Engineering *N*-salicylidene aniline derivatives: from solid-state molecular switches to multifunctional organic-inorganic architectures

Thèse présentée en vue de l'obtention du grade
de docteur en sciences par

François Robert

Université Catholique de Louvain
Institut de la Matière Condensée et des Nanosciences,
Pôle MOlécules, Solides et RéacTivité.

Il faut savoir ce que l'on veut.
Quand on le sait, il faut avoir le courage de le dire.
Quand on le dit, il faut avoir le courage de le faire.

Georges Clémenceau
Président du Conseil de France (1906-1909)

Arrivant au terme de ces quatre années de thèse, il est bon de regarder en arrière afin de se rendre compte du travail réalisé. Celui-ci a été particulièrement enrichissant tant au niveau scientifique qu'au niveau humain. Cependant, une telle tâche ne peut se construire que sur les bases de nombreuses heures de travail qui se sont révélées être tantôt palpitantes, attrayantes et prometteuses, tantôt pesantes, exténuantes et désespérantes. C'est donc avec beaucoup d'émotions que je tiens à remercier les personnes sur lesquelles j'ai pu compter durant les bons et les moins bons moments de cette période qui s'achève en même temps que les dernières lignes de ce manuscrit.

Je commencerai par remercier mon promoteur de thèse, le Prof. Yann Garcia, pour m'avoir permis de rejoindre son équipe de recherche internationale ainsi que m'avoir donné la possibilité de présenter mes travaux tant sous la forme écrite, à l'aide des nombreuses publications réalisées, que sous la forme de communications orales lors de conférences (GFSM, GDR, etc). Ce travail n'aurait, bien sûr, pas pu être réalisé sans la collaboration d'autres personnes qui m'ont permis de me former et d'évoluer vers les techniques qu'a nécessité ce projet. Tout d'abord, je désire exprimer toute ma gratitude au Dr. Anil D. Naik pour l'aide précieuse qu'il m'a fournie durant les synthèses organiques et inorganiques ainsi qu'au Prof. Bernard Tinant pour le nombre d'heures incalculable que nous avons passé ensemble pour tenter d'enfin pécher les « moches cristaux verts qui sentent mauvais » (sic). Un tout grand merci pour leur patience, leur travail mais aussi leur bonne humeur qui m'a accompagné durant ces quatre années. Merci aussi au Prof. Raphaël Robiette qui a su m'accueillir dans le monde de

la chimie quantique à un moment où les données contradictoires bouchaient notre horizon. Grâce à sa patience et toutes nos conviviales discussions, nous aurons pu éviter l'adage qui dit : « c'est pendant qu'on calcule, qu'on analyse les pour et les contres, que la vie passe, et qu'il ne se passe rien »[*]. Merci également aux Professeurs Jean-Louis Habib Jiwan et Jean-Philippe Soumillion ainsi qu'à Benoît Muls sans qui la fluorescence serait restée pour moi un vague phénomène physique amusant, observé durant mes travaux pratiques de master. Merci aussi aux personnes extérieures à l'UCL avec qui j'ai eu l'occasion de travailler: Prof. J.-C. Bünzli et F. Gummy (EPFL, Lausanne) pour les mesures de rendement quantique de fluorescence, Prof. K. Boukheddaden (Université de Versailles) pour les mesures optiques réalisées dans son laboratoire, Prof. J. Wouters et B. Norberg (FUNDP, Namur) pour la diffraction des rayons X de Ksaltrz et enfin Dr. R. Clérac (CNRS Bordeaux) pour les mesures magnétiques des complexes de cuivre. Merci également à tous les autres professeurs que j'ai côtoyés durant ces dernières années, Prof. M. Devillers, S. Hermans, J-F. Gohy, B. Mahieu, J.-P. Declercq, D. Peteers, J. Ladrière, I. Marko, O. Riant, J. Marchand, pour leurs cours ainsi que leur patience lors de mes séances de questions. Merci enfin aux membres de mon jury de thèse d'avoir accepté de consacrer un peu de leur précieux temps à la lecture de ce manuscrit.

Comparer le Lavoisier à un bâtiment où des personnes se croisent pour converser du travail serait réducteur. Malgré les nombreuses occupations scientifiques des chimistes 'lavoisiens', une ambiance particulière émane de ce lieu devenu, pour la plupart d'entre nous, presque mythique… Certains seraient même parvenus à comparer ce petit groupe de personnes à un grand

[*] Levy M., *Et si c'était vrai*, Robert Laffont, **2000**.

village gaulois où se croisent moultes occupations allant de la découverte de nouveaux nano-assemblages à la préparation de toxines sous-marines. Une situation « à la belge » donc, où chacun se forgera sa propre opinion sur la fraîcheur des produits vendus par le poissonnier.[†] Après m'être baigné dans cette « horde », je tiens tout particulièrement à remercier les personnes qui ont été impliquées de près ou de loin à ce travail. Merci dès lors aux étudiants que j'ai encadrés et qui ont réussi à supporter mes longs soupirs lorsqu'ils avaient raté leurs manipulations. Merci à Florence, Pierre-Loïc, Alice, Michèle, Pierre, Jérémie et Maxime. Merci surtout à ChocoNico© et Kevin pour leur amitié et toutes les heures passées, ensemble, autour d'une table de restaurant ou devant un buffet garni de mille et une sauces thaïlandaises. Merci aussi à Jacqueline, Jean-François, ChanChan, (les) Cécile(s), Axel, Hubert, Alain, Jacques N., Alexandre S., Raoul et Brigitte ainsi qu'aux autres membres de l'ex-unité CMAT pour leurs aides quotidiennes.

Merci enfin à ma femme Caroline pour son amour et sa patience face à aux obstacles qui ont jalonnés la réalisation de ce travail et qu'elle m'a aidé à surmonter. Merci aussi à mes parents ainsi qu'à toute ma famille, belle-famille et amis pour leur soutien.

[†] Goscinny R., A. Uderzo, *Astérix et Obélix*, Hachette, **1961**-.

Jury Members:

Prof. Y. Garcia	Supervisor Université Catholique de Louvain
Prof. E. Gaigneaux	Chair Université Catholique de Louvain
Prof. J.-L. Habib Jiwan	Secretary Université Catholique de Louvain
Prof. M. Devillers	Université Catholique de Louvain
Prof. D. Bonifazi	Facultés Universitaires Notre-Dame de la Paix Namur, Belgium
Dr. R. Lapouyade	CNRS Bordeaux, France
Prof. F. Tuczek	Christian Albrechts Universität zu Kiel Kiel, Germany

Table of contents

Introduction _____ *1*

Foreword: Technology of information storage and displays **1**

Introduction to photochromism **2**

Organic molecules 3

Inorganic compounds 6

Introduction to thermochromism **7**

Few words about other types of chromic phenomena **9**

N-salicylidene aniline and derivatives **9**

Versatile thermo- and photochromic molecules 9

The chemical pathways point of view 11

Impact of the crystal structure and of the molecular environment 12

The spin crossover phenomenon **15**

Generalities and influence of molecular composition and supramolecular interactions 15

Ligand-Driven Light-Induced Spin Change phenomenon (LD-LISC) 17

Aim and strategy _____ *19*

N-salicylidene aniline derivatives based organic materials **21**

Organic-inorganic materials built with N-salicylidene aniline derivatives **23**

Part I: Organic Materials _____ *25*

Chapter I: The intriguing case of N-salicylidene aminopyridines ____ *25*

Introducing remarks **25**

Syntheses and crystallization methods **26**

Crystal structures study N-salicylidene 2-aminopyridine (L^2) **28**

N-salicylidene 3-aminopyridine (L^3) 29

N-salicylidene 4-aminopyridine (L^4) 30

5-chloro-*N*-salicylidene 3-aminopyridine (L^5) 32

Optical properties **34**

Computational study of the photo-isomerisation 39

Isolated molecules 39

Influence of the crystal packing 43

Discussion 45

Chapter II: A crystal engineering approach: the case of N-salicylidene N-heterocycle derivatives _____49

Introducing remarks 49

The supramolecular chemistry concept 49

A crystal engineering approach 51

Syntheses and crystallization methods 52

Crystal structures study 54

Crystal structures study 54

N-salicylidene 4-amino-1,2,4-triazole (Hsaltrz) 54

N-salicylidene 4-amino-3,5-bis(pyridin-2-yl)-1,2,4-triazole (Habs) 57

N-salicylidene 5-amino-1,10-phenanthroline (Hsalphen) 59

N-salicylidene 5-amino-tetrazole (Hsaltz) 61

Potassium salt of *N*-salicylidene 5-amino-tetrazolate (Ksaltrz) 62

Wavelength and time dependent Kubelka-Munk spectra of Hsaltrz, Habs, Hsalphen, Hsaltz, Ksaltz related to macroscopic considerations .64

Computational study of the photo-isomerisation 71

Isolated molecules 71

Influence of the crystal packing 76

Effect of the chemical substitution on Hsaltrz 77

Discussion 80

Chapter III: Effect of a non aromatic linker on the structural and optical properties of N-salicylidene aminopyridines _____87

Introducing remarks 87

Syntheses and crystallization methods 88

Crystal structures study **89**

N-salicylidene 2-amino-methylpyridine (CH_2L^2) 89

5-chloro-N-salicylidene 2-amino-3-aminomethyl-pyridine (CH_2L^5) **90**

Comparison with the reported crystal structure of *N*-salicylidene 3-aminomethylpyridine (CH_2L^3) 92

Wavelength and time dependent diffuse reflectance spectroscopy **93**

Temperature dependent fluorimetry **97**

Discussion **105**

Chapter IV: Anionic N-salicylidene anils: Synthesis and optical studies. ***111***

Introducing remarks **111**

Syntheses and crystallization methods **112**

Optical study of salts of the N-salicylidene anil anions **115**

N-salicylidene *p*-aminobenzenesulfonates (Na1, K1 and Ca1, Na1Cl and Na1Br) 115

N-salicylidene *m*-aminobenzene sulfonate (Na2) 122

Discussion **126**

Part II: Coordination compounds ***129***

Chapter V: Tuning optical properties of N-salicylidene aniline derivatives: study of complexes with ligands derived from aminopyridines ***129***

Introducing remarks **129**

Syntheses and crystallization methods **131**

Crystal structures study **132**

Crystal structure of $[Co^{II}(L^3)_2(NCS)_2(CH_3OH)_2]$ (C^1) 132

Crystal structure of $[Co^{II}(L^3)_2(NCSe)_2(CH_3OH)_2]$ (C^2), $[Mn^{II}(L^3)_2(NCS)_2(CH_3OH)_2]$ (C^3), $[Ni^{II}(L^3)_2(NCS)_2(CH_3OH)_2]$ (C^4) and $[Cu^{II}(L^3)_2(NCS)_2(CH_3OH)_2]$ (C^5) 134

Optical properties **137**

Diffuse reflectance study 137

Fluorimetry 139

Computational details about the impact of the metal ions coordination.140

Discussion 144

Chapter VI: N-salicylidene 4-amino-1,2,4-triazole as precursor for spin crossover complexes _____147

Introducing remarks.....147

Syntheses and crystallization methods 149

Crystal structures study.....150

$[Fe_2(Hsaltrz)_5(NCS)_4]\cdot 4\ CH_3OH$ (C^7)..... 150

$[Fe_2(Hsaltrz)_5(NCS)_4]\cdot 3H_2O\cdot CH_3OH$ (C^8) 153

$[Fe_2(Hsaltrz)_5(NCS)_4]\cdot 4H_2O$ (C^9) 156

$[Co_2(Hsaltrz)_5(NCS)_4]\cdot 4H_2O\cdot CH_3OH$ (C^{10})..... 159

SQUID magnetometry and ^{57}Fe Mössbauer spectroscopy of C^7 162

Differential scanning calorimetry 171

Optical properties 172

Discussion 182

Chapter VII: Inorganic complexes with N-salicylidene 4-amino-3,5-bis(pyridin-2-yl)-1,2,4-triazole (Habs)_____190

Introducing remarks.....191

Syntheses and crystallization methods 192

Discussion about the materials formulation 193

Study of the spin crossover phenomenon.....197

Optical properties 198

Discussion 212

Chapter VIII: N-salicylidene aniline derivatives as precursors for new magnetic supramolecular architectures_____215

Introducing remarks.....215

Syntheses and crystallization methods 217

Crystal structures study **218**

$[Cu^{II}_4(L\text{-}^2)_4(NO_3)_3(CH_3OH)][Cu^{II}(L\text{-}^2)(NO_3)_2]$(2-aminopyridinium)$(NO_3)$•5 CH_3OH (C^{17}). 218

$[Cu^{II}_4(L\text{-}2)_4(NO_3)_2(OH)_2]$(2-aminopyridinium) (OH)•CH_3OH (C^{18}) 222

$[Ni^{II}_2(CH_2L^3)_4(NCS)_2(CH_3OH)_2]$ • 2 CH_3OH (C^{19}) 224

SQUID magnetometry **225**

Discussion **228**

Part III: Hybrid Materials ***231***

Chapter IX: Anionic N-salicylidene aniline derivatives as thermo-sensibilisator precursors into inorganic frameworks ***231***

Introducing remarks **231**

Syntheses and crystallization methods **233**

Crystal structures study of hybrid materials built with 1,10-phenanthroline complexes **235**

Hybrid materials with anion 1 235

Hybrid materials with anion 2 237

Optical properties **239**

^{57}Fe Mössbauer spectroscopy **247**

Discussion **252**

General discussion ***257***

Conclusions and perspectives ***269***

Notes and references ***273***

List of publications, communications and awards ***295***

Written communications **295**

Papers in international journals 295

Poster communications 300

Oral communications 302

Awards 303

Appendix _____ *i*

Crystal structures data ..... **i**

Additional material ..... **xlviii**

Materials ..... **xlix**

Experimental section ..... **lvii**

Organic molecules lvii

Inorganic molecules lxxx

Hybrid materials xc

Abstract

In a world involving an increasing amount of new technologies, the search for new molecular switches for the optimisation of information storage and display setups becomes very challenging. In this work, we have been interested to derivatives of the *N*-salicylidene aniline, known for its solid-state thermo- and photochromism. *N*-salicylidene aminopyridines ($L^{2\text{-}4}$) and *N*-salicylidene aminomethylpyridines ($CH_2L^{2\text{-}6}$) have revealed a more complicated structure-properties relationship than the one previously reported because of the combination of structural factors (associated to the molecular packing) and electronic factors, induced by the molecular architecture itself (presence of substituents, etc). A study of the influence of the molecular flexibility has led to consider new conditions needed to observe thermo- and photochromism (with short or long lifetimes). This study was performed with fluorimetry (observation of new radiative deexcitations) and supported by a computational approach in order to simulate the thermo- and photo-induced phenomenon appearing in the solid state materials.

A second step of rationalisation and control of involved parameters was then investigated by using a supramolecular engineering approach based on 1,10-phenanthroline (Hsalphen), 1,2,4-triazole (Hsaltrz, Habs and their derivatives) and tetrazole (Hsaltz and Ksaltz) moieties. These molecules allowed us to study the role of each type of supramolecular interactions in the crystal structure. It also gave access to a novel phenomenon such as a 'spring type effect' involving a photo-switchable material (Habs) which resists to the light irradiation constraint.

These organic molecules were also studied after incorporation as ligands in inorganic complexes. The impact of the coordination as well as the nature of complexes components on the optical behaviours (tuning of the intensity of the thermo- and the photochromism as well as of the fluorescence of materials) was demonstrated experimentally and supported by a theoretical approach on $[M^{II}(L^3)_2(CH_3OH)_2(NCS)_2]$ and $[Zn^{II}(Habs)_2F_2]$. Moreover, the use of spin transition ions paves interesting way to the observation of thermo- and/or photo-induced

magnetic phenomenon. We were also able, for the first time, to follow a thermo-induced spin crossover by temperature dependent fluorimetry via the use of a ligand acting as a local probe in $[Fe^{II}_2(Hsaltrz)_5(NCS)_4]$ dinuclear compound. *N*-salicylidene aniline derivatives were also presented as excellent precursors for complex self-assemblies formation as demonstrated by the synthesis of magnetic and asymmetric nanogrids such as $[Cu^{II}_4(L^2)_4(NO_3)_3(CH_3OH)]$.

Finally, *N*-salicylidene aminobenzenesulfonates (A^{1-2}) were inserted as non coordinated anionic units in organic-inorganic hybrid materials: $[M^{II}(phen)_3](A^2)_2$ and $[Fe^{II}_3(hyetrz)_6(H_2O)_6](A^1)_4Cl_2$. These molecules have shown a strong sensitivity to the molecular environment as well as a preservation of their chromic behaviours after insertion. This study paves the way to the synthesis of multifunctional molecular materials with magnetic properties tuned by the thermo- and/or the photo-sensitivity of the inserted anions.

Résumé

Dans un monde imprégné de nouvelles technologies, la recherche de nouveaux matériaux moléculaires bistables pour l'amélioration des dispositifs de stockage et affichage de l'information devient une nécessité. Lors de ce travail, nous avons étudié de façon approfondie et pluridisciplinaire de nouveaux dérivés de la *N*-salicylidene aniline, connue pour ses propriétés de thermo- et de photochromisme à l'état solide.

Les dérivés de type aminopyridine ($L^{2\text{-}5}$) et aminométhylpyridine ($CH_2L^{2\text{-}6}$) ont ainsi démontré la présence d'une relation structure/propriété plus complexe que précédemment proposé vu l'implication de facteurs structuraux, liés à l'empilement moléculaire, ainsi qu'électroniques induits par l'architecture moléculaire elle-même (présence de substituants, etc). Une étude de l'influence de la flexibilité moléculaire a également été réalisée, ce qui a conduit à s'interroger sur les pré-requis liés à l'observation des phénomènes de thermo- et de photochromisme (à court et long temps de vie). Cette étude a été soutenue par des mesures fluorimétriques (observation de nouvelles désexcitations radiatives) et via une approche théorique visant à modéliser les phénomènes thermo- et photo-induits au sein des matériaux en phase solide.

Une seconde étape de rationalisation et de contrôle des différents paramètres impliqués a ensuite été envisagée via une approche d'ingénierie supramoléculaire développée à partir de motifs azotés de type 1,10-phénanthroline (Hsalphen), 1,2,4-triazole (Habs, Hsaltrz et ses dérivés) et tétrazole (Hsaltz et Ksaltz). Ces composés nous ont donné la possibilité d'étudier le rôle des différentes interactions supramoléculaires présentes au sein des structures cristallographiques, permettant ainsi de mettre à jour des phénomènes inédits tel qu'un effet ressort impliquant un matériau photo-commutable (Habs) qui résiste aux contraintes lumineuses appliquées.

Ces molécules organiques ont également été étudiées après leur incorporation en tant que ligands au sein de complexes inorganiques. L'impact de la coordination

ainsi que de la nature des différents constituants moléculaires sur les propriétés optiques (ajustement de l'intensité du thermo- et du photochromisme ainsi que de la fluorescence des matériaux) a été démontrée expérimentalement et confortée par calculs théoriques sur des composés tels que $[M^{II}(L^3)_2(CH_3OH)_2(NCS)_2]$ et $[Zn^{II}(Habs)_2F_2]$. Dans ce cadre, l'utilisation d'ions à transition de spin ouvre la voie vers l'observation de phénomènes magnétiques thermo- et/ou photo-induits. Ainsi, nous avons suivi, pour la première fois, une transition de spin thermo-induite par fluorescence via l'utilisation d'un ligand (Hsaltrz) opérant comme sonde luminescente locale au sein de nouveaux binucléaires de type $[Fe^{II}_2(Hsaltrz)_5(NCS)_4]$. De plus, les dérivés de la *N*-salicylidène aniline se sont montrés être d'excellents précurseurs pour la formation d'auto-assemblages complexes vu l'obtention de nano-grilles asymétriques, de formulation $[Cu^{II}_4(L^2)_4(NO_3)_3(CH_3OH)]$, dont le magnétisme a pu être étudié.

Enfin, des *N*-salicylidene aminobenzènesulfonates (A^{1-2}) on été insérées en tant qu'entités anioniques non coordinées au sein de matériaux hybrides organiques-inorganiques de type $[M^{II}(phen)_3](A^2)_2$ et $[Fe^{II}_3(hyetrz)_6(H_2O)_6](A^1)_4Cl_2$. Ces molécules ont montrés une forte sensibilité à leur environnement chimique ainsi que la conservation de leurs propriétés optiques après incorporation. Cette étude ouvre la voie vers la synthèse de matériaux multifonctionnels aux propriétés magnétiques régies par la thermo- et/ou photosensibilité de l'anion.

List of abbreviations, symbols and molecules

Abbreviations and symbols

τ_A: Addison structural index
AD-LISC: Anion-Driven Light-Induced Spin Change
AD-TISC: Anion-Driven Temperature-Induced Spin Change
AF: Antiferromagnetism
COSY: Correlation Spectroscopy (2D NMR)
Φ: Dihedral angle (°)
DSC: Differential Scanning Calorimetry
DTA: Differential Thermal Analysis
Dist.: Distance (Å)
Σ: Distortion parameter for octahedral coordination sphere
ΔH: Enthalpy difference ($kJ.mol^{-1}$)
ΔS: Entropy difference ($J.mol^{-1}.K^{-1}$)
cis*: Excited state of the *cis*-keto form
trans*: Excited state of the *trans*-keto form
EXAFS: Extended X-ray Absorption Fine Structure
S^1: First singlet excited state
T^1: First singlet excited triplet
Φ_f: Fluorescence quantum yield
FTIR: Fourier Transformed Infrared Spectroscopy
GS: Ground State
Γ/2: Half width at half maximum ($mm.s^{-1}$)
HS: High-spin
δ: Isomer shift (Mössbauer, $mm.s^{-1}$) and chemical shift (NMR, ppm)
k: Kinetic constant
F(R): Kubelka-Munk (KM) Function, defined as $F(R)= (1-R^2)/2R$ where R = absolute reflectance
τ: Lifetime of excited state
LD-LISC: Ligand-Driven Light-Induced Spin Change
LIESST: Light-Induced Excited Spin State Trapping
LITH: Light-Induced Thermal Hysteresis
LS: Low-spin
J: Magnetic coupling constant (cm^{-1})
MS: Mass spectrometry
MLCT: Metal-to-Ligand Charge Transfer
γ_{HS}: Molar fraction of HS iron(II) ions

χ: Molar magnetic susceptibility
M: Molecular ion
NLO: Non linear optics
NMR: Nuclear magnetic resonance
ORTEP: Oak Ridge thermal ellipsoid plot
pyr: Pyridine
ΔE_Q: Quadrupole splitting ($mm.s^{-1}$)
Ref.: Reference
Rel. E_{stat}: Relative stabilisation energy
salicyl: Salicylic ring
SOF: Site Occupation Factor (%)
C_p: Specific Heat at constant pressure
SCO: Spin crossover
SQUID: Superconducting Quantum Interference Device
ΔT^{80}: Temperature range where 80 % of sites undergo a SCO[1] (from γ_{HS} = 10 % to 90%)
$T_{1/2}$: Temperature where half of SCO ions have changed their spin state
TGA: Thermogravimetric analysis
Γ: Torsion angle (°)
TS: Transition state
UV: Ultraviolet
vib.: Vibrational
XRD: X-ray diffraction
XPS: X-ray Photoelectron Spectroscopy
ZF-μSR: Zero Field Muon Spin Relaxation
ZFS: Zero Field Splitting

Organic molecules

L^2: *N*-salicylidene 2-aminopyridine
L^3: *N*-salicylidene 3-aminopyridine
L^4: *N*-salicylidene 4-aminopyridine
L^5: 5-chloro-*N*-salicylidene 3-aminopyridine
Hsaltrz: *N*-salicylidene 4-amino-1,2,4-triazole
Habs: *N*-salicylidene 4-amino-3,5-bis(pyridin-2-yl)-1,2,4-triazole
Hsalphen: *N*-salicylidene 5-amino-1,10-phenanthroline
Hsaltz: *N*-salicylidene 5-amino-tetrazole
Ksaltz: potassium salt of *N*-salicylidene 5-amino-tetrazolate
Clsaltrz: 5-chloro-*N*-salicylidene 4-amino-1,2,4-triazole
Brsaltrz: 5-bromo-*N*-salicylidene 4-amino-1,2,4-triazole
3OHsaltrz: 3-hydroxy-*N*-salicylidene 4-amino-1,2,4-triazole
4OHsaltrz: 4-hydroxy-*N*-salicylidene 4-amino-1,2,4-triazole
34OHsaltrz: 3,4-dihydroxy-*N*-salicylidene 4-amino-1,2,4-triazole
omesaltrz: 3-methoxy-*N*-salicylidene 4-amino-1,2,4-triazole
naphsaltrz: 1-naphtalene-*N*-salicylidene 4-amino-1,2,4-triazole
CH_2L^2: *N*-salicylidene 2-aminomethylpyridine
CH_2L^3: *N*-salicylidene 3-aminomethylpyridine
CH_2L^4: *N*-salicylidene 4-aminomethylpyridine
CH_2L^5: 5-chloro-*N*-salicylidene 3-aminomethylpyridine
CH_2L^6: 5-chloro-*N*-salicylidene 4-aminomethylpyridine
Na1 : sodium salt of *N*-salicylidene *p*-aminobenzenesulfonate
Na2 : sodium salt of *N*-salicylidene *m*-aminobenzenesulfonate
K1 : potassium salt of *N*-salicylidene *p*-aminobenzenesulfonate
Ca1 : calcium salt of *N*-salicylidene *p*-aminobenzenesulfonate
Na1Cl : sodium salt of 5-chloro-*N*-salicylidene *p*-aminobenzenesulfonate
Na1Br : sodium salt of 5-bromo-*N*-salicylidene *p*-aminobenzenesulfonate
hyetrz: 4-(2'-hydroxy-ethyl)-1,2,4-triazole
phen: 1,10-phenanthroline
abpt: 4-amino-3,5-bis(pyridin-2-yl)-1,2,4-triazole

Inorganic complexes and hybrid materials

C[1]: $[Co^{II}(\mathbf{L^3})_2(NCS)_2(CH_3OH)_2]$

C[2]: $[Co^{II}(\mathbf{L^3})_2(NCSe)_2(CH_3OH)_2]$

C[3]: $[Mn^{II}(\mathbf{L^3})_2(NCS)_2(CH_3OH)_2]$

C[4]: $[Ni^{II}(\mathbf{L^3})_2(NCS)_2(CH_3OH)_2]$

C[5]: $[Cu^{II}(\mathbf{L^3})_2(NCS)_2(CH_3OH)_2]$

C[6]: $[Fe^{II}(\mathbf{L^3})_2(NCS)_2(CH_3OH)_2]$

C[7]: $[Fe^{II}_2(\mathbf{Hsaltrz})_5(NCS)_4]\bullet 4CH_3OH$

C[8]: $[Fe^{II}_2(\mathbf{Hsaltrz})_5(NCS)_4]\bullet 3H_2O\bullet CH_3OH$

C[9]: $[Fe^{II}_2(\mathbf{Hsaltrz})_5(NCS)_4]\bullet 4H_2O$

C[10]: $[Co^{II}_2(\mathbf{Hsaltrz})_5(NCS)_4]\bullet 4H_2O$

C[11]: $[Fe^{II}(\mathbf{Habs})_2(NCS)_2]\cdot 4H_2O$

C[12]: $[Fe^{II}(\mathbf{Habs})_2Cl_2]\cdot 1.5H_2O$

C[13]: $[Zn^{II}(\mathbf{Habs})_2F_2]$

C[14]: $[Zn^{II}(\mathbf{Habs})_2Cl_2]\cdot 12\ H_2O$

C[15]: $[Zn^{II}(\mathbf{Habs})_2Br_2]\cdot 12\ H_2O$

C[16]: $[Zn^{II}(\mathbf{Habs})_2I_2]\cdot 2\ H_2O$

C[17]: $[Cu^{II}_4(\mathbf{L\text{-}^2})_4(NO_3)_3(CH_3OH)][Cu^{II}(\mathbf{L\text{-}^2})(NO_3)_2]$(2-aminopyridinium)$(NO_3)\bullet 5\ CH_3OH$

C[18]: $[Cu^{II}_4(\mathbf{L\text{-}^2})_4(NO_3)_2(OH)_2]$(2-aminopyridinium)$(OH)\bullet CH_3OH$

C[19]: $[Ni^{II}_2(\mathbf{CH_2L^3})_4(NCS)_2(CH_3OH)_2]\bullet 2CH_3OH$

H[1]: $[Cu^{II}(phen)_3](\mathbf{1})Cl\bullet 5H_2O\bullet 2CH_3CH_2OH$

H[2]: $[Ni^{II}(phen)_3](\mathbf{1})Cl\bullet 7H_2O\bullet CH_3OH$

H[3]: $[Cu^{II}(phen)_3](\mathbf{2})_2$

H[4]: $[Ni^{II}(phen)_3](\mathbf{2})_2$

H[5]: $[Fe^{II}_3(hyetrz)_6(H_2O)_6](\mathbf{1})_4Cl_2$

H[6]: $[Fe^{II}_3(hyetrz)_6(H_2O)_6](\mathbf{1Br})_4Cl_2$

Introduction

Foreword: Technology of information storage and displays

The treatment, storage and display of information probably belong to one of the most important achievements of the last century. Indeed, electronic systems which perform numeric tasks are now present everywhere and can be considered as integral parts of modern life. Improving these setups is one of the main challenges nowadays. Indeed, during past decades, novel information supports have been discovered, involving different technologies, such as *Compact Disk* (CD), *Digital Versatile Disc* (DVD) or *Blu-ray Disc* as optical supports, *Hard Disk* (HDD) and *Floppy Disk* as magnetic supports or *Flash Memory Data Storage Devices* (e.g. *USB keys*). In the same time, new devices were built in order to treat more and more information at the same time (characterized by a frequency which corresponds to the operations number per second). Microprocessors have known a very large evolution from a frequency of few MHz to GHz. Finally, information display setups radically change too from *Cathode Ray Tube Screen* to *Liquid Crystal Display* (LCD), *Plasma Display Panel* or *Light-emitting Diode Screen* (LED).

In the context of information storage and display, it is of the highest importance to increase the information density per volume or surface unity. The lower limit to reach is then the molecular level which promises the maximum of data density. Designed materials for this purpose must present special features. Since actual data treatment setups use a binary system, based on two possible states (0 or 1), they must present two different states too, assigned to 0 and 1, respectively. The switch between them must be

reversible and specific to an external stimulus. Moreover, a very good thermal stability, a low fatigability, a rapid response, a non-destructive readout capability of each form and a low energy demand are also needed.[2]

Molecular switches could be considered as highly promising compounds in data storage and display research. They are characterized by a range of external stimulus (e.g. temperature, pressure, pH, light, etc) and of the system response (e.g. light emission, colour, electric or magnetic properties changes, etc). In the next sections, we will describe a few compounds which fall in to these categories.

Introduction to photochromism

Photochromism is defined as a light-induced reversible colour change of a material composed by one species which present two different forms absorbing at different wavelengths.[3-6] This appealing switching phenomenon can be associated with a reversible modification of the geometrical structure, redox potential, dielectric constant, magnetic susceptibility and refractive index.[7] Photo-induced processes can involve interesting phenomena such as redox reaction,[8] electron–hole pair generation,[9] spin crossover,[10] coordination change,[11] photo-cyclisation,[7, 12] photo-isomerisation,[13] tautomerisation[14] and bond cleavage.[14] Solid-state photochromism, which is rarely encountered, enables prospective potential applications in information storage,[15, 16]molecular machines,[17] optical switches, displays, sensors[18] and in nonlinear optics.[19-22] However, only a few photochromic systems operating in the solid state fulfil criteria for data storage applications as previously described.[2] Next sections are devoted to the description of some compounds which present such photo-

sensitivity. Nevertheless, the aim of these sections is not to be an exhaustive survey of known photochromic molecules but a critical overview of selected photo-switchable materials.

Organic molecules

A large panel of photochromic organic molecules in solution has been reported. As said above, it could be explained by the large variety of chemical origins of photochromism. Two of them appear to be more represented: the photo-isomerisation and the photo-cyclisation. In this section, we give a brief description of the most reported molecular systems.

Stilbene molecule undergoes an isomerisation from *cis* to *trans* isomers (a and b) by light activation in solution (Scheme 1).[7, 15] However, this molecule is not very studied for data recording because of the presence of a side reaction lead by the oxidation of the *trans* isomer into phenanthrene (c) as shown in Scheme 1.[7]

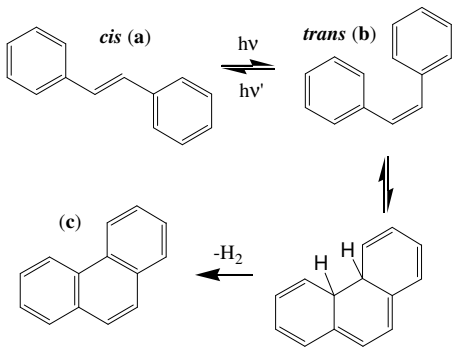

Scheme 1 Photo-isomerisation of stilbene involving the *cis* and *trans* isomers (a and b) and the oxidation side reaction leading to the phenanthrene formation (c).[23]

Azobenzenes are similar molecules to stilbene but the replacement of the C=C bond by a N=N double bond (Scheme 2) leads to the suppression of side reaction and the appearance of a strong photochromism. Indeed, the non-substituted azobenzene irradiated at 313 nm gives approximately 80% of the *cis* isomer.[15] The reverse reaction can also be observed when the material is irradiated with visible light (Scheme 2).[23] For these reasons, azobenzene derivatives, such as styrylpyridines, were studied in polymers,[24] liquid crystals[25], macrocyclic[26, 27] chemistry. Nevertheless, another promising photochromic system for data recording involving a photo-isomerisation process is the *N*-salicylidene aniline, because of the good efficiency of the photo-induced process in the solid state. More details about this class of molecules will be given in next sections.

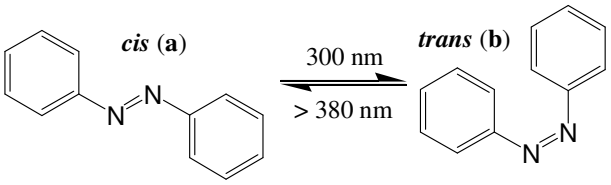

Scheme 2 Photo-isomerisation of non substituted azobenzene involving the *cis* and *trans* isomers (a and b).[23]

Photochromic molecules involving photo-cyclisation are very numerous and often usable in the solid state.[23] For example, spiropyrans and spirooxazines can be observed in their closed and open (called merocyanine) forms which show a yellow and blue colour, respectively.[15] They are accessible by light irradiation (Scheme 3) and give strong photochromic properties to the system.[28-35] Moreover, although some spiropyrans or spirooxazines based materials present a significant fatigability,[23] they were actively studied for data recording applications as demonstrated by several patents.[36, 37]

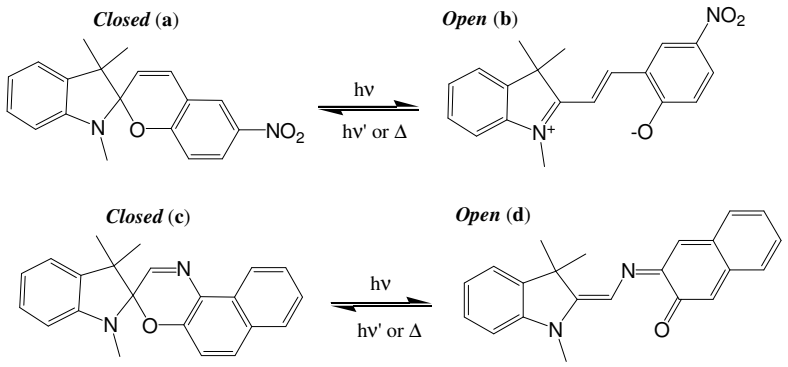

Scheme 3 Photochromism of a spirobenzopyrane (a and b) and of a spironaphtooxazine (c and d) involving a photo-cyclisation between an open and a closed forms.

Finally, diarylethene derivatives are certainly the most promising molecules for data recording application.[7] Their photochromism, involving the open and the closed forms represented in Scheme 4, has been widely studied in the past decade.[7] However, although diarylethenes present very attracting switchable properties such as a very good cyclisation and ring opening efficiency in solution and in the solid state[7] (associated to the very low geometrical changes during the photoreaction),[38, 39] a good thermal stability and fatigability,[7] they bring very complicated synthetic difficulties because of the numerous conformations they can take.[7, 40] Indeed, thiophene rings (or other similar moieties) can be arranged following parallel (where strong π-π stacking interactions are created) or anti-parallel conformations.[7] However, only the second one is photochromic. Moreover, many conformations of open and closed forms in the ground and excited states were observed.[7, 40, 41] They can be stabilised or destabilised following the presence of substituent,[7] the nature and the chirality of them (electronic conjugation, inductive and mesomeric effect, etc),[7, 38] the presence of a specific molecular environment (nature and polarity of solvent, crystal

structure, dilution in polymer, enantiomeric medium, etc).[7, 38, 42-45] These parameters have not only a large impact on the photochromism efficiency but also on the photo-induced chemical pathway[40, 41] and the colour of compounds in their different forms (which can extend over all the visible spectrum).[38, 43]

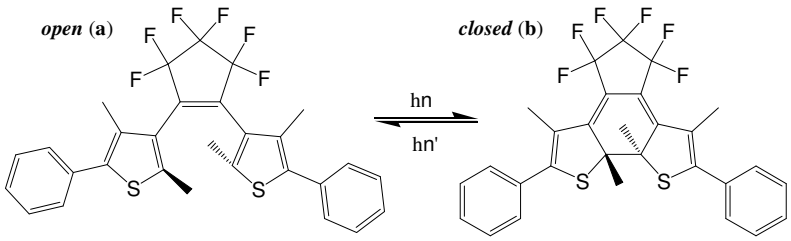

Scheme 4 Photochromism of a diarylperfluocyclopentene involving a reversible switch between the open and closed forms (a and b, respectively).

Inorganic compounds

Although photochromic materials are mostly organic molecules, inorganic materials displaying photochromic behaviour present some advantages such as a better thermal stability, chemical resistance and macroscopic shape modelling.[3, 8, 46-48] Two types of photochromic inorganic compounds can be distinguished: materials where the photo-sensitivity is conducted by the metal ions and complexes where the photochromism is brought by an organic molecule localized near the metal (as a ligand, anion or guest molecule). The first class is composed of different types of materials such as oxides, mercury compounds, alkaline earth titanates and sulphides, zinc sulphide, copper complexes, etc.[49] Photo-induced mechanisms are various and can involve electron-hole pairs generation (in semiconductor transition-metal oxides such as WO_3 which turn from transparent to blue under light irradiation with an energy of approximately 3 eV),[9, 46, 50, 51] metal ion photo-

reduction (e.g. in CuCl where the reaction '$2Cu^{+} + h\nu \rightarrow Cu^{2+} + Cu^{*}$' lead to a blackening of the material),[49, 52, 53] other redox reactions (e.g. $ZnS + 2ZnO \rightarrow 3Zn + SO_2$),[53] etc. Incorporation of organic photo-switchable dyes into inorganic matrices at the nanometre scale, giving rise to hybrid materials, allows to combine advantages brought by both organic (large variety of colours, photochromic behaviours and chemical natures) and inorganic components (thermal and (photo-)chemical stability, controlled molecular structures and crystal phases, etc).[34, 54] It opens versatile synthesis ways in order to fabricate tailor-made materials in terms of their chemical and physical properties.[55] Such approach was mainly developed for zeolite matrices, known for their good inclusion capacity, where *N*-salicylidene aniline derivatives,[56]stilbenes[57, 58] and spiropyrans[59] were successfully encapsulated. Interestingly, thanks to these results, it was demonstrated that optical behaviours of some organic chromophores were strongly influenced by their molecular environments and then directed by the nature of inorganic matrices giving rise to a new way to tune optical properties of this class of materials.[56] However, organic photochromic molecules were also incorporated in other inorganic frameworks like sol-gel glasses with various compositions such as silica[54, 55] or more complex assemblies such as Pb_7I_{18}.[60] Nevertheless, the main part of these data was obtained by different synthetic strategies such as the 'ship-in-a-bottle' synthesis which imply a statistical number of incorporated chromophores.[56, 59] This point of view will be discussed in more details in chapters 4 and 9.

Introduction to thermochromism

Thermochromism is defined as a change of colour of a substance, or a mixture of substances, when heated to a certain temperature.[61] This

phenomenon is usually considered as reversible but irreversible thermochromism was also reported.[61, 62] To briefly develop an overview of known thermochromic compounds appears to be very challenging because of the very large variety of physical or chemical mechanisms involved. Some tendencies could however be observed. Indeed, thermochromism in inorganic compounds is usually based on a change of electron distribution into valence and conduction bands (e.g. for pure metals such as copper, gold, silver or for metal oxides such as chromium oxide)[63] or into molecular orbitals (e.g. in the metal ion spin crossover phenomenon which will be introduced in details in a next section)[64]. Other possibility is a change of coordination sphere geometry. In addition to the large influence of the solvent nature, it is also interesting to note that supramolecular interactions, in solution as well in the solid state, can also change with temperature leading to other thermochromism phenomena as demonstrated for $[Cu(daco)_2](NO_3)_2$ (daco = 1,5-diazacyclooctane) where the hydrogen bond breaking induced by temperature increase leads to a colour change from orange to violet.[61, 67] Lastly, structural changes (order/disorder, phase transition, lattice expansion, etc) can also lead to thermo-induced chromic behaviour as shown for Ag_2HgI_4 which undergoes a phase transition over a considerable range of temperature giving rise to a colour change from yellow to orange on heating.[63] Thermochromic organic molecules are also numerous. In this case, two important mechanisms are involved: a thermo-induced chemical reaction such as keto-enol tautomerisation (e.g. for *N*-salicylidene anils which are discussed in detail in the next section),[68, 69] radical stabilisation,[70] cyclisation,[35] etc or structural and/or conformational change.[71-78] This last phenomenon was principally observed for some

polymers in different forms such as solid state, solution, gel, thin film, etc.[71-79]

Few words about other types of chromic phenomena

In this manuscript, we will focus on the thermo- and photochromic properties but many other chromic phenomena can be invoked with different external stimuli which could be a physical constraint such as pressure (piezochromism),[80] mechanical strain (mechanochromism),[76, 81] electricity (electrochromism),[82] or due to reaction / interaction with solvent molecules (solvatochromism) (which eventually involves a temperature effect as shown with $[Ni(diam)_2(C_2H_5OH)_2]$ (blue), where diam = ethylenediamine, stabilised at low temperatures in solution although only $[Ni(diam)_2]$ (violet) is formed at high temperatures)[61, 65, 66,70, 83], chemical vapours (vapochromism),[84] ions (ionochromism) or other molecular reagents (affinochromism).[78] Nevertheless, it is interesting to note that, very usually, compounds are characterised by a combination of chromic properties (e.g. thermo- and photochromism).[68]

N-salicylidene aniline and derivatives

Versatile thermo- and photochromic molecules

In this thesis, we were particularly interested by *N*-salicylidene aniline derivatives which have been used in various fields such as nonlinear optics,[22] catalysis,[85] biology[86] and several applications have been proposed (chemical sensor,[87] stimuli responsive polymer,[88] molecular machines,[17] information storage and display.[15, 16] This latter application is probably the most promising one thanks to the thermo- and photochromism

switching ability of a few *N*-salicylidene aniline derivatives[89] that occurs in the solid state and without fatigue.[90]

Thermochromism is observed thanks to a thermal tautomeric equilibrium between the uncoloured enol and the yellow *cis*-keto forms (Figure 1).[89] Photochromism arises from photo-isomerization of both the enol and *cis*-keto forms (Figure 1) to the red *trans*-keto form.[89] For *N*-salicylidene aniline, photochromism is induced by light irradiation at 365 and 436 nm but derivatives can absorb at other wavelengths, as demonstrated by the large range of colours shown by these molecules.[89, 91, 92] The strong light sensitivity of the *N*-salicylidene aniline allow thus to selectively irradiate a surface in order to write an information as demonstrated in Figure 2 for the CMAT logo in memorial of our Chemistry of Materials Laboratory.

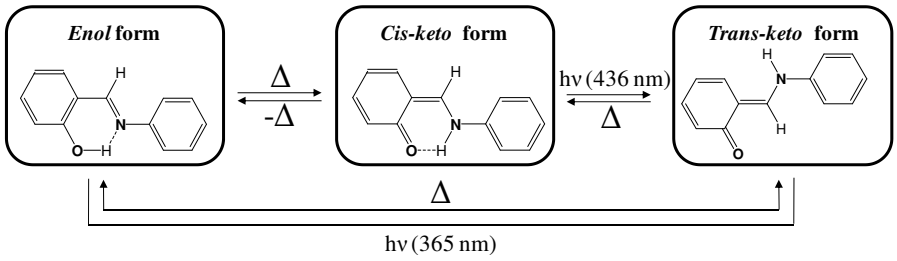

Figure 1 Thermochromism and photochromism of *N*-salicylidene aniline.

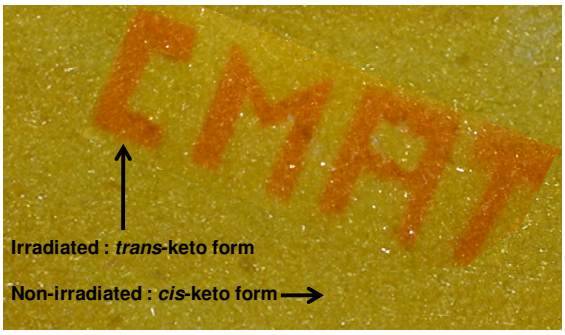

Figure 2 Photograph of *N*-salicylidene aniline powder showing yellow non-irradiated surfaces (where the colour is given by the *cis*-keto form) and irradiated (254 nm, 1h) red surfaces (where the colour is given by a mixture of *cis*- and *trans*-keto forms).

The chemical pathways point of view

The photochemical process associated to photochromism has been described.[93-95] UV irradiation (Figure 3) of the enol form leads to the formation of the excited enol form (enol*). This species can complete a fast tautomerization to the excited *cis*-keto form (cis*). The cis* to cis relaxation is mainly radiative and is always detected by fluorescence spectroscopy.[91] The cis* form can also undergo photo-isomerization to produce the excited *trans*-keto (trans*), which is described as non-fluorescent. It is assumed that the trans*–trans relaxation is mostly non-radiative. Back reaction from *trans*-keto to *cis*-keto and enol forms is either thermally or photo-chemically induced (Figure 3).

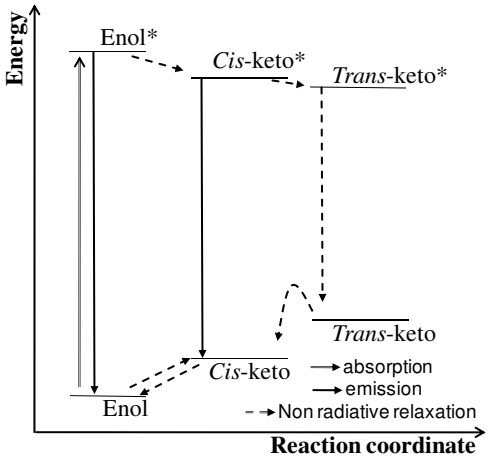

Figure 3 Photochemical process leading to the formation of the *trans*-keto form from the enol form for the *N*-salicylidene aniline. The solid arrows indicate absorption phenomena or emission relaxation and the dotted arrows represent non-radiative relaxation.

Impact of the crystal structure and of the molecular environment

N-Salicylidene aniline derivatives were firstly claimed to be thermochromic or photochromic but not both.[68, 91, 96] This exclusive classification was recently clarified[89] and *N*-salicylidene aniline derivatives were shown to be either photochromic and thermochromic or only thermochromic (except for few rare examples that are neither thermo- nor photochromic, and present a strong deep red coloration[91] probably originating from a very large *cis*-keto form population). Being aware of the importance to predict these optical properties, a structure–properties classification was proposed.[68] Thermochromic compounds were observed as planar molecules that are closely packed in the crystal lattice, with a low dihedral angle between aromatic rings ($\Phi < 25°$). These structures are stabilised by strong π-π or

C-H···π supramolecular interactions. Aromatic rings and imine groups are particularly involved in these interactions, assisted by charge-transfer phenomenon.[97] A typical example of this type of packing is represented by the *N*-salicylidene 2-aminopyridine crystal structure (Figure 4).[68, 98] Thermo- and photochromic molecules were described as highly twisted molecules, with large dihedral angles ($\Phi \geq 25°$), packed within an open structure. Molecules appear to be quite isolated because of long intermolecular distances, as observed for instance in the model compound *N*-salicylidene 2-chloroaniline (Figure 5).[99] Some molecules such as *N*-salicylidene aniline present polymorphism and can crystallize in one thermochromic phase (β_1) as well as two photochromic phases (α_1 and α_2).[100-102] Interestingly, *N*-salicylidene aniline derivatives are only thermochromic in solution because of the low stability of the *trans*-keto form in this medium.

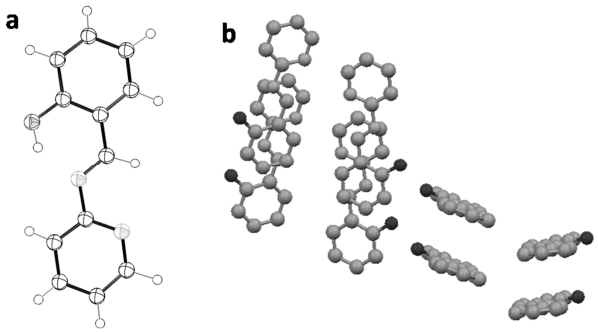

Figure 4 ORTEP view of the asymmetric part of the unit cell of the *N*-salicylidene 2-aminopyridine[98], showing 50% probability displacement ellipsoids (a). View of the crystal packing of the *N*-salicylidene 2-aminopyridine.[98] H atoms were omitted for clarity. The presence of π-π stacking interactions is clearly indicated by the superposition of molecules (b).

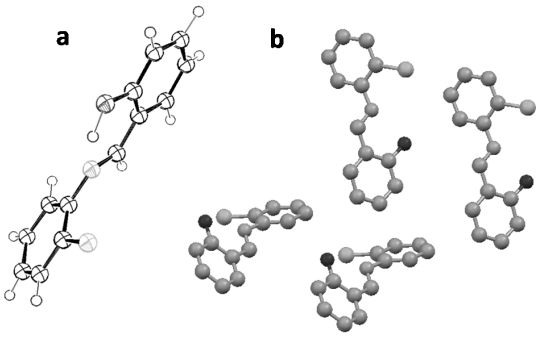

Figure 5 ORTEP view of the asymmetric part of the unit cell of the *N*-salicylidene 2-chloroaniline,[99] showing 50% probability displacement ellipsoids (a). View of the crystal packing of the *N*-salicylidene 2-chloroaniline.[99] H atoms were omitted for clarity. The absence of strong supramolecular interaction can be noted by the large intermolecular distances (b).

Solid-state optical properties of *N*-salicylidene aniline derivatives are also influenced by the molecular environment, as shown by the incorporation of these molecules in polymethylmethacrylate,[14] MCM41 mesoporous silica,[103-105] liquid crystals,[106] organogelators and clathrates,[107-113] Na-Y zeolite[56, 105] or micelles.[104] Consequences of this incorporation take their origin in the modification of the steric hindrance during the photo-isomerisation (e.g. photochromism is always present in diluted materials)[96] and in the modification of the energy levels of the different forms of molecules (enol, *cis*- and *trans*-keto, transition states, zwitterionic form, etc)[56]. This strategy can lead to the appearance of persistent photochromism or to the quenching of this phenomenon and remains thus difficult to use in order to predict optical behaviour of this class of compounds.[56, 114, 115]

The spin crossover phenomenon

Generalities and influence of molecular composition and supramolecular interactions

As described later, spin crossover (SCO) inorganic complexes have been synthesized during this work. SCO is a very attracting research field[10, 62, 116-126] in view of the fact that many applications could be aimed in many fields such as molecular electronic[127-129] and sensors,[62] data storage and display,[127-129] biology and medicine,[130] non linear optics,[127, 131] etc. This phenomenon, which involves a transition from a Low-Spin (LS) to a High-Spin (HS) state, was encountered with many metal ions such as chromium, manganese, iron and cobalt[64, 117, 132-134] but the most studied metal ion is, unquestionably, the iron(II) ($3d^6$) in an octahedral environment because of its ability to cross from a diamagnetic LS (S = 0) to a paramagnetic HS (S = 2) state (Figure 6).[10, 64, 118]

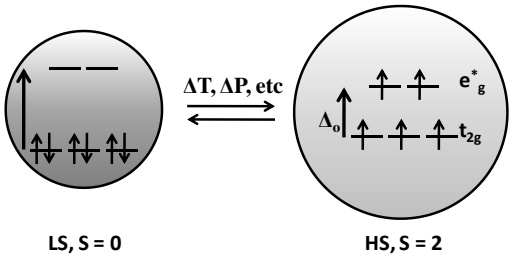

Figure 6 Schematic representation of the SCO of an iron(II) ion in an octahedral environment. Diamagnetic LS and paramagnetic HS states are shown in left and right of the figure, respectively.

In order to observe this phenomenon, the ligand field of the metal ion (Δ_o) must be finely tuned to an 'intermediate' range where both electronic configurations are stable and accessible thanks to a small external

stimulus.[10, 64] A large variety of external perturbation were described, for example, temperature,[121, 135] pressure,[62, 64] or light irradiation (*via* LIESST and LD-LISC effects)[136]. As shown in Figure 6, the SCO involves a large modification of the electron distribution leading to a change of numerous physical characteristics of the materials such as light absorption (colour change), magnetism, vibration of surrounding ligands and/or anions, structural changes, etc.[10] SCO phenomenon can then be studied by a large variety of analytical techniques (magnetometry, ^{57}Fe Mössbauer, infrared, Raman and UV/Visible spectroscopies, etc).[10] The SCO phenomenon can be regarded as gradual or abrupt (Figure 7), complete (transition of 100 % of active ion sites) or not, in one or more steps.[10, 64]

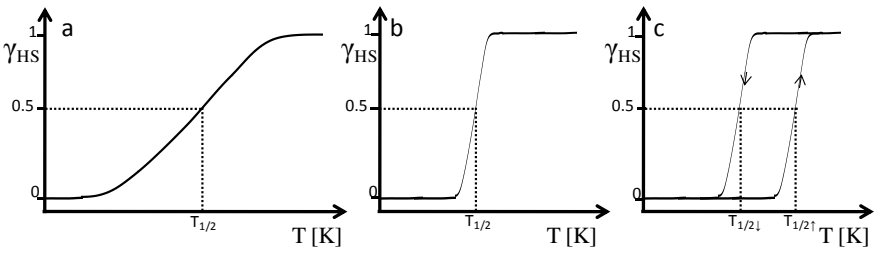

Figure 7 Gradual (a), abrupt (b) and with hysteresis (c) thermally induced SCO. The HS fraction (γ_{HS}) is plotted as a function of the temperature. The $T_{1/2}$ value indicates the temperature where half of SCO ions have changed their spin state. Different values are obtained on cooling and warming mode for the SCO with hysteresis.

The abrupt character of the transition, corresponding to a deviation from a Maxwell-Boltzmann statistic, originates from an elastic interaction between metallic nodes, giving a certain 'cooperativity' to the LS-HS switch.[10, 64, 121, 137] The cooperativity can be transmitted by covalent or supramolecular bonds[138] and can drive to the presence of a hysteresis loop giving a bi-stability to the system (Figure 7).[64, 121] Thus, SCO phenomenon is not only

modified by the inorganic complex nature (metal ion, ligand and dimensionality) but also by a large variety of parameters such as the presence of guest molecules,[139] anions and guest molecules nature,[121, 135, 139] crystal structure and synthetic pathway used,[139] etc. This characteristic allows a fine tuning of the SCO parameters and gives rise to a very attracting freedom in the design of such materials.

Ligand-Driven Light-Induced Spin Change phenomenon (LD-LISC)

The use of light as external stimulus for SCO phenomenon is one of the most challenging research field for this class of compounds because of the large expected perspectives in the data storage setups.[128, 129] LIESST effect (Light-Induced Excited Spin State Trapping) corresponds to a trapping of a meta-stable HS state formed by light excitation of a LS ion at low temperature.[10, 64, 136, 140-142] However, a dramatic limitation of this photo-magnetic phenomenon takes its origin in the relaxation of the meta-stable HS configurations into the initial LS state.[142] Compounds must then be cooled below a critical temperature (T_{LIESST}) which corresponds to the limit above which the light-induced HS ions are not stable.[142] In spite of the numerous compounds exhibiting this phenomenon,[142-147] the T_{LIESST} values remain very low and thus difficult to use for industrial perspectives (e.g. T_{LIESST} $[Fe^{II}(bpp)_2](BF_4)_2$ = 110 K where bpp = 2,6-bis(pyrazol-3-yl)pyridine).[142] In order to reach room temperature light-induced SCO, another way was proposed by using a photo-sensitive molecule coordinated to the SCO metal ion.[148-154] The idea is then to induce the SCO phenomenon by a photo-induced modification of the ligand. It was successfully shown with the 4-styrylpyridine (stpy) molecule which leads to the formation of two

complexes, of formula $[Fe^{II}(stpy)_4(NCBPh_3)_2]$, containing the *cis* (c-stpy) and *trans* (t-stpy) isomers.[154] In this case, the two inorganic units present different magnetic behaviour (thermally induced SCO and HS state over the whole studied temperature range for the complex with t-stpy and c-stpy, respectively), the spin change is thus obtained by a photo-isomerisation of stpy below the $T_{1/2}$ temperature (where the two complexes have a LS and HS states, respectively).[154] Nevertheless, although recent data show the possibility to observed LD-LISC phenomenon at room temperature,[150, 152] it appears that the photo-induced transition cannot occur in pure solid phase because of the large steric hindrance induced by the isomerisation.[154] Until now, authors have thus investigated their system in solution[154] or as inorganic complexes embedded in polymeric matrix.[153] The research of new inorganic architectures allowing this type of photo-magnetic phenomenon at room temperature and as pure materials remains thus challenging and necessary.

Aim and strategy

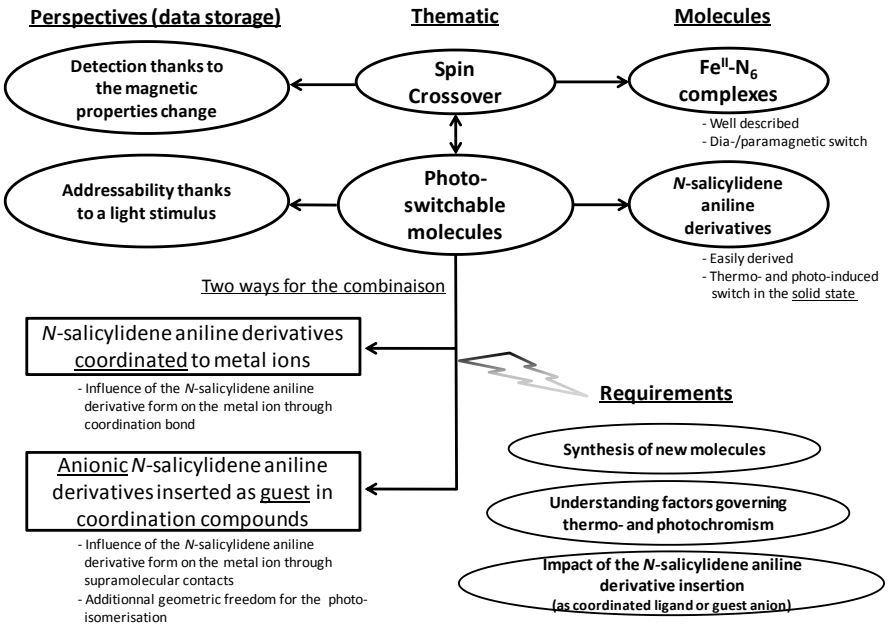

Figure 8 Synoptic view of the thematic of this work and associated requirements.

The genesis of this project was to develop new SCO inorganic complexes operating with a molecular switch in pure solid phase. This type of multifunctional material is thought for data storage perspectives because it could combine the high magnetic detection capability of the SCO phenomenon (e.g. iron(II) which drives to a dia- to paramagnetic switch) with the very good addressability brought by a photosensitive switchable molecule in the solid state (Figure 8). For this purpose, we had to select a suitable system in order to synthesize new solid-state thermo- and photo-sensitive molecules with coordinating atoms compatible with a SCO metal ion environment. The *N*-salicylidene aniline was selected because of its very promising optical properties in the solid state and the possibility to design

coordinating moieties bound on the thermo- and photo-sensitive moiety (Figure 8). The assets of this class of materials could become large and thus more suitable than the widely studied organic-inorganic azobenzene switches.[149, 149, 150, 153, 154] However, the search of a photo-magnetic phenomenon with such materials is a very challenging task in view of the fact that no information about the influence of 1/ chemical derivation (adding of coordinating moieties) and 2/ metal ion coordination on the optical properties was available (Figure 8). This work will thus aim to clarify these questions. This manuscript will be divided in two main parts devoted to the synthesis of new *N*-salicylidene aniline derivatives followed by the study of their optical properties and the formation of inorganic complexes built with these molecules, respectively. Moreover, the perspective to modify the magnetic behaviour of SCO complexes by using novel type of anionic derivatives of the *N*-salicylidene aniline will be also investigated (Figure 8).

N-salicylidene aniline derivatives based organic materials

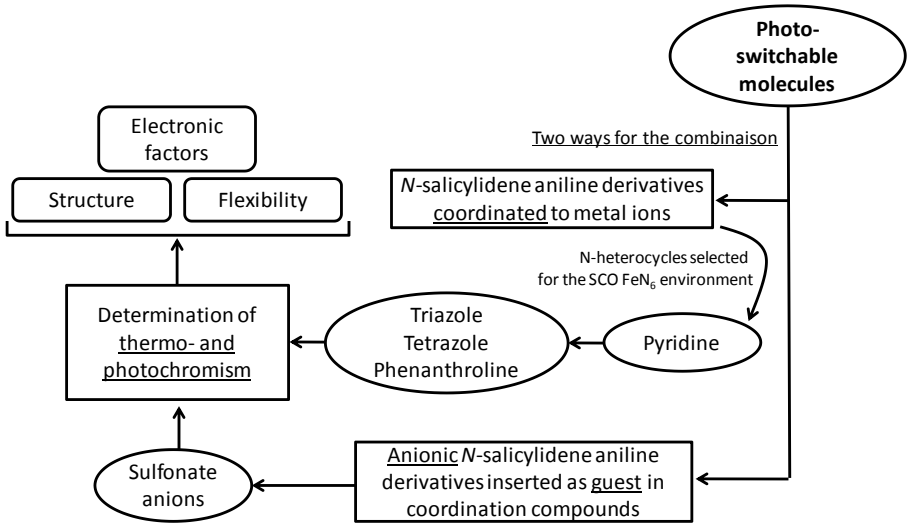

Figure 9 Schematic view of the organic part of this work as descibed in the text.

N-heterocycle *N*-salicylidene aniline derivatives were very less studied earlier. New molecules of this class were thus designed in order to be compatible with the 3d ion coordination perspectives describe in the next section. We will investigate pyridine (Chapters 1 and 3), 1,2,4-triazole and tetrazole (Chapter 2) rings (Figure 9). The influence of the nitrogen rich moieties on the structural and optical properties will be finely analysed in order to understand their impact on the optical properties of this class of materials. The goal is thus to rationalise the observations and to make links between chemical and physical characteristics (electronic resonance, molecular rigidity and packing, etc) of molecules (Figure 9). It should lead to an overview of parameters which govern the appearance of thermo- and photochromism. Moreover, a supramolecular engineering approach will be proposed in order to, at least partially, control the presence and the strength

of these phenomena. Finally, the synthesis of new anionic derivatives of *N*-salicylidene aniline, comprising non-coordinating sulfonate groups, will be also investigated (Chapter 4) and the role of the local environment (such as the influence of the counter-ion nature) will be analysed (Figure 9).

Organic-inorganic materials built with N-salicylidene aniline derivatives

The second step of this study is the investigation of inorganic complexes built with the *N*-salicylidene aniline derivatives described above. For this work, a methodical approach was applied in order to analyse 1/ the influence of the coordination and 2/ of the nature of the metal ions and their coordination spheres on the structural and optical properties of the thermo- and/or photo-sensitive ligands, 3/ the possibility to form complex supramolecular architectures built with *N*-salicylidene anils frameworks and 4/ the impact of the metal ion SCO phenomenon on the thermochromic moieties. These studies will thus lead to thinking about 5/ the possibility to bring a photo-sensitivity to an inorganic complex through the ligand and to perspectives in LD-LISC effect. Moreover, the incorporation of a *N*-salicylidene anil anion into such inorganic materials will also be investigated in order to carry a thermo-sensitivity to the complexes through the anion (perspectives in AD-TISC effect, *Anion-Driven Temperature-Induced Spin-Change*).

Part I: Organic Materials

Chapter I: The intriguing case of *N*-salicylidene aminopyridines‡

Introducing remarks

In this chapter, we focus on *N*-salicylidene aminopyridines and more precisely on *N*-salicylidene 2-aminopyridine (**L**^{2}), *N*-salicylidene 3-aminopyridine (**L**^{3}), *N*-salicylidene 4-aminopyridine (**L**^{4}) and 5-chloro-*N*-salicylidene 3-aminopyridine (**L**^{5}) (Scheme 5).

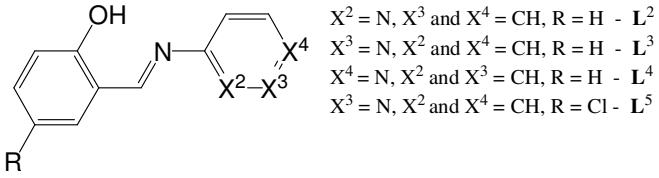

Scheme 5 Molecular scheme of *N*-salicylidene aminopyridines.

L$^{2\text{-}4}$ molecules were previously reported in the literature but only the **L**^{2} and **L**^{3} crystal structures were known.[96, 98] The growing of the **L**^{4} and **L**^{5} crystal structures opens new relationships between structure and optical properties. In the next sections, we discuss all crystal structures but only the optical properties of **L**$^{3\text{-}5}$ will be analysed because **L**^{2} is a known thermochromic molecule.[155]

‡ Adapted from F. Robert, A.D. Naik, B. Tinant, R. Robiette, Y. Garcia *Chem. Eur. J.* **2009**, *15*, 4327-4342.

Syntheses and crystallization methods

Whereas $\mathbf{L^3}$ and the new molecule $\mathbf{L^5}$ were synthesised by using a reported method,[156] $\mathbf{L^4}$ could not be obtained in a pure form by following ref. [106] and so a new synthetic approach had to be developed. The use of a Dean–Stark setup, which allows the trapping of water released during the Schiff base condensation, was found to be the most efficient method. Recrystallisation from cold toluene afforded the pure compound with a good yield (66%). Obtaining single crystals of $\mathbf{L^4}$ was challenging because other attempts like solvent evaporation or diffusion were unsuccessful.[96] We obtained beautiful yellow needles of a diffractable quality of $\mathbf{L^4}$ (Figure 10a) by using a suitable home-made sublimation setup. Extreme caution was taken while handling the crystal for X-ray determination since crystals are unstable at room temperature and atmospheric pressure. Indeed, the compound becomes oily after a few minutes, even in a desiccator. We thus limited the transportation time between sublimation setup and diffractometer, quickly selected crystals and put them into a suitable mineral oil before mounting. The same setup was used to obtain single crystals of $\mathbf{L^3}$ (Figure 10b), which were found to be isostructural to the reported structure.[56] $\mathbf{L^5}$ was obtained as long yellow/orange needles by slow evaporation of a concentrated solution in methanol (Figure 11).

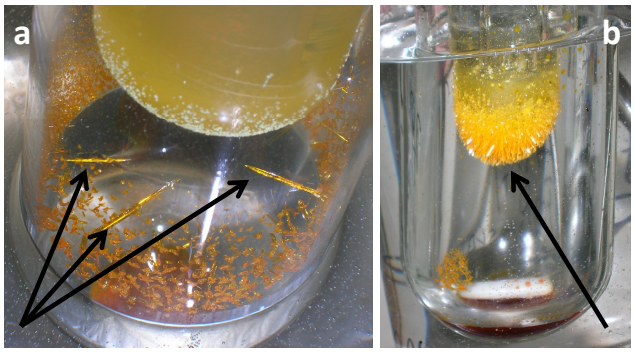

Figure 10 Photograph of the home-made sublimation setup allowing $\mathbf{L}^4$ (a) and $\mathbf{L}^3$ (b) crystals growing.

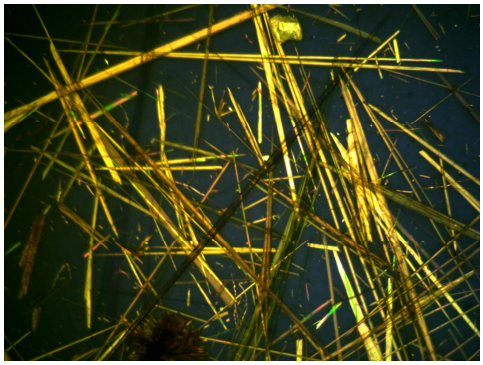

Figure 11 Photograph of $\mathbf{L}^5$ single crystals.

Crystal structures study N-*salicylidene 2-aminopyridine* (L^2)[§]

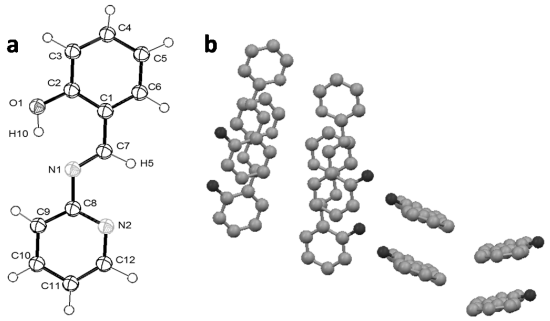

Figure 12 (a) ORTEP view of the asymmetric part of the unit cell of $\mathbf{L^2}$ [98], showing 50% probability displacement ellipsoids. (b) View of the crystal packing of $\mathbf{L^2}$.[98] H atoms were omitted for clarity. The presence of π-π stacking interactions is clearly visible by the superposition of molecules.

As briefly described in the introduction part, *N*-salicylidene 2-aminopyridine[98] is a typical example of an exclusively thermochromic molecule (as confirmed by our own diffuse reflectance experiments). The structure, reported by Hadjoudis[98] (Table 19), is composed by highly planar molecules in the enol form (the dihedral angle between aromatic rings Φ = 5°) due to the presence of two intramolecular H-bonds (see Scheme 6a and Table 20) which force the planarity and forbid any photo-isomerisation and photochromism phenomenon. Molecules are packed very closely and develop strong π-π stacking interactions between aromatic rings and imine functions (Table 21).

[§] In order to help the reading, tables, containing crystals data, are located at the beginning of the appendix part (Table 19 to Table 63, p. i to xlvii).

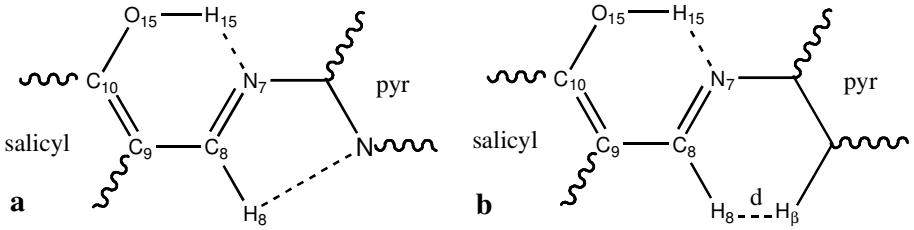

Scheme 6 Intramolecular hydrogen bonding in $\mathbf{L^2}$ (a) and $\mathbf{L^{3\text{-}5}}$ (b). The strong intramolecular H-bond between N and H8 atoms locks the planarity of the $\mathbf{L^2}$ molecule because no rotation of the pyridine ring around the N7-C axis is allowed.

N-salicylidene 3-aminopyridine ($\mathbf{L^3}$)

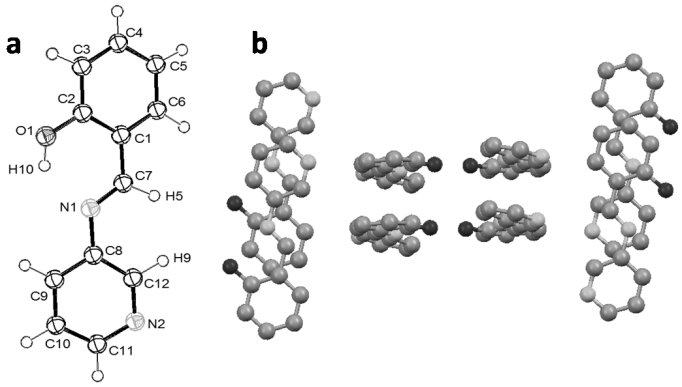

Figure 13 (a) ORTEP view of the asymmetric part of the unit cell of $\mathbf{L^3}$ [98, 157] showing 50% probability displacement ellipsoids. (b) View of the crystal packing of $\mathbf{L^3}$.[157] H atoms were omitted for clarity. The presence of π-π stacking interactions is clearly indicated by the superposition of molecules.

N-salicylidene 3-aminopyridine crystal structure[157] is composed by almost planar molecules in the enol form (the dihedral angle between aromatic rings $\Phi = 15°$). As in $\mathbf{L^2}$, molecules are packed very closely and develop strong π-π stacking interactions between aromatic rings and imine functions (see Table 21).

N-salicylidene 4-aminopyridine (L^4)

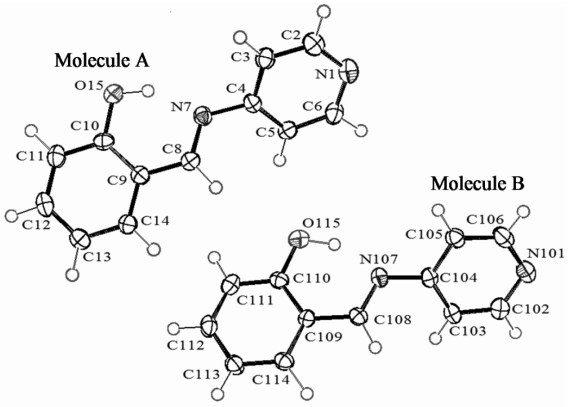

Figure 14 ORTEP view of the asymmetric part of the unit cell containing the two types of molecule of $\mathbf{L^4}$, showing 50% probability displacement ellipsoids.

Crystal structureof $\mathbf{L^4}$ was solved at 120(2) and 250(2) K by Prof. B. Tinant (UCL). It crystallises in orthorhombic space group $P2_12_12_1$ (Table 19 and Figure 14). At 120 K, in the asymmetric part of the unit cell, two molecules (A and B) in the fundamental enol form are found. The bond length of C10-O15 is approximately 1.36 Å and that of C8-C9 is 1.45 Å, which indicates single bonds, whereas a double bond is revealed from C8-N7 being approximately 1.29 Å (Table 23).[158] These two molecules only differ by the dihedral angle between the aromatic rings (Φ_A = 41(1)° and Φ_B = 49(1)°, Table 23), which should imply different energy states for these molecules since this angle is believed to depend on the strength of the conjugation of the molecule.[107] The conformation difference also has an influence on the intramolecular hydrogen-bond strength between the alcohol and the imine functions.[68] In our case, the most planar molecule, A, has the longer N···H distance and thus has a softer hydrogen bond (H15···N7 = 1.72(3) Å > H115···N107 = 1.64(3) Å; Table 20 and Scheme 6). It is surprising because

thermochromic molecules with a planar structure are known to have a stronger hydrogen bond than photochromic molecules with a twisted structure.[68] A similar observation was noticed for the α_1 phase of *N*-salicylidene aniline.[100-102] An inconsistency is noted between the reported conclusion for the intramolecular hydrogen-bond strength in **L³** [157] and our results with **L⁴**. Indeed, **L³** is much more planar than **L⁴** but the hydrogen bond is stronger for **L⁴** (**L³**: H15···N7 = 1.91 Å > **L⁴**: H115···N107 = 1.72(3) Å) (Table 20). Long intermolecular distances (≈ 5 Å between centroids) are noted in the non-centrosymmetric crystal packing of **L⁴** but some weak π–π stacking and CH–π interactions are observed (Figure 15, Table 21 and Table 22). Four types of π–π interactions can be envisaged with molecules A and B: two between imine functions and pyridine or salicyl rings, respectively. However, only one interaction is significant between the imine function (C108-N107) and a salicyl ring (C9-C10-C11-C12-C13-C14) at a distance of 3.63(3) Å (at 120 K), where planes are almost parallel (12°; Table 21). Overall, we can conclude that the molecules are only slightly linked in contrast to the structures of **L³**[157] and **L⁵** (see next section) in which molecules interact strongly by π–π stacking characterized by short inter-fragment distances and very small dihedral angles. No significant difference was observed for the bond lengths and dihedral angles of the enol function for **L⁴** at 120(2) and 250(2) K. This observation is consistent with the fact that the concentration of the *cis*-keto form is too low to be detected by X-ray diffraction (Table 19 and Table 20).[68] The slight differences observed in cell parameters (thermal dilatation of the cell) and in intermolecular distances (Table 19, Table 21 and Table 22) leads to a decrease of π–π stacking and CH–π interactions. This structural change could be at the origin of the melting of crystals noted at room temperature.

Interestingly, moving the N atom from position 3 ($\mathbf{L^3}$) to 4 ($\mathbf{L^4}$) results in a weakening of the intramolecular H8···H_β interaction, which is not surprising because in this case, a large dihedral angle is observed ($\Phi > 40°$).

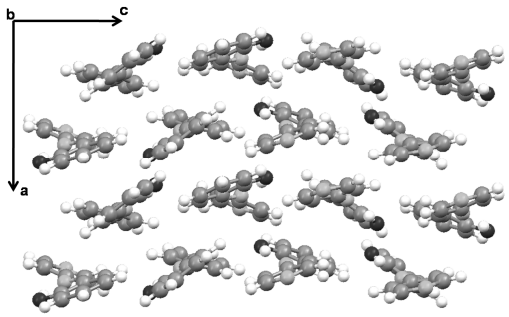

Figure 15 View of the crystal packing of $\mathbf{L^4}$ along the *b* axis.

5-chloro-*N*-salicylidene 3-aminopyridine ($\mathbf{L^5}$)

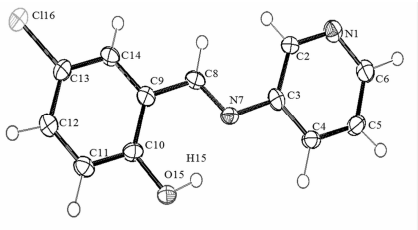

Figure 16 ORTEP view of the asymmetric part of the unit cell of $\mathbf{L^5}$, showing 50% probability displacement ellipsoids.

Crystal structure determination of $\mathbf{L^5}$ (Figure 16) was undertaken to understand the impact of the electron density modification on both the structure and optical properties. The chlorine substituent was driven for synthetic reason (product purification ability). Although the potential formation of a crystal directing effect induced by this atom is known,[180] it was not targeted in this case. Overall, this molecule, which crystallises in the

monoclinic $P2_1/n$ space group, presents a similar structure than $\mathbf{L^3}$ (Table 19). [157] In this structure, solved by Prof. B. Tinant (UCL), planar molecules in the enol form with $\Phi = 5(1)°$ are found (Table 23). It is interesting to note that the nitrogen atom of the pyridine ring is, as for $\mathbf{L^3}$, located in a *cis* position with respect to H8 of the imine function and no disorder can be identified, contrary to the structure of *N*-(5-methoxysalicylidene)-3-aminopyridine.[157] A study of the hydrogen-bond strength of $\mathbf{L^5}$ in comparison with $\mathbf{L^3}$ and $\mathbf{L^4}$ reveals that the chloride derivative $\mathbf{L^5}$ is more planar and has a H15···N7 distance of 1.83(5) Å, which is smaller than that observed for $\mathbf{L^3}$ (1.91 Å) but longer than that for $\mathbf{L^4}$ (1.72(3) Å; Table 20). The 'closed' packing of this molecule is also interesting because of a compact arrangement, in which molecules interact in pairs (π-π stacking) due to short inter-molecular distances (Figure 17, Table 21 and Table 23), is observed. The effect of the chloride substituent on the molecular structure results then in a decrease of the dihedral angle between aromatic rings (Φ), a denser packing and a shorter intramolecular hydrogen bond. Indeed, the intramolecular H8···H2 distance (1.950(5) Å) of $\mathbf{L^5}$ is even shorter than the H7···H9 distance found for $\mathbf{L^3}$ and *N*-salicylidene aniline (≈ 2.4 Å),[101, 157] which is in agreement with the lowest dihedral angle of the series (5(1)°), thus ensuring full planarity. Interestingly, the dihedral angle and the hydrogen-bond strength is similar to that of $\mathbf{L^2}$.[98] In conclusion, we have investigated the influence of the chloride substituent with $\mathbf{L^5}$, which is a rare example of the chemical derivation of $\mathbf{L^3}$.[97, 159, 160] This new thermochromic molecule is clearly more planar than $\mathbf{L^3}$ and is packed as a closed structure, as expected for thermochromic molecules.

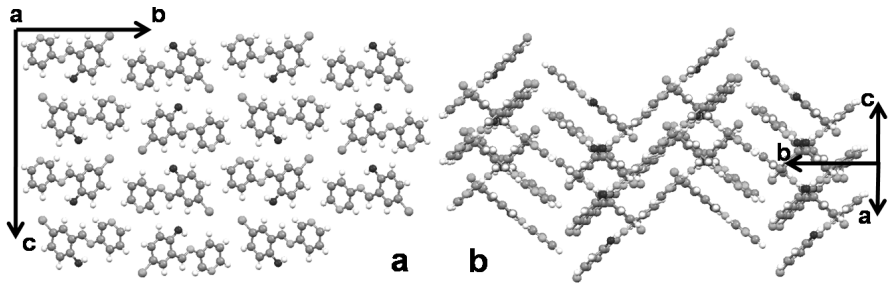

Figure 17 View of the crystal packing of $\mathbf{L^5}$ along *a* axis (a) and showing strong π-π stacking interactions (b).

Optical properties

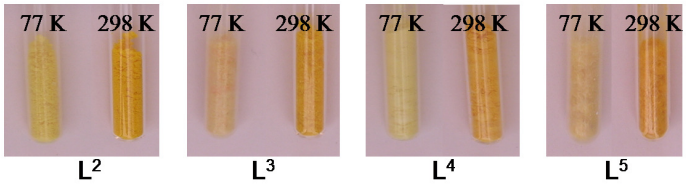

Figure 18 Photographs showing thermochromism of the crystalline powders of $\mathbf{L^{2\text{-}5}}$ at 77 K and 298 K.

As shown in Figure 18, the crystalline powders of $\mathbf{L^{2–5}}$ reveal thermochromism from yellowish orange at room temperature, to yellowish green on cooling to 77 K.[96, 161] This colour change arises from the enol/*cis*-keto tautomerisation,[89] with the yellowish-green colour, clearly observed for $\mathbf{L^2}$ and $\mathbf{L^4}$, being attributed to a contribution of the fluorescence of the compounds.[92] These organic molecules ($\mathbf{L^{3–5}}$) were analysed by diffuse reflectance spectroscopy in the crystalline form (Figure 19a). Two regions can be distinguished at room temperature: a broad absorption range corresponding to the enol form, which is located in the UV region, and a second one in the visible region originating from the absorption of the *cis*-keto form, and from the *trans*-keto form (for $\mathbf{L^3}$). In $\mathbf{L^3}$, enol absorption may

be composed of three unresolved bands ranging from the UV region to approximately 450 nm. The *cis*-keto band is clearly distinguished at $\lambda_{max} \approx$ 480 nm, but it could also be observed at $\lambda_{max} \approx$ 450 nm. In $\mathbf{L^4}$ and $\mathbf{L^5}$, these bands are less resolved and ranged from the UV region to approximately 560 nm.

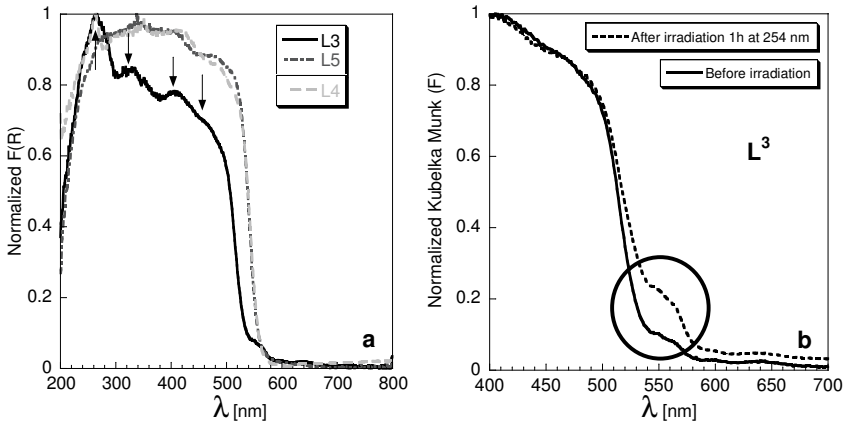

Figure 19 Kubelka–Munk spectra of $\mathbf{L^{3-5}}$ crystals (a) and Kubelka–Munk spectra of $\mathbf{L^3}$ crystals before and after irradiation at 254 nm for 1 h (b). The circle in part (b) highlights the increase of the *trans*-keto band. In part (a), the arrows indicate the maxima of observed bands in $\mathbf{L^3}$.

Surprisingly, formation of the red *trans*-keto form under UV irradiation (λ = 254 nm, 1 h) is found for $\mathbf{L^3}$ by means of diffuse reflectance measurements. Indeed, a growing of the band located at $\lambda_{max} \approx$ 550 nm is observed as a result of photo-isomerisation (Figure 19b). We note, however, traces of the *trans*-keto form before irradiation, indicating a mixture of both keto isomers. Thus, $\mathbf{L^3}$ is not only thermochromic as earlier observed[96] but also photochromic. In contrast, there is no change in the diffuse reflectance spectra of $\mathbf{L^4}$ and $\mathbf{L^5}$ before and after light irradiation. $\mathbf{L^4}$ is therefore exclusively thermochromic and not photochromic as claimed earlier.[96] It is

important to note that $\mathbf{L^{3–5}}$ have the same optical properties regardless of their crystalline or powder state even though the diffractograms of $\mathbf{L^3}$ and $\mathbf{L^4}$ are different as shown by X-ray powder diffraction (see experimental section). Reversibility of the *cis*/*trans* isomerisation for $\mathbf{L^3}$ was checked. As shown in Figure 20, irradiation at $\lambda_{max} \approx 365$ nm leads to a large increase of the Kubelka–Munk function (F) to approximately 0.18. This increase is clearly attributed to the formation of the *trans*-keto form of $\mathbf{L^3}$. As a result, a conversion of the surface colour from yellow to red-orange is observed. Thermal relaxation to the *cis*-keto form is extremely slow and these data can be fitted properly by a first-order exponential equation (see inset of Figure 20a). The kinetic constant ($k = 9.9 \times 10^{-8}$ s^{-1}) is very weak and corresponds to an almost persistent photochromism. Reverse photo-switching to the *cis*-keto form can be achieved by irradiating the *trans*-keto form absorption band at $\lambda_{max} = 546$ nm. Consequently, a dramatic decrease of F from 0.175 to approximately 0 is observed. The cycle can be repeated by irradiation once again at 365 nm (Figure 20b). Such very slow relaxation kinetics ($k \approx 10^{-7}$ s^{-1}) was similarly observed for *N*-(3,5-di-tert-butylsalicylidene)-3-nitroaniline ($k = 2 \times 10^{-7}$ s^{-1}),[162] the lowest value being found for *N*-(3,5-di-tert-butylsalicylidene)-4-aminopyridine ($k = 1.8 \times 10^{-8}$ s^{-1}).[20] The extraordinary stability of the NH form in the crystalline state was explained by the presence of a resonance hybrid of two canonical structures (non-polar quinoidal and polar zwitterionic forms).[163] In the present case, such structures cannot be excluded. Interestingly, this experiment demonstrates that the presence of bulky tert-butyl groups on the phenol group is not necessary to obtain a high thermal stability for the *trans*-keto form as earlier claimed.[20]

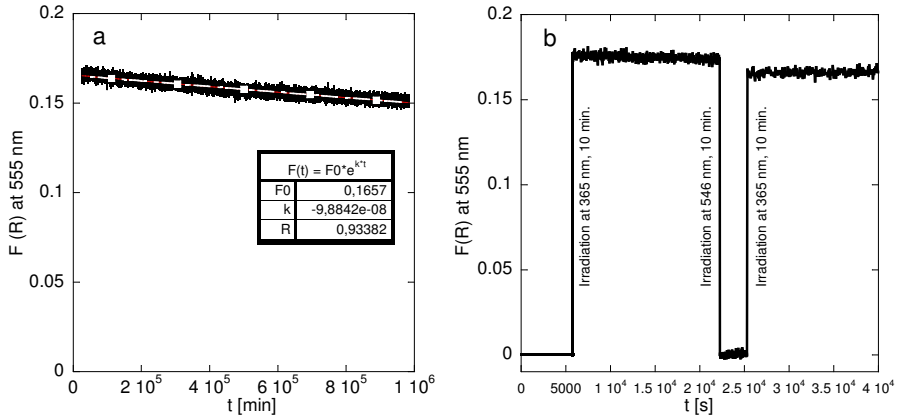

Figure 20 Time dependence of the Kubelka–Munk function (F) of crystals of $\mathbf{L^3}$ at 555 nm showing a slow exponential thermal relaxation of the meta-stable *trans*-keto form. The inset shows the output of the fitting procedure.(a) Reversibility of the *cis*/*trans* isomerisation as shown by the evolution of the Kubelka–Munk function (F) at 555 nm with cycles of irradiation of $\mathbf{L^3}$ at 365 and 546 nm, respectively.(b)

A comparative study of $\mathbf{L^{3–5}}$ by emission spectroscopy has been conducted. Emission spectra were recorded at the excitation wavelengths of 300 nm (Figure 21b) and 400 nm (Figure 21a), which correspond to the enol and *cis*-keto form absorptions, respectively. For a solution of $\mathbf{L^3}$ in methanol (Figure 22), two bands are observed corresponding to the enol* → enol ($\lambda_{\max}^{300nm}$ = 373 nm) and *cis*-keto* → *cis*-keto ($\lambda_{\max}^{400nm}$ = 510 nm) emissions. In contrast, when $\mathbf{L^3}$ and $\mathbf{L^5}$ are analysed in their crystalline forms, only the second major contribution to the fluorescence is observed ($\lambda_{\max}^{400nm}$ = 580 and 572 nm for $\mathbf{L^3}$ and $\mathbf{L^5}$, respectively). A shoulder is detected at $\lambda_{\max}^{400nm} \approx$ 540 nm for the emission of the *cis*-keto* for $\mathbf{L^3}$. The origin of this band may come from the radiative relaxation of a less stable and constrained conformation of the *cis*-keto form as earlier explained for

N-(5-chloro-2-hydroxybenzylidene)aniline.[92] For $\mathbf{L^4}$ crystals, a major intense emission is observed at λ_{max}^{400nm} = 582 nm (Figure 21a) but a very weak fluorescence at $\lambda_{max}^{300nm} \approx 430$ nm can also be detected. Crystals of $\mathbf{L^3}$ show the same behaviour because of a weak emission centred at 358 nm. Table 1 summarizes all maximum emission wavelengths for $\mathbf{L^{3\text{-}5}}$.

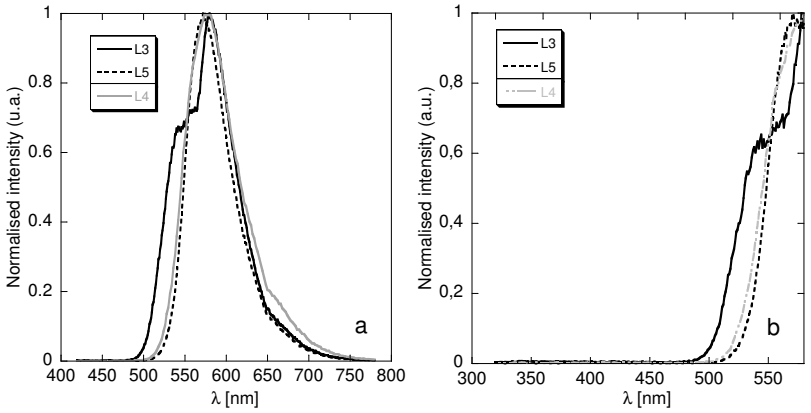

Figure 21 Emission spectra of crystalline powders of $\mathbf{L^{3\text{-}5}}$ at an excitation wavelength of 400 nm (a) and 350 nm (b).

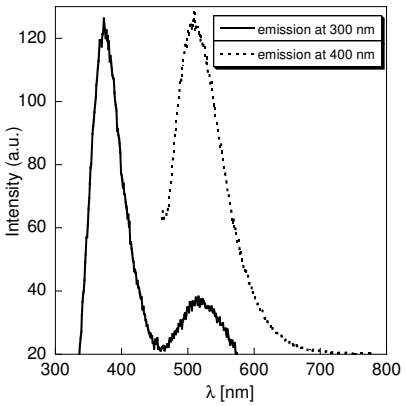

Figure 22 Emission spectra of $\mathbf{L^3}$ in methanol (10^{-4} M) at 300 and 400 nm.

Table 1 Emission maximum wavelengths [nm] of $\mathbf{L^{3\text{-}5}}$.

	$\mathbf{L^4}$	$\mathbf{L^3}$		$\mathbf{L^5}$
State	Crystalline	Solution[a]	Crystalline	Crystalline
λ_{max}^{400nm} [nm][b]	582	510	580	572
λ_{max}^{300nm} [nm][c]	(430)	373	(358)	-

[a] In methanol (10^{-4} M). [b] Wavelength of maximum emission at an excitation wavelength of 400 nm. [c] Wavelength of maximum emission at an excitation wavelength of 300 nm. Values in brackets correspond to peaks observed as traces.

Computational study of the photo-isomerisation

To understand the observed differences in optical properties according to the position of the hetero-nitrogen atom of the pyridine ring, we have investigated, in collaboration with Prof. R. Robiette (UCL), the photo-isomerisation of $\mathbf{L^{2\text{–}4}}$ by computational means. The primary goal of this study was to determine the real influence of the steric hindrance induced during photo-isomerisation process. Thus, this phenomenon was simulated for isolated molecules and the approach was next apply to molecules incorporated in their real crystal packings. Data described below give thus new trends allowing having a better understanding of the parameters governing the photochromism.

Isolated molecules

First, we have considered isolated $\mathbf{L^{2\text{–}4}}$ molecules and examined their enol, *cis*- and *trans*-keto forms in the ground state (GS) and first singlet (S^1) and first triplet (T^1) excited states (Table 2). Transition states (TS) for *cis*-keto/*trans*-keto isomerisation were also studied. Figure 23 shows the calculated energy evolution for these species during the photo-isomerisation

of $\mathbf{L^3}$ (relative to the torsion angle C14-C9-C8-N7). All stable forms were found to be fully planar, thus allowing maximisation of electron conjugation leading to a minimisation of energy. In the GS, the enol form is more stable than the corresponding *cis*-keto form. In S^1 and T^1, the situation is reversed; hydrogen transfer from the oxygen atom to the nitrogen atom is energetically favoured, resulting in an exothermic enol to *cis*-keto tautomerisation. This is in good agreement with the observed thermochromism for all molecules. Energy barriers calculated for the *cis*-keto/*trans*-keto chemical equilibrium provide relevant information on the photo-isomerisation probability. Indeed, our results reveal a highly disfavoured isomerisation for the GS and T^1 with a high energy barrier of 30–42 kcal/mol. However, the activation barrier to isomerisation for S^1 is found to be much lower (20–23 kcal/mol) indicating that photo-isomerisation must take place in the first singlet excited state. Comparison of the energy barrier between both keto forms, according to the position of the nitrogen atom on the pyridine ring, demonstrates that isomerisation in the case of $\mathbf{L^3}$ is slightly more accessible than for $\mathbf{L^2}$ and $\mathbf{L^4}$ (see Table 2).

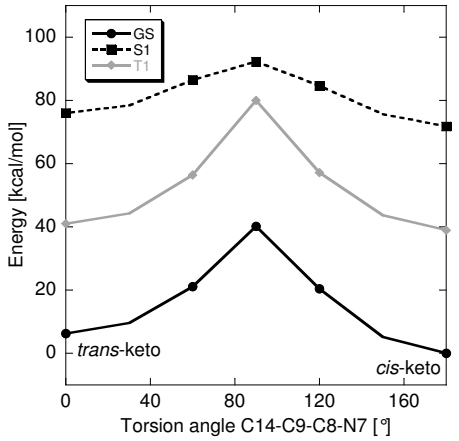

Figure 23 Calculated energy evolution for the ground state (GS), the first singlet (S1) and the first triplet (T1) excited states during the photo-isomerisation of $\mathbf{L^3}$.

Table 2 Calculated energies (in kcal/mol relative to enol) for the enol, *cis*-keto and *trans*-keto forms of $\mathbf{L^{2\text{-}4}}$ as isolated molecules in the ground state (GS), first singlet (S^1) and triplet (T^1) excited states.

		$\mathbf{L^2}$	$\mathbf{L^3}$	$\mathbf{L^4}$
GS	enol	0	0	0
	cis-keto	6.8	8.8	7.0
	barrier[a]	42.0	40.2	42.2
	trans-keto	7.7	15.1	12.6
S^1	enol	84.2	83.4	84.2
	cis-keto	72.7	80.6	78.9
	barrier[a]	21.3 (23.1)[b]	20.5 (20.3)[b]	21.1 (22.3)[b]
	trans-keto	78.2	84.8	87.3
T^1	enol	52.6	47.7	52.1
	cis-keto	45.8	38.9	48.6
	barrier[a]	34.7	41.1	29.4
	trans-keto	42.5	41.0	50.6

[a] Activation barrier from the *cis*- to *trans*-keto form. [b] Values in brackets correspond to an energy barrier involving a 'pedal motion'.

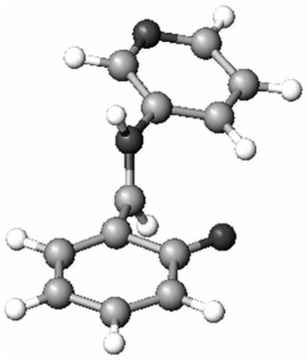

Figure 24 View of the isomerisation TS involving a pedal-motion mechanism for $\mathbf{L^3}$.

This prediction is consistent with the photochromism of $\mathbf{L^3}$ and the thermochromism of $\mathbf{L^4}$ and $\mathbf{L^2}$. Based on structural changes, Harada et al. have proposed that isomerisation involves a concerted movement of the bridge atoms and the aromatic rings resembling the pedal motion of a bicycle.[164] Investigation of such an isomerisation mechanism for $\mathbf{L^3}$ reveals its likelihood, as shown in Figure 24. Indeed, in each case, the rotation barrier was found to be very close (within 2 kcal/mol) to the barrier obtained using the pedal motion (Table 2).

Influence of the crystal packing

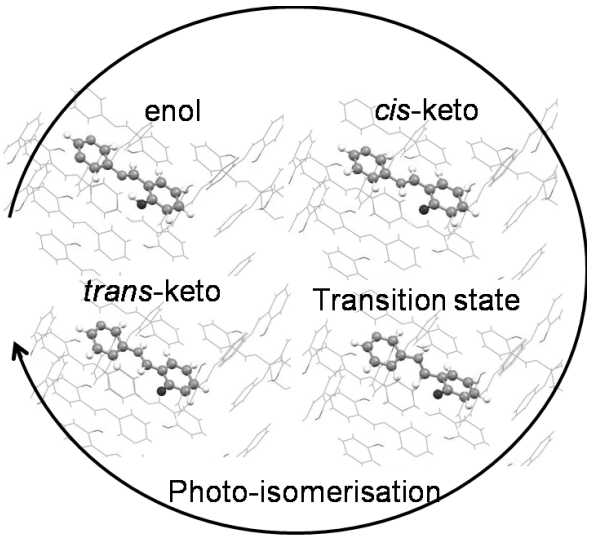

Figure 25 View of the calculated photo-isomerisation of $\mathbf{L^3}$ in the real crystal packing[157].

Table 3 Calculated stabilisation energies (in kcal/mol relative to enol) for the enol, *cis*-keto and *trans*-keto forms of $\mathbf{L^{2\text{-}4}}$ obtained when molecules in the ground state (GS) are placed in their real crystal packing.

		$\mathbf{L^2}$	$\mathbf{L^3}$	$\mathbf{L^4}$	$\mathbf{L^4}$
rel. $E_{stab.}$[a]	enol	0	0	0	0
	cis-keto	-1.5	-4.3	-3.6	-4.7
	barrier[c]	-0.6	-9.1	-11.6	-14.2
	trans-keto	-1.7	-7.7	-5.1	-7.1

[a] Following equation developed in the experimental section. [b] 'Planar' corresponds to the more planar molecule observed in the $\mathbf{L^4}$ crystal packing whereas 'twisted' is the more twisted molecule. [c] Activation barrier from the *cis*- to *trans*-keto form.

Because of the importance of crystal packing on the photochromic properties of salicylidene anilines,[68] photo-isomerisation was also investigated on the molecules included in the crystal packing obtained by single-crystal

X-ray diffraction analyses. The influence of crystal packing on *cis*-keto/*trans*-keto isomerisation was probed by estimating the relative stabilisation of enol, *cis*-keto and *trans*-keto forms as well as TS species in the crystal (see Table 3 and Figure 25). Calculations were considered for an isomerisation occurring through either a simple rotation or a pedal motion,[164] as found for isolated molecules. However, all attempts to optimise a TS structure corresponding to a simple rotation revealed a high destabilisation of such a structure by the crystal, leading instead to a TS involving a pedal motion. Our results thus provide strong support for the pedal-motion mechanism.[164] Obtained stabilisation energies show that **L^2** is not significantly influenced by the crystal; *cis*-keto, *trans*-keto and the TS are stabilised by ~ 2 kcal/mol, and thus, no reduction of the energy barrier is noted. Crystal packing stabilises **L^3** to a greater extent and the energy barrier is lowered in the crystal, due to a higher stabilization of the TS than the *cis*-keto form. This is again in good agreement with the observed thermo- and photochromism of **L^3** and the absence of photochromism for **L^2**. For **L^4**, the high stabilisation of the TS structure by crystal packing also indicates an activation of the isomerisation, thus suggesting that isomerisation should be possible in the solid state, although it was not observed experimentally in this work. These results seem to suggest that modification from **L^2** to **L^4** in our isolated-molecules study has more influence on the photochromic behaviour than variation of the crystal packing. It is worth noting, however, that this disagreement between computed activation by crystal packing and experiment may also originate from the fact that distortion of the surrounding molecules and crystal-packing dilatation were not taken into account in our calculations.

Discussion

Intrigued by the absence of photochromism for **L**^{4} and by the surprising observation of thermochromism for this molecule, which was previously reported to be only photochromic,[96] we have improved crystallisation methods to obtain single crystals suitable for X-ray diffraction analyses. This task was successfully completed by developing a new and straightforward crystallisation method to overcome reported difficulties due to the instability of the crystals at room temperature.[96] Interestingly, the structure is made of highly twisted molecules arranged in an open network, built with only one weak π-π stacking interaction and CH···π interactions. These structural characteristics were claimed to be typical of photochromic molecules,[68] but we have found, however, that **L**^{4} is exclusively thermochromic. Contradictions with the literature were also noted for *N*-salicylidene-3-aminopyridine (**L**^{3}), which was claimed to be exclusively thermochromic,[96] but which is actually photochromic, too, irrespective of its form (crystalline powder or single crystals). Surprisingly, molecules are closely packed in their crystal structure, with such characteristics being a signature, according to Hadjoudis, of thermochromic molecules.[68, 96] The existence of polymorphs could explain the conflicting observations between ref. [96] and our results for **L**^{4}. However, for **L**^{3}, this can be fully excluded since single crystals used in this work are isomorphous to those of ref. [157] as checked by X-ray diffraction. For **L**^{4}, this possibility cannot be excluded since Hadjoudis et al. did not report an X-ray diffraction pattern due to the instability of the molecule at room temperature. It is also interesting to note that, despite that the crystals and powders have the same optical properties, their structures are clearly different (see experimental section). These findings thus challenge the structure–property relationship ‘open

structure/photochromism'–'closed structure/thermochromism' that is widespread in the literature.[68] Crystal structures are thus not sufficient for predicting optical properties of *N*-salicylidene aniline derivatives and other complementary techniques must be used. Fluorescence analyses are a very interesting way to probe these systems and to understand their optical properties. Indeed, emission spectroscopy allows information to be gained about the energetic level of fundamental and excited species formed during photochemical processes. Diffuse reflectance spectra also give energetic information but these are more difficult to interpret because of the unresolved absorption bands. Two important emission bands have been observed when $\mathbf{L^3}$ is in solution but only one is observed for $\mathbf{L^{3\text{-}5}}$ in the solid state. The enol* → enol emission is no longer observed when these organic molecules are in the crystal form. Thus, this emission must be quenched when the second emission, corresponding to the radiative relaxation of the *cis*-keto* form, is too energetically favoured. We assume that this situation occurs when the *cis*-keto* form is much more stable than the enol* form. On the contrary, the radiative relaxation of the excited enol* is only observed when the energy difference between the excited enol* and the excited *cis*-keto* form is very low and thus, when the enol* is not too unstable relative to the *cis*-keto* form, as shown in Figure 26. Thus, the switch from a solution of $\mathbf{L^3}$ in methanol to a crystalline form, which implies a change in supramolecular interactions,[165] leads to a significant increase in the energy gap between both excited levels and leads to the quenching of the enol* emission. It is surprising that the switch from $\mathbf{L^3}$ to $\mathbf{L^4}$ crystals has no influence on the fluorescence of the *cis*-keto* form despite the difference in dihedral angle observed by XRD analyses (Table 23). On the other hand, the change from $\mathbf{L^3}$ to $\mathbf{L^5}$ affects the observed emission and proves that

electronic changes have an influence on the emission properties of the system. However, no information can be obtained on the energy gap between the fundamental enol and *cis*-keto form because the [enol]/[*cis*-keto] ratio could be governed by an activation barrier and not by the gap between these energy levels.[93] Theoretical calculations allowed the factors controlling photochromism to be investigated. Our results on isolated molecules show that isomerisation must take place in the S^1 excited state with computed activation barriers being in good agreement with observed **L^3** and **L^4** experimental optical properties. Studies on real crystal structures support a pedal-motion photo-isomerisation mechanism[164] and show a significant decrease of the activation barrier to isomerisation induced by the crystal packing for **L^3** and **L^4**. This allows the two crystals to be described as structures in which the photo-isomerisation is helped by the molecular environment. In contrast, in **L^2**, no activation by the packing is noted. These results are another inconsistency with the reported classification in which **L^2** and **L^3** are claimed to be closed structures and **L^4** an open structure. This computational study does not give definite predictions about the photochromism of **L^3** and **L^4** but provides a useful trend that can help chemists in the understanding of photochromic phenomena. Interestingly, we note that **L^4** crystallises in a non-centrosymmetric space group, which is a favourable situation for non-linear optical (NLO) properties. Unfortunately, this molecule is not bi-functional since **L^4** does not undergo a photochromic reaction in the solid state. However, **L^3** could be useful for optical memories due to its infinitely slow thermal back reaction.

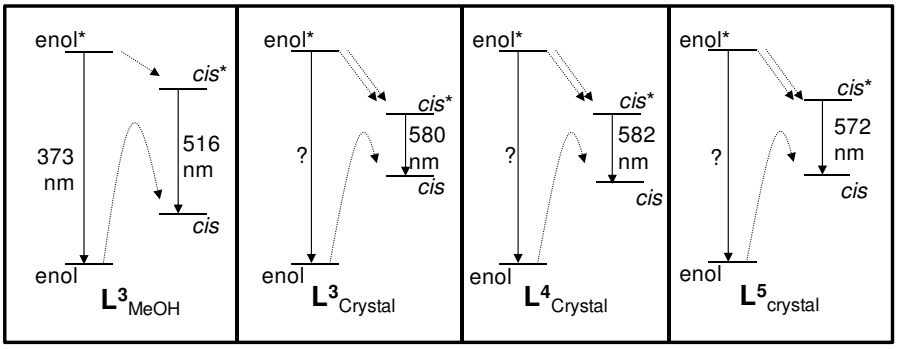

Figure 26 Schematic view of energy levels involved in the fluorescence of $\mathbf{L^{3\text{-}5}}$. The solid arrows indicate emission relaxation. Single and double dotted arrows indicate slow and fast non-radiative relaxation, respectively. The curve lines represent the crossing of the energy barrier. The enol level has been fixed arbitrarily.

To summarize, structure-property relationships of these molecules widely acknowledged in the literature[68] are contradicted by the present investigation: 1/ $\mathbf{L^3}$ presents a crystal structure characteristic of thermochromic molecules, with a small dihedral angle between aromatic moieties and a dense packing typical of closed structures.[68] This molecule is, however, not only thermochromic but also photochromic. 2/ In contrast, $\mathbf{L^4}$, which is a highly twisted molecule and packed in an open structure, as expected for a photochromic molecule, is exclusively thermochromic, contrary to the exclusive photochromic properties claimed earlier.[96] 3/ Thanks to a computational approach, we demonstrate that the optical properties of *N*-salicylidene aniline derivatives cannot be predicted on the basis of the crystal structure solely, as claimed earlier.[68] Crystallography is certainly the most important tool to investigate such molecules but it must be accompanied by a wide variety of physical and theoretical methods.

Chapter II: A crystal engineering approach: the case of *N*-salicylidene N-heterocycle derivatives**

Introducing remarks

In the previous chapter, we have shown that both electronic and structural aspects must be considered to properly predict optical properties. In this chapter, we thus propose a new strategy to gain a better control of the crystal structure of such molecules using crystal packing directing effect moieties. This possibility was thought after the analysis of the crystal structure of *N*-salicylidene 2-aminopyridine,[97, 155, 156] where an intramolecular H-bond between imine and pyridine ring locks the molecule in a planar geometry and gives a closed structure. Here, a rational crystal engineering approach is applied for the first time to the *N*-salicylidene aniline derivatives system.

The supramolecular chemistry concept

Supramolecular chemistry constitutes a highly versatile research field where new complex chemical systems are made from simple components interacting through non-covalent intermolecular forces.[166] Supramolecular chemistry concepts have been largely used in materials science,[167] polymer science[168] and biology[169] and provide novel types of applications (receptors,[170-172] chemo-responsive sensors,[173] zeolite analogues,[174] etc). Supramolecular architectures are constructed thanks to steric and electronic information contained in basic molecular building blocks.[175] These primary

** Adapted from F. Robert, A.D. Naik, F. Hidara, B. Tinant, R. Robiette, J. Wouters, Y. Garcia *Eur. J. Org. Chem.* **2010**, 621-637.

covalent units are made of an internal algorithm that controls the final supramolecular assembly.[166] In such architectures, molecular entities (made by covalent bonds) are connected through a large panel of supramolecular interactions such as H-bonds,[176] π–π stacking,[177] hydrophilic,[178] ionic[179] and halogen–halogen interactions.[180] This diversity of interactions explains the complexity of supramolecules which can be either artificial (nanogrids,[181-183] nanoracks,[184] nanocages[185]) or natural[186] (DNA, recognition proteins, etc). Supramolecular interactions can be very stable (thermodynamic) or very labile (kinetic),[187] which allows the system to (re)organize either itself[188] or under a given constraint (temperature,[188] light irradiation,[177, 189] pH[190] and solvent change,[188] concentration[188]) to form complex self-assemblies. The self-reorganization ability of supramolecular systems plays also an important role in molecular recognition encountered in some host–guest complexes.[187] The nature of the supramolecular architecture can also be used to predict physical properties (cooperativity and spin-transition temperature,[191] magnetic behaviours,[183] porosity,[192] etc.) thanks to crystal structure control. This approach, called crystal engineering,[193, 194] based on supramolecular chemistry concepts, allows simplifying the complex problem of structure prediction into a problem of network architecture[193, 194] where molecules, metals, ions and so on are considered as nodes and the intermolecular interactions or coordination bonds represent node connections. In this chapter, we make use of this strategy to obtain new switchable functional materials based on the *N*-salicylidene moiety, whose optical properties could be finely tuned thanks to a proper electronic and structural control.

A crystal engineering approach

In this chapter, we discuss about new N-heterocycle derivatives that are predesigned to lead to a controlled crystal structure with selected supramolecular interactions. In the crystal network, *N*-salicylidene aniline derivatives are considered as nodes and supramolecular interactions (H-bonds, π–π stacking, CH–π and ionic interactions) as linkers. *N*-salicylidene 4-amino-1,2,4-triazole (**Hsaltrz**) and *N*-salicylidene 5-aminotetrazole (**Hsaltz**) (Scheme 7a,b) present dense supramolecular networks based on intermolecular H-bonding interactions, although *N*-salicylidene 4-amino-3,5-bis(pyridin-2-yl)-1,2,4-triazole (**Habs**) and *N*-salicylidene (1,10)-phenanthrolin-5-amine (**Hsalphen**) (Scheme 7c,d) reveal mostly π-π stacking interactions. The potassium salt of *N*-salicylidene 5-aminotetrazolate (**Ksaltz**) (Scheme 7e) was studied to probe the impact of ionic interactions. All compounds are discussed as family members selected to lead to specific optical properties. From non-functional **Hsaltrz**, we could make either thermochromic molecules (**Hsaltz** and **Ksaltz**) by adding strong intermolecular H-bonds and ionic interactions or a photochromic molecule (**Habs**) by isolating the triazole moiety by two pyridine rings. **Hsalphen** is similar to **Habs** from a crystallographic point of view but however presents only weak photochromic properties.

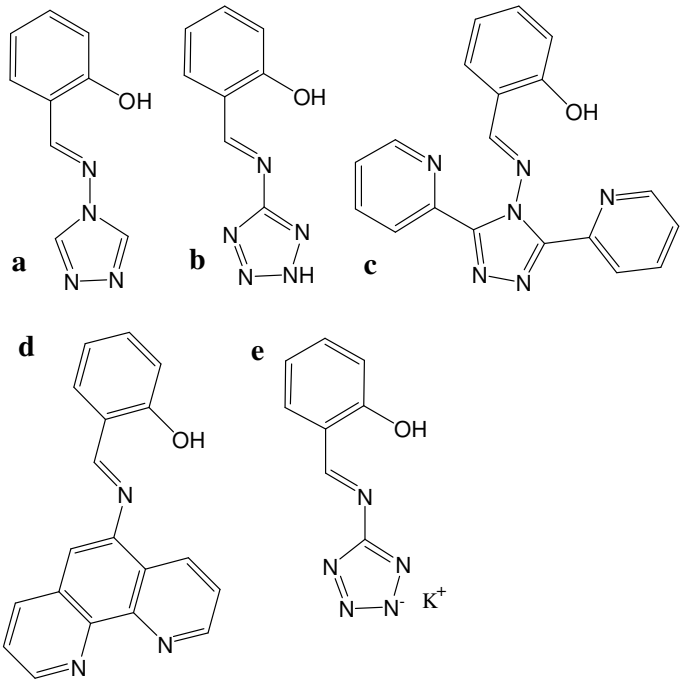

Scheme 7 Molecular scheme of **Hsaltrz** (a), **Hsaltz** (b), **Habs** (c), **Hsalphen** (d) and **Ksaltz** (e).

Syntheses and crystallization methods

Purification of **Hsaltz** and **Hsalphen** was very difficult because the crude products systematically contained a large amount of unreacted salicylaldehyde in contrast to other *N*-salicylidene aniline derivatives. These impurities were successfully extracted by sonication in hexane and single crystals were obtained by slow evaporation of concentrated ethyl ether solutions. Slow sublimation of **Habs** at 110 °C under vacuum led to the growing of single crystals on the cold finger condenser of our sublimator setup. Single crystals of **Hsaltrz** were obtained by an unconventional method. For this experiment, we used the nucleophilicity of 4- amino-1,2,4-triazole, which can trap salicylaldehyde molecules, slowly released by the

hydrolysis of a sodium salt of *N*-salicylidene *p*-aminobenzenesulfonate (**Na1**) in methanol. A copper(II) salt, inserted in the reaction medium, is assumed to ease the production of pure **Hsaltrz**, which slowly crystallizes (Scheme 8, see experimental part for details).

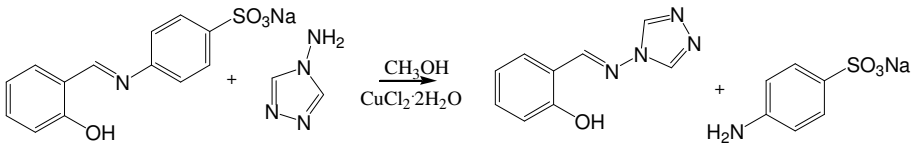

Na1 **NH_2trz** **Hsaltrz**

Scheme 8 Synthetic pathway allowing the **Hsaltrz** single crystals growing.

Crystal structures study[††]

N-salicylidene 4-amino-1,2,4-triazole (Hsaltrz)

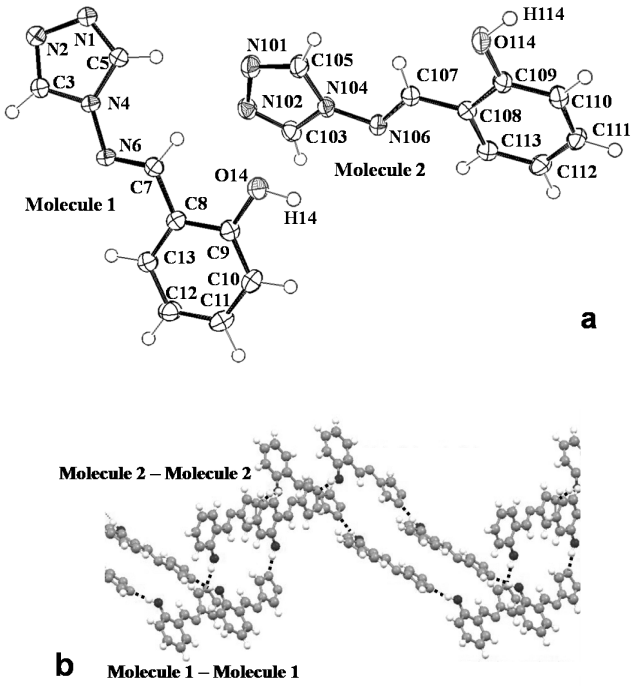

Figure 27 (a) ORTEP view of the asymmetric part of the unit cell of **Hsaltrz**, showing 50% probability displacement ellipsoids. (b) Crystal packing of **Hsaltrz** involving intermolecular H-bonds (dotted line) and the formation of supramolecular double chains. The organization by pairs with (molecule 1/molecule 1) and (molecule 2/molecule 2) is clearly identified.

[††] Crystal structures were solved by Prof. B. Tinant except Ksaltz which was solved by Prof. J. Wouters (FUNDP)

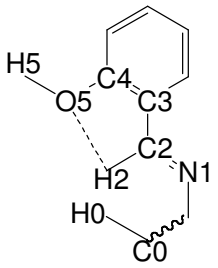

Scheme 9 Topology of **Hsaltrz**.

Hsaltrz crystallizes in the monoclinic space group *P*21/n (Table 24). Two molecules in the enol form were distinguished in the asymmetric part of the unit cell (Figure 27). The bond lengths C9–O14 and C109–O114 of 1.351(2) and 1.350(2) Å respectively, confirm the presence of the enol form (Table 25, Scheme 9). In addition, the lengths of C8–C7 (1.458(2) Å) and C108–C107 (1.456(6) Å) are in the range for single bonds, whereas the lengths for C7–N6 (1.279(2) Å) and C107–N106 (1.279(2) Å) are in the range for double bonds[158] (Table 25). No bond length difference is noted between the two molecules of the asymmetric part of the unit cell. In contrast, a change in the dihedral angle between the aromatic rings is clearly distinguished (Φ_1 = 16(1)°, Φ_1' = 6(1)°, where Φ_1 and Φ_1' are measured on molecules 1 and 2, respectively) and is accompanied by different torsion angles C(10)5–N(10)4–N(10)6–C(10)7: Γ_1 = 15(1)° and Γ_1' = 6(1)° (Table 25). The distances between H2, H102 and the nearest H from the triazole ring are 2.15(2) Å and 2.19(2) Å (Table 25). According to some authors,[107] these differences can be interpreted as a slight change in the electronic conjugation of the molecule. Interestingly, **Hsaltrz** develops a new type of molecular geometry for the two molecules included in the asymmetric part of the unit cell where the intramolecular H-bond between the alcohol and imine

functions is broken by rotation of the phenolic ring (Figure 27) and replaced by softer intramolecular H-bonds between the CH_{imine} and $O_{alcohol}$ atoms (C7–H7···O14 2.38(2) Å and C107–H107···O114 2.40(2) Å) (Table 26). Considering the loss of energy led by the absence of the usual intramolecular H-bond, the system has counterbalanced it by the formation of a strong intermolecular H-bond between a nitrogen atom of the triazole ring and the alcohol function (O14–H14···N102 1.74(2) Å, O114–H114···N1 1.76(2) Å) (Table 26 and Figure 27b). The triazole ring has a strong structure-directing effect that drives molecules to leave their normal molecular geometry to allow the formation of strong intermolecular H-bonds. The packing is also highly modified because of the formation of supramolecular zigzag double chains (leading to a supramolecule; Figure 27). In each chain, a sequence of ···–Hsaltrz-2–Hsaltrz-1–Hsaltrz-2–Hsaltrz-1–··· is identified (Table 26 and Figure 27b). The double chain architecture is not only stabilised by H-bonds but also by π-π stacking interactions (Table 27) between the imine function of a molecule of a chain and salicyl or a triazole ring of a molecule of the other chain (Figure 27b). In contrast, double chains are almost isolated from each other. Only a weak intermolecular H-bond between the alcohol function of a molecule of one chain and a CH from the salicyl ring of a molecule of another chain (C111–H111···O114 2.45(2) Å) is found (Table 26). A weak CH···π interaction between a salicyl ring of a molecule in a chain and a CH of a triazole ring of the nearest chain (C108–C109–C110–C111–C112–C113···H105–C105 2.87(2) Å) is also noted (Table 27).

N-salicylidene 4-amino-3,5-bis(pyridin-2-yl)-1,2,4-triazole (Habs)

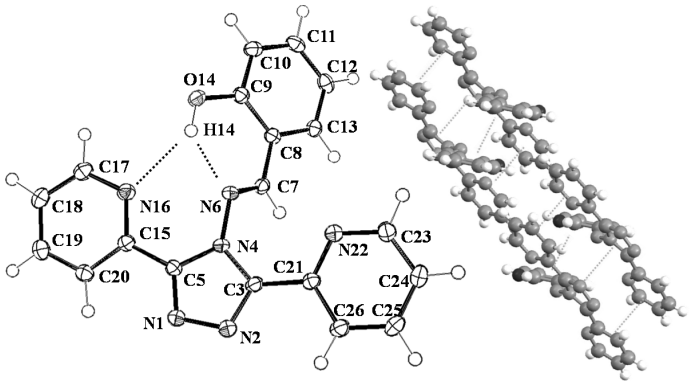

Figure 28 ORTEP view of the asymmetric part of the unit cell of **Habs**, showing 50% probability displacement ellipsoids. Intramolecular bifurcated H-bonds are indicated as dotted lines. The inset shows a view along the *b* axis of the crystal packing showing extended intermolecular π-π stacking interactions (indicated as dotted lines).

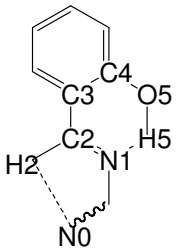

Scheme 10 Topology of **Habs**.

Habs crystallizes in the triclinic space group $P\bar{1}$ (Table 24). The asymmetric part of the unit cell contains one molecule in the enol form (Figure 28). It is possible to clearly identify it: the C9–O14 (1.352(2) Å) and C8–C7 (1.452(3) Å) bond lengths are characteristic of single bonds and the N6–C7 (1.279(3) Å) bond length reveals a double bond[158] (Table 25). Small dihedral angles

are observed between the triazole and pyridine rings (Φ_2 = 10(1)° between C15–N16–C17–C18–C19–C20 pyridine and the triazole ring and Φ_3 = 9(1)° between C21–N22–C23– C24–C25–C26 pyridine and triazole ring) (Table 25). In contrast, a large dihedral angle is identified between the salicyl and the triazole rings (Φ_1 = 41(1)°) (Table 25). In addition, the imine function is observed to be away from the 'pyridine- triazole-pyridine' plane (N22···H7 2.80(3) Å). The torsion angle C3–N4–N6–C7 (Γ) is equal to 62(1)° (Table 25). A strong intramolecular H-bond exists between the alcohol and imine functions, as commonly identified in *N*-salicylidene aniline derivatives (O14–H14···N6 1.95(3) Å) (Figure 28 and Table 26).[68] Another soft intramolecular H-bond is also observed between the alcohol function and the nearest nitrogen of one pyridine ring (O14–H14···N16 2.36(3) Å). Finally, two weak intermolecular H-bonds are observed between the imine group and a pyridine ring of the nearest molecule (C7–H7···N22 2.45(3) Å) and between triazole and the pyridine ring of another molecule (C26–H26···N2 2.60(3) Å) (Figure 28 and Table 26). These interactions explain the position of the nitrogen of the pyridine rings in the molecule. Crystal packing is very dense because of short intermolecular distances ($d_{centroid–centroid}$ = 3.80 Å) (Table 25). Strong π-π stacking interactions are noted between all aromatic rings of one molecule and the same rings in nearest symmetric molecules (Figure 28 and Table 27). In contrast to **Hsaltrz**, no CH···π interaction is observed.

N-salicylidene 5-amino-1,10-phenanthroline (Hsalphen)

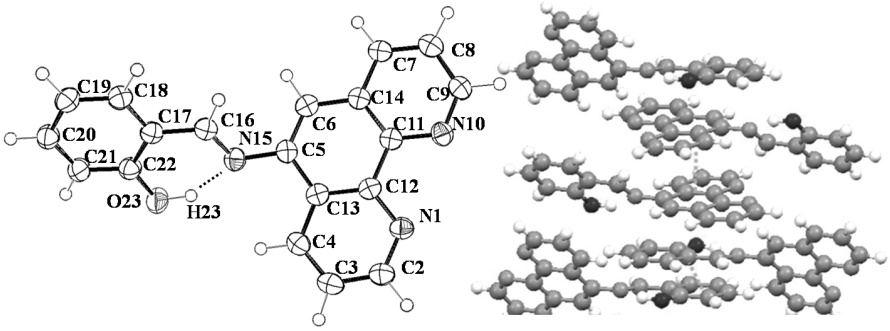

Figure 29 ORTEP view of the asymmetric part of the unit cell of **Hsalphen**, showing 50% probability displacement ellipsoids. Intramolecular H-bond is indicated as a dotted line. View along the *b* axis of the crystal packing showing intermolecular π-π stacking interactions (indicated as dotted lines).

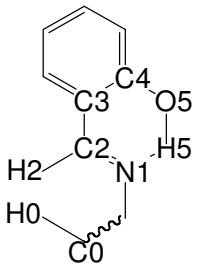

Scheme 11 Topology of **Hsalphen**.

Hsalphen was studied in collaboration with F. Hidara during her undergraduate studies.[195] It crystallizes in the orthorhombic space group *P*bca (Table 24). As in **Habs**, one molecule in the enol form is observed in the asymmetric part of the unit cell (Figure 29). The C22–O23 (1.355(3) Å) and C16–C17 (1.450(3) Å) bond lengths indicate single bonds and C16–N15 (1.283(3) Å) reveals a double bond[158] (Table 25). Two planes are present in the molecule: the first one is formed by the salicyl ring and the imine

function, which are coplanar, and the second one is created by the phenanthroline moiety, which is perfectly planar. A large dihedral angle Φ_1 = 48(1)° and a large torsion angle (C6–N5–N15–C16) Γ_1 = 45(1)° are noted between them (Table 25). The distance between H16 and H6 is found as 2.39(2) Å (Table 25). A strong intramolecular H-bond (O23–H23···N15 1.80(3) Å) is observed between the alcohol and imine functions as in **Habs** (Figure 29 and Table 26). Although the dihedral angle with the salicyl ring is similar in **Habs** and **Hsalphen**, the distance between H23 and N15 is significantly shorter (1.80(3) Å) in **Hsalphen** in comparison to the distance between H14 and N6 in **Habs** (1.95(3) Å) (Table 26). This observation clearly shows the absence of link between Φ and the intramolecular H-bond strength which was claimed in the literature[68]. Crystal packing of **Hsalphen** is directed by the formation of strong intermolecular π-π stacking interactions between phenanthroline moieties, imine functions and salicyl rings (phen···phen 3.90 Å between centroids; $d_{\text{between molecular centroids}}$ = 4.72 Å) (Table 25 and Figure 29). In addition, two weak intermolecular H-bonds (C6–H6···N1 2.51(3) Å and C16–H16···N1 2.46(2) Å) (Table 26) and a CH···π interaction between phenanthroline moieties (C2–H2···N10–C11–C14–C7–C8–C9) complete such a dense supramolecular network (Table 27).

N-salicylidene 5-amino-tetrazole (Hsaltz)

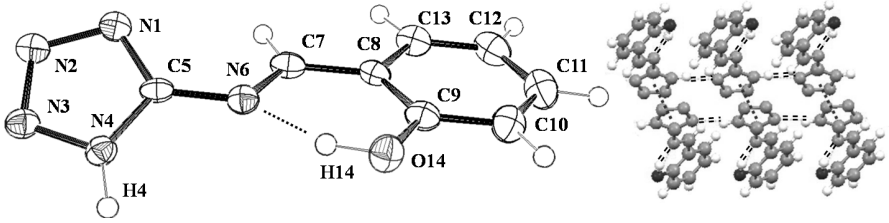

Figure 30 ORTEP view of the asymmetric part of the unit cell of **Hsaltz**, showing 50% probability displacement ellipsoids. Intramolecular H-bond is indicated as a dotted line. The inset is a view of the crystal packing showing the formation of supramolecular double chains built with intermolecular π-π stacking interactions (indicated as dotted lines) and with intermolecular H-bonds (indicated as double dotted lines).

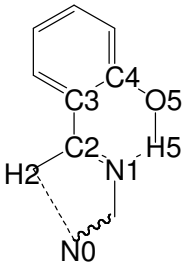

Scheme 12 Topology of **Hsaltz**.

Hsaltz crystallizes in the monoclinic space group *C*2/c (Table 24). In the asymmetric part of the unit cell, one highly twisted molecule in the enol form is observed (Figure 30). The C9–O14 (1.354(3) Å) and C7–C8 (1.431(4) Å) bond lengths indicate single bonds and C7–N6 (1.293(3) Å) reveals a double bond[158] (Table 25). The molecule is characterized by a large dihedral angle (Φ_1 = 35(1)°), a large torsion angle N1–C5–N6–C7 Γ_1 = 33(1)° and a strong intramolecular H-bond (O14–H14···N6 1.75(3) Å) between the imine and alcohol functions (Table 25 and Table 26, Figure 30),

which is clearly stronger than in **Hsalphen** and **Habs**. Crystal packing is directed, as in **Hsaltrz**, by the formation of an intermolecular H-bond between the proton of the tetrazole moiety and the nearest tetrazole ring (N4–H4···N1 1.90(3) Å) (Figure 30 and Table 26). The distance between molecular centroids is evaluated as 4.13 Å and the distance between N1 and H7 was found as 2.64(3) Å (Table 25). Intermolecular H-bonds lead to a supramolecular network where supramolecular double chains (supramolecules) are clearly distinguished (Figure 30). Cohesion between these two chains originates from intermolecular π-π stacking interactions between the tetrazole moieties (tz···tz 3.47 Å between centroids) (Figure 30 and Table 27). No CH···π interaction is observed.

Potassium salt of *N*-salicylidene 5-amino-tetrazolate (Ksaltrz)

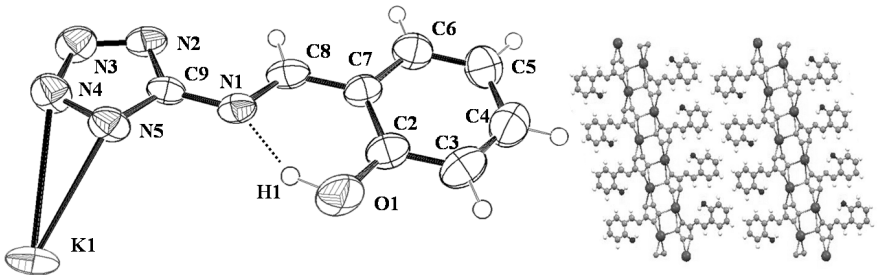

Figure 31 ORTEP view of the asymmetric part of the unit cell of **Ksaltz**, showing 50% probability displacement ellipsoids. Intramolecular H-bond is indicated as a dotted line. The inset is a view of the crystal packing, along the *b* axis, showing a planar arrangement of ionic planes containing potassium and tetrazolate ions and organic planes containing other functions.

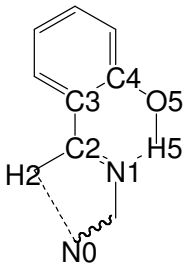

Scheme 13 Topology of **Ksaltz**.

Ksaltz also crystallizes in the monoclinic space group *C*2/c (Table 24). However, it is not isostructural to **Hsaltz**. An almost planar molecule is observed in the asymmetric part of the cell. A small dihedral angle between the aromatic rings (Φ_1) of 6(1)° was measured (Figure 31 and Table 25), which is clearly lower than that in the **Hsaltz** structure (35(1)°). The molecule is in the fundamental enol form (Figure 31). The C2–O1 and C7–C8 bond lengths (1.347(5) and 1.437(6) Å) are typical of single bonds and C8–N1 (1.283(5) Å) of a double bond[158](Table 25). Two intramolecular H-bonds are noted in **Ksaltz**. A strong H-bond is present between the alcohol and imine functions (O1-H1···N1 1.76(5) Å), which is highly similar to the intramolecular H-bond observed in **Hsaltz**. A soft intramolecular H-bond is also observed between a nitrogen of the tetrazolate ring and the hydrogen of the imine function (C8–H8···N2 2.49 Å) (Table 26), which was not present in **Hsaltz** because of the large dihedral angle. Crystal packing is clearly directed by ionic interactions between potassium and tetrazolate ions. The structure is packed in planes: a stack of ionic planes and organic planes with salicyl and imine moieties as observed in Figure 31. Potassium ions are present within disorganized atomic spheres and no clear geometric environment can be derived (Table 25). The closed packing is not only

stabilised by ionic interactions but also by strong π-π stacking interactions between the imine group and the salicyl ring ($d_{inter\ planes}$ = 3.694(2) Å) and between the imine group and the tetrazolate ring ($d_{inter\ planes}$ = 3.504(2) Å) (Table 27).

Wavelength and time dependent Kubelka-Munk spectra of Hsaltrz, Habs, Hsalphen, Hsaltz, Ksaltz related to macroscopic considerations

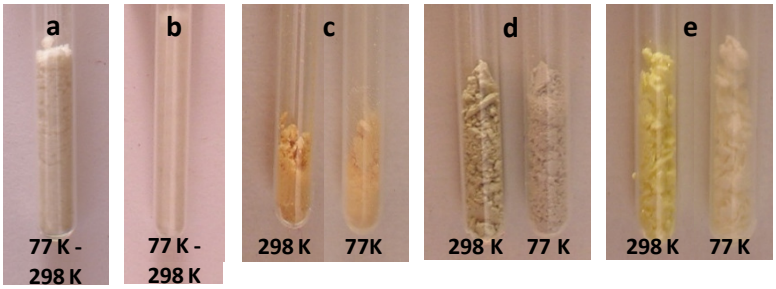

Figure 32 Photograph of powders of **Hsaltrz** (a) and **Habs** (b) over the temperature range 298–77 K and of **Hsalphen** (c), **Hsaltz** (d) and **Ksaltz** (e) at 298 and 77 K. Thermochromism is identified for c, d (very weak) and e (strong).

As shown in Figure 32, **Hsaltrz** and **Habs** remain white over the whole investigated temperature range (298–77 K). In contrast, **Hsalphen**, **Hsaltz** and **Ksaltz** exhibit moderate to strong thermochromism upon cooling to 77 K. **Hsalphen** has a yellow/orange coloration that evolves from dark to light orange when the temperature is decreased. **Hsaltz** is only slightly thermo-sensitive. Its colour varies from very pale yellow at room temperature to white at liquid-nitrogen temperature. In contrast, **Ksaltz** clearly changes its colour: the sample is yellow at room temperature and turns to white at low temperature. Colour difference between **Hsaltz** and **Ksaltz** is clearly distinguished by naked eyes at room temperature.

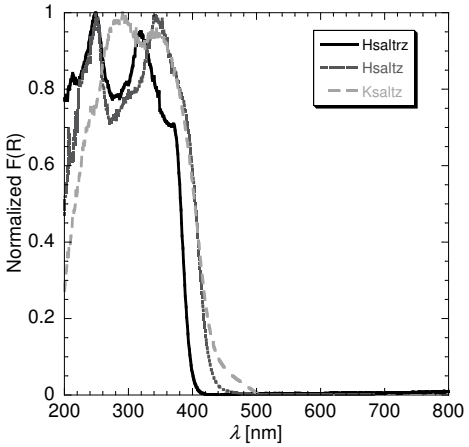

Figure 33 Kubelka-Munk spectra at 298 K of **Hsaltrz**, **Hsaltz** and **Ksaltz**.

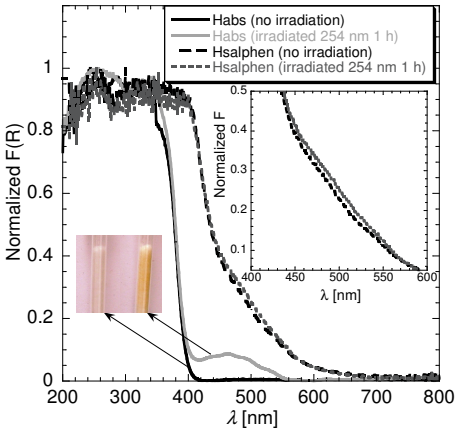

Figure 34 Diffuse reflectance spectra of **Habs** and **Hsalphen** before and after UV irradiation. Photochromism is clearly identified for **Habs**. The inset in Figure 34 reveals weak photochromism for **Hsalphen** at 298 K.

All compounds were analyzed by diffuse reflectance spectroscopy as pure solid powder samples[196] to avoid matrix and environment effects that are known to intensively modify the optical properties of *N*-salicylidene aniline derivatives.[14, 56, 104-106, 108-113, 197]

Figure 33 shows the diffuse reflectance spectra of **Hsaltrz**, **Hsaltz** and **Ksaltz**. A bathochromic shift is observed from **Hsaltrz** to **Hsaltz** and **Ksaltz**. **Hsaltrz** only absorbs in the UV range (below 400 nm). This band is typical of the enol form, which is largely predominant as described in the crystallographic section. In **Hsaltz**, the enol band is shifted by approximately 18 nm to lower energies (an intense band is noted to approximately 430 nm), which leads to the slightly yellow coloration of the product. No band from the keto forms is observed. The colour difference between **Hsaltz** and **Ksaltz** is ascribed to the presence of a band with a maximum in the visible range of the spectrum at approximately 460 nm for **Ksaltz**. This band is typical of the *cis*-keto form of the molecule. **Hsaltrz**, **Hsaltz** and **Ksaltz** are observed to be non photochromic at room temperature. Indeed, irradiation at 254 nm for 1 h does not lead to modification of the Kubelka-Munk spectra.

Figure 34 shows the Kubelka-Munk spectra of **Habs** and **Hsalphen**. **Habs** presents an intense band in the UV range, a feature that fits with the white colour of the compound. Irradiation of the sample at 254 nm during 1 h leads to a clear spectral change in the visible range. A new maximum is noted at 465 nm and is attributed to the formation of a photo-induced meta-stable form: the *trans*-keto isomer.[68] The absence of the *cis*-keto form is assumed for this compound. For **Hsalphen**, an unresolved intense band in the UV range of the spectrum is noted with a bathochromic shift of approximately 50 nm. A second broad band is observed in the visible (maximum unresolved at approximately 450 nm) and is attributed to the *cis*-keto form. Irradiation at 254 nm for 1 h leads to a very slight change in the Kubelka-Munk function intensity around 500 nm, which is attributed to the formation

of the *trans*-keto isomer. The increase in the *trans*-keto band is less intense in **Hsalphen** than in **Habs** but is still detected with the naked eye.

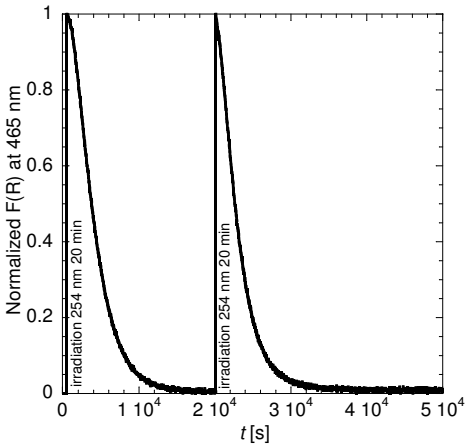

Figure 35 Time dependence of the Kubelka-Munk function (F) of **Habs** at 465 nm, showing the reproducible thermal relaxation of the meta-stable *trans*-keto form.

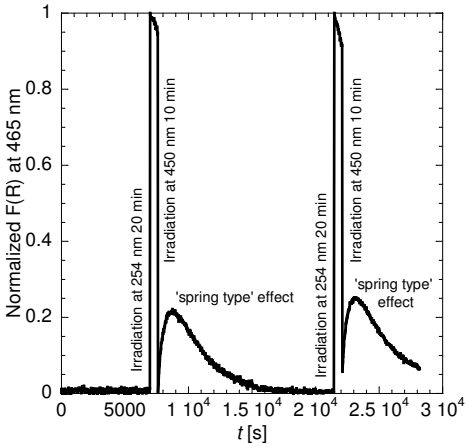

Figure 36 Time dependence of the Kubelka-Munk function (F) of **Habs** at 465 nm, showing the reproducible photo-chemical relaxation of the meta-stable *trans*-keto form leading to an unexpected "spring-type" effect.

Thanks to the clear spectral change under UV irradiation of **Habs**, a study of the thermal relaxation of the system in the *trans*-keto form was conducted by using time dependent diffuse reflectance spectroscopy. Figure 35 shows the evolution of the Kubelka-Munk function at 465 nm, which is near the band maximum of the *trans*-keto form (Figure 34). Irradiation at 254 nm for 20 min induces a large increase in F. After stopping the irradiation, leading to rapid thermal relaxation, complete recovery of the initial value in approximately 4 h is observed. This cycle is fully reproducible, as shown in Figure 35. The relaxation appears to be complicatedd and contains more than one chemical relaxation pathway. Attempts to fit this curve with an exponential function failed. The photo-isomerization process is also photo-chemically reversible, as shown in Figure 36. After photo-excitation at 254 nm and thermal relaxation over 10 min, illumination at 450 nm induces a fast return to the initial F value (Figure 36). Afterwards, an unexpected "spring-type" effect is observed without further stimulus. Over a few minutes, the signal increased to approximately 20% of the maximum value reached. The system reacts spontaneously to the energy flow induced by the second irradiation by trying to return to the meta-stable state. After this abnormal increase, a subsequent thermal relaxation of the *trans*-keto form is observed.

Fluorimetry of Hsaltrz, Habs, Hsalphen, Hsaltz and Ksaltz

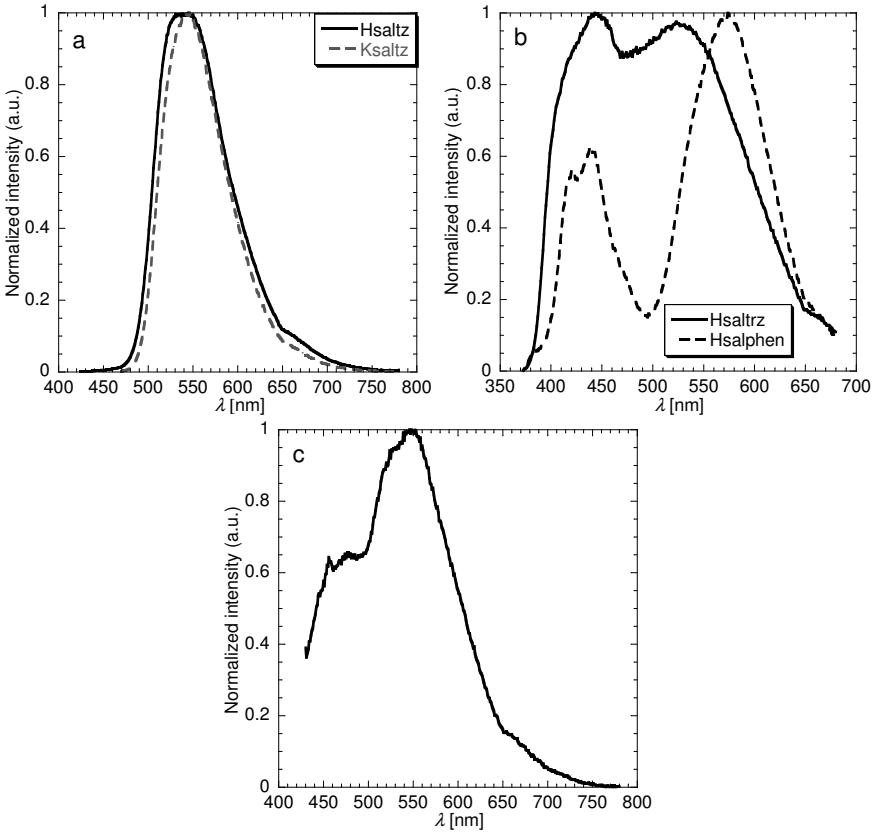

Figure 37 Solid-state emission spectra at 298 K of (a) **Hsaltz** and **Ksaltz** at 400 nm (b) **Hsaltrz** and **Hsalphen** at 350 nm and of (c) **Habs** at 400 nm.

Table 4 Emission maximum wavelengths [nm] of **Hsaltz**, **Ksaltz**, **Hsaltrz**, **Hsalphen** and **Habs**. The excitation wavelengths are 350 nm for **Hsaltrz** and **Hsalphen** and 400 nm for **Habs**, **Hsaltz** and **Ksaltz**.

λ [nm]	**Hsaltz**	**Ksaltz**	**Hsaltrz**	**Hsalphen**	**Habs**
λ^1_{max}	536	540	523	569	544
λ^2_{max}	-	-	441	438	476
λ^3_{max}	-	-	-	420	-

Fluorimetry was used to study energy levels involved during the thermo- and photo-induced processes. Analyses were conducted on pure solid powder samples. Figure 37a shows the emission spectra at 400 nm of **Hsaltz** and **Ksaltz**. One intense emission is observed, centred at 536 nm for **Hsaltz** and at 540 nm for **Ksaltz**, which is assigned to the emission of the excited *cis*-keto* form (Table 4). Thus, the two compounds seem to have very similar emission properties. Figure 37b presents the emission spectra of **Hsaltrz** and **Hsalphen** at 350 nm, which are clearly different. More than one contribution is noted. A first intense emission band, centred at 523 nm and 569 nm for **Hsaltrz** and **Hsalphen**, respectively, is attributed to the radiative relaxation of the excited *cis*-keto* form (Table 4). Thus, a shift of this band is clearly noted between **Hsaltrz** and **Hsalphen**. A second band is observed in both spectra at very narrow wavelengths, 441 and 438 nm for **Hsaltrz** and **Hsalphen**, respectively (Table 4). This emission is attributed to the radiative relaxation of the excited enol* form. Finally, it is important to notice that a third emission contribution is only observed in **Hsalphen**, centred at 420 nm, which is believed to be a radiative relaxation of an enol form in a more relaxed conformation (Table 4). Figure 37c represents the emission spectrum of **Habs** at 400 nm. The main emission band noted at 544 nm is attributed to the excited *cis*-keto* radiative relaxation. A second major contribution is observed at 476 nm (Table 4). This less-intense band could originate from three excited molecules: the enol form, a more relaxed *cis*-keto form or the molecule in an intermediate state as described in the next section. Unfortunately, we are not able to distinguish between these three molecules because of the proximity or the superposition of some absorption bands. It is important to notice that in all spectra (**Hsaltrz**, **Habs**, **Hsalphen**, **Hsaltz** and **Ksaltz**), a low emission is observed at approximately 650 nm that cannot be

assigned with confidence. The origin of this emission could be the radiative deexcitation of either an excited *cis*-keto form with a different conformation or the excited *trans*-keto* form.

Computational study of the photo-isomerisation

Isolated molecules

In order to gain a better understanding of factors that control the intriguing optical properties of **Hsalphen** and **Habs**, we have investigated their photo-isomerization by the same computational approach than the one developed in the previous chapter for the *N*-salicylidene aminopyridines. Firstly, we have examined the enol, *cis*-keto and *trans*-keto equilibria for isolated **Hsalphen** and **Habs** molecules in the ground state (GS) and in the first singlet (S^1) and the first triplet (T^1) excited states. Table 5 reports the computed relative energy of the different species and the activation barrier for *cis*-keto/*trans*-keto isomerization in the respective states. The energy profiles for this latter step are depicted in Figure 38.

Table 5 Calculated energies (in kcal/mol relative to enol) for **Habs** and **Hsalphen** as isolated molecules.

		Habs	**Hsalphen**
GS	Enol	0,0	0,0
	Cis-keto	11.3	7,6
	TS[a]	30.0	43.5
	Cyclised	18.1	-
	TS[b]	0.1	-
	Trans-keto	16.8	16.5
S^1	Enol	92.1	84.4
	Cis-keto	83.8	81.3
	TS[a]	16.9	21.0
	Trans-keto	88.5	89.2
	cyclised	-	-
T^1	Enol	55.6	44.6
	Cis-keto	49.7	49.0
	TS[a]	34.2	38.6
	Trans-keto	51.6	43.9
	cyclised	-	-

[a] Transition state for *cis*-keto to cyclised rearrangement. [b] Transition state for cyclised to *trans*-keto rearrangement.

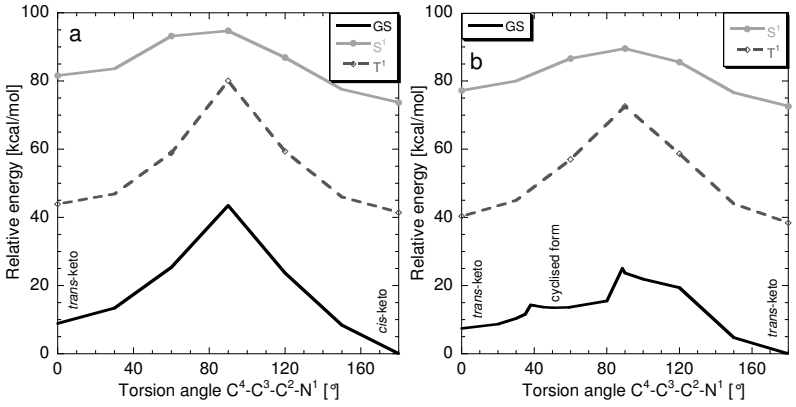

Figure 38 Calculated energy evolution for the ground state (GS) and for the first singlet (S^1) and first triplet excited states (T^1) during the photo-isomerization of **Hsalphen** (a) and **Habs** (b). The torsion angle C4–C3–C2–N1 is given relative to Scheme 9-Scheme 13.

These results reveal that, in both cases, the proton transfer step (enol to *cis*-keto) is energetically disfavoured in the ground state and favoured in the first singlet and first triplet excited states.[198] Interestingly, the proton transfer in the GS for **Habs** is significantly more endothermic (11.3 kcal/mol) than for **Hsalphen** (7.6 kcal/mol) or for previously studied aminopyridines derivatives (7–9 kcal/mol) (see previous chapter). This could account for the absence of thermochromism in **Habs**, whereas all the other considered molecules, except **Hsaltrz**, show thermochromism.

The computed activation barrier for *cis*-keto to *trans*-keto isomerization indicates that, for both molecules, photo-isomerization must take place through the S^1 state (as described in previous chapter) (Table 5, Figure 38). For **Hsalphen**, the activation barrier in the S^1 state (21.0 kcal/mol) nicely corresponds to those of *N*-salicylidene aminopyridine derivatives (20–21 kcal/mol) (see previous chapter), whereas in the case of **Habs** it is much lower (16.9 kcal/ mol). This result supports the observation of

photochromism for these molecules. It is interesting to note that the energy profile for photo-isomerization of **Habs** in the ground state unexpectedly reveals the presence of an intermediate in the pathway to the *trans*-keto form (Figure 38 and Figure 39). Formation of a cyclised intermediate can be accounted for by the developing zwitterionic character of **Habs** (heterolytic breaking of the C7–C8 double bond) with rotation (see details in the experimental section). Indeed, the presence of a nucleophilic nitrogen atom (N22) in this case allows addition of this latter onto the developing positive charge on C7, which is rapidly followed by addition of the phenolic oxygen (O14) onto the pyridine ring (C23) to form a six-member ring (Figure 39b). This cyclised intermediate can then lead to the *trans*-keto form through a very low activation barrier (0.1 kcal/mol), which suggests that the equilibrium between these two forms must be thermally accessible. The influence of this new cyclised form on the experimental results will be discussed in the next section. Note that, even if this mechanism allows a low activation barrier in the GS (lower than that for **Hsalphen** or aminopyridine derivatives), no thermochromism upon heating is observed for this compound (≈100 °C).

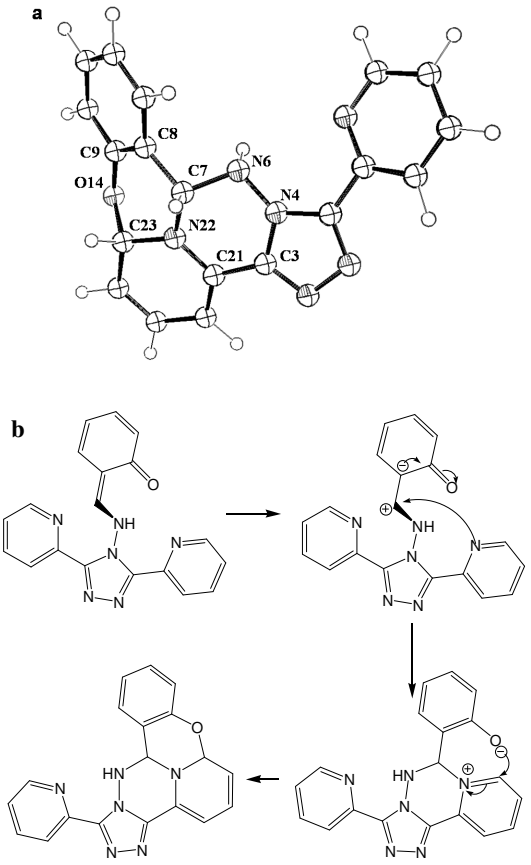

Figure 39 (a) Optimized structure of the cyclised form of **Habs**. (b) Suggested mechanism for the formation of the cyclised form involving a zwitterionic form of **Habs**.

Influence of the crystal packing

Table 6 Calculated energies (in kcal/mol relative to enol) for **Habs** and **Hsalphen** as molecules in their crystal packing.

		Habs	**Hsalphen**
Rel. E_{stab}	Enol	0	0
	Cis-keto	-1.6	2.6
	TS[a]	-5.8	-7.2
	Trans-keto	*undetermined*	2.5
	TS[b, c]	-3.5	-
	Cyclised [c,d]	-5.5	-

[a] Transition state for *cis*-keto to cyclised rearrangement. [b] Transition state for cyclised to *trans*-keto rearrangement. [c] Optimisation was performed in the ground state. [d] Coordinates of N1 were frozen during optimisation.

Because of the expected importance of crystal packing on the photochromic properties of **Habs** and **Hsalphen**, we also investigated, in collaboration with Prof. R. Robiette (UCL), the *cis*-keto/*trans*-keto isomerization by computational means taking in account a model of the crystal packing obtained by single-crystal X-ray diffraction analyses (see Figure 28 and Figure 29). The influence of crystal packing on the photo-isomerization was probed by estimating the relative stabilization induced by placing the different species in their crystal (Table 6).[199] Obtained stabilization energies (from 0 to 7.2 kcal/mol) indicate that although the packing is closed, due to the strong π-π stacking network, it does not prevent isomerization. Analysis of the transition-state structure shows that, as previously observed for *N*-salicylidene aminopyridine derivatives, the preferred mechanism for isomerization resembles the pedal motion of a bicycle. In both cases (although to a larger extent for **Hsalphen**), the TS structure is better stabilised by crystal packing than for the *cis*-keto form. This means that

crystal packing should lead to an activation of the isomerization, which is in good agreement with the observed photochromism at room temperature.

Effect of the chemical substitution on Hsaltrz

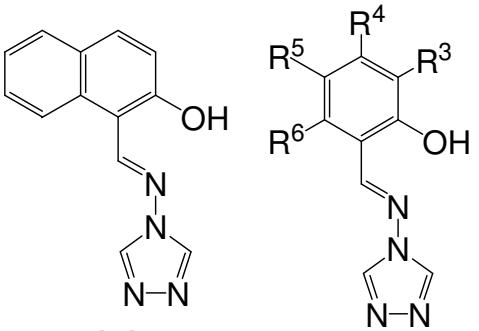

naphsaltrz

Clsaltrz : R^3, R^4 and R^6 = H, R^5 = Cl
Brsaltrz : R^3, R^4 and R^6 = H, R^5 = Br
3OHsaltrz : R^4, R^5 and R^6 = H, R^3 = OH
4OHsaltrz : R^3, R^5 and R^6 = H, R^4 = OH
34OHsaltrz : R^5 and R^6 = H, R^3 and R^4 = OH
omsaltrz : R^4, R^5 and R^6 = H, R^3 = OCH_3

Scheme 14 Molecular scheme of **Clsaltrz**, **Brsaltrz**, **3OHsaltrz**, **4OHsaltrz**, **34OHsaltrz**, **omsaltrz** and **naphsaltrz** (**Rsaltrz**). **naphsaltrz** is considered as a derivative with a second aromatic ring as substituent.

In order to probe the effect of chemical substituents on the structural and optical properties of **Hsaltrz**, a group of molecules (named **Rsaltrz**) was prepared, in collaboration with Alice Bargibant,[200, 201] by changing the R moieties on the salicyl ring as shown in Scheme 14.

The presence of substituents leads to drastic change in the crystal structures as shown by powder X-ray diffraction patterns (Figure 40). Thus, R groups may influence the crystal packing by steric effect but also by the formation of a new supramolecular network involving the substituents atoms (additional H bonds, π-π stacking, C-H···π interactions, halogen···halogen interactions, etc). Nevertheless, the crystal structures of **Rsaltrz** molecules are unknown except for **Brsaltrz**.[202] The crystals growing was then attempted and reached for **naphsaltrz** and **3OHsaltrz** by diffusion of

diethylether into a methanol solution of these molecules. However, although a large number of crystallisation attempts with various conditions were carried out, the quality of these crystals was not good enough for X-ray diffraction.

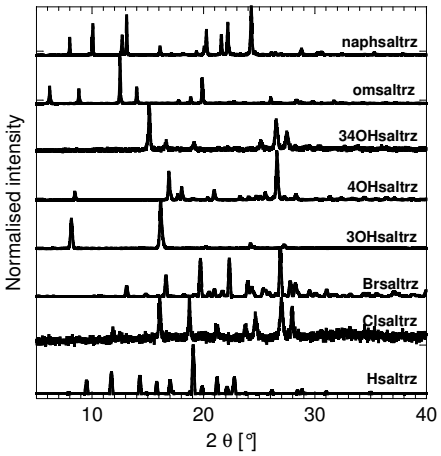

Figure 40 X-ray diffractograms of powders of **Hsaltrz**, **Clsaltrz**, **Brsaltrz**, **3OHsaltrz**, **4OHsaltrz**, **34OHsaltrz**, **omsaltrz** and **naphsaltrz**.

In addition to a crystal structure change, the substituents have necessarily an electronic influence (by inductive and mesomeric effect) which can have an impact on the optical properties of materials and thus on the shape of the diffuse reflectance spectra. Kubelka-Munk spectra were thus recorded at 298 K for all compounds. As shown in Figure 41, the large band observed in the UV range and attributed to the enol forms of **Rsaltrz**, weakly shifts following the nature of the substituents. Indeed, this signal appears from UV to 391 nm (for **omsaltrz**), 398 nm (for **4OHsaltrz**), 408 nm (for **3OHsaltrz**) and 410 nm (for **Clsaltrz**, **Brsaltrz** and **3OHsaltrz**). This evolution was expected but remains not predictable because more than one parameter

(electronic) is changed after substitution (crystal structure, molecular conformation, supramolecular network, etc).

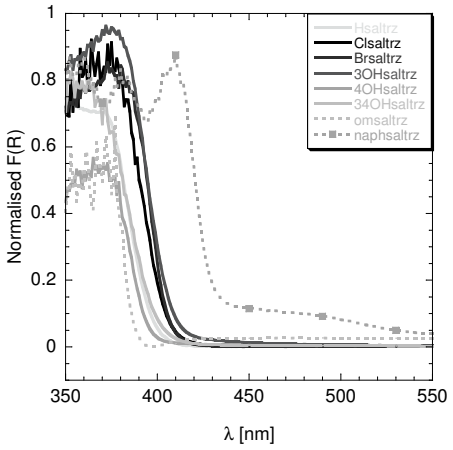

Figure 41 Diffuse reflectance spectra of **Hsaltrz**, **Clsaltrz**, **Brsaltrz**, **3OHsaltrz**, **4OHsaltrz**, **34OHsaltrz**, **omsaltrz** and **naphsaltrz** showing the influence of the substituents on the position of the enol band and on the presence of the *cis*-keto band for **naphsaltrz**.

As for **Hsaltrz**, the derivatives **Clsaltrz**, **Brsaltrz**, **3OHsaltrz**, **4OHsaltrz**, **34OHsaltrz** and **omsaltrz** spectra present only the enol band, and no keto band is observed in the visible part of the spectra. It could be explained following two hypotheses: 1/ **Rsaltrz** derivatives present a molecular conformation similar to **Hsaltrz** where the intramolecular H-bond between the alcohol and imine functions is broken and where the tautomerisation from the enol to the *cis*-keto form is thus not possible in the ground state; 2/ the *cis*-keto form of **Rsaltrz** is to high in energy in comparison to the enol form and the tautomerisation enol/*cis*-keto is not thermally accessible as observed for **Habs**. Crystal structures are necessary to conclude. In **naphsaltrz**, in addition to the enol band, a second signal, centred at 407 nm, is observed in the visible part of the spectrum (Figure 41). This band can be

attributed to the presence of the *cis*-keto form. Moreover, a broad and weak signal is also observed between 430 and 530 nm. It could take its origin in the presence of an impurity (present only as trace on the basis of the good results obtained by the elementary analyses and NMR) or a weak amount of inactive *trans*-keto form which could have been trapped in the solid compound during the synthesis.

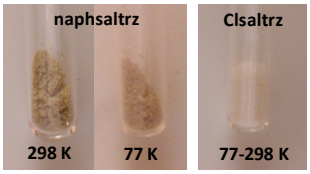

Figure 42 Photograph of powder samples of **naphsaltrz** and **Clsaltrz** in the temperature range 77-300 K showing the very weak thermochromism of **naphsaltrz** and the white colour of other **Hsaltrz** derivatives as discussed in the text.

As expected because of the white colour of the major part of **Rsaltrz** compounds, only **naphsaltrz** seems to be very weakly thermochromic (from yellow at room temperature to pale yellow at 77 K) (Figure 42) while other **Rsaltrz** remain white over the whole temperature range (Figure 42). Moreover, no room temperature photochromism was observed for **Rsaltrz**. Light irradiation of these materials does not lead to any diffuse reflectance spectra change at room temperature.

Discussion

Novel, nitrogen-rich *N*-salicylidene aniline derivatives have been synthesized. Each molecule has been selected to promote a given supramolecular interaction (intra- or intermolecular H-bonds (**Hsaltrz** and **Hsaltz**), π-π stacking (**Habs** and **Hsalphen**), ionic interaction (**Ksaltz**)) that allows their optical properties to be tuned.

Hsaltrz is distinguished from other *N*-salicylidene aniline derivatives thanks to a novel molecular geometry. Complete rotation of the salicyl ring leads to breakage of the intramolecular H-bond between the alcohol and imine moieties and allows the formation of supramolecular double chains with π-π stacking interactions. Thus, a crystal-directing effect of the electron-rich triazole ring is effective. This feature associated with phenolic ring rotation leads to a large change in the optical properties because the prototropic phenomenon is no longer thermally accessible. Photochromism at room temperature is also quenched because the molecular geometry and packing do not allow the photo-isomerization to proceed.

Habs could be seen as a derivative of **Hsaltrz**, where the triazole ring is isolated thanks to two pyridine rings. The intermolecular H-bond between the triazole rings in **Hsaltrz** is no longer possible and thus no rotation of the salicyl ring is observed. However, the presence of triazole and pyridine rings linked to each other leads to a close molecular packing directed by the formation of strong π-π stacking interactions. Interestingly, the close crystal packing made with highly planar molecules is not sufficient to properly predict the optical properties of **Habs**, because, despite the fact that it is expected to be thermochromic following the classification of Ogawa,[68, 89] it is exclusively photochromic. This intriguing situation was met in the case of *N*-salicylidene aminopyridines discussed in the previous chapter. Our calculations suggest that this unexpected absence of thermochromism associated with an absence of coloration of the compound in the whole studied temperature range (77–400 K), which is observed for the first time for this class of molecules, could be due to a higher reaction energy (more endothermic) for proton transfer in the ground state. On the other hand, in

the first singlet excited state, the proton transfer is found to be exothermic, as for other studied derivatives, and the barrier to *cis*-keto/*trans*-keto isomerization is consistent with the observed photochromism at room temperature.

Kinetic study of the thermal relaxation of the photo-induced meta-stable *trans*-keto form indicates that the relaxation pathway is very complex. Our computational calculations have revealed the presence of a cyclised intermediate on the energy profile of **Habs** (see Figure 38). This intermediate is predicted to be in equilibrium with the *trans*-keto form through a very low activation barrier. This new molecular scheme allows a rationalization of the complex thermal relaxation kinetics and in particular the unprecedented 'spring-type' effect observed during the photochemical reversibility study to be proposed (see Figure 36). Figure 43a suggests a schematic evolution of the population of the enol, the cyclised and the *trans*-keto forms during each step observed in Figure 35. We assume that the irradiation at 254 nm (step 1) leads to a large increase in the *trans*-keto form population and the formation of a small amount of the cyclised form. During the first minutes of the relaxation (step 2), the cyclised form rapidly relaxes to the *trans*-keto form. The input of the *trans*-keto form into the system slightly compensates for the thermal relaxation of this form to the enol form and then modifies the shape of the thermal relaxation from a normal exponential to a curve as observed in Figure 35. Finally, during the last step (step 3), normal kinetic relaxation from the *trans*-keto to the enol form is observed. The unexpected 'spring-type' effect can also be thought by a similar reasoning (Figure 43b). Although steps 1 and 2 are the same as those described in Figure 43a, irradiation at 450 nm (step 3) leads to a zeroing of

the *trans*-keto form population, but we assume that a significant population of the cyclised form remains present. A small amount of *trans*-keto form could be then reformed by relaxation of the cyclised form after a few minutes without any external stimulus (step 4), as observed in the experimental data (see Figure 36, 'spring-type' effect). Finally, the *trans*-keto form population then relaxes to the enol form to return to the initial situation (step 5).

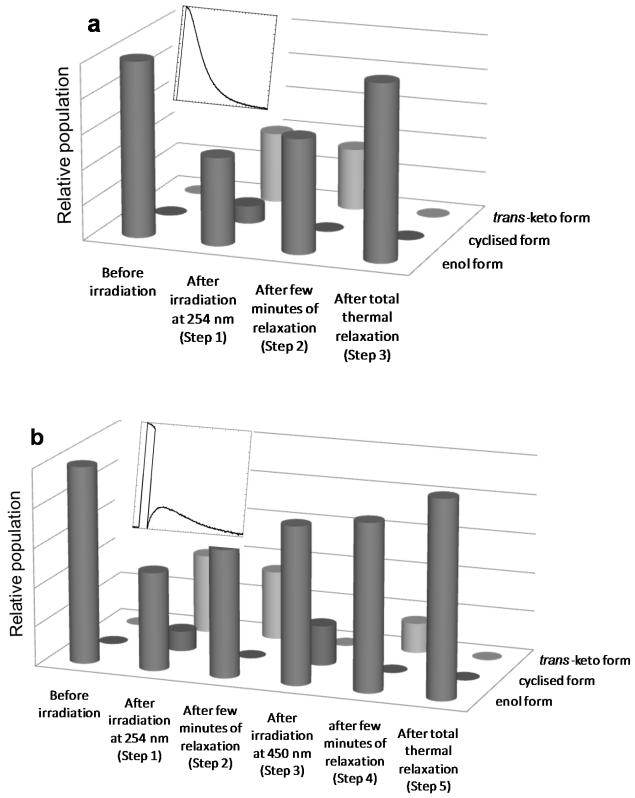

Figure 43 (a) Suggested evolution of the population of the enol, cyclised and *trans*-keto forms of **Habs** during each step of the thermal relaxation study (see Figure 35) and of the photo-chemical relaxation study (b) (see Figure 36). Populations have been fixed arbitrarily.

Hsaltz is closely related to **Hsaltrz**. The tetrazolate ring is indeed more electron rich than a triazole ring, but it contains an N–H moiety that has an important crystal packing directing effect. Indeed, crystal packing is directed by the formation of an intermolecular H-bond between the tetrazole rings, which replaces the intermolecular H-bond between the OH function and the triazole ring noted in **Hsaltrz**. We observe the formation of supramolecular double chains made by π-π stacking interactions with highly twisted molecules. Because of the absence of stacking of salicyl rings, **Hsaltz** can be classified as an open structure[68] that is typical of photochromic compounds but no photochromism was observed at room temperature with the powder sample of this compound.

Ksaltz is an interesting molecule because of its similarity to **Hsaltz** from an electronic point of view. The main difference between **Hsaltz** and **Ksaltz** originates from the difference in the involved supramolecular interactions. In **Hsaltz**, N–H intermolecular H-bonds appear to be very important in contrast to the ionic interactions present in **Ksaltz**. In addition, the appearance of ions leads to a drastic change in the medium polarisability, which can have a large influence on the photochromic behaviour.[56] Whereas the intramolecular H-bonding between the alcohol and imine functions is similar in both structures, the **Ksaltz** structure contains planar molecules (Φ_1 = 6(1)°) although **Hsaltz** is constituted of highly twisted ones (Φ_1 = 35(1)°). In addition to structural differences and, more precisely, to supramolecular network linkers, the major change between both compounds is observed in absorption optical properties. **Ksaltz** is shown to be strongly thermochromic, whereas **Hsaltz** is only slightly thermochromic. Surprisingly, this difference, associated to stabilization of the *cis*-keto form with respect to the enol form,

is not correlated to a difference in intramolecular H-bonding strength. No change in emission properties is observed between both tetrazole compounds. Finally, **Hsalphen** appears to be similar to **Habs** due to its crystal packing directed by strong π-π stacking interactions. The highly closed structure obtained is typical of thermochromic compounds[89] except that the dihedral angle is large (Φ_1 = 48(1)°). The π-π stacking interactions seem to decrease the photochromism at room temperature but do not quench it. This observation is supported by the height of the energy barrier predicted by our calculations.

Fluorimetry on solid samples is a very interesting method to analyze *N*-salicylidene aniline derivatives because of their strong fluorescence, which allows probing energy levels involved during the photochemical processes. All molecules have a strong emission around 540 nm (from 523 to 569 nm) that can be attributed to the radiative relaxation of the excited *cis*-keto form. **Habs** and **Hsalphen** have more bathochromic emissions, whereas **Hsaltrz** has a more energetic emission (523 nm). This phenomenon can be attributed to the enlarged electronic conjugation generated by the presence of pyridine moieties in **Habs** and of aromatic rings placed side by side in **Hsalphen**. Interestingly, the emission of the enol form appears only in **Hsaltrz** and **Hsalphen** at very narrow wavelengths (438 and 441 nm, respectively).We thus suspect that the optical properties of the enol forms are less affected by described molecular changes than the ones of keto forms. We assume that the presence or the absence of enol emission is controlled by the energy gap between excited enol and *cis*-keto form levels as described in the chapter 1 for the *N*-salicylidene aminopyridines. Indeed, if this gap is large, as predicted by our calculations for **Habs**, excited enol molecules are very

rapidly relaxed to the excited *cis*-keto form by tautomerism, which quenches the enol emission.

Finally, chemical derivation was thought in order to tune the optical properties by changing the electronic density in the organic molecules by inductive and mesomeric effects. Influences of chemical substituents on the shape of the diffuse reflectance spectra were observed (position of the enol band, presence of the *cis*-keto band, thermochromism) but appear to be not predictable and thus not controlled. Indeed, in addition to an electronic impact, the substituents lead also to structural impacts (change of supramolecular network and steric hindrance creation). The combination of these factors competes with the crystal directing effect demonstrated for **Hsaltrz** and prevents the crystal packing control introduced in the first sections of this chapter. Another approach must then be thought in order to tune more efficiently the electronic density in the organic derivatives. In response to this problem, an inorganic approach will be introduced in chapter 5.

Chapter III: Effect of a non aromatic linker on the structural and optical properties of *N*-salicylidene aminopyridines

Introducing remarks

As described earlier, authors have stressed the role of the crystal packing density for the control of photochromism of *N*-salicylidene aniline derivatives because solid state photo-isomerisation requires a significant space in molecular packing.[68] However, we assume that the voids in the crystal can be limited if the organic molecules have a large flexibility thanks to specific molecular architectures. The role of flexibility was briefly considered in the literature but no systematic study was carried out.[93] The aim of this section, realized in collaboration with Pierre-Loïc Jacquemin,[203] is to analyse the influence of the increase of flexibility in *N*-salicylidene aminopyridines by adding a methyl spacer group between salicyl and pyridine rings as suggested in Scheme 15.

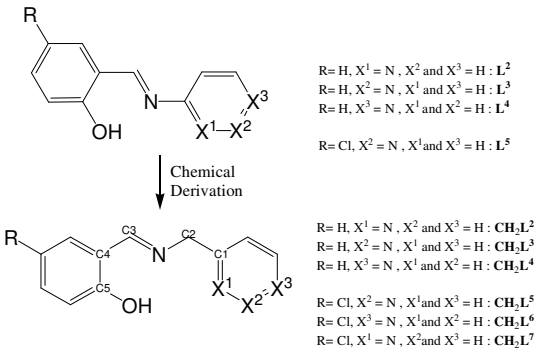

Scheme 15 Molecular scheme of *N*-salicylidene aminomethylpyridines compared to *N*-salicylidene aminopyridines described in chapter 1. The position of methyl spacer group (C2) is clearly identified in the architecture of aminomethylpyridine derivatives.

Syntheses and crystallization methods

The synthesis of aminomethylpyridines derivatives was firstly carried out following reported procedures[204, 204-207] (e.g. reflux in ethanol followed by recrystallisation or solvent free synthesis). Unfortunately, these methods were not adapted because of the very strong sensitivity of such molecules to high temperatures (a very fast degradation was observed) and of the strong difficulties to obtain pure products without salicylaldehyde impurities. Thus, we had to develop a new synthesis procedure with a first step involving a synthesis in refluxing benzene in a Dean-Stark setup. In a second step, the remaining amount of salicylaldehyde, giving rise to a crude yellow oil, was extracted by few sonications in hexane as described in the experimental section. All compounds were obtained in large amount with excellent purity except **CH_2L^7** which will not be discussed in this manuscript.

Because of the thermal instability of these molecules, sublimation crystallisations failed but single crystals of **CH_2L^2** and **CH_2L^5** were obtained by slow evaporation of hexane solutions. Interestingly, we have also obtained single crystals of **CH_2L^3** by the same method demonstrating the same polymorph than the reported structure.[204]

Crystal structures study[‡‡]

N-salicylidene 2-amino-methylpyridine (CH_2L^2)

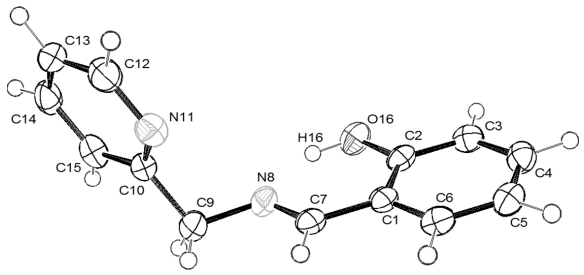

Figure 44 ORTEP view of the asymmetric part of the unit cell of $\mathbf{CH_2L^2}$, showing 50% probability displacement ellipsoids.

The crystal structure of $\mathbf{CH_2L^2}$ was solved at 125 (2) K. It crystallizes in monoclinic space group $P2_1/n$ (Table 28). The bond lengths C2-O16 (1.352 (2) Å) and C1-C7 (1.458 (2) Å) indicate single bonds (Table 31) whereas a double bond is found for C7-N8 with 1.278 (2) Å which indentifies the enol form (Figure 44).[158] The dihedral angle between aromatic rings (Φ = 81(1)°) is very high and far from the angle range observed for aminopyridines derivatives (Table 31) (5-49°, see chapter 1). It could take its origin from the increase of molecular flexibility induced by the methyl spacer between aromatic rings which implies a large torsion angle Γ of 114(1)° (Table 31). An intramolecular hydrogen bond (O16-H16···N8 = 1.74 (3) Å) (Table 29) between the imine and the alcohol functions is observed with similar parameters than for aminopyridine derivatives (see chapter 1). Two intermolecular C-H···π interactions are also present between H14 and salicyl ring (C1-C2-C3-C4-C5-C6) (d = 2.88 Å) and between H7

[‡‡] Structures were solved by Prof. B. Tinant (UCL).

and pyridine (N11-C10-C12-C13-C14-C15) (d = 2.65 Å) (Table 30). The intermolecular distances are long (~ 6 Å) (Table 31) and the crystal packing can be qualified as an open structure, typical of thermo- and photochromic molecules (Figure 45). [68]

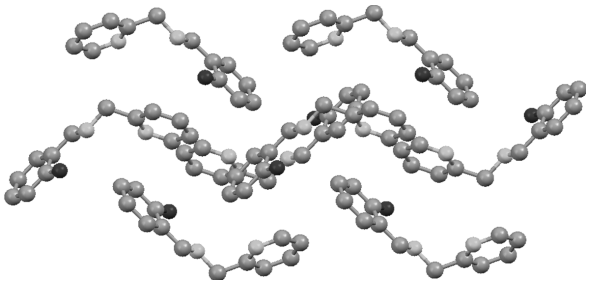

Figure 45 View of the crystal packing of $\mathbf{CH_2L^2}$ along the *c* axis. H atoms were omitted for clarity.

5-chloro-N-salicylidene 2-amino-3-aminomethyl-pyridine (CH_2L^5)

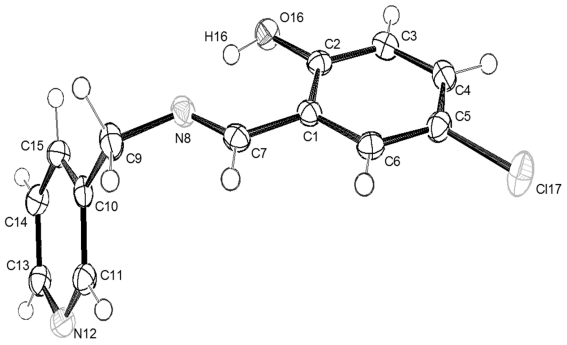

Figure 46 ORTEP view of the asymmetric part of the unit cell of $\mathbf{CH_2L^5}$, showing 50% probability displacement ellipsoids.

The crystal structure of $\mathbf{CH_2L^5}$ was solved at 120(2) K. It crystallizes in monoclinic space group $P2_1/c$ (Table 28). The molecule in the asymmetric part is in its enol form as suggested by the bond lengths N8-C9 (1.279(2) Å)

and C2-O16 (1.354(2) Å) (Table 31 and Figure 46).[158] The molecule is not planar because of the important dihedral angle between the two aromatic rings Φ = 72(1)° (Table 31). An intramolecular hydrogen bond is observed with a O16-H16···N8 distance of 1.81(3) Å which is in the same range than for $\mathbf{CH_2L^{2\text{-}3}}$. A stronger supramolecular network than for $\mathbf{CH_2L^{2\text{-}3}}$, built with one H-bond (involving pyridine atoms), one π-π stacking and two C-H···π interactions, is identified for $\mathbf{CH_2L^5}$ (Table 29 and Table 30) and leads to a closed structure (Figure 47), typical of thermochromic molecules.[68] Hopefully, although we have not obtained single crystals of $\mathbf{CH_2L^6}$ suitable for X-ray diffraction, measurements made on crystalline powders (see experimental part) show the same diffractograms for $\mathbf{CH_2L^5}$ and $\mathbf{CH_2L^6}$. The two molecules are thus isomorphous.

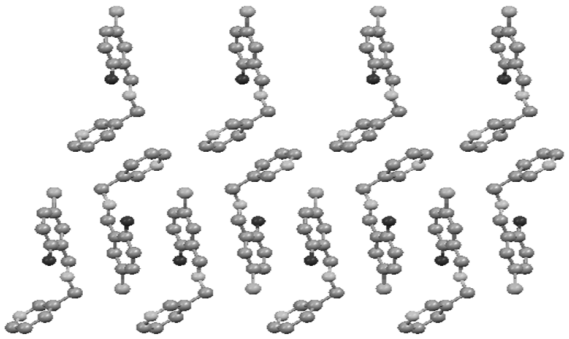

Figure 47 View of the crystal packing of $\mathbf{CH_2L^5}$ along the *b* axis. H atoms were omitted for clarity.

Comparison with the reported crystal structure of *N*-salicylidene 3-aminomethylpyridine (CH_2L^3)

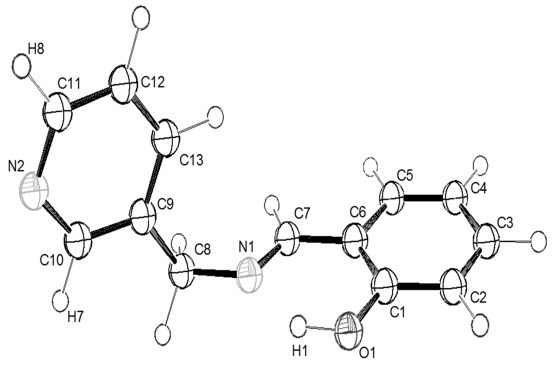

Figure 48 ORTEP view of the asymmetric part of the unit cell of $\mathbf{CH_2L^3}$ [204], showing 50% probability displacement ellipsoids.

The crystal structure of $\mathbf{CH_2L^3}$ was solved at 297 (1) K by Cimerman *et al.*[204] The compound crystallizes in monoclinic space group $P2_1/n$ (Table 28). As $\mathbf{CH_2L^2}$, the molecule is present in the asymmetric part of its unit cell in the enol form (Figure 48) as suggested by the bond lengths listed in Table 31. The dihedral angle between aromatic rings (Φ = 72(1)°) is high in comparison with aminopyridines derivatives (Table 31) (5-49°, see chapter 1) but remains lower than the angles observed for $\mathbf{CH_2L^2}$ and $\mathbf{CH_2L^5}$. A large torsion angle Γ of 112(1)° (Table 31) is also noted thanks to the presence of the methyl spacer group. It is highly similar to the torsion angle observed for $\mathbf{CH_2L^2}$ and $\mathbf{CH_2L^5}$. An intramolecular hydrogen bond (O16-H16···N8 = 1.73 Å) (Table 29) between the imine and the alcohol functions is observed. In addition to a weak supramolecular network, containing only one C-H···π interaction, the intermolecular distances are quite long (~ 6 Å) (Table 31) leading to an open crystal packing (Figure 49), typical of thermo- and photochromic molecules.[68]

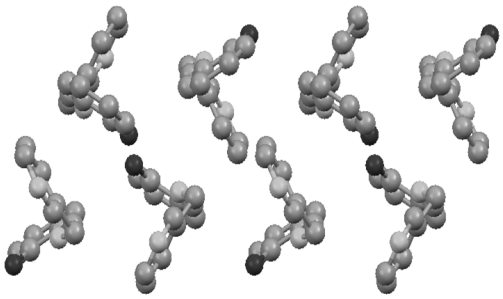

Figure 49 View of the crystal packing of $\mathbf{CH_2L^3}$ along the *c* axis. H atoms were omitted for clarity.

Wavelength and time dependent diffuse reflectance spectroscopy

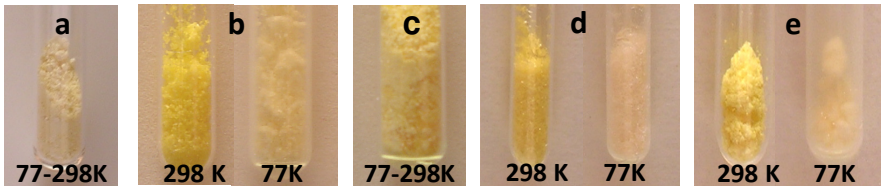

Figure 50 Photograph of powders of $\mathbf{CH_2L^{2,4}}$ (a and c) over the temperature range 298–77 K and of $\mathbf{CH_2L^{3,5\text{-}6}}$ (b, d and e) at 298 and 77 K. Thermochromism is clearly identified for b, d and e.

Although $\mathbf{CH_2L^2}$ and $\mathbf{CH_2L^4}$ are not thermochromic, the crystalline powders of $\mathbf{CH_2L^3}$, $\mathbf{CH_2L^5}$ and $\mathbf{CH_2L^6}$ reveal thermochromism from yellow at room temperature to white on cooling to 77 K (Figure 50). This colour change is due to the thermal enol/*cis*-keto tautomerisation.

Diffuse reflectance spectroscopy was used for all molecules. In each spectrum, a large and intense band, attributed to the enol form, is observed in the UV range (Figure 51). Interestingly, a bathochromic shift (of about 35 nm) of the right limit of this band is noted between $\mathbf{CH_2L^2}$, $\mathbf{CH_2L^6}$ and

CH_2L^5. In the visible, another band is present and attributed to the *cis*-keto form. Although this signal is observed in all spectra, the intensity seems to be different, increasing from **CH_2L^6** to **CH_2L^2**, **CH_2L^5**, **CH_2L^4** and **CH_2L^3**.

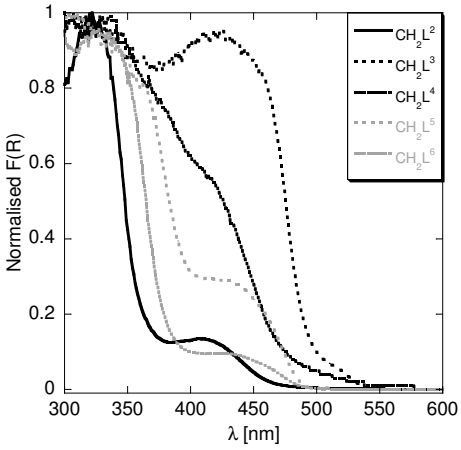

Figure 51 Kubelka–Munk spectra of **CH_2L^{2-6}** at 298 K.

After irradiation at 450 nm of a **CH_2L^3** sample during 5 minutes, a new band appears at 520 nm and can be attributed to the absorption of the *trans*-keto form (Figure 52a). The signal of this meta-stable form is also obtained with irradiation at 365 nm but the intensity attributed to the *trans*-keto population increase is less pronounced (Figure 52a). However, it is difficult to draw conclusion about the efficiency of the irradiation according to the wavelength used because of the lack of information about the quantity of photons delivered by the light source at these wavelengths, the quality of the surface and the molar absorptivity of light. After irradiation at 450 nm of **CH_2L^5** during 5 minutes, a new absorption region above 500 nm, composed by two unresolved bands at 510 and 540 nm, arises (Figure 52b). The presence of these two bands could be attributed to the formation of two different conformations of the *trans*-keto form which are strongly suggested

by the large flexibility given by the methyl group present between aromatic rings and which were never observed before. The increasing of the *trans*-keto signal is more important than in **CH_2L^3**, the photochromism of **CH_2L^5** being apparently more intense than for **CH_2L^3**. Finally, **CH_2L^6** was also observed as photochromic (Figure 52c). After 5 minutes of irradiation at 450 nm, the photo-isomerisation can be observed by the rising of a signal in the *trans*-keto form absorption range. As in **CH_2L^3**, two bands, located at 505 and 530 nm, can be detected showing also the potential presence of two *trans*-keto conformations.

The reversibility of the *cis/trans* isomerisation was checked by time dependent diffuse reflectance spectroscopy. The thermal and photochemical relaxation of the *trans*-keto form of **CH_2L^3** and **CH_2L^6** cannot be analysed by our spectrophotometer because of the too fast thermal relaxation of this form. As shown in Figure 53a, irradiation at 450 nm of **CH_2L^5** during 20 min leads to a large increase of the intensity of the signal of the *trans*-keto form (at 546 nm). The thermal relaxation to the *cis*-keto form is complete after 3600 s. Interestingly, although a exponential kinetic scheme was demonstrated in the case of **L^3** (see chapter 1), no reliable fit can be obtained for the thermo-induced decrease observed in Figure 53a for **CH_2L^5**. The presence of many conformations leading to more than one relaxation pathways is proposed. The reverse photo-switching of the *trans*-keto form can also be reached by irradiating the *trans*-keto band at 546 nm. The cycle can be repeated many times without significant degradation as suggested in Figure 53b.

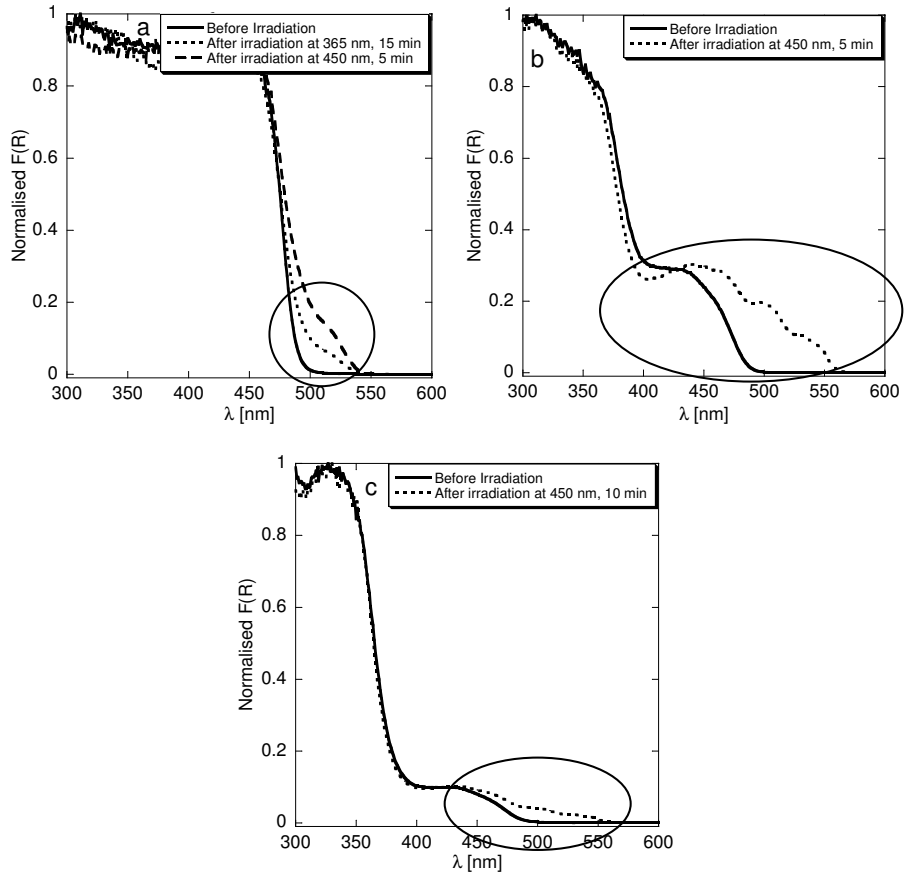

Figure 52 Kubelka–Munk spectra of $\mathbf{CH_2L^3}$ (a) at 298 K before and after irradiation at 365 nm and at 450 nm for 15 min and 5 min, respectively and of $\mathbf{CH_2L^5}$ (b) and $\mathbf{CH_2L^6}$ (c) at 298 K before and after irradiation at 450 nm for 10 min The circle highlights the increase of the *trans*-keto band.

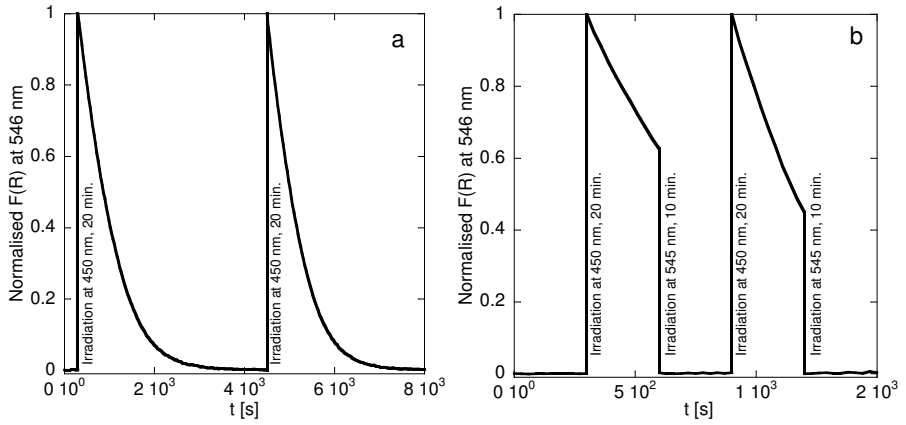

Figure 53 (a) Time dependence of the Kubelka–Munk function (F) of $\mathbf{CH_2L^5}$ at 546 nm showing a fast thermal relaxation of the meta-stable *trans*-keto form. (b) Reversibility of the *cis*/*trans* isomerisation as shown by the evolution of the Kubelka–Munk function (F) at 546 nm with cycles of irradiation of $\mathbf{CH_2L^5}$ at 450 and 545 nm, respectively.

Temperature dependent fluorimetry

Fluorimetry is a very important technique in order to study photochemical processes happening during the photochromism phenomenon. Moreover, using a temperature dependent analyser allow probing thermo-induced modifications in the ground and excited states population. In this section, the emission and excitation modes are presented. In the emission experiments, sketched in Figure 54, the excitation wavelength is locked in the absorption range of a molecule (in Figure 54, the enol form at 350 nm). The emission wavelength is scanned and the spectrum then contains all emissions driven from the excited enol* (enol* → enol: A and *cis*-keto* → *cis*-keto: B). In the excitation mode, the emission wavelength is fixed using information obtained with emission spectra about maximum emission wavelengths. For example, in Figure 54, we focus on the *cis*-keto*→*cis*-keto emission at 550 nm and we scan excitation wavelengths. Excitation spectrum

thus contains two bands corresponding to pathways C (enol→enol*→*cis*-keto*) and D (*cis*-keto→*cis*-keto*) leading to the formation of emitting excited states. We can thus obtain not only information about photochemical processes leading to emission phenomenon but also about the population of the molecules in their different forms as described later in this section.

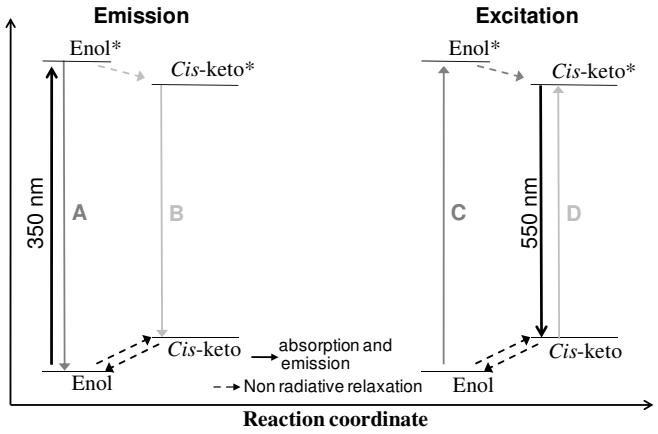

Figure 54 Photochemical processes evidencing two radiative relaxation pathways (A and B) in emission mode at 350 nm and two absorption pathways (C and D) in excitation mode at 550 nm for *N*-salicylidene aniline derivatives.

$CH_2L^{2\text{-}6}$ were first analysed by room temperature fluorimetry. Emission spectra were recorded with excitation wavelengths selected on the basis of maxima observed in diffuse reflectance spectra displayed in Figure 51. Results will be presented following two distinct groups based on the presence or absence of photochromism.

Photochromic molecules (**CH_2L^3** and **$CH_2L^{5\text{-}6}$**) were analysed by emission spectroscopy using excitation wavelengths 370 nm, 430 nm and 520 nm, corresponding to the absorption ranges of the enol, *cis*- and *trans*-keto forms,

respectively (see Figure 53). All spectra present a very similar broad and complicated emission band. In this section, we have decided to only discuss the emission spectra with an excitation wavelength of 430 nm because this excitation wavelength leads to a better resolution (Figure 55).

Three bands can be detected in the emission spectra shown in Figure 55 with emission maxima of approximately 520 nm, 540 nm and 610 nm for **CH_2L^3**, 530 nm, 570 nm and 660 nm for **CH_2L^5** and **CH_2L^6**. A clear influence of the chloride substituent is observed.

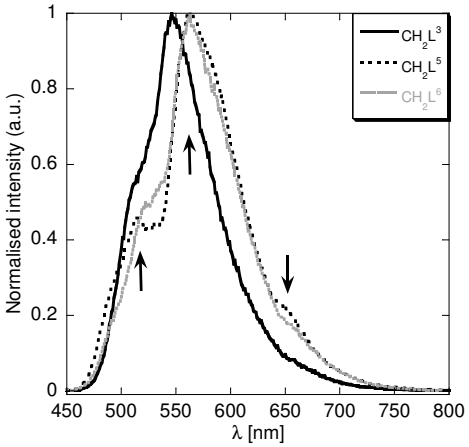

Figure 55 Emission spectra of solid samples of **CH_2L^3** and **CH_2L^{5-6}** at an excitation wavelength of 430 nm at 298 K. The arrows indicate the three emission contributions as discussed in the text.

Excitation spectra were carried out at the maximum emission wavelengths in order to determine the origins of these signals. Excitation spectra of **$CH_2L^{3, 5-6}$** at 520 nm and 540 nm give very similar results (Figure 56a). Two ranges in the excitation spectra are observed. Indeed, a very high intensity is detected from UV to ~ 400-450 nm which can be attributed to the enol form absorption (Figure 56a). This signal seems to present more than one

contribution. It could be due to few electronic transitions of this form. In addition to that, a second excitation range is observed between 450 nm and 500 nm. This band fits well with the signal which was attributed to the *cis*-keto form by diffuse reflectance spectroscopy. Thus, the emissions centred at 520 nm and 540 nm (observed in Figure 55) come from the radiative deexcitation of the *cis*-keto* form (pathway B in Figure 54) which is produced from the absorption of light by the enol (which undergoes then an excited state fast tautomerisation) and the *cis*-keto forms in the ground state.

Excitation spectra at 650 nm (Figure 56b) show also the two contributions discussed in the previous paragraph but a third intense band, centred at λ^{max} ~ 500 nm, is also distinguished. This contribution can be attributed to the absorption of the *trans*-keto form as suggested by the position of the *trans*-keto band in the diffuse reflectance spectrum shown in Figure 56b. The emission at 610 and 660 nm, observed in Figure 55, can then be assigned to the radiative relaxation of the *trans*-keto* form which can be formed through the light absorption of the enol, *cis*- and *trans*-keto forms in the ground state. It is here the first time that the emission of the *trans*-keto form of a *N*-salicylidene anil is clearly observed and attributed.

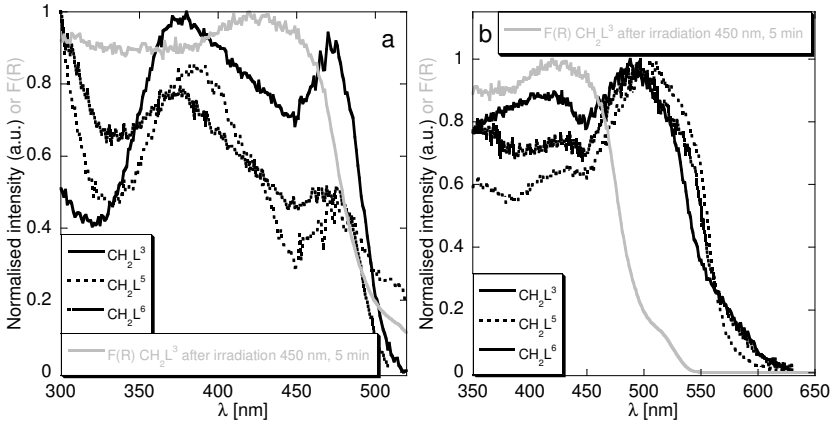

Figure 56 Excitation spectra of solid samples of $\mathbf{CH_2L^3}$ and $\mathbf{CH_2L^{5\text{-}6}}$ at 298 K with emission wavelengths of 540 nm (a) and 650 nm (b). The grey curve represents the Kubelka-Munk spectrum of $\mathbf{CH_2L^3}$ after irradiation at 450 nm during 5 min. The enol, *cis*- and *trans*-keto ranges are observed from UV to ~ 400 nm, from 400 nm to 500 nm and between 500 and 550 nm, respectively.

Similar experiments were done with non-photochromic molecules ($\mathbf{CH_2L^2}$, $\mathbf{CH_2L^4}$). At 400 nm, both spectra are very similar and present a broad signal (Figure 57a). This band seems to be constituted by two contributions at approximately 580 nm and 660 nm for $\mathbf{CH_2L^2}$ and 550 nm and 650 nm for $\mathbf{CH_2L^4}$. The origin of these contributions was analysed by excitation spectra at ~ 600 nm and ~ 650 nm. Interestingly, although the most intense emission peak (around 600 nm) comes from the radiative relaxation of the *cis*-keto form as observed for the photochromic molecules described above, the excitation spectra at 650-670 nm (Figure 57b) show high intensity in the whole visible range studied. Indeed, in addition to a signal between 350 nm and 450 nm, coming from enol and *cis*-keto absorption, an intense band is also noted between 450 nm and 650 nm, centred at 560 nm and 530 nm for $\mathbf{CH_2L^2}$ and $\mathbf{CH_2L^4}$, respectively. This range is typical of the *trans*-keto absorption and we can then conclude that the shoulder observed at lowest

energies in the emission spectra of $\mathbf{CH_2L^2}$ and $\mathbf{CH_2L^4}$ comes from the radiative deexcitation of the *trans*-keto* coming from the absorption of the enol, *cis*- and *trans*-keto forms, as described for the photochromic molecules $\mathbf{CH_2L^3}$ and $\mathbf{CH_2L^{5\text{-}6}}$. This observation is surprising because the absence of photochromism for $\mathbf{CH_2L^2}$ and $\mathbf{CH_2L^4}$ induces the absence of *trans*-keto form in the diffuse reflectance spectra which is however observed by fluorimetry. We assume that, although no photochromism is observed by diffuse reflectance spectroscopy (and by naked eyes), a very little amount of this form is present in the solid and appears to be very fluorescent and then intense in the excitation spectra shown in Figure 57. The origin of the *trans*-keto form could come from the formation of crystalline defects or from a stabilization mechanism yet to be established. A study of the distribution of these species into the crystals could bring some more information about it.

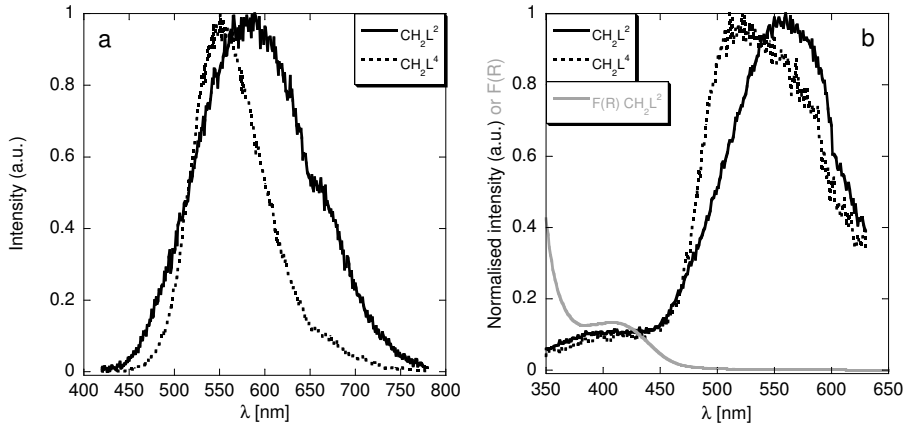

Figure 57 (a) Emission spectra of solid samples of $\mathbf{CH_2L^2}$ and $\mathbf{CH_2L^4}$ at 298 K with an excitation wavelength of 400 nm. (b) Excitation spectra of $\mathbf{CH_2L^2}$ and $\mathbf{CH_2L^4}$ at 298 K with an emission wavelength of 655 nm and 670 nm, respectively. The grey curve represents the Kubelka-Munk spectrum of $\mathbf{CH_2L^2}$. The *cis*- and *trans*-keto ranges are observed from 400 nm to 450 nm and between 450 and 650 nm, respectively.

The influence of temperature on the photochemical pathways leading to the fluorescence was checked by temperature dependent fluorimetry on solids. Indeed, decreasing temperature leads to a strong increase of emission intensity as expected by the decrease of the probability of non radiative relaxation induced by thermal activation.

As shown for example for **CH_2L^5** in Figure 58, in addition to a change in intensity, the broad emission bands indicate more than one contribution arising from the presence of many conformations of enol, *cis*- and *trans*-keto forms in the ground and excited states. The temperature change seems to stabilise certain conformations with respect to others and thus slightly change the shape of emission bands. However, it is not possible at this stage to draw more conclusions about these evolutions. More details about the photophysics of this class of molecules could be obtained by computional means but the large number of molecular conformations brings difficulties and errors in the energy states estimations.

The same experiments were also carried out for the excitation spectra. Indeed, in **CH_2L^3** and **CH_2L^5** spectra with an emission wavelength fixed at 540 nm, corresponding to the *cis*-keto form emission, (Figure 59) a slight decrease of the enol band from UV to ~ 400 nm and a significant increase of the *cis*-keto excitation band between 400 and 500 nm are clearly observed.

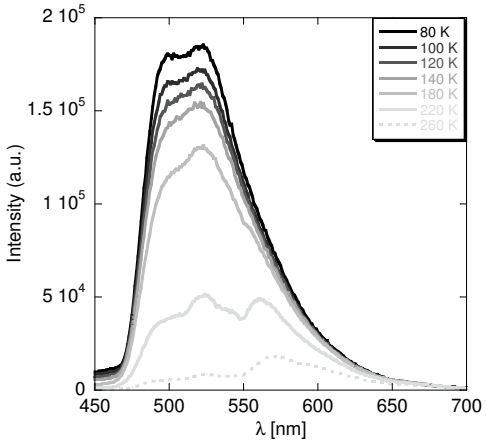

Figure 58 Emission spectra of a solid sample of $\mathbf{CH_2L^5}$ over a 80-260 K temperature range with an excitation wavelength of 400 nm.

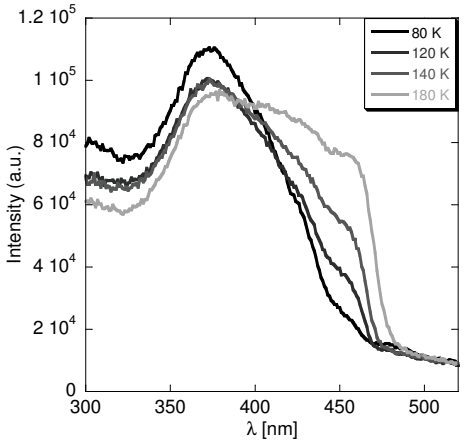

Figure 59 Excitation spectra of a solid sample of $\mathbf{CH_2L^3}$ over a 80-180 K temperature range with an excitation wavelength of 540 nm.

This increase can be interpreted as an increase of *cis*-keto population induced by the thermal tautomerisation. This hypothesis is, indeed, the only one which can explain the *cis*-keto band enhancement because the increase of temperature must enhance the non radiative relaxation pathways and then

decrease emission phenomenon. However, this observation was not checked for **CH_2L^2**, **CH_2L^4** and **CH_2L^6** where the variation of the non radiative relaxation pathways seems to hide the keto/enol tautomerisation. In these cases, the evolution of the intensity of the different bands is either not predictable (intensity increase, stabilisation and decrease) or only shows a decrease with temperature.

Discussion

In this chapter, we have reported five derivatives of *N*-salicylidene aniline. These compounds are closely related to the *N*-salicylidene aminopyridines described in chapter 1 but contain a methyl spacer group between the aromatic rings. The influence of this group was analysed through a detailed structural and optical study.

Three of the five *N*-salicylidene derivatives, **CH_2L^3**, **CH_2L^5** and **CH_2L^6**, are thermo- and photochromic in contrast to **CH_2L^2** and **CH_2L^4** which are not switchable. Surprisingly, it contradicts the previous study of **CH_2L^2** which claimed photochromism of this molecule.[205] Impact of the methyl spacer group on photochromism was difficult to predict because two factors must be taken in account. Indeed, in addition to the loss of electronic conjugation, the CH_2 group also provides more flexibility to the molecules. It leads to new molecular conformations, supramolecular interaction networks and crystal packing as described in the crystal structures section. In case of aminomethylpyridines, the crystal packing seems to have less influence on photochromism. It could be due to the increase of the degree of freedom induced by the methyl spacer group which decreases steric hindrance disturbing the pedal motion during the photo-isomerisation.[68] Thus,

contradictions with literature also appear in the analysis of the structure-optical properties relationship.[68]

Diffuse reflectance spectroscopy combined with solid phase fluorimetry also gives unexpected information about the formation and properties of the *trans*-keto form. Indeed, all *N*-salicylidene aminomethylpyridines show, for the first time, a low energy emission which can be clearly attributed to the radiative deexcitation of the *trans*-keto* form. Absence of previous observation of this emission in literature could be explained by either the lack of resolution of solid state fluorimetry and the proximity of the *cis*-keto and *trans*-keto emission bands or by the absence of radiative relaxation of *trans*-keto* in other *N*-salicylidene aniline derivatives. The *trans*-keto form emission is more intense in the case of non-photochromic molecules $\mathbf{CH_2L^2}$ and $\mathbf{CH_2L^4}$, suggesting that formation of *trans*-keto* form from *cis*-keto* from is highly favourable. It suggests that, although *trans*-keto form is produced by light irradiation in both photochromic and non photochromic molecules, this form is only stabilised in the ground state in the first class of molecules. However, even in photochromic molecules, the photo-produced *trans*-keto form appears to be less stabilised as demonstrated by the very fast thermal relaxation of $\mathbf{CH_2L^3}$ and $\mathbf{CH_2L^{5\text{-}6}}$. It leads us to conclude that the absence of photochromism can be driven by two different factors as follow. As previously discussed in chapter 1, the photo-isomerisation in the excited state from the *cis*- to *trans*-keto* forms can be blocked by a too large activation barrier (see barrier 1 in Figure 60) (e.g. for $\mathbf{L^4}$ where a large activation barrier was evaluated by computational means). In addition to this hypothesis, the importance of the activation barrier 2 in Figure 60 is highlighted by the case of the aminomethylpyridines where the formation of

the *trans*-keto form is confirmed but where this form appears to be too unstable to be accumulated and observed by diffuse reflectance spectroscopy in the case of $\mathbf{CH_2L^2}$ and $\mathbf{CH_2L^4}$. Interestingly, excitation spectra show also the *trans*-keto excitation band for both photochromic and non-photochromic molecules. It strongly suggests that, although the *trans*-keto form in the ground state is unstable and not visible by diffuse reflectance spectroscopy, this strongly fluorescent form is present as a trace in non photochromic molecules and then revealed in excitation spectra. These traces could be stabilised by the presence of crystalline defects.

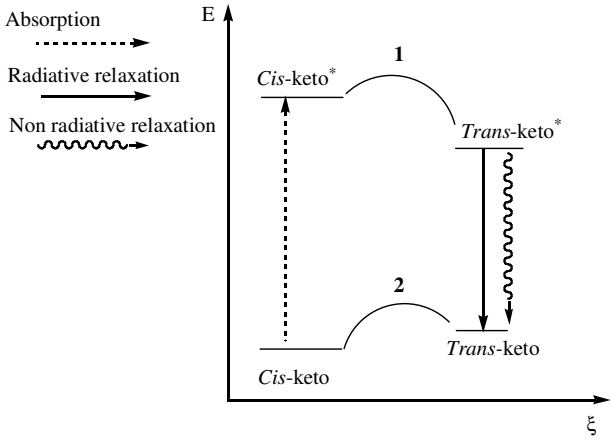

Figure 60 Photochemical process leading to the formation of the *trans*-keto form from a *cis*-keto absorption and to the accumulation of this form leading to the photochromism observation. The presence of activation barriers 1 and 2 is clearly highlighted in the formation and relaxation chemical pathways of the *trans*-keto form.

In conclusion, the presence of the methyl group induces a loss of electronic conjugation between aromatic rings and drives to a large change in the energy of electronic levels and then to modification of the shape of diffuse reflectance spectra (shifts of the bands, modification of the enol/*cis*-keto

population ratio, etc). Moreover, the influence of electronic substituents is also strongly modified by the addition of a methyl spacer group. Indeed, although a strong bathochromic shift was observed for the enol band for $\mathbf{L^3}$ and $\mathbf{L^5}$, no clear shift is observed from $\mathbf{CH_2L^3}$ to $\mathbf{CH_2L^5}$ (Figure 61). A change of enol/*cis*-keto signals ratio induced by adding the chloride substituent and the methyl group is also noted (Figure 61b). It could be explained by the electronic conjugation in the molecule. Indeed, in the *cis*-keto form, the electron donor amine group is stabilised by the acceptor effect of the ketone function and, in the case of conjugated molecules (e.g. $\mathbf{L^3}$ and $\mathbf{L^5}$), by the acceptor effect of the pyridine ring. Introducing a chloride substituent provides a loss of the amine stabilization, compensated in $\mathbf{L^5}$ by the presence of the conjugated pyridine ring. The destabilisation of the *cis*-keto form is however very important in derivatives comprising the methyl spacer group (e.g. $\mathbf{CH_2L^3}$ and $\mathbf{CH_2L^5}$) because, in these cases, the acceptor effect of the pyridine ring cannot play any role in the amine stabilisation due to the fact that this ring is electronically isolated from the salicyl ring by the CH_2 group (Figure 61b). These effects are also strongly visible in fluorescence experiments where large shifts of emission and excitation bands are observed.

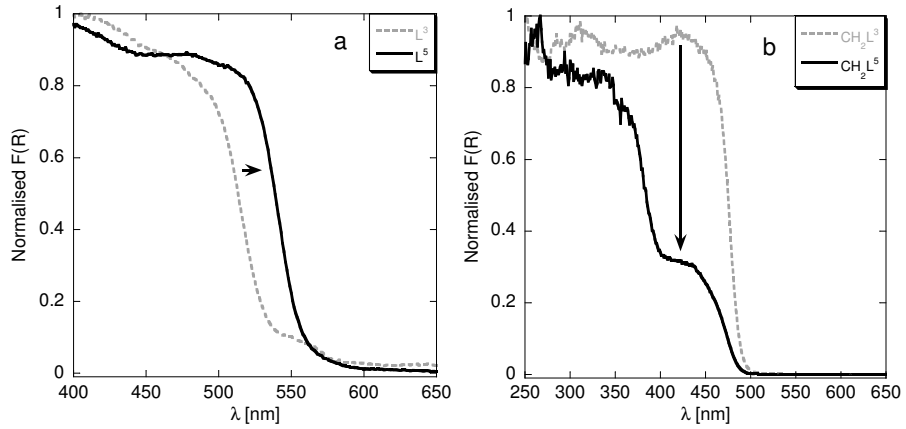

Figure 61 Effect of the chloride substituent on the diffuse reflectance spectra of $\mathbf{L^3}$ ($\mathbf{L^5}$) (a) and $\mathbf{CH_2L^3}$ ($\mathbf{CH_2L^5}$) (b). The arrows indicate the bathochromic shift and the apparent modification of the enol/*cis*-keto signals ratio induced by the addition of a chloride substituent.

Chapter IV: Anionic *N*-salicylidene anils: Synthesis and optical studies.

Introducing remarks

A challenging perspective brought by *N*-salicylidene aniline derivatives is the preparation of hybrid molecular materials based on the thermo- or/and photo-sensitivity of this class of molecules that could be incorporated as guest anionic molecules in various cationic host functional matrices. In this chapter, we will thus focus on the study of the organic *N*-salicylidene anils anions. For this purpose, the sulfonate group was selected because of its low coordination ability and its permanent charge which we will be useful for the organic-inorganic hybrid materials described in next chapters.

In order to obtain information about the influence of the molecular topology and environment on the optical properties of this class of molecule, the change of the charged sulfonate position (from para to meta, *N*-salicylidene *p*-aminobenzenesulfonate: **1** and *N*-salicylidene *m*-aminobenzenesulfonate: **2**) as well as the nature of the counter anion (from sodium: **Na1** and **Na2** to potassium: **K1** and calcium: **Ca1**) and the presence of substituents (chloride: **Na1Cl** and bromide: **Na1Br**) were investigated (Scheme 16). The results obtained with these molecules lead to an interesting overview of the factors governing the thermo-sensitivity of the *N*-salicylidene anions which must be known before studying hybrid materials.

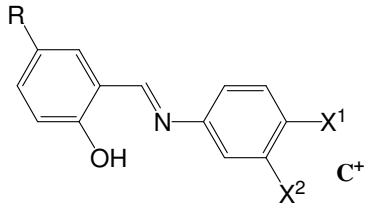

R= H, $X^1 = SO_3^-$, X^2 = H, C^+ = Na : **Na1**
R= H, $X^2 = SO_3^-$, X^1 = H, C^+ = Na : **Na2**
R= H, $X^1 = SO_3^-$, X^2 = H, C^+ = K : **K1**
R= H, $X^1 = SO_3^-$, X^2 = H, $C^+ = Ca_{1/2}$: **Ca1**
R= Cl, $X^1 = SO_3^-$, X^2 = H, C^+ = Na : **Na1Cl**
R= Br, $X^1 = SO_3^-$, X^2 = H, C^+ = Na : **Na1Br**

Scheme 16 Molecular scheme of **Na1-2**, **K1**, **Ca1**, **Na1Cl** and **Na1Br**.

Syntheses and crystallization methods

Sodium salts of anions **1** and **2** (**Na1** and **Na2**, respectively) were synthesized as pure yellow powders following an adapted method involving a first step of deprotonation of sulfanilic acid or 3-aminobenzenesulfonic acid by sodium hydroxide and a second step of condensation of the amine and aldehyde functions which leads to precipitation of crude products. The pure compounds are therefore obtained by re-crystallisation in hot methanol to give large amount of very small yellow tangled needles. **Na1** and **Na2** have a very high thermal stability for an organic salt as confirmed by TGA/DTA (degradation temperature = 384(1)°C and 340(1)°C, respectively). Indeed, it is in the same range of some reported polysulfonates phenolphthalein derivatives which are degraded around 350°C.[208] Although **Na1Cl**, **Na1Br** and **Ca1** were also obtained following a similar method (but where the re-crystallisation step was not necessary), **K1** was more difficult to obtain because of its higher solubility in organic solvents (e.g. methanol and ethanol). Indeed, the clear solution obtained after the condensation step was cooled down, filtered in order to eliminate remaining reactants and

concentrated to give a crude yellow oil. The mixture was then sonicated twice in diethylether and the supernate was extracted in order to separate the unreacted salicylaldehyde and the pure yellow powder of **K1**. Interestingly, **K1, Ca1, Na1Cl** and **Na1Br** have also very high thermal degradation temperatures as confirmed by TGA/DTA (349(1)°C, 346(1)°C, 400(1)° and 401(1)°, respectively). The change of counter-ion and the presence of chemical substituents have thus a significant impact on the thermal stability of this class of materials.

Numerous crystallisation attempts were carried out with *N*-salicylidene aminobenzene sulfonates. However, the solubility (increasing from **Ca1** to **Na1** and **K1**) and the very low vapour pressure of this class of materials appear to make tough the single crystals growth despite the large variety of techniques tested (solvent evaporation, liquid or gaseous diffusion of non-solvent, rate controlled syntheses, sublimation experiments, etc). Nevertheless, a small single crystal of **K1** was obtained by solvent evaporation but, due to the poor quality of the material, the structure was not refined up to a value of 14%. The rough packing obtained appears to be similar to those obtained for **Ksaltz** (see chapter 2) thanks to the appearance of planes containing either the anionic sulfonate groups and the potassium ions or the organic parts of **1** (Figure 62, A and B planes, respectively). Because of the poor R factor, the structure will not be described (crystal refinement data are available in the appendix section, Table 63). The literature contains however recent reports about crystal structures of *N*-salicylidene *p*-aminobenzenesulfonate crystallised with coordinated ions through the sulfonate function (Pb and Ca)[209, 210] or with hexahydrate metal complexes (with M^{II} = Ni, Zn, Cd and Mg)[211-215]. Moreover, the related

sulfonic acid has also been recently reported.[216] These structures strongly support our observations about the packing organized in planes for these anions (**K1** and **Ksaltz**) although a large variety of powders X-ray diffractograms were observed, pointing out differences in crystal structures (Figure 63).

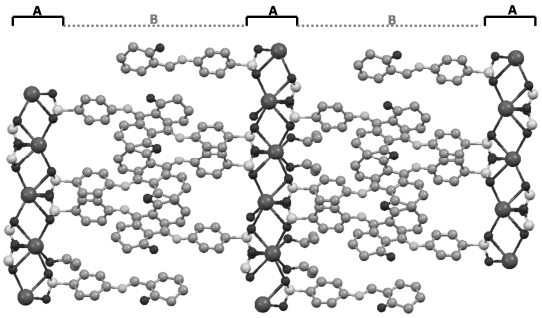

Figure 62 View of the crystal packing in the crystal structure of **K1** along the *c* axis. The stacking of hydrophilic planes containing the potassium ions and the sulfonate groups (A) with hydrophobic planes containing the organic part of **1** (B) is clearly suggested despite the low resolution of the structure.

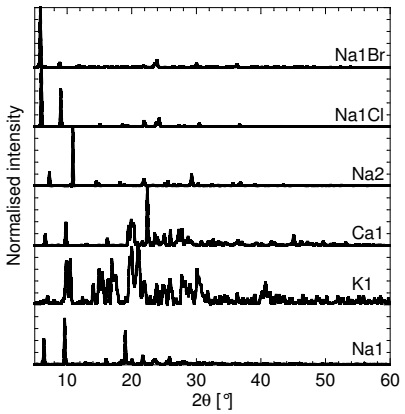

Figure 63 Powder X-ray diffractograms of **Na1**-**2**, **K1**, **Ca1**, **Na1Cl** and **Na1Br**.

Optical study of salts of the N-salicylidene anil anions

N-salicylidene *p*-aminobenzenesulfonates (Na1, K1 and Ca1, Na1Cl and Na1Br)

As shown in Figure 64, **Na1** is pale yellow at room temperature. The colour turns to a perfect white at 77 K. The intensity of the thermochromism phenomenon is very weak in this temperature range. In the diffuse reflectance spectrum at 298 K, a large intensity, coming for the enol form, is observed in the UV range (Figure 65). A very weak band could also be observed in the visible range (420-500 nm). This band can be attributed to a trace of *cis*-keto form. Light irradiation of **Na1** does not lead to any change in the diffuse reflectance spectrum, showing the absence of photochromism at room temperature.

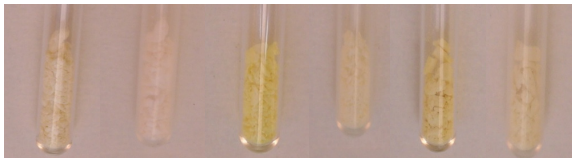

Figure 64 Photographs showing thermochromism of the powder samples of **Na1**, **K1** and **Ca1** at 298 K and 77 K.

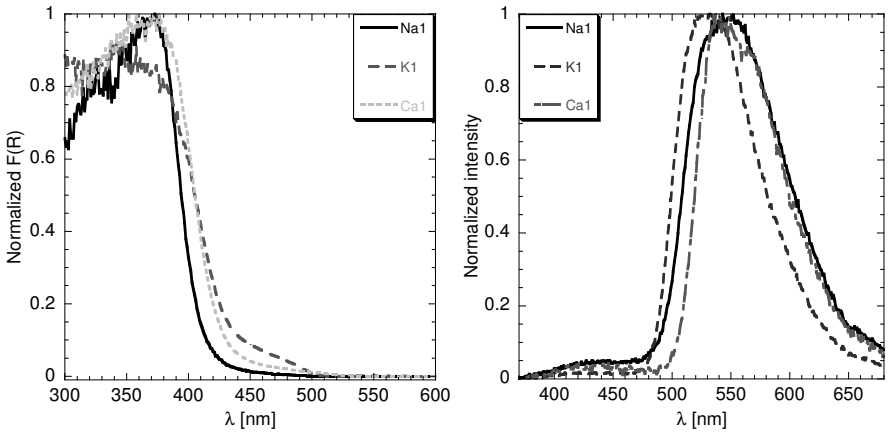

Figure 65 Diffuse reflectance spectra at 298 K (on the left) and Emission spectra with an excitation wavelength of 350 nm at 298 K (on the right) of **Na1**, **K1** and **Ca1**.

With a light excitation wavelength of 350 nm (corresponding to the excitation of the enol form), pure solid sample of **Na1** presents an intense emission centred at approximately 543 nm, which can be attributed to the radiative relaxation of the excited *cis*-keto form (cis*) (Figure 65). **Na1** emission spectrum also contains a second significant weak emission approximately centred at 430 nm, attributed to the radiative relaxation of the excited enol form (enol*). In all cases, bands appear to be very broad which could reveal the presence of several *N*-salicylidene anils conformations, close in energy in the ground and excited states as suggested by ref. [92]. Temperature dependent fluorescence experiments confirm this hypothesis because a modification of the emission bands shape is observed (Figure 66a). A stabilisation of some conformations with respect to others leading a change in the emission intensities is assumed (Figure 66a). Moreover, the presence of various emission maxima in the lowest temperature spectra (from 130 to 77 K) suggests the formation of a vibrational substructure.

Temperature dependent excitation spectra at 550 nm, corresponding to the emission wavelength of the radiative relaxation of the excited *cis*-keto form, were also recorded for **Na1** (Figure 66b). A large influence of temperature is observed in the UV range (decrease of the excitation signal) which can be explained by the increase of non radiative pathways induced by high temperatures. Moreover, in the visible range, an increase of the excitation signal with temperature could be distinguished for **Na1** but remains unclear.

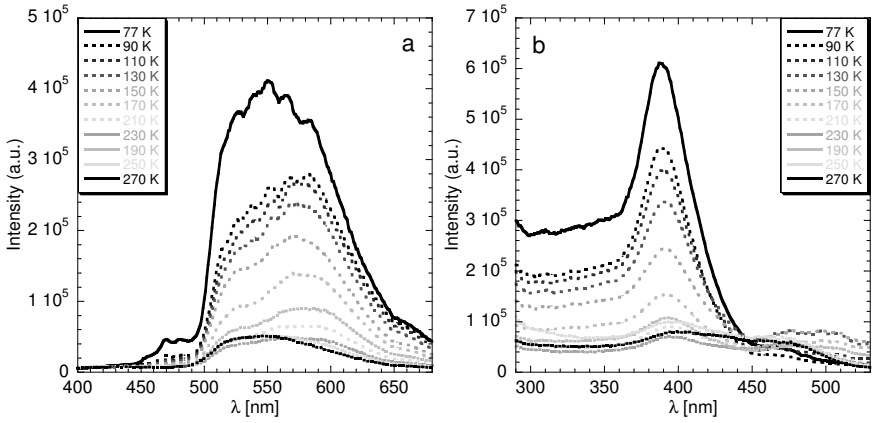

Figure 66 Temperature dependent (from 77 to 270 K) (a) emission spectra of **Na1** with an excitation wavelength of 350 nm. In the lowest temperature spectra, the presence of a vibrational substructure is suggested by the shape of the most intense band. (b) excitation spectra of **Na1** with an emission wavelength of 550 nm, corresponding to the emission wavelength of the excited *cis*-keto form.

The replacement of counter-ion from Na to K and Ca appears to change the colour of the material as demonstrated by the strength of thermochromism (Figure 64). As shown in Figure 65, it has also a significant impact on the diffuse reflectance spectrum. As stressed above, **Na1** presents mainly an intense broad band in the UV range, attributed to the enol form. This band is also observed in **K1** and **Ca1** but with a bathochromic shift of approximately

12 nm. Although with **Na1** only a very weak signal was detected in the visible range, a significant band is observed between 410 nm and 510 nm for **K1** and **Ca1** which reveals the presence of the *cis*-keto form at room temperature (Figure 65). It could be explained by a change in the energies of states involved in the thermochromism phenomenon (enol, *cis*-keto). As for **Na1**, light irradiation of **K1** and **Ca1** does not lead to any change in the diffuse reflectance spectrum. The impact of counter-ion replacement is also clearly noted in the emission spectra shown in Figure 67a. Indeed, although a similar curve is observed for **K1** and **Na1**, emission maxima are separated by a hypsochromic shift of approximately 20 nm. **Na1** and **Ca1** have approximately the same emission maximum (~ 550 nm) but some differences can however be observed (e.g. band width of 108 nm for **Na1** and 94 nm for **Ca1**). The change of temperature has significant impact on the shape of the emission and excitation spectra. As expected because of the increase of non radiative pathways, the emission intensities decrease with temperature as observed for **Na1** (Figure 67a). A change of the shape is also noted (presence of two well resolved emission bands between 470 and 600 nm in the lowest temperature spectra), showing that some conformations and then some emissions are favoured through the modification of temperature. The same experiment was conducted for the excitation spectra (Figure 67b). As for **Na1**, the temperature increase leads to a strong quenching of the excitation signal in the UV range of the spectrum but also to a significant increase of the intensity between 450 and 500 nm for **K1** which is however less pronounced than the one observed with the *N*-salicylidene aminomethylpyridines (see previous chapter) and could be attributed to a thermally induced *cis*-keto form population increase. The same observation

can be done in the UV range of the **Ca1** excitation spectrum but the evolution of the intensity in the visible range remains not clear.

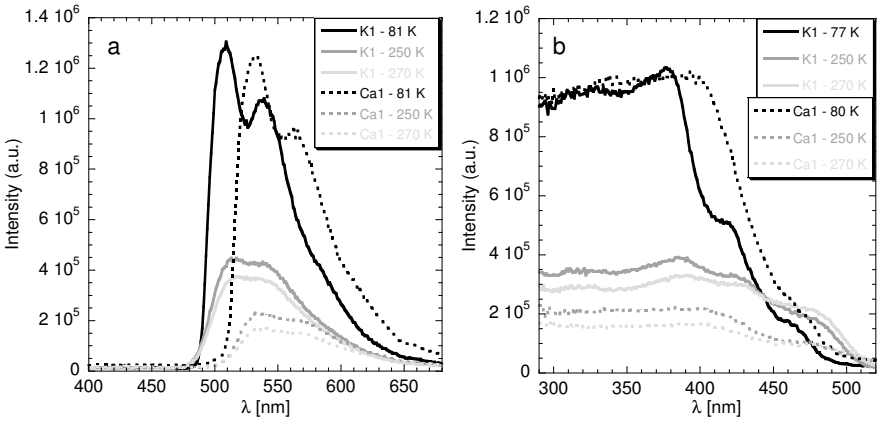

Figure 67 Temperature dependent (a) emission spectra of **K1** and **Ca1** with an excitation wavelength of 350 nm in a range of 81-270 K. The formation of two resolved emission bands in the lowest temperature spectra is clearly observed. (b) excitation spectra of **K1** and **Ca1** with an emission wavelength of 540 nm in a range of 77-270 K and 80-270 K, respectively.

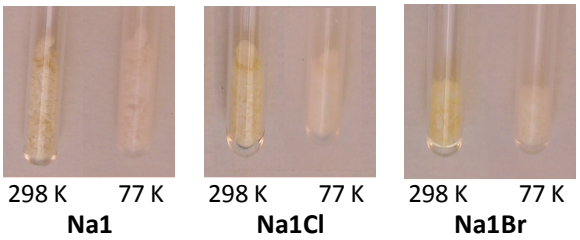

Figure 68 Photographs showing the thermochromism of the powder samples of **Na1**, **Na1Cl** and **Na1Br** at 298 K and 77 K.

As expected, the presence of a chemical substituent in the molecular scheme of *N*-salicylidene *p*-aminobenzenesulfonate (Scheme 16) involves a modification of electronic densities in the molecule. Indeed, as described earlier for $\mathbf{L}^3$ and **Hsaltrz** (see chapters 1 and 2), it leads to significant

modifications of the colour of the compounds (the substituted molecules is darker than the original **Na1** although it is not clearly detectable in photographs shown in Figure 68) as well as in the Kubelka-Munk signal (Figure 69). In these spectra, the enol band which is observed from UV to approximately 420 nm for **Na1** appears to be shifted of few nanometres to the lower energy range for **Na1Cl** and **Na1Br**. Moreover, the *cis*-keto band, which was almost quenched in **Na1**, is significantly present in **Na1Cl** and **Na1Br** spectra, explaining the colour differences observed between these materials. These changes, attributed to a modification of the energy levels of enol and *cis*-keto forms, cannot be totally explained by thinking about electronic resonance and must be also driven by the crystal structure change. A *cis*-keto band intensity change also seems to be present between **Na1Cl** and **Na1Br** but cannot be clearly demonstrated at this stage because of the limitation of the technique. Moreover, it was also noted that light irradiation of the samples does not lead to any significant spectral change. **Na1Cl** and **Na1Br** are not photochromic at room temperature.

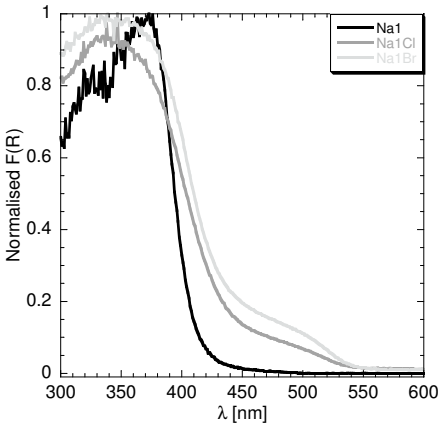

Figure 69 Kubelka-Munk spectra of **Na1**, **Na1Cl** and **Na1Br** at 298 K.

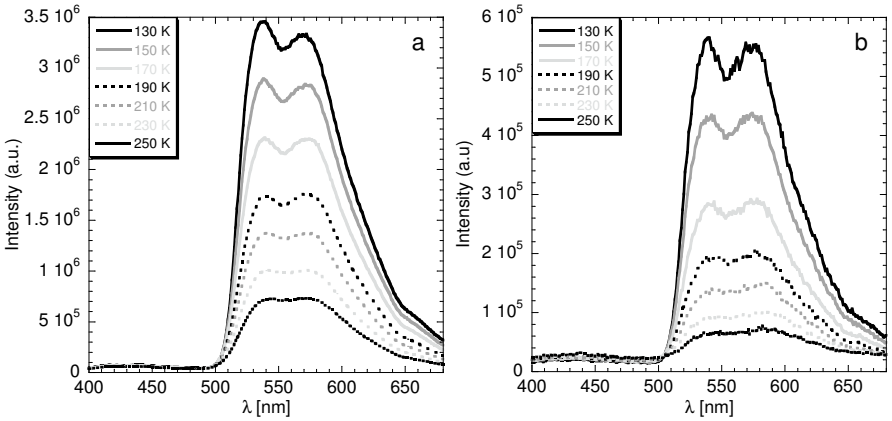

Figure 70 Temperature dependent emission spectra of **Na1Cl** (a) and **Na1Br** (b) with an excitation wavelength of 350 nm in a temperature range of 130-250 K.

The presence of the substituents is also felt by fluorimetry. Indeed, if we compare Figure 66a and Figure 70, a clear modification of the emission band shape is noted. Although **Na1** presented complicated emission spectra composed by numerous emission maxima, **Na1Cl** and **Na1Br** spectra show only two main emission bands at low temperature at approximately 535 nm, 566 nm and 536 nm, 573 nm, respectively. The chemical substituents seem

then to favour two emission pathways suggesting two *cis*-keto conformations, as previously discussed for **K1** and **Ca1**. These two emission bands seem, however, to evolve with the same behaviour with temperature (slow decrease at higher temperatures, induced by the increase of the non radiative relaxation pathways).

N-salicylidene *m*-aminobenzene sulfonate (Na2)

In contrast to **Na1**, **Na2** is dark yellow at room temperature and becomes white at 77 K, showing an intense thermochromism.

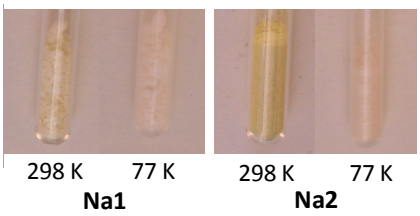

Figure 71 Photographs showing the weak and the strong thermochromism of the powder samples of **Na1** and **Na2**, respectively, at 298 K and 77 K.

The colour difference between **Na1** and **Na2** is also visible in the diffuse reflectance spectra at 298 K (Figure 72). The broad enol contribution (from UV) appears in **Na2** with a bathochromic shift of approximately 19 nm with respect to **Na1** which translates a significant change in the electronic levels induced by the position change of the sulfonate group. In addition to the enol band shift, the *cis*-keto band (centred at approximately 450 nm) is very large in **Na2** although this contribution was almost quenched in **Na1**. A strong stabilisation of the *cis*-keto form with respect to the enol form is then suggested for **Na2**. UV irradiation of the sample does not lead to any diffuse reflectance spectrum change traducing the absence of photochromism for **Na2** at room temperature.

Solid state emission spectra were recorded for **Na2** with an excitation wavelength of 350 nm which corresponds to the band of the enol form in diffuse reflectance spectra (Figure 72). Temperature dependent fluorimetry analyses were carried out on warming from 77 K to 300 K in order to study the influence of temperature on the photochemical processes as discussed above.

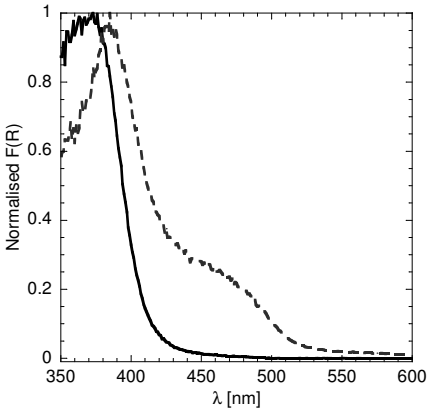

Figure 72 Kubelka-Munk spectra of **Na1** (black line) and **Na2** (dotted line) at 298K.

Na2 presents an emission spectrum in agreement with reported data[92] (Figure 73). A major broad contribution (β, λ^{max} = 547 nm) is observed between ~ 490 nm and ~ 650 nm over the whole temperature range investigated, which is assigned to the radiative relaxation of the excited *cis*-keto* form. A sharper band (α, λ^{max} = 529 nm), attributed to a *cis*-keto* planar conformation[92], is also noted at 77 K but disappears on warming. The temperature dependent emission spectrum also contains a weak, badly resolved contribution between ~ 370 nm and 490 nm (γ and δ), which is attributed to the radiative relaxation of the excited enol* form. This contribution grows at higher temperatures in comparison to the *cis*-keto

band. Several reasons could be invoked to explain this unexpected temperature dependent behaviour: (i) a decreased proton transfer efficiency in the excited state (which leads to a smaller population of the *cis*-keto* form), (ii) the presence of enol conformers for which the excited state proton transfer reaction does not occur at all.

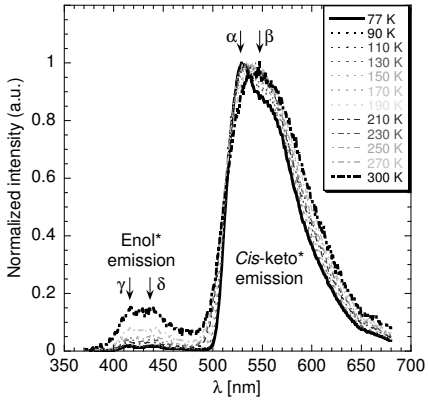

Figure 73 Temperature dependent emission spectra of pure solid samples of **Na2** recorded on warming over 77- 300 K, with a light excitation at 350 nm. The arrows indicate the major α, β, γ and δ emission bands as discussed in the text.

The thermo-induced tautomerisation of the anion was followed by temperature dependent fluorimetry in excitation mode from 77(1) K to room temperature (Figure 74). As for the *N*-salicylidene aminomethylpyridines (see previous chapter), we have focused on the *cis*-keto* → cis-keto emission pathway and did not consider the enol emission because its absorption band is known to not vary very much with temperature[89]. Thus, the emission wavelength was fixed at 560 nm. A signal ranging from UV to ~430 nm is attributed to the absorption of the enol form (λ^{max} = 384 nm) and its associated fluorescence (Figure 74). This signal is very high because the enol form should be present in majority compared to the *cis*-keto form and

this situation is expected to be much favoured on cooling. Thus, photochemical pathway from the enol form excitation appears to be favoured. On warming, it is seen that the intensity of the enol form decreases as expected with the growing of the *cis*-keto form. Actually, the *cis*-keto absorption range (from ~ 430 nm to ~ 520 nm) shows no signal at low temperature (77 – 150 K). This form appears at 170 K and slowly increases with temperature to reach an intensity value of ~27000 at 250 K (Figure 74). The proton transfer (leading to the enol/cis-keto tautomerisation) at high temperature is then clearly observed as for $\mathbf{CH_2L^3}$ in the previous chapter. Other phenomena could, however, also be considered to explain the decrease of the enol excitation band such as a decrease of the proton transfer efficiency in the excited state or the presence of other non radiative relaxation pathways.

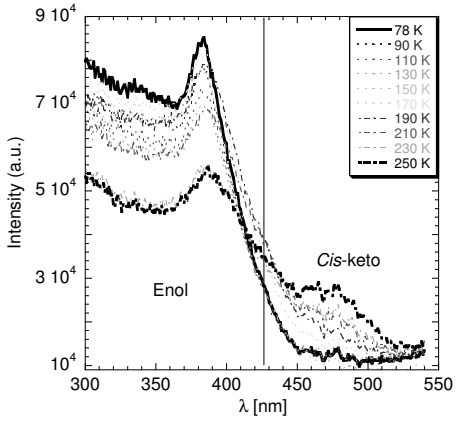

Figure 74 Temperature dependent excitation spectra of pure solid samples recorded on warming from 77(1) K for **Na2**, with an emission wavelength of 560 nm. The vertical line shows the approximate signals ranges of enol and *cis*-keto forms.

Discussion

In this section, we have described seven novel organic salts with a *N*-salicylidene anil framework. All these compounds present thermochromism, which is more or less intense following the molecular topology, but are not photochromic. The absence of photo-sensitivity could be explained by the expected rigidity of the crystal structure where the packing seems to be directed by the formation of strong ionic interactions as previously described in the chapter 2 for **Ksaltz**.

Interestingly, properties of this class of anions appear to be very sensitive to molecular topology. Indeed, the replacement of the counter-ion leads to changes in the structure, as shown by powder X-ray diffractograms, in the thermal stability, which is very high for organic salts (340 – 401 °C) and largely higher than for most of *N*-salicylidene aniline derivatives (e.g. 220 and 254°C for **Hsaltrz** and **Habs**, respectively), but also in optical behaviours of materials. Indeed, in addition to a visible modification of the colour of compounds at room temperature, the replacement of sodium by potassium and calcium cations leads to a shift of the enol band and a significant increase of the intensity of the *cis*-keto band in the diffuse reflectance spectra. It translates a modification of the electronic levels induced by the counter-ion nature. It could be due to a combination of structural changes, induced by the radius and the charge of the selected cation, and medium polarisability modifications in the organic material which was reported to be very influent on the photochemical processes in *N*-salicylidene anils.[56] The cation nature has also an influence on the shape of the emission spectra. Indeed, **Na1** shows a broad complicated band coming from the radiative relaxation of the excited *cis*-keto form which

suggests that many conformations are accessible during photochemical processes leading to the fluorescence phenomenon. The situation is changed for **K1** and **Ca1** where the *cis*-keto* band is only constituted by two main contributions.

The presence of chemical substituents such as chloride and bromide can be compared to the situation induced by the cation change. Indeed, as for **Hsaltrz**, the chloride and bromide groups induce a shift of the enol band and a significant increase of the intensity of the *cis*-keto band. Moreover, the insertion of a substituent also leads to a modification of the emission and excitation spectra as observed for **K1** and **Ca1**. The impact of the presence of the substituent in **Na1Cl** and **Na1Br** is then similar to the one of the change of cation nature which should be then considered accurately when hybrid materials will be considered (see chapter 9).

Finally, the position of the charged sulfonate group also leads to strong modification of structural and optical properties. Indeed, an enol band bathochromic shift combined with a large *cis*-keto band increase is noted in the diffuse reflectance spectrum of **Na2** in comparison with the same measurement made with **Na1** at room temperature. It translates a significant modification of the electronic levels involved in the fluorescence phenomenon and a stabilisation of the *cis*-keto form with respect to the enol form, explaining the strong thermochromism of this compound. Moreover, **Na2** is an anion where the enol* emission band is significant with respect to the *cis*-keto* band at room temperature as discussed above. The observation of the enol* signal is another proof of the strong impact of this slight molecular topology change on the energy states of the molecules. Temperature dependent excitation spectra of **Na2** are also particularly

interesting because, as for **CH_2L^3** in chapter 3, the thermally induced enol/*cis*-keto tautomerisation can be clearly followed. It paves the way to the generalisation of this analytical technique in order to probe this type of phenomenon as it will be confirmed for the hybrid materials in chapter 9.

Part II: Coordination compounds

Chapter V: Tuning optical properties of *N*-salicylidene aniline derivatives: study of complexes with ligands derived from aminopyridines[§§]

Introducing remarks

N-salicylidene aminopyridines described in chapter 1 are not only organic molecular switches but also potential ligand for transition metals. Thanks to the presence of three coordinating atoms (Scheme 17), alcohol and imine functions could chelate a metal ion through the coordination of oxygen and nitrogen atoms (Scheme 17, complex 1). The nitrogen atom of the pyridine can also participate to the formation of inorganic complex because the lone pair of this atom is not involved in the ring aromaticity and then available for a metal-ligand bond (Scheme 17, complex 2). A third possibility is to make complexes using the three coordinating atoms in order to obtain oligo- or polynuclear compounds (Scheme 17, complex 3). Finally, we could also think about other less probable coordination modes which imply the use of two of the three coordinating atoms (e.g. the oxygen atom and the nitrogen of the pyridine, the two nitrogen atoms) but where a molecular distortion is necessary in order to reach the geometry needed for the complexes formation. In view of the fact that the composition and the properties of the materials will strongly depend of the coordination mode, it is very challenging to control such parameters thanks to the experimental conditions

[§§]Adapted from F. Robert, A.D. Naik, B. Tinant, R. Robiette, Y. Garcia *Chem. Eur. J.* **2009**, *15*, 4327-4342.

(number and nature of ligands and metal salts, presence of other coordinating molecules, solvent, temperature, pH, etc).

In this section, we will focus on the study of complexes built by coordination only through the nitrogen of the pyridine rings (complex 2 in Scheme 17). This class of compounds is, indeed, the most suitable one for the appearance of thermo- and photochromism because the salicyl moiety is free and then available for the tautomeric equilibrium and for the photo-isomerisation reaction. This chapter will highlight the impact of the coordination on the properties of the *N*-salicylidene molecular switches. Indeed, the metal ion is known to influence the ligand electronically (through coordination bonds), geometrically and sterically.[217]

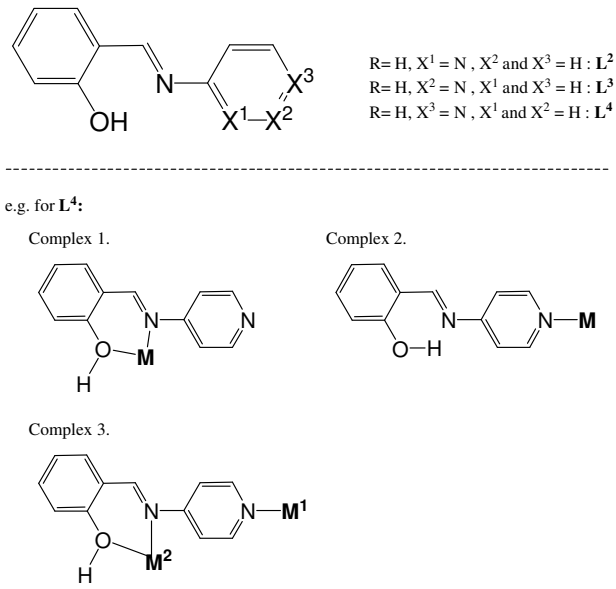

Scheme 17 Molecular scheme of *N*-salicylidene aminopyridines (on the top) and most probable coordination modes for $\mathbf{L^4}$. The coordinated alcohol function of complexes 1 and 3 is shown in its protonated form although the phenolate form can also be observed.

Syntheses and crystallization methods

Inorganic syntheses were carried out with $\mathbf{L^2}$, $\mathbf{L^3}$ and $\mathbf{L^4}$ as ligands (see Scheme 17 and Chapter 1) with various copper(II), nickel(II) and iron(II) metal ions. However, the pyridine moiety appears to be not a very good ligand for 3d transition metals. It leads to strong competition for the complexation between all coordination molecules present in the synthetic medium (pyridine moiety but also alcohol and imine functions of $\mathbf{L^2}$, $\mathbf{L^3}$ or $\mathbf{L^4}$, the anion (e.g. chloride, nitrate, etc) and the solvent, such as methanol, ethanol, etc.). On the basis of our analyses, the three studied molecules, $\mathbf{L^{2\text{-}4}}$, give different types of inorganic complexes. The use of $\mathbf{L^2}$ favours the formation of very complicated polynuclear architectures where the alcohol and the imine functions are involved in the metal ion coordination spheres. Such materials will be discussed in chapter 8. Despite all our efforts, $\mathbf{L^4}$ seems to generate mixtures of inorganic complexes which are then not possible to characterise properly and reproductively. In this section, we will then focus on $\mathbf{L^3}$ complexes and more precisely on compounds with molecular formula $[M^{II}(\mathbf{L^3})_2(NCX)_2(CH_3OH)_2]$ which were obtained as crystals (for M^{II} = Co ($\mathbf{C^1}$ and $\mathbf{C^2}$), Mn ($\mathbf{C^3}$), Ni ($\mathbf{C^4}$), Cu ($\mathbf{C^5}$) and X = S ($\mathbf{C^1}$, $\mathbf{C^{3\text{-}5}}$), Se ($\mathbf{C^2}$)) or powder (for M^{II} = Fe ($\mathbf{C^6}$) and X = S). Although iron(II) compound was obtained by precipitation in methanol, single crystals of other complexes were grown in methanol by either slow evaporation or using gaseous diethylether diffusion.

Crystal structures study[***]

Crystal structure of $[Co^{II}(L^3)_2(NCS)_2(CH_3OH)_2]$ (C^1)

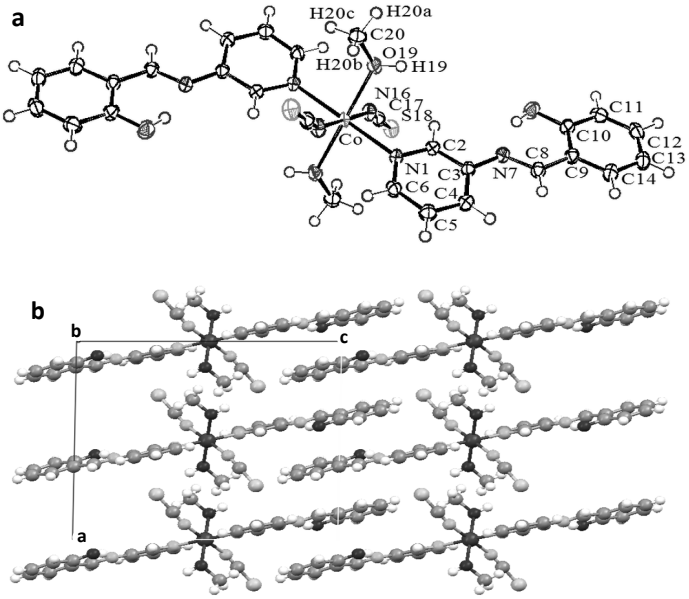

Figure 75 (a) ORTEP view of the asymmetric part of the unit cell of $\mathbf{C^1}$, showing 50 % probability displacement ellipsoids. (b) View of the crystal packing of $\mathbf{C^1}$ along the *b* axis showing the π-π stacking interactions allowed by the short inter-ligand distances.

The complex crystallizes under a monoclinic system ($P2_1/a$) at room temperature (Table 32). The structure consists of a mononuclear cobalt(II) unit with a N_4O_2 octahedral environment built by two equivalent ligands in enol form coordinated through nitrogen pyridine atoms, two isothiocyanato anions and two methanol molecules, all respectively in *trans* position (Figure 75a). The presence of methanol molecules in the coordination sphere

[***] Structures were solved by Prof. B. Tinant (UCL).

confirms our discussion about the low coordination ability of this class of pyridine ligands. Compared to the free molecule $\mathbf{L^3}$ (see chapter 1), a complete rotation of the pyridine ring is observed as a result of the coordination to cobalt: the hetero nitrogen being in *trans* with respect to the H8 of the imine function. The dihedral angle between aromatic rings is highly modified by coordination because it decreases from 15(1)° ($\mathbf{L^3}$) to 7(1)° ($\mathbf{C^1}$). This change is followed by a modification of the H-bond strength which is found to increase (Scheme 18 and Table 33) ($\mathbf{L^3}$: H15···N7 = 1.91 Å > $\mathbf{C^1}$: H15···N7 = 1.83(4) Å) as for $\mathbf{L^5}$ (see chapter 1, 5-chloro *N*-salicylidene 3-aminopyridine: H15···N7 = 1.83(5) Å) (Table 33). The octahedral coordination sphere is very symmetric, with no appreciable angle deviation, the distortion parameter Σ[218] being very low: 6.2(5)°. About bond lengths, we notice a small Jahn-Teller distortion for the NCS group (Co-N16 is approximately 3 % smaller than the other Co-N and Co-O distances). The molecular packing shows a closed structure characterized by short distances (~ 3.96 Å) between ligands which lead to the formation of π-π stacking between salicyl rings and imine double bonds (distances between centroids = 3.38 (3) Å, angle between planes = 2 (1)°) (Table 34 and Figure 75b). It is also interesting to notice that there is one intermolecular H-bond between sulphur atom and hydrogen of the alcohol function of the methanol molecule (O19-H19···S18 ≈ 2.4 Å) (Table 33). Co-N and Co-O distances (Table 35) confirm the Co^{II} oxidation and HS spin states by comparison with $[Co^{II}(pdms)_2](ClO_4)_2 \cdot H_2O$ (where pdms = 1-((E)-2-pyridinylmethylidene)semicarbazide) with Co-$N_{pyridine}$ = 2.138 Å, Co-N_{imine} = 2.047 Å and Co-O = 2.141 Å).[219]

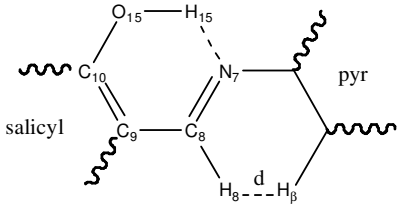

Scheme 18 Intramolecular hydrogen bonds in *N*-salicylidene aminopyridines complexes.

Crystal structure of $[Co^{II}(L^3)_2(NCSe)_2(CH_3OH)_2]$ (C^2), $[Mn^{II}(L^3)_2(NCS)_2(CH_3OH)_2]$ (C^3), $[Ni^{II}(L^3)_2(NCS)_2(CH_3OH)_2]$ (C^4) and $[Cu^{II}(L^3)_2(NCS)_2(CH_3OH)_2]$ (C^5)

The complexes $[Co^{II}(\mathbf{L^3})_2(NCSe)_2(CH_3OH)_2]$ ($\mathbf{C^2}$) and $[Mn^{II}(\mathbf{L^3})_2(NCS)_2(CH_3OH)_2]$ ($\mathbf{C^3}$) are isostructural to $\mathbf{C^1}$, discussed above, an isoselecyonato anion being found in the coordination sphere of the cobalt ion in $\mathbf{C^2}$ (Table 32, Table 35 and Figure 76). The $\mathbf{L^3}$ ligand is also found in enol form. The cobalt(II) oxidation state is confirmed for $\mathbf{C^2}$ (see Table 35) and manganese(II) for $\mathbf{C^3}$ as compared with $[Mn^{II}(H_2O)_2(dca)_2(ima)_2]$ (dca = dicyanamide and ima = 4-(1H-imidazol-1-yl)aniline) with Mn-N_{pyr} = 2.231 Å, Mn-N_{imine} = 2.214 Å and Mn-O = 2.197 Å).[220] No major difference in the dihedral angle between aromatic rings (7.4 (10)° for $\mathbf{C^1}$, 6.7 (10)° for $\mathbf{C^2}$ and 7.1 (10)° for $\mathbf{C^3}$) is noted (Table 35). In contrast, changes in H-bond strength (Table 33) are significant. This strength decreases from $\mathbf{C^2} > \mathbf{C^1} > \mathbf{C^3}$ and is related to an electronic density change in the ligand. We have also obtained single crystals of $[Ni^{II}(\mathbf{L^3})_2(NCS)_2(CH_3OH)_2]$ ($\mathbf{C^4}$) and $[Cu^{II}(\mathbf{L^3})_2(NCS)_2(CH_3OH)_2]$ ($\mathbf{C^5}$) which are isostructural to $\mathbf{C^1}$, $\mathbf{C^2}$ and $\mathbf{C^3}$, but a good refinement of these structures was not possible (Table 32). Therefore, these crystal structures are not discussed in detail further. Interestingly enough, when coordination occurs, the dihedral angle Φ

decreases from 15 to 7 (1)°, but the H8···H_β interaction decreases which do not correspond with the tendency observed for the free ligands.

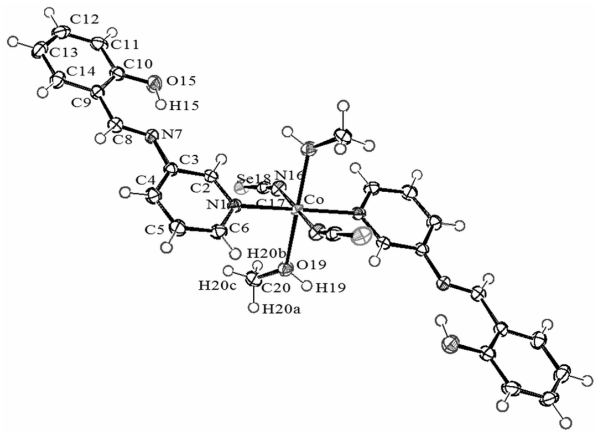

Figure 76 ORTEP view of the asymmetric part of the unit cell of $\mathbf{C^2}$, showing 50 % probability displacement ellipsoids.

Powders of $\mathbf{C^6}$ were found to be isostructural to the other compounds $\mathbf{C^{1\text{-}5}}$ (see powder diffraction peaks in experimental section). Figure 77 shows the Mössbauer spectrum recorded at 298 K for $\mathbf{C^6}$. It reveals a doublet with isomer shift δ = 1.10(1) mm/s and quadrupole splitting ΔE_Q = 2.25(1) mm/s, that corresponds to an asymmetric HS $Fe^{II}N_4O_2$ coordination sphere.[221] ^{57}Fe Mössbauer spectroscopy confirms the presence of one crystallographic site as observed in the crystal structures of $\mathbf{C^{1\text{-}5}}$. The decrease of temperature leads to small expected parameter changes (Figure 77, Table 7).[222]

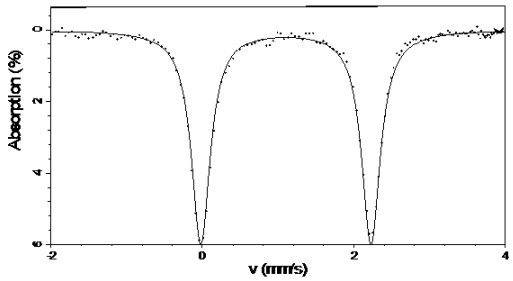

Figure 77 ^{57}Fe Mössbauer spectrum of **C^6** at 298 K (calibrated with respect to α-Fe).

Table 7 Evolution of ^{57}Fe Mössbauer parameters of **C^6** spectra in a temperature range of 143-298 K.

T [K]	**δ [mm.s^{-1}][a]**	**ΔE_Q [mm.s^{-1}]**	**Γ/2 [mm.s^{-1}]**
143 (1)	1.18 (1)	2.57 (1)	0.20 (1)
163 (1)	1.17 (1)	2.53 (1)	0.16 (1)
298 (1)	1.10 (1)	2.25 (1)	0.15 (1)

[a] Values are given with respect to α-Fe.

Optical properties

Diffuse reflectance study

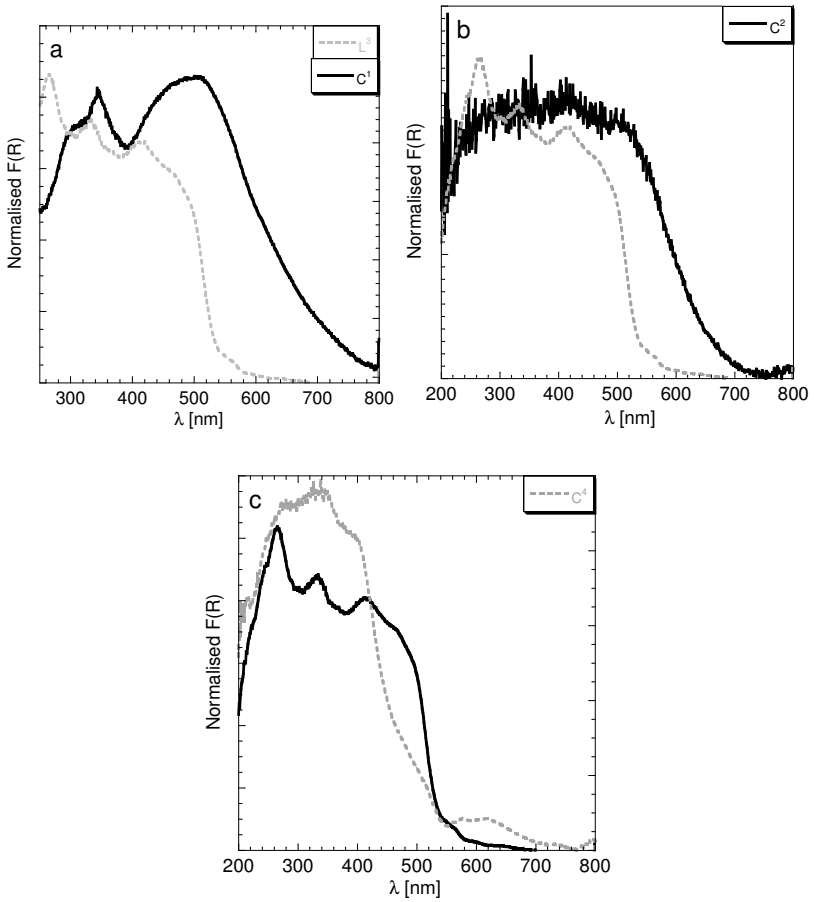

Figure 78 Diffuse reflectance spectra of crystals of $\mathbf{C^1}$ (Co/NCS) (a), $\mathbf{C^2}$ (Co/NCSe) (b) and $\mathbf{C^4}$ (Ni/NCS) (c) (solid lines) in comparison with $\mathbf{L^3}$ (dotted lines).

In coordination complexes, enol and *cis*-keto signals arising from the $\mathbf{L^3}$ ligand (see chapter 1) are not the only contributions to consider, there are also d-d transitions and often charge transfer phenomena which can be more

or less intense depending on the nature of the metal ion and ligands used. Bands of the keto forms are difficult to assign when they are located in the same wavelength range. This is the case for $\mathbf{C^1}$ (M = Co/NCS) and $\mathbf{C^2}$ (M = Co/NCSe) (Figure 78a and b). Indeed, added to an unresolved intense signal in UV attributed to the enol form of $\mathbf{L^3}$ (which is more resolved in the case of $\mathbf{C^1}$), a very intense band centred at 501 nm, which can be attributed to a charge transfer transition, is observed. This band hides the *cis*-keto and *trans*-keto bands. In $\mathbf{C^3}$, (M = Ni), this problem could be partly avoided because d-d transitions are only responsible for a weak absorption between 550-700 nm, and no charge transfer is assumed (Figure 78). These characteristics enable to observe the enol form, which is responsible for an intense signal ranging from UV to ~ 450 nm, and the *cis*-keto form, which seems to be in a smaller proportion than in the free ligand $\mathbf{L^3}$ (see chapter 1), and gives a band between ~ 450 nm and 545 nm. For complexes $\mathbf{C^{1\text{-}2}}$ and $\mathbf{C^4}$, UV irradiation at 254 nm (corresponding to the enol form absorption) for 1 h did not lead to a spectral change suggesting the absence of photochromism. Crystals of $\mathbf{C^3}$ (M = Mn) and $\mathbf{C^5}$ (M = Cu) were obtained in insufficient quantity to be analyzed by spectroscopic techniques. Interestingly, inorganic materials built with $\mathbf{L^3}$ appear to be thermochromic on cooling to liquid nitrogen. A colour change is observed from burgundy to brown for $\mathbf{C^1}$, from orange-bronze to pale orange for $\mathbf{C^2}$ and from green to pale green for $\mathbf{C^4}$ as shown in Figure 79. However, no thermally induced discoloration was observed for $\mathbf{C^6}$ (M = Fe).

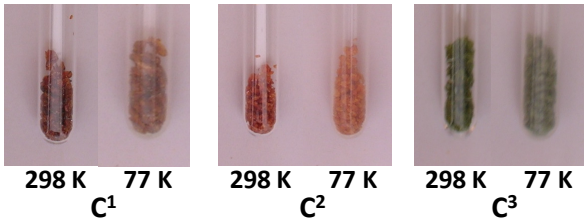

Figure 79 Photographs showing the weak thermochromism of the crystal samples of $\mathbf{C}^{1\text{-}3}$ at 298 K and 77 K.

Fluorimetry

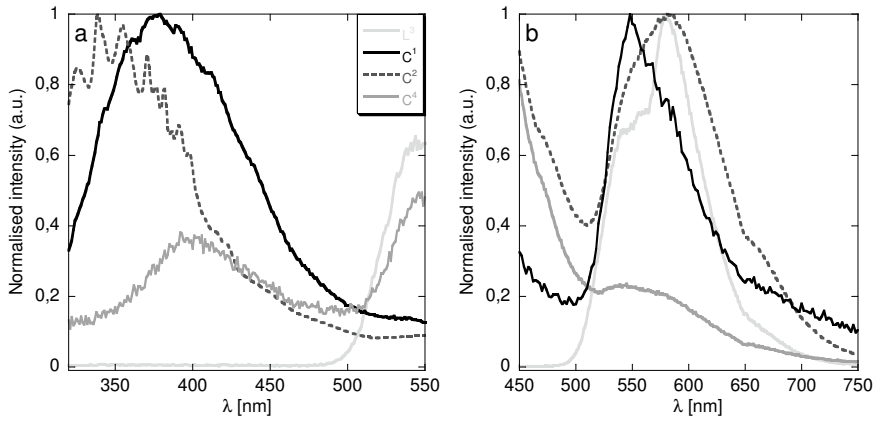

Figure 80 Comparison of emissions at 300 nm (a) and 400 nm (b) for crystals of $\mathbf{L}^{3}$, $\mathbf{C}^{1\text{-}2}$ and $\mathbf{C}^{4}$.

When $\mathbf{L}^{3}$ is embedded in complex $\mathbf{C}^{1}$, two emission contributions are observed (λ^{max} = 379 nm and λ^{max} = 545 nm) although only one, coming from the radiative relaxation of the excited *cis*-keto form, was observed for $\mathbf{L}^{3}$ in the solid state (Figure 80). In fact, the emission spectrum looks like the one obtained for $\mathbf{L}^{3}$ in methanol solution where both enol and *cis*-keto emission bands were noted (see chapter 1). For $\mathbf{C}^{4}$, similar bands are obtained with a slight red-shift (λ^{max} = 393 nm and λ^{max} = 548 nm, see Figure 80). For compound $\mathbf{C}^{2}$, the situation is more complicated since, in addition to

the band at λ^{max} = 581 nm, a shoulder is noticed at ~ 650 nm (Figure 80). This new band may stems, in this case, from the radiative relaxation of a more stable and more relaxed *cis*-keto form conformation, as discussed in previous chapters. Interestingly, several oscillations are noted for **C²** at λ^{max} = 339 nm. These oscillations may indicate the presence of a fine structure related to the vibrations levels of the complex molecule. Such phenomenon is also present in **C¹** but much less pronounced and absent in **C⁴**. Thus, complexation has a dramatic impact on the shape of the spectrum but also on the emission wavelengths (Table 8).

Table 8 Emission maximum wavelengths [nm] of **C¹⁻²** and **C⁴** in comparison with **L³**.

	L³		**C¹**	**C²**	**C⁴**
State	Solution (10^{-4} M methanol)	Crystals	Crystals	Crystals	Crystals
$\lambda_{max}^{400\,nm}$ [nm][a]	510	580	545	581	548
$\lambda_{max}^{300\,nm}$ [nm][b]	373	-	379	339	393

[a] Wavelength of maximum emission at an excitation wavelength of 400 nm or [b] 300 nm.

Computational details about the impact of the metal ions coordination

Previous sections of this chapter give experimental data about the influence of the complexation of the *N*-salicylidene anils. We were also interested by a theoretical treatment of this phenomenon in order to see if the coordination to a metal ion has a strong influence on the conformation and on the energy levels of these molecules. This work was performed in collaboration with Prof. R. Robiette. For practical reasons due to the large number of accessible

excited states of inorganic complexes, the system $[M^{II}(\mathbf{L^3})_2(NCS)_2(CH_3OH)_2]$ was only examined as isolated molecules in the ground state and with M^{II} = Ni ($\mathbf{C^4}$) or Cu ($\mathbf{C^5}$). $\mathbf{L^3}$ was then simulated, in the studied complexes, in its enol, *cis*- and *trans*-keto forms and in the transition state (TS) found in the chemical pathway going from the *cis*- to the *trans*-keto forms.

Table 9 Calculated energies (in kcal/mol relative to enol) for the enol, *cis*- and *trans*-keto forms of $\mathbf{L^3}$ and $\mathbf{C^{4-5}}$ as isolated molecules in the ground state (GS).

	enol	*cis*-keto	Activation barrier[a]	*trans*-keto
$\mathbf{L^3}$	0.0	4.4	40.6	15.3
$\mathbf{C^4}$	0.0	5.8	39.9	13.0
$\mathbf{C^5}$	0.0	5.5	39.0	13.0

[a] Activation barrier from the *cis*- to the *trans*-keto forms.

Results, listed in Table 9, demonstrate that although no significant differences are observed between $\mathbf{C^4}$ and $\mathbf{C^5}$, a slight but significant modification of the energy of the *cis*- and *trans*- keto forms is observed between $\mathbf{L^3}$ as free molecule and as ligand in complexes. Indeed, the *cis*-keto form appears to be destabilised by the complexation (compared to the enol) ($\mathbf{C^{4-5}}$: ~5.5 kcal/mol > $\mathbf{L^3}$: 4.4 kcal/mol) whereas the *trans*-keto form is stabilised ($\mathbf{C^{4-5}}$: 13.0 kcal/mol < $\mathbf{L^3}$: 15.3 kcal/mol). This energy change could lead to a decrease of the thermochromism strength. Moreover, the activation barrier for the isomerisation is also slightly modified: from 40.6 kcal/mol for $\mathbf{L^3}$ to 39.9 and 39.0 kcal/mol for $\mathbf{C^4}$ and $\mathbf{C^5}$, respectively. A slight but significant sensitivity to the nature of the metal ion is thus suggested for the activation barrier.

Interestingly, the metal ion nature seems to have a significant role on the most stable conformations of the different forms of $\mathbf{L^3}$ in the complexes.

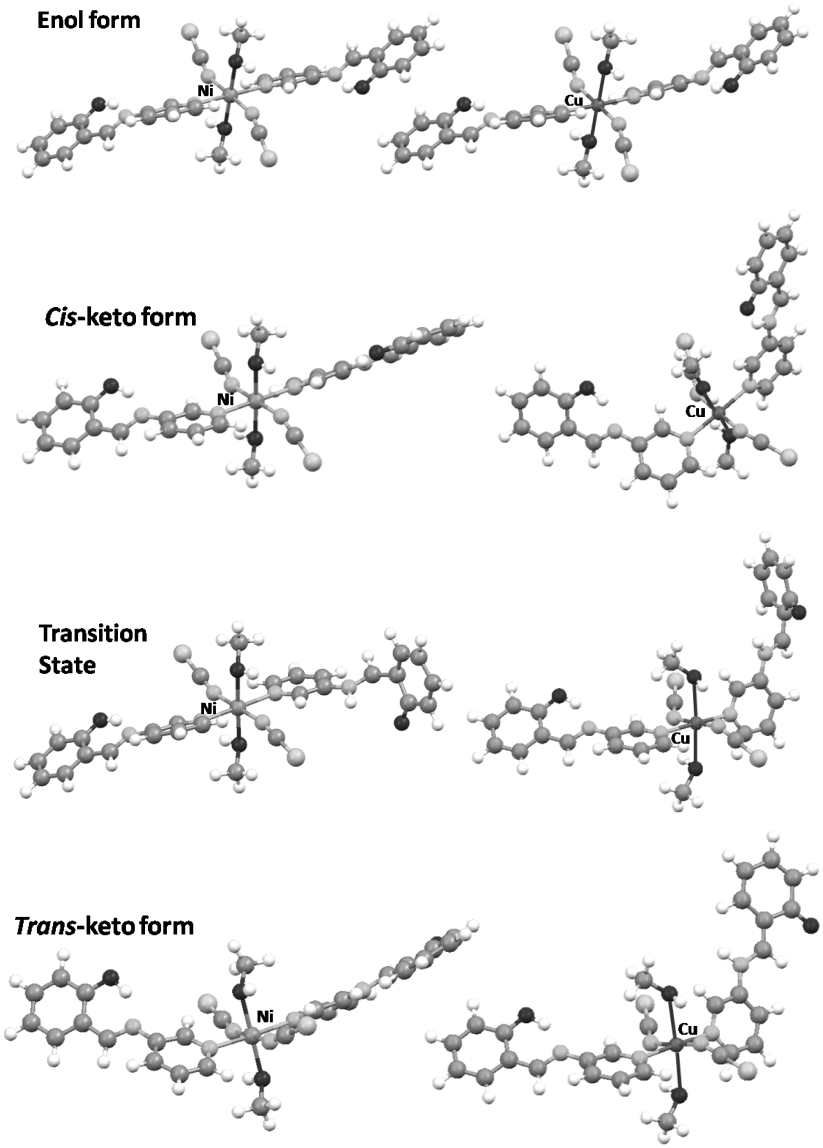

Figure 81 View of the most stable calculated structures of $\mathbf{C^4}$ (on the left) and $\mathbf{C^5}$ (on the right) as isolated molecules in the ground state. The picture shows the evolution of one $\mathbf{L^3}$ ligand from its enol to its *cis*- and *trans*-keto *via* the transition state (TS). A clear conformation difference is noted between $\mathbf{C^4}$ and $\mathbf{C^5}$ with the TS, *cis*- and *trans*-keto forms.

Indeed, as shown in Figure 81, differences appear in the conformation of $\mathbf{C^4}$ and $\mathbf{C^5}$ when $\mathbf{L^3}$ is in its TS, *cis*- and *trans*-keto forms although no significant difference was observed for the enol form. As suggested by Figure 81, the difference of conformation between $\mathbf{C^4}$ and $\mathbf{C^5}$ mainly comes from a change of torsion angle C-N_{pyr}-M-$N_{thiocyanate}$. We have thus investigated the energy difference between all conformations induced by the variation of this angle for the *cis*-keto form of $\mathbf{L^3}$ in complexes $\mathbf{C^4}$ and $\mathbf{C^5}$ (Figure 82).

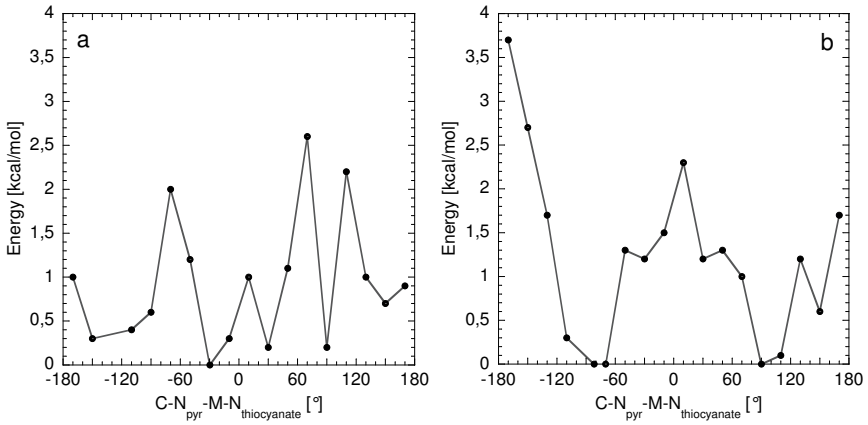

Figure 82 Calculated relative energy evolution for the ground state (GS) during the change of torsion angle C-$N_{pyridine}$-M-$N_{thiocyanate}$ in $\mathbf{C^4}$ (a) and $\mathbf{C^5}$ (b).

In $\mathbf{C^4}$ (Figure 82a), no clear tendency is obtained. The situation seems different for $\mathbf{C^5}$ (Figure 82b) where two energy minima are evidenced at -82° and + 90°. It suggests that the nature of the metal can induce modification in the energy levels of $\mathbf{L^3}$ ligand and then in the optical behaviours of the system. However, it is important to note that this computational study was done with inorganic complexes in the ground state and we have thus no information about the influence of the

complexation and of the nature of the metal ion on excited states although it is assumed that phenomena observed in GS must be reflected in other states (S^1, S^2, T^1, etc).

Discussion

A few coordination compounds containing *N*-salicylidene aminopyridines derivatives[223, 224] such as **L^3** [225] have been previously synthesized but their photosensitive and thermo-sensitive moiety was very often engaged in coordination, thus preventing any switchable chromic properties. Crystallography allows, in addition, studying the influence of both metal and auxiliary ligand (like NCS, NCSe, MeOH) on the photosensitive moiety. Complexation leads to a clear change in **L^3** dihedral angle (Φ) and to a modification of the intramolecular H-bonds (see text above). The metal ion thus leads to an electron density change in the ligand which strongly affects the photosensitive moiety and quenches the photochromism of **L^3**. Replacement of cobalt(II) by manganese(II) and of NCS by NCSe in $[Co(\mathbf{L^3})_2(NCS)_2(CH_3OH)_2]$ (**C^1**) is highly interesting because no dihedral angle modification is observed but a gradual H-bond strength modification is clearly identified as revealed by the O15-H15 and H15···N7 bond lengths. This situation may result from an electronic density change in coordinated **L^3** due to a change of the strength of σ bond between the metal and pyridine nitrogen. It could also be due to a modification of π back bonding between the metal and **L^3**. This observation leads to a new structural hint: the reported link between dihedral angle and H-bond strength is not systematic,[68, 101, 102] and must be considered with care since both factors can be independent. Φ is observed to be principally the result of one torsion angle (C8-N7-C4-C3) as noted for our complexes as well as for **L^3** and **L^4**

(see chapter 1). The presence of a zwitterionic form of the molecule could be taken in account to explain this observation. Finally, when interactions between pyridine and salicyl cycles, involved in the electronic resonance (C_{pyr}-N7-C8-C9-C10-O15), are studied in $\mathbf{L^{3\text{-}5}}$ (see chapter 1) and in $\mathbf{C^{1\text{-}3}}$, no significant differences are observed. Thus, the resonance seems to be not much influenced by molecular changes.

Interestingly, the coordination of $\mathbf{L^3}$ leads to a dramatic decrease of the energy difference between the excited species with a slow non radiative relaxation between these two. Indeed, the same phenomenon was previously discussed in chapter 1 when the emission properties of $\mathbf{L^3}$ in solution and as crystalline solid sample were compared. Although solid sample of $\mathbf{L^3}$ give only one main emission contribution arising from the radiative relaxation of the *cis*-keto* form, emission spectra of complexes at 350 nm show two bands attributed to the enol* and *cis*-keto* relaxation. We also note that replacement of Co^{II} ($\mathbf{C^1}$) by Ni^{II} ($\mathbf{C^4}$), has no influence on dihedral angles of $\mathbf{L^3}$ but leads to a slight emission shift for enol* and *cis*-keto* bands which is more important when replacing the S by a Se atom in $[Co(\mathbf{L^3})_2(NCS)_2(MeOH)_2]$. This observation confirms the electronic density change in $\mathbf{L^3}$ postulated to explain the observed H-bond strength change.

Theoretical calculations confirm our experimental investigations. Indeed, a significant impact of the metal ion coordination was seen in the energy of the enol, *cis*- and *trans*-keto forms as well as in the activation barrier between them in the ground state. Moreover, the nature of the metal ion also induces slight modifications in the height of this barrier. However, the most important effect of this parameter seems to be observed in the most stable conformation taken by $\mathbf{L^3}$ ligand in the complex. Indeed, although no clear

preference was noted for the nickel(II) complex (**C**^{4}), the copper complex (**C**^{5}) adopts preferential conformations, for example, with torsion angles C-$N_{pyridine}$-M-$N_{thiocyanate}$ of - 82° and + 90° in the case of the *cis*-keto form in the ground state. No information was, however, obtained for excited states preventing any prediction regarding the photochromism for **L**^{3} in the complexes.

Chapter VI: *N*-salicylidene 4-amino-1,2,4-triazole as precursor for spin crossover complexes

Introducing remarks

Molecules built with 1,2,4-triazole moiety are probably the most promising for the synthesis of iron(II) SCO complexes because of the suitable ligand field strength they provide.[121] They have offered a large variety of complexes dimensionalities[226] ranging from mononuclear[147] and oligonuclear (mostly dinuclear[227] and trinuclear[1, 228, 229]) to polynuclear systems. The polynuclear 1D chain is the most studied architecture.[123] These materials appear to be highly sensitive to ligands[230-232], anions[121, 122, 135, 138, 233-236] and solvent guest molecules nature, geometry and number.[237] These parameters can tune the SCO phenomenon and many industrial perspectives are thought. The influence of external constraints such as light irradiation (leading to photo-magnetic phenomena such as LIESST or LITH effects),[238-240] hydrostatic pressure[62] and sampling were also investigated for this class of materials. Indeed, metal or material dilution as well as the formation of films,[241-243] gels and supramolecular architectures,[244-249] nanoparticules,[250-254] and dendrimers[255, 256] were also studied. Triazole based SCO compounds were probed by EXAFS,[257, 258]Raman and infrared spectroscopies,[259-261] X-ray diffraction methods,[262]NMR,[263] XPS,[264] ellipsometry[265] and ZF-μSR and LF-μSR techniques[266, 267] but also simulated by computational means[268, 269]. A few reviews were published[123, 226] as well as some patents[251, 270, 271].

In this study, we were interested by the study of new dinuclear compounds built with **Hsaltrz** as ligands for iron(II) ions. This class of system has been rarely crystallized with only one reported example: $[Fe_2(pttrz)_5(NCS)_4]$, where pttrz = (4-*p*-tosyl)-1,2,4-triazole, which co-crystallizes and strongly interacts with a mononuclear $[Fe^{II}(pttrz)_2(NCS)_4]$.[227] It is important to notice that the crystal structure was only solved at room temperature in the [HS-HS] state.[227] The dinuclear contains two type of triazole ligands: two of them are terminal and monodentate although the three others are bidentate and ensure the bridge between the two metal ions.[227] This bridging framework was also identified in two other structures made with other 3d metal ions.[272, 273] Interestingly, the SCO phenomenon in dinuclear complexes is extensively studied[124, 274-286] because of the potential multi-step phenomenon[287, 288] which can occurs by formation of [HS-HS] and [LS-LS] pairs[124, 274] or stabilisation of an intermediate phase constituted with [LS-HS] dinuclear units[274, 275] which can interplay with long-range magnetic phenomena such as anti-ferromagnetism[275].

Moreover, we are interested by the use of the temperature dependent fluorimetry which is very less used for the study of the SCO phenomenon. Up to now, only two results are reported for this class of inorganic compounds but the SCO curve has not yet been precisely followed by this method on pure sample.[273, 289] Thus, we have decided to select *N*-salicylidene 4-amino-1,2,4-triazole (**Hsaltrz**) as fluorescent ligand (see chapter 2). In this chapter, we will then discuss about an unusual triazole based dinuclear of formula $[Fe^{II}_2(\mathbf{Hsaltrz})_5(NCS)_4]\bullet 4CH_3OH$ ($\mathbf{C^7}$) which was first prepared by Prof. Y. Garcia and later crystallised at UCL and analysed by SQUID magnetometry by Dr. G. Zhou in 2004.[290] The

temperature induced SCO phenomenon will be analyzed by ^{57}Fe Mössbauer spectroscopy and calorimetry. In addition to these 'traditional' techniques, we will finely discuss temperature dependent fluorimetry measurements in order to follow the SCO phenomenon. The crystal structure of **C^{7}** will also be compared with crystal structure of other $[Fe^{II}(\mathbf{Hsaltrz})_5(NCS)_4]\cdot S$, where solvent guest molecules S are constituted by 4 water molecules (**C^{8}**), 3 water and 1 methanol molecules (**C^{9}**), and of $[Co^{II}(\mathbf{Hsaltrz})_5(NCS)_4]\cdot 4H_2O\cdot CH_3OH$ (**C^{10}**). These three crystal structures have been obtained in our laboratory by Dr. G. Zhou[290], B. Muls,[291] and Dr. G. Marinescu,[292] respectively, and have been refined during this work and precisely analysed in the light of our knowledge about **Hsaltrz** in order to investigate the SCO phenomenon of this class of materials.

Syntheses and crystallization methods

The reproducibility of the synthesis of **C^{7}** was difficult to reach because of the strong sensitivity of this material to the quality of solvent used. The previous synthesis described by Dr. G. Zhou[290] could not be reproduced and was modified. In addition to Schlenk conditions (dried argon atmosphere), the methanol had to be dried on molecular sieves in order to avoid the formation of crystals containing water as guest molecules. After mixing all reactants, the yellow solution was kept for few weeks under a dried argon atmosphere to give beautiful yellow blocks which are used as fresh sample for all analyses. Compounds **C$^{8\text{-}10}$** were obtained using appropriated metal salt and with modified synthesis conditions which allow water to be trap in the materials (see experimental section).[290-292]

Crystal structures study

$[Fe_2(Hsaltrz)_5(NCS)_4]\cdot 4\ CH_3OH$ (C^7)

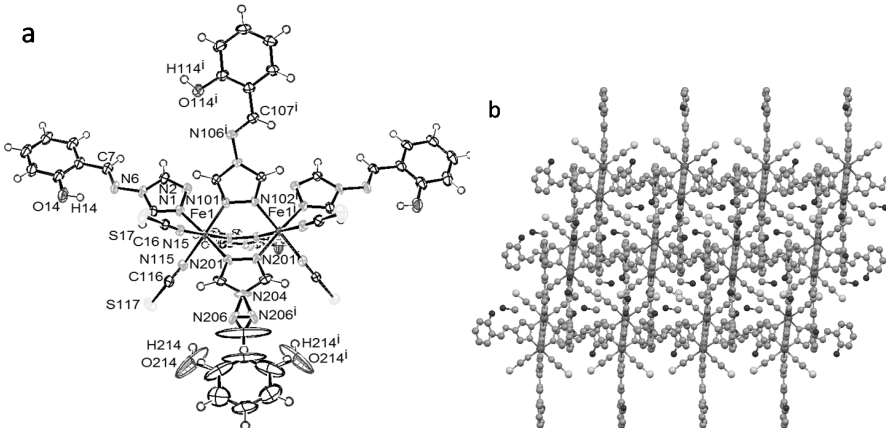

Figure 83 (a) ORTEP view of the asymmetric part of the unit cell of $\mathbf{C^7}$, showing 50% probability displacement ellipsoids. The disorder on the O214-H214 atoms of the alcohol function is clearly observed. (b) View of the crystal packing of the $\mathbf{C^7}$ along the *b* axis. H atoms were omitted for clarity. The presence of an organization by planes where methanol guest molecules are localised in voids can be identified.

The crystal structure of $\mathbf{C^7}$ was solved at 125 (2) and 240 (2) K by Prof. Tinant thanks to single crystals provided by Dr. G. Zhou. It crystallises in the monoclinic space group *C*2/c (Table 36). At 125 (2) K, an unusual triazole based dinuclear complex is identified with an inter-metal atoms distance of 3.648 (7) Å (Figure 83a). The two iron ions are identical and built by symmetry. They are bridged by three bidentate **Hsaltrz** ligands (through N101 and N102 (Hsaltrz 2), N201 and N202 (Hsaltrz 3)). The octahedral coordination spheres are completed by two isothiocyanato anions (in *cis* positions as in ref. [227]) and one monodentate **Hsaltrz** (in *cis* position as in ref. [227]) (coordination through N1 of Hsaltrz 1) affording a Fe^{II}-N_6 environment (Figure 83a and Table 37). The iron-nitrogen bond lengths are

comprised between 1.948 (3) Å and 1.985 (3) Å which are typical of LS state[64] of the metal ion and shows a [LS-LS] state for the dinuclear (Table 37). In the terminal and bridging **Hsaltrz** ligands, the bond lengths C9-O14, C109-O114 and C209-O214 of 1.360 (5) and 1.357 (5) Å respectively, confirm the enol form of these molecules (Table 37). In addition, single bonds are also indicated by C8-C7 (1.471 (5) Å), C108-C107 (1.447 (5) Å) and C208-C207 (1.458 (5) Å) bond lengths while double bonds are revealed by C7-N6 (1.283 (5) Å), C107-N106 (1.276 (5) Å) and C207-N206 (1.458 (5) Å) bond lengths[158] (Table 37). A change in the dihedral angle between aromatic rings is clearly distinguished between **Hsaltrz** molecules (Φ_1 = 8 (1)°, Φ_2 = 19 (1)° and Φ_3 = 1 (1)°) (Table 37). According to some authors[107], these differences can be interpreted as a slight change in electron conjugation in the molecule. Interestingly, these bonds lengths differences are combined with a change in the position of the H atom of the alcohol functions and a disorder on the imine function. Indeed, terminal Hsaltrz 1 presents a normal molecular scheme, showing the formation of a strong intramolecular H bond between the alcohol and the imine functions ($d_{H14\cdots N6}$ = 1.94 Å) (Table 38 and Figure 83a). The bridging Hsaltrz 2 presents an unusual conformation, previously observed for the free **Hsaltrz** molecule (see chapter 2), where the intramolecular H-bond is broken by a rotation of the alcohol function in order to create a intermolecular H-bond ($d_{H114\cdots O121}$ = 2.36 Å) (Table 38 and Figure 83a). The bridging Hsaltrz 3 ligand develops a conformation involving a disorder around the imine function translated by the observation of two N206 positions (Site Occupation Factor: 0.5/0.5) (Table 39 and Figure 83a) and two alcohol positions (O214-H214//H998, Site Occupation Factor: 0.5/0.5). The two alcohol positions present, as in the molecule Hsaltrz 1 (terminal molecule), a strong intramolecular H-bond

($d_{H214\cdots N206}$ = 2.52 Å) (Table 38). These three significantly different conformations could be explained by the presence of a dense supramolecular network (Table 38 and Table 40), built with 11 H-bonds, 4 π-π stacking and 3 C-H···π interactions, which binds differently Hsaltrz 1, 2 or 3. Indeed, Hsaltrz 2 is involved in 10 intermolecular interactions in place of 5 for Hsaltrz 1 and 7 for Hsaltrz 3. The supramolecular network induces a crystal packing organized by planes which contains iron ions and bridging **Hsaltrz** while the NCS^- fragments and the methanol guest molecules are placed between planes in order to build hydrophilic inter-plane spaces (Figure 83b).

At 240 (2) K, $\mathbf{C^7}$ crystal structure shows the same monoclinic *C*2/c space group (Table 36). No phase transition is observed within the 120 K-240 K temperature range. The increase of temperature leads to a longer Fe···Fe distance (3.966 (8) Å), which becomes similar to the value observed in ref. [227], and by a drastic change in the Fe-N bond lengths which are comprised between 2.107 (3) Å and 2.219 (3) Å (Table 37). These Fe-N data appear also to be in good adequacy with the reported values.[227] These thermally induced inter-atomic distances increase of approximately 9 % is typical of a SCO phenomenon[10] which leads to the formation of [HS-HS] pairs in the dinuclear complex. Interestingly, the SCO does not lead to any change neither in the distortion parameter nor in the angle observed with the isocyanato ligands (Table 37). The temperature has also no influence on the dihedral angles in **Hsaltrz** (Φ_1 = 8 (1)°, Φ_2 = 19 (1)° and Φ_3 = 3 (1)°) (Table 37), in the disorder observed in Hsaltrz 3 (Site Occupation Factor = 0.5/0.5) (Table 39) and on the positions of the H atoms of the alcohol functions of Hsaltrz 1, 2 and 3. Moreover, the enol form of all **Hsaltrz** ligand is preserved at 240 (2) K as shown by the C9-O14 (1.362 (6) Å), C109-O114

(1.356 (6) Å), C209-O214 (1.324 (8) Å), C8-C7 (1.457 (5) Å), C108-C107 (1.444 (5) Å), C208-C207 (1.458 (5) Å), C7-N6 (1.274 (6) Å), C107-N106 (1.270 (5) Å) and C207-N206 (1.458 (5) Å) (Table 37). The crystal packing is very less modified by the temperature change. We observe a slight dilatation of the inter-dinuclear distances (approximately 8.67 Å and 8.81 Å between Fe1 at 120 (2) K and 240 (2) K respectively). It leads to a slight decrease of supramolecular interactions intensity as shown by the inter-atomic distances in Table 38 and Table 40.

$[Fe_2(Hsaltrz)_5(NCS)_4]\cdot 3H_2O\cdot CH_3OH$ (C^8)

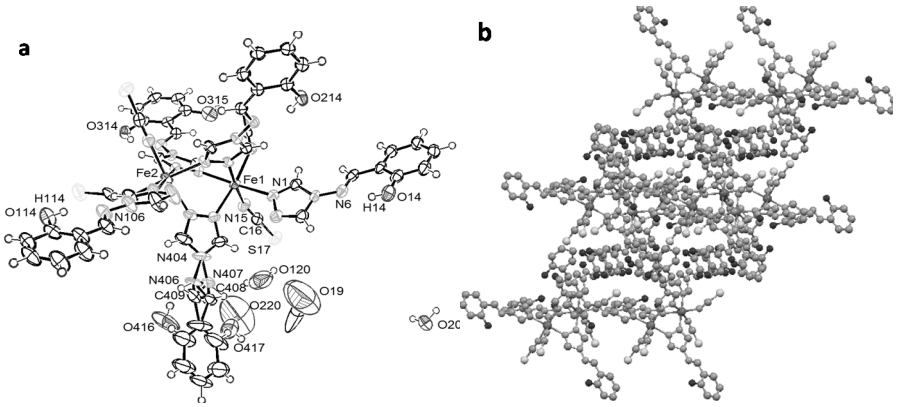

Figure 84 (a) ORTEP view of the asymmetric part of the unit cell of $\mathbf{C^8}$, showing 50% probability displacement ellipsoids. The disorder on the two alcohol (O314/O315 and O416/O417) and imine (N406/N407) functions is clearly observed. (b) View of the crystal packing of the $\mathbf{C^8}$ along the *c* axis. H atoms were omitted for clarity

The crystal structure of $\mathbf{C^8}$ was solved by Prof. B. Tinant, thanks to single crystals provided by Dr. G. Marinescu, at 125 (2) K and 240 (2) K. It crystallises in a triclinic space group $P\bar{1}$ (Table 36). At 125 (2) K, an unusual triazole based dinuclear complex is identified with an inter-metal atoms of 3.976 (5) Å (Figure 84a and Table 37). Two structurally different iron(II)

ions constitute the oligomer. Fe1 is characterized by a distorted (Σ = 35 (1)°) octahedral coordination sphere built by one terminal, monodentate **Hsaltrz** (Hsaltrz 1), coordinated by the N1 atom (Fe1-N1 = 2.196 (3) Å), three bridging **Hsaltrz** ligands (Hsaltrz 3-5), coordinated by N201 (Fe1-N201 = 2.220 (3) Å), N301 (Fe1-N301 = 2.170 (3) Å) and N402 (Fe1-N402 = 2.189 (3) Å), respectively, and by two isothiocyanato anions coordinated through the N15 (Fe1-N15 = 2.106 (3) Å) and N115 (Fe1-N115 = 2.166 (3) Å) atoms (Table 37). The Fe^{II}-N_6 environment which presents Fe-N bonds lengths in the 2.106 (3) Å – 2.220 (3) Å range is typical of a iron(II) ion in its HS state.[10] Fe2 present a similar coordination sphere than Fe1 but significantly less distorted (Σ = 28 (1)°) (Table 37). This metal ion is coordinated by one terminal, monodentate **Hsaltrz** (Hsaltrz 2) through N101 (Fe2-N101 = 2.154 (3) Å), the three bridging **Hsaltrz** (3-5) through N202 (Fe2-N202 = 2.216 (3) Å), N302 (Fe2-N302 = 2.181 (3) Å) and N401 (Fe2-N401 = 2.230 (3) Å) and by two isothiocyanato anions through N215 (Fe2-N215 = 2.111 (3) Å) and N315 (Fe2-N315 = 2.147 (3) Å) (Table 37). Interestingly, when we analyse the isothiocyanato anions, an important difference is seen in the Fe-N-C angles which are identified as Fe1-N15-C16 = 150.8 (3)° and Fe1-N115-C116 = 142.4 (3)° around Fe1 and Fe2-N215-C216 = 175.5 (3)°, Fe2-N315-C316 = 149.4 (3)° around Fe2 (Table 37). A large difference is then observed not only between iron(II) coordination sphere (Fe1 or Fe2) but also between the two NCS coordinated on a same iron site. The study of the **Hsaltrz** ligands demonstrates that all ligands are in the enol form as confirmed by the C-O and C=N single and double bonds, respectively (C-O = 1.333 (9) Å – 1.40 (1) Å and C=N = 1.264 (8) Å – 1.282 (4) Å) (Table 37).[158] Terminal **Hsaltrz** appear to be very similar in dihedral angle between aromatic rings (Φ = 16-17 (1)°) and in bonds lengths (Table 37).

These ligands are characterised by a conformation usually observed for the *N*-salicylidene aniline derivatives, which involves the presence of a strong intramolecular H-bond between the alcohol and imine functions (O14-H14•••N6 = 1.92 Å and O114-H114•••N106 = 1.93 Å) (Table 38). One of the bridging ligands, Hsaltrz 3, presents the same conformation than the terminal ones but appears to be slightly less twisted (Φ = 11 (1)°, O214-H214•••N206 = 1.94 Å) (Table 38). Hsaltrz 4 is significantly more twisted than other **Hsaltrz** ligands (Φ = 29 (1)°) (Table 37) and present also an new conformation which involves a disorder on the alcohol function which is 91 % of time targeted to Fe2 and 9 % of time to Fe1 (Table 39). Moreover, as shown in the crystal structure, it implies that the intramolecular H-bond (O314-H314···N306 = 1.95 Å) is present in the molecule only 91 % of time (Table 38 and Table 39). Hsaltrz 5 is also found with another conformation induced by a double disorder observed on the alcohol function (Site Occupation Factor (SOF): O416/O417 = 37/63 (1) %) and on the imine function (SOF: N406/N407 = 43/57 (1) %) (Table 39). This structural configuration was already met with **C**[7], described in the previous section. The iron(II) dinuclear complex is surrounded by one methanol and three water uncoordinated guest molecules which allow the formation of a supramolecular network of H-bonds (Table 38). These interactions are completed by ten C-H···π and π-π stacking interactions directed by the **Hsaltrz** molecules (Table 41). We notice that three of the isothiocyanato anions are actively involved in the supramolecular network (Table 38 and Table 41). The supramolecular network induces a crystal packing organized by planes which contains iron ions and bridging **Hsaltrz** while the NCS^- fragments and the methanol guest molecules are placed between planes in order to build hydrophilic inter-plane spaces (Figure 84b).

At 240 K, the crystal structure is isostructural to the structure measured at 125 K (Table 36). All parameters, such as asymmetric cell composition, enol form of **Hsaltrz** molecules, coordination bonds lengths and angles, dihedral angles, supramolecular network and SOF values, are almost identical (Table 37, Table 38, Table 39 and Table 41). The temperature seems to have only a slight influence on the cell volume which is dilated at high temperature (Table 36). No spin crossover phenomenon of the iron(II) ions is observed because of the HS states observed over the whole temperature range (125-240 (2) K) (Table 37). This result has been confirmed by temperature dependent magnetic susceptibility measurements.[290]

$[Fe_2(Hsaltrz)_5(NCS)_4]\cdot 4H_2O$ (C^9)

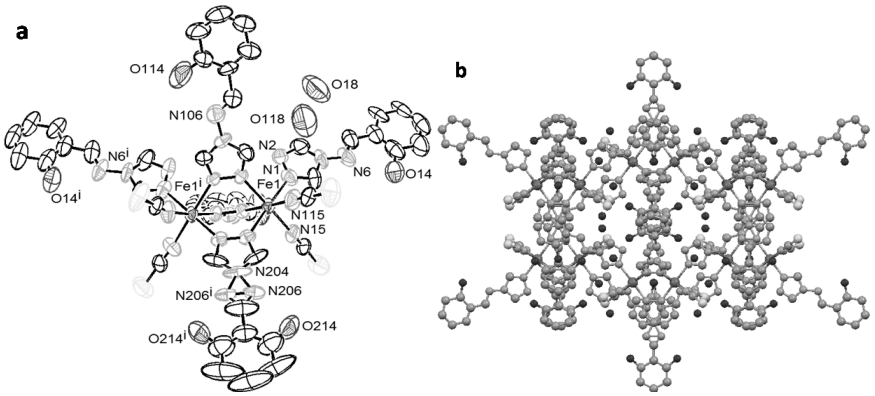

Figure 85 (a) ORTEP view of the asymmetric part of the unit cell of $\mathbf{C^9}$, showing 50% probability displacement ellipsoids. The disorder on the alcohol (O214) and imine (N206) functions is clearly observed. H atoms were omitted for clarity. (b) View of the crystal packing of the $\mathbf{C^9}$ along the *c* axis. H atoms were omitted for clarity. The presence of water guest molecules in voids can be identified.

The crystal structure of $\mathbf{C^9}$ was solved at 293 (2) K by Prof. B. Tinant thanks to single crystals provided by B. Muls.[293] It crystallises in a monoclinic space group *C*2/c (Table 42). As in $\mathbf{C^{7\text{-}8}}$, a triazole based dinuclear complex,

built by symmetry, is identified in the crystal structure cell with an inter-metal atoms of 3.97 (3) Å (Figure 85a and Table 43). The only iron(II) site is characterized by a weakly distorted (Σ = 19.1 (7)°) octahedral coordination sphere (Table 43). Iron(II) ions are coordinated by one terminal, monodentate **Hsaltrz** (Hsaltrz 1), coordinated by the N1 atom (Fe1-N1 = 2.17 (1) Å), three bridging **Hsaltrz** ligands (Hsaltrz 2-3), coordinated by N101 (Fe1-N101 = 2.20 (1) Å) and N201 (Fe1-N201 = 2.16 (1) Å), respectively, and by two isothiocyanato anions coordinated through the N15 (Fe1-N15 = 2.11 (2) Å) and N115 (Fe1-N115 = 2.11 (2) Å) atoms (Table 43). The Fe^{II}-N_6 environment which presents Fe-N bonds lengths in the 2.11 (2) Å – 2.24 (1) Å range is typical of a iron(II) ion in its HS state (Table 43)[10]. The two isothiocyanato anions are linear and show a very large Fe-N(1)15=C1(16) angle, close than 180° (Fe1-N15-C16 = 168 (2)° and Fe1-N115-C116 = 174 (2)°) (Table 43). As in **C**[7-8], all **Hsaltrz** molecules appear to be in their enol forms. It is clearly demonstrated by the C-O and C=N single and double bonds, respectively (C-O = 1.32 (4) Å – 1.39 (1) Å and C=N = 1.10 (2) Å – 1.26 (3) Å) (Table 43).[158] Monodentate **Hsaltrz** (Hsaltrz 1) present a very weak dihedral angle Φ = 3 (1)° and has a normal conformation involving the presence of a strong intramolecular H-bonds between the alcohol and the imine functions (O14-H14···N6 = 2.00 Å) (Table 43 and Table 44). The first type of bridging **Hsaltrz** (Hsaltrz 2) present a slightly more twisted conformation (Φ = 15 (1)°) also involving a strong intramolecular H-bond (O114-H114···N116= 1.97 Å) (Table 43 and Table 44). Finally, as in **C**[8], Hsaltrz 3 is characterised by the presence of a very weak dihedral angle between aromatic rings (Φ = 2 (1)°) and by a disorder on the alcohol and the imine functions (Table 43 and Table 39). The site occupation factor was evaluated as 0.5 for the position 1 (N206, O214

and H214) and 0.5 for the second one (N206i, O214i, H214i) (Table 39). These positions are, indeed, generated in the crystal structure by symmetry. In contrast to **C[8]**, the strong intramolecular H-bond is then observed in all **Hsaltrz** in all their positions (O214-H214•••N206 = 1.81 Å) (Table 44). The iron(II) dinuclear complex is surrounded by four water uncoordinated guest molecules, no methanol molecule was identified in this structure. A developed supramolecular network of H-bonds is identified in **C[9]** (Table 44). These interactions are completed by 6 C-H$\cdots\pi$ and π-π stacking interactions directed by the **Hsaltrz** molecules (Table 45). We notice that the isothiocyanato anions are not involved in supramolecular interaction with water guest molecules. As in **C[7-8]**, a crystal packing organized by planes which contains iron ions and bridging **Hsaltrz** while the NCS^- fragments and the methanol guest molecules are placed between planes in order to build hydrophilic inter-plane spaces is identified along the *c* axis (Figure 85b). The magnetic properties of **C[9]** are described in ref. [291] and reveal a thermo-induced SCO phenomenon characterised by a $T_{1/2}$ of 174(1) K and by a non-active HS ratio of 30 % even at 5 K.

$[Co_2(Hsaltrz)_5(NCS)_4]\cdot 4H_2O\cdot CH_3OH$ (C^{10})

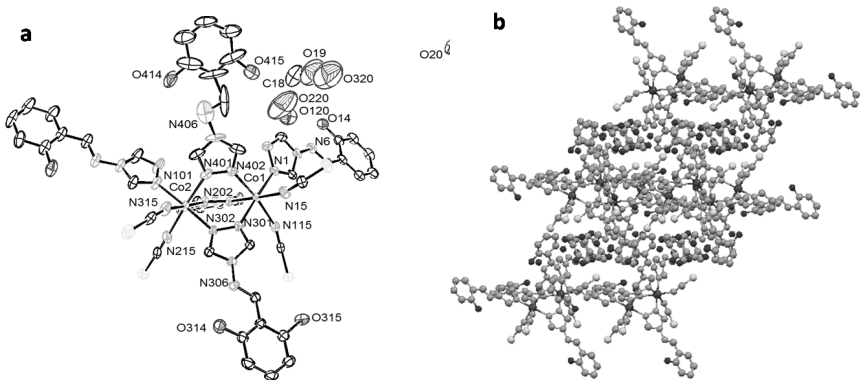

Figure 86 (a) ORTEP view of the asymmetric part of the unit cell of $\mathbf{C^{10}}$, showing 50% probability displacement ellipsoids. The disorder on the alcohol (O314/O315 and O414/O415) functions is clearly observed. H atoms were omitted for clarity. (b) View of the crystal packing of the $\mathbf{C^{10}}$ along the *c* axis. H atoms were omitted for clarity.

The crystal structure of $\mathbf{C^{10}}$ was solved at 293 (2) K by Prof. B. Tinant thanks to single crystals prepared by Dr. G. Marinescu. It crystallises in a triclinic space group $P\bar{1}$ (Table 42). As for the two previous compounds, the crystal structure of $\mathbf{C^{10}}$ is composed of a triazole based dinuclear complex (Figure 86). The two cobalt(II) ions, distant of 3.895 (5) Å, are surrounded by strongly distorted coordination spheres (Σ = 30.5 (4)° and 23.6 (4)° for Co1 and Co2, respectively) (Table 43). Co1 is coordinated to one terminal, monodentate **Hsaltrz** (Hsaltrz 1), coordinated through the N1 atom (Co1-N1 = 2.143 (3) Å), three bridging **Hsaltrz** ligands (Hsaltrz 3-5), coordinated by N201 (Co1-N201 = 2.160 (3) Å), N301 (Co1-N301 = 2.117 (3) Å) and N402 (Co1-N402 = 2.147 (3) Å), respectively, and by two isothiocyanato anions coordinated through the N15 (Co1-N15 = 2.072 (3) Å) and N115 (Co1-N115 = 2.150 (3) Å) atoms (Table 43). Co-N bonds lengths enter in a 2.072 (3) Å – 2.160 (3) Å range which is typical of cobalt(II) ions in HS state (Table

43).[218] Co2 is similar to Co1 but significantly less distorted (Σ = 23.6 (4)°) (Table 43). This metal ion is coordinated by one terminal, monodentate **Hsaltrz** (Hsaltrz 2) through N101 (Co2-N101 = 2.126 (3) Å), the three bridging **Hsaltrz** (3-5) through N202 (Co2-N202 = 2.145 (3) Å), N302 (Co2-N302 = 2.142 (3) Å) and N401 (Co2-N401 = 2.151 (3) Å) and by two isothiocyanato anions through N215 (Co2-N215 = 2.086 (4) Å) and N315 (Co2-N315 = 2.092 (4) Å) (Table 43). As in **C**$^{7-9}$, all **Hsaltrz** ligands are present in the enol form as confirmed by the C-O and C=N single and double bonds, respectively (C-O = 1.350 (5) Å – 1.42 (2) Å and C=N = 1.150 (6) Å – 1.292 (5) Å) (Table 43)[158, 294]. The four isothiocyanato anions are significantly different as seen in the Co-N-C angles which are identified as Co1-N15-C16 = 153.1 (3)°, Co1-N115-C116 = 141.7 (3)°, Co2-N215-C216 = 173.5 (3)° and Co2-N315-C316 = 152.4 (4)° (Table 43). When we look at the **Hsaltrz** ligands, we observe that terminal molecules are different in dihedral angle between aromatic rings (Φ_1 = 19 (1)° and Φ_2 = 10 (1)° for Hsaltrz 1 and 2, respectively) but are similar in bonds lengths (Table 43). The terminal ligands show the usual conformation for the *N*-salicylidene aniline derivatives involving the presence of a strong intramolecular H-bond between the alcohol and imine functions (O14-H14···N6 = 1.94 Å and O114-H114···N106 = 1.93 Å) (Table 44). As in **C**^{8}, one of the bridging ligands, Hsaltrz 3, presents the same conformation than the terminal ones but is almost planar (Φ = 1 (1)°, O214-H214···N206 = 1.94 Å) (Table 43 and Table 44). Both Hsaltrz 4 and 5 show a disorder on the alcohol function only with SOF values of O314-H314 = 92.5 (8) % and O315-H315 = 7.5 (8) % for Hsaltrz 4 and of O414-H414 = 54 (1) % and O415-H415 = 46 (1) % for Hsaltrz 5 (Table 39). In both case, a strong intramolecular H-bond is observed only for the first position (O314-H314···N306 = 1.94 Å and O414-

H414···N406 = 1.88 Å) although no supramolecular interaction is observed for the second positions (Table 44). It is interesting to notice also that Hsaltrz 4 and 5 are very different in dihedral angle (Φ = 31 (1)° and 4 (1)°, respectively) and in bond lengths (see Table 43). Crystal structure of **C[10]** also contains one methanol and four water uncoordinated guest molecules leading to an intense supramolecular network of H-bonds (Table 44). Ten C-H···π and π-π stacking interactions directed by the **Hsaltrz** molecules are also identified in the crystal network (Table 45). We notice that, as in **C[8]**, three of the isothiocyanato anions are actively involved in the supramolecular network. The crystal packing is organized by planes containing metal ions and bridging **Hsaltrz**. The NCS^- anions and the guest molecules are then distributed between planes leading to the formation of hydrophilic inter-plane spaces (Figure 86b). The magnetic properties of this cobalt dinuclear complex reveal an overall AF behaviour between spin carriers.[290]

SQUID magnetometry and ^{57}Fe Mössbauer spectroscopy of C^7

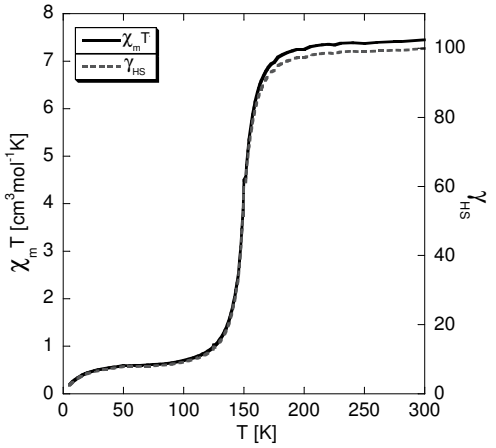

Figure 87 Temperature dependence of χ_MT and of molar fraction of HS iron(II) ions obtained by SQUID magnetometry of a fresh **C^7** sample.

The temperature dependent SQUID measurements were carried out on a fresh sample of **C^7** between 5 K and 300 K (Figure 87). The data have been obtained by Dr. G. Zhou and Prof. Y. Garcia at EPL in the laboratory of Prof. L. Piraux (UCL).[290] The susceptibility was converted to a Fe^{II}_{HS} ratio (γ_{HS}) curve by means of Equation (1): $\gamma_{HS} = \frac{\chi_M(T) - \chi_M^{LS}(T)}{\chi_M^{HS}(T) - \chi_M^{LS}(T)}$ where $\chi_M^{LS}(T)$ = 184 x 10^{-6} cm^3mol^{-1} below 50 K[295] and χ_M^{HS} = 7.46 cm^3mol^{-1}. As shown in Figure 87, the SCO observed in X-ray diffraction measurements is confirmed by magnetometry. At 300 K, $\chi_M T$ = 7.46 $cm^3mol^{-1}K$ that corresponds to the value of 2 non coupled Fe(II) ions. On cooling, $\chi_M T$ drops from 7.37 $cm^3mol^{-1}K$ to 0.60 $cm^3mol^{-1}K$ at 250 and 50 K respectively, indicating an incomplete SCO. We also note a

slight decrease of the $\chi_M T$ below 50 K which could be attributed to a zero field splitting phenomenon and possibility to an AF coupling of remaining HS iron(II) ions. The SCO is observed between 138 (1) K and 161 (1) K (over a temperature range of 23 (1) K; ΔT^{80}, which is defined as the temperature range where 80 % of sites undergo a SCO[1] (from γ_{HS} = 10 % to 90%), equals 35 (1) K) and present a transition temperature $T_{1/2}$ (at which 50% of active LS and HS molecules are present) of 150 (1) K. No thermal hysteresis was observed. Figure 87 shows that the SCO is almost completed over the whole temperature range. The remaining Fe^{II}_{HS} ratio at 50 K is ~ 7.6 % while at 300 K, all iron ions are in the HS state.

^{57}Fe Mössbauer spectra were recorded in the SCO range (93-208 K, see experimental section for details) in order to probe the behaviour of iron ions in the dinuclears. At 93 (1) K, the spectrum consists of four quadrupole doublets of different resonance area fractions (Figure 88, see Table 10 to Table 13). A first doublet (in dark grey in Figure 88), with δ = 0.43 (1) mm.s^{-1}, ΔE_Q = 0.16 (9) mm.s^{-1} and a relative area fraction of 45 (3) %, is attributed to a LS iron site (Fe^{II}_{LS1}). A second doublet (in black in Figure 88) with isomer shift δ = 0.41 (2) mm.s^{-1}, a quadrupole splitting ΔE_Q = 0.5 (1) mm.s^{-1} and a relative area fraction of 36 (3) % is attributed to a second LS iron (II) site (Fe^{II}_{LS2}) more distorted than Fe^{II}_{LS1}.[222] Two other quadrupole doublets which can be attributed to two HS iron (II) sites (Fe^{II}_{HS2} and Fe^{II}_{HS3})[222] are also observed with δ^{HS2} = 1.13 (8) mm.s^{-1} and δ^{HS3} = 1.34 (5) mm.s^{-1}, $\Delta E_Q{}^{HS2}$ = 3.3 (1) mm.s^{-1} and $\Delta E_Q{}^{HS3}$ = 3.2 (1) mm.s^{-1} and relative area fractions of 14 (9) % and 5 (7) %, respectively. Interestingly, we notice that two different iron LS sites are detected although the two iron ions observed by crystallography were built by symmetry.

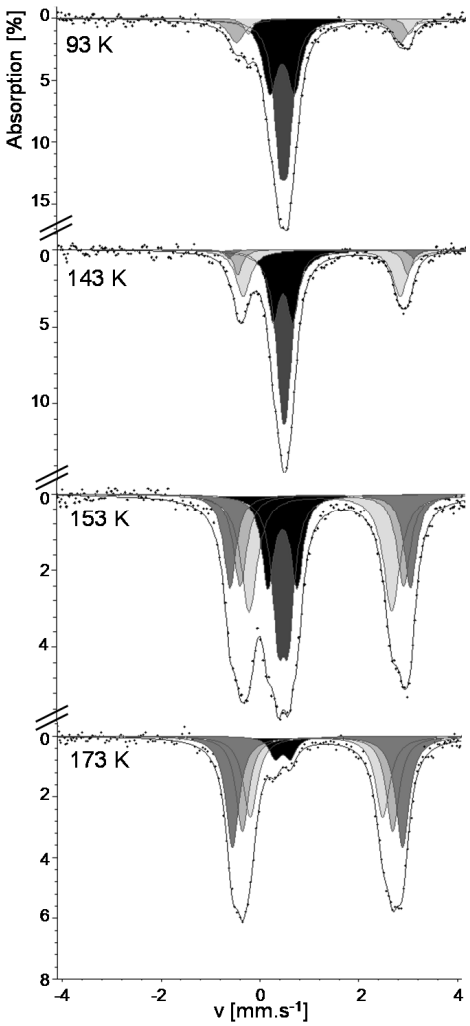

Figure 88 ^{57}Fe Mössbauer spectra of **C^{7}** at selected temperatures recorder on warming from 93 K. Signals LS1 and LS2 are in darkest grey and black, respectively, signals HS1-3 are represented in light to dark grey.

Table 10 Temperature dependence of δ in ^{57}Fe Mössbauer spectra of **C**[7] over the temperature range 93-208 K.

T [K]	Fe^{II}_{LS1}	Fe^{II}_{LS2}	Fe^{II}_{HS1}	Fe^{II}_{HS2}	Fe^{II}_{HS3}
93 (1)	0.43 (1)	0.41 (2)	-	1.13 (8)	1.34 (5)
98 (1)	0.43 (1)	0.40 (2)	-	1.06 (7)	1.28 (5)
103 (1)	0.44 (1)	0.41 (1)	-	1.12 (5)	1.30 (7)
108 (1)	0.44 (1)	0.41 (1)	-	1.14 (5)	1.34 (7)
113 (1)	0.44 (1)	0.41 (1)	-	1.12 (5)	1.32*
118 (1)	0.44 (1)	0.41 (1)	-	1.12 (4)	1.31 (5)
123 (1)	0.43 (1)	0.41 (1)	-	1.13 (9)	1.27*
128 (1)	0.42 (1)	0.40 (1)	-	1.07 (3)	1.25 (2)
138 (1)	0.43 (1)	0.40 (1)	-	1.18 (1)	1.19 (1)
143 (1)	0.43 (1)	0.41 (2)	1.18 (7)	1.20 (3)	1.18 (2)
148 (1)	0.42 (1)	0.38 (1)	1.18 (2)	1.20 (2)	1.18 (2)
153 (1)	0.43 (1)	0.42 (1)	1.17 (2)	1.21 (2)	1.18 (1)
158 (1)	0.42*	0.41*	1.16 (1)	1.18 (1)	1.16 (1)
163 (1)	0.42 (3)	0.4 (1)	1.17 (1)	1.18 (1)	1.16 (1)
168 (1)	0.44 (3)	-	1.15 (1)	1.17 (1)	1.14 (1)
173 (1)	0.46 (5)	-	1.16 (1)	1.17 (1)	1.14 (2)
178 (1)	0.38 (5)	-	1.16 (1)	1.17 (1)	1.15 (1)
183 (1)	0.4 (2)	-	1.16 (1)	1.17 (1)	1.14 (1)
188 (1)	0.4 (2)	-	1.16 (2)	1.16 (2)	1.14 (2)
193 (1)	0.4 (1)	-	1.15 (1)	1.15 (1)	1.13 (1)
198 (1)	0.4 (1)	-	1.15 (1)	1.14 (1)	1.13 (1)
208 (1)	0.4*	-	1.15 (1)	1.15 (1)	1.13 (1)

* symbol shows values which were fixed during data fitting.

Table 11 Temperature dependence of ΔE_Q in ^{57}Fe Mössbauer spectra of **C**[7] over the temperature range 93-208 K.

T [K]	Fe^{II}_{LS1}	Fe^{II}_{LS2}	Fe^{II}_{HS1}	Fe^{II}_{HS2}	Fe^{II}_{HS3}
93 (1)	0.16 (4)	0.5 (1)	-	3.3 (1)	3.2 (1)
98 (1)	0.14 (3)	0.4 (1)	-	3.3 (1)	3.3 (1)
103 (1)	0.14 (1)	0.5 (1)	-	3.3 (1)	3.3 (1)
108 (1)	0.14 (2)	0.4 (1)	-	3.2 (1)	3.2 (1)
113 (1)	0.16 (2)	0.5 (1)	-	3.2 (1)	3.2 (1)
118 (1)	0.14 (1)	0.5 (1)	-	3.3 (1)	3.2 (1)
123 (1)	0.17 (4)	0.5 (1)	-	3.3 (1)	3.3*
128 (1)	0.14 (1)	0.5 (1)	-	3.3 (1)	3.3 (1)
138 (1)	0.13 (2)	0.4 (1)	-	3.5 (1)	3.2 (1)
143 (1)	0.1 (1)	0.4 (1)	3.7 (2)	3.4 (1)	3.1 (2)
148 (1)	0.2 (1)	0.5 (1)	3.6 (1)	3.3 (1)	3.0 (1)
153 (1)	0.2 (1)	0.6 (1)	3.6 (1)	3.3 (1)	2.8 (1)
158 (1)	0.2 (1)	0.6 (1)	3.6 (1)	3.2 (1)	2.8 (1)
163 (1)	0.2 (1)	0.7 (2)	3.6 (1)	3.2 (1)	2.8 (1)
168 (1)	0.3 (1)	-	3.4 (1)	3.0 (1)	2.6 (1)
173 (1)	0.3 (1)	-	3.4 (1)	3.0 (1)	2.7 (1)
178 (1)	0.3 (1)	-	3.6 (1)	3.2 (1)	2.8 (1)
183 (1)	0.3*	-	3.6 (1)	3.1 (1)	2.7 (1)
188 (1)	0.3*	-	3.4 (1)	3.1 (1)	2.8 (1)
193 (1)	0.3*	-	3.4 (1)	3.1 (1)	2.7 (1)
198 (1)	0.3*	-	3.4 (1)	3.1 (1)	2.7 (1)
208 (1)	0.3*	-	3.3 (1)	3.1 (1)	2.7 (1)

* symbol shows values which were fixed during data fitting.

Table 12 Temperature dependence of Γ/2 in ^{57}Fe Mössbauer spectra of **C**[7] over the temperature range 93-208 K.

T [K]	Fe^{II}_{LS1}	Fe^{II}_{LS2}	Fe^{II}_{HS1}	Fe^{II}_{HS2}	Fe^{II}_{HS3}
93 (1)	0.14 (6)	0.18 (4)	-	0.20 (8)	0.1 (1)
98 (1)	0.15 (6)	0.16 (4)	-	0.1 (1)	0.16 (6)
103 (1)	0.14 (2)	0.14 (2)	-	0.18 (4)	0.17 (6)
108 (1)	0.13 (1)	0.14 (2)	-	0.14 (5)	0.12 (9)
113 (1)	0.15 (1)	0.15 (2)	-	0.20 (6)	0.18 (9)
118 (1)	0.14 (2)	0.14 (2)	-	0.18 (3)	0.16 (5)
123 (1)	0.14 (5)	0.15 (4)	-	0.2 (1)	0.24 (8)
128 (1)	0.13 (2)	0.14 (1)	-	0.14 (3)	0.17 (2)
138 (1)	0.13 (3)	0.14 (2)	-	0.14 (5)	0.17 (3)
143 (1)	0.15 (7)	0.14 (6)	0.17 (4)	0.1 (2)	0.1 (2)
148 (1)	0.14 (4)	0.14 (3)	0.12 (6)	0.1 (1)	0.12 (6)
153 (1)	0.14 (6)	0.15 (4)	0.15 (4)	0.2 (1)	0.20 (3)
158 (1)	0.2 (1)	0.1 (1)	0.15 (2)	0.17 (2)	0.17 (2)
163 (1)	0.2 (2)	0.1 (2)	0.16 (4)	0.2 (1)	0.17 (4)
168 (1)	0.18 (5)	-	0.15 (2)	0.16 (4)	0.16 (2)
173 (1)	0.14 (7)	-	0.16 (4)	0.2 (1)	0.17 (5)
178 (1)	0.14 (7)	-	0.16 (1)	0.17 (3)	0.16 (2)
183 (1)	0.3 (3)	-	0.16 (1)	0.18 (3)	0.17 (2)
188 (1)	0.2 (4)	-	0.14 (4)	0.14 (6)	0.16 (4)
193 (1)	0.2 (2)	-	0.15 (3)	0.13 (8)	0.14 (2)
198 (1)	0.11 (7)	-	0.14 (3)	0.13 (8)	0.14 (3)
208 (1)	0.2 (2)	-	0.15 (2)	0.15 (6)	0.15 (3)

Table 13 Temperature dependence of the relative area of signals observed in ^{57}Fe Mössbauer spectra of **C**[7] over the temperature range 93-208 K. The presence of many signals in δ and ΔE_Q narrow ranges could explain the larger errors observed.

T [K]	Fe^{II}_{LS1}	Fe^{II}_{LS2}	Fe^{II}_{HS1}	Fe^{II}_{HS2}	Fe^{II}_{HS3}
93 (1)	45 (3)	36 (3)	0	14 (9)	5 (7)
98 (1)	49 (2)	33 (2)	0	5 (6)	13 (7)
103 (1)	52 (9)	27 (9)	0	12 (8)	9 (8)
108 (1)	50*	30 (2)	0	14 (8)	6 (8)
113 (1)	53*	25 (2)	0	15 (6)	7 (6)
118 (1)	48 (9)	29 (8)	0	14 (6)	8 (6)
123 (1)	45 (2)	30 (2)	0	9 (9)	16 (9)
128 (1)	48 (7)	25 (7)	0	8 (4)	18 (5)
138 (1)	43 (1)	26 (1)	0	11 (9)	19 (9)
143 (1)	41 (3)	26 (3)	2 (8)	7 (2)	23 (2)
148 (1)	40 (1)	24 (1)	8 (8)	7 (1)	21 (1)
153 (1)	21 (1)	16 (1)	17 (1)	18 (2)	28 (1)
158 (1)	13 (1)	6 (1)	26 (5)	28*	27 (5)
163 (1)	10 (9)	2 (8)	30 (2)	28 (5)	29 (4)
168 (1)	8 (1)	0	28 (1)	33 (2)	31 (8)
173 (1)	6 (2)	0	36 (2)	30 (5)	28 (3)
178 (1)	4 (1)	0	32*	30 (9)	34 (9)
183 (1)	5 (3)	0	32*	27 (3)	35*
188 (1)	4 (5)	0	28*	32 (8)	37*
193 (1)	4 (2)	0	33 (2)	29 (4)	35 (2)
198 (1)	3 (1)	0	29 (2)	34 (4)	34 (4)
208 (1)	3 (2)	0	30*	30 (2)	37 (2)

* symbol shows values which were fixed during data fitting.

Our hypothesis is that the differentiation could come from the crystallographic disorder observed by X-ray diffraction but the presence of the tautomeric equilibrium between the enol and the *cis*-keto forms could

also play a role in this observation. Up to 143 (1) K, similar spectra are obtained but at this temperature, a fifth contribution, attributed to a Fe^{II}_{HS1} signal,[222] is observed with δ = 1.18 (7) mm.s^{-1}, ΔE_Q = 3.7 (2) mm.s^{-1} and a relative area fraction of 2 (8) % (Figure 88, Table 10 to Table 13). From 143 K to 173 K, a drastic transformation is observed in Mössbauer spectra. The relative area fractions of the two Fe^{II}_{LS} signals appear to strongly decrease to 6 (2) % and 0 %, respectively (Figure 88 and Table 13). In contrast, Fe^{II}_{HS1} and Fe^{II}_{HS2} signals increase to 36 (2) % and 30 (5) % respectively (increases are significantly higher to errors as shown in Table 13). Finally, spectra between 173 (1) K and 208 (1) K, which are similar to the one at 173 (1) K, are obtained. Figure 89 shows the evolution of the relative area fraction of all sites. The SCO is clearly confirmed by the drastic increase of the Fe^{II}_{HS1} and Fe^{II}_{HS2} relative area fractions and the decrease of the Fe^{II}_{LS1} and Fe^{II}_{LS2} which begin at the onset temperature of 147 (1) K and stop at the onset temperature of 161 (1) K. $T_{1/2}$ is observed at 154 (1) K which fits well with the data obtained by SQUID measurements (150 K). Fe^{II}_{HS3} (Figure 88 in light grey) presents a linear increase of its relative area fraction. It translates that this increase could be an artefact lead by a difference of *f* factor (ratio of γ absorption without recoil).[222] This possibility is also supported by the presence of single crystals which usually lead to very efficient γ absorption phenomenon at low temperature, as observed during this work. Interrestingly, when we examine the evolution of the Mössbauer parameters δ and ΔE_Q, we could distinguish a discontinuity for Fe^{II}_{HS3} and Fe^{II}_{HS2} between about 120 and 140 K. This phenomenon should take its orign in the presence of a hidden additional site or in significant modification of these sites. However, new X-ray diffraction data should be obtained in this temperature range in order to clarify the observation.

The addition of all relative area fractions of HS iron (II) sites leads to a γ_{HS} which fits well with the same value obtained by SQUID measurements as shown in Figure 90. We can notice than below 140 K, the γ_{HS} obtained by Mössbauer spectroscopy is slightly higher than the other one but it takes in origin in the presence of Fe^{II}_{HS3} site which is probably over-estimated. It is well suggested by the corrected Mössbauer values shown in Figure 90 which takes in account relative area fractions data where the contribution of Fe^{II}_{HS3} is neglected. A perfect match between the magnetic and the Mössbauer curves is obtained.

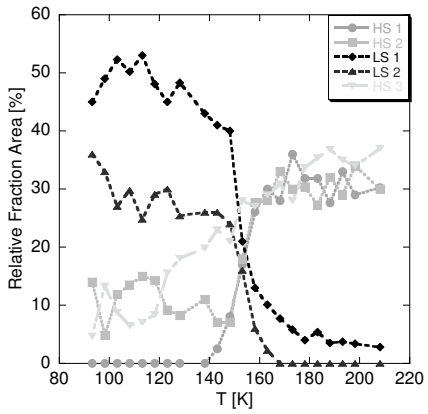

Figure 89 Temperature dependence of the relative area fractions of iron signals obtained on ^{57}Fe Mössbauer spectra of **C^7** from 93 K to 208 K.

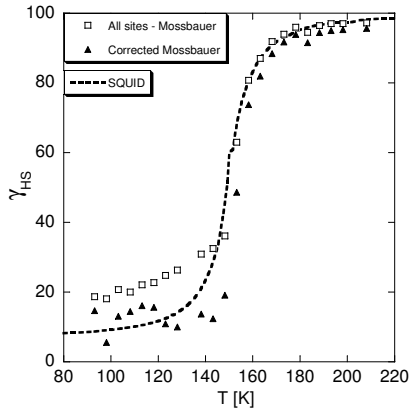

Figure 90 Temperature dependence of the molar fraction of HS iron(II) ions for **C**[7] obtained by the SQUID and ^{57}Fe Mössbauer experiments. The 'corrected' Mössbauer data points correspond to the data obtained when the Fe^{II}_{HS3} contribution is neglected.

Differential scanning calorimetry

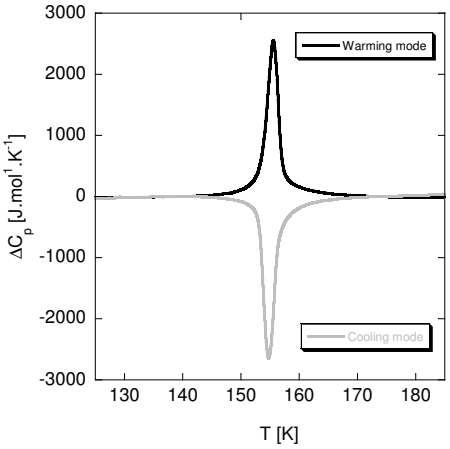

Figure 91 DSC measurements of **C**[7] in the 104 K to 300 K temperature range. The cooling and warming modes are in grey and black respectively.

C[7] was investigated by Differential Scanning Calorimetry over the T range 100 (1) - 300 (1) K on cooling and warming modes with a scanning rate of 5

K.min^{-1}. The DSC response for **C^7** is given in Figure 91. A remarkable exothermic peak is observed on cooling at a maximum temperature of 155 (1) K which corresponds very well with the $T_{1/2}$ value obtained by SQUID and Mössbauer measurements (150 and 154 K, respectively). In the warming mode, a very similar endothermic peak with a maximum at 155 (1) K is observed, confirming the absence of hysteresis phenomenon. The enthalpy and entropy variations have been evaluated as ΔH = 8.6 kJ.mol^{-1} and ΔS = 56 J.mol^{-1}K^{-1} considering the transition of the active iron(II) ions (97.5 %) obtained by SQUID and Mössbauer measurements. The experimental entropy variation can be accounted for by an electronic contribution, R x ln 5 = 13.4 J.mol^{-1}K^{-1}, and a vibrational contribution (42 J.mol^{-1}K^{-1})[10].

Optical properties

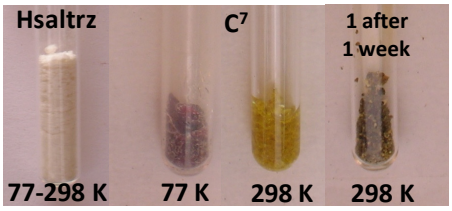

Figure 92 Photographs of a powder sample of **Hsaltrz** over the temperature range 77-298 K and of a crystalline sample of **C^7** at 77 K and 298 K and, after keeping in air during one week, at 298 K. The thermochromism and the aging effect are clearly identified.

As shown in Figure 92, while **Hsaltrz** is white in the temperature range 77-298 K, crystalline sample of **C^7** presents a strong yellow colour at room temperature which turns to deep burgundy at 77 K. Moreover, crystals of **C^7** are unstable in air at room temperature. Indeed, a clear colour change is observed from yellow to a dark brown colour as shown in Figure 92. It is

assumed to take its origin in a loss of solvent molecules seen in the crystal structure (supported by diffuse reflectance spectra described below). The phenomenon is a surface effect because it does not lead to significant ^{57}Fe Mössbauer spectra change (corresponding to a bulk measurement) and because a broken aged crystal appears to still have a yellow core. Unfortunately, the ageing effect is not reversible. Indeed, adding a drop of methanol solvent to brown crystals does not lead to a recovery of the yellow coulour.

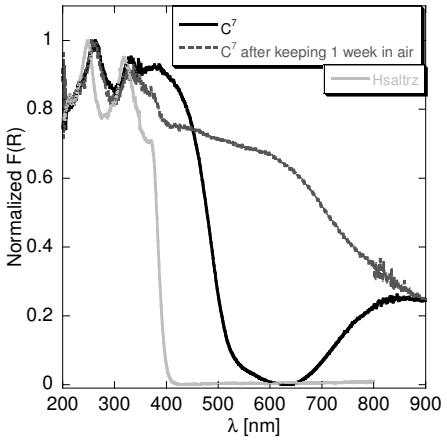

Figure 93 Diffuse reflectance spectra at 298 K of **Hsaltrz** and **C^7** before and after keeping the sample during 1 week in air.

Diffuse reflectance spectra were also carried out (Figure 93). As described in chapter 2, **Hsaltrz** shows a spectrum built with an intense signal in the UV range (to approximately 400 nm) which was attributed to the enol form of the molecule, stabilised by the absence of intramolecular H-bonds between alcohol and imine functions (Figure 93). Fresh sample of **C^7** shows a similar signal in the UV range (maxima are shifted to a higher wavelength of few nanometres) but presents also an intense band between 400 nm and

approximately 535 nm attributed to the *cis*-keto form of **Hsaltrz**, which was however expectedly not observed in the crystal structure[68] (Figure 93). A third broad contribution is also identified from approximately 630 nm to the infrared region which can be attributed to a charge transfer band (MLCT) from iron to **Hsaltrz**. No effect of UV irradiation was noted neither for **Hsaltrz** nor $\mathbf{C^7}$ showing the absence of photochromism at room temperature for these compounds. If the sample is kept in air (the colour change seems to start just after the evaporation of the mother solution and continues during few days), we observed the appearance of an complicated spectrum containing a new non resolved band in the visible range which supports the observation of a brown material in Figure 93. Oxidation of iron(II) into iron(III) and/or a direct influence of the solvent molecules are assumed.

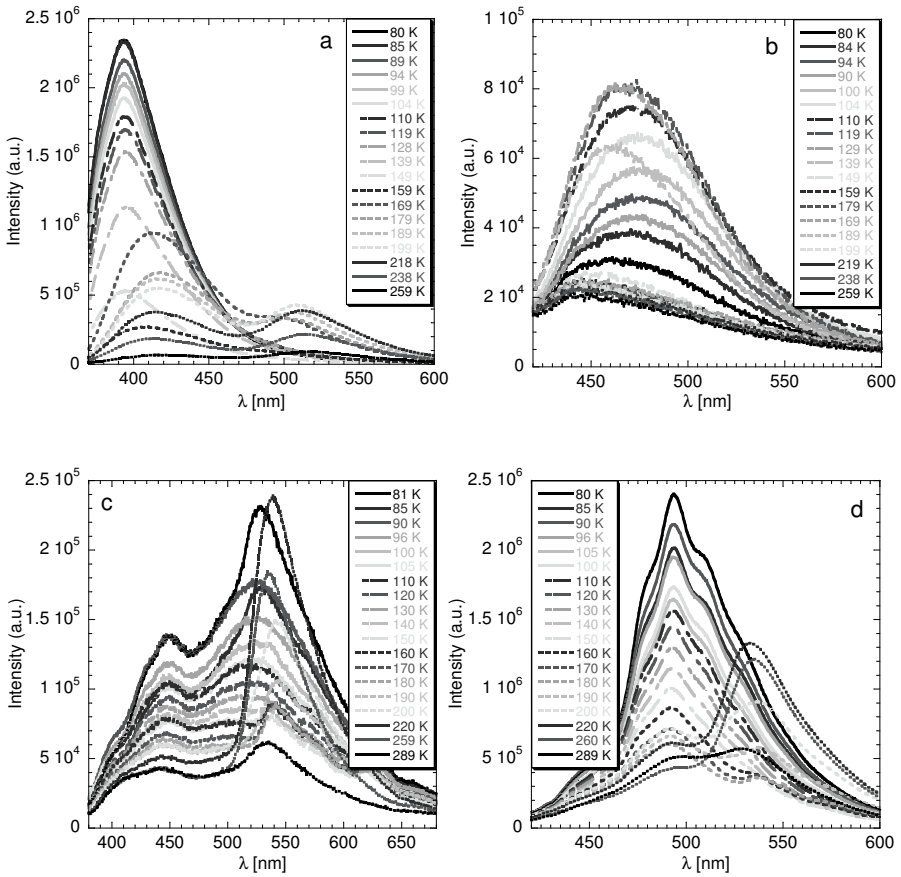

Figure 94 Temperature dependent ***emission*** spectra at 350 nm and 400 nm for **C**[7] (a and b, respectively) and **Hsaltrz** (c and d, respectively).

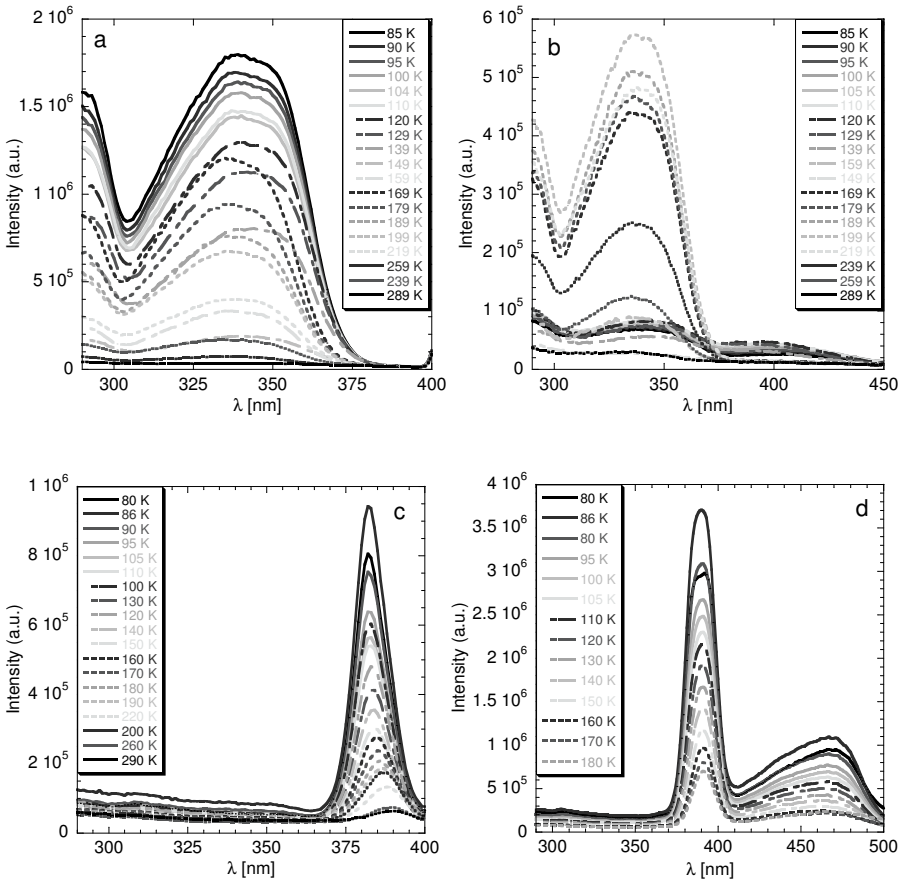

Figure 95 Temperature dependent ***excitation*** spectra at 410 nm and 515 nm for **C**[7] (a and b, respectively) and **Hsaltrz** (c and d, respectively).

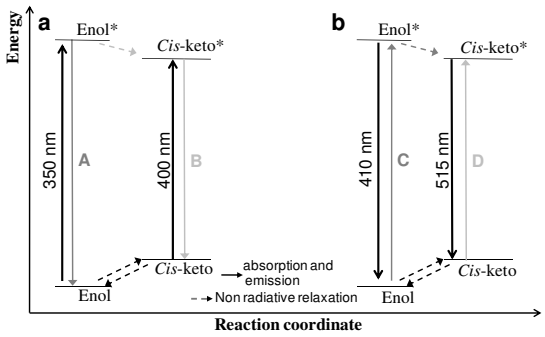

Scheme 19 Chemical pathways involved during the measurements of emission (a) and excitation (b) spectra of $\mathbf{C^7}$ and **Hsaltrz**.

Fluorescence measurements on pure crystalline sample of $\mathbf{C^7}$ and on **Hsaltrz** were also carried out in order to analyse the energetic levels involved during light absorption and emission phenomena and the influence of the temperature on these processes (Figure 94 and Figure 95). Emission spectra at 350 nm of $\mathbf{C^7}$ (Figure 94a) present one major contribution at low temperature (λ^{max} = 394 nm at 80 K) which could be attributed to the radiative deexcitation of the excited enol form (enol*) (Pathway A in Scheme 19a). At high temperature, we observe a significant bathochromic shift of this emission band of about 25 nm (λ^{max} = 419 nm at 288 K) but also the appearance of a second band at a λ^{max} of 495 nm at 288 K which can be attributed to the radiative relaxation of the excited *cis*-keto form (cis*) following the chemical pathway B in Scheme 19a. The presence of this band at high temperatures translates an increase of the proton transfer in the excited state (enol* → *cis*-keto*) (Scheme 19a). For **Hsaltrz** at 350 nm (Figure 94c), the two bands are observed in the whole studied temperature range (80 K – 290 K) (λ^{max} = 444.5 nm and 526.5 nm) and no enol* emission band shift with temperature is detected. The wavelengths of the maximum

emission are largely different between **C^7** and **Hsaltrz** showing the major impact of the coordination of **Hsaltrz** to iron ions. Emission spectra of **C^7** at 400 nm were also recorded (Figure 94b). A broad band, attributed to the radiative relaxation of the cis* (Pathway B in Scheme 19a) is observed with a λ^{max} = 461 nm at 80 K. For **Hsaltrz**, a similar spectrum is obtained at low temperature (Figure 94d), showing the presence of a broad peak, centred at 493.5 nm, containing more than four non resolved contributions which could be attributed to the presence of several molecular conformations.[92] Moreover, the temperature increase seems to stabilize less energetic emissions which could be attributed to more planar conformations of the *cis*-keto form as earlier described.[92]

Temperature dependent excitation spectra were also recorded on **C^7** and **Hsaltrz** (Figure 95). In both cases, at 410 nm, corresponding to the emission wavelength of the enol* (see Figure 94), an intense signal is observed in the UV range of the spectrum (Figure 95a and Figure 95c). For **C^7**, an intense broad peak is noted with a λ^{max} = 338.5 nm at 80 K. Another band is also partially observed below 300 nm. These excitation signals are attributed to the enol form, following the chemical pathway C in Scheme 19b. A similar situation is obtained for **Hsaltrz** but the peak centred at 382 nm appears to be largely more intense than the other signals (Figure 95c). When the emission wavelength is fixed at 515 nm (Figure 95b and Figure 95d), corresponding to the emission of the cis* (see Figure 94), the maximum attributed to the enol form is also observed in **C^7** and **Hsaltrz** at 335.5 nm and 392 nm, at 80 K, respectively. In addition to the enol contribution, another weaker signal is observed at approximately 389 nm at 129 K for **C^7** and at 471 nm at 80 K for **Hsaltrz** (Figure 95d). This signal can be attributed

to the contribution of the *cis*-keto form (Pathway D in Scheme 19b) which is present in significant amount in **C**[7] but only as trace in **Hsaltrz** (see Figure 93).

The evolution of the emission and excitation signals with temperature were analysed in order to study an eventual influence of the SCO of the iron ions on the fluorescence properties. The study of the influence of the temperature on the wavelength of the maximum emission of enol* shows a clear influence of the coordination of iron ions and of the thermo-induced SCO (Figure 96). As shown in Figure 96a, in **C**[7], the enol* emission band remains at approximately 395 nm below 150 K and at approximately 415 nm above 200 K. A drastic jump of about 20 nm is then observed between the onset temperatures 135.5 K and 179 K. Remarkably, the strong increase of the wavelength follows precisely the γ_{HS} curve obtained by SQUID measurements. The SCO curve is then, for the first time, tracked by fluorimetry. The $T_{1/2}$ is estimated at 157 (1) K which is also in good adequacy with the values obtained by other analytical techniques discussed above (154 (1) K for Mössbauer spectroscopy). In contrast to **C**[7], the study of the enol* emission band wavelength in **Hsaltrz** shows no abrupt phenomenon but only a slow decrease from approximately 450 nm at 80 K to 441 nm at 290 K which could be attributed to a slight change of the strength of supramolecular interactions in crystal structure induced by the temperature change (Figure 96b). This experiment strongly supports our hypothesis about the origin of the strong wavelength change in **C**[7].

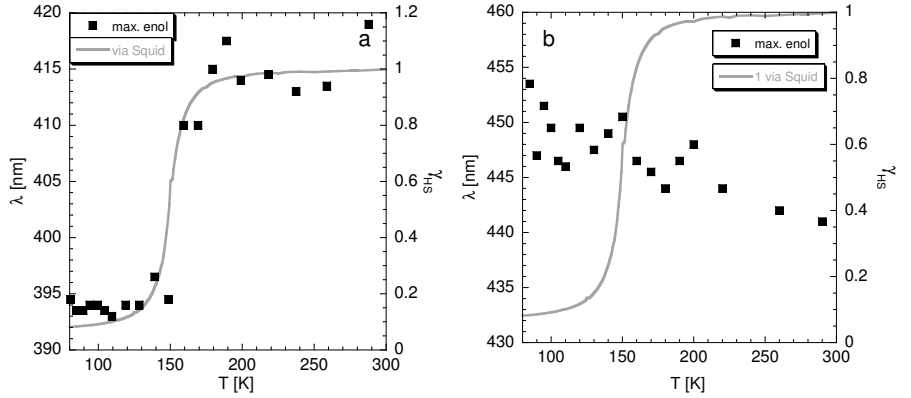

Figure 96 Temperature dependence of the wavelength of the maximum emission of enol* in the emission spectra at 350 nm of **C**^{7} (a) and **Hsaltrz** (b) versus the molar fraction of HS iron(II) ions for **C**^{7} obtained by SQUID measurements.

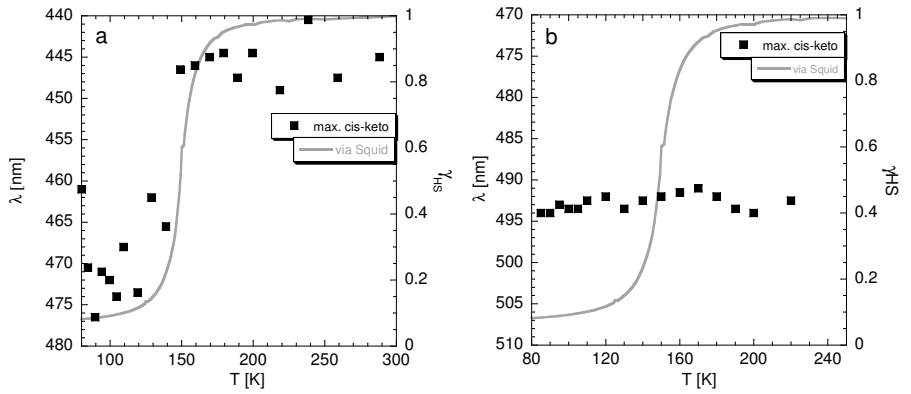

Figure 97 Temperature dependence of the wavelength of the maximum emission of cis* in the emission spectra at 400 nm of **C**^{7} (a) and **Hsaltrz** (b) versus the molar fraction of HS iron(II) ions for **C**^{7} obtained by SQUID measurements.

Similar observations were also done with selected parameters derived from the emission spectra at 400 nm. Indeed, the wavelength of the maximum emission of cis* in **C**^{7} also shows a drastic modification around the SCO temperature as shown in Figure 97a. In this case, we observed that the wavelength drops from approximately 472 nm at 80-120 K to about 445

nm in the 200-300 K range. Although the distribution of the experimental points is significantly larger in this case, the jump seems to match the γ_{HS} curve obtained by SQUID measurements. In contrast, **Hsaltrz** presents an almost stable emission wavelength as shown in Figure 97b. Moreover, the emission intensity at 470 nm, which approximately corresponds to the wavelength of emission maximum of cis* at low temperature of **C**[7], also shows an interesting temperature induced variation (Figure 98). Indeed, although the temperature dependent curve for **Hsaltrz** presents also variations with unknown origins (see appendix section), the curve of **C**[7] shows a strong jump of the emission intensity between 80 K and 150 K (from 3.10^4 to 8.10^4). One hypothesis is that this observation could take its origin in an elastic stress created in the SCO network in a temperature range near the start of the transition. Indeed, this type of stress, which can originate from the elastic cooperativity phenomenon,[10] could induce a more rigid network that leads to enhance the fluorescence phenomenon. It is however interesting to notice that the temperature range, where the fluorescence enhancement is observed, corresponds to the one where an unexplained Mössbauer parameter change was detected for the Fe^{II}_{HS2} and Fe^{II}_{HS3} sites. It may thus not be excluded that these two observations are linked and ascribable to a unique phenomenon. The study of the evolution of selected parameters were also done for the excitation spectra but, considering that many thermo-induced phenomena are visible (efficiency change in proton transfer in the fundamental and excited states, change of emission pathways, SCO, etc), the evolution with temperature becomes more complicated and thus difficult to use, at this stage, in order to probe the SCO.

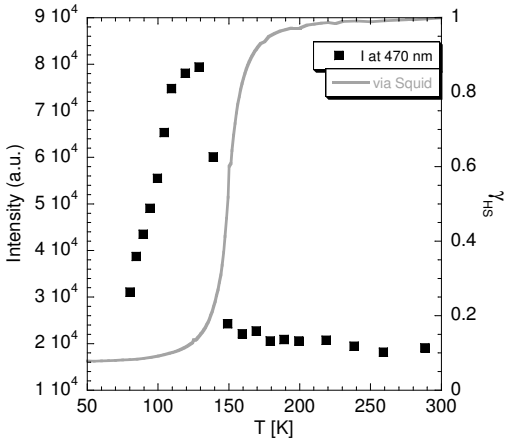

Figure 98 Temperature dependence of the intensity of emission of cis* in the emission spectra at 400 nm of **C**^{7} (emission wavelength = 470 nm) versus the molar fraction of HS iron(II) ions obtained by the SQUID measurements.

Discussion

We have discussed the structure, magnetic and optical properties of new triazole based dinuclear compound of formula $[Fe_2(\mathbf{Hsaltrz})_5(NCS)_4]\bullet 4CH_3OH$ (**C**^{7}). The crystal structure can be compared with the only iron(II) triazole based dinuclear complex with a $[Fe^{II}_2(Rtrz)_5(NCS)_4]$ formula reported in ref. [227] (**K**^{1}). In our case, the dinuclear is the only component of the crystal structure in contrast to **K**^{1} which is also composed of a mononuclear unit which ensures the cohesion between dinuclear units thanks to water molecules driven supramolecular interactions.[227] The stability of **C**^{7} can be guaranteed by the presence of a strongly developed supramolecular network. Interestingly, it was claimed that the presence of a mononuclear unit was responsible for the relatively abrupt SCO of **K**^{1}.[227] Our study demonstrates that the contribution of the mononuclear to the cooperativity can be replaced by a large supramolecular

network. The SCO phenomenon in **C[7]** is more abrupt than in **K[1]** and the transition appears at a higher temperature (150 (2) K). It can be explained by the change in the electronic density of the inorganic complexes involved by the change of supramolecular interactions and by the chemical derivation of the triazole ligand.

As noted before, although the crystal structure of **C[7]** contains only one iron(II) site, ^{57}Fe Mössbauer spectra present two slightly different HS and LS iron(II) signals. This observation could take its origin in the presence of the disorder observed in Hsaltrz 3 which could lead to a iron(II) sites differentiation into dinuclears or to the presence of two types of dinuclear units in the crystal structure (one with Hsaltrz 3 in position 1 and another with the ligand in position 2) but the presence of the tautomeric equilibrium between the enol and the *cis*-keto forms could also play a role in this observation. Moreover, the presence of spin domains can not be excluded.[296] It is interesting to notice that ref. [227] presents also two different iron(II) Mössbauer signals which are coherent with the observations obtained for **C[7]**. It also interesting to see that three types of conformations are observed for **Hsaltrz** in the complexes although the free ligand is blocked in a 'non functional' geometry (see chapter 2).

^{57}Fe Mössbauer spectra (see Figure 88 and Table 10 to Table 13) are complicated because of the presence of five signals which lead to some inaccuracies in certain parameters but the evolution of these peaks confirms very well the SCO observed by SQUID magnetometry. The two LS iron(II) signals are represented by two doublets with small or very small quadrupole splitting explained by the absence of orbital contribution to this value.[222] These two peaks are in the same isomer shift range (about 0.4 mm.s^{-1}),

which is slightly higher than the value obtained for **K[1]**,[227] but differ by their quadrupole splitting (0.16 (4) $mm.s^{-1}$ and 0.5 (1) $mm.s^{-1}$ for Fe^{II}_{LS1} and Fe^{II}_{LS2}, respectively at 93 (1) K) which can be attributed to a difference of electrical field environment induced by the surrounding network.[222] Indeed, Fe^{II}_{LS1} site appears to be placed in a more symmetric environment than Fe^{II}_{LS2}. It leads to a difference in the relative area fraction evolution which goes to zero at 168 (1) K for Fe^{II}_{LS2} in contrast to Fe^{II}_{LS1} which is still present with a weak relative area fraction of 3.3 (1) % at 208 (1) K (see Table 13). Similar conclusions can be drawn with the two HS iron(II) signals (Fe^{II}_{HS1} and Fe^{II}_{HS2}) which are very similar in isomer shift (approximately 1.15 $mm.s^{-1}$ at 208(1) K which is higher than the reported values for **K[1]**) but differ in their quadrupole splitting (3.3 (1) $mm.s^{-1}$ and 3.1 (1) $mm.s^{-1}$ for Fe^{II}_{HS1} and Fe^{II}_{HS2}, respectively at 208 (1) K which are significantly higher than the reported values for **K[1]**). Fe^{II}_{HS2} is then in a more symmetric environment than Fe^{II}_{HS1} and can be linked to the Fe^{II}_{LS1}. The Fe^{II}_{HS1} is linked to the Fe^{II}_{LS2} signal. Differences between Fe^{II}_{HS1} and Fe^{II}_{HS2} are also seen in the relative area fraction evolution with a zeroing of the value at 138 (1) K for Fe^{II}_{HS1} although ~ 14 % of Fe^{II}_{HS2} is still noted at 93 (1) K (Table 13). The mechanism of the SCO phenomenon seems to be relatively similar for both iron(II) ions allowing a spin change from [LS-LS] to [HS-HS] pairs without intermediate [LS-HS] phase. Calorimetric measurements of **C[7]** show a very well resolved endothermic or exothermic peak in the warming or cooling mode, respectively. This analysis properly confirms that no hysteresis phenomenon is present in the SCO of **C[7]**. Moreover, the thermodynamic analyses of the calorimetric data have confirmed the large vibrational contribution to the entropy (42 $J.mol^{-1}.K^{-1}$).

Optical properties are certainly other attractive characteristics of compound **C^7**. In addition to a marked thermochromism coupled to the SCO phenomenon (see Figure 92) and the absence of photochromism at room temperature (it cannot be excluded that these molecules are photochromic at higher or lower temperature), the crystalline solid compound **C^7** presents an ageing effect. It is probably linked to a solvent lost phenomenon and is visible by diffuse reflectance spectroscopy as well as with naked eyes. Compound **C^7** is also unique because of the strong fluorescence of the inorganic compound which is given by the *N*-salicylidene aniline derivative ligand. Indeed, the light emission property of a solid-state SCO compound was very rarely reported[273, 289] and not yet used in order to precisely follow the SCO curve in pure solid sample. Moreover, it is the first time that the studied fluorescence comes clearly from a ligand centred photo-induced electronic transition and not from a charge transfer phenomenon[289]. Moreover, in this case, the experiments have been conducted with pure crystalline samples without sampling processes, such as thin films,[289] which are known to influence SCO properties.[10]

As previously described, we have made a systematic analysis of some selected parameters obtained in four types of temperature dependent fluorimetry spectra. These experiments were carried out in order probe the radiative deexcitation of enol* (Pathways A and B in Scheme 19a) and cis* (pathway B in Scheme 19a) for the emission spectra at 350 nm and 400 nm respectively, and to probe the excitation of the enol form (pathway C in Scheme 19b) and of the *cis*-keto form (pathways C and D in Scheme 19b) for the excitation spectra at 410 and 515 nm respectively. We have focussed our discussion on the temperature dependence of the wavelength of the

maximum emission of enol* (λ^{max}_{enol*}) observed in the emission spectra at 350 nm. As shown in Figure 96a, an unexpected increase of λ^{max}_{enol*} of approximately 20 nm is noted between the onset temperatures 135.5 K and 179 K which exactly corresponds to the SCO temperature range. This wavelength modification, which corresponds to a transition energy decrease (of about 15 kJ/mol), can be attributed to a change in the energy levels of the **Hsaltrz** in the complex induced by the electronic redistribution in the metal orbitals conducted by the thermo-induced SCO phenomenon. It is well suggested by the fact that such modification was already probed by a modification of the vibrational constants in the ligand of an iron(II) complex during its SCO.[10] Indeed, it is assumed that information concerning the electronic distribution in the metal ion is transmitted to the ligand through the δ and π coordination bonds which bind the metal ion with the ligands. Interestingly, a similar SCO curve was obtained by following the temperature dependence of wavelength of the maximum emission of cis* (λ^{max}_{cis*}) in the emission spectra at 400 nm (Figure 97a). In this case, we observe that the SCO of the metal ion leads to a drastic drop of the λ^{max}_{cis*} of approximately 27 nm. This phenomenon corresponds to an increase of energy of about 15 kJ/mol which is exactly the same value as the one found in the case of the radiative relaxation of the enol* but the transition becomes more energetic in the case of the cis*→ cis and less energetic in the case of enol*→ enol. Finally, the temperature dependence of a third parameter found in the emission spectra at 400 nm shows an unexpected shape. Indeed, if we follow the emission intensity at 470 nm, which corresponds to the emission band of the cis* excited state, we observe a very intense signal from low temperature to approximately 150 K where to intensity drop to about 37 % of its maximum value (Figure 98). An elastic stress created in

the SCO network in a temperature range near the start of the transition is proposed in order to explain the fluorescence enhancement. Moreover, Mössbauer parameters seem to confirm the presence of such phenomenon although no confirmation about the nature of the phenomenon was obtained by this method.

Finally, the study of the crystal structures of **C**$^{8\text{-}10}$ shows that following different synthetic pathways (metal salt, synthetic conditions, etc) leads to a change in the formula of the compounds as well as the crystal structure parameters (e.g. the space group). Indeed, a modification of the nature and the number of solvent guest molecules is clearly identified. These changes have a clear impact on the thickness of the supramolecular network involving the solvent guest molecules which is very developed in $[Fe_2(Hsaltrz)_5(NCS)_4]\bullet 4CH_3OH$ (**C**^{7}) with 12 H-bonds per dinuclear at 100(2) K. The replacement of three methanol molecules by three water molecules (**C**^{7} → **C**^{8}) leads to only seven H-bonds involving the guest molecules at 125(2) K and only six H-bonds if the dinuclear is surrounded by four water molecules (**C**^{9}) (see Table 38 and Table 44).[297] Interestingly, the use of cobalt(II) salt leads to the formation of a similar dinuclear (**C**^{10}) surrounded by four water molecules and one methanol. It strongly supports that the synthetic pathway plays a crucial role in the composition of this class of materials.

As shown by the crystal structure of **C**^{8} at 125(2) K and 240(2) K, no SCO phenomenon is observed for the two iron(II) ions in this temperature range. In contrast to **C**^{8}, the SQUID magnetometry experiments on **C**^{9}, which were previously carried out,[290, 291] have confirmed the presence of a SCO phenomenon of both iron(II) ions between 160(1) K and 187(1) K ($T_{1/2}$ =

174(1) K). It is similar than the phenomenon observed in **C**[7] where the SCO was identified between 138(1) K and 161(1) K ($T_{1/2}$ = 150(1) K). If we compare the SCO parameters of the two compounds (**C**[7] and **C**[9]), an important temperature shift of the $T_{1/2}$ of about 24 K to the higher temperatures is noted for **C**[9]. Moreover, the SCO of **C**[9] appears to be not completed (with a remaining γ_{HS} of about 30% at low temperature) in contrast to the SCO of **C**[7] which leads to almost completed [LS-LS] dinuclears at 100 K. An influence of the supramolecular network is proposed to explain these differences. Moreover, the presence or the absence of SCO phenomenon should be translated by a change of ligand field of the iron(II) ions which becomes too low in **C**[8], in comparison to the one obtained for **C**[7] and **C**[9], to favour the SCO. This is supported by structural differences in the dinuclear units. In the SCO complexes **C**[7] and **C**[9], the isothiocyanato anions are observed as linear and aligned with the iron(II) ions (M1-N15-C16 = 171.2(3)° and 168(2)° and M1-N115-C116 = 173.4(4)° and 174(2)° at 293(2) K and 200(2) K for **C**[7] and **C**[9], respectively). The situation is very different in the non SCO complex **C**[8] where the linear isothiocyanato anions are observed with large angles with the metal ions (M1-N15-C16 = 152.2(3)°, M1-N115-C116 = 142.8(3)°, M2-N215-C216 = 176.2(3)°, M2-N315-C316 = 149.6(3)° at 240(2) K). A difference is also seen in the octahedral coordination spheres of metal ions which are less distorted in **C**[7] and **C**[9] in contrast to **C**[8] ($\sum_{Fe1}$ = 18(2)° and 19.1(7)° at 293(2) K and 200(2) K for **C**[7] and **C**[9], respectively ; $\sum_{Fe1}$ = 34(1)° and $\sum_{Fe2}$ = 28(1)° at 293 K for **C**[8]). In addition to these differences, the terminal **Hsaltrz** ligands appear to be more twisted in **C**[7] and **C**[9] than in **C**[8] (Φ_1 = 8(1)° and 3(1)° at 293(2) K and 200(2) K for **C**[7] and **C**[9], respectively and Φ_1 = 17(1)° at 240(2) K for

C[8]). We also note that **C**[7] and **C**[9] are in the *C*2/c space group in contrast to **C**[8] which crystallises in the *P*$\bar{1}$ one. On the basis of our knowledge, it is the first time that these differences between SCO complexes and HS complexes are observed in a group of similar Fe^{II}-$N_4(NCS)_2$ complexes.

Chapter VII: Inorganic complexes with *N*-salicylidene 4-amino-3,5-bis(pyridin-2-yl)-1,2,4-triazole (Habs)

Introducing remarks

Habs, which was extensively studied in chapter 2, was selected as potential ligand for transition metal complexes. It is derivated from an important ligand in coordination chemistry: the 4-amino-3,5-bis(pyridin-2-yl)-1,2,4-triazole (**abpt**).[298-301] Indeed, the **abpt** molecule presents attracting perspectives in the synthesis of mixed coordination spheres as demonstrated by the large variety of complexes of formula $[M(\mathbf{abpt})_x(L)_y]$ where L is another ligand with oxygen, nitrogen, phosphorous or halogen donor atoms.[302-307] **abpt** and related molecules (**Rabpt**) were also widely investigated as ligand in SCO complexes. It was presented either in $[Fe^{II}(\mathbf{Rabpt})_3]$ units, where the nature of the triazole substituent appears to have a large influence on the SCO parameters,[308] or as component in mixed coordination spheres.[143, 309-315] However, the SCO **abpt** complexes have been identified in few cases as polymorphic compounds which implies strong changes of SCO phenomenon parameters following the crystal packing present in the structure of the materials.[125, 316, 317] The difficulty to obtain reproducible SCO materials is also induced by the presence of various coordination mode of **abpt** and related molecules which can lead to the formation of complexes with various compositions and dimensionalities[318-321] such as mononuclear (with one,[322, 323] two [324-326] or three **abpt** ligands per metal ion[327]), dinuclear,[328] oligonuclear or polynuclear compounds[329]. The dimensionality can however be partially controlled by the synthesis

conditions.[330, 331] It drives to promising perspectives in application domains such as electroluminescence devices (*LED*).[332]

In this section, we have investigated **Habs** ligand for the preparation of new transition metal complexes. Interestingly, the use of **abpt** derivatives with substituted imine function is quite rare[333, 334] and confirms the interest of this way of derivation. A large variety of complexes was proposed[335] following two types of formula: $[M^{II}(\mathbf{Habs})_3]A_2$ and $[M^{II}(\mathbf{Habs})_2(L)_2]$ where M^{II} = Fe, Co, Ni, Cu and Zn, A = BF_4^-, Cl^- and L = NCS, NCSe. However, because the difficulty to find a reliable formulation for some complexes or the absence of remarkable properties, we will only discuss first about $[Fe^{II}(\mathbf{Habs})_2(NCS)_2]$ (**C**[11]). In a second part, we will also investigate the possibility to form new compounds with formula $[Fe^{II}(\mathbf{Habs})_2Cl_2]$ (**C**[12]) and $[Zn^{II}(\mathbf{Habs})_2X_2]$ where X = F (**C**[13]), Cl (**C**[14]), Br (**C**[15]) and I (**C**[16]). This class of materials presents very attracting properties as described later. This chapter will be divided in two main parts devoted to a discussion about material composition and properties, respectively.

Syntheses and crystallization methods

$[Fe^{II}(\mathbf{Habs})_2(NCS)_2]$ was synthesized in air with an oxidation inhibitor reagent (ascorbic acid) (**C**[11]). An attempt was also realised under inert atmosphere (Schlenk technique) but it leads to an unpure product without any switchable behaviour, showing a strong sensitivity to the synthesis conditions as suggested by **abpt** complexes. [330, 331]

Growth of diffractable quality crystals was investigated for all transition metal ions $3d^{5\text{-}10}$ (Mn^{II}, Fe^{II}, Co^{II}, Ni^{II}, Cu^{II}, Zn^{II}) by a large variety of techniques such as slow evaporation of concentrated solutions made with

different solvents (methanol, ethanol, octanol, acetone, etc), gaseous diffusion of a solvent where molecules are insoluble (e.g. diethylether) in concentrated complexes solutions, diffusion of reactants (H-tubes technique), solvothermal syntheses, etc. However, **Habs** complexes lead to crystallisation difficulties as suggested by the systematic formation of **abpt** complexes by imine function hydrolysis and their associated crystallisation.

In a second part, another inorganic complexes series was investigated with a proposed formula of $[M^{II}(\mathbf{Habs})_2X_2]$ where M^{II} = Fe, Zn and X = F, Cl, Br and I. In this case, it was more difficult to obtain a precipitate. Indeed, it has needed a synthesis in ethanol under reflux for one to four days based on the complexes nature (see experimental section).

Discussion about the materials formulation

As suggested before, the main difficulty with **Habs** complexes is the determination of the material composition because of the possibility of large variety of dimensionalities and natures. In order to clarify this point, a large number of analytical experiments such as elementary and thermo-gravimetric analyses, Raman and infrared spectroscopies, mass spectrometry, powder X-ray diffraction and nuclear magnetic resonance measurements were carried out.

A good matching between theoretical and experimental data, obtained by elementary analyses, was found for $\mathbf{C^{11}}$ to $\mathbf{C^{14}}$ but the exact formulation for $\mathbf{C^{15}}$ and $\mathbf{C^{16}}$ remains however undetermined.[336] Nevertheless, the presence of numerous solvent guest molecules of different nature could partially explain this difficulty as suggested by mass spectrometry combined with

thermo-gravimetric measurements. Moreover, the presence of a mix of different complexes natures cannot be excluded for **C**[15-16].

The complexation of **Habs** on the metal ion was confirmed by the displacement of vibrational peaks in IR spectra. Similar conclusions were also drawn from Raman spectroscopy data but no confirmation about the presence of metal-halogen bonds in $[Zn^{II}(\mathbf{Habs})_2X_2]$ complexes (**C**[14-15]) was obtained because no peak were clearly attributed to the vibration of this class of molecular bonds. Nevertheless, the probability to have a $M\text{-}N_4X_2$ coordination sphere is suggested by reported crystal structures of **abpt** halogenated complexes[330, 337] and by the mass spectrometry experiments. Indeed, although the molecular ions were never observed, complexes **C**[14-16] mainly give peaks attributed to $[Zn^{II}(\mathbf{Habs})_2X]$ and $[Zn^{II}(\mathbf{Habs})_2]$ units. Moreover, some sodium and potassium adducts of the molecular ion were also identified in some cases (e.g. for **C**[16]). The formation of non-hydrolysed **Habs** complexes is then demonstrated. Typical example is given by $[Zn^{II}(\mathbf{Habs})_2Cl_2]$ (**C**[14]) showing the presence of fragments of the molecular ion (M): M - 1 Cl + 1 H^+ (m/z = 785), M - 2 Cl -1 H^+ (747), M – 2 Cl (374), **Habs** (343) and **abpt** (239). Moreover, the shape of the fragments peaks shows an complicated isotopic distribution which is in adequacy with the presence of one zinc ion per complex.

Zinc complexes were the most studied because of the possibility to use NMR techniques, in particular the Correlation Spectroscopy (*COSY*) which is a two-dimensional NMR experiment showing the H-H atoms correlations. These measurements were carried out in order to analyze the spin systems, defined as groups of correlated spins, present in **Habs** molecule before and after complex formation. This experiment was successfully run with

$[Zn^{II}(\mathbf{Habs})_2Cl_2]$ ($\mathbf{C^{14}}$) and $[Zn^{II}(\mathbf{Habs})_2Br_2]$ ($\mathbf{C^{15}}$) whereas similar measurements with $[Zn^{II}(\mathbf{Habs})_2F_2]$ ($\mathbf{C^{13}}$) and $[Zn^{II}(\mathbf{Habs})_2I_2]$ ($\mathbf{C^{16}}$) were not possible because of the too low solubility of these compounds in deuterated solvents. Five potentially different spin systems can be thought in **Habs**, as shown in Figure 99.

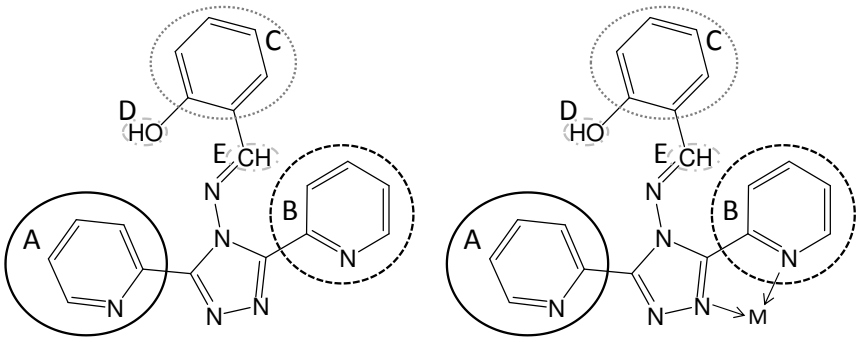

Figure 99 View of the five potentially different spin systems (A-E) in **Habs**. The left figure shows that pyridine rings (systems A and B) are chemically equivalent in the free organic molecule whereas A and B become different in a mononuclear complex, represented on the right.

As suggested by Figure 99, in free **Habs**, only four different spin systems can be distinguished because of the equivalence of A and B spins group.[338] This degeneracy is however suppressed if we imagine that a metal ion is coordinated through the triazole and one pyridine ring whereas it reappears if two metal ions are coordinated though each side of the triazole moiety and the pyridine rings (observed in the case of dinuclears formation).

COSY and ^{1}H-NMR measurements were first carried out for $\mathbf{C^{14}}$. A first spin system is observed, constituted of two doublets at 8.95 and 8.68 ppm and two multiplets at 7.75 and 8.21 ppm (see experimental section for details). A second system is also noted with two doublets at 6.97 and 7.94 ppm and two multiplets at 7.51 and 7.04 ppm and a third system is experimentally

observed with two doublets at 8.36 and 8.81 ppm and two multiplets at 7.68 and 8.16 ppm. Finally, one peak can be attributed to the hydrogen atom of the alcohol function at 10.05 ppm whereas the proton of the CH_{imine} is observed as a singlet at 9.08 ppm. The results obtained by COSY experiments seem then to support the formation of a mononuclear complex with the targeted formula $[Zn^{II}(\mathbf{Habs})_2Cl_2]$ as defined by elementary analysis. Indeed, three isolated spin system are observed. Nevertheless, we are not able to attribute with accuracy which are the A, B and C systems. ^{1}H-NMR shows, however, integration values for spin systems in inadequacy with a 1/1/1 ratio expected for **Habs**, as observed in the free organic molecule (see experimental section for details). These data, surprisingly, do not correspond to any proposed complexes natures. Two hypothesis are proposed: the targeted formula $[Zn^{II}(\mathbf{Habs})_2Cl_2]$ remains correct and the integration values are distorted for an unknown reason or the compound is present in solution with a more complicated composition which is not possible to define at this stage. The formation of a mixture of compounds with different dimensionalities in the solution can also not be totally excluded although the solid-state compound seems to have a well-resolved architecture as suggested by our elementary analyses.

Similar data were obtained for $\mathbf{C^{15}}$ where spin systems are observed with a similar composition: the first group of spins is composed by two doublets at 8.74 and 8.97 ppm and two multiplets at 7.78 and 8.22 ppm, the second one is characterized by two doublets at 6.97 and 8.01 ppm and two multiplets at 7.52 and 7.05 ppm, and the last one is present with doublets at 8.40 and 8.84 ppm and multiplets at 8.19 and 7.72 ppm. The H_{imine} is also noted with a singlet at 9.16 ppm whereas the proton of the alcohol function is not

observed in the spectrum. The four spin systems are thus very similar than the ones obtained for **C[14]** but the integration values are also in inadequacy with the targeted formula.

Moreover, **Habs** complexes present various crystal stuctures as demonstrated by powder X-ray diffraction experiments (see experimental section). This parameter could also play a role in the properties of such materials.

Study of the spin crossover phenomenon

Interestingly, **C[11]** shows a thermally induced SCO phenomenon associated with a thermochromism from pale to dark pink at room and liquid nitrogen temperatures, respectively. ^{57}Fe Mössbauer spectroscopy was then carried out in order to demonstrate this observation. As shown in Figure 100, at 113 K, a significant amount of LS iron(II), characterized by a isomer shift (δ^{113K}_{LS}) of 0.495 (2) mm.s^{-1}, a quadrupole splitting ($\Delta E_Q{}^{113K}_{LS}$) of 0.40 (4) mm.s^{-1} and a relative area fraction of 13 (2) %, is observed. Interestingly, at 193 K, the LS iron(II) signal is quenched, leading to an increase of the three HS iron(II) sites observed in dark grey in Figure 100 (δ^{193K}_{HS} = 1.0 (1) mm.s^{-1}, $\Delta E_Q{}^{193K}_{HS}$ = 3.1-3.8 (1) mm.s^{-1}, Relative fraction area = 19-30 (2) %) and suggesting a thermally-induced SCO phenomenon. The origin of these three different sites may come from the presence of three types of complexes environments. However, a crystal structure determination is necessary to clarify this observation. The ^{57}Fe Mössbauer spectra also present a significant contribution of iron(III) ($\delta^{298K}_{Fe(III)}$ = 0.03 (4) mm.s^{-1}, $\Delta E_Q{}^{298K}_{Fe(III)}$ = 0.71 (6) mm.s^{-1}, relative area fraction at 298 K = 22 (3) %), in light grey in Figure 100, but this oxidised specie is present in small amount although the

iron(III) signal is enhanced in the Mössbauer spectra at high temperature because of the difference of *f* factor between material components.

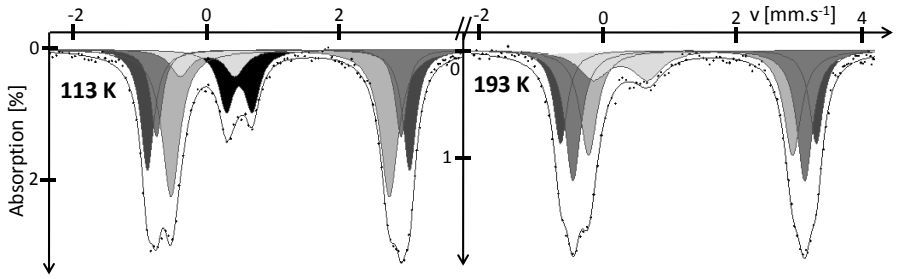

Figure 100 Selected temperature dependent ^{57}Fe Mössbauer spectra of compounds $[Fe^{II}(\mathbf{Habs})_2(NCS)_2]$ ($\mathbf{C^{11}}$) in a temperature range of 113-193K. Mössbauer parameters are given in the experimental part and discussed in the text.

Habs complexes are thus potentially good SCO candidates for the observation of targeted optically induced magnetic properties. Nevertheless, the lack of clear information about the crystal structure leads to difficulties in the discussion about the ^{57}Fe Mössbauer signals.

Optical properties

Optical properties of **Habs** complexes appear to be versatile in view of the fact that various optical behaviours were observed during our investigations. Diffuse reflectance spectra of compound $[Fe^{II}(\mathbf{Habs})_2(NCS)_2]$ ($\mathbf{C^{11}}$) was carried out (Figure 101). Indeed, the spectrum is very complicated, containing an intense band in the UV region, attributed to the light absorption by the ligand in the enol form, and a very broad signal in the visible part of the spectrum. This contribution is probably constituted of a large charge transfer band combined with d-d transition bands and, perhaps, of a band resulting from the light absorption by the *cis*-keto form of the

ligand (which was not observed for the free organic molecule but which can be allowed by the modification of the electronic levels induced by metal complexation – see chapters 2 and 5).

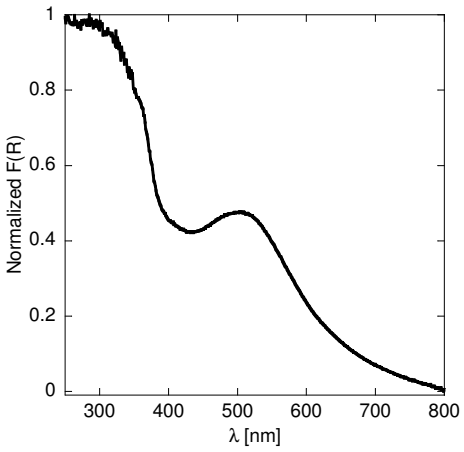

Figure 101 Diffuse reflectance spectra at 298 K of $[Fe^{II}(\mathbf{Habs})_2(NCS)_2]$ ($\mathbf{C^{11}}$).

Compounds $[Zn^{II}(\mathbf{Habs})_2X_2]$ where X = F, Cl, Br, I ($\mathbf{C^{13\text{-}16}}$) were also analysed by diffuse reflectance spectroscopy (Figure 102). Spectra are similar to the one obtained in Figure 101 but, in the case of these compounds, the charge transfer band seems to be quenched. The *cis*-keto form of **Habs** is then visible between 400 and 500 nm and appears to be sensitive to halogen nature. Indeed, as shown in Figure 102, this band is almost quenched in $[Zn^{II}(\mathbf{Habs})_2I_2]$ ($\mathbf{C^{16}}$), strongly enhanced in $[Zn^{II}(\mathbf{Habs})_2F_2]$ ($\mathbf{C^{13}}$) and intermediate in the two other zinc complexes ($\mathbf{C^{14\text{-}15}}$). Moreover, the position of the enol band seems to be also influenced by the halogen nature as suggested by the hypsochromic shift of approximately 10 nm of the upper wavelength limit observed between $\mathbf{C^{14}}$ and $\mathbf{C^{15}}$ (see Figure 102).

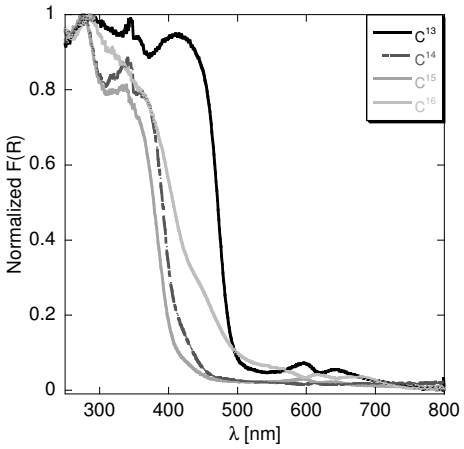

Figure 102 Diffuse reflectance spectra at 298 K of $[Zn^{II}(\mathbf{Habs})_2F_2]$ ($\mathbf{C^{13}}$), $[Zn^{II}(\mathbf{Habs})_2Cl_2]$ ($\mathbf{C^{14}}$), $[Zn^{II}(\mathbf{Habs})_2Br_2]$ ($\mathbf{C^{15}}$) and $[Zn^{II}(\mathbf{Habs})_2I_2]$ ($\mathbf{C^{16}}$).

Finally, optical behaviour of $[Fe^{II}(\mathbf{Habs})_2Cl_2]$ ($\mathbf{C^{12}}$) is very interesting because it presents a diffuse reflectance spectrum constituted by two main bands, in the UV range, attributed to the enol form of the **Habs** ligand, and in the visible (between 400 and 600 nm). This last contribution takes its origin in a combination of the *cis*-keto band and a charge transfer band (Figure 103). Although a very weak signal is also observed after 700 nm, attributed to the d-d transitions, the compound is pale yellow in contrast to the other **Habs** iron(II) complex ($\mathbf{C^{11}}$) which is pink or dark pink following the temperature. Under UV light irradiation, $\mathbf{C^{12}}$ shows a strong modification of the intensity of the main signal localized in the visible part of the spectrum (Figure 103) whereas no significant difference was observed in the spectra of other **Habs** complexes[339].

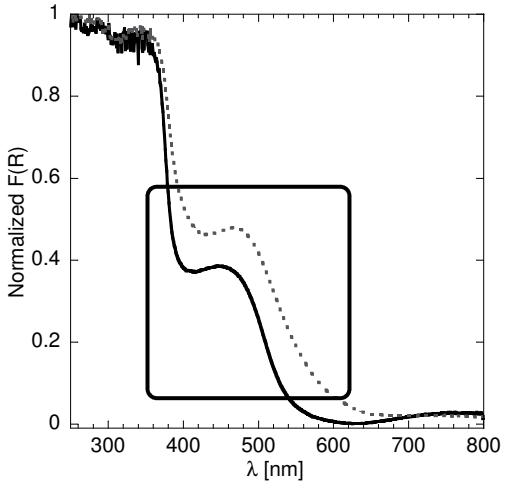

Figure 103 Diffuse reflectance spectra at 298 K of [Fe^{II}(**Habs**)$_2Cl_2$] (**C^{12}**) before (black line) and after light irradiation at 254 nm for 1 h (dotted line), showing the increase of the band in the visible part of the spectrum (indicated by the black square).

The photo-induced phenomenon observed in Figure 103 was investigated by time dependent diffuse reflectance spectroscopy on a fresh sample. Surprisingly, when we measure the evolution of the Kubelka-Munk function at 550 nm without any light irradiation, an unexpected and complicated evolution is observed as shown in Figure 104. It seems then that the phenomenon observed in Figure 103 is, at least partially, not directed by the light irradiation itself but by an ageing effect induced by keeping the sample in air during the experiment.[340] Photochromism is however suggested because a weak reversibility has been detected by a light irradiation at 546 nm for 15 min (same experimental condition than for **Habs**, see chapter 2) (Figure 105).

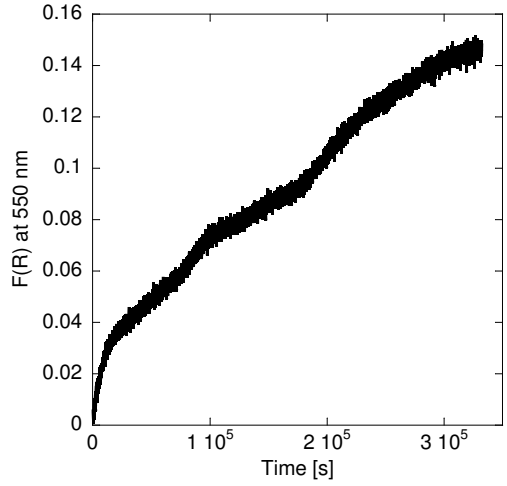

Figure 104 Evolution with time of the Kubelka-Munk function at 550 nm for a fresh sample of $[Fe^{II}(\mathbf{Habs})_2Cl_2]$ ($\mathbf{C^{12}}$) kept in air at 298 K.

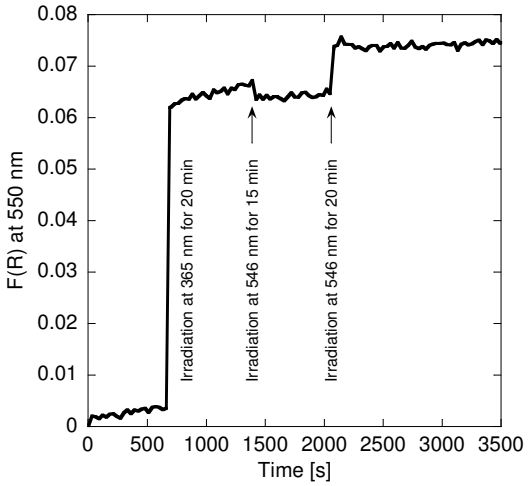

Figure 105 Evolution with time of the Kubelka-Munk function at 550 nm for a fresh sample of $[Fe^{II}(\mathbf{Habs})_2Cl_2]$ ($\mathbf{C^{12}}$) at 298 K in air with successive light irradiation at 365 nm and 546 nm for 20, 15 and 20 min, respectively. The weak reversibility of the photo-induced phenomenon is suggested by the decrease of the signal after the second light irradiation.

Although **C[12]** appears then to be not the perfect candidate for the photochromism observation, it is the very first time that this phenomenon is suspected for a inorganic complex built with a *N*-salicylidene aniline derivative molecule.

In a second step, the ageing effect in air of **C[12]** was analysed by ^{57}Fe Mössbauer spectroscopy on a fresh sample, before and after irradiating at 365 nm for 1 h at room temperature. As shown in Table 14 and Figure 106, the fresh sample gives a spectrum composed by a main doublet signal (δ^{298K}_{HS1} = 1.031 (2) mm.s^{-1}, $\Delta E_Q{}^{298K}_{HS1}$ = 3.940 (4) mm.s^{-1}, relative fraction area = 84 (1) %). This signal could be attributed to a HS Fe^{II}-N_4Cl_2 site (comparison with $[Fe^{II}(py)_4Cl_2]$: δ^{298K} = 1.04 mm.s^{-1}, $\Delta E_Q{}^{298K}$ = 3.14 mm.s^{-1})[222, 341] and support our previous discussion about the formulation of this compound. Moreover, a second weak peak can also be distinguished with Mössbauer parameters of δ^{77K}_{HS2} = 1.06 (3) mm.s^{-1}, $\Delta E_Q{}^{77K}_{HS2}$ = 2.35 (6) mm.s^{-1}, Relative fraction area = 6 (2) %. It probably comes from a HS Fe^{II}-N_6 complex[222], present in the material as an impurity. As shown in Table 14, the temperature has a low impact on the spectrum. A normal evolution of the Mössbauer parameters is noted[222] and weak modification of the relative fraction areas of the two sites seems to be present because of the expected *f* factor difference.

Table 14 Evolution of ^{57}Fe Mössbauer parameters of **C^{12}** spectra in a temperature range of 77-298 K before and after a light irradiation at 365 nm for 1 h. Parameters for each Mössbauer signal are given separated by a '/' symbol.

Irradiated	T [K]	δ [mm.s^{-1}][a]	ΔE_Q [mm.s^{-1}]	$\Gamma/2$ [mm.s^{-1}]	Relative Fraction Area [%]
✘	77	1.149(2)/1.06(3)	3.963(4)/2.35(6)	0.138(3)/0.13(5)	94(1)/6(2)
✘	90	1.144(2)/1.06(2)	3.965(4)/2.33(5)	0.138(3)/0.11(4)	94(2)/6(1)
✘	110	1.134(2)/1.06(4)	3.964(5)/2.36(8)	0.136(4)/0.15(6)	93(2)/7(2)
✘	130	1.126(2)/1.07(3)	3.970(3)/2.33(5)	0.136(2)/0.16(4)	93(1)/7(1)
✘	150	1.117(2)/1.01(4)	3.967(4)/2.28(8)	0.134(3)/0.18(6)	92(2)/8(2)
✘	170	1.106(2)/1.06(3)	3.975(4)/2.35(6)	0.134(3)/0.20(5)	90(2)/10(2)
✘	190	1.093(2)/1.04(2)	3.964(3)/2.33(4)	0.137(2)/0.14(3)	93(1)/7(1)
✘	210	1.081(2)/1.03(3)	3.965(4)/2.33(6)	0.140(3)/0.18(5)	92(2)/8(2)
✘	230	1.068(2)/1.02(5)	3.960(4)/2.3 (1)	0.136(4)/0.26(8)	89(2)/11(3)
✘	250	1.056(2)/1.02(4)	3.962(4)/2.30(9)	0.134(3)/0.27(7)	89(2)/11(2)
✘	270	1.042(2)/1.01(4)	3.951(4)/2.33(7)	0.135(3)/0.20(6)	91(2)/9(2)
✘	298	1.031(2)/1.01(6)	3.940(4)/2.2 (1)	0.131(4)/0.38(9)	84(2)/16(3)
✓	90	1.143(1)/1.08(2) 0.39 (3)	3.960(3)/2.40(4) 0.1 (4)	0.142(2)/0.11(3) 0.2 (1)	89(1)/4(1) 7 (1)
✓	298	1.026(2)/0.95(2) 0.28 (2)	3.935(3)/2.34(4) 0.31 (4)	0.149(3)/0.14(3) 0.21 (4)	82(1)/6(1) 12 (1)

[a] Values are given with respect to α-Fe.

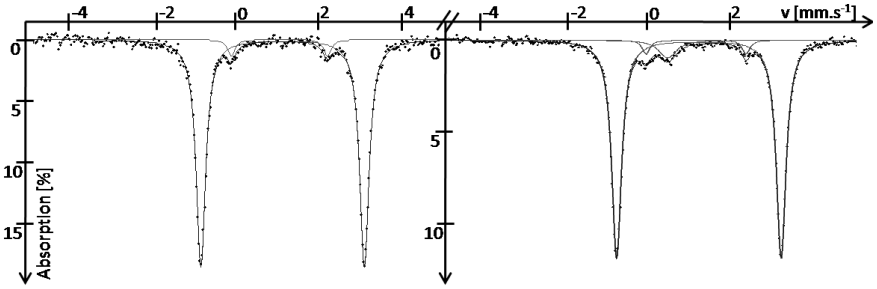

Figure 106 ^{57}Fe Mössbauer spectra of **C^{12}** at 90 K before (on the left) and after light irradiation in air at 365 nm for 1h at room temperature (on the right). The formation of a third signal is noted in the centre of the spectrum.

The light irradiation at 365 nm in air and at room temperature leads to a slight change in the spectrum shape (Figure 106) induced by the presence of a third absorption peak, characterised by $\delta^{298K}_{Fe(III)}$ = 0.28(2) mm.s^{-1}, $\Delta E_Q{}^{77K}_{Fe(III)}$ = 0.31(4) mm.s^{-1}, Relative fraction area = 12(1) %, which could be attributed to an iron(III) site[222]. The formation of this signal is probably induced by air atmosphere which leads to an oxidation as suggested by our time dependent diffuse reflectance spectroscopy measurements. Nevertheless, a photo-oxidation can not be rejected. No other change seems to be induced by light irradiation. However, the formation of the photo-induced *trans*-keto form of **Habs** in the complex cannot be rejected too because of the expected small efficiency of the photo-isomerisation process[68] combined with the sensitivity of the Mössbauer spectrocopy.

Compounds [Zn^{II}(**Habs**)$_2X_2$] (**C$^{13\text{-}16}$**), where X = F, Cl, Br and I, and [Fe^{II}(**Habs**)$_2Cl_2$] (**C^{12}**) were analyzed by fluorimetry at room temperature (Figure 107 and Figure 108). With an excitation wavelength of 350 nm, different emission behaviours have been observed. Indeed, as shown in Table 15, **C^{12}** presents only one emission contribution at a maximum emission wavelength of 413 nm (λ_1^{max}), **C^{16}** have two emission bands centred at 387 (λ_1^{max}) and at 499 nm (λ_2^{max}) whereas the other complexes show only the less energetic contribution between 454 nm and 503 nm (λ_2^{max}) (although some broad emission bands could contain both contributions). According to excitation spectra made with emission wavelength adjusted to values shown in Table 15, it has been demonstrated that emission bands 1 and 2, corresponding to maximum emission wavelength λ_1^{max} and λ_2^{max} respectively, can be attributed to the radiative

relaxation of the excited enol* and *cis*-keto*, as previously discussed in the work (see chapters 1 and 2). Interestingly, **C[12]** appears to be the first compound presenting only the enol* emission band. The excited state proton transfer, giving rise to the *cis*-keto* form which can fluoresce, does not occur. However, no deeper conclusions about this observation can be drawn because of the lack of information about the crystal structure of this molecule. The other complexes present both enol* and *cis*-keto* forms (or exclusively the *cis*-keto* emission) which correspond to the same behaviours than described in details in chapter 5. However, it is interesting to notice that although significant differences in maximum emission wavelengths were observed between **Habs** complexes, no correlation between electro-negativity of X and this parameter can be drawn.

Table 15 Maxima emission wavelength for **C[12-16]** with an excitation wavelength of 350 nm at room temperature.

	C[12]	**C[13]**	**C[14]**	**C[15]**	**C[16]**
λ_1^{max}	-	503	495	454	499
λ_2^{max}	413	-	-	-	387

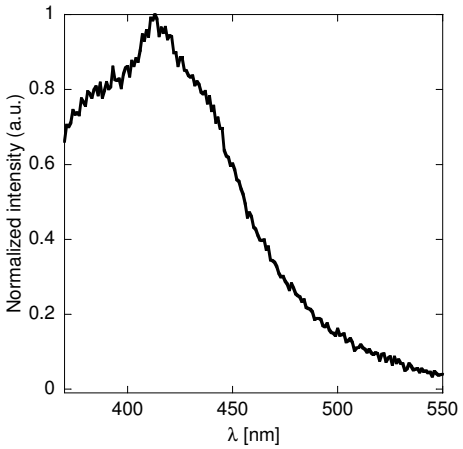

Figure 107 Emission spectra at room temperature of solid samples of $\mathbf{C^{12}}$ with an excitation wavelength of 350 nm. The shape of the emission band indicates a substructure which could take its origin in the presence of few molecular conformations.

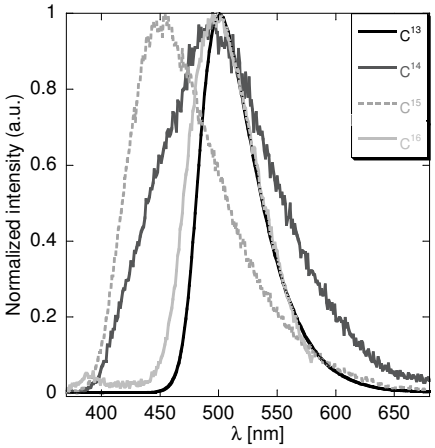

Figure 108 Emission spectra at room temperature of solid samples of $\mathbf{C^{13\text{-}16}}$ with an excitation wavelength of 350 nm.

Compounds $[Zn^{II}(\mathbf{Habs})_2X_2]$ and, in particular, when X = F ($\mathbf{C^{13}}$), was observed to be highly fluorescent as suggested in Figure 109. This property appears to be very attractive[342] because of the promising perspectives of Light-Emitting Diodes (*LED*).[332, 342] Fluorescence quantum yields of compounds $\mathbf{C^{13\text{-}16}}$ were then analysed by using a home-made integration sphere setup built in the Prof. J.-C. Bünzli's laboratory at EPFL in Switzerland (see experimental section). Experimental values, listed in Table 16, show a very strong enhancement of the fluorescence quantum yield by the coordination of **Habs** to the zinc metal ion. However, a strong sensitivity to the halogen anion (X) is also demonstrated. Because of the decrease of Φ_f with the mass of X, a 'heavy atom effect', which leads to an inter-crossing system phenomenon increase and then to a fluorescence intensity decrease,[343] is strongly suspected. The best value is obtained for the compound with the targeted formula $[Zn^{II}(\mathbf{Habs})_2F_2]$ which presents a very good fluorescence quantum yield of 15.4 % (comparing to Ref. [344]).

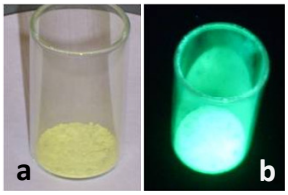

Figure 109 Photograph of a sample of $\mathbf{C^{13}}$ under the daylight (a) and under a light of 254 nm (b) showing the very strong green luminescence of the material.

Table 16 Fluorescence quantum yield (Φ_f) of $\mathbf{C^{13\text{-}16}}$ and **Habs** at 500 nm with an excitation wavelength of 430 nm.

	$\mathbf{C^{13}}$ Zn/F	$\mathbf{C^{14}}$ Zn/Cl	$\mathbf{C^{15}}$ Zn/Br	$\mathbf{C^{16}}$ Zn/I	**Habs**
Φ_f [%]	15.4	5.0	3.6	0.8	- [a]

[a]Value below the detection limit of the experimental setup.

Considering the attractive luminescence properties of $[Zn^{II}(\mathbf{Habs})_2X_2]$ complexes, we have also investigated the lifetimes of excited states in the solid state in collaboration with Dr. B. Muls and Prof. J.-L. Habib Jiwan. For this purpose, **Habs** was analysed in methanol and in the solid state with an excitation and emission wavelengths corresponding to maxima of absorption and emission of the *cis*-keto form, respectively. As shown in Figure 110, the switch from the solution to the solid state induces a very large modification of the photo-chemical processes. Indeed, as described in Table 17, excited states with long lifetimes seem to be favoured in solution as demonstrated by the presence of a τ_4 of 3.49 ns (P_4 = 83 %) in contrast to the longest lifetime obtained in the solid state τ_4 = 2.83 ns (P_4 = 63 %). Moreover, in the solid state, a more distributed range of short lifetimes is observed (τ_2 and τ_3 = 0.21 and 0.97 ns, respectively) (Table 17). A very short lifetime of τ_1 = 0.02 ns is also noted with a negative value of P, attributed to a delay of the fluorescence phenomenon which could be induced by an energy transfer phenomenon between **Habs** molecules before light emission. This hypothesis is supported by the solid state where the measurements were carried out and which could imply the presence of slightly different molecular environments around luminophores. It is, however, important to note that an exponential fitting procedure as followed, with a so large number of contributions, cannot be considered as accurate. Indeed, more than one fit can be obtained from the experimental data and, thus, cannot conduct to deep discussions about kinetic schemes leading to such fluorescence decays. Nevertheless, very interesting tendencies can be obtained giving some additional details about photochemical processes in free organic molecules and in related inorganic complexes.

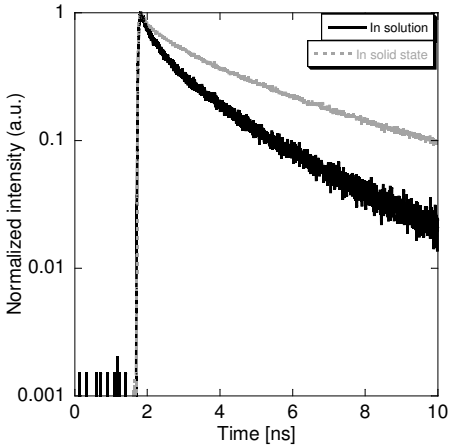

Figure 110 Fluorescence decay at 560 nm with an excitation wavelength of 430 nm for **Habs** in methanol solution (10^{-5} M) and in the solid state.

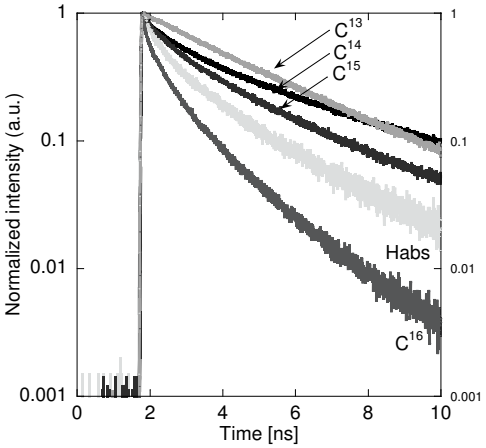

Figure 111 Fluorescence decay at 560 nm with an excitation wavelength of 430 nm for **Habs** and **C$^{13\text{-}16}$** in the solid state.

Table 17 Excited states lifetimes for **Habs** in methanol solution (10^{-5} M) and in the solid state and for $\mathbf{C^{13\text{-}16}}$ in the solid state found with an excitation and emission wavelengths of 430 and 560 nm, respectively.

	$\mathbf{C^{13}}$	$\mathbf{C^{14}}$	$\mathbf{C^{15}}$	$\mathbf{C^{16}}$	**Habs**	
	Zn/F	Zn/Cl	Zn/Br	Zn/I	Solution	Solid state
τ_1 [ns]	-	0.02	0.01	0.06	0.05	0.02
P_1[a] [%]		-1	-1	4	8	-2
τ_2 [ns]	0.13	0.13	0.16	0.30	0.07	0.21
P_2[a] [%]	1	2	2	11	4	10
τ_3 [ns]	0.94	0.96	0.95	0.99	0.67	0.97
P_3[a] [%]	16	13	42	48	5	27
τ_4 [ns]	3.20	4.09	3.25	2.27	3.49	2.83
P_4[a] [%]	83	85	56	38	83	63

[a]P was defined as the percentage of deexcitation of excited states found by the multiplication of the amplitude of the fluorescence with the associated lifetime.

Metal ion coordination as well as the nature of the halogen atoms have strong influences on the lifetimes of excited states of **Habs**. Indeed, as shown in Figure 111 and Table 17, $\mathbf{C^{13}}$ appears to be constituted with a main long lifetime (τ_4 = 3.20 ns, P_4 = 83 %) and two shorter ones (τ_2 = 0.13 ns, P_2 = 1 % and τ_3 = 0.94 ns, P_3 = 16 %). $\mathbf{C^{14}}$ is similar with a very long lifetime (τ_4 = 4.09 ns, P_4 = 85 %), two shorter ones (τ_2 = 0.13 ns, P_2 = 2 % and τ_3 = 0.96 ns, P_3 = 13 %) and a very short one associated with a negative P value as observed for the **Habs** molecule (τ_1 = 0.02 ns and P_1 = -1 %). $\mathbf{C^{16}}$ is different because of the presence of the shorter lifetime τ_1 (2.27 ns) and other important *P* values associated with τ_1 = 0.06 ns (P_1 = 4 %), τ_2 = 0.30 ns (P_2 = 11 %) and τ_3 = 0.99 ns (P_3 = 48 %). Finally, $\mathbf{C^{15}}$ appears to be an intermediate between $\mathbf{C^{14}}$ and $\mathbf{C^{16}}$ with τ_1 = 0.01 ns (P_1 = -1 %), τ_2 = 0.16 ns (P_2 = 2 %), τ_3 = 0.95 ns (P_3 = 42 %) and τ_4 = 3.25 ns (P_4 = 56 %). The tendency is then clearly distinguished: the larger halogen atom mass leads to more distributed lifetimes from a mainly mono-exponential fitting curve for $\mathbf{C^{13}}$ (F) to complicated fluorescence decay for $\mathbf{C^{16}}$ (I). It

could take its origin in the presence of more disordered **Habs** conformations induced by the steric hindrance brought by the larger halogen atoms. The shortest lifetimes seem also to be favoured by the heavier halogen atoms.

Discussion

Habs molecule was chosen as ligand because of its expected good coordination capability in order to make complexes with mixed coordination spheres built with different ligands such as NCS or halogen anions (X). **Habs** complexes correspond to a new promising class of materials because of the very wide type of accessible complexes (mononuclear, dinuclear, etc). However, it leads also to difficulties for some formulation determination. In the case of studied compounds, the large variety of analytical techniques used gives information about the mononuclear nature of the inorganic unit (thanks to NMR and elementary analyses) and the formation of expected mixed sphere (^{57}Fe Mössbauer, reported **abpt** complexes structures, etc) but some uncertainties remains about the exact formulation of some molecules.

As claimed above, **Habs** complexes are promising materials because of the various optical and magnetic properties detected during our investigation. Indeed, we have confirmed the possibility to form SCO complexes by choosing a Fe^{II}-N_6 mixed coordination sphere built with NCS ligands (**C^{11}**). Moreover, the observation of a weak reversibility in a photo-induced phenomenon with [Fe^{II}(**Habs**)$_2$Cl$_2$] complex (**C^{12}**) has stimulated the project to observe a photochromism on a *N*-salicylidene aniline based inorganic complex. This observation remains however strongly disturbed by the presence of a strong oxidation process. A measurement under vacuum with an in-situ photo-excitation could be proposed in order to clarify this point.

Finally, zinc complexes of formula $[Zn^{II}(\mathbf{Habs})_2X_2]$ with X = halogen anions have been observed as strongly fluorescent with up to 15.4 % of fluorescence quantum yield which is close to well-known molecular luminophores in solution such as $[Ru(phen)_3]^{2+}$ ($\Theta_P \leq 12$ %).[344] The study of the lifetime of excited states shows complicated fluorescence decays which are not possible to fit by mono-exponential function. Indeed, the presence of many relaxation pathways is strongly supported by our previous observations about the presence of few conformations of all forms (enol*, *cis*-keto*, *trans*-keto* and cyclised* forms, see discussions in previous chapters). The lifetimes found are in the range of 0.01-4.09 ns which confirm the presence of fluorescence processes. However, the presence of phosphorescence processes, which are characterised by very long excited states lifetime (μs to ms time range),[345] cannot be rejected because of the limitation of our measurement apparatus (see experimental section).

Chapter VIII: *N*-salicylidene aniline derivatives as precursors for new magnetic supramolecular architectures†††

Introducing remarks

A major concept in crystal engineering is that covalent blocks can be encoded to interact in a given orientation affording crystal packing control.[194] In such self assemblies, building blocks are directly connected through intermolecular interactions or by the use of metal ions that can present diverse coordination sphere geometries and natures. Following this synthetic plan, various functional nano-structures (e.g. racks,[184, 346, 347] cages[348] and grids[182, 183, 349-352]), which can often reorganize under a given stimulation,[188-190] were synthesized. Grid-like metal ion arrays are particularly attractive in this respect for molecular electronic applications because of the well controlled 2D arrangement that can be extended on a given surface.[353, 354] In the frame of molecular magnetism, these molecules can behave as single-molecule magnets[355] and be potentially interesting for data storage applications by addressing electronic properties of metal ions (spin state,[120, 356-360] oxidation state[361]). The magnetic properties of [2x2] grid-like complexes[362] are relatively rich. In particular, ferromagnetic[363] and/or anti-ferromagnetic[363, 364] couplings have been observed within and between the supramolecules. High-nuclearity transition metal complexes are also of common interest in bio-inorganic chemistry as they can mimic multimetallic active sites of metalloproteins.[365] A biomimetic application

††† Adapted from F. Robert, B. Tinant, R. Clérac, P.-L. Jacquemin, Y. Garcia *Polyhedron,* **2010**, *29*, 2739-2746.

was considered in this context for a Cu(II) [2x2] grid-like complex.[366] Thus, the synthesis of asymmetric [2x2] nanogrids with different metals,[355] spin states,[120, 356-359] coordination spheres[364] and geometries remains a challenging perspective, particularly in the frame of magneto-chirality.[367, 368] There exist various ways of generating chiral coordination complexes and assemblies.[369, 370] Transfer of chiral information from predesigned optically active ligands or coordination building blocks is generally targeted.[371] This strategy has been successful for developing chiral tetranuclear Cu(II) complexes,[372] most examples being found for cubanes.[373-375]

We present herein two new examples of metal directed supramolecular grid self-assemblies, using *N*-salicylidene 2-aminopyridine ligand ($\mathbf{L^2}$) (in this chapter, $\mathbf{L^x}$ = molecule with alcohol function and $\mathbf{L\text{-}^x}$ = molecule with alcoholate function), showing the potentiality of *N*-salicylidene aniline derivatives in the development of new magnetic architectures. First, an unique asymmetric [2x2] grid-like complex that co-crystallizes with a Cu(II) mononuclear anion: $[Cu_4(\mathbf{L\text{-}^2})_4(NO_3)_3(CH_3OH)]$ $[Cu(\mathbf{L\text{-}^2})(NO_3)_2]$ (2-aminopyridinium) $(NO_3)\bullet 5CH_3OH$ ($\mathbf{C^{17}}$). It is a sophisticated architecture comprising not less than three Cu(II) coordination sphere geometries. This asymmetric self-assembly is generated without any ligand conformation asymmetry[376] and affords a strong anti-ferromagnetic (AF) coupling between spin carriers. A more symmetric [2x2] grid-like complex was obtained with $\mathbf{L^2}$ using modified synthetic conditions: $[Cu_4(\mathbf{L\text{-}^2})_4(NO_3)_2(OH)_2]$(2-aminopyridinium)$(OH)\bullet CH_3OH$ ($\mathbf{C^{18}}$). A Ni(II) dinuclear complex, $[Ni_2(\mathbf{CH_2L\text{-}^3})_2(\mathbf{CH_2L^3})_2(NCS)_2(CH_3OH)_2]\bullet 2CH_3OH$ ($\mathbf{C^{19}}$), was also prepared with the related Schiff base *N*-salicylidene

3-(aminomethyl)pyridine (**CH_2L^3**). It structurally represents half of the [2x2] grid-like complex **C^{17}** and **C^{18}**, and is helpful to understand the complex grid architecture.

Syntheses and crystallization methods

Reacting $Cu(NO_3)_2 \bullet 3H_2O$, **L^2** and 2-aminopyridine in a 4:4:1 ratio in methanol afforded large green crystals of $[Cu_4(\mathbf{L}\text{-}^{2})_4(NO_3)_3(CH_3OH)][Cu(\mathbf{L}\text{-}^{2})(NO_3)_2](2\text{-aminopyridinium})(NO_3) \bullet 5CH_3OH$ (**C^{17}**). These crystals transform to powder after filtration in air. This behaviour originates from the lost of lattice solvent methanol molecules as concluded from thermogravimetric and elemental analyses. Crystals thus had to be directly taken out from the mother solution and quickly transferred to a diffractometer to enable a crystal structure determination that revealed an interesting [2x2] grid-like complex. Surprisingly, reacting $Cu(NO_3)_2 \bullet 3H_2O$, **L^2** and 2-aminopyridine in a different ratio (5:5:1) also in methanol afforded $[Cu_4(\mathbf{L}\text{-}^{2})_4(NO_3)_2(OH)_2](2\text{-aminopyridinium})(OH) \bullet CH_3OH$ (**C^{18}**) whose crystal structure was determined. Although we assume that its crystal structure is not representative of the major reaction product, it is discussed below because, like **C^{17}**, it is a [2x2] grid-like complex, and confirms the formation of such self-assembled architecture in the reaction scheme. Note that, in both cases, 2-aminopyridinium acted as a seeding agent. Indeed, all crystallization attempts without this molecule failed whatever the method employed. Single crystals of $[Ni_2(\mathbf{CH_2L}\text{-}^{3})_2(\mathbf{CH_2L}^{3})_2(NCS)_2(CH_3OH)_2] \bullet 2CH_3OH$ (**C^{19}**) were obtained in collaboration with P.-L. Jacquemin[203] by reacting $NiCl_2$, NH_4NCS and **CH_2L^3** in a 1:2:4 ratio in methanol.

Crystal structures study[‡‡‡]

$[Cu^{II}_4(L^{-2})_4(NO_3)_3(CH_3OH)][Cu^{II}(L^{-2})(NO_3)_2](2\text{-aminopyridinium})(NO_3)\bullet 5\ CH_3OH$ (C^{17})

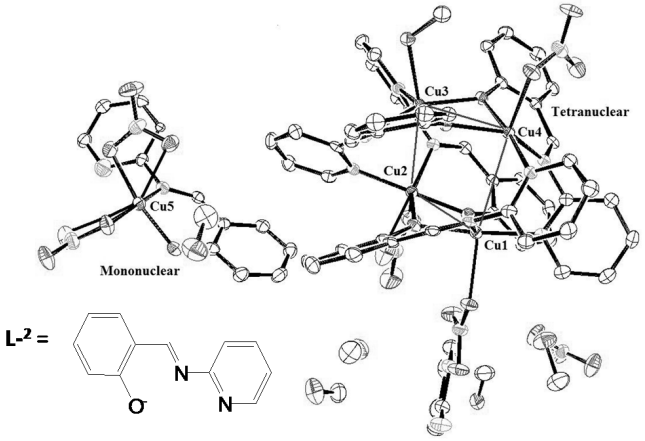

Figure 112 ORTEP view of the asymmetric part of the unit cell for $\mathbf{C^{17}}$, showing 50% probability displacement ellipsoids. The Cu^{II} grid-like complex (grey square) is shown on the right side and the mononuclear unit on the left side. H atoms were omitted for clarity. The inset shows a scheme of the $\mathbf{L^{-2}}$ ligand.

The asymmetric part of the unit cell of $\mathbf{C^{17}}$, which crystallizes in the triclinic space group $P\bar{1}$ (Table 46), is crowded. It contains a non-centrosymmetric cationic Cu(II) [2x2] grid-like complex with 4 copper ions labelled as Cui (i = 1-4), an anionic Cu(II) mononuclear unit, several uncoordinated species (five methanol molecules and one nitrate anion), as well as a disordered 2-aminopyridinium cation, required to ease crystallization (Figure 112). The coordination sphere of the anionic mononuclear entity around Cu5, $[Cu(\mathbf{L^{-2}})(NO_3)_2]$, contains one $\mathbf{L^{-2}}$ and two bidentate nitrato anions.

[‡‡‡] Crystal structures were solved by Prof. B. Tinant (UCL).

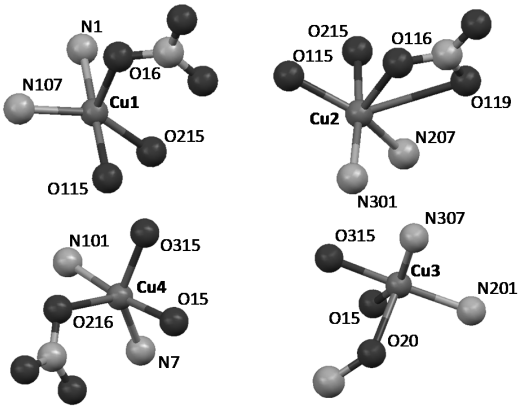

Figure 113 View of the coordination sphere in the tetranuclear unit of **C**[17].

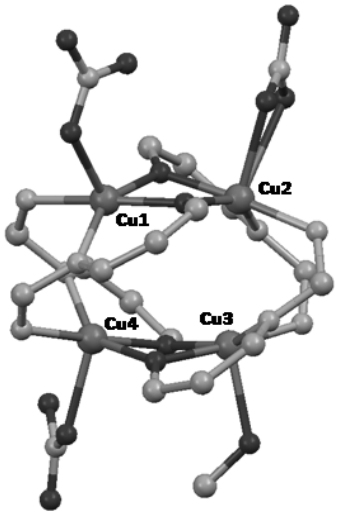

Figure 114 View of the magnetic pathway in **C**[17], between the magnetic dinuclear units (Cu1, Cu2) and (Cu3, Cu4).

Interestingly, **L-**^{2} appears to be twisted (the dihedral angle between salicyl and pyridine rings, Φ = 42(1)°) even though the pyridine moiety is not involved in the coordination sphere. In order to simplify the discussion of the tetranuclear complex, structurally different ligands have been labelled as Lj

(j = a-e) (Table 47). Relevant bond length differences and angles are given in Table 48 and Table 49. The coordination sphere of Cu1 is built of five atoms in a square pyramidal geometry which is confirmed by the Addison structural index,[377] $\tau_A = 0.35$. It involves O16 of a monodentate nitrate, N1 from the pyridine of **L-^{2}a**, N107 from the imine function of **L-^{2}b**, O115 and O215 from alcoholate functions of **L-^{2}b** and **L-^{2}c**, respectively (Figure 113). Interestingly, Cu2 adopts a distorted hexa-coordinated coordination sphere with O116 and O119 from a bidentate nitrato anion, N301 from the pyridine of **L-^{2}d**, N207 from the imine function of **L-^{2}c**, O115 and O215 from alcoholate functions of **L-^{2}b** and **L-^{2}c**, respectively. The coordination sphere of Cu3, also displayed on Figure 113, resembles the one of Cu1. It is also penta-coordinated ($\tau_A = 0.04$) but the nitrato anion has now been replaced by a methanol molecule. Indeed, we find one oxygen atom arising from a methanol molecule (O20), N201 from the pyridine of **L-^{2}c**, N307 from the imine function of **L-^{2}d**, O15 and O315 from the alkoxo groups of **L-^{2}a** and **L-^{2}d**. As Cu1, Cu4 also presents a square pyramidal coordination sphere ($\tau_A = 0.40$) made with O216 from a monodentate nitrato anion, N101 from the pyridine of **L-^{2}b**, N7 from the imine function of **L-^{2}a**, O15 and O315 from alkoxo groups of **L-^{2}a** and **L-^{2}d**. However, their connection through μ_2-alkoxo groups to different copper ions (Cu2 and Cu3), makes Cu1 and Cu4 different from a crystallographic point of view (Table 48 and Table 49). The whole [2x2] grid forms a slightly distorted square (Figure 112) with Cu···Cu distances of 3.064(3) Å, 3.067(3) Å, 3.253(3) Å and 3.343(3) Å (Table 47) which are in the same range than the distances observed for $[Cu_4(\mathbf{L1})_4(H_2O)_4](NO_3)_4$ (**C^{26}**).[378] The tetranuclear unit can be viewed as a pair of dinuclear complexes,[218] the bridging geometry within each dinuclear unit being made of two μ_2-alkoxo groups with Cu-O-Cu angles around

101.8-102.8° (Table 49) that suggest strong AF interactions between metal ions. Both dimers are linked by two N-C-N bridges including the imine and pyridine moieties of $\mathbf{L}^{-2}$ (Figure 114). A racemic mixture of two enantiomers, generated by the $P\bar{1}$ symmetry, has been crystallised with a right hand helicate (Δ enantiomer) or a left hand helicate (Λ enantiomer) (Figure 115). This situation results from the large twist of $\mathbf{L}^{-2}$ (see torsion angles in Table 47). A dense supramolecular network is also revealed based on 14 intermolecular H-bonds, one N-H···π and two C-H···π interactions (Table 50 and Table 51).

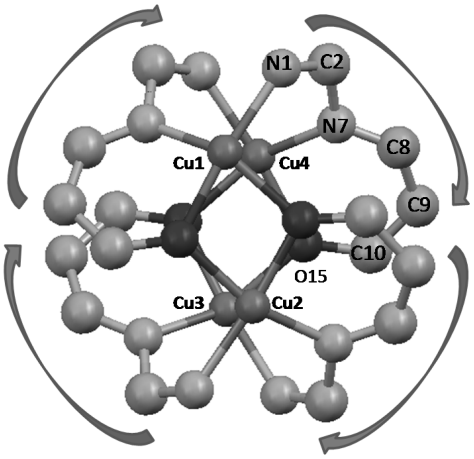

Figure 115 View of the tetranuclear core of $\mathbf{C}^{17}$ revealing a right hand quadruple helicate structure thanks to the torsion of four $\mathbf{L}^{-2}$ ligands. The arrows indicate the clockwise rotation, e.g. from Cu1 (top) to Cu3 (bottom) following the labelled sequence. A similar view can be depicted for $\mathbf{C}^{18}$.

$[Cu^{II}_4(L\text{-}2)_4(NO_3)_2(OH)_2]$(2-aminopyridinium)$(OH)\bullet CH_3OH$ (C^{18})

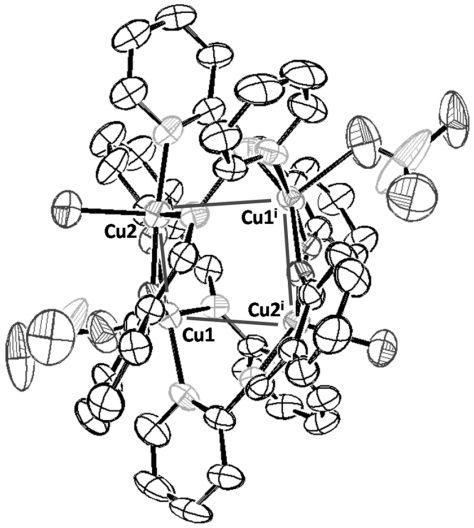

Figure 116 ORTEP view of the tetranuclear unit (grey square) in **C[18]**, showing 50% probability displacement ellipsoids. H atoms and guest molecules were omitted for clarity.

C[18] crystallizes in the orthorhombic space group *P*bcn and contains a Cu(II) tetranuclear unit, made with **L-[2]**, that forms a [2x2] grid-like arrangement with Cu···Cu distances of 3.067(9) Å and 3.213(9) Å (Figure 116, Table 46 and Table 47). Two different coordination spheres are identified. Cu1 presents a square pyramidal geometry (τ_A = 0.40) made of a monodentate nitrato anion (O202) in apical position, two oxygen atoms originating from alkoxo groups of **L-[2]a** (O15) and **L-[2]b** (O115), a nitrogen N1 of the pyridine of **L-[2]a** and a nitrogen N107 of the imine function of **L-[2]b**. Cu2 which is also penta-coordinated presents a similar coordination sphere (τ_A = 0.01) with a hydroxide (O20) in apical position, two oxygen atoms from alkoxo functions of **L-[2]a** (O15) and **L-[2]b** (O115), a nitrogen N101 of the pyridine of **L-[2]b** and

a nitrogen N7 of the imine function of **L-^{2}a**. The bridge between Cu ions is ensured, like in **C^{17}**, by two alkoxo groups in one direction and by an imine and a pyridine group (N-C-N bridge) in the other direction. Even if only two Cu ions are present in the asymmetric part of the unit cell, the grid-like complex is generated by symmetry. Each ligand **L-^{2}** is coordinated to three Cu ions. Interestingly, the coordination involves a large dihedral angle Φ between aromatic rings of **L-^{2}** (Φ_a = 35(1)° and Φ_b = 40(1)°) (Table 47). Because of this angle, as in **C^{17}**, a quadruple helicate is formed within this chiral tetranuclear unit. The two enantiomers, which crystallize in a racemic mixture, are generated by symmetry in the *P*bcn group.

The [2x2] grid unit also co-crystallizes with a hydroxide ion, a methanol and a 2-aminopyridinium cation. The electro-neutrality is reached between positive charges (copper ions and pyridinium moiety) and negative charges (**L-^{2}**, coordinated nitrates and hydroxide, free hydroxide). The structure shows a few supramolecular interactions that ensure the cohesion between building blocks. Indeed, three intramolecular and three intermolecular H-bonds in addition to two intramolecular and three intermolecular π-π interactions are found (Table 50 and Table 51).

$[Ni^{II}_2(CH_2L^3)_4(NCS)_2(CH_3OH)_2] \bullet 2\ CH_3OH$ (C^{19})

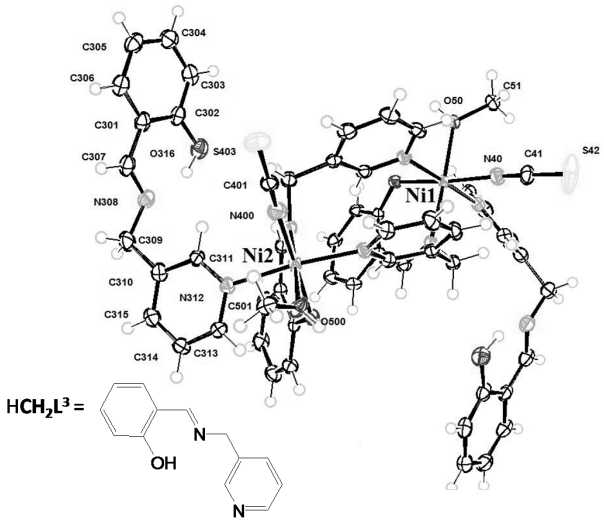

Figure 117 ORTEP view of the asymmetric part of the unit cell for $\mathbf{C^{19}}$, showing 50% probability displacement ellipsoids. The two solvent methanol molecules were omitted for clarity. The inset shows a scheme of the $\mathbf{CH_2L^3}$ ligand.

The asymmetric part of the unit cell of $\mathbf{C^{19}}$, which crystallizes in the triclinic space group $P\bar{1}$, contains a Ni^{II} dinuclear complex (Figure 117). Each nickel ion sits in a distorted octahedral coordination sphere (distortion parameter,[218] $\Sigma_{Ni1} = 72°$, $\Sigma_{Ni2} = 60°$) built from a methanol molecule, a linear isothiocyanato anion, a pyridine group originating from a terminal $\mathbf{CH_2L^3}$ as well as a pyridine, a μ-alkoxo and an imino group belonging to two different bridging $\mathbf{CH_2L^3}$ ligands (Table 47). Two disordered methanol solvent molecules are also found in the crystal lattice. $\mathbf{CH_2L^3}$ ligands are structurally different. Indeed, large differences are observed in the dihedral angle, between phenoxide and pyridine aromatic rings, as well as in the C7-N8-C9-C10 torsion angle allowed by the presence of the flexible methyl group (Table 47). Terminal $\mathbf{CH_2L^3}$ ($\mathbf{CH_2L^3a}$ and $\mathbf{CH_2L^3d}$) are similar with

dihedral angles of 60(1)° and 69(1)° and torsion angles of 125(1)° and 126(1)° although bridging $\mathbf{CH_2L\text{-}^3}$ ($\mathbf{CH_2L\text{-}^3b}$ and $\mathbf{CH_2L\text{-}^3c}$) have dihedral angles of 76(1)° and 90(1)° and torsion angles of 97(1)° and 109(1)°. A larger metal distance (6.758(3) Å) is observed compared to the ones found for $\mathbf{C^{17}}$ and $\mathbf{C^{18}}$ (Table 47). This difference originates from the presence of a methyl spacer group in the related donor ligand $\mathbf{CH_2L^3}$. The dinuclear motif is slightly asymmetric as confirmed by the bond lengths differences noted in the coordination spheres of Ni1 and Ni2 (Table 48 and Table 52) and presents an helicate geometry provided by the $\mathbf{CH_2L^3}$ torsion angle. A racemic mixture of left (Λ) and right hand (Δ) enantiomers is generated by symmetry within the centrosymmetric $P\bar{1}$ space group. The structure is also characterised by a supramolecular interactions network. Indeed, three intramolecular H-bonds and one intramolecular π-π stacking interaction ensure the stability and the geometry of the supramolecular architecture. In addition to the intramolecular interactions, the cohesion between the dinuclear units and between complexes and guest molecules is obtained by three intermolecular H-bonds and three π-π stacking interactions (Table 50 and Table 51).

SQUID magnetometry

The magnetic properties of a polycrystalline sample of $\mathbf{C^{17}}$ were measured over the 1.8 - 300 K range, with an applied magnetic field of 1000 Oe by Dr. R. Clérac (CRPP, Bordeaux). At room temperature, χT was 0.63 $cm^3.K.mol^{-1}$ that is far from the theoretical value of 1.875 cm^3 K mol^{-1}, which is expected for five isolated paramagnetic Cu(II) ions (d^9, S = 1/2) with g = 2. This behaviour indicates that dominant anti-ferromagnetic (AF) exchange interactions exist between the Cu(II) ions which are confirmed on

cooling by the continuous decrease of the χT product that reaches a value around 0.40 cm^3 K mol^{-1} below 100 K. This value is in good agreement with the residual magnetism coming from the mononuclear Cu(II) S = 1/2 unit. As shown in the crystal analysis, complex **C[17]** can be topologically viewed as two dinuclear moieties composed of two S = 1/2 Cu(II) ions (Figure 114).[379-381] The magnetic data have been thus approximately modelled using an isotropic Heisenberg S = 1/2 dimer model and the following Hamiltonian:

$$H = -2J(S_{CuA}.S_{CuB})$$

where $\boldsymbol{J}$ is the average exchange interaction within dinuclear Cu units: Cu1-Cu2 and Cu3-Cu4 that are considered identical in this simplified approach; $\boldsymbol{S_i}$ the spin operators for each centres. The application of the van Vleck equation[379] to the Kambe's vector coupling scheme,[380] allows a determination of the low field analytical expression of the magnetic susceptibility[381] taking into account the presence of the residual S = 1/2 mononuclear unit:

$$\chi T = \frac{4Ng^2\mu_B^2}{k_B}\frac{1}{3+\exp\left(\frac{-2J}{k_BT}\right)} + \frac{Ng^2\mu_B^2}{4k_B}$$

This approximated model reproduces rather well the experimental results over the 1.5-300 K range as shown in Figure 118. The best set of parameters are g = 2.06(3) and J/k_B = - 489(3) K (J = - 340(2) cm^{-1}). The sign of the magnetic interaction implies that these copper binuclear units and thus the tetramer complex possesses a $S_T = 0$ ground state.

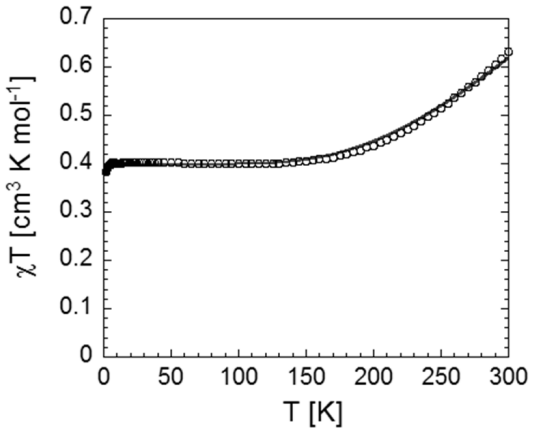

Figure 118 Temperature dependence of χT for **C**[17] at 1000 Oe (with χ defined as M/H) The open dots indicate the experimental data points and the line represents the best fitting curve obtained with the Heisenberg model described in the text.

It is worth mentioning that two other analyses of the magnetic data have been attempted: (i) considering two different dinuclear moieties with two independent magnetic interactions and (ii) considering identical dinuclear units that possess inter-dimer magnetic interactions through the N-C-N bridges. While the first approach leads to identical magnetic intra-dimer interactions and thus the same result displayed in Figure 118, the second model converges to an unphysically large value of the inter-dimer interaction (of the order of the intra-dimer interactions). Therefore, we assume that the inter-binuclear magnetic coupling is too weak in comparison to the intra-dimer interactions to be correctly estimated. The magnetic properties of the related grid **C**[20] support an AF exchange interactions between Cu(II) ions,[378] but no comparison can be made due to severe uncertainties both in the fit and acquisition of magnetic data (contamination of diamagnetic impurities) in Ref. [378].

Discussion

Reacting a Cu(II) salt with $\mathbf{L^2}$ in methanol afforded tetranuclear [2x2] grid-like complexes ($\mathbf{C^{17}}$ and $\mathbf{C^{18}}$). The composition of these complexes is different from the one reported by Hatfield[376] and Drummond[378] which was obtained following a different synthetic method in isopropanol. Indeed, ref.[378] reports on a highly symmetric tetranuclear complex $[Cu_4(\mathbf{L\text{-}^2})_4(H_2O)_4](NO_3)_4$ ($\mathbf{C^{20}}$) (as shown by the $P4_22_12$ space group) where all Cu(II) ions are identical and generated by symmetry). In $\mathbf{C^{17}}$, three Cu(II) coordination spheres with two distinct geometries around metal ions were identified, whereas two types of coordination spheres and two different $\mathbf{L\text{-}^2}$ ligands ($\mathbf{L\text{-}^2a\text{-}b}$) were identified for $\mathbf{C^{18}}$. Such an asymmetry is not only visible in Cu^{II} coordination spheres (see Table 48 and Table 49) but also in ligands, which can be differentiated by their dihedral angles Φ (Table 47). This structural feature provides chirality to the tetranuclear unit thanks to a $\mathbf{L\text{-}^2}$ torsion angle of approximately 40° (Table 47). The same structural feature is present in $\mathbf{C^{20}}$ but it was not discussed in Ref. [378]. In addition to the depicted 'intramolecular asymmetry', the intermolecular interactions network appears also to be asymmetric in $\mathbf{C^{17}}$. Such a network is less dense in the centrosymmetric tetranuclear $\mathbf{C^{18}}$. The difficulty to isolate $\mathbf{C^{18}}$ in large amount compared to $\mathbf{C^{17}}$ may stem from the dense supramolecular network (Table 50 and Table 51), developed in $\mathbf{C^{17}}$, which strongly stabilizes the structure and thus eases the crystallization. Comparison with the network developed in $\mathbf{C^{20}}$ is not feasible because the deposited CIF file in Ref. [378] does not contain any nitrato anions due to disorder.[378]

As seen in the crystal structures, the tetranuclear assembly is built by connecting two dinuclear units by a double N-C-N bridge, with short Cu···Cu

distances (~ 3 Å) (Figure 114) allowing a strong AF coupling as revealed by the study of the magnetic properties (J = - 340(2) cm^{-1}) for **C[17]**. This coupling constant reaches the same order of magnitude than observed for a related [4 x 4] grid-like complex (J = - 271 cm^{-1}).[382] Interestingly, the position in the Cu^{II} coordination spheres, occupied by the nitrato anion and methanol molecules in **C[17]** and by methanol and hydroxide molecules in **C[18]**, can be considered as labile. It suggests that a large variety of molecules may be formed in solution but that a selective crystallization of more stable complexes has occurred affording **C[17]** and **C[18]**. In this scheme, the influence of the synthetic solvent could explain the large composition and structural differences with respect to **C[20]**.[378] Interestingly, an intermediate mononuclear compound was also isolated in the crystal lattice of **C[17]**. Because of the apparent complexity of the crystal structures of **C[17]** and **C[18]**, we have investigated the coordination chemistry with another related ligand, **CH_2L^3**, which has a flexible methyl group between aromatic rings, in order to block the formation of tetranuclear units at a lower nuclearity stage. To reach this goal, a nickel ion in combination with a thiocyanato anion were selected and afforded the dinuclear complex **C[19]**. Even though the systems **C[17-18]** and **C[19]** are quite different, we observe the formation of a similar framework involving all donor atoms present in **L^2** and **CH_2L^3**. Taking into account that both dinuclear units in **C[17]** and **C[18]** are linked by two N-C-N bridges, here the dinuclear moiety **C[19]** is linked by two N-C-C-C-N bridges (Figure 117). This compound completes the short list of crystal structures of nickel dinuclear complexes with N-C_x-N bridges.[383-390] Interestingly, this bridging configuration imitates rather well the lateral side of the grid in **C[17]** and **C[18]** (Figure 114). Bridging ligands **CH_2L-^{3}b** and **CH_2L-^{3}c** in **C[19]** are indeed similar than **L-^{2}a** and **L-^{2}b** in **C[17]** except that the alkoxo group, that

was bidentate, becomes monodentate. The bridge between metal ions is longer in **C[19]** than in **C[17]** and **C[18]** (6.758(3) Å compared to 3.2-3.3 Å - Table 47) because of the methyl spacer group in **CH_2L^{-3}**.

In this chapter, we thus show that *N*-salicylidene aniline derivatives bearing coordinating groups such as pyridine rings can also be used as covalent units leading to the formation of strongly complicated inorganic architectures. Moreover, thanks to the conjugated bridge achieved in the case of assemblies built with **L^2** molecules, a strong magnetic coupling can be formed and opened the way to the synthesis of highly versatile materials. The multi-functionality of this class of material could be reached thanks to the structural and electronic properties of complexes such as chirality, redox properties, etc.

Part III: Hybrid Materials

Chapter IX: Anionic *N*-salicylidene aniline derivatives as thermo-sensibilisator precursors into inorganic frameworks

Introducing remarks

As briefly introduced in chapter 4, the preparation of organic-inorganic hybrid molecular materials, defined as a mix of organic and inorganic molecules at the nano-scale,[54] based on the thermo- or/and the photo-sensitivity of *N*-salicylidene anils that could be inserted as guest anionic molecules in various cationic host functional matrices is very challenging. The possibility to insert *N*-salicylidene anils in hybrid materials was proposed for different types of host frameworks like organogelators and clathrates,[107-113] polymers,[14, 104, 106] zeolite,[56, 104] mesoporous silica,[103-105], and following different synthetic strategies such as the 'ship-in-a-bottle' synthesis.[59] However, the use of inorganic complexes (where the ligand is an organic molecule) as host material is actually very rare and the optical behaviour of such material was not yet studied.[391] Interestingly, introducing an anion in a host charged inorganic matrix would give a better control of the number of incorporated functional molecules compared to the reported insertion modes described above that provide a random composition of guest molecules.

Based on the lack of information about the influence of a molecular inorganic host on *N*-salicylidene anil guests, we decided first to use a classic inorganic complex built with mononuclear units $[M^{II}(phen)_3]$, where M is a 3d metal ion and phen = 1,10-phenanthroline, because it can easily

crystallize and is very stable thanks to the chelating effect of the phen ligands. In order to rationalize our results, the two sulfonate anions (compounds **1** and **2**, *N*-salicylidene *p*- and *m*-aminobenzenesulfonate, respectively) studied in chapter 4 have been employed. The influence of the nature of the components on the material composition as well as on their properties has been finely investigated by a large variety of analytical techniques as shown in next sections. Indeed, in this work, we have prepared and studied the optical properties of the thermochromic sulfonate anion **2** (*N*-salicylidene *m*-aminobenzene sulfonate) that has been introduced into $[Cu^{II}(phen)_3]$ and $[Ni^{II}(phen)_3]$ inorganic cationic frameworks. The related **1** anion was also introduced in these matrices but discussions have been restricted to structures descriptions because of the low amount of hybrid materials available has prevented optical experiments.

We also decided to extend the study to the synthesis of hybrid materials built with functional inorganic units in order to combine properties brought by each material component. In this work, we are focussed on the study of SCO materials, and more precisely iron(II) SCO compounds, because of their very promising application perspectives in data storage and display.[10] The use of an anion as thermo- and/or photo-sensibilisator in such compound was not investigated in the literature in contrast to the use of functional ligand which was already proposed.[153, 154]

Triazole based trinuclear compounds $[Fe^{II}_3(hyetrz)_6(H_2O)_6]^{6+}$ where hyetrz = 4-(2'-hydroxy-ethyl)-1,2,4-triazole (Figure 119), which were prepared during my master thesis,[392] were selected because of the very well described SCO properties of this type of architectures[1, 228, 229] and the large potentiality brought by using triazole ligands (see chapter 6).[123, 226]

Moreover, some reported data show the sensitivity of the electronic properties of this class of complexes to the anion nature.[228]

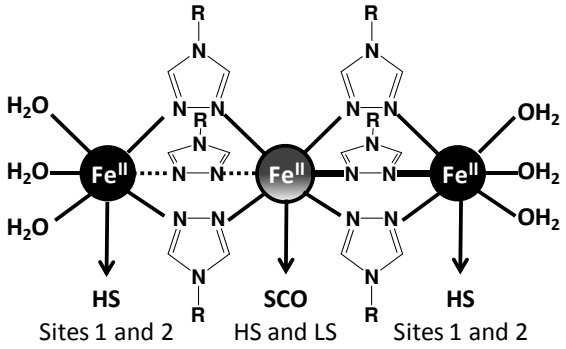

Figure 119 Schematic view of a 4-R-1,2,4-triazole iron(II) trinuclear compound with R = CH_2CH_2OH.

Syntheses and crystallization methods

Na1 was reacted with phen and $CuCl_2 \cdot 2H_2O$ or $NiCl_2$ to afford compounds $\mathbf{H^1}$ and $\mathbf{H^2}$. Interestingly, compound $\mathbf{H^1}$ contains ethanol guest molecules although the synthesis was run in methanol, but containing ethanol as impurities. Crystallization attempts were carried out in other experimental conditions but it was shown that ethanol was needed to promote crystals formation although all syntheses in pure ethanol were unsuccessful because of the too low complexes solubility. **Na2** was also reacted with phen and $CuCl_2 \cdot 2H_2O$ or $NiCl_2$ to give compounds $\mathbf{H^3}$ and $\mathbf{H^4}$, respectively. $\mathbf{H^3}$ was obtained as long green needles whereas $\mathbf{H^4}$ crystallized as large pale orange needles. While $\mathbf{H^1}$ and $\mathbf{H^2}$ were obtained as few single crystals stuck on the glassware, crystals of inorganic complexes containing **2** can be synthesized in very large amount in only a few days.

The hybrid materials $\mathbf{H^1}$, $\mathbf{H^2}$ and $\mathbf{H^3}$, $\mathbf{H^4}$ have been successfully prepared without modifying the nature of the inserted organic guest **1** and **2**, respectively as found by single crystal X-ray diffraction (see next sections). Interestingly, hybrid compounds $\mathbf{H^3}$ and $\mathbf{H^4}$ present, as **1**, a very good thermal stability (degradation temperatures = 309 (1)°C and 370 (1)°C, respectively).

Trinuclear compounds $[Fe^{II}_3(hyetrz)_6(H_2O)_6](\mathbf{1})_4Cl_2$ ($\mathbf{H^5}$) and $[Fe^{II}_3(hyetrz)_6(H_2O)_6](\mathbf{1Br})_4Cl_2$ ($\mathbf{H^6}$) were obtained although a ratio of one equivalent of iron(II) chloride salt for three equivalents of hyetrz and two equivalents of the sodium salt of the anions **1** or **1Br** was engaged in the reaction medium (methanol, technical grade). It strongly suggests that **1** and **1Br** prevents the formation of the usually reported 1D chain.[62]

Crystal structures study of hybrid materials built with 1,10-phenanthroline complexes[§§§]

Hybrid materials with anion 1

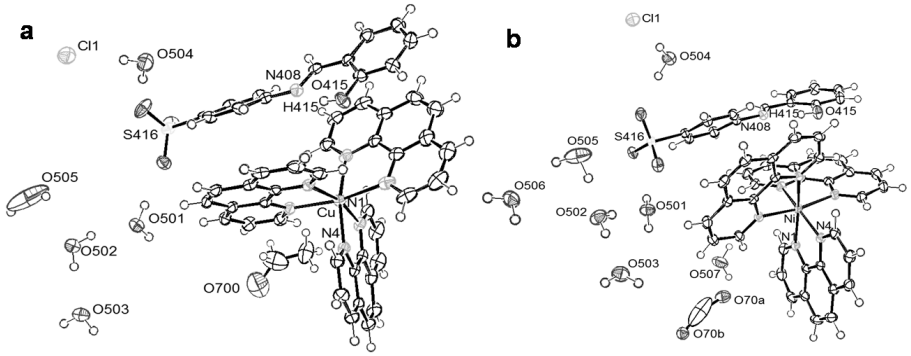

Figure 120 ORTEP view of the asymmetric part of the unit cell of $\mathbf{H^1}$ (a) and $\mathbf{H^2}$ (b), showing 50 % probability displacement ellipsoids.

$[Cu^{II}(phen)_3](\mathbf{1})Cl\cdot 5H_2O\cdot 2C_2H_5OH$ ($\mathbf{H^1}$), crystallizes in the triclinic $P\bar{1}$ space group (Table 53). At 120 (2) K and 250 (2) K, the asymmetric part of the unit cell (Figure 120) contains a copper(II) mononuclear complex built with three bidentate phen ligands. The metal ion is surrounded by six nitrogen atoms forming a distorted octahedral coordination sphere as shown in Table 54. The complex is surrounded by one anion **1** and by a chloride ion which ensure the electro-neutrality in the material. The distance **1**···Cu is rather short (5.07 (1) Å and 5.12 (1) Å at 120 (2) and 250 (2) K respectively). **1** is observed in the twisted enol form (Φ = 32 (1)°) as indicated by the O-H distance (0.80 (6) Å and 0.83 (6) Å), the single bonds C3-C4 (1.457 (6-7) Å) and C5-O6 (1.352 (6) Å and 1.354 (6) Å) and the double bond N2-C3 (1.281

[§§§] Crystal structures were solved by Prof. B. Tinant (UCL).

(6) Å and 1.274 (6) Å at 120 (2) K and 250 (2) K respectively) (Table 54).[158] Crystal structure of $\mathbf{H^1}$ is characterized by the presence of plentiful solvent guest molecules (5 water and 2 ethanol molecules, one of whom presents a C01a/C01b disorder). Thanks to these molecules, the packing is highly directed by the strong supramolecular network built with 11 or 9 H-bonds, 4 π-π and 3 or 2 C-H···π interactions at 120 (2) K or 250 (2) K, respectively (Table 55 and Table 56). An arrangement by planes is clearly noted (Figure 121). Hydrophilic planes, containing chloride ions, sulfonate groups and solvent molecules, are packed with hydrophobic planes containing inorganic complexes and organic parts of **1**. Interestingly, H-bonds, which are strongly developed in hydrophilic planes, bind **1** to the structure, through to the sulfonate group (Table 55). The temperature has a very low influence on the crystal structure of $\mathbf{H^1}$. A normal cell dilatation is observed in combination with a slight decrease of the number of significant supramolecular interactions (Table 53, Table 55 and Table 56). As expected, no influence on the bond lengths in **1** is observed (Table 54).[68]

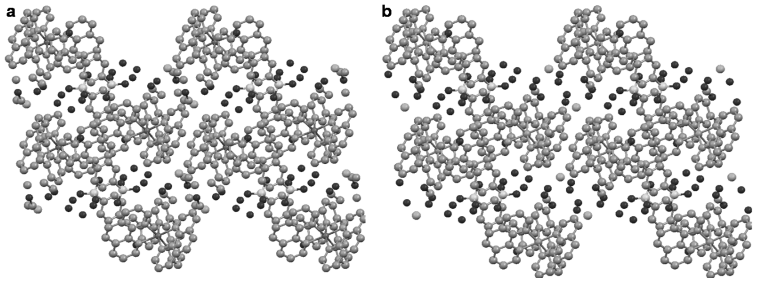

Figure 121 Projection of the crystal structure packing of $\mathbf{H^1}$ (a) and $\mathbf{H^2}$ (b) along the *b* axis.

$[Ni^{II}(phen)_3](\mathbf{1})Cl\cdot 7H_2O\cdot CH_3OH$ ($\mathbf{H^2}$), crystallizes in the triclinic $P\bar{1}$ space group (Table 53). At 120 (2) K, the asymmetric part of the unit cell (Figure 120) contains a nickel(II) mononuclear built with the same architecture than

the copper(II) complex observed in $\mathbf{H^1}$. The nickel complex is surrounded by one anion **1** and one chloride ion. The distance **1**···Ni is short (5.05 (1) Å). **1** is observed in a twisted enol form (Φ = 32 (1)°) as indicated by the O-H distance (0.83 (4) Å), the single bonds C3-C4 (1.439 (3) Å) and C5-O6 (1.347 (3) Å) and the double bond N2-C3 (1.268 (3) Å) (Table 54).[158] In $\mathbf{H^2}$, seven water molecules and one disordered methanol are incorporated in the structure. The methanol and one water molecule seem then to replace the ethanol molecule observed in $\mathbf{H^1}$. The crystal packing in $\mathbf{H^2}$ is similar to the one of $\mathbf{H^1}$ (Figure 121). The supramolecular architecture is also built by numerous supramolecular interactions but their number appears to be significantly higher in $\mathbf{H^2}$ than in $\mathbf{H^1}$ (same π-π stacking and C-H···π interactions but 18 H bonds in contrast to 11 in $\mathbf{H^1}$) (Table 57 and Table 58).

Hybrid materials with anion 2

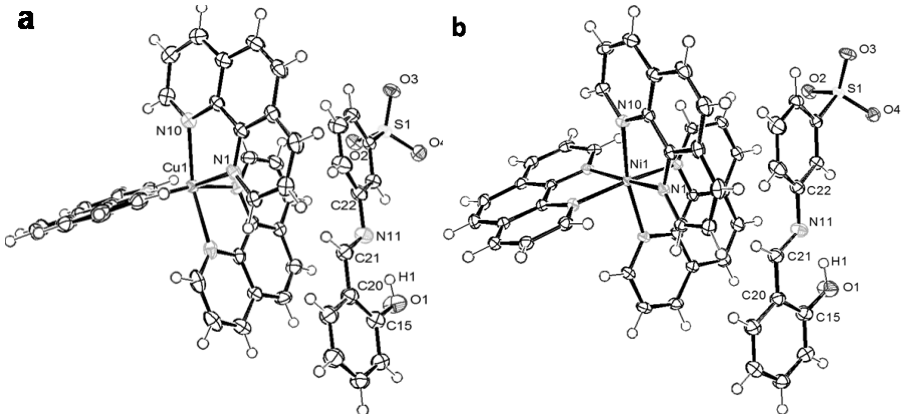

Figure 122 ORTEP view of the asymmetric part of the unit cell of $\mathbf{H^3}$ (a) and $\mathbf{H^4}$ (b), showing 50 % probability displacement ellipsoids.

The insertion of the anion **2** into inorganic frameworks was also proved by X-ray crystallography. Single crystals of $\mathbf{H^3}$ ($[Cu^{II}(phen)_3](\mathbf{2})_2$) and $\mathbf{H^4}$

($[Ni^{II}(phen)_3(\mathbf{2})_2$) were prepared and analysed by X-ray diffraction. The asymmetric part of the unit cell (Figure 122) shows a copper(II) complex and a nickel(II) complex for $\mathbf{H^3}$ and $\mathbf{H^4}$, respectively, with a distorted octahedral coordination sphere made with three phenanthroline ligands (Table 59). The structure also contains two *N*-salicylidene anil anions per copper ion (Figure 122). The anions are found in the enol form and are generated by symmetry thanks to the *C*2/c space group (the metal ions are localised on the two fold axis). The enol form of the anion is confirmed by the presence of single and double bonds (C15-O1 = 1.341(3) Å and 1.344 (2) Å, C21-N11 = 1.278(3) Å and 1.282 (2) Å, N11•••H1 = 1.88 Å and 1.73 Å, O1-H1 = 0.84 Å and 0.96 Å, for $\mathbf{H^3}$ and $\mathbf{H^4}$, respectively).[158]

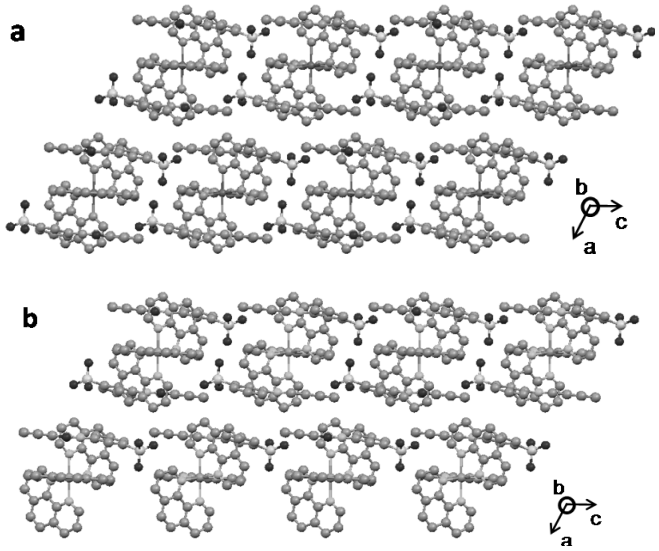

Figure 123 Projection of the crystal structure packing of $\mathbf{H^3}$ (a) and $\mathbf{H^4}$ (b) along the *b* axis.

The molecule is almost planar with a dihedral angle between aromatic rings of 13 (1)° and 12 (1)°, for $\mathbf{H^3}$ and $\mathbf{H^4}$, respectively. The anions in $\mathbf{H^3}$ and $\mathbf{H^4}$

are similar in angles and bond lengths (except for the H-bonds O1-H1···N11). The distances between the centroid of the anions and the nearest metal ion (A···M = 5.79 (1) Å and 5.74(1) Å for **H^3** and **H^4**, respectively) is very close but seems to be slightly different for **H^3** and **H^4**. It favours the formation of a strong supramolecular network involving the anions and the copper complexes (Table 60, Table 61 and Table 62). The crystal packing (Figure 123), organized by planes which contain either the sulfonate groups or the organic part of anions and the metal complexes, is similar for **H^3** and **H^4**. It is governed by the combination of strong electrostatic and supramolecular interactions such as H-bonds, π-π stacking.

Optical properties

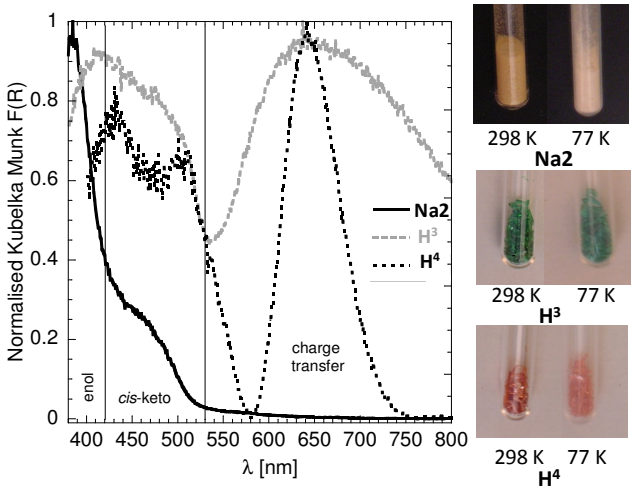

Figure 124 Diffuse reflectance spectra of pure solid samples of **Na2** (full line), **H^3** and **H^4** (dotted lines) at 298 K. The inset shows photographs at 298 K and 77 K for **Na2**, **H^3** and **H^4**.

Because of the very low amount of **H^1** and **H^2**, diffuse reflectance spectroscopy was carried out only on pure powder samples of **H^3** and **H^4** along with a Kubelka-Munk (KM) treatment of the data. As described in the chapter 4, the KM spectrum of **Na2** contains two important contributions showing the presence of an enol form, from UV to ~ 425 nm, and a *cis*-keto form, form 425 nm to ~ 530 nm (Figure 124). This assignment agrees with reported band ranges on diluted samples of *N*-salicylidene aniline.[89] The intensity of the *cis*-keto band is much lower than the enol band and is expected to decrease with temperature due to the thermally induced proton transfer, fully described in previous chapters. UV irradiation of **Na2** did not change the diffuse reflectance spectrum which confirms the absence of *trans*-keto form at room temperature.

The diffuse reflectance spectrum of **H^3** displayed in Figure 124 contains three intense non-resolved bands which can be attributed to the enol (in UV) and the *cis*-keto form (to approximately 530 nm), which is very less resolved, and to an intense broad charge transfer band (between phenanthroline and copper ion, λ^{max} ~ 637 nm). The signal of the *cis*-keto form seems to be more intense than in **Na2**. The green colour of **H^3** which originates from all bands observed in the visible range of the KM spectrum, is maintained on cooling to 77 K indicating no clear apparent thermochromism (Figure 124). As shown in Figure 124, diffuse reflectance spectrum of **H^4** gives a very similar signal to compound **H^3**. Indeed, three intense non-resolved bands are also observed: the enol and *cis*-keto bands (from UV to approximately 570 nm) and an intense broad charge transfer band (λ^{max} ~ 647 nm). The difference between charge transfer bands

observed in compounds $\mathbf{H^3}$ and $\mathbf{H^4}$ takes its origin in the modification of the metal ion nature.

Solid state emission spectra were recorded for **Na2**, $\mathbf{H^3}$ and $\mathbf{H^4}$ at λ^{exc} = 350 nm which corresponds to the band of the enol form in diffuse reflectance spectra (Figure 124). These emission spectra were also recorded on pure samples in order to avoid matrix effect which can strongly modify the population of keto/enol forms.[14, 56, 105-107] Temperature dependent fluorimetry analyses were carried out on warming from 77 K to 300 K in order to study the influence of temperature on the photochemical processes. As described in the chapter 4, **Na2** presents an emission spectrum in agreement with reported data[164] (Figure 125a). A major broad contribution (β, λ^{max} = 547) is observed between ~ 490 nm and ~ 650 nm over the whole temperature range investigated, which is assigned to the radiative relaxation of the excited *cis*-keto* form (Pathway B in Figure 126a). A sharper band (α, λ^{max} = 529 nm), attributed to a *cis*-keto* planar conformation,[92] is also noted at 77 K but disappears on warming. The temperature dependent emission spectrum also contains a weak, badly resolved contribution between ~ 370 nm and 490 nm (γ and δ), which is attributed to the radiative relaxation of the excited enol* form (see chapter 1) (Pathway A in Figure 126a). This contribution grows at higher temperatures in comparison to the *cis*-keto band. Several reasons could be invoked to explain this unexpected temperature dependent behaviour: (i) a decreased proton transfer efficiency in the excited state (which leads to a smaller population of the *cis*-keto* form, Figure 126a). (ii) the presence of enol conformers for which the excited state proton transfer reaction does not occur at all. Temperature dependent emission spectrum of $\mathbf{H^3}$ looks different (Figure 125b). An

intense contribution of the radiative relaxation of the *cis*-keto* form is clearly identified between ~ 490 nm and ~ 650 nm (λ^{max} = 530 nm at 300 K) (α and β) (Pathway B in Figure 126a). A hypsochromic shift of about 17 nm is observed between the *cis*-keto emissions in the anion **Na2** and the complex $\mathbf{H^3}$.

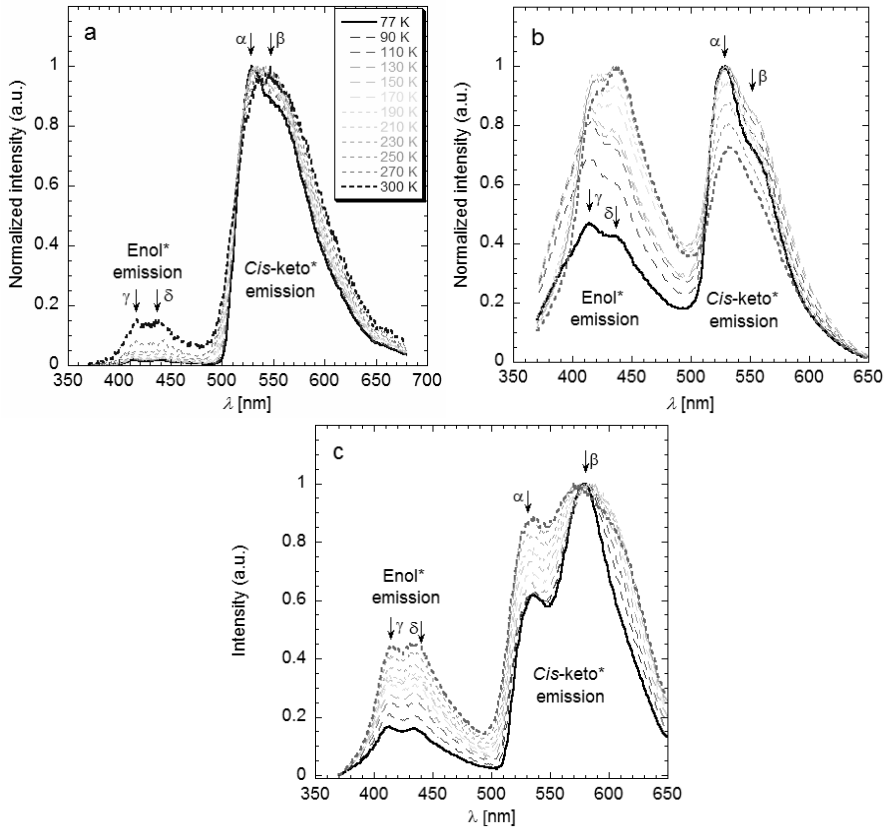

Figure 125 Temperature dependent emission spectra of pure solid samples of **Na2** (a), $\mathbf{H^3}$ (b) and $\mathbf{H^4}$ (c) recorded on warming over 77- 300 K and 77 – 270 K respectively, with a light excitation at 350 nm. The arrows indicate the major α, β, γ and δ emission bands as discussed in the text.

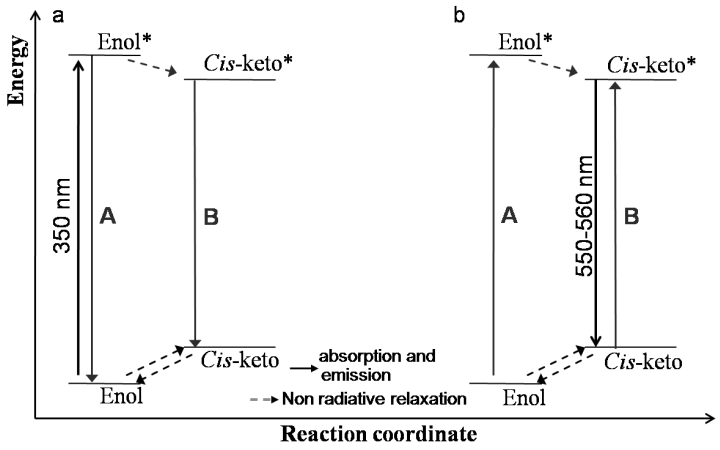

Figure 126 Photochemical process evidencing two radiative relaxation pathways in emission mode (a) or two excitation pathways in excitation mode (b) for *N*-salicylidene aminobenzenesulfonates.

This difference can be explained by the modification of the supramolecular network around anions but also by the change of the medium polarisability induced by the replacement of the sodium cation by the inorganic copper complex. The emission spectrum of **H^3** also contains an intense contribution, between ~ 370 nm and ~ 490 nm, coming from the radiative relaxation of enol* form of the anion (Pathway A in Figure 126a). This emission band appears to be constituted by two badly resolved contributions (λ^{max} = 418 nm (γ) and 435 nm (δ), at 210 K). The origin of these emissions could come from the presence of two different excited states conformations, as seen for the *cis*-keto* form. The temperature has also a large impact on the relative intensity of the enol* and *cis*-keto* emissions. High temperatures strongly favour the emission of the enol* form at the expense of the emission of the *cis*-keto* form for **H^3**. It suggests that the energy of both enol* and *cis*-keto* excited forms are very similar in **H^3**, in contrast to **Na2** as reported for *N*-salicylidene aminopyridines (see chapter 1). Similar observations can be

done for **H^4** where the emissions from the enol* and *cis*-keto* forms are also observed but with significant maximum emission wavelengths shifts (536 nm, 580 nm, 413 nm and 435 nm for α, β, γ and δ bands, respectively). This shift must take its origin in the metal nature change and could be explained either by a slight modification of steric hindrance, which is however less observed by X-ray crystallography (see previous sections), or by the slight polarisability change of the molecular environment induced by the replacement of the copper(II) by the nickel(II) complexes. Indeed, medium polarisability has already been reported to have a strong influence on the optical behaviours of *N*-salicylidene anils.[56]

As in chapters 3 and 4, the thermo-induced tautomerisation of the anion was followed by temperature dependent fluorimetry in excitation mode from 77(1) K to room temperature (Figure 127). Indeed, we did not use diffuse reflectance spectroscopy to track the tautomerisation[89] because of the very complicated diffuse reflectance spectrum of **H^3** (Figure 124), that unables to fully resolve the enol and *cis*-keto bands at room temperature. We have focused on the *cis*-keto* → *cis*-keto emission pathway (B in Figure 126a) and did not consider the enol emission because its absorption band is known to not vary very much with temperature.[89] Thus, the emission wavelength was fixed at ~550-560 nm. As described in chapter 4, for **Na2**, a signal ranging from UV to ~430 nm is attributed to the absorption of the enol form (λ^{max} = 384 nm) and its associated fluorescence (Figure 127a). This signal is very high because the enol form should be present in majority compared to the *cis*-keto form (Figure 124) and this situation is expected to be much favoured on cooling. Thus, pathway A on Figure 126b is favoured.

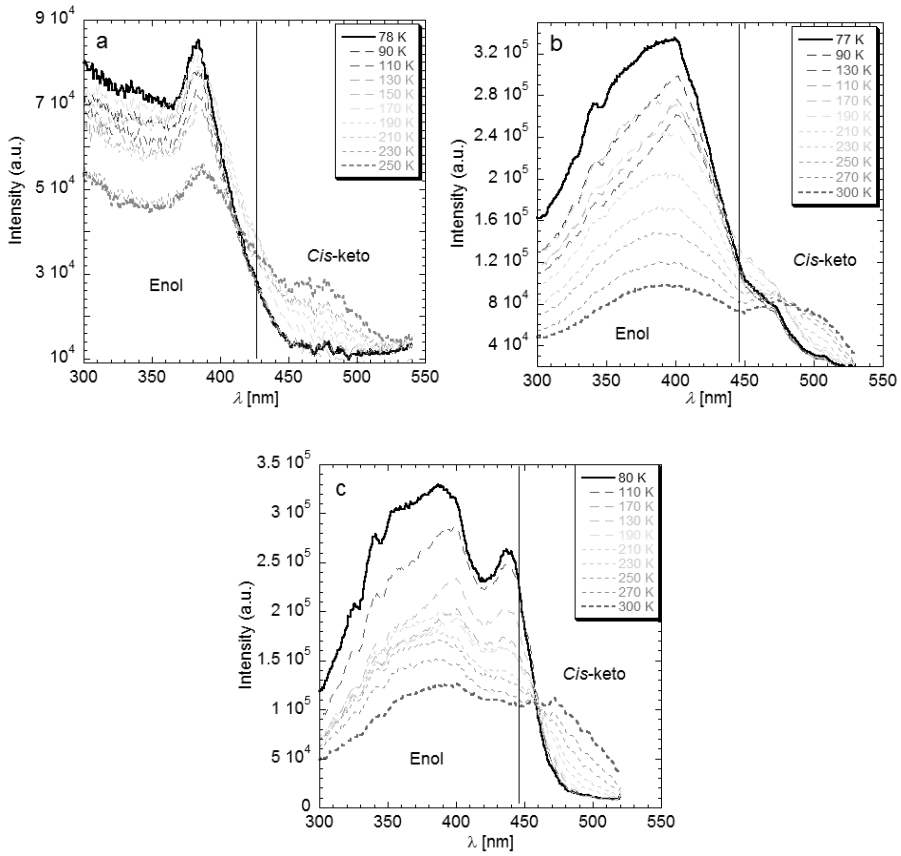

Figure 127 Temperature dependent excitation spectra of pure solid samples recorded on warming from 77(1) K for **Na2**, λ^{em} = 560 nm (a), **H^3**, λ^{em} = 550 nm (b) and **H^4**, λ^{em} = 535 nm (c).

On warming, it is seen that the intensity of the enol form decreases as expected with the growing of the *cis*-keto form. Actually, the *cis*-keto absorption range (from ~ 430 nm to ~ 520 nm) shows no signal at low temperature (77 – 150 K). This form appears at 170 K and slowly increases with temperature to reach an intensity value of ~27000 at 250 K (Figure 127a). The proton transfer (leading to the enol/*cis*-keto tautomerisation) at high temperature is thus clearly observed. However, other phenomena could

also be considered to explain the decrease of the enol excitation band such as a decrease of the proton transfer efficiency in the excited state or the presence of other non radiative relaxation pathways. Temperature dependent excitation spectra were also recorded on a pure sample of **H^3** and **H^4** (Figure 127b and Figure 127c). Using excitation spectra allows suppressing the broad charge transfer band observed in diffuse reflectance spectra (Figure 124). The enol excitation band is clearly identified (λ^{max} ~ 400 nm) but appears to be shifted to ~ 16 nm to lower energies in comparison to **Na2** for compound **H^3**. The enol excitation band decreases on warming from 77 K which could be due to a smaller population of the enol form in the ground state (Figure 126) and to other reasons invoked above. As for **Na2**, the excitation band intensity of the *cis*-keto form (λ^{max} ~ 490 nm) surprisingly increases with temperature whereas non radiative relaxation is expected to increase with temperature. This phenomenon can only be explained by an increase of the *cis*-keto population induced by the tautomeric equilibrium. Thus, these excitation spectra demonstrate that the tautomeric equilibrium is still observed in the hybrids **H^3** and **H^4** thanks to the *cis*-keto excitation band that grows on warming from 77 K to room temperature.

Optical properties of trinuclear (**H$^{5-6}$**) were measured at room temperature and previously described in our master thesis.[392] As expected, the diffuse reflectance spectrum is complicated, containing a large band in the UV range attributed to the enol form of the anion and to the absorption of ligands. In the visible part of the spectrum, a non resolved signal is detected. Its origin can be attributed to the combination of the *cis*-keto, the d-d and a broad MLCT bands. No light irradiation effect was observed. The compound was characterised by a weak fluorescence showing a broad complicated emission

band (corresponding to the cis* → cis relaxation pathway) when the *cis*-keto form was excited by light irradiation. The effect of the temperature on this spectrum can however not be measured because of the low fluorescence capacity combined to the low available quantity of this class of compounds.[392]

^{57}Fe Mössbauer spectroscopy[****]

H^5 was analysed by temperature dependent ^{57}Fe Mössbauer spectroscopy (Figure 128). At 145 K, the central metal ion gives rise to two ^{57}Fe Mössbauer signals: a narrow doublet (δ_{LS} = 0.43(1) mm.s^{-1} and $\Delta E_{Q\text{-}LS}$ = 0.32(2) mm.s^{-1}) and a large quadrupole doublet ($\Delta E_{Q\text{-}HS\text{-}central}$ = 2.66(4) mm.s^{-1}) with a higher isomer shift ($\delta_{HS\text{-}central}$ = 1.71(2) mm.s^{-1}) which appears to be unusually large and higher than reported values[227] (Table 18). These contributions are attributed to a LS iron(II) and a HS iron(II) produced by a thermally induced HS↔LS spin conversion.[222] This is consistent with the Fe^{II}-N_6 coordination sphere which is very often encountered for SCO centres.[10] The external iron(II) ions have a N_3O_3 coordination sphere which is not suitable for SCO in the present case (Figure 119). Surprisingly, for **H^5**, the external $Fe^{II}_{HS\text{-}ext.}$ Mössbauer contribution appears to be split into two slightly different doublets labelled $Fe^{II}_{HS\text{-}Ext.1}$ and $Fe^{II}_{HS\text{-}Ext.2}$ (Figure 128). These two signals are detected at a lower isomer shift ($\delta_{HS\text{-}ext.1}$ = 1.14(1) mm.s^{-1} and $\delta_{HS\text{-}ext.2}$ = 1.17(1) mm.s^{-1}) and a higher quadrupole splitting ($\Delta E_{Q\text{-}HS\text{-}ext.1}$ = 3.15(8) mm.s^{-1} and $\Delta E_{Q\text{-}HS\text{-}ext.2}$ = 3.39(4) mm.s^{-1}) than for the central iron(II) HS ion because of the strongly different coordination spheres of

[****]Adapted from F. Robert, A.D. Naik, Y. Garcia *J. Phys. Conf. Ser.* **2010**, 217, 012031.

these ions (Table 18). The difference between the two $Fe^{II}_{HS\text{-}ext.}$ is clearly identified in the ΔE_Q values and translates the presence of two types of long-range molecular environments through a different H-bonding network at the end of the trinuclear entities. The influence of temperature on **H^5** was analysed by ^{57}Fe Mössbauer spectroscopy on warming over the temperature range 145-275 K (Figure 128). Mössbauer spectra of **H^5** are fitted best by the combination of the four contributions described above although the presence of a small amount of Fe^{III}_{HS} impurity is identified in the 275 K spectrum thanks to the higher *f* factor of this iron site (Table 18).

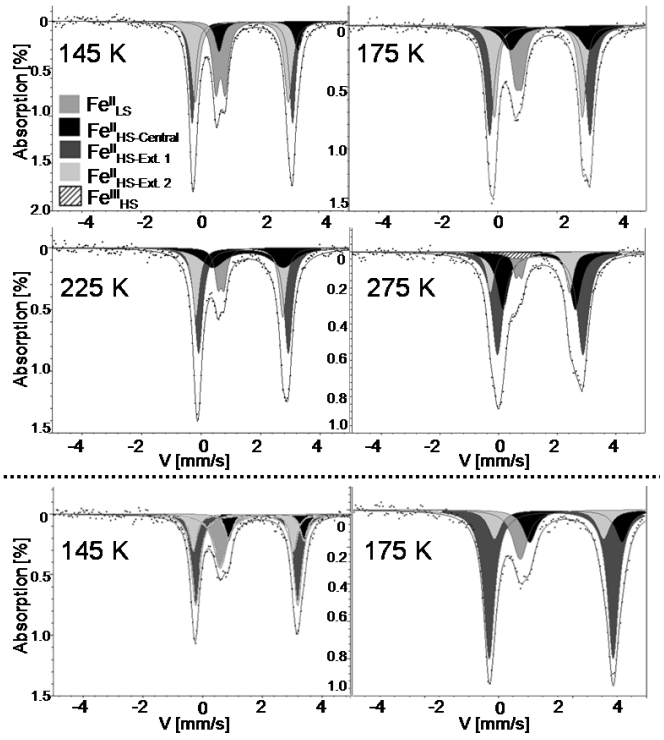

Figure 128 Selected ^{57}Fe Mössbauer spectra of **H^5** (top) and **H^6** (bottom).

Table 18 Temperature dependent ^{57}Fe Mössbauer parameters for **H^5** and **H^6**. Isomer shift (δ) values are given respective to α-Fe. *Fixed parameters. ΔE_Q = quadrupole splitting. Γ/2 = half width at half maximum.

δ [mm.s^{-1}]	T [K]	Fe^{II}_{LS}	$Fe^{II}_{HS\text{-central}}$	$Fe^{II}_{HS\text{-Ext. 1}}$	$Fe^{II}_{HS\text{-Ext. 2}}$	Fe^{III}_{HS}
H^5	145(1)	0.43(1)	1.71(2)	1.14(1)	1.17(1)	-
	175(1)	0.45(2)	1.50(9)	1.12(1)	1.16(1)	-
	225(1)	0.41(2)	1.32(1)	1.03(2)	1.17(1)	-
	275(1)	0.41(4)	1.14(2)	0.817*	1.18(2)	0.403*
H^6	145(1)	0.33(3)	1.88(2)	1.12(6)	1.22(5)	-
	175(1)	0.33(4)	1.83(4)	1.111*	1.17(1)	-
ΔE_Q [mm.s^{-1}]						
H^5	145(1)	0.32(2)	2.66(4)	3.15(8)	3.39(4)	-
	175(1)	0.23(4)	2.6(2)	2.96(2)	3.38(2)	-
	225(1)	0.20(4)	2.28(2)	2.93(2)	3.01(2)	-
	275(1)	0.22(7)	2.52(5)	2.70(3)	2.94(3)	0.448*
H^6	145(1)	0	2.52(5)	3.35(1)	3.42(3)	-
	175(1)	0	2.49(7)	2.95(2)	3.35(2)	-
Γ/2 [mm.s^{-1}]						
H^5	145(1)	0.14(1)	0.16(4)	0.16(2)	0.13(2)	-
	175(1)	0.18(4)	0.35*	0.15*	0.18(1)	-
	225(1)	0.12(3)	0.48(9)	0.145*	0.17(1)	-
	275(1)	0.15(7)	0.22(3)	0.16(3)	0.22(3)	0.36*
H^6	145(1)	0.27(3)	0.14(3)	0.15(6)	0.17(3)	-
	175(1)	0.25(5)	0.22*	0.20(9)	0.18(2)	-
Relative Area Fraction [%]						
H^5	145(1)	22(1)	12(3)	33(2)	32(2)	-
	175(1)	17(1)	17*	27*	39(2)	-
	225(1)	10(1)	23*	24*	43*	-
	275(1)	7(2)	29*	18(5)	43(7)	4*
H^6	145(1)	22(2)	12(3)	19(3)	47(4)	-
	175(1)	13(2)	16(3)	13(1)	58(9)	-

An optimization of Mössbauer parameters all together was successfully achieved for the 145(1) K spectrum but did not lead to a good fit for other

spectra. Some parameters need indeed to be fixed during the optimization. A gradual and incomplete SCO phenomenon is clearly identified for the central metal ion because of the slow decrease of the $Fe^{II}_{LS\text{-}central}$ relative area fraction (from 22 to 7 %) compensated by a slow increase of the Fe^{II}_{HS} relative area fraction (from 12 to 29 %) (Figure 129a). The two $Fe^{II}_{HS\text{-}ext.}$ doublets seem to be involved in a thermal equilibrium although the error on their relative area fraction seems to be large. $Fe^{II}_{HS\text{-}ext.1}$ relative area fraction decreases from 33 to 18 % whereas the relative area fraction of $Fe^{II}_{HS\text{-}ext.2}$ increases from 32 to 43 % (Figure 129a). Interestingly, a large sensitivity of the isomer shift values is noted for the $Fe^{II}_{HS\text{-}central}$ and $Fe^{II}_{HS\text{-}Ext.\ 1}$ (Table 18). Although this variation is supported by the presence of a second order Doppler effect, the modification is higher than the expected one. An influence of the thermo-sensitivity of the anion could be invoked to explain this observation. Moreover, the half width at half maximum, Γ/2, of the central HS iron(II) ion increases on cooling and reaches a maximum at 225(1) K, before returning to a similar value on further cooling (Figure 129b). This dramatic line broadening reflects a pronounced relaxation phenomenon that might be promoted by the tautomeric equilibrium between the enol and keto forms of the anion. Accurate population of respective species shall be derived using an appropriate relaxation model[393] to fit our spectra in order to take into account the present dynamics. A second trinuclear SCO compound $[Fe^{II}_3(hyetrz)_6(H_2O)_6](\mathbf{1Br})_4Cl_2$ ($\mathbf{H^6}$) was prepared by mixing one equivalent of iron(II) chloride salt, three equivalents of hyetrz and two equivalents of the sodium salt of the anions **1Br** in methanol and investigated by Mössbauer spectroscopy from 145 K to 175 K. The presence of four iron(II) signals as in $\mathbf{H^5}$ is confirmed (Figure 128). The change of the anion from **1** to **1Br** leads to a significant change into some Mössbauer

parameters. The Fe^{II}_{LS} site is a singlet and has a lower isomer shift than for **H^5**. The isomer shift of $Fe^{II}_{HS\text{-}central}$ increases and shows a lower quadrupole splitting (Table 18). The SCO phenomenon is still observed with a decrease of the Fe^{II}_{LS} relative area fraction: from ~ 22 to 13 % and an increase of the $Fe^{II}_{HS\text{-}central}$ relative area fraction: from ~ 12 to 16 %, which appears to be less influenced by the anion equilibrium (Table 18). Although the isomer shifts of $Fe^{II}_{HS\text{-}ext.}$ do not differ much comparing **H^6** and **H^5**, a large change in the relative $Fe^{II}_{HS\text{-}ext.1}/Fe^{II}_{HS\text{-}ext.2}$ ratio is observed (from 33/32 for **H^5** to 19/47 for **H^6** at 145(1) K). The variation of the relative area fraction of $Fe^{II}_{HS\text{-}ext.}$ sites with the temperature which was observed for **H^5** is preserved in **H^6**.

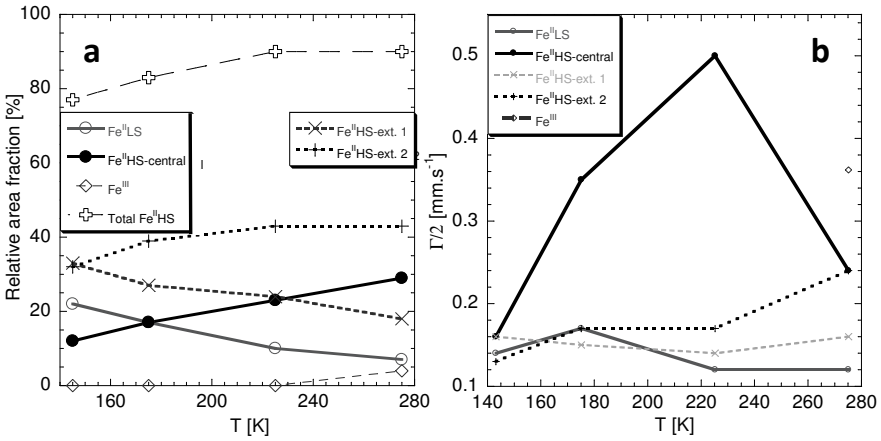

Figure 129 (a) Evolution of the relative area fraction for **H^5** over the temperature range 140-275 K. (b) Evolution of Γ/2 for **H^5** over the same temperature range.

Discussion

A clear impact of the insertion of a *N*-salicylidene aniline derivative into an inorganic framework built with $[Cu^{II}(phen)_3]$ and $[Ni^{II}(phen)_3]$ complexes was noted though drastic changes in the energy levels of the enol and keto forms. Optical properties are thus modified by the incorporation in the inorganic framework. The Kubelka-Munk spectra of $\mathbf{H^3}$ and $\mathbf{H^4}$ are very complicated because of the presence of intense signal in the UV range (originates from the enol form of **2** and the phenanthroline ligand), a broad band between approximately 400 nm and 550 nm (from *cis*-keto form) and a very large charge transfer phenomenon between approximately 550 and 700-800 nm. Spectrum of $\mathbf{H^4}$ is similar to the one of $\mathbf{H^3}$ but slightly more resolved.

Fluorescence shows also a large change induced by the incorporation of **2** in $\mathbf{H^3}$ and $\mathbf{H^4}$. Indeed, a shift of the maximum wavelength of the *cis** emission is noted in $\mathbf{H^4}$. However, this phenomenon appears to be inexistent in $\mathbf{H^3}$ at 77 K (λ^{max} = 530, 529 and 580 nm for **Na2**, $\mathbf{H^3}$ and $\mathbf{H^4}$, respectively, at 77 K). Differences between optical properties of $\mathbf{H^3}$ and $\mathbf{H^4}$ are then identified although the crystal structure and molecular formula are almost identical. The same phenomenon was previously observed in chapter 4 where a shift of 12 nm was observed for the enol emission band from **Na1** to **K1** and **Ca1**. Moreover, other modifications, induced by the counter-ion replacement, such as the presence of the weak *cis*-keto band which was only present in **K1** and **Ca1** diffuse reflectance spectra (see chapter 4) were also shown. It thus clearly demonstrates a strong sensitivity of the anion properties to the nature of counter ion and surrounding inorganic complex. Moreover, the temperature dependent fluorimetry also showed that many conformations of

2 in the ground and excited states are present in the hybrid materials, leading to broad emission bands which change their shape with temperature. This phenomenon suggests that the temperature change leads to a stabilisation of some conformations with respect to others.

The preservation of the keto-enol equilibrium after insertion was proved by the analysis of temperature dependent excitation spectra. This result is important because conservation of the thermo-induced tautomeric equilibrium after insertion of the anion into the inorganic framework was *a priori* not guaranteed. Indeed, although it is known that tautomerisation in *N*-salicylidene anilines derivatives can occur in solution,[394] the situation in the solid state is different because the matrix itself can strongly influence the energy levels of the enol and *cis*-keto forms,[56, 107-112] which thereby can modify optical properties and, in a few cases, leads to the absence of thermochromism (e.g. **Habs**, see chapter 2). Moreover, it would not have been possible to follow the thermo-induced tautomerization by single crystal X-ray diffraction because when the *cis*-keto form is present in low concentration, it is only possible to detect the enol form.[68]

In conclusion, the synthesis of a crystalline material, such as $\mathbf{H^3}$ and $\mathbf{H^4}$, where the number of inserted *N*-salicylidene anils could be controlled through the oxidation state of the metal ion, properly validates our hypotheses about the possibility to use *N*-salicylidene anils as thermo- or photo-sensibilisator into multi-functional materials. The study of $\mathbf{H^4}$, which is very similar to $\mathbf{H^3}$ but built with nickel metal ions, shows an unexpected sensitivity of the optical behaviours of the anion to the nature of the complex. The interaction between the anion and the inorganic complex is then very sensitive and must be strongly considered. This conclusion is also

supported by the study of hybrid compounds **H^1** and **H^2** which contain a very large quantity of solvent guest molecules (until 8 moles per mole of metal ion). The presence of these molecules leads to the formation of strong hydrophilic and hydrophobic planes in the crystal packing. The importance of the solvent in the single crystals syntheses is clearly illustrated by the difficulty to obtain **H^1** and **H^2** in large quantity. The preparation of a single crystal of **H^1**, in methanol, but with ethanol as guest molecules (present in synthesis solvent as impurity) also indicates that crystals act as molecular sponge, absorbing needed molecules in order to grow. In contrast to **H^1** and **H^2**, compounds **H^3** and **H^4** contains no solvent molecules but interestingly, two anions **2** in place of only one anion **1**. This difference could be attributed to the crystal packing differences lead by the sulfonate position. We assume that anion **1** in the inorganic framework $[M^{II}(phen)_3]$ induces a too large steric hindrance in the widely developed supramolecular network in order to include a second organic anion in the structure. It is important to notice that the incorporation of the chromophores (**1** or **2**) is not statistical such as in previous study (ship-in-a-bottle,…)[56, 59, 114] but the number of inserted functional molecule is comprised between one and the oxidation stage of the metal ion (in this case, two). In addition, there is a very significant difference in the distance between organic anion centroids and the metal ion (near 5 Å for **H^1** and **H^2**, 5.79 (1) Å for **H^3** and 5.74 (1) Å for **H^4**) which can lead to significant properties modification in the case of functional inorganic complexes as presented for a novel type of multifunctional material built with a triazole based trinuclear SCO compound and probed by ^{57}Fe Mössbauer spectroscopy for the very first time.

In this case, the stabilization of the trinuclear pattern, revealed by a ratio $Fe^{II}_{central}/Fe^{II}_{ext.}$ of ~ 1/3, is the first consequence of the successful insertion of the organic anions **1** and **1Br** which is believed to prevent the formation of the 1D chain. A reaction mechanism involving a steric hindrance of anions must be considered. A second very interesting impact of the presence of the anions is highlighted by the splitting of the doublet corresponding to the $Fe^{II}_{HS\text{-}ext.}$ into two slightly different doublets ($Fe^{II}_{HS\text{-}ext.1}$ and $Fe^{II}_{HS\text{-}ext.2}$). This behaviour translates the presence of two slightly different molecular environments for the external metal ions. The electronic density of the organic anion has a strong influence on the relative area fraction of the two $Fe^{II}_{HS\text{-}ext.}$ doublets as shown by $\mathbf{H^6}$ where the anion was substituted by a bromide. Thus, a new type of multifunctional material which combines a thermo-sensitive anion and a SCO inorganic compound was synthesized, for the first time. A direct influence of the presence of the anion was revealed thanks to ^{57}Fe Mössbauer spectroscopy. The communication between the anion and the complexes is thought to be favoured by the expected dense supramolecular network developed by these molecules.[1] It opens very attracting way to the development of 'AD-TISC' and 'AD-LISC' effects (*anion-driven Temperature* or *Light-induced Spin Changes*). These phenomena, not yet described, are similar to the LD-LISC effect, which implies a photo-sensitive ligand,[154] but where the difficulty to conserve this property after coordination and in the solid state could be decreased.

General discussion

This thesis work was divided in nine chapters each studying a class of organic, inorganic or hybrid materials. Many observations and discussions were summarized at the end of each chapter. Arriving at the end of this manuscript, we will underline most important results in order to outline the large perspectives brought by *N*-salicylidene aniline derivatives in such materials. Indeed, these molecules are very attractive solid-state molecular switches but, however, their thermo- and photochromism is not observed for all compounds. The first aim of this work was thus to investigate the factors governing these optical phenomena.

In chapter 1, *N*-salicylidene aminopyridines ($\mathbf{L}^{2\text{-}5}$) were the starting point of soul-searching about the relationship between numerous crystal structures and optical behaviours which was claimed by authors in many papers, including leading reviews[68] (closed packing = thermochromic molecules, open packing = thermo- and photochromic compounds). Indeed, by resolving the *N*-salicylidene 4-aminopyridine ($\mathbf{L}^{4}$) crystal structure, we have shown that an open structure with long intermolecular distances and less supramolecular interactions can be exclusively thermochromic. In contrast to $\mathbf{L}^{4}$, $\mathbf{L}^{3}$ (*N*-salicylidene 3-aminopyridine) which presents a closed structure with short intermolecular distances and strong supramolecular interactions was found with an almost 'persistent' photochromism and a significant thermochromism. Moreover, some traditional structural relationships such as the link between the dihedral angle between aromatic rings (Φ) and the strength of the intra-molecular H-bonds[68] were also disregarded. The situation clearly shows that the 'open/closed structural relationship'[68] does not take into account all factors governing the presence of the

photochromism and cannot be sufficient in order to predict optical properties of these materials. This conclusion was also supported by other molecules packed in closed structures such as the photochromic **Habs** and **Hsalphen**, described in chapter 2.

Our work has demonstrated, thanks to a computational study, on isolated molecules as well as on molecules inserted into their crystal packing, that the energy barrier present in the photo-chemical pathway involved in the photochromism phenomenon (see A in Figure 130) (between cis* and trans*) was significantly modified by the molecular topology as shown by comparing results for $\mathbf{L^3}$ and $\mathbf{L^4}$ or **Habs** and **Hsalphen** in chapters 1 and 2.

The crystal structure can however also influence the optical behaviours by two mechanisms. 1/ As shown with **Hsaltrz**, the intramolecular H-bond between the alcohol and the imine functions is essential to the thermo- and the photochromism appearance. Molecule presenting a strong (accessible) crystal packing directing effect moiety such as 1,2,4-triazole, which drives to the intramolecular H-bond breaking, leads to the formation of non switchable materials (see **Hsaltrz**). 2/ The packing also leads to stabilisation of energy levels attributed to the enol, *cis*-, *trans*-keto forms and transition states. This phenomenon, demonstrated by our computational studies, can help the system during the photo-isomerisation process by decreasing the activation barriers. It is also interesting to note that the thermochromism of *N*-salicylidene aniline derivatives can also be quenched for other reasons than an intramolecular H-bond breaking. Indeed, as shown with **Habs**, the molecular topology can induce a larger difference between the enol and *cis*-keto forms in the ground state which becomes not accessible by a thermal way (see energy difference *1* in Figure 130). Moreover, it can also add other

unknown relaxation pathways as shown with the cyclised form of **Habs**, leading to the appearance of the unexpected 'spring type effect'.

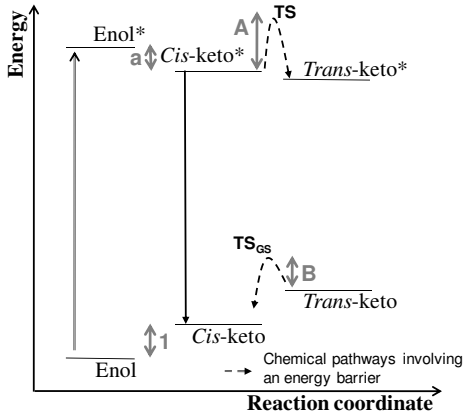

Figure 130 Chemical processes leading to the thermo- and the photochromism of the *N*-salicylidene aniline derivatives. 1 = energy difference driven the thermochromism, a = energy difference governing the excited state proton transfer, A and B = energy barriers involved in the photochromism process.

The study of more flexible molecules, the *N*-salicylidene aminomethyl pyridines (**$CH_2L^{2\text{-}6}$**) have also supported our discussion about the discrepancy of the previous 'open/closed structure relationships'[68] with the observation of non photochromic molecules packed with long intermolecular distances. This observation was understood thanks to fluorescence measurements. Indeed, fluorimetry was used in order to probe the radiative relaxations, allowing a better understanding of the energy scheme involved during thermo- and photochromic processes. Regretfully, the literature was relatively poor in systematic fluorescence studies for this class of compounds. It was thus claimed that *N*-salicylidene aniline derivatives showed exclusively one emission band attributed to the deexcitation of the excited *cis*-keto form.[68, 92, 395] In this work, we have successfully completed the emission scheme by finding two other emissions coming from the

excited enol (enol*) and *trans*-keto (trans*) forms. We assume that the first one is actually observed when the difference between the enol* and cis* levels is low (see energy difference *a* in Figure 130) and thus when the excited state proton transfer is not too fast (lifetime of enol* long enough to observe the fluorescence of this form). It was for example the case for $\mathbf{L^3}$ in methanol solution (see chapter 1). The trans* emission band is more difficult to detect and was, up to now, only clearly observed for $\mathbf{CH_2L^{2\text{-}6}}$. It could be explained by the fact that 1/ the *trans*-keto band is better distinguished by fluorimetry for these compounds or 2/ this emission is not present in other investigated compounds (where a non radiative relaxation is favoured). The observation of the trans* emission band was unexpectedly done in fluorescence spectra of photochromic molecules ($\mathbf{CH_2L^3}$ and $\mathbf{CH_2L^{5\text{-}6}}$) but also of non-photochromic molecules ($\mathbf{CH_2L^2}$ and $\mathbf{CH_2L^4}$). It leads us to conclude that the *trans*-keto form is produced by photo-isomerisation even in these non photochromic molecules but this form appears to be too unstable to be accumulated and to drive to the photochromism appearance. In order to stabilise them, a large energy barrier (B in Figure 130) must take place between the *cis*- and *trans*-keto forms in the ground state. It is thus a new parameter to take into account in order to properly control the photochromic behaviours of *N*-salicylidene aniline derivatives. It is however important to note that, in the solid state, it appears that there exists a large variety of accessible conformations presenting slightly different electronic properties (induced by different electronic resonance strengths). It was indeed clearly demonstrated by the broad emission bands obtained during this work (see for example emission spectra of $\mathbf{CH_2L^{2\text{-}6}}$, $\mathbf{Na^{1\text{-}2}}$, etc). This observation was also supported by the modification of the emission bands shape with the temperature (showing a variation of the most favoured

relaxation scheme) as well as by the observation of highly complicated fluorescence decay (for **Habs** and inorganic related molecules).

Regarding the complexity of the parameters governing the thermo- and photochromism, we thus developped a supramolecular approach leading to the synthesis of molecules for which the crystal packing is mainly directed by specific supramolecular interactions (see chapter 2, H-bonds → **Hsaltrz** and **Hsaltz**, π-π stacking → **Habs** and **Hsalphen** or ionic interactions → **Ksaltz**). This way allows controlling the crystal structure and thus simplifying the prediction of the optical behaviour. However, the exclusively photochromic **Habs** has demonstrated that the electronic factors, induced by the molecular topology, must always be considered. A possible approach in order to tune the electronic properties was also brought by using chemical substituents (**L^3**-**L^5**, **CH_2L^{2-6}** and **Rsaltrz**). However, the presence of the substituents also often lead to structure changes and remains thus difficult to control.

Another interesting way was thought in order to control structural and electronic properties of *N*-salicylidene aniline derivatives by using the coordination capability of investigated molecules. Indeed, organic molecular switches discussed above are characterised by the presence of N-heterocycle presenting suitable properties for 3d metal ion complexation. This class of compounds is very rich as shown by the large diversity of dimensionalities (mononuclear, oligonuclears, polynuclear) and complex natures which can be targeted. In chapter 5, we have focussed our attention on the impact of the coordination on the structural and optical behaviours of materials. It was successfully done thanks to the synthesis of a series of crystalline compounds $[M^{II}(\mathbf{L^3})_2(NCX)_2(CH_3OH)_2]$ where the nature of M and X atoms

has been tuned. Modification of the $\mathbf{L^3}$ conformation, driven by the complexes formation, was detected. Indeed, the dihedral angle between aromatic rings switches from 15° to 7° which is in the same range than $\mathbf{L^5}$ and could be then assimilated to a 'substituent' effect. The coordination has also an influence on the optical properties as demonstrated by the quenching of the photochromism of $\mathbf{L^3}$ and the change of emission spectrum shape (enol* emission band appears). These observations were also supported by a computational study which showed the modification of the energy levels induced by the complexation. The thermochromism was however preserved allowing the first preparation of a thermochromic inorganic complex built with a *N*-salicylidene aniline derivative.

Similar conclusions were drawn by studying the influence of the complex nature (tuning of the M and X atoms nature in $[M^{II}(\mathbf{L^3})_2(NCX)_2(CH_3OH)_2]$). Indeed, although no change of dihedral angle was observed, the switch from manganese to copper metal ions ($3d^5 \rightarrow 3d^9$) leads to a significant modification of the strength of the intramolecular H-bond between the alcohol and imine functions which is strongly involved of the thermo- and photochromic phenomena. This variation is combined with other optical properties changes as demonstrated by the modification of the shape of the emission spectra of complexes. Moreover, these observations were also supported by a computational study which has demonstrated that the replacement of a nickel by a copper metal ion can lead to the stabilisation of different conformations in the enol, *cis*- and *trans*-keto forms and thus to a change of energy levels involved in the optical behaviours of $\mathbf{L^3}$. It is also important to note that the influence of the metal ion nature was also clearly detected in **Habs** complexes where a shift of the bands (mainly enol signal)

and a strong variation of the *cis*-keto band intensity were shown in the diffuse reflectance spectra. Moreover, the synthesis of complexes with formula $[M^{II}(\mathbf{Habs})_2X_2]$ ($\mathbf{C^{12\text{-}16}}$) also lead to the preparation of strongly fluorescent materials (with Φ_f up to 15.4 %) but where the intensity of the light emission was tuned by the complex nature. In conclusion, considering the fact that it is possible to synthesize isostructural compounds (e.g. $[M^{II}(\mathbf{L^3})_2(NCX)_2(CH_3OH)_2]$), it appears that, by changing the complex nature, it is possible to finely tune the electronic density in the chromophores. It opens then very interesting ways in order to properly control the optical behaviours of *N*-salicylidene molecular switches.

The perspectives leading by the synthesis of inorganic complexes built with *N*-salicylidene aniline derivatives are very numerous. Indeed, such molecules can be used in order to grow more complicated inorganic assemblies than mononuclear described above. During this work, we have used the *N*-salicylidene 2-aminopyridine ($\mathbf{L^2}$) as covalent block in the building of new magnetic tetranuclear self-assemblies of formula $[Cu_4(\mathbf{L\text{-}^2})_4(NO_3)_3(CH_3OH)]$ $[Cu(\mathbf{L\text{-}^2})(NO_3)_2]$ (2-aminopyridinium)$(NO_3)\bullet 5CH_3OH$ ($\mathbf{C^{17}}$) and $[Cu_4(\mathbf{L\text{-}^2})_4(NO_3)_2(OH)_2]$ (2-aminopyridinium)$(OH)\bullet CH_3OH$ ($\mathbf{C^{18}}$). Interestingly, $\mathbf{C^{17}}$ was a [2x2] nanogrid which presents an unexpected chirality, thanks to the $\mathbf{L^2}$ torsion, combined with an unusual asymmetry linked to the existence of three types of coordination sphere natures and geometries. The formation of such architecture was fully discussed in light of $\mathbf{C^{18}}$ and of a dinuclear model compound built with $\mathbf{CH_2L^3}$ ($\mathbf{C^{19}}$). Moreover, the very intense antiferromagnetic coupling between spin carriers through $\mathbf{L^2}$ has been investigated and leads to J = -340(1) cm^{-1}.

Inorganic complexes built with *N*-salicylidene aniline derivatives can also show other magnetic behaviours such as thermally induced SCO, as shown with the mononuclears $[Fe^{II}(\mathbf{Habs})_2(NCS)_2]$ ($\mathbf{C^{11}}$) and confirmed with the dinuclears $[Fe^{II}_2(\mathbf{Hsaltrz})_5(NCS)_4]$ ($\mathbf{C^{7\text{-}10}}$). These last materials were crystallised and showed a very important sensitivity to the solvent guest molecules inserted into the inorganic frameworks. Indeed, the replacement of three of the four methanol by three water molecules appears to quench the SCO phenomenon, leading to a compound exclusively HS in the whole temperature range. During this work, this phenomenon was correlated to structural parameters such as the Fe-N=C(=S) angle which is almost equal to 180° in SCO compounds. Crystal structures are, however, relatively complicated because of the presence of disorder on **Hsaltrz**. $[Fe^{II}_2(\mathbf{Hsaltrz})_5(NCS)_4]\cdot 4CH_3OH$ ($\mathbf{C^7}$) was investigated by a large variety of analytical techniques in order to analyse the SCO phenomenon leading to the switch from [HS-HS] to [LS-LS] electronic configuration. SQUID magnetometry demonstrated the presence of a SCO (where 93 % of iron ions are active) at $T_{1/2}$ = 150 (1) K. These results were confirmed by DSC (ΔH = 8.6 kJ.mol^{-1} and ΔS = 56 J.mol^{-1}.K^{-1}) and ^{57}Fe Mössbauer spectroscopy but a differentiation of two iron(II) HS and LS sites were observed, coming from either the crystallographic disorder, the presence of two slightly different dinuclear units or the tautomeric equilibrium in **Hsaltrz**. The SCO phenomenon has also a significant influence on the optical behaviour of the material. Indeed, in addition to a clear thermochromism associated to the SCO itself, the electronic configuration change of the metal ion is felt by the chromophores **Hsaltrz**. Although no structural difference was noted between the molecular conformation of **Hsaltrz** at 125 and 254 K, the temperature dependent fluorescence properties translate an electronic density change into

the ligand. It allows following the SCO curve by fluorimetry which has not yet been reported up to now. Actually, clear SCO impacts on the emission spectra were detected in the position of the enol* (with a bathochromic shift of 20 nm), and the cis* emission band (with a hypsochromic shift of 27 nm) and in the intensity of the cis* emission band which is enhanced few Kelvin before the SCO. We have suggested that this last and unexpected phenomenon could be attributed to a mechanic stress appearing in the SCO network around the SCO jump. Interestingly, the shift of emission bands can be converted to an energy change of 15 $kJ.mol^{-1}$. This value can however not be compared with the thermodynamic data obtained by DSC. Finally, it is also important to highlight the observation of a presumed photochromic phenomenon in $[Fe^{II}(\mathbf{Habs})_2Cl_2]$ which could become the first photochromic inorganic compound built with a *N*-salicylidene switch. However, this material was observed as unstable during the photo-excitation experiments and the oxidation process detected roughly hides the effect of the light irradiation.

Lastly, the development of anionic derivatives of *N*-salicylidene aniline was also successfully investigated with the *N*-salicylidene aminobenzenesulfonates (**Na1-2**, **K1**, **Ca1**, **Na1Cl**, **Na1Br**). Interestingly, this class of thermochromic compounds appears to be very sensitive to their molecular environment. Indeed, a significant properties change was observed in the degradation temperatures (which are very high – e.g. 384(1)°C for **Na2**), crystal structures (a packing of hydrophilic and hydrophobic planes seems to be present), colour, diffuse reflectance and emission spectra (shift, intensity enhancement, etc) when the cation nature was changed (from Na to K and Ca). This effect can be compared to the

influence of chemical substituents such as chlorine or bromine (**Na1Cl** and **Na1Br**).

N-salicylidene aminobenzenesulfonates were inserted into inorganic complexes frameworks built with $[M^{II}(phen)_3]$ units where M = Cu, Ni and phen = 1,10-phenanthroline. The number of incorporated functional anions per metal ion was comprised between 1 and the oxidation stage of this ion. It remains thus not statistical in contrast to previous studies.[14, 56, 103-113] The use of thermo- and/or photochromic anions presents also the advantages that this anion is in strong interaction with the inorganic complexes, as demonstrated by the dense supramolecular network around anions **1** and **2** in the crystal structures $\mathbf{H^{1\text{-}4}}$, but remains less encaged than a coordinated switchable molecule. The hybrid compounds built with $[M^{II}(phen)_3]$ units ($\mathbf{H^{1\text{-}4}}$) showed crowded diffuse reflectance spectra because of the presence of a broad charge transfer band which hides a large part of the visible part of the spectrum. We have thus decided to use the fluorimetry in order to investigate optical behaviours of these materials. Interestingly, a strong sensitivity to the metal ion was observed in the emission spectra (where the cis* emission band is shifted), confirming the discussion about the influence of the counter-ion in the case of **Na1**, **K1** and **Ca1**. The conservation of the thermally induced tautomeric equilibrium of anions into the hybrid materials was proved by temperature dependent excitation spectra. These experiments, which were validated with $\mathbf{CH_2L^{2\text{-}6}}$, have shown an increase of the *cis*-keto form population with the temperature which can only be explained by the tautomeric phenomenon. This success has driven us to extend the study with SCO trinuclear complexes of formula $[Fe^{II}_3(hyetrz)_6(H_2O)_6](\mathbf{1})_4Cl_2$ and $[Fe^{II}_3(hyetrz)_6(H_2O)_6](\mathbf{1Br})_4Cl_2$ where hyetrz = 2'-hydroxyethyl-1,2,4-

triazole. In this material, although no influence of the thermo-sensitive anion was detected on the SCO phenomenon, the interaction between **1** and inorganic units lead to a dynamic relaxation phenomenon in the ^{57}Fe Mössbauer spectra combined with a split of the signal coming from the external iron(II) sites of the trinuclear pattern. The relative area fractions of these two signals were in thermal equilibrium which could be attributed to an influence of the tautomeric equilibrium of **1**. These conclusions were supported by the replacement of anion **1** by **1Br** which leads to similar observations.

Finally, we would like to notice that, in this work, all UV/Visible optical measurements, in reflection or emission, were carried out on pure solid samples in order to avoid matrix effects induced by materials dilution.[14, 56, 103-113] This approach could be criticized in the case of diffuse reflectance measurements because it is well known that observed reflectance is composed by diffuse and regular reflections.[396] The Kubelka-Munk transformation [F(R)] gives spectra which can be regarded as absorption spectra only when regular reflections can be neglected. This aim is reached by using strongly diluted materials (e.g. 0.1 wt % in NaCl).[89, 396] However, these experimental conditions could lead to dramatic interpretation errors such as the observation of photochromism for a compound which is actually non photochromic in pure solid phase. Indeed, we assume that such problems could be at the origin of some contradictions between our results and previous studies (e.g. $\mathbf{L^3}$ and $\mathbf{L^4}$ which were previously analysed in polymeric matrices).[96] Nevertheless, some distortions could appear in pure solid sample diffuse reflectance spectra. In this work, these eventual problems can be neglected because we avoid comparing Kubelka-Munk with

absorption spectra. Moreover, these eventual distortions could lead to modification of band intensity but have no influence on the bands wavelengths[396] which can be safely compared.

Conclusions and perspectives

Novel *N*-salicylidene aniline derivatives containing N-heterocycles were successfully synthesized. In a first step, the factors governing the presence of photo- and thermochromism were searched. The widespread previous conclusions about the predictions of photochromism exclusively based on the crystal packing were unexpectedly disregarded thanks to inadequacies with compounds obtained during this work. An extended analytical approach of these solid-state materials was then carried out and reliable data about structural and electronic properties of *N*-salicylidene aniline derivatives were obtained. The link between these results were fully discussed and new conclusions about the role of 1/ the crystal packing and the molecular topology, 2/ the energy barriers involved during the thermo- and photochemical processes and 3/ the influence of the chemical environment were drawn. They were supported by computational means and temperature dependent solid-state fluorimetry which has, for the very first time, showed the presence of the radiative relaxation of the excited enol and *trans*-keto forms. Moreover, this better understanding of photo- and thermochromism has allowed a novel supramolecular approach giving rise to a control of the crystal packing through specific supramolecular interactions conducted by N-heterocycle nature. Novel non switchable, thermo- and/or photosensitive molecules with various properties were discovered.

N-heterocycle moieties of *N*-salicylidene aniline derivatives were also successfully involved in inorganic coordination complexes. A large variety of inorganic units were prepared (with various dimensionalities, metal and anion nature, geometries, etc). The impact of the coordination as well as of the complexes nature on the structural and optical behaviours of the *N*-

salicylidene molecular switches was fully discussed. Moreover, the possibility to synthesize multifunctional materials combining optical (thermo-, photochromism, strong fluorescence, etc) and magnetic properties (magnetic couplings, SCO, etc) brought by the ligand and the metal ion, respectively, was also introduced. Indeed, in addition to the possibility to grow very attracting supramolecular architectures, the synthesis of SCO complexes containing *N*-salicylidene aniline derivatives demonstrated the possibility to use the ligand as local fluorescent probe in order to characterise the magnetic behaviour of the metal ions. It is interesting to note that the observation of a fluorescent iron(II) complex is quiet rare[342] and that the study of the light emission in pure solid phase was challenging because of the high sensitivity of such materials to the sampling method.[273, 289] It also opens very promising perspectives in photo-switchable SCO complexes which was suggested by the preparation of an assumed photo-sensitive complexes built **Habs** ligand. Finally, the insertion of thermo-sensitive anion derivated from the *N*-salicylidene aniline was also successfully reached. The conservation of the thermo-induced behaviour and the strong interactions between inorganic complexes and switchable anions allow extending this study to SCO materials. The transmission of the thermo-sensitivity to such inorganic complexes was shown and paves the way the observation of an *AD-LISC* effect, namely a SCO induced by a light-induced modification of the anions incorporated in the inorganic frameworks.

Perspectives of this work are numerous because the analytical procedure developed could be applied to a large number of solid-state molecular switches. This possibility was actually already proposed with new inorganic

complexes built with switchable diarylethene ligand. Moreover, a large variety of modifications in the molecular topology of the *N*-salicylidene N-heterocycle derivatives can be thought. Indeed, the addition of a methyl spacer group between salicyl and heterocycle rings could be extended to all molecules synthesized in this work (**Hsaltrz**, **Habs**, **Hsalphen**, **Hsaltz** and **Ksaltz**, anions **1** and **2**) in order to add flexibility to the switchable moieties. It should be particularly interesting in the case of molecules included in inorganic complexes, such as the **Hsaltrz** SCO dinuclears or *N*-salicylidene anions based hybrid materials, which could become photo-sensitive thanks to the larger salicyl ring flexibility. Moreover, it should also lead to modification of the SCO properties. The methyl group could also be replaced by other spacer moieties, such as alkyl, olefinic chains or other conjugated groups (aromatic rings, etc), and thus lead to other structural and electronic properties.

Inorganic complexes series, prepared in this work, should also be enlarged in order to grow the numbers of potentially thermo- and/or photo-sensitive materials. It is specially the case for **Habs** complexes because of the very large variety of accessible molecular dimentionalities (see chapter 7). The *N*-salicylidene anions should also be investigated deeper. Indeed, a large variety of cationic host can be thought in order to prepare novel multi-functional materials. This class of molecules could then be inserted into charged polymeric matrices or other inorganic compounds. These last entities could present SCO phenomenon and various dimensionalities. Tridimensional networks appear to be very promising because the functional anions could be encaged in voids leading to strong interactions between molecular components. Mononuclear compounds should also be considered

in order to investigate deeper the influence of such anions on SCO properties. The aim of such studies should be, of course, the research of a SCO phenomenon induced by the thermo- and/or photo-sensitivity of the anions (AD-TISC and AD-LISC effects).

The synthesis of new *N*-salicylidene aniline derivatives incorporating other coordinating moieties should also be considered. Indeed, we could prepare new molecules with a combination of coordinating moieties such as pyridine, triazole and tetrazole, as previously discussed, but also other donor groups like aliphatic amine, imidazole or isoxazole rings. These molecules could react with SCO metal ions in order to give novel switchable inorganic complexes.[124, 309, 397, 398] Other organic molecules presenting specific molecular organisations should be also developed. For example, chiral molecules could be prepared by reacting corresponding aldehyde with chosen chiral amines. *N*-salicylidene chiral molecules could be derived from amino acids which are known to be bio-compatible, easily grafted on coordinating moieties and to metal ions, and which could crystallise in non centro-symmetric packings.[399-402] It would open the way to future researches on NLO. Finally, the syntheses of such organic, inorganic or hybrid materials could be tuned in order to drive to other specific molecular arrangement such as liquid crystals (built thanks to long aliphatic chains and which are less studied up to now[403]) or nanoparticles which could lead to novel interesting properties linked to the large presence of particles interfaces.

Notes and references

[1] Y. Garcia, P. Guionneau, G. Bravic, D. Chasseau, J. A. K. Howard, O. Kahn, V. Ksenofontov, S. Reiman and P. Gutlich, *Eur. J. Inorg. Chem.* **2000**, *1*, 1531-1538.

[2] H. Tian and Y. L. Feng, *J. Mater. Chem.* **2008**, *18*, 1617-1622.

[3] Brown, B. H. *Photochromism.*, Wiley, New York **1971**.

[4] Dürr, B. and B. Laurent. *Photochromism: Molecules and System.*, Elsevier, Amsterdam, The Netherlands **2010**.

[5] H. Bouas-Laurent and H. Durr, *Pure Appl. Chem.* **2001**, *73*, 639-

[6] *Organic Photochromism and Thermochromism compounds.*, Plenum, **1998**.

[7] M. Irie, *Chem. Rev.* **2000**, *100*, 1683.

[8] O. Sato, *J. Photochem. Photobio. C.* **2004**, *5*, 203-223.

[9] T. He and J.-N. Yao, *Res. Chem. Intermediat.* **2004**, *30*, 459-488.

[10] P. Gütlich, Y. Garcia, H. Spiering. *Spin Transition Phenomena and New Trends in Spin Crossover Research.*, *Magnetism : Molecules to Materials IV - Nanosized Magnetic Materials*, Wiley-VCH Verlag GmbH & Co, **2002**, 2 46-69 90.

[11] O. Sato, *Acc. Chem. Res.* **2003**, *36*, 692-700.

[12] H. Bouas-Laurent, A. Castellan, J. P. Desvergne and R. Lapouyade, *Chem. Soc. Rev.* **2001**, *30*, 248-263.

[13] J. Saltiel, T. S. R. Krishna, A. M. Turek and R. J. Clark, *Chem. Comm.* **2006**, 1506-1508.

[14] K. Amimoto and T. Kawato, *J. Photochem. Photobio. C.* **2005**, *6*, 207-226.

[15] B. L. Feringa, W. F. Jager and B. Delange, *Tetrahedron* **1993**, *49*, 8267-8310.

[16] S. Kawata and Y. Kawata, *Chem. Rev.* **2000**, *100*, 1777-1788.

[17] B. L. Feringa, *Accounts Chem. Res.* **2001**, *34*, 504-513.

[18] V. A. Bren, A. D. Dubonosov, V. I. Minkin, T. N. Gribanova, V. P. Rybalkin, E. N. Shepelenko, A. V. Tsukanov and R. N. Borisenko, *Mol. Cryst. Liq. Cryst.* **2005**, *431*, 417-422.

[19] K. Nakatani and J. A. Delaire, *Chem. Mater* **1997**, *9*, 2682-2684.

[20] M. Sliwa, S. Letard, I. Malfant, M. Nierlich, P. G. Lacroix, T. Asahi, H. Masuhara, P. Yu and K. Nakatani, *Chem. Mater.* **2005**, *17*, 4727-4735.

[21] M. Sliwa, A. Spangenberg, I. Malfant, P. G. Lacroix, R. Metivier, R. B. Pansu and K. Nakatani, *Chem. Mater.* **2008**, *20*, 4062-4068.

[22] A. Plaquet, M. Guillaume, B. Champagne, L. Rougier, F. Mancois, V. Rodriguez, J. L. Pozzo, L. Ducasse and F. Castet, *J. Phys. Chem. C.* **2008**, *112*, 5638-5645.
[23] S. Kobatake and M. Irie, *Annu. Rep. Prog. Chem. , Sect. C* **2003**, *99*, 277-313.
[24] J. I. Mamiya, A. Yoshitake, M. Kondo, Y. Yu and T. Ikeda, *J. Mater. Chem.* **2008**, *18*, 63-65.
[25] T. Ikeda, H. Shin, K. Durga B., K. Seiji and T. Shigeo, *Macromolecules* **1990**, *23*, 36-42 (a), 42-48 (b) and 3939-3943 (c).
[26] S. Shinkai, T. Ogawa, Y. Kusano, O. Manabe, K. Kikukawa, T. Goto and T. Matsuda, *J. Am. Chem. Soc.* **1982**, *104*, 1960-1967.
[27] S. Shinkai, *Pure Appl. Chem.* **1987**, *59*, 425-430.
[28] B. S. Lukyanov and M. B. Lukyanova, *Chem. Heterocyclic Compd.* **2005**, *41*, 281-310.
[29] L. Hou, H. Schmidt, B. Hoffmann and M. Mennig, *J. Sol-Gel Sci. Technol.* **1997**, *8*, 927-929.
[30] G. Favaro, G. Chidichimo, P. Formoso, S. Manfredi, U. Mazzucato and A. Romani, *J. Photoch. Photobio. A.* **2001**, *140*, 229-236.
[31] G. Sciaini, D. E. Wetzler, J. Alvarez, R. Fernandez-Prini and M. L. Japas, *J. Photoch. Photobio. A.* **2002**, *153*, 25-31.
[32] E. A. Gonzalez-de los Santos, M. J. Lozano-Gonzalez and A. F. Johnson, *J. Appl. Polym. Sci.* **1999**, *71*, 267-272.
[33] L. de Leon and M. C. Biewer, *Tetrahedron Lett.* **2000**, *41*, 3527-3530.
[34] R. B. Morgunov, F. B. Mushenok, S. M. Aldoshin, E. A. Yur'eva, G. V. Shilov and Y. Tanimoto, *J. Solid State Chem.* **2009**, *182*, 1424-1429.
[35] V. I. Minkin, *Chem. Rev.* **2004**, *104*, 2751-2776.
[36] M. Kumiko, S. Masaaki, A. Eiji and H. Junichi, *Jpn Patent 04-116546,* **1992**.
[37] M. Masata, M. Hiroyuki and T. Nobuyoshi, *Jpn Patent 09-124654,* **1997**.
[38] M. Morimoto and M. Irie, *Chem. Comm.* **2005**, 3895-3905.
[39] S. L. Gilat, S. H. Kawai and J. M. Lehn, *Chem. Eur. J.* **1995**, *1*, 275-284.
[40] Y. Asano, A. Murakami, T. Kobayashi, A. Goldberg, D. Guillaumont, S. Yabushita, M. Irie and S. Nakamura, *J. Am. Chem. Soc.* **2004**, *126*, 12112-12120.

[41] M. Murakami, H. Miyasaka, T. Okada, S. Kobatake and M. Irie, *J. Am. Chem. Soc.* **2004**, *126*, 14764-14772.
[42] Y. F. Feng, Y. L. Yan, S. Wang, W. H. Zhu, S. X. Qian and H. Tian, *J. Mater. Chem.* **2006**, *16*, 3685-3692.
[43] K. Uchida and M. Irie, *Chem. Lett.* **1995**, 969-970.
[44] T. Yamaguchi, K. Uchida and M. Irie, *J. Am. Chem. Soc.* **1997**, *119*, 6066-6071.
[45] S. Kobatake, K. Shibata, K. Uchida and M. Irie, *J. Am. Chem. Soc.* **2000**, *122*, 12135-12141.
[46] T. He and J. N. Yao, *Prog. Mater. Sci.* **2006**, *51*, 810-879.
[47] S. D. Cohen and G. A. Newman, *J. Photogr. Sci.* **1967**, *15*, 290-298.
[48] C. C. Ko and V. W. W. Yam, *J. Mater. Chem.* **2010**, *20*, 2063-2070.
[49] R. Exelby and R. Grinter, *Chem. Rev.* **1965**, *G5*, 247-260.
[50] Z. K. Luo, J. J. Yang, H. H. Cai, H. Y. Li, X. Z. Ren, J. H. Liu and X. Liang, *Thin Solid Films* **2008**, *516*, 5541-5544.
[51] V. Coue, R. Dessapt, M. Bujoli-Doeuff, M. Evain and S. Jobic, *J. Solid State Chem.* **2008**, *181*, 1116-1122.
[52] A. S. Poulos, D. Constantin, P. Davidson, M. Imperor, B. Pansu, P. Panine, L. Nicole and C. Sanchez, *Langmuir* **2008**, *24*, 6285-6291.
[53] L. Jr. Chalkley, *Chem. Rev.* **1929**, *6*, 217-280.
[54] C. Sanchez, B. Lebeau, F. Chaput and J. P. Boilot, *Adv. Mater.* **2003**, *15*, 1969-1994.
[55] B. Lebeau and C. Sanchez, *Curr. Opin. Solid State Mater. Sci.* **1999**, *4*, 11-23.
[56] I. Casades, M. Alvaro, H. Garcia and M. N. Pillai, *Eur. J. Org. Chem.* **2002**, *0*, 2074-2079.
[57] A. Corma, V. Fornes, H. Garcia, M. A. Miranda, J. Primo and M. J. Sabater, *J. Am. Chem. Soc.* **1994**, *116*, 2276-2280.
[58] A. Corma, V. Fornes, H. Garcia, M. A. Miranda and M. J. Sabater, *J. Am. Chem. Soc.* **1994**, *116*, 9767-9768.
[59] I. Casades, S. Constantine, D. Cardin, H. Garcia, A. Gilbert and F. Marquez, *Tetrahedron* **2000**, *56*, 6951-6956.
[60] Z. J. Zhang, S. C. Xiang, G. C. Guo, G. Xu, M. S. Wang, J. P. Zou, S. P. Guo and J. S. Huang, *Angew. Chem. Int. Ed.* **2008**, *47*, 4149-4152.
[61] U. El-Ayaan, F. Murata and Y. Fukuda, *Monatsh. Chem.* **2001**, *132*, 1279-1294.

[62] Y. Garcia, V. Ksenofontov and P. Gutlich, *Hyperfine Interact.* **2002**, *139*, 543-551.
[63] J. H. Day, *Chem. Rev.* **1968**, *68*, 649-657.
[64] P. Gütlich, Y. Garcia and H. A. Goodwin, *Chem. Soc. Rev.* **2000**, *29*, 419-427.
[65] M. Sorai, *J. Chem. Thermodyn.* **2002**, *34*, 1207-1253.
[66] M. Kojima, H. Taguchi, M. Tsuchimoto and K. Nakajima, *Coord. Chem. Rev.* **2003**, *237*, 183-196.
[67] A. Tsuda, *Bull. Chem. Soc. Jpn.* **2009**, *82*, 11-29.
[68] E. Hadjoudis and I. M. Mavridis, *Chem. Soc. Rev.* **2004**, *33*, 579-588.
[69] V. Bertolasi, P. Gilli and G. Gilli, *Curr. Org. Chem.* **2009**, *13*, 250-268.
[70] C. Reichardt, *Chem. Soc. Rev.* **1992**, *21*, 147-153.
[71] M. Leclerc, *Adv. Mater.* **1999**, *11*, 1491-1498.
[72] F. C. Schilling, A. J. Lovinger, D. D. Davis, F. A. Bovey and J. M. Zeigler, *J. Inorg. Organomet.* **1992**, *2*, 47-57.
[73] S. Okada, S. Peng, W. Spevak and D. Charych, *Acc. Chem. Res.* **1998**, *31*, 229-239.
[74] M. Leclerc, *J. Polym. Sci. Part A.* **2001**, *39*, 2867-2873.
[75] J. Liu, J. W. Y. Lam and B. Z. Tang, *Chem. Rev.* **2009**, *109*, 5799-5867.
[76] R. W. Carpick, D. Y. Sasaki, M. S. Marcus, M. A. Eriksson and A. R. Burns, *J. Phys. - Condens. Mat.* **2004**, *16*, R679-R697.
[77] D. J. Sandman, J. M. Njus and B. Tran, *Macromol. Symp.* **2004**, *216*, 77-85.
[78] D. J. Ahn, S. Lee and J. M. Kim, *Adv. Funct. Mater.* **2009**, *19*, 1483-1496.
[79] A. Seeboth, J. Kriwanek, D. Lotzsch and A. Patzak, *Polym. Adv. Technol.* **2002**, *13*, 507-512.
[80] J. K. Grey and I. S. Butler, *Coord. Chem. Rev.* **2001**, *219*, 713-759.
[81] S. H. Foulger, P. Jiang, A. Lattam, D. W. Smith, J. Ballato, D. E. Dausch, S. Grego and B. R. Stoner, *Adv. Mater.* **2003**, *15*, 685-689.
[82] C. G. Granqvist, *Sol. Energ. Mat. Sol. C.* **2008**, *92*, 203-208.
[83] H. El-Gezawy, W. Rettig and R. Lapouyade, *J. Phys. Chem. A* **2006**, *110*, 67-75.

[84] H. Mastuzaki, H. Kishida, H. Okamoto, K. Takizawa, S. Matsunaga, S. Takaishi, M. A. Hitoshi, K. Sugiura and M. Yamashita, *Angew. Chem. Int. Ed.* **2005**, *44*, 3240-3243.
[85] C. Baleizao and H. Garcia, *Chem. Rev.* **2006**, *106*, 3987-4043.
[86] R. K. Parashar, R. C. Sharma, A. Kumar and G. Mohan, *Inorg. Chim. Acta* **1988**, *151*, 201-208.
[87] Z. Cimerman, N. Galic and B. Bosner, *Anal. Chim. Acta* **1997**, *343*, 145-153.
[88] F. D. Jochum and P. Theato, *Macromolecules* **2009**, *42*, 5941-5945.
[89] T. Fujiwara, J. Harada and K. Ogawa, *J. Phys. Chem. B* **2004**, *108*, 4035-4038.
[90] D. S. Lo, D. M. Manikowski and M. M. Hanson, *Appl. Optics* **1971**, *10-4*, 978-979.
[91] E. Hadjoudis, *Mol. Eng.* **1995**, *5*, 301-337.
[92] J. Harada, T. Fujiwara and K. Ogawa, *J. Am. Chem. Soc.* **2007**, *129*, 16216-16221.
[93] M. E. Kletskii, A. A. Millov, A. V. Metelitsa and M. I. Knyazhansky, *J. Photoch. Photobio. A.* **1997**, *110*, 267-270.
[94] N. Otsubo, C. Okabe, H. Mori, K. Sakota, K. Amimoto, T. Kawato and H. Sekiya, *J. Photoch. Photobio. A.* **2002**, *154*, 33-39.
[95] V. Vargas, *J. Phys. Chem.* **2004**, *108*, 281-288.
[96] E. Hadjoudis, M. Vittorakis and I. Moustakali-Mavridis, *Tetrahedron* **1987**, *43*, 1345-1360.
[97] T. Inabe, N. Hoshino, T. Mitani and Y. Maruyama, *Bull. Chem. Soc. Jpn.* **1989**, *62*, 2245-2251.
[98] I. Moustakali-Mavridis and E. Hadjoudis, *Acta Crystallogr. B.* **1978**, *34*, 3709-3715.
[99] J. Bregman, L. Leiserowitz and K. Osaki, *J. Chem. Soc.* **1964**, *0*, 2086-2100.
[100] R. Destro, A. Gavezzotti and M. Simonetta, *Acta Crystallogr. B.* **1978**, *34*, 2867-2869.
[101] F. Arod, M. Gardon, P. Pattison and G. Chapuis, *Acta Crystallogr. C.* **2005**, *61*, O317-O320.
[102] F. Arod, P. Pattison, K. J. Shenk and G. Chapuis, *Cryst. Growth Des.* **2007**, *7*, 1679-1685.
[103] E. Hadjoudis, A. B. Bourlinos and D. Petridis, *J. Incl. Phenom. Macro.* **2002**, *42*, 275-279.
[104] M. Ziolek, J. Kubicki, A. Maciejewski, R. Naskrecki and A. Grabowska, *J. Chem. Phys.* **2006**, *124*, (124518)-1-9.

[105] L. Z. Zhang, Y. Xiang, P. Cheng, G. Q. Tang and D. Z. Liao, *Chem. Phys. Lett.* **2002**, *358*, 278-283.
[106] S. Sakagami, T. Koga and A. Takase, *Mol. Cryst. Liq. Cryst.* **2002**, *373*, 71-81.
[107] E. Hadjoudis, V. Verganelakis, C. Trapalis and G. Kordas, *Mol. Eng.* **1999**, *8*, 459-469.
[108] P. Xue, R. Lu, G. Chen, Y. Zhang, H. Nomoto, M. Takafuji and H. Ihara, *Chem. Eur. J.* **2007**, *13*, 8231-8239.
[109] T. Kawato, H. Koyama and H. Kanatomi, *Chem. Lett.* **1994**, 665-668.
[110] G. Pistolis, D. Gegiou and E. Hadjoudis, *J. Photochem. Photobio. A.* **1996**, *93*, 179-184.
[111] E. Hadjoudis, T. Dziembowska and Z. Rozwadowski, *J. Photochem. Photobio. A* **1999**, *128*, 97-99.
[112] T. Haneda, M. Kawano, T. Kojima and M. Fujita, *Angew. Chem. Int. Ed.* **2007**, *46*, 6643-6645.
[113] P. Chen, R. Lu, P. C. Xue, T. H. Xu, G. J. Chen and Y. Y. Zhao, *Langmuir* **2009**, *25*, 8395-8399.
[114] O. Ohmori, M. Kawano and M. Fujita, *J. Am. Chem. Soc.* **2004**, *126*, 16292-16293.
[115] M. Handa, A. Honda, Z. J. Zhong, H. Okawa and S. Kida, *Inorg. Chim. A. - Art. Let.* **1985**, *101*, 39-43.
[116] Y. Garcia, V. Ksenofontov and P. Gütlich, *C. R. Acad. Sci. Paris, IIc* **2001**, *4*, 227-233.
[117] Y. Garcia and P. Gütlich, *Top. Curr. Chem.* **2004**, *234*, 49-62.
[118] P. Gütlich. *Spin Crossover in Iron (II) Complexes*., *Structure Bonding, Springer Verlag, Berlin*.,**1981**, 83.
[119] P. Gütlich, A. Hauser and H. Spiering, *Angew. Chem. Int. Ed.* **1994**, *33*, 2024-2054.
[120] E. Breuning, M. Ruben, J. M. Lehn, F. Renz, Y. Garcia, V. Ksenofontov, P. Gutlich, E. Wegelius and K. Rissanen, *Angew. Chem. Int. Ed.* **2000**, *39*, 2504-2507.
[121] M. M. Dîrtu, A. Rotaru, D. Gillard, J. Linares, E. Codjovi, B. Tinant and Y. Garcia, *Inorg. Chem.* **2009**, *48*, 7838-7852.
[122] Y. Garcia, V. Ksenofontov, S. Mentior, M. Dîrtu, C. Gieck, A. Bhatthaccharjee and P. Gutlich, *Chem. Eur. J.* **2008**, *14*, 3745-3758.
[123] Y. Garcia, V. Niel, M. C. Muñoz and J. A. Real, *Top. Curr. Chem.* **2004**, *233*, 229-257.

[124] Y. Garcia, C. M. Grunert, S. Reiman, O. van Campenhoudt and P. Gutlich, *Eur. J. Inorg. Chem.* **2006**, 3333-3339.
[125] G. Dupouy, M. Marchivie, S. Triki, J. Sala-Pala, J. Y. Salaun, C. J. Gomez-Garcia and P. Guionneau, *Inorg. Chem.* **2008**, *47*, 8921-8931.
[126] P. Gütlich and Y. Garcia, *J. Phys. Conf. Ser.* **2010**, *217*, (012001)-1-21.
[127] J.-F. Létard, P. Guionneau and L. Goux-Capes, *Top. Curr. Chem.* **2004**, *235*, 221-249.
[128] O. Kahn, E. Codjovi, Y. Garcia, P. J. van Koningsbruggen, R. Lapouyade and L. Sommier, *ACS Symp. Ser.* **1996**, *64*, 298-310.
[129] O. Kahn, J. Krober and C. Jay, *Adv. Mater.* **1992**, *4*, 718-728.
[130] R. N. Muller, L. Vander Elst and S. Laurent, *J. Am. Chem. Soc.* **2003**, *125*, 8405-8407.
[131] F. Averseng, C. Lepetit, P. G. Lacroix and J. P. Tuchagues, *Chem. Mater.* **2000**, *12*, 2225-2229.
[132] P. N. Martinho, C. J. Harding, H. Muller-Bunz, M. Albrecht and G. G. Morgan, *Eur. J. Inorg. Chem.* **2010**, 675-679.
[133] G. G. Morgan, K. D. Murnaghan, H. Muller-Bunz, V. Mckee and C. J. Harding, *Angew. Chem. Int. Ed.* **2006**, *45*, 7192-7195.
[134] K. Wolfgang, E. Werner and P. Gütlich, *Inorg. Chem.* **1987**, *26*, 3977-3982.
[135] M. M. Dîrtu, C. Neuhausen, A. D. Naik, A. Rotaru, L. Spinu and Y. Garcia, *Inorg. Chem.* **2010**, *49*, 5723-5736.
[136] P. Gütlich, Y. Garcia and T. Woike, *Coord. Chem. Rev.* **2001**, *219*, 839-879.
[137] J.-F. Létard, J. S. Costa, S. Marcen, C. Carbonera, C. Desplanches, A. Kobayashi, N. Daro and P. Guionneau, *J. Phys. Conf. Ser.* **2005**, *21*, 23-29.
[138] Y. Garcia, P. J. van Koningsbruggen, R. Lapouyade, L. Rabardel, O. Kahn, M. Wieczorek, R. Bronisz, Z. Ciunik and M. F. Rudolf, *C. R. Acad. Sci. Paris, IIc* **1998**, *1*, 523-532.
[139] A. D. Naik, B. Tinant, K. Muffler, J. A. Wolny, V. Schunemann and Y. Garcia, *J. Solid State Chem.* **2009**, *182*, 1365-1376.
[140] S. Decurtins, P. Gutlich, C. P. Kohler, H. Spiering and A. Hauser, *Chem. Phys. Lett.* **1984**, *105*, 1-4.
[141] S. Decurtins, P. Gutlich, K. M. Hasselbach, A. Hauser and H. Spiering, *Inorg. Chem.* **1985**, *24*, 2174-2178.
[142] J. F. Létard, *J. Mater. Chem.* **2006**, *16*, 2550-2559.

[143] G. Dupouy, M. Marchivie, S. Triki, J. Sala-Pala, C. J. Gomez-Garcia, S. Pillet, C. Lecomte and J. F. Letard, *Chem. Comm.* **2009**, 3404-3406.
[144] Kondo M. and Yoshizawa K., *Chem. Phys. Lett.* **2003**, *372*, 519-523.
[145] S. Marcen, L. Lecren, L. Capes, H. A. Goodwin and J. F. Letard, *Chem. Phys. Lett.* **2002**, *358*, 87-95.
[146] M. Matsumoto, T. Sato, S. Hashimoto, M. Kojima and S. Iijima, *J. Phys. Conf. Ser.* **2009**, *148*, 1-5.
[147] O. Roubeau, M. deVos, A. F. Stassen, R. Burriel, J. G. Haasnoot and J. Reedijk, *J. Phys. Chem. Solids* **2003**, *64*, 1003-1013.
[148] C. Roux, J. Zarembowitch, B. Gallois, T. Granier and R. Claude, *Inorg. Chem.* **1994**, *33*, 2273-2279.
[149] M. L. Boillot, C. Roux, J. P. Audiere, A. Dausse and J. Zarembowitch, *Inorg. Chem.* **1996**, *35*, 3975-3980.
[150] M. L. Boillot, S. Chantraine, J. Zarembowitch, J. Y. Lallemand and J. Prunet, *New J. Chem.* **1999**, *23*, 179-183.
[151] J. S. Kolb, M. D. Thomson, M. Novosel, K. Senechal-David, E. Riviere, M. L. Boillot and H. G. Roskos, *CR. Chim.* **2007**, *10*, 125-136.
[152] Y. Hasegawa, S. Kume and H. Nishihara, *Dalton Trans.* **2009**, 280-284.
[153] M. L. Boillot, S. Pillet, A. Tissot, E. Riviere, N. Claiser and C. Lecomte, *Inorg. Chem.* **2009**, *48*, 4729-4736.
[154] M. L. Boillot, J. Zarembowitch and A. Sour, *Top. Curr. Chem.* **2004**, *234*, 261-276.
[155] E. Hadjoudis, J. Argyroglou, E. Lambi and I. M. Mavridis, *Mol. Eng.* **1991**, *1*, 67-74.
[156] E. Hadjoudis, J. Petrou and J. Xexakis, *Mol. Cryst. Liq. Cryst.* **1983**, *93*, 73-81.
[157] I. Moustakali-Mavridis, E. Hadjoudis and A. Mavridis, *Acta Crystallogr. B* **1980**, *36*, 1126-1130.
[158] K. Ogawa, Y. Kasahara, Y. Ohtani and J. Harada, *J. Am. Chem. Soc.* **1998**, *120*, 7107-7108.
[159] Z. Cimerman, N. Galesic and B. Bosner, *J. Mol. Struct.* **1992**, *274*, 131-144.
[160] H. Unver, M. Yildiz, D. M. Zengin, S. Ozbey and E. Kendi, *J. Chem. Crystallogr.* **2001**, *31*, 211-216.
[161] E. Hadjoudis, *J. Photochem.* **1981**, *17*, 355-363.

[162] T. Kawato, H. Koyama, H. Kanatomi and M. Isshiki, *J. Photochem.* **1985**, *28*, 103-110.
[163] M. Mikami and S. Nakamura, *Phys. Rev. B* **2004**, *69*, (134205)-1-8.
[164] J. Harada, H. Uekusa and Y. Ohashi, *J. Am. Chem. Soc.* **1999**, *121*, 5809-5810.
[165] V. Vargas and L. Amigo, *J. Chem. Soc. , Perkin Trans. 2* **2001**, 1124-1129.
[166] J. M. Lehn, *Science* **2002**, *295*, 2400-2403.
[167] K. Ono, M. Yoshizawa, M. Akita, T. Kato, Y. Tsonubuchi, S. Ohkoshi and M. Fujita, *J. Am. Chem. Soc.* **2009**, *131*, 2782-2783.
[168] J. Qian and F. P. Wu, *Chem. Mater.* **2009**, *21*, 758-762.
[169] J.-L. Li, X.-Y. Liu, R.-Y. Wang and J.-Y. Xiong, *J. Phys. Chem. B.* **2005**, *109*, 24231-24235.
[170] S. Goswami, S. Jana, S. Dey, I. A. Razak and H. K. Fun, *Supramol. Chem.* **2006**, *18*, 571-574.
[171] P. Crochet, J. P. Malval and R. Lapouyade, *Chem. Comm.* **2000**, 289-290.
[172] J. P. Malval, C. Chaimbault, B. Fischer, J. P. Morand and R. Lapouyade, *Res. Chem. Intermediat.* **2001**, *27*, 21-34.
[173] K. S. Suslick, N. A. Rakow and A. Sen, *Tetrahedron* **2004**, *60*, 11133-11138.
[174] M. E. Kosal, J.-H. Chou, S. R. Wilson and K. S. Suslick, *Nat. Mater.* **2002**, *1*, 118-121.
[175] N. Lin, A. Langner, S. L. Tait, C. Rajadurai, M. Ruben and K. Kern, *Chem. Commun.* **2007**, 4860-4862.
[176] A. Rochefort, E. Bayard and S. Hadj-Messaoud, *Adv. Mater.* **2007**, *19*, 1992-1995.
[177] S. Yagai, T. Karatsu and A. Kitamura, *Chem. Eur. J.* **2005**, *11*, 4054-4063.
[178] A. Mukherjee, M. K. Saha, M. Nethaji and A. R. Chakravarty, *New J. Chem.* **2005**, *29*, 596-603.
[179] Y. Zakrevskyy, J. Stumpe and C. F. J. Faul, *Adv. Mater.* **2006**, *18*, 2133-2136.
[180] P. Metrangolo, F. Meyer, T. Pilati, G. Resnati and G. Terraneo, *Angew. Chem. Int. Ed.* **2008**, *47*, 6114-6127.
[181] M. Schmittel, V. Kalsani and J. W. Bats, *Inorg. Chem.* **2005**, *44*, 4115-4117.
[182] M. Barboiu, E. Petit, A. van der Lee and G. Vaughan, *Inorg. Chem.* **2006**, *45*, 484-486.

[183] J. I. van der Vlugt, S. Demeshko, S. Dechert and F. Meyer, *Inorg. Chem.* **2008**, *47*, 1576-1585.
[184] H. Sleiman, P. N. W. Baxter, J. M. Lehn, K. Airola and K. Rissanen, *Inorg. Chem.* **1997**, *36*, 4734-4742.
[185] V. Chandrasekar, L. Nagarajan, R. Clérac, S. Ghost and S. Verma, *Inorg. Chem.* **2008**, *47*, 1067-1073.
[186] M. kinoshita, *Int. J. Mol. Sci.* **2009**, *10*, 1064-1080.
[187] J. D. Crowley and B. Bosnich, *Eur. J. Inorg. Chem.* **2005**, 2015-2025.
[188] T. Weilandt, R. W. Troff, H. Saxell, K. Rissanen and C. A. Schalley, *Inorg. Chem.* **2008**, *47*, 7588-7598.
[189] K. Yamauchi, Y. Takashima, A. Hashidzume, H. Yamaguchi and A. Harada, *J. Am. Chem. Soc.* **2008**, *130*, 5024-5025.
[190] Z. S. Ge, J. M. Hu, F. H. Huang and S. Y. Liu, *Angew. Chem. Int. Ed.* **2009**, *48*, 1798-1802.
[191] C. Rajadurai, F. Schramm, S. Brink, O. Fuhr, M. Ghafari, R. Kruk and M. Ruben, *Inorg. Chem.* **2006**, *45*, 10019-10021.
[192] P. A. N. Reddy, M. Nethaji and A. R. Chakravarty, *Inorg. Chem. Comm.* **2003**, *6*, 698-701.
[193] F. S. Delgado, C. Ruiz-Perez, J. Sanchiz, F. Lloret and M. Julve, *Cryst. Eng. Comm.* **2006**, *8*, 530-544.
[194] Desiraju, G. R. *The Crystal as a Supramolecular Entity*., Wiley, Chichester, United Kingdom **1996**.
[195] F. Hidara., *IPL Report* **2008**.
[196] Although the presence of polymorphs cannot be rejected, on the basis of the difference between simulated and experimental X-ray powder diffractograms, a very nice correspondence between optical and structural properties have been observed.
[197] E. Hadjoudis, I. M. Mavridis, T. Dziembowska, Z. Rozwadowski and R. Anulewicz, *Mol. Eng.* **1999**, *8*, 97-104.
[198] Except for **Hsalphen** in the T^1 state.
[199] These values are, however, only rough estimates of this stabilization and have to be taken with caution. Indeed, these calculations do not take into account the distortion of the surrounding molecules nor the crystal-packing dilatation.
[200] A. Bargibant., *IPL Report* **2009**.
[201] A preliminary foray was also carried out by Dr. G. Zhou as described in 'G. Zhou., *Internal Report, CMAT Laboratory, UCL* **2003**'.
[202] O. van Campenhoudt., *Master Thesis UCL* **2005**.

[203] P.-L. Jacquemin., *Master Thesis UCL* **2009**.
[204] Z. Cimerman, R. Kiralj and N. Galic, *J. Mol. Struct.* **1994**, *323*, 7-14.
[205] E. Lambi, D. Gegiou and E. Hadjoudis, *J. Photochem. Photobio. A.* **1995**, *86*, 241-246.
[206] R. W. Oehmke and J. C. Jr. Bailar, *J. Inorg. Nucl. Chem.* **1965**, *27*, 2209-2215.
[207] L. Shi, H. M. Ge, S. H. Tan, H. Q. Li, Y. C. Song, H. L. Zhu and R. X. Tan, *Eur. J. Med. Chem.* **2007**, *42*, 558-564.
[208] D. R. Godhani, M. R. Sanariya, Y. V. Patel and P. H. Parsania, *Eur. Polym. J.* **2002**, *38*, 2171-2178.
[209] X. S. Tai, Y. M. Feng and Z. P. Liang, *Acta Crystallogr. E.* **2009**, *65*, M275-U485.
[210] X. S. Tai, J. Yin, Y. M. Feng and F. Y. Kong, *Chin. J. Inorg. Chem.* **2007**, *23*, 1812-1814.
[211] X. S. Tai, J. Xu, Y. M. Feng and Z. P. Liang, *Acta Crystallogr. E.* **2008**, *64*, M893-U364.
[212] X. S. Tai, J. Yin and M. Y. Hao, *Acta Crystallogr. E.* **2008**, *64*, M273-M273.
[213] X. S. Tai, J. Xu, Y. M. Feng and Z. P. Liang, *Acta Crystallogr. E.* **2008**, *64*, M694-M694.
[214] X. S. Tai, Y. M. Feng and F. Y. Kong, *Acta Crystallogr. E.* **2008**, *64*, M645-M645.
[215] L. H. Wang, J. Yin and X. S. Tai, *Acta Crystallogr. E.* **2007**, *63*, M1664-M1164.
[216] X. Zhang and Z. Li, *Acta Crystallogr. E.* **2008**, *64*, o1159.
[217] Brégeault, J. M. *Catalyse homogène par les complexes des métaux de transition*., Masson, Paris, France **1992**.
[218] P. Guionneau, M. Marchivie, G. Bravic, J.-F. Létard and D. Chasseau, *Top. Curr. Chem.* **2004**, *234*, 97-128.
[219] J. Zhou, Z. F. Chen, Y. S. Tan, X. W. Wang, Y. H. Tan, H. Liang and Y. Zhang, *Acta Crystallogr. E.* **2004**, *60*, M519-M521.
[220] L. L. Zheng, C. K. Tan and M. L. Tong, *Chin. J. Inorg. Chem.* **2006**, *22*, 1426-1430.
[221] G. Lemercier, E. Mulliez, C. Brouca-Cabarrecq, F. Dahan and J. P. Tuchagues, *Inorg. Chem.* **2004**, *43*, 2105-2113.
[222] Greenwood, N. N. and T. C. Gibbs. *Mössbauer Spectroscopy*., Chapman and Hall Ltd, **1971**.
[223] Y. Hai-jian, W. Hong-Gen and S. Wen-Hue, *Chin. J. Struct. Chem.* **2004**, *23*, 183-184.

[224] T. Akitsu and Y. Einaga, *Acta Crystallogr. E.* **2004**, *60*, M1552-M1554.
[225] S. I. Noro, M. Kondo, S. Kitagawa, T. Ishii, H. Matsuzaka and M. Yamashita, *Mol. Cryst. Liq. Cryst.* **2000**, *342*, 231-236.
[226] J. G. Haasnoot, *Coord. Chem. Rev.* **2000**, *200*, 131-185.
[227] J. J. A. Kolnaar, M. I. de Heer, H. Kooijman, A. L. Spek, G. Schmitt, V. Ksenofontov, P. Gutlich, J. G. Haasnoot and J. Reedijk, *Eur. J. Inorg. Chem.* **1999**, 881-886.
[228] J. J. A. Kolnaar, G. vanDijk, H. Kooijman, A. L. Spek, V. G. Ksenofontov, P. Gutlich, J. G. Haasnoot and J. Reedijk, *Inorg. Chem.* **1997**, *36*, 2433-2440.
[229] G. A. Berezovskii, M. B. Bushuev, D. P. Pishchur and L. G. Lavrenova, *J. Therm. Anal. Calorim.* **2008**, *93*, 999-1002.
[230] E. Rentschler and C. von Malotki, *Inorg. Chim. Acta* **2008**, *361*, 3646-3653.
[231] Y. Garcia, J. Moscovici, A. Michalowicz, V. Ksenofontov, G. Levchenko, G. Bravic, D. Chasseau and P. Gutlich, *Chem. Eur. J.* **2002**, *8*, 4992-5000.
[232] H. M. Wang, P. Cheng, L. C. Li, S. P. Yan, Z. H. Jiang, D. Z. Liao, G. L. Wang and J. P. Tuchagnes, *Inorg. Chem. Comm.* **2000**, *3*, 198-201.
[233] L. G. Lavrenova, O. G. Shakirova, V. N. Ikorskii, V. A. Varnek, L. A. Sheludyakova and S. V. Larionov, *Russ. J. Coord. Chem.* **2003**, *29*, 22-27.
[234] S. Toyazaki, M. Nakanishi, T. Komatsu, N. Kojima, D. Matsumura and T. Yokoyama, *Synthetic Met.* **2001**, *121*, 1794-1795.
[235] P. J. vanKoningsbruggen, Y. Garcia, E. Codjovi, R. Lapouyade, O. Kahn, L. Fournes and L. Rabardel, *J. Mater. Chem.* **1997**, *7*, 2069-2075.
[236] Y. Murakami, T. Komatsu and N. Kojima, *Synthetic Met.* **1999**, *103*, 2157-2158.
[237] O. Roubeau, J. G. Haasnoot, E. Codjovi, F. Varret and J. Reedijk, *Chem. Mater.* **2002**, *14*, 2559-2566.
[238] A. Desaix, O. Roubeau, J. Jeftic, J. G. Haasnoot, K. Boukheddaden, E. Codjovi, J. Linarès, M. Noguès and F. Varret, *Eur. Phys. J.* **1998**, *6*, 183-193.
[239] Y. Moritomo, Y. Isobe, X. J. Liu, T. Kawamoto, A. Nakamoto, N. Kojima, K. Kato and M. Takata, *J. Lumin.* **2004**, *108*, 229-232.

[240] N. O. Moussa, D. Ostrovskii, V. M. Garcia, G. Molnar, K. Tanaka, A. B. Gaspar, J. A. Real and A. Bousseksou, *Chem. Phys. Lett.* **2009**, *477*, 156-159.
[241] A. Nakamoto, N. Kojima, X. J. Liu, Y. Moritomo and A. Nakamura, *Polyhedron* **2005**, *24*, 2909-2912.
[242] O. Roubeau, B. Agricole, R. Clerac and S. Ravaine, *J. Phys. Chem. B* **2004**, *108*, 15110-15116.
[243] A. Nakamoto, Y. Ono, N. Kojima, D. Matsumura, T. Yokoyama, X. J. Liu and Y. Moritomo, *Synthetic Met.* **2003**, *137*, 1219-1220.
[244] O. Roubeau, J. M. A. Gomez, E. Balskus, J. J. A. Kolnaar, J. G. Haasnoot and J. Reedijk, *New J. Chem.* **2001**, *25*, 144-150.
[245] H. Matsukizono, K. Kuroiwa and N. Kimizuka, *J. Am. Chem. Soc.* **2008**, *130*, 5622-5623.
[246] K. Kuroiwa, T. Shibata, S. Sasaki, M. Ohba, A. Takahara, T. Kunitake and N. Kimizuka, *J. Polym. Sci. A.* **2006**, *44*, 5192-5202.
[247] O. Roubeau, A. Colin, W. Schmitt and R. Clerac, *Angew. Chem. Int. Ed.* **2004**, *43*, 3283-3286.
[248] T. Fujigaya, D. L. Jiang and T. Aida, *J. Am. Chem. Soc.* **2003**, *125*, 14690-14691.
[249] P. Grondin, O. Roubeau, M. Castro, H. Saadaoui, A. Colin and R. Clérac, *Langmuir* **2010**, *26*, 5184-5195.
[250] A. Suzuki, M. Fujiwara and M. Nishijima, *Colloid Polym. Sci.* **2008**, *286*, 525-534.
[251] J.-F. Létard, O. Nguyen and N. Daro, *Eur. Patent WO2007065996,* **2007**.
[252] E. Coronado, J. R. Galan-Mascaros, Monrabal-capilla M., Garcia-Martinez J. and Pardo-Ibànez P., *Adv. Mater.* **2007**, *19*, 1359-1361.
[253] C. Thibault, G. Molnar, L. Salmon, A. Bousseksou and C. Vieu, *Langmuir* **2010**, *26*, 1557-1560.
[254] T. Forestier, A. Kaiba, S. Pechev, D. Denux, P. Guionneau, C. Etrillard, N. Daro, E. Freysz and J. F. Letard, *Chem. Eur. J.* **2009**, *15*, 6122-6130.
[255] P. Sonar, C. M. Grunert, Y. L. Wei, J. Kusz, P. Gutlich and A. D. Schluter, *Eur. J. Inorg. Chem.* **2008**, 1613-1622.
[256] T. Fujigaya, D. L. Jiang and T. Aida, *J. Am. Chem. Soc.* **2005**, *127*, 5484-5489.
[257] N. Kojima, Y. Murakami, T. Komatsu and T. Yokoyama, *Synthetic Met.* **1999**, *103*, 2154-2154.

[258] A. Michalowicz, J. Moscovici, J. Charton, F. Sandid, F. Benamrane and Y. Garcia, *J. Synchrotron Radiat.* **2001**, *8*, 701-703.
[259] E. Smit, B. Manoun and D. de Waal, *J. Raman Spectrosc.* **2001**, *32*, 339-344.
[260] E. Smit, D. de Waal and A. M. Heyns, *Mater. Res. Bull.* **2000**, *35*, 1697-1707.
[261] L. A. Sheludyakova and L. G. Lavrenova, *J. Struct. Chem.* **1997**, *38*, 853-856.
[262] O. G. Shakirova, L. G. Lavrenova, Y. G. Shvedenkov, V. N. Ikorskii, V. A. Varnek, L. A. Sheludyakova, V. L. Varand, T. A. Krieger and S. V. Larionov, *J. Struct. Chem.* **2000**, *41*, 790-797.
[263] S. Takeda, T. Ueda, A. Watanabe and G. Maruta, *Polyhedron* **2001**, *20*, 1263-1267.
[264] L. N. Mazalov, I. P. Asanov and V. A. Varnek, *J. Electron Spectrosc.* **1998**, *96*, 209-214.
[265] E. D. Loutete-Dangui, F. Varret, E. Codjovi, P. R. Dahoo, H. Tokoro, S. Ohkoshi, C. Eypert, J. F. Letard, J. M. Coanga and K. Boukheddaden, *Phys. Rev. B* **2007**, *75*, (184425)-1-7.
[266] V. Ksenofontov, Y. Garcia, S. J. Campbell, Y. Boland, J. S. Lord and P. Gutlich, *Physica B.* **2006**, *374*, 126-129.
[267] Y. Garcia, S. J. Campbell, J. S. Lord, Y. Boland, V. Ksenofontov and P. Gutlich, *J. Phys. Chem. B* **2007**, *111*, 11111-11119.
[268] C. Timm and U. Schollwock, *Phys. Rev. B* **2005**, *71*, (224414)-1-8.
[269] H. O. Jeschke, L. A. Salguero, B. Rahaman, C. Buchsbaum, V. Pashchenko, M. U. Schmidt, T. Saha-Dasgupta and R. Valenti, *New J. Phys.* **2007**, *9*, 448-461.
[270] J.-F. Létard, N. Daro and S. Auffret, *Eur. Patent WO2009007534,* **2009**.
[271] A. Bousseksou, C. Vieu, J.-F. Létard, P. Demont, J.-P. Tuchagues, M. Laurent, M. Jerome and S. Lionel, *Eur. Patent WO03019695,* **2003**.
[272] D. W. Engelfriet, G. C. Verschoor and W. Denbrinker, *Acta Crystallogr. B.* **1980**, *36*, 1554-1560.
[273] T. Kosone, C. Kanadani, T. Saito and T. Kitazawa, *Polyhedron* **2009**, *28*, 1930-1934.
[274] A. B. Gaspar, M. C. Muñoz and J. A. Real, *J. Mater. Chem.* **2006**, *16*, 2522-2533.

[275] J. A. Real, A. B. Gaspar, M. C. Muñoz, P. Gütlich, V. Ksenofontov and H. Spiering, *Top. Curr. Chem.* **2004**, *233*, 167-193.
[276] G. Chastanet, C. Carbonera, C. Mingotaud and J.-F. Létard, *J. Mater. Chem.* **2004**, *14*, 3516-3523.
[277] K. Nakano, S. Kawata, K. Yoneda, A. Fuyuhiro, T. Yagi, S. Nasu, S. Morimoto and S. Kaizaki, *Chem. Comm.* **2004**, 2892-2893.
[278] A. B. Gaspar, V. Ksenofontov, V. Martinez, M. C. Muñoz, J. A. Real and P. Gütlich, *Eur. J. Inorg. Chem.* **2004**, 4770-4773.
[279] K. Nakano, N. Suemura, K. Yoneda, S. Kawata and S. Kaizaki, *Dalton Trans.* **2005**, 740-743.
[280] B. Weber and E. Kaps, *Heteroatom Chem.* **2005**, *16*, 391-397.
[281] N. Ortega-Villar, A. L. Thompson, M. C. Munoz, V. M. Ugalde-Saldivar, A. E. Goeta, R. Moreno-Esparza and J. A. Real, *Chem. Eur. J.* **2005**, *11*, 5721-5734.
[282] K. Yoneda, K. Nakano, J. Fujioka, K. Yamada, T. Suzuki, A. Fuyuhiro, S. Kawata and S. Kaizaki, *Polyhedron* **2005**, *24*, 2437-2442.
[283] K. Yoneda, K. Adachi, S. Hayami, Y. Maeda, M. Katada, A. Fuyuhiro, S. Kawata and S. Kaizaki, *Chem. Comm.* **2006**, 45-47.
[284] M. Quesada, P. de Hoog, P. Gamez, O. Roubeau, G. Aromi, B. Donnadieu, C. Massera, M. Lutz, A. L. Spek and J. Reedijk, *Eur. J. Inorg. Chem.* **2006**, 1353-1361.
[285] J. L. M. Amoore, C. J. Kepert, J. D. Cashion, B. Moubaraki, S. M. Neville and K. S. Murray, *Chem. Eur. J.* **2006**, *12*, 8220-8227.
[286] A. B. Gaspar, V. Ksenofontov, S. Reiman, P. Gütlich, A. L. Thompson, A. E. Goeta, M. C. Muñoz and J. A. Real, *Chem. Eur. J.* **2006**, *12*, 9289-9298.
[287] K. S. Murray, *Eur. J. Inorg. Chem.* **2008**, 3101-3121.
[288] J. A. Real, A. B. Gaspar, V. Niel and M. C. Munoz, *Coord. Chem. Rev.* **2003**, *236*, 121-141.
[289] M. Hasegawa, F. Renz, T. Hara, Y. Kikuchi, Y. Fukada, J. Okubo, T. Hoshi and W. Linert, *Chem. Phys.* **2002**, *277*, 21-30.
[290] G. Zhou., *Internal Report, CMAT Laboratory, UCL* **2003**.
[291] B. Muls., *Master Thesis UCL* **2003**.
[292] G. Marinescu., *Internal Report, CMAT Laboratory, UCL* **2003**.
[293] The structure was partially described in 'B. Muls, *Master thesis, UCL*, **2003**.
[294] The bond lengths of atoms involved in disorder were neglected in the distance range

[295] Carlin, R. L. and A. J. van Duyneveldt. *Magnetic properties of transition metal compounds*., Springer - Verlag (Berlin), **1977**.
[296] Gütlich, P. and A. H. Goodwin. *Spin Crossover in Transition Metal Compounds*., Springer, **2004**.
[297] Although some hydrogen atoms were not placed in some structures and then that numbers of H-bonds must be taken in account with care, a clear modification of the supramolecular network surrounded the dinuclear units can be claimed.
[298] F. Bentiss, M. Lagrenee and D. Barbry, *Tetrahedron Lett.* **2000**, *41*, 1539-1541.
[299] R. A. Bowie, M. D. Gardner, D. G. Neilson, K. M. Watson, S. Mahmood and V. Ridd, *J. Chem. Soc. , Perkin Trans. 1* **1972**, 2395-2399.
[300] L. Cheng, W. X. Zhang, B. H. Ye, J. B. Lin and X. M. Chen, *Inorg. Chem.* **2007**, *46*, 1135-1143.
[301] G. Giuffrida, G. Calogero, G. Guglielmo, V. Ricevuto, M. Ciano and S. Campagna, *Inorg. Chem.* **1993**, *32*, 1179-1183.
[302] M. Shakir, S. Parveen, N. Begum and P. Chingsubam, *Trans. Met. Chem.* **2004**, *29*, 196-199.
[303] M. Shakir, S. Parveen, N. Begum and Y. Azim, *Polyhedron* **2003**, *22*, 3181-3186.
[304] H. M. Burke, J. F. Gallagher, M. T. Indelli and J. G. Vos, *Inorg. Chim. Acta* **2004**, *357*, 2989-3000.
[305] U. Garcia-Couceiro, O. Castillo, J. Cepeda, A. Luque, S. Perez-Yanez and P. Roman, *Inorg. Chim. Acta* **2009**, *362*, 4212-4218.
[306] G. Gupta, K. T. Prasad, B. Das and K. M. Rao, *Polyhedron* **2010**, *29*, 904-910.
[307] G. Calogero, G. Giuffrida, S. Serroni, V. Ricevuto and S. Campagna, *Inorg. Chem.* **1995**, *34*, 541-545.
[308] J. A. Kitchen, N. G. White, M. Boyd, B. Moubaraki, K. S. Murray, P. D. W. Boyd and S. Brooker, *Inorg. Chem.* **2009**, *48*, 6670-6679.
[309] G. S. Matouzenko, A. Bousseksou, S. A. Borshch, M. Perrin, S. Zein, L. Salmon, G. Molnar and S. Lecocq., *Inorg. Chem.* **2004**, *43,* 227-236.
[310] N. Moliner, M. C. Munoz, S. Letard, J. F. Letard, X. Solans, R. Burriel, M. Castro, O. Kahn and J. A. Real, *Inorg. Chim. Acta* **1999**, *291*, 279-288.
[311] S. Zein, G. S. Matouzenko and S. A. Borshch, *Chem. Phys. Lett.* **2004**, *397*, 475-478.

[312] Y. Miyazaki, T. Nakamoto, S. Ikeuchi, K. Saito, A. Inaba, M. Sorai, T. Tojo, T. Atake, G. S. Matouzenko, S. Zein and S. A. Borshch, *J. Phys. Chem. B* **2007**, *111*, 12508-12517.
[313] P. J. Kunkeler, P. J. vanKoningsbruggen, J. P. Cornelissen, A. N. vanderHorst, A. M. vanderKraan, A. L. Spek, J. G. Haasnoot and J. Reedijk, *J. Am. Chem. Soc.* **1996**, *118*, 2190-2197.
[314] N. Moliner, M. C. Munoz, P. J. van Koningsbruggen and J. A. Real, *Inorg. Chim. Acta* **1998**, *274*, 1-6.
[315] N. Moliner, A. B. Gaspar, M. C. Munoz, V. Niel, J. Cano and J. A. Real, *Inorg. Chem.* **2001**, *40*, 3986-3991.
[316] S. Pillet and C. Lecomte, *J. Phys. Conf. Ser.* **2007**, *21*, 221-226.
[317] A. B. Gaspar, M. C. Muñoz, N. Moliner, V. Ksenofontov, G. Levchenko, P. Gutlich and J. A. Real, *Monatsh. Chem.* **2003**, *134*, 285-294.
[318] A. L. Rheingold, P. Saisuwan and N. C. Thomas, *Inorg. Chim. Acta* **1993**, *214*, 41-45.
[319] U. Hartmann and H. Vahrenkamp, *Inorg. Chim. Acta* **1995**, *239*, 13-17.
[320] M. H. Klingele, P. D. W. Boyd, B. Moubaraki, K. S. Murray and S. Brooker, *Eur. J. Inorg. Chem.* **2006**, 573-589.
[321] M. L. Tong, C. G. Hong, L. L. Zheng, M. X. Peng, A. Gaita-Arino and J. M. C. Juan, *Eur. J. Inorg. Chem.* **2007**, 3710-3717.
[322] A. J. Muller, J. Conradie, W. Purcell, S. S. Basson and J. A. Venter, *S. Afr. J. Chem.* **2010**, *63*, 11-19.
[323] S. Rubino, P. Portanova, A. Albanese, G. Calvaruso, S. Orecchio, G. Fontana and G. C. Stocco, *J. Inorg. Biochem.* **2007**, *101*, 1473-1482.
[324] U. Garcia-Couceiro, O. Castillo, A. Luque, G. Beobide and P. Roman, *Acta Crystallogr. E.* **2004**, *60*, M720-M722.
[325] J. Hua, L. Gao and B. Y. Li, *Acta Crystallogr. E.* **2009**, *65*, M1106-MU848.
[326] P. J. van Koninsbruggen, K. Goubitz, J. Haasnoot and J. Reedijk, *Inorg. Chim. Acta* **1998**, *268*, 37-42.
[327] N. G. White, J. A. Kitchen and S. Brooker, *Eur. J. Inorg. Chem.* **2009**, 1172-1180.
[328] R. Prins, P. J. M. W. L. Birker, J. G. Haasnoot, G. C. Verschoor and J. Reedijk, *Inorg. Chem.* **1985**, *24*, 4128-4133.
[329] Z. S. Meng, L. Yun, W. X. Zhang, C. G. Hong, R. Herchel, Y. C. Ou, J. D. Leng, M. X. Peng, Z. J. Lin and M. L. Tong, *Dalton Trans.* **2009**, 10284-10295.

[330] J. A. Kitchen, A. Noble, C. D. Brandt, B. Moubaraki, K. S. Murray and S. Brooker, *Inorg. Chem.* **2008**, *47*, 9450-9458.
[331] M. X. Peng, C. G. Hong, C. K. Tan, J. C. Chen and M. L. Tong, *J. Chem. Crystallogr.* **2006**, *36*, 703-707.
[332] M. A. Omary, *Eur. Patent WO2010016990,* **2010**.
[333] W. J. Wang, C. H. Lin, J. S. Wang and S. W. Tang, *Mol. Cryst. Liq. Cryst.* **2006**, *456*, 209-219.
[334] G. Gasser, J. D. Carr, S. J. Coles, S. J. Green, M. B. Hursthouse, S. M. Cafferkey, H. Stoeckli-Evans and J. H. R. Tucker, *J. Organomet. Chem.* **2010**, *695*, 249-255.
[335] A synthesis from $(NH_4)_2Fe(SO_4)_2.6H_2O$ was previously attempted in 'B. Muls, *Master Thesis UCL*, **2003**' giving a mixture of complexes containing ammonium cation.
[336] Other compositions or dimensionalities such as dinuclears were also investigated.
[337] F. S. Keij, R. A. G. de Graaf, J. G. Haasnoot and J. Reedijk, *J. Chem. Soc. , Dalton T.* **1984**, 2093-2097.
[338] This observation is supported by the expected fast rotation around the N-N, CH-Csalicyl anc C-C_{pyr} bonds in solution.
[339] Although a very weak and short-live photochromism is perhaps present for $\mathbf{C}^{13}$ but not possible to detect with our experimental setup.
[340] An enhancement of this oxidation phenomenon by light or by local temperature increase cannot be excluded.
[341] R. M. Golding, K. F. Mok and J. F. Duncan, *Inorg. Chem.* **1966**, *5*, 774-778.
[342] A. Barbieri, G. Accorsi and N. Armaroli, *Chem. Comm.* **2008**, 2185-2193.
[343] Lakowicz, J. R. *Principles of Fluorescence Spectroscopy*., Springer, Singapore **2006**.
[344] R. C. Evans, P. Douglas and C. J. Winscom, *Coord. Chem. Rev.* **2006**, *250*, 2093-2126.
[345] Blasse, G. and B. C. Grabmaier. *Luminescent Materials*., Springer-Verlag, **1994**.
[346] G. S. Hanan, C. R. Arana, J. M. Lehn and D. Fenske, *Angew. Chem. Int. Ed. Engl.* **1995**, *34*, 1122-1124.
[347] H. Sleiman, P. Baxter, J. M. Lehn and K. Rissanen, *Chem. Comm.* **1995**, 715-716.
[348] P. Baxter, J. M. Lehn, A. De Cian and J. Fisher, *Angew. Chem. Int. Ed.* **1993**, *32*, 89-90.

[349] P. Baxter, J. M. Lehn, J. Fisher and M.-T. Youinou, *Angew. Chem. Int. Ed.* **1994**, *106*, 2432-2434.
[350] L. N. Dawe and L. K. Thompson, *Angew. Chem. Int. Ed.* **2007**, *46*, 7440-7444.
[351] L. N. Dawe, K. V. Shuvaev and L. K. Thompson, *Inorg. Chem.* **2009**, *38*, 2334-2359.
[352] Y. S. Moroz, K. Kulon, M. Haukka, E. Gumienna-Kontecka, H. Kozlowski, F. Meyer and I. O. Fritsky, *Inorg. Chem.* **2008**, *47*, 5656-5665.
[353] M. Ruben, J. Rojo, F. J. Romero-Salguero, L. H. Uppadine and J. M. Lehn, *Angew. Chem. Int. Ed.* **2004**, *43*, 3644-3662.
[354] U. Ziener, J. M. Lehn, A. Mourran and M. Moller, *Chem. Eur. J.* **2002**, *8*, 951-957.
[355] O. Roubeau and R. Clérac, *Eur. J. Inorg. Chem.* **2008**, 4325-4342.
[356] M. Ruben, E. Breuning, J. M. Lehn, V. Ksenofontov, F. Renz and P. Gütlich, *Chem. Eur. J.* **2003**, *9*, 4422-4429.
[357] M. Ruben, E. Breuning, J. M. Lehn, V. Ksenofontov, F. Renz and P. Gütlich, *Chem. Eur. J.* **2003**, *9*, 5176-5176.
[358] M. Ruben, U. Ziener, J. M. Lehn, V. Ksenofontov, P. Gütlich and B. M. Vaughan Gavin, *Chem. Eur. J.* **2004**, *11*, 94-100.
[359] M. Ruben, E. Breuning, J. M. Lehn, V. Ksenofontov, P. Gütlich and G. Vaughan, *Magnetism and Magnetic Materials* **2004**, *272-276*, E715-E717.
[360] A. R. Stefankiewicz and J. M. Lehn, *Chem. Eur. J.* **2009**, *15*, 2500-2503.
[361] A. K. Boudalis, J. M. Clemente-Juan, F. Dahan, V. Psycharis, C. P. Raptopoulou, B. Donnadieu, Y. Sanakis and J. P. Tuchagues, *Inorg. Chem.* **2008**, *47*, 11314-11323.
[362] L. K. Thompson, *Coord. Chem. Rev.* **2002**, *233-234*, 193-206.
[363] B. Graham, M. T. W. Hearn, P. C. Junk, C. M. Kepert, F. E. Mabbs, B. Moubaraki, K. S. Murray and L. Spiccia, *Inorg. Chem.* **2001**, *40*, 1536-1543.
[364] K. L. V. Mann, E. Psillakis, J. C. Jeffery, L. H. Rees, N. M. Harden, J. A. McCleverty, M. D. Ward, D. Gatteschi, F. Totti, F. E. Mabbs, E. J. L. Mcinnes, P. C. Riedi and G. M. Smith, *J. Chem. Soc. , Dalton T.* **1999**, 339-348.
[365] R. H. Holm, P. Kennepohl and E. I. Solomon, *Chem. Rev.* **1996**, *96*, 2239-2314.
[366] V. Chandrasekhar, L. Nagarajan, R. Clérac, S. Ghosh and S. Verma, *Inorg. Chem.* **2008**, *47*, 1067-1073.

[367] G. L. J. A. Rikken and E. Raupach, *Nature* **1997**, *390*, 493-494.
[368] L. D. Barron, *Nature Materials* **2008**, *7*, 691-692.
[369] von Zelewsky, A. *Stereochemistry of Coordination Compounds*., J. Wiley & Sons, Chichester **1996**.
[370] Sokolov, V. I. *Chiral and Optical Activity in Organometallic Compounds*., Gordon & Beach Science Publishers, New York **1990**.
[371] J. Crassous, *Chem. Soc. Rev.* **2009**, *38*, 830-845.
[372] A. Fragoso, M. L. Kahn, A. Castineiras, J. P. Sutter, K. Olivier and R. Cao, *Chem. Comm.* **2000**, 1547-1548.
[373] S. J. Loeb and C. J. Willis, *Inorg. Chem.* **1981**, *20*, 2791-2794.
[374] A. Burkhardt, E. T. Spielberg, H. Gorls and W. Plass, *Inorg. Chem.* **2008**, *47*, 2485-2493.
[375] L. L. Fan, F. S. Guo, L. Yun, Z. J. Lin, R. Herchel, J. D. Leng, Y. C. Ou and M. L. Tong, *Dalton Trans.* **2010**, *39*, 1771-1780.
[376] W. E. Hatfield and F. L. Bunger, *Inorg. Chem.* **1969**, *8*, 1194-1995.
[377] A. W. Addison, T. N. Rao, J. Reedijk, J. Vanrijn and G. C. Verschoor, *J. Chem. Soc. , Dalton Trans.* **1984**, 1349-1356.
[378] J. Drummond and J. S. Wood, *J. Chem. Soc. , Dalton Trans.* **1972**, 365-369.
[379] van Vleck, J. H. *The theory of electric and magnetic susceptibility*., Oxford University Press, **1932**.
[380] K. Kambe, *Phys. Soc. Jpn.* **1950**, *5*, 48-51.
[381] C. J. O'Connor, *Prog. Inorg. Chem.* **1982**, *29*, 203-283.
[382] S. H. Gou, M. Qian, Z. Yu, C. Y. Duan, X. F. Sun and W. Huang, *J. Chem. Soc. , Dalton T.* **2001**, 3232-3237.
[383] L.-P. Lu, X. P. Lu and M.-L. Zhu, *Acta Cryst. C.* **2007**, *63*, m374-
[384] A. R. Paital, M. Mikuriya and D. Ray, *Eur. J. Inorg. Chem.* **2002**, 5360-
[385] S. V. Larionov, T. E. Kokina, L. A. Glinskaya and R. F. Klevtsova, *Russ. J. Coord. Chem.* **2002**, *28*, 560-564.
[386] A. R. Paital, W. T. Wong, G. Aromi and D. Ray, *Inorg. Chem.* **2007**, *46*, 5727-5733.
[387] M. Fondo, N. Ocampo, A. M. Garcia-Deibe, R. Vicente, M. Corbella, M. R. Bermejo and J. Sanmartin, *Inorg. Chem.* **2006**, *45*, 255-262.
[388] C. H. Ng, T. S. Chong, S. G. Teoh and S. W. Ng, *J. Coord. Chem.* **2005**, *58*, 1455-1461.

[389] M. Fondo, A. M. Garcia-Deibe, N. Ocampo, J. Sanmartin, M. R. Bermejo and A. L. Llamas-Saiz, *Dalton Trans.* **2006**, 4260-4270.
[390] M. Fondo, A. M. Garcia-Deibe, N. Ocampo, J. Sanmartin and M. R. Bermejo, *Dalton Trans.* **2007**, 414-416.
[391] N. Matsushita and A. Taira, *Synthetic Met.* **1999**, *102*, 1787-1788.
[392] F. Robert., *Master Thesis UCL* **2006**.
[393] P. Adler, H. Spiering and P. Gütlich, *Inorg. Chem.* **1987**, *26*, 3840-3845.
[394] K. Ogawa, J. Harada, T. Fujiwara and S. Yoshida, *J. Phys. Chem. A* **2001**, *105*, 3425-3427.
[395] T. Sekikawa, T. Kobayashi and T. Inabe, *J. Phys. Chem. A* **1997**, *101*, 644-649.
[396] K. Ogawa, J. Harada, T. Fujiwara and H. Takahashi, *Chem. Lett.* **2004**, *33*, 1446-1447.
[397] A. Thiel, A. Bousseksou, M. Verelst, F. Varret and J. P. Tuchagues, *Chem. Phys. Lett.* **1999**, *302*, 549-554.
[398] F. Tuna, M. R. Lees, G. J. Clarkson and M. J. Hannon, *Chem. Eur. J.* **2004**, *10*, 5737-5750.
[399] A. D. Naik, J. Marchand-Brynaert and Y. Garcia, *Synthesis* **2008**, *1*, 149-154.
[400] H. Imai, K. Inoue, K. Kikuchi, Y. Yoshida, M. Ito, T. Sunahara and S. Onaka, *Angew. Chem. Int. Ed.* **2004**, *43*, 5618-5621.
[401] A. D. Cutland-Van Noord, J. W. Kampf and V. L. Pecoraro, *Angew. Chem. Int. Ed.* **2002**, *41*, 4667-4670.
[402] J. D. Ranford, J. J. Vittal, D. Q. Wu and X. D. Yang, *Angew. Chem. Int. Ed.* **1999**, *38*, 3498-3501.
[403] C. V. Yelamaggad, A. S. Achalkumar, D. S. S. Rao and S. K. Prasad, *J. Org. Chem.* **2009**, *74*, 3168-3171.
[404] Pretsh, E., T. Clerc, J. Seibl, and W. Simon. *Spectral data for structure determination of organic compounds.*, Springer Verlag (Berlin), **1989**.
[405] Nakamoto, K. *Infrared and Raman Spectra of Inorganic and Coordination Compounds. Part B: Applications in Coordination, Organomettalic, and Bioinorganic Chemistry.*, John Willey & Sons, Inc., New-York **1997**.
[406] Recoïl, Mössbauer Spectral Analysis Software for Windows, 1.0, K LagarecD. G. Rancourt, Department of Physics, University of Ottawa, Canada, **1998**.
[407] Becker, K. and H. Hickl. *Time-correlated Single Photon Counting Modules; Multi SPC Software. SPC 630 - User Manual*., **2003**.

[408] Muls, B. *Single-Molecules Spectroscopy: Novel methods and their application to the analysis of polyfluorene conjugated polymers*., PhD Thesis, UCL, **2008**.
[409] ShelX97; Program system for crystal structure determination,G. M. Sheldrick, University of Göttingen, **1997**.
[410] A. L. Spek, *Acta Crystallogr. D.* **2009**, *65*, 148-155.
[411] Jaguar, 6.5, Schrodinger, LLC, **2005**.
[412] Gaussian 03, B.04, M. J. Frisch, G. W. Trucks, H. B. Schlegel, G. E. Scuseria, M. A. Robb, J. R. Cheeseman, J. A. Jr. Montgomery, T. Vreven, K. N. Kudin, J. C. Burant, J. M. Millam, S. S. Iyengar, J. Tomasi, V. Barone, B. Mennucci, M. Cossi, G. Scalmani, N. Rega, G. A. Petersson, G. A. Petersson, H. Nakatsuji, M. Hada, M. Ehara, N. Toyota, R. R. Fukuda, J. Hasegawa, M. Ishida, T. Nakajima, Y. Honda, O. Kitao, H. Nakai, M. Klene, X. Li, J. E. Knox, H. P. Hratchian, J. B. Cross, V. Bakken, C. Adamo, J. Jaramillo, R. Gomperts, R. E. Stratmann, O. Yazyev, A. J. Austin, R. Cammi, C. Pomelli, J. W. Ochterski, P. Y. Ayala, K. Morokuma, G. A. Voth, P. Salvador, J. J. Dannenberg, V. G. Zakrzewski, S. Dapprich, A. D. Daniels, M. C. Strain, O. Farkas, D. K. Malick, A. D. Rabuck, K. Raghavachari, J. B. Foresman, J. V. Ortiz, Q. Cui, A. G. Baboul, S. Clifford, J. Cioslowski, B. B. Stefanov, G. Liu, A. Liashenko, P. Piskorz, I. Komaromi, R. L. Martin, D. J. Fox, T. Keith, M. A. Al-Laham, C. Y. Peng, A. Nanayakkara, M. Challacombe, P. M. W. Gill, B. Johnson, W. Chen, M. W. Wong, C. Gonzalez,J. A. Pople, Gaussian, Inc., **2003**.
[413] H. O. Bayer, R. S. Cook and W. C. Von Meyer, *US Patent 3,821,376,* **1974**.

List of publications, communications and awards

Written communications

Papers in international journals

'Insights into the Origin of Solid-State Photochromism and Thermochromism of N-Salicylideneanils: The Intriguing Case of Aminopyridines'

Robert F., Naik A.D., Tinant B., Robiette R., Garcia Y. Chem. Eur. J. 2009, 15, 4327-4342.

Abstract: The relationships between the crystal structure and optical properties of switchable *N*-salicylidene anils have been revised and discussed on the basis of new experimental results and a computational approach. *N*-Salicylidene-3-aminopyridine ($\mathbf{L^3}$) is a versatile thermo- and photochromic molecule. It also exhibits an infinitely slow thermal back relaxation ($k = 9.9 \times 10^{-8}\ s^{-1}$) after photo-switching that is suitable for optical memories. Contrary to reports in the literature, *N*-salicylidene-4-aminopyridine ($\mathbf{L^4}$) is exclusively thermochromic. To explain these unexpected optical properties in the solid state, crystallography combined with UV-visible spectroscopic data was exploited. $\mathbf{L^3}$ was also used as a ligand in new thermochromic coordination complexes $[M^{II}(CH_3OH)_2(\mathbf{L^3})_2(NCX)_2]$, in which M^{II} = Fe, Co, Ni, Cu or Mn and X = S or Se (**1**–**6**), which allowed the fine tuning of the electron density in the photochromic moiety. The influence of the coordination through the nitrogen of the pyridine ring is also fully discussed.

Cited by: Sun M.-L., Zhang L., Lin Q.-P., Zhang J., Yao Y.-G. *Cryst. Growth Des.***2010**, *10*, 1464-1467.

Gavara R., Laia C.A.T., Parola A.J., Pina F. *Chem. Eur. J.* **2010**, *16*, 7760-7766.

'Insights into Crystal Structure/Optical Properties Relationships of New N-salicylidene Anils'

Tinant B., Robert F., Naik A.D., Garcia Y. Acta Cryst. A. 2009, A65, s248.

N-salicylidene aniline derivatives are highly versatile thermo- and photochromic molecules. These are actively studied for many applications like non linear optics, biological activities, information storage and display, etc. Thermo and photochromism occurring in the solid state thanks to reversible equilibria between the uncoloured enol, the yellow *cis*-keto and the red *trans*-keto forms are the main interests of these compounds. All derivatives are described as thermochromic but only a few of them are photochromic. Many authors stress the importance of crystal packing to explain these properties but the molecular environment is also to be considered. Crystallographic study of *N*-salicylidene aniline derivatives is essential for the understanding of molecular properties in solution or in solid state. In this work, we have observed that the dihedral angle between aromatic rings and the crystal packing are not sufficient to predict the photochromism behaviour of the compounds. This is clearly seen with the *N*-salicylidene 4-aminopyridine ($\mathbf{L^4}$) and 2-(3,5-bis(pyridin-2-yl)-1,2,4-triazole-4-ylimino-methyl)-phenol (**Habs**). $\mathbf{L^4}$, a highly twisted molecule, present an open structure with large intermolecular distances and weak C-H···π and π-π stacking interactions. Photo-isomerisation to the *trans*-keto form should be easier thanks to the crystal packing. However, $\mathbf{L^4}$ is only thermochromic. In contrast, **Habs** crystal is formed with highly twisted molecules, packed very closely with strong supramolecular interactions (π-π stacking) but is only photochromic. This observation clearly disagrees with reported conclusions. Finally, a novel interesting molecular conformation has been discovered with the *N*-salicylidene 4-amino- 1,2,4-triazole (**Hsaltrz**) which is packed as supramolecular zig-zag double chains.

'Engineering Solid-State Molecular Switches: N-salicylidene H-heterocycle derivatives'

Robert F., Naik A.D., Hidara F., Tinant B., Robiette R., Wouters J., Garcia Y. Eur. J. Org. Chem. 2010, 621-637 and 579 (coverpage).

Abstract: A supramolecular engineering approach has been developed for a novel family of *N*-salicylidene aniline derivatives to control their thermo- and photochromic behaviours. **Hsaltrz**, **Habs**, **Hsalphen**, **Hsaltz** and **Ksaltz** are versatile molecules built from *N*-heterocycles, which drive the molecular arrangement to form a controlled crystal packing with predesigned optical properties. A complete structural, optical and computational study of powders of these new molecular nano-switches is presented. An *N*-salicylidene aniline derivative possessing no thermo- or photo-induced chromic properties thanks to a specific molecular geometry was sought, and Habs and Hsalphen were designed to enhance π-π stacking interactions. A theoretical study of the crystal packing, combined with time-dependent diffuse reflectance studies of **Habs**, have confirmed the appearance of photochromism at room temperature completed with an unprecedented "spring-type effect" observed during the photochemical relaxation of the metastable *trans*-keto form. The absence of thermochromism in an *N*-salicylidene aniline derivative, induced by the absence of *cis*-keto form, is a unique behaviour, firstly identified and explained for these types of compounds. Finally, **Hsaltz** and **Ksaltz** are the result of a molecular derivation of **Hsaltrz** which allow enhancing the amplitude of thermochromism of these functional materials.

'Influence of a thermochromic anion on the spin crossover of iron(II) trinuclear complexes probed by Mössbauer spectroscopy'

Robert F., Naik A.D., Garcia Y. J. Phys. Conf Ser. 2010, 217, 012031.

Abstract: The insertion of thermochromic anions (**1** and **2**) into triazole based iron(II) trinuclear spin crossover complexes $[Fe^{II}_3(hyetrz)_6(H_2O)_6]$(**1** or **2**)$_4Cl_2$ paves the way to a large panel of multifunctional materials. In addition to a gradual thermo-induced spin conversion of the central metal ion on cooling below room temperature, an unexpected split of the Mössbauer signal of the external iron(II) ions as well as pronounced relaxation phenomenon for the central HS iron(II) ion was discovered. This phenomenon is suggested to be induced by the tautomeric equilibrium between enol and keto forms of the anion.

'Self assembly of asymmetric tetranuclear Cu(II) [2x2] grid-like complexes and of a dinuclear Ni(II) complex from pyridyl-phenol Schiff base ligands'

***Robert F., Tinant B., Clérac R., Jacquemin P-L., Garcia Y., Polyhedron, 2010, 29*, 2739-2746.**

Abstract: Self assembly of *N*-salicylidene 2-aminopyridine (**L1H**) with $Cu(NO_3)_2$•$3H_2O$ affords $[Cu_4$(**L1**$)_4(NO_3)_3(CH_3OH)][Cu$(**L1**$)(NO_3)_2]$(2-aminopyridinium)(NO_3)•$5CH_3OH$ (**1**) which is composed of an asymmetric [2x2] grid-like cationic complex that co-crystallizes with a Cu(II) mononuclear anion. This remarkable tetranuclear unit presents three penta-coordinated and one hexa-coordinated Cu(II) sites. This quadruple helicate structure reveals strong antiferromagnetic coupling (J = - 340(2) cm^{-1}) between Cu(II) ions through a double alkoxo bridge. Reacting L1H with $Cu(NO_3)_2$•$3H_2O$ in slightly different conditions affords however a more symmetric tetranuclear grid-like complex: $[Cu_4$(**L1**$)_4(NO_3)_2(OH)_2]$(2-aminopyridinium)(OH)•CH_3OH (**2**). A dinuclear Ni(II) complex, $[Ni_2$(**L2**$)_2$(**L2H**$)_2(NCS)_2(CH_3OH)_2]$•$2CH_3OH$ (**3**), obtained with another

related donor ligand (**L2H** = *N*-salicylidene 3-aminomethylpyridine) was also prepared.

'Crystal structure of chloro-bis(1,10-phenanthroline) copper(II) o-aminobenzene sulfonate - methanol (2:3), $[Cu(C_{12}H_8N_2)_2Cl]_2[C_6H_3NO_3S]_2 \cdot 3CH_3OH$, at 120 K'

Tinant B., Robert F., Garcia Y. , Z. Kristallogr. NCS, 2010, in press.

'Crystal structure of tris(1,10-phenanthroline)-nickel(II) bis(o-aminobenzenesulfonate) - ethanol (1:1), $[Ni(C_{12}H_8N_2)_3][C_6H_3NO_3S]_2 \cdot C_2H_6OH$, at 120 K'

Tinant B., Robert F., Garcia Y. , Z. Kristallogr. NCS, 2010, in press.

'Crystal structure 2-(2'-pyridyl)-imidazole'

Tinant B., Decamp C., Robert F., Garcia Y. , Z. Kristallogr. NCS, 2010, in press.

'Synthesis and magnetic properties of an iron 1,2-bisthienylperfluorocyclopentene photochromic coordination compound'

Garcia Y., Ksenofontov V., Lapouyade R., Naik A.D., Robert F., Gütlich P., submitted.

Poster communications

'The N-salicylidene aminopyridine : highly versatile thermo- and photo-switchable molecules'

2007 – Université de Mons-Hainaut – *Société Royale de Chimie* meeting.
2007 – Université de Liège – '*Ecole Doctorale CHIM'* meeting.

'Improvement in thermo- and photochromism understanding: the complementary use of UV/Visible spectroscopies, crystallography and Mössbauer spectroscopy'

2008 – Université Catholique de Louvain – PhD students day.
2008 – Université Catholique de Louvain – '*Groupe Francophone de Spectrométrie Mössbauer'* meeting.

'Comparative optical and structural study of thermo- and photo-switchable molecules based on 1,2,4-triazole and pyridine moieties'

2008 – Faculté Notre-Dame de la Paix (Namur) – *Société Royale de Chimie* meeting.

'Comparative optical and structural study of new thermo- and phtochromic molecules based on triazole and pyridine moieties'

2008 – 5th Belgian Crystallographic Symposium - Bruxelles.

'Insertion of N-salicylidene aniline derivatives into iron(II) trinuclear spin crossover materials : towards a novel type of hybrid materials'

2009 – Université de Liège – *Ecole doctorale CHIM* meeting.

'Influence d'un anion thermochrome sur la transition de spin de trinucléaires de Fe(II) sondée par spectroscopie Mössbauer'

2009 – Université Joseph Fourier (Grenoble, France) – *Groupe Francophone de Spectrométrie Mössbauer* meeting.

'Insight into crystal structure/optical properties relationships of new N-salicylidene anils'

2009 – XXV European Crystallographic Symposium – Istanbul (Turkey).

'An unprecedented Optical 'Spring type' Effect in N-salicylidene aniline derivatives'

2009 – Université de Liège – *Société Royale de Chimie* meeting

'A Novel Self-assembled Magnetic Asymmetric and Chiral Nanogrid'

2009 – Université de Liège – *Société Royale de Chimie* meeting

'Self-assembled Magnetic, Asymmetric and Chiral Nanogrids'

2009 – '*Groupe de Recherche Magnétisme et Commutation Moléculaire'* meeting, Dourdan, France.

2010 – Université de Mons – *Ecole Doctorale CHIM* meeting

'N-salicylidene anils as potential thermo/photo-responsive components of functional hybrid materials'

2010 – '*MOLMAT'* conference – Monpellier, France.

'Influence of the insertion of a non aromatic linker on structural and optical properties of N-salicylidene aniline derivatives'

2010 – '*MOLMAT'* conference – Monpellier, France.

Oral communications

'Les dérivés de la N-salicylidène aniline : du photochromisme en phase solide au photomagnétisme'

2007 – Université Catholique de Louvain.

'The N-salicylidene aniline derivatives : highly versatile thermo- and photo-switchable molecules'

2008 – Université Catholique de Louvain – IAP meeting.

'Towards a control of the thermo- and the photochromic properties of N-salicylidene aniline derivatives'

2009 – Université Catholique de Louvain – PhD students day.

'Influence d'un anion thermochrome sur la transition de spin de trinucléaires de Fe(II) sondée par spectroscopie Mössbauer'

2009 – Université Catholique de Louvain – '*Groupe Francophone de Spectrométrie Mössbauer'* meeting.

'Engineering novel solid-state molecular switches : N-salicylidene N-heterocyle derivatives'

2009 – Dourdan (France) – '*Groupe de Recherche Magnétisme et Commutation Moléculaire'* meeting.

'Syntheses of N-salicylidene anils based switches : inorganic-organic hybrid architectures'

2010 – Université Catholique de Louvain – IAP meeting.

'N-salicylidene aniline derivatives: from organic molecular switches to multifunctional organic-inorganic architectures'

2010 – Université de Mons – *Ecole Doctorale CHIM* meeting.

'Transmission d'une thermo-sensibilité d'un anion vers un compose hybride à transition de spin: les premiers pas vers les effets AD-LISC et AD-TISC.

2010 – Université de Lisbonne (Portugal) – '*Groupe Francophone de Spectrométrie Mössbauer'* meeting.

Awards

Belgochlor Award – Award of the best poster communication

2007 – Université de Mons-Hainaut – *Société Royale de Chimie* meeting.

Award of the best poster communication

2008 – 5th Belgian Crystallographic Symposium - Bruxelles.

Appendix

Crystal structures data

Table 19 Crystal data and structure refinement for $\mathbf{L^{2\text{-}5}}$.

	$\mathbf{L^4}$		$\mathbf{L^5}$	$\mathbf{L^3}$ [157]	$\mathbf{L^2}$ [98]
Empirical formula	$C_{12}H_{10}N_2O$	$C_{12}H_{10}N_2O$	$C_{12}H_9ClN_2O$	$C_{12}H_{10}N_2O$	$C_{12}H_{10}N_2O$
fw	198.22	198.22	232.66	198.22	198.22
T [K]	120(2)	250(2)	120(2)	298	298
Crystal system	Ortho-rhombic	Ortho-rhombic	Mono-clinic	Mono-clinic	Ortho-rhombic
space group	$P2_12_12_1$ (No 19)	$P2_12_12_1$ (No 19)	$P2_1/n$ (No 14)	$P2_1/n$ (No 14)	$Pbca$ (No 61)
a [Å]	7.052(3)	7.157(3)	4.519(2)	15.233(8)	6.329(1)
b [Å]	12.184(4)	12.223(4)	19.091(8)	4.692(2)	14.778(3)
c [Å]	22.712(6)	22.872(6)	11.935(5)	14.316(7)	21.808(5)
β [°]	-	-	94.80(2)	98.19(4)	-
V [Å³]	1952(1)	2001(1)	1026.0(8)	1012.9	2039.7
Z	8	8	4	4	8
ρ_{calc} [Mg.m^{-3}]	1.35	1.32	1.51	1.30	1.30
F(000)	832	832	480	416	832
μ [mm^{-1}]	0.089	0.086	0.348	0.092	0.691
Crystal size [mm]	0.22 x 0.15 x 0.08	0.22 x 0.15 x 0.08	0.5 x 0.15 x 0.05	0.7 x 0.25 x 0.15	0.5 x 0.25 x 0.15
θ max [°]	22.2	22.2	23.3	-	-
Reflections collected/ unique	12393/ 2455	7225/ 2423	12064/ 1408	1329	1274
R_{int}	0.059	0.068	0.084	-	-
R_1 [I>2σ(I)]	0.0332 [2299]	0.0448 [2021]	0.0575 [1240]	0.059	0.049
wR_2	0.0771	0.1084	0.1583	-	-
Largest peak and hole	0.18 and -0.19	0.145 and -0.14	0.47 and -0.34	-	-

Table 20 Intra-molecular hydrogen bonds in $\mathbf{L}^{2\text{-}5}$ crystal structures.

	T [K]	D-H•••A	D-H [Å]	H•••A [Å]	D•••A [Å]	D-H•••A [°]
$\mathbf{L}^4$	120(2)	O15H15•••N7	0.96(3)	1.72(3)	2.596(4)	149(1)
		O115H115•••N107	1.04(3)	1.64(3)	2.602(4)	151(1)
	250(2)	O15H15•••N7	0.98(3)	1.72(3)	2.604(6)	149(1)
		O115H115•••N107	0.99(3)	1.67(3)	2.607(6)	155(1)
$\mathbf{L}^3$ [157]	298	O1H10•••N1	0.91	1.91	2.604	132
$\mathbf{L}^2$ [98]	298	O1H10•••N1	0.90	1.81	2.581	141
$\mathbf{L}^5$	120(2)	O15H15•••N7	0.89(5)	1.83(5)	2.612(6)	146(1)

Table 21 Intra- and inter-molecular π-π stacking interactions in $\mathbf{L^{2\text{-}5}}$ crystal structures.

	T [K]	Imine ••• $ring_{pyr}$ [Å][a]	Imine ••• $ring_{pyr}$ [°][b]	Imine ••• $ring_{salicyl}$ [Å][c]	Imine ••• $ring_{salicyl}$ [°][d]	$Ring_{salicyl}$ ••• $ring_{pyr}$ [Å]	$Ring_{salicyl}$ ••• $ring_{pyr}$ [°][e]
$\mathbf{L^4}$	120(2)	4.17 (3)	36 (1)	4.26 (3)	12 (1)	-	-
		3.72 (3)	36 (1)	3.63 (3)	12 (1)	-	-
	250(2)	4.24 (3)	36 (1)	4.32 (3)	13 (1)	-	-
		3.77 (3)	36 (1)	3.69 (3)	13 (1)	-	-
$\mathbf{L^3}$[157]	298	3.44	13	3.44	2	-	-
$\mathbf{L^2}$[98]	298	-	-	-	-	3.89	5
$\mathbf{L^5}$	120(2)	3.34 (5)	3 (1)	3.35 (5)	2 (1)	-	-

[a] C8-N7···N101-C102-C103-C104-C105-C106. [b] Angle between imine and pyridine planes. [c] C108-N107···C9-C10-C11-C12-C13-C14. [d] Angle between imine and salicyl planes. [e] Angle between rings.

Table 22 Intra- and inter-molecular C-H···π interactions in $\mathbf{L^{2\text{-}4}}$ crystal structures.

	T [K]	Atoms involved[a]	d between centroids [Å]	C-H•••ring [°][b]
$\mathbf{L^4}$	100 (2)	N1-C2-C3-C4-C5-C6[a]//C2-H2	2.78 (3)	13 (1)
	100 (2)	N101-C102-C103-C104-C105-C106[b]//C8-H8	2.80 (3)	7 (1)
	100 (2)	C109-C110-C111-C112-C113-C114[c]//C105-H105	2.97 (3)	9 (1)
	250 (2)	N1-C2-C3-C4-C5-C6[a]//C2-H2	2.82 (4)	12 (1)
	250(2)	N101-C102-C103-C104-C105-C106[b]//C8-H8	2.86 (4)	7 (1)
$\mathbf{L^2}$ [98]	298	N2-C8-C9-C10-C11-C12[d]//C4-H2	2.94	4
		C1-C2-C3-C4-C5-C6[e]// C11-H8	2.76	6

[a] Atoms marked with a superscripted letter are generated by the following symmetry operations: a = 1/2 + x, 3/2 - y, 1 - z; b = 1 - x, y – 1/2, 1/2 - z; c=1 - x, 1/2 + y, 1/2 - z; d = 3/2 - x, y – 1/2, z; e = 1/2 - x, 1/2 + y, z. [b] Angle between C-H axis and aromatic ring normal.

Table 23 Selected bond lengths and angles for $\mathbf{L^{2\text{-}5}}$ crystal structures.

	$\mathbf{L^4}$		$\mathbf{L^3}$[157]	$\mathbf{L^2}$ [98]	$\mathbf{L^5}$
T [K]	120 (2)	250 (2)	298	298	120 (2)
Φ [°]	41 (1) and 49(1)	41 (1) and 49(1)	15	5	5 (1)
Dist. [Å][a]	4.99	5.06	4.69	5.59	4.52
N7-$C_{pyr.}$ [Å] [b]	1.422 (3) and 1.421 (3)	1.418 (5) and 1.421 (5)	1.410	1.413	1.417 (6)
N7-C8 [Å] [b]	1.292 (3) and 1.288 (3)	1.282 (5) and 1.289 (4)	1.277	1.285	1.297 (6)
C8-C9 [Å] [b]	1.449 (4) and 1.455 (3)	1.457 (5) and 1.457 (5)	1.449	1.448	1.453 (6)
C9-C10 [Å] [b]	1.408 (4) and 1.405 (3)	1.393 (5) and 1.401 (5)	1.409	1.401	1.403 (6)
C10-O15 [Å] [b]	1.358 (3) and 1.362 (3)	1.362 (5) and 1.362 (4)	1.340	1.349	1.363 (5)

[a] Average distance between molecular centroids. [b] Distances with respect to Scheme 6.

Table 24 Crystal data and structure refinement for **Hsaltrz**, **Habs**, **Hsalphen**, **Hsaltz** and **Ksaltz.**

	Hsaltrz	**Habs**	**Hsalphen**	**Hsaltz**	**Ksaltz**
Empirical formula	$C_9H_8N_4O$	$C_{19}H_{14}N_6O$	$C_{19}H_{13}N_3O$	$C_8H_7N_5O$	$C_8H_6N_5OK$
fw	188.19	342.36	299.32	189.19	227.27
T [K]	120 (2)	120 (2)	120 (2)	120 (2)	293 (2)
Crystal system	Monoclinic	Triclinic	Ortho-rhombic	Monoclinic	Monoclinic
Space group	$P2_1/n$ (No 14)	$P\bar{1}$ (No 2)	*P*bca (No 61)	*C*2/c (No 15)	*C*2/c (No 15)
a [Å]	5.101 (2)	3.805 (2)	10.487 (3)	17.392 (6)	39.760 (2)
b [Å]	28.807 (9)	11.563 (5)	12.271 (3)	4.943 (2)	4.006 (1)
c [Å]	12.029 (5)	18.897 (7)	22.980 (5)	20.540 (8)	12.455 (1)
α [°]	90	71.28 (2)	90	90	90
β [°]	93.20 (2)	86.15 (2)	90	106.12 (2)	104.07 (1)
γ [°]	90	88.70 (2)	90	90	90
V [Å³]	1765 (1)	785.7 (6)	2957 (1)	1696 (1)	1924 (1)
Z	8	2	8	8	8
ρ_{calc} [Mg.m^{-3}]	1.417	1.447	1.345	1.482	1.569
F(000)	784	356	1248	784	928
μ [mm^{-1}]	0.099	0.096	0.086	0.107	0.531
Crystal size [mm]	0.40 x 0.10 x 0.08	0.35 x 0.15 x 0.10	0.15 x 0.15 x 0.10	0.40 x 0.05 x 0.03	0.15 x 0.10 x 0.07
θ max [°]	26.39	26.39	23.24	23.34	24.71
Reflections collected/ unique	25283/ 3490	11439/ 2954	21539/ 2076	2736/ 1101	7411/ 1650
R_{int}	0.047	0.047	0.061	0.061	0.064
R_1 [I>2σ(I)]	0.0426 [3210]	0.0518 [2769]	0.0425 [1634]	0.0493 [925]	0.0642 [1270]
wR_2	0.1084	0.1492	0.1000	0.1165	0.1248
Largest peak and hole	0.348 and -0.277	0.428 and -0.397	0.185 and -0.204	0.371 and -0.306	0.339 and -0.214

Table 25 Selected bond lengths [Å] and angles [°] for **Hsaltrz**, **Habs**, **Hsalphen**, **Hsaltz** and **Ksaltz**.

	Hsaltrz	**Habs**	**Hsalphen**	**Hsaltz**	**Ksaltz**
Intermolecular distance (Å)[a]	5.10	3.80	4.72	4.13	4.06
Φ_1 [°][b]	16 (1) 6 (1)	41 (1)	48 (1)	35 (1)	6 (1)
Φ_2 [°][c]	-	10 (1)	-	-	-
Φ_3 [°][d]	-	9 (1)	-	-	-
Γ [°][e]	15 (1) 6 (1)	62 (1)	45 (1)	33 (1)	1 (1)
C4-O5 [Å][f]	1.351 (2) 1.350 (2)	1.352 (2)	1.355 (3)	1.354 (3)	1.347 (5)
C2-N1 [Å][f]	1.279 (2) 1.279 (2)	1.279 (3)	1.283 (3)	1.293 (3)	1.283 (5)
C2-C3 [Å]f	1.458 (2) 1.456 (6)	1.452 (3)	1.450 (3)	1.431 (4)	1.437 (6)
H2···nearest H [Å][f]	2.15 (2) 2.19 (2)	-	2.39 (2)	-	-
N0···H2 [Å][f]	-	2.80 (3)	-	2.64 (3)	2.49 (5)
K···N2[Å][g]	-	-	-	-	2.940 (3)
K···N3[Å][g]	-	-	-	-	2.806 (3)
K···N3#2[Å][g]	-	-	-	-	3.170 (4)
K···N4[Å][g]	-	-	-	-	2.853 (4)
K···N4#2[Å][g]	-	-	-	-	3.100 (4)
K···N5[Å][g]	-	-	-	-	2.886 (3)
K···N5#2[Å][g]	-	-	-	-	2.869 (4)

[a] Distances between nearest molecular centroids. [b] Dihedral angle between phenolic plane and triazole (for **Hsaltrz** and **Habs**) or tetrazole (for **Hsaltz** and **Ksaltz**) or benzoic rings (for **Hsalphen**). [c] Dihedral angle between C15–N16–C17–C18–C19–C20 pyridine ring and the triazole ring. [d] Dihedral angle between C21–N22–C23–C24–C25–C26 pyridine ring and triazole ring. [e] Torsion angle centred on the imine function. [f] Distances with respect to Scheme 9-Scheme 13. [g] Distances between K and the nearest nitrogen atoms.

Table 26 Intra- and intermolecular H-bonds in **Hsaltrz**, **Habs**, **Hsalphen**, **Hsaltz** and **Ksaltz**.

	D-H···A	D-H [Å]	H···A [Å]	D···A [Å]	D-H···A
Hsaltrz	O14-H14···N102[a]	0.96 (2)	1.74 (2)	2.667 (2)	163 (2)
	O114-H114···N1[b]	0.93 (2)	1.76 (2)	2.685 (2)	174 (2)
	C7-H7···O14	0.97 (2)	2.38 (2)	2.736 (3)	101 (2)
	C107-H107···O114	0.96 (2)	2.40 (2)	2.743 (2)	100 (1)
	C111-H111···O114[c]	0.96 (2)	2.45 (2)	3.244 (2)	140 (2)
Habs	O14-H14···N6	0.89 (2)	1.95 (3)	2.682 (2)	138 (2)
	O14-H14···N16	0.89 (2)	2.36 (3)	3.098 (3)	140 (2)
	C7-H7···N22[d]	0.97 (3)	2.45 (3)	3.400 (3)	167 (2)
	C26-H26···N2[e]	1.00 (3)	2.60 (3)	3.333 (3)	131 (2)
Hsalphen	O23-H23···N15	0.97 (3)	1.80 (3)	2.650 (3)	146 (2)
	C6-H6···N1[f]	1.00 (3)	2.51 (3)	3.352 (3)	141 (2)
	C16-H16···N1[g]	1.02 (3)	2.46 (2)	3.401 (3)	152 (2)
Hsaltz	O14-H14···N6	0.94 (3)	1.75 (3)	2.602 (3)	151 (3)
	N4-H4···N1[h]	0.92 (3)	1.90 (3)	2.805 (3)	167 (3)
Ksaltz	O1-H1···N1	0.96 (5)	1.76 (5)	2.615 (4)	147 (5)
	C8-H8···N2	0.93	2.49	2.837 (6)	102

Atoms marked with a superscripted letter are generated by the following symmetry operations: a = x – 1, y, z; b = x – 3/2, –y + 1/2, z + 1/2; c = x – 1/2, 1/2 – y, 1/2 + z; d = x + 1, y, z; e = 1 – x, 2 – y, –z; f = 1/2 – x, 1/2 + y, z; g = –x, 2 – y, 1 – z; h = x, 1 + y, z.

Table 27 Intra- and intermolecular π-π stacking and C-H···π interactions in **Hsaltrz**, **Habs**, **Hsalphen**, **Hsaltz** and **Ksaltz**.

	Moiety 1	Moiety 2	Distance between centroids [Å]	Angle between moiety [°]
Hsaltrz	C8-C7-N6-N4	N1-N2-C3-N4-C5	3.782 (2)	12 (1)
	C108-C107-N106-N104	N101-N102-C103-N104-C105	3.552 (2)	6 (1)
	C8-C7-N6-N4	C8-C9-C10-C11-C12-C13	3.934 (2)	4 (1)
	C108-C107-N106-N104	C108-C109-C110-C111-C112-C113	3.481 (2)	12 (1)
	C108-C109-C110-C111-C112-C113	C105-H105	2.87 (2)	3 (1)
Habs	C15-N16-C17-C18-C19-C20	C15-N16-C17-C18-C19-C20	3.805 (2)	0 (1)
	C21-N22-C23-C24-C25-C26	C15-N16-C17-C18-C19-C20	3.805 (2)	0 (1)
	N1-N2-C3-N4-C5	N1-N2-C3-N4-C5	3.805 (2)	0 (1)
	C8-C9-C10-C11-C12-C13	C8-C9-C10-C11-C12-C13	3.805 (2)	0 (1)
	C7-C8-N4-N6	C7-C8-N4-N6	3.805 (2)	0 (1)
Hsalphen	C5-C6-C11-C12-C13-C14	C5-C6-C11-C12-C13-C14	3.603 (2)	0 (1)
	N1-C2-C3-C4-C12-C13	C5-C6-C11-C12-C13-C14	3.985 (2)	2 (1)
	N1-C2-C3-C4-C12-C13	N10-C9-C8-C7-C14-C11	4.228 (2)	1 (1)
	N1-C2-C3-C4-C12-C13	C17-C18-C19-C20-C21-C22	4.239 (2)	6 (1)
	C5-N15-C16-C17	N1-C2-C3-C4-C12-C13	3.713 (2)	8 (1)
	N10-C9-C8-C7-C14-C11	C2-H2	2.86 (3)	3 (1)
Hsaltz	N1-N2-N3-N4-C5	N1-N2-N3-N4-C5	3.468 (2)	0 (1)
Ksaltz	C9-N1-C8-C7	C7-C3-C2-C4-C5-C6	3.694 (2)	5 (1)
	C9-N1-C8-C7	N5-N4-N3-C9-N2	3.504 (2)	2 (1)

Table 28 Crystal data and structure refinement for **CH_2L^{2-3}** and **CH_2L^5**.

	CH_2L^2	**CH_2L^3** [204]	**CH_2L^5**
Empirical formula	$C_{13}H_{12}N_2O$	$C_{13}H_{12}N_2O$	$C_{13}H_{11}N_2OCl$
fw	212.25	212.25	246.69
T [K]	125(2)	297(1)	120(2)
Crystal system	Monoclinic	Monoclinic	Monoclinic
space group	$P2_1/n$	$P2_1/n$	$P2_1/c$
a [Å]	9.863(3)	10.49(1)	13.864(4)
b [Å]	10.363(3)	9.002(4)	6.004(2)
c [Å]	11.563(3)	12.42(1)	14.041(4)
β [°]	113.28(2)	109.10(4)	103.95(2)
V [Å³]	1085.6(5)	1109(2)	1134.3(6)
Z	4	4	4
ρ_{calc} [Mg.m^{-3}]	1.299	1.271	1.445
F(000)	448	448	512
μ [mm^{-1}]	0.084	0.08	0.32
Crystal size [mm]	0.4 x 0.3 x 0.3	0.1 x 0.3 x 0.4	0.5 x 0.4 x 0.1
θ max [°]	26.37	25	26.39
Reflections collected/ unique	8564/2120	2411/886	19898/2257
R_{int}	0.045	0.053	0.053
R_1 [I>2σ(I)]	0.0475 [1931]	0.049 [156]	0.0409 [2167]
wR_2	0.051	-	0.042
Largest peak and hole	0.353 and -0.214	-	0.251 and -0.287

Table 29 Intra- and inter-molecular hydrogen bonds in **CH_2L^{2-3}** and **CH_2L^5** crystal structures.

	D-H•••A	D-H [Å]	H•••A [Å]	D•••A [Å]	D-H•••A [°]
CH_2L^2	O16H16•••N8	0.96(3)	1.74(3)	2.602(2)	149(2)
CH_2L^3[204]	O16H16•••N8	1.02(5)	1.73(5)	2.571(5)	137(4)
CH_2L^5	O16H16•••N8	0.87 (2)	1.81(3)	2.616(2)	153(2)
	C13H13•••N112[a]	0.98(2)	2.56(2)	3.459(2)	152(2)

[a] N112 is generated by the symmetry operation 3-x, 1-y, -z.

Table 30 Intra- and inter-molecular π-π stacking and C-H···π interactions in **CH_2L^{2-3}** and **CH_2L^5** crystal structures.

	Atoms involved 1	Atoms involved 2	d [Å][a]	Angle [°][b]
CH_2L^2	N11-C10-C15-C14-C13-C12	C7-H7	2.88(2)	2(1)
	C1-C2-C3-C4-C5-C6	C14-H14	2.65(2)	8(1)
CH_2L^3[204]	C1-C2-C3-C4-C5-C6	C11-H8	2.85(1)	3(1)
CH_2L^5	C1-C2-C3-C4-C5-C6	C1-C2-C3-C4-C5-C6	3.83(1)	0(1)
	C1-C2-C3-C4-C5-C6	C7-H7	2.81(2)	5(1)
	N12-C11-C10-C15-C14-C13	C15-H15	2.78(1)	6(1)

[a] For π-π stacking, distances between rings centroids. For C-H···π interactions, distances between H atoms and rings centroids. [b] For π-π stacking, angles between rings planes. For C-H···π interactions, angles between C-H axis and aromatic rings normals.

Table 31 Selected bond lengths and angles for $\mathbf{CH_2L^{2\text{-}3}}$ and $\mathbf{CH_2L^5}$ crystal structures.

	$\mathbf{CH_2L^2}$	$\mathbf{CH_2L^3}$[204]	$\mathbf{CH_2L^5}$
Φ [°]	81(1)	90(1)	72(1)
Γ [°]	114(1)	112(1)	117(1)
Dist. [Å][a]	5.99	5.51	5.54
C2-C1 [Å][b]	1.509(2)	1.507(5)	1.512(2)
N-C2 [Å][b]	1.459(2)	1.459(7)	1.469(2)
C3-N [Å][b]	1.278(2)	1.269(5)	1.279(2)
C4-C3 [Å][b]	1.458(2)	1.450(7)	1.463(2)
C5-C4 [Å][b]	1.410(3)	1.403(6)	1.406(2)
C5-O[Å][b]	1.352(2)	1.348(5)	1.354(2)

[a] Average distance between molecular centroids. [b] Distances with respect to Scheme 15.

Table 32 Crystal data and structure refinement for **C**[1-5].

	C[1]	**C**[2]	**C**[3]	**C**[4]	**C**[5]
Empirical formula	$C_{14}H_{14}Co_{0.5}N_3SO_2$	$C_{14}H_{14}Co_{0.5}N_3SeO_2$	$C_{14}H_{14}Mn_{0.5}N_3SO_2$	$C_{14}H_{14}Ni_{0.5}N_3SO_2$	$C_{14}H_{14}Cu_{0.5}N_3SO_2$
fw	317.81	317.70	364.71	315.81	320.11
T [K]	120 (2)	120 (2)	120 (2)	120 (2)	120 (2)
Crystal system	Monoclinic	Monoclinic	Monoclinic	Monoclinic	Monoclinic
space group	$P2_1/a$ (No. 14)	$P2_1/a$ (No. 14)	$P2_1/a$ (No. 14)	$P2_1/a$ (No. 14)	$P2_1/a$ (No. 14)
a [Å]	13.474 (4)	13.595 (4)	13.624 (4)	13.444 (4)	13.714 (4)
b [Å]	7.092 (2)	7.170 (2)	7.088 (2)	7.095 (2)	7.116 (2)
c [Å]	14.928 (4)	15.037 (4)	15.022 (4)	14.850 (4)	14.594 (4)
β [°]	90.98 (2)	91.75 (2)	91.45 (2)	90.81 (2)	93.54(2)
V [Å³]	1426.3 (7)	1465.1 (7)	1450.2 (7)	1416.3 (7)	1421.5 (7)
Z	4	4	4	4	4
ρ_{calc} [Mg.m^{-3}]	1.48	1.65	1.45	1.49	1.50
F(000)	658	730	654	660	662
μ [mm^{-1}]	0.794	3.115	0.644	0.878	0.961
Crystal size [mm]	0.35 x 0.25 x 0.25	0.30 x 0.30 x 0.25	0.32 x 0.14 x 0.14	0.30 x 0.15 x 0.15	0.30 x 0.25 x 0.05
θ max [°]	26.4	26.4	26.4	25.4	24.4
Reflections collected/ unique	17432/ 2890	10248/ 2988	25535/ 2891	9957/ 2534	6449/ 2292
R_{int}	0.055	0.071	0.043	0.084	0.066
R_1 [I>2σ(I)]	0.0457 [2790]	0.0408 [2857]	0.426 [2730]	0.1237 [2440]	0.1149 [1992]
wR_2	0.1294	0.1170	0.1213	0.3460	0.3044
Largest peak and hole	0.59 and -0.82	0.97 and -0.89	1.10 and -0.38	1.88 and -0.77	3.05 and -0.95

Table 33 Intra- and inter-molecular hydrogen bonds in **C**$^{1-3}$ crystal structures.

	D-H•••A	D-H [Å]	H•••A [Å]	D•••A [Å]	D-H•••A [°]
C^{1}	O15H15•••N7	0.82 (4)	1.83 (4)	2.596 (3)	156 (1)
	O19H19•••S18[a]	0.88 (4)	2.38 (4)	3.244 (3)	171 (1)
C^{2}	O15H15•••N7	0.91 (3)	1.77 (3)	2.600 (4)	151 (1)
	O19H19•••S18[a]	0.90 (3)	2.49 (3)	3.352 (3)	161 (1)
C^{3}	O15H15•••N7	0.72 (4)	1.92 (4)	2.597 (4)	156 (1)
	O19H19•••S18[a]	0.88 (2)	2.37 (4)	3.250 (4)	174 (1)

[a] S18 is generated by the symmetry operation 0.5 + x, 0.5 – y, z.

Table 34 Intra- and inter-molecular π-π stacking interactions in **C**$^{1-3}$ crystal structures.

	Imine ••• ring$_{salicyl}$ [Å][a]	Imine ••• ring$_{salicyl}$ [°][b]
C^{1}	3.38 (3)	2 (1)
C^{2}	3.36 (3)	2 (1)
C^{3}	3.41 (4)	2 (1)

[a] C108-N107⋯C9-C10-C11-C12-C13-C14. [b] Angle between imine and salicyl planes.

Table 35 Selected bond lengths and angles for $\mathbf{C^{1-3}}$ crystal structures.

	$\mathbf{C^1}$	$\mathbf{C^2}$	$\mathbf{C^3}$
Φ [°]	7 (1)	7 (1)	7 (1)
Dist. [Å][a]	3.96	4.15	3.94
N7-$C_{pyr.}$ [Å] [b]	1.411 (3)	1.415 (4)	1.416 (3)
N7-C8 [Å] [b]	1.289 (3)	1.286 (4)	1.288 (3)
C8-C9 [Å] [b]	1.448 (3)	1.453 (4)	1.449 (3)
C9-C10 [Å] [b]	1.409 (4)	1.409 (4)	1.411 (3)
C10-O15 [Å] [b]	1.357 (3)	1.354 (4)	1.355 (3)
M···M [Å]	7.092 (2)	7.170 (2)	7.088 (2)
M-N1 [Å]	2.161 (2)	2.160 (2)	2.269 (2)
M-N16 [Å]	2.078 (2)	2.077 (2)	2.170 (2)
M-O19 [Å]	2.134 (2)	2.122	2.230 (2)
N1-M-N16 [°]	88.60 (8)	88.71 (9)	88.79 (7)
N1-M-O19 [°]	88.80 (7)	88.86 (9)	88.87 (7)
N16-M-O19 [°]	89.51 (8)	89.78 (9)	89.50 (7)
Σ [°]	6.2 (5)	5.3 (5)	5.7 (4)
M-N16-C17 [°]	159.95 (8)	160.44 (9)	159.92 (7)
N16-C17-S18 [°]	178.66 (8)	179.18 (9)	179.61 (7)
H8···H_β [Å]	2.129 (4)	2.127 (3)	2.120 (4)

[a] Average intermolecular distances between nearest $\mathbf{L^3}$ ligand centroids. [b] Distance as shown in Scheme 18.

Table 36 Crystal data and structure refinement for $[Fe_2(Hsaltrz)_5(NCS)_4]\cdot 4CH_3OH$ (**C**[7]) and $[Fe_2(Hsaltrz)_5(NCS)_4]\cdot 3H_2O\cdot CH_3OH$ (**C**[8])

	C[7]		**C**[8]	
Empirical formula	$C_{53}H_{56}Fe_2N_{24}O_9S_4$		$C_{50}H_{50}Fe_2N_{24}O_9S_4$	
fw	1413.16		1371.08	
T [K]	100 (2)	200 (2)	125 (2)	240 (2)
Crystal system	Monoclinic		Triclinic	
Space group	*C*2/c (No 15)		*P*$\bar{1}$ (No 2)	
a [Å]	19.287 (5)	19.630 (5)	11.455 (4)	11.503 (4)
b [Å]	17.924 (5)	18.131 (5)	13.594 (5)	13.576 (5)
c [Å]	19.221 (5)	19.500 (5)	21.214 (8)	21.225 (8)
α [°]	90	90	95.08 (2)	94.68 (2)
β [°]	110.26 (2)	110.74 (2)	104.85 (2)	104.72 (2)
γ [°]	90	90	107.33 (2)	106.90 (2)
V [Å^3]	6192 (3)	6491 (3)	2999 (2)	3024 (2)
Z	4		2	
ρ_{calc} [Mg.m^{-3}]	1.516	1.446	1.518	1.106
F(000)	2904		1412	
μ [mm^{-1}]	0.679	0.648	0.699	0.693
Crystal size [mm]	0.24 x 0.20 x 0.14		0.24 x 0.20 x 0.12	
θ max [°]	25.35	25.35	24.91	24.82
Reflections collected/ unique	23328/ 5599	40601/ 5938	28458/ 9755	42059/ 9989
R_{int}	0.038	0.054	0.046	0.053
R_1 [I>2σ(I)]	0.0547 [5015]	0.0566 [5048]	0.0472 [7971]	0.0473 [7795]
wR_2	0.1405	0.1625	0.1340	0.1259
Largest peak and hole	1.762 and -2.130	0.849 and -0.854	0.959 and -0.782	0.538 and -0.571

Table 37 Selected bond lengths and angles for **C**[7] and **C**[8].

	C[7]		**C**[8]	
T [K]	100 (2)	200 (2)	125 (2)	240 (2)
Intermolecular distance [Å][a]	11.035 (7)	11.305 (8)	10.730 (5)	10.731 (5)
M···M [Å]	3.648 (7)	3.966 (8)	3.976 (5)	3.960 (5)
Φ_1 [°][b]	8 (1)	8 (1)	17 (1)	17 (1)
Φ_2 [°][b]	19 (1)	19 (1)	16 (1)	14 (1)
Φ_3 [°][b]	1 (1)	3 (1)	11 (1)	11 (1)
Φ_4 [°][b]	-	-	29 (1)	29 (1)
Φ_5 [°][b]	-	-	13 (1)	11 (1)
C7-N6 [Å]	1.283 (5)	1.274 (6)	1.268 (4)	1.268 (5)
C9-O14 [Å]	1.360 (5)	1.362 (6)	1.346 (5)	1.349 (5)
C107-N106 [Å]	1.276 (5)	1.270 (5)	1.269 (5)	1.270 (5)
C109-O114 [Å]	1.357 (5)	1.356 (6)	1.342 (5)	1.347 (5)
C207-N206 [Å]	1.001 (7)	1.035 (6)	1.279 (4)	1.263 (4)
C209-O214 [Å]	1.341 (9)	1.324 (8)	1.365 (4)	1.354 (4)
C307-N306 [Å]	-	-	1.282 (4)	1.281 (4)
C309-O314 [Å]	-	-	1.353 (4)	1.349 (5)
C313-O315 [Å]	-	-	1.40 (1)	1.42 (1)
C408-N406 [Å]	-	-	1.277 (9)	1.272 (9)
C409-N407 [Å]	-	-	1.264 (8)	1.258 (8)
C411-O416 [Å]	-	-	1.333 (9)	1.315 (8)
C415-O417 [Å]	-	-	1.363 (9)	1.346 (8)
Fe1-N1 [Å]	1.985 (3)	2.177 (3)	2.196 (3)	2.189 (3)
Fe1-Na [Å][c]	1.976 (3)	2.219 (3)	2.220 (3)	2.212 (3)
Fe1-Nb [Å][c]	1.972 (3)	2.209 (3)	2.170 (3)	2.169 (3)
Fe1-Nc [Å][c]	1.962 (3)	2.161 (3)	2.189 (3)	2.201 (3)
Fe1-N15 [Å]	1.951 (3)	2.107 (3)	2.106 (3)	2.090 (3)
Fe1-N115 [Å]	1.948 (3)	2.121 (3)	2.166 (3)	2.177 (3)
Fe2-N101 [Å]	2.154 (3)	2.174 (3)	-	-
Fe2-N202 [Å]	2.216 (3)	2.209 (3)	-	-
Fe2-N302 [Å]	2.181 (3)	2.199 (3)	-	-
Fe2-N401 [Å]	2.230 (3)	2.218 (3)	-	-

Fe2-N215 [Å]	2.111 (3)	2.097 (3)	-	-
Fe2-N315 [Å]	2.147 (3)	2.135 (3)	-	-
Σ_{Fe1} [°][d]	35 (1)	34 (1)	18.2 (4)	18 (2)
Σ_{Fe2} [°][d]	28 (1)	28 (1)	-	-
Fe1-N15-C16 [°]	150.8 (3)	152.2 (3)	172.8 (3)	171.2 (3)
Fe1-N115-C116 [°]	142.4 (3)	142.8 (3)	174.1 (3)	173.4 (4)
Fe2-N215-C216 [°]	175.5 (3)	176.2 (3)	-	-
Fe2-N315-C316 [°]	149.4 (3)	149.6 (3)	-	-

[a] Minimal distance between dinuclear centroids. [b] Dihedral angle between phenolic and triazole rings. [c] Na = N101 and N201, Nb = N102 and N301, Nc = 201 and N402 for **C**[7] and **C**[8], respectively. [d] Distortion parameter following the equation $\Sigma = \sum_{i=1}^{12} (|\varphi_i - 90|)$ where φ corresponds to N-Fe-N angles.

Table 38 Intra- and inter-molecular H-bonds for **C**[7] and **C**[8] crystal structures.

	T [K]	D-H•••A	D-H [Å]	H•••A [Å]	D•••A [Å]	D-H•••A [°]
C[7]	100 (2)	O14-H14•••N6	0.84	1.94	2.666 (5)	144
		O21-H21•••S117	0.99 (5)	2.52 (4)	3.474 (4)	164 (5)
		O114-H114•••O121[a]	0.84	2.36	3.152 (5)	157
		O121-H121•••O114[a]	0.90 (4)	2.30 (6)	3.152 (5)	159 (5)
		O214-H214•••N206	0.84	2.52	3.15 (2)	132
		C103-H103•••O21	0.95	2.39	3.234 (6)	147
		C105-H105•••S17[b]	0.95	2.76	3.572 (4)	144
		C107-H107•••O21	0.95	2.56	3.326 (6)	138
		C118-H119•••O214[c]	0.99 (4)	2.51 (4)	3.50 (2)	172 (2)
		C203-H203•••O121[d]	0.95	2.24	3.193 (5)	177
		C210-H210•••S117[d]	0.95	2.87	3.755 (8)	156
	200 (2)	O14-H14•••N6	0.84	1.95	2.670 (5)	144
		O114-H114•••O119[a]	0.84	2.44	3.235 (5)	159
		O214-H214•••N206	0.84	2.41	3.07 (2)	136
		C3-H3•••S117[e]	0.95	2.86	3.789 (6)	165
		C103-H103•••O19	0.95	2.35	3.218 (7)	151
		C105-H105•••S17[b]	0.95	2.75	3.583 (4)	147
		C203-H203•••O119[d]	0.95	2.27	3.218 (7)	175
C[8]	125 (2)	O14-H14•••N6	0.84	1.92	2.656 (4)	145
		O20-H20•••O214[f]	0.91 (3)	2.00 (3)	2.874 (4)	163 (4)
		O20-H20•••S217[g]	0.90 (4)	2.52 (4)	3.403 (3)	167 (4)
		O114-H114•••N106	0.84	1.93	2.658 (5)	144
		O120-H120•••O220	1.08 (6)	1.87 (6)	2.60 (1)	121 (4)
		O120-H121•••S17	0.88 (3)	2.68 (4)	3.294 (7)	129 (3)
		O214-H214•••N206	0.84	1.94	2.672 (4)	144
		O314-H314•••N306	0.84	1.95	2.673 (4)	143
		O417-H417•••O220[h]	0.84	2.54	3.29 (2)	149

	C3-H3•••S217[i]	0.95	2.79	3.724 (4)	169
	C305-H305•••O20[j]	0.95	2.31	3.228 (5)	162
	C403-H403•••O120	0.95	2.42	3.32 (1)	157
	C412-H412•••N2[h]	0.95	2.49	3.319 (8)	145
240 (2)	O14-H14•••N6	0.83	1.93	2.647 (4)	144
	O20-H20•••O214[f]	0.94 (3)	2.00 (3)	2.890 (4)	158 (4)
	O20-H20•••S217[g]	0.91 (3)	2.67 (4)	3.423 (4)	141 (4)
	O114-H114•••N106	0.83	1.92	2.638 (5)	145
	O120-H120•••O220	1.08 (6)	1.95 (6)	2.68 (2)	121(4)
	O214-H214•••N206	0.83	1.94	2.657 (4)	145
	O314-H314•••N306	0.83	1.95	2.668 (4)	145
	C3-H3•••S217[i]	0.94	2.82	3.749 (4)	170
	C305-H305•••O20[j]	0.94	2.34	3.249 (5)	162
	C403-H403•••O120	0.94	2.42	3.31 (1)	157
	C412-H412•••N2[h]	0.94	2.59	3.378 (8)	142

[a] O121, O114 and O119 are generated following the symmetry operation: -x, -y, -z. [b] S17: -1/2+x, 1/2-y, -1/2+z. [c] O214: 1/2-x, -1/2+y, 1/2-z. [d] O121, S117 and O119: 1/2-x, 1/2+y, 1/2-z. [e] S117: 1/2-x, -1/2+y, 1/2-z. [f] O214: 1-x, 1-y, 1-z. [g] S217: 1+x, -1+y, z. [h] O220 and N2: -x, 1-y, -z. [i] S217: x, -1+y, z. [j] O20: x, 1+y, z.

Table 39 Site Occupation Factor for atoms involved in disorder phenomenon in **C**[7-10] crystal structures.

	T [K]	Atom 1	SOF [%]	Atom 2[a]	SOF [%]
C[7]	100 (2)	N206	50	N206^{i}	50
		O214	50	O214^{i}	50
		H214	50	H214^{i}	50
		H998	50	H998^{i}	50
	200 (2)	N206	50	N206^{i}	50
		O214	50	O214^{i}	50
		H214	50	H214^{i}	50
		H998	50	H998^{i}	50
C[8]	125	O314	91.0 (7)	O315	9.0 (7)
		H314	91.0 (7)	H315	9.0 (7)
		N406	43 (1)	N407	57 (1)
		C408	43 (1)	C409	57 (1)
		H408	43 (1)	H409	57 (1)
		O416	37 (1)	O417	63 (1)
		H416	37 (1)	H417	63 (1)
		H999	37 (1)	H998	63 (1)
	240 (2)	O314	94.4 (7)	O315	5.6 (7)
		H314	94.4 (7)	H315	5.6 (7)
		N406	46 (1)	N407	54 (1)
		C408	46 (1)	C409	54 (1)
		H408	46 (1)	H409	54 (1)
		O416	44 (1)	O417	56 (1)
		H416	44 (1)	H417	56 (1)
		N999	44 (1)	H998	56 (1)
C[9]	293 (2)	N206	50	N206^{i}	50
		O214	50	O214^{i}	50
		H214	50	H214^{i}	50
C[10]	293 (2)	O314	92.5 (8)	O315	7.5 (8)
		H314	92.5 (8)	H315	7.5 (8)
		H998	92.5 (8)	H999	7.5 (8)
		O414	54 (1)	O415	46 (1)
		H414	54 (1)	H415	46 (1)
		H997	54 (1)	H996	46 (1)

[a] Atoms with a superscripted ‘i’ are generated by symmetry in the crystal structure.

Table 40 Inter-molecular π-π stacking and C-H···π interactions in **C**[7] crystal structures.

T [K]	Atoms involved	d between centroids [Å]	C-H•••ring [°][b]
100 (2)	N201-C203-N204-C203-N201// C8-C9-C10-C11-C12-C13[a]	3.695 (2)	8.9 (2)
	N201-C203-N204-C203-N201// C8-C9-C10-C11-C12-C13[b]	3.695 (2)	8.9 (2)
	C8-C9-C10-C11-C12-C13// C8-C9-C10-C11-C12-C13[c]	3.554 (2)	0
	C108-C109-C110-C111-C112-C113// C108-C109-C110-C111-C112-C113[d]	4.320 (2)	0
	C211-H211//C108-C109-C110-C111-C112-C113[e]	2.95	19.3
	C211-H211// C108-C109-C110-C111-C112-C113[f]	2.95	19.3
	C16-S17//N1-N2-C3-N4-C5[g]	3.503 (2)	20.4
200 (2)	N101-N102-C103-N104-C105//C108-C109-C110-C111-C112-C113[d]	4.522 (3)	19.2 (2)
	N201-C203-N204-C203-N201// C8-C9-C10-C11-C12-C13[h]	3.675 (2)	9.3 (2)
	N201-C203-N204-C203-N201// C8-C9-C10-C11-C12-C13[b]	3.675 (2)	9.3 (2)
	C8-C9-C10-C11-C12-C13// C8-C9-C10-C11-C12-C13[c]	3.566 (3)	0
	C108-C109-C110-C111-C112-C113// C108-C109-C110-C111-C112-C113[d]	4.403 (3)	0
	C211-H211//C108-C109-C110-C111-C112-C113[e]	2.97	20.3
	C211-H211// C108-C109-C110-C111-C112-C113[f]	2.97	20.3
	C16-S17//N1-N2-C3-N4-C5[g]	3.498 (2)	20.3

[a] ring is generated following the symmetry operation: x-1/2, 1/2+y, z. [b] 1/2-x, 1/2+y, 1/2-z. [c] 1-x, -y, 1-z. [d] -x, -y, -z. [e] -x, 1-y, -z. [f] x, 1-y, 1/2+z. [g] 1/2-x, 1/2-y, 1-z.

Table 41 Inter-molecular π-π stacking and C-H···π interactions in **C[8]** crystal structures.

T [K]	Atoms involved[a]	d between centroids [Å]	C-H•••ring [°][b]
125 (2)	N1-N2-C3-N4-C5//C8-C9-C10-C11-C12-C13[a]	4.322 (3)	17.3 (2)
	N1-N2-C3-N4-C5//C308-C309-C310-C311-C312-C313[b]	4.461 (3)	15.7 (2)
	N101-N102-C103-N104-C105//C108-C109-C110-C111-C112-C113[c]	4.420 (3)	15.7 (2)
	N201-N202-C203-N204-C205//C208-C209-C210-C211-C212-C213[d]	3.923 (2)	11.4 (2)
	N301-N302-C303-N304-C305//C108-C109-C110-C111-C112-C113[e]	3.845 (3)	19.0 (2)
	N401-N402-C403-N404-C405//C410-C411-C412-C413-C414-C415[f]	4.273 (4)	13.0 (3)
	C8-C9-C10-C11-C12-C13// C8-C9-C10-C11-C12-C13[a]	4.840 (3)	0
	C8-C9-C10-C11-C12-C13//C308-C309-C310-C311-C312-C313[g]	4.503 (3)	13.6 (2)
	C216-S217//C308-C309-C310-C311-C312-C313[h]	3.913 (2)	25.2
	C316-S317//N101-N102-C103-N104-C105[e]	3.517 (2)	17.0
240 (2)	N1-N2-C3-N4-C5//C8-C9-C10-C11-C12-C13[a]	4.339 (3)	17.2 (2)
	N1-N2-C3-N4-C5//C308-C309-C310-C311-C312-C313[b]	4.498 (3)	15.8 (2)
	N101-N102-C103-N104-C105//C108-C109-C110-C111-C112-C113[c]	4.407 (3)	13.8 (2)

N201-N202-C203-N204-C205//C208-C209-C210-C211-C212-C213[d]	3.948 (2)	10.9 (2)
N301-N302-C303-N304-C305//C108-C109-C110-C111-C112-C113[e]	3.878 (2)	20.1 (2)
N401-N402-C403-N404-C405//C410-C411-C412-C413-C414-C415[f]	4.317 (4)	10.8 (3)
C8-C9-C10-C11-C12-C13// C8-C9-C10-C11-C12-C13[a]	4.792 (3)	0
C8-C9-C10-C11-C12-C13//C308-C309-C310-C311-C312-C313[g]	4.472 (3)	13.2 (2)
C216-S217//C308-C309-C310-C311-C312-C313[h]	3.955 (3)	24.6
C316-S317//N101-N102-C103-N104-C105[e]	3.533 (3)	18.0

[a] ring is generated following the symmetry operation: 1-x, 1-y, 1-z. [b] x-1, y-1, z. [c] -1-x, 2-y, -z. [d] -x, 2-y, 1-z. [e] -x, 2-y, -z. [f] -x, 1-y, -z. [g] 1-x, 2-y, 1-z. [h] x-1, y, z.

Table 42 Crystal data and structure refinement for $[Fe_2(Hsaltrz)_5(NCS)_4]\cdot 4H_2O$ (**C[9]**) and $[Co_2(Hsaltrz)_5(NCS)_4]\cdot 4H_2O\cdot CH_3OH$ (**C[10]**)

	C[9]	**C[10]**
Empirical formula	$C_{49}H_{40}Fe_2N_{24}O_9S_4$	$C_{50}H_{52}Co_2N_{24}O_{10}S_4$
fw	1348.99	1395.26
T [K]	293 (2)	240 (2)
Crystal system	Monoclinic	Triclinic
Space group	*C*2/c (No 15)	*P*$\bar{1}$ (No 2)
a [Å]	19.023 (5)	11.455 (4)
b [Å]	18.396 (5)	13.594 (5)
c [Å]	19.386 (5)	21.214 (8)
α [°]	90	95.08 (2)
β [°]	108.73 (2)	104.85 (2)
γ [°]	90	107.33 (2)
V [Å³]	6425 (3)	2999 (2)
Z	4	2
ρ_{calc} [Mg.m^{-3}]	1.395	1.545
F(000)	2744	1436
μ [mm^{-1}]	0.651	0.770
Crystal size [mm]	0.32 x 0.18 x 0.16	0.20 x 0.18 x 0.05
θ max [°]	20.81	25.37
Reflections collected/ unique	6284/3230	22005/10410
R_{int}	0.0284	0.045
R_1 [I>2σ(I)]	0.1180 [2680]	0.0546 [8750]
wR_2	0.3832	0.1448
Largest peak and hole	1.020 and -0.459	1.519 and -1.156

Table 43 Selected bond lengths and angles for **C^{9}** and **C^{10}**.

	C^{9}	**C^{10}**		**C^{9}**	**C^{10}**
Intermolecular distance [Å][a]	11.40 (3)	10.615 (5)	M1-N1 [Å]	2.17 (1)	2.143 (3)
M···M [Å]	3.97 (3)	3.895 (5)	M1-Na [Å][c]	2.24 (1)	2.160 (3)
Φ_1 [°][b]	3 (1)	19 (1)	M1-Nb [Å][c]	2.20 (1)	2.117 (3)
Φ_2 [°][b]	15 (1)	10 (1)	M1-Nc [Å][c]	2.16 (1)	2.147 (3)
Φ_3 [°][b]	2 (1)	11 (1)	M1-N15 [Å]	2.11 (2)	2.072 (3)
Φ_4 [°][b]	-	31 (1)	M1-N115 [Å]	2.11 (2)	2.150 (3)
Φ_5 [°][b]	-	4 (1)	M2-N101 [Å]	-	2.126 (3)
C7-N6 [Å]	1.26 (3)	1.277 (5)	M2-N202 [Å]	-	2.145 (3)
C9-O14 [Å]	1.39 (3)	1.351 (5)	M2-N302 [Å]	-	2.142 (3)
C107-N106 [Å]	1.17 (2)	1.284 (5)	M2-N401 [Å]	-	2.151 (3)
C109-O114 [Å]	1.39 (3)	1.350 (5)	M2-N215 [Å]	-	2.086 (4)
C207-N206 [Å]	1.10 (2)	1.280 (5)	M2-N315 [Å]	-	2.092 (4)
C209-O214 [Å]	1.32 (4)	1.360 (4)	Σ_{Fe1} [°][d]	19.1 (7)	30.5 (4)
C307-N306 [Å]	-	1.292 (5)	Σ_{Fe2} [°][d]	-	23.6 (4)
C309-O314 [Å]	-	1358 (5)	M1-N15-C16	168 (2)	153.1 (3)
C313-O315 [Å]	-	1.42 (2)	M1-N115-C116	174 (2)	141.7 (3)
C407-N406 [Å]	-	1.150 (6)	M2-N215-C216	-	173.5 (3)
C409-O414 [Å]	-	1.293 (9)	M2-N315-C316	-	152.4 (4)
C413-O415 [Å]	-	1.25 (1)			

[a] Minimal distance between dinuclear centroids. [b] Dihedral angle between phenolic and triazole rings. [c] Na = N101 and N201, Nb = N102 and N301, Nc = N201 and N402 for **C^{9}** and **C^{10}**, respectively. [d] Distortion parameter following the equation $\Sigma = \sum_{i=1}^{12} (|\varphi_i - 90|)$ where φ corresponds to N-M-N angles.

Table 44 Intra- and inter-molecular H-bonds in **C^{9}** and **C^{10}** crystal structures.

	D-H•••A	D-H [Å]	H•••A [Å]	D•••A [Å]	D-H•••A [°]
C^{9}	O14-H14•••N6	0.82	2.00	2.68 (3)	140
	O114-H114•••N106	0.82	1.97	2.67 (3)	143
	O214-H214•••N206	0.82	1.81	2.59 (4)	158
	C3-H3•••S117[a]	0.93	2.82	3.70 (2)	158
	C103-H103•••O118	0.93	2.47	3.40 (4)	173
	C105-H105•••S17[b]	0.93	2.84	3.65 (2)	147
	C203-H203•••O18[c]	0.93	2.37	3.29 (4)	174
	C210-H210•••S117[c]	0.93	2.76	3.66 (5)	164
C^{10}	O14-H14•••N6	0.82	1.94	2.649 (4)	145
	O114-H114•••N106	0.82	1.93	2.648 (5)	145
	O214-H214•••N206	0.82	1.94	2.649 (4)	145
	O314-H314•••N306	0.82	1.94	2.649 (4)	145
	O414-H414•••N406	0.82	1.88	2.592 (9)	145
	C3-H3•••S217[d]	0.93	2.83	3.752 (4)	169
	C103-H103•••O220[e]	0.93	2.52	3.37 (1)	151
	C107-H107•••O220[e]	0.93	2.50	3.43 (1)	173
	C303-H303•••O19[f]	0.93	2.50	3.33 (1)	148
	C305-H305•••O20[f]	0.93	2.34	3.238 (5)	163
	C403-H403•••O120	0.93	2.33	3.233 (8)	163
	C407-H407•••O120	0.93	2.56	3.485 (9)	173

[a] S117 is generated following the symmetry operation: 1/2-x, -1/2+y, 1/2-z. [b] S17: -1/2+x, 1/2-y, -1/2+z. [c] O18, S117: 1/2-x, 1/2+y, 1/2-z. [d] S217: x, -1+y, z. [e] O220: -1+x, y, z. [f] O20 and O19: x, 1+y, z.

Table 45 Inter-molecular π-π stacking and C-H···π interactions in **C[9]** and **C[10]** crystal structures.

	Atoms involved	d between centroids	C-H•••ring [°][b]
C[9]	N101-N102-C103-N104-C105// C108-C109-C110-C111-C112-C113[a]	4.43 (1)	15 (1)
	N201-C203-N204-C203-N201// C8-C9-C10-C11-C12-C13[b]	3.75 (1)	8 (1)
	N201-C203-N204-C203-N201// C8-C9-C10-C11-C12-C13[c]	3.75 (1)	8 (1)
	C8-C9-C10-C11-C12-C13// C8-C9-C10-C11-C12-C13[d]	3.70 (2)	0
	C108-C109-C110-C111-C112-C113//C108-C109-C110-C111-C112-C113[a]	4.35 (1)	0
	C16-S17//N1-N2-C3-N4-C5[e]	3.52 (1)	17.0
C[10]	N1-N2-C3-N4-C5// C8-C9-C10-C11-C12-C13[f]	4.379 (3)	19.1 (2)
	N1-N2-C3-N4-C5//C308-C309-C310-C311-C312-C313[g]	4.422 (3)	15.9 (2)
	N101-N102-C103-N104-C105// C108-C109-C110-C111-C112-C113[h]	4.298 (3)	10.1 (3)
	N201-N202-C203-N204-C205// C208-C209-C210-C211-C212-C213[i]	3.901 (3)	11.0 (2)
	N301-N302-C303-N304-C305// C108-C109-C110-C111-C112-C113[j]	3.930 (3)	23.7 (2)
	N401-N402-C403-N404-C405// C408-C409-C410-C411-C412-C413[k]	4.242 (4)	4.2 (3)
	C8-C9-C10-C11-C12-C13// C8-C9-C10-C11-C12-C13[f]	4.757 (3)	0
	C8-C9-C10-C11-C12-C13//C308-C309-C310-C311-C312-C313[l]	4.495 (3)	15.5 (2)
	C216-S217//C308-C309-C310-C311-C312-C313[m]	3.938 (3)	27.0
	C316-S317//N101-N102-C103-N104-C105[j]	3.940 (3)	17.6

[a] ring is generated following the symmetry operation: -x, -y, -z. [b] x–1/2, y+1/2, z. [c] 1/2-x, 1/2+y, 1/2-z. [d] 1-x, -y, 1-z. [e] 1/2-x, 1/2-y, 1-z. [f] 1-x, 1-y, 1-z. [g] x-1, y-1, z. [h] -1-x, 2-y, -z. [i] -x, 2-y, 1-z. [j] -x, 2-y, -z. [k] -x, 1-y, -z. [l] 1-x, 2-y, 1-z. [m] x-1, y, z.

Table 46 Crystal data and structure refinement for **C[17-19]**.

Compound	**C[17]**	**C[18]**	**C[19]**
Empirical formula	$C_{71}H_{76}Cu_5N_{18}O_{29}$	$C_{60}H_{64}Cu_4N_{14}O_{16}$	$C_{57.5}H_{60}N_{10}O_{7.5}S_2Ni_2$
fw	1963.20	1491.42	1192.70
T [K]	120(2)	120(2)	115(2)
Crystal system	Triclinic	Orthorhombic	Triclinic
Space group	*P*$\bar{1}$	*P*bcn	*P*$\bar{1}$
a [Å]	15.002(2)	14.139(5)	13.639(4)
b [Å]	15.894(5)	24.896(7)	14.517(4)
c [Å]	17.764(3)	16.452(5)	15.404(4)
α [°]	70.20(2)	90	68.32(2)
β [°]	87.83(2)	90	87.47(2)
γ [°]	81.25(2)	90	81.35(2)
V [Å³]	3938(2)	5791(3)	2802(1)
Z	2	4	2
ρ_{calc} [Mg.m^{-3}]	1.655	1.711	1.413
F(000)	2010	3064	1246
μ [mm^{-1}]	1.425	1.536	0.809
Crystal size [mm]	0.2 x 0.2 x 0.2	0.5 x 0.2 x 0.2	0.4 x 0.1 x 0.1
θ max [°]	24.40	23.55	24.42
Reflections collected/ unique	79617/12257	29887/4280	27850/8730
R_{int}	0.046	0.069	0.052
R_1 [I>2σ(I)]	0.0424 [10535]	0.0898 [3611]	0.0397 [7501]
wR_2	0.1104	0.2772	0.1060
Largest peak and hole	1.16 and -0.70	1.86 and -1.29	0.42 and -0.41

Table 47 Selected angles (°) and distances (Å) for **C$^{17\text{-}19}$**.

Φ[a] [°]	**L-^{2}a**	**L-^{2}b**	**L-^{2}c**	**L-^{2}d**	**L-^{2}e**
C^{17}	48(1)	48(1)	42(1)	35(1)	42(1)
C^{18}	35(1)	40(1)	-	-	-
C^{19}	60(1)	76(1)	90(1)	69(1)	-
C7-N8-C9-C10[b] [°]					
C^{19}[c]	125(1)	97(1)	109(1)	126(1)	-
$d_{Himine\text{-}H\beta}$ [Å]					
C^{17}	2.52(5)	2.48(5)	2.38(5)	2.36(5)	2.33(5)
C^{18}	2.34	2.38	-	-	-
C^{19}	2.41(2)	2.44(2)	2.43(2)	2.52(2)	-
$d_{M\cdots M}$ [Å]	Cu1-Cu2	Cu2-Cu3	Cu3-Cu4	Cu4-Cu1	Cu2-Cu5
C^{17}	3.064(3)	3.253(3)	3.067(3)	3.343(3)	9.082(3)
C^{18}	3.067(9)	3.213(9)	-	-	-

[a]Dihedral angle between phenolic and pyridine aromatic rings. [b]Torsion angle involving the CH_2 spacer group between the imine function and the pyridine ring. [c]concerns either **CH_2L^3a**, **CH_2L-^{3}b**, **CH_2L-^{3}c** and **CH_2L^3d**.

Table 48 Selected bond lengths (Å) for **C**[17-19].

C[17]				**C**[18]		**C**[19]	
Cu1-O16	2.267(3)	Cu3-O15	1.978(3)	Cu1-O202	2.28(1)	Ni1-N12	2.140(3)
Cu1-N1	2.026(3)	Cu3-O315	1.947(3)	Cu1-N1	2.016(8)	Ni1-N40	2.042(3)
Cu1-N107	2.005(3)	Cu4-O216	2.211(3)	Cu1-N107	2.001(7)	Ni1-N108	2.082(3)
Cu1-O115	1.941(3)	Cu4-N101	2.015(3)	Cu1-O15	1.965(5)	Ni1-N212	2.132(2)
Cu1-O215	1.981(3)	Cu4-N7	1.997(3)	Cu1-O115	1.942(6)	Ni1-O50	2.089(2)
Cu2-O116	2.341(5)	Cu4-O15	1.945(3)	Cu2-O20	2.167(7)	Ni1-O116	2.009(2)
Cu2-O119	2.786(3)	Cu4-O315	2.003(3)	Cu2-N7	1.997(7)	Ni2-N112	2.132(2)
Cu2-N301	2.031(3)	Cu5-O415	1.893(3)	Cu2-N101	2.024(8)	Ni2-N208	2.082(3)
Cu2-N207	2.012(3)	Cu5-N407	1.958(3)	Cu2-O15	1.948(6)	Ni2-N312	2.159(2)
Cu2-O115	1.998(3)	Cu5-O416	1.988(3)	Cu2-O115	1.980(6)	Ni2-N400	2.040(3)
Cu2-O215	1.947(3)	Cu5-O418	2.588(3)			Ni2-O216	2.021(2)
Cu3-O20	2.202(3)	Cu5-O516	2.010(3)			Ni2-O500	2.098(2)
Cu3-N201	2.021(3)	Cu5-O518	2.453(3)				
Cu3-N307	1.987(3)						

Table 49 Selected bond angles (°) for **C**[17-18].

C[17]						**C**[18]	
O16-Cu1-N1	93.5 (1)	N301-Cu2-O115	99.4 (1)	O216-Cu4-O15	93.5 (1)	O202-Cu1-N1	92.7 (3)
O16-Cu1-N107	85.3 (1)	O115-Cu2-O215	75.2 (1)	O216-Cu4-O315	91.9 (1)	O202-Cu1-N107	84.4 (4)
O16-Cu1-O115	92.5 (1)	O20-Cu3-N201	93.9 (1)	N7-Cu4-N101	94.9 (1)	O202-Cu1-O15	122.8 (4)
O16-Cu1-O215	119.4 (1)	O20-Cu3-N307	101.8 (1)	N101-Cu4-O315	98.4 (1)	O202-Cu1-O115	91.5 (3)
N1-Cu1-N107	94.8 (1)	O20-Cu3-O15	97.0 (1)	O315-Cu4-O15	75.4 (1)	N1-Cu1-N107	95.4 (3)
N107-Cu1-O115	88.6 (1)	O20-Cu3-O315	90.0 (1)	O15-Cu4-N7	88.5 (1)	N107-Cu1-O115	89.4 (3)
O115-Cu1-O215	75.8 (1)	N201-Cu3-N307	94.5 (1)	N407-Cu5-O415	92.8 (1)	O115-Cu1-O15	75.4 (2)
O215-Cu1-N1	98.6 (1)	N307-Cu3-O315	88.9 (1)	O415-Cu5-O416	88.0 (1)	O15-Cu1-N1	98.5 (3)
O116-Cu2-N301	89.4 (1)	O315-Cu3-O15	76.0 (1)	O416-Cu5-O516	89.7 (1)	O20-Cu2-N7	101.1 (3)
O116-Cu2-N207	123.2 (1)	O15-Cu3-N201	99.2 (1)	O516-Cu5-N407	91.6 (1)	O20-Cu2-N101	96.8 (3)
O116-Cu2-O115	87.2 (1)	O216-Cu4-N7	122.7 (1)	O418-Cu5-O416	54.6 (1)	O20-Cu2-O15	89.3 (3)
O116-Cu2-O215	93.1 (1)	O216-Cu4-N101	89.6 (1)	O518-Cu5-O516	57.0 (1)	O20-Cu2-O115	101.7 (3)
N207-Cu2-N301	94.7 (1)					N7-Cu2-N101	95.7 (3)
						N101-Cu2-O115	97.9 (3)
						O115-Cu2-O15	74.9 (2)
						O15-Cu2-N7	89.0 (3)

Table 50 Intra- and intermolecular H-bonds in the crystal structures of **C[17-19]**.

	D-H···A[a]	D-H [Å]	H···A [Å]	D···A [Å]	D-H···A [°]
	N607-H07B···O18	0.94(5)	1.99(5)	2.924(6)	172(4)
	N601-H601···O19	0.95(5)	1.91(5)	2.844(6)	169(4)
	O700-H700···O316	0.97(5)	1.83(5)	2.785(5)	172(5)
	O710-H710···O116	0.95(4)	2.54(5)	3.389(6)	149(4)
	O710-H710···O118	0.95(4)	2.09(3)	2.980(6)	156(5)
	O720-H720···O710	0.96(6)	1.78(5)	2.733(7)	171(4)
	N607-H07A···O415[a]	0.93(4)	1.98(4)	2.853(5)	157(4)
	O20-H20···O318[b]	0.87(3)	1.82(3)	2.676(4)	171(4)
	O20-H20···O319[b]	0.87(3)	2.52(5)	3.160(5)	131(4)
	O740-H740···O416[c]	1.04(6)	1.81(6)	2.846(6)	173(4)
C[17]	C6-H6···O16	0.95	2.34	3.029(5)	129
	C106-H106···O216	0.95	2.51	3.016(5)	113
	C206-H206···O20	0.95	2.44	3.044(6)	122
	C211-H211···O700	0.95	2.52	3.417(5)	156
	C304-H304···O518	0.95	2.49	3.352(6)	150
	C12-H12···O519[d]	0.95	2.44	3.212(5)	139
	C204-H204···O316[e]	0.95	2.45	3.388(5)	170
	C206-H206···O319[b]	0.95	2.43	3.234(5)	143
	C308-H308···O419[c]	0.95	2.41	3.317(6)	159
	C403-H403···O730[b]	0.95	2.02	2.961(6)	172
	C604-H604···O518[f]	0.95	2.51	3.435(6)	164
	C6-H6···O202	0.95	2.22	2.93(2)	131
	C11-H11···O203	0.95	2.46	3.15(2)	129
	C106-H106···O20	0.95	2.52	3.12(1)	121
C[18]	C8-H8···N607[g]	0.95	2.46	3.40(2)	169
	C108-H108···O204[a]	0.95	2.50	3.44(1)	168
	C14-H14···N602[g]	0.95	2.38	3.29(2)	159

	C111-H111···N606[h]	0.95	2.46	3.08(3)	123
	C112-H112···N602[i]	0.95	2.34	3.14(2)	141
C[19]	O16-H16···N8	0.99(4)	1.70(4)	2.607(4)	150(4)
	O316-H316···N308	0.88(5)	1.83(4)	2.634(4)	150(4)
	C109-H10A···N40	0.99(1)	2.51(1)	3.096(4)	118(1)
	O50-H50···O116[j]	0.79(3)	1.87(3)	2.657(4)	171(3)
	O500-H500···O216[e]	0.82(4)	1.83(4)	2.634(4)	150(4)
	C314-H314···O700[k]	0.95(1)	2.39(1)	3.278(7)	156(1)

[a]Atoms marked with a superscripted letter are generated by the following symmetry operations: a = 2-x, 1-y, -z ; b = 1+x, y, z ; c = 3-x, 1- y, -z ; d = 3-x, 1-y, 1-z ; e = 2-x, 1-y, 1-z ; f = x-1, y, z ; g = 1-x, y, 1/2-z ; h = 1/2+x, 1/2+y, 1/2-z; i = 1/2-x, 1/2+y, z ; j = 1-x, 2-y, 1-z ; k = 1-x, 1-y, -z.

Table 51 Intra- and intermolecular C-H···π and π-π stacking interactions in the crystal structures of **C[17-19]**.

	Atoms involved[a]	*d* between centroids [Å]	C-H···ring [°]
C[17]	C9-C10-C11-C12-C13-C14// C209-C210-C211-C212-C213-C214	4.846(3)	1(1)
	C109-C110-C111-C112-C113-C114// C309-C310-C311-C312-C313-C314	4.752(3)	9(1)
	N1-C2-C3-C4-C5-C6// N401-C402-C403-C404-C405-C406[a]	4.603(3)	10(1)
	C106-H106//Cu4-O216- N217-O218	2.55	119(1)
	C305-H305// C409-C410-C411-C412-C413-C414	2.94	124(1)
	C306-H306//Cu2-O116-N117-O119	2.39	120(1)
	N607-H07A//Cu5-O416-N417-O418[b]	2.85(4)	8(1)
	C21-H21B// N401-C402-C403-C404-C405-C406[c]	2.89(4)	11(1)
C[18]	C9-C10-C11-C12-C13-C14// C9-C10-C11-C12-C13-C14[b]	4.710(6)	9(1)
	C109-C110-C111-C112-C113-C114// C109-C110-C111-C112-C113-C114[b]	4.863(6)	4(1)
	C11-H11//N1-C6-C5-C4-C3-C2	3.00	28(1)
	C11-H11//C2-C3-C4-C5-C6-N1[b]	3.00	28(1)
	C13-H13// N602-C601-C600-C605-C604-C603[d]	2.75	15(1)
C[19]	C110-C111-N112-C113-C114-C115// C210-C211-N212-C213-C214-C215	3.511(2)	11(1)
	C204-H204// C201-C202-C203-C204-C205-C206[e]	2.90(1)	2(1)
	C206-H206//C1-C2-C3-C4-C5-C6[e]	2.76(1)	2(1)
	C306-H306//C310-C311-C312-C313-C314-C315-C316[f]	2.60(1)	2(1)

[a]Atoms marked with a superscripted letter are generated by the following symmetry operations: a = x-1, 1+y, z ; b = 2-x, y, 1/2-z ; c = x, 1+y, z ; d = 1+x, y, z ; e = 1-x, 1-y, 1-z ; f = 2-x, 1-y, -z.

Table 52 Selected bond angles for **C[19]**.

C[19]			
N40-Ni1-N108	94.1 (1)	N208-Ni2-N400	93.9 (1)
N108-Ni1-O116	91.1 (1)	N400-Ni2-O500	89.3 (1)
O116-Ni1-O50	84.4 (1)	O500-Ni2-O216	87.3 (1)
O50-Ni1-N40	90.3 (1)	O216-Ni2-N208	89.5 (1)
N12-Ni1-N40	91.6 (1)	N112-Ni2-N208	91.6 (1)
N12-Ni1-N108	90.6 (1)	N112-Ni2-N400	93.2 (1)
N12-Ni1-O116	86.8 (1)	N112-Ni2-O500	90.8 (1)
N12-Ni1-O50	88.2 (1)	N112-Ni2-O216	87.3 (1)
N212-Ni1-N40	92.6 (1)	N312-Ni2-N208	89.0 (1)
N212-Ni1-N108	89.4 (1)	N312-Ni2-N400	93.6 (1)
N212-Ni1-O50	91.5 (1)	N312-Ni2-O216	85.8 (1)
N212-Ni1-O116	89.1 (1)	N312-Ni2-O500	88.2 (1)
Ni1-N40-C41	175.7 (1)	Ni2-N400-C401	171.4 (1)
N40-C41-S42	178.1 (1)	N400-C401-S403	179.2 (1)

Table 53 Crystal data and structure refinement for **H[1-4]**.

	H[1]		**H[2]**	**H[3]**	**H[4]**
T [K]	120(2)	250(2)	120(2)	120(2)	120(2)
Empirical formula	$C_{53}H_{56}ClCuN_7O_{11}S$		$C_{50}H_{52}ClNiN_7O_{12}S$	$C_{62}H_{44}N_8CuO_8S_2$	$C_{62}H_{44}N_8NiO_8S_2$
Fw	1098.10		1069.21	1156.71	1151.88
Crystal system	Triclinic		Triclinic	Monoclinic	Monoclinic
Space group	*P*$\bar{1}$ (No 2)		*P*$\bar{1}$ (No 2)	*C*2/c (No 15)	*C*2/c (No 15)
a [Å]	11.198(3)	11.302(3)	11.185(3)	26.553(7)	26.475(7)
b [Å]	12.969(4)	13.011(4)	12.835(4)	10.812(2)	10.747(2)
c [Å]	16.759(5)	16.949(5)	16.700(5)	21.889(6)	21.930(6)
α [°]	86.69(2)	86.62(2)	86.66(2)	90	90
β [°]	83.75(2)	83.48(2)	83.82(2)	124.59(2)	124.24(2)
γ [°]	81.74(2)	82.18(2)	81.13(2)	90	90
V [Å³]	2392(1)	2451(1)	2377(1)	5173(2)	5158(2)
Z	2	2	2	4	4
ρ_{calc} [Mg.m^{-3}]	1.525	1.488	1.477	1.485	1.483
F(000)	1146	1146	1116	2388	2384
μ [mm^{-1}]	0.63	0.614	0.575	0.5272	0.527
Crystal size [mm]	0.32 x 0.18 x 0.08		0.25 x 0.20 x 0.20	0.44 x 0.32 x 0.30	0.55 x 0.5 x 0.3
θ max [°]	23.25	21.96	24.43	27.50	26.73
Reflections collected/ unique	20500/6398	17370/5660	29231/7634	106674/ 5868	91450/5328
R_{int}	0.0409	0.061	0.055	0.040	0.037
R_1 [I>2σ(I)]	0.0542 [5304]	0.052 [4592]	0.047 [6450]	0.0442 [5594]	0.0359 [5204]
wR_2	0.1440	0.1389	0.1228	0.1208	0.1010
Largest peak and hole	1.439 and -0.788	0.557 and -0.527	0.775 and -0.593	0.481 and -0.668	0.451 and -0.549

Table 54 Selected bond lengths and angles for $\mathbf{H^1}$ and $\mathbf{H^2}$

	$\mathbf{H^1}$		$\mathbf{H^2}$
T [K]	120(2)	250(2)	120(2)
M···**1** [Å]	9.09(1)	10.34(1)	9.15(1)
Anion···**1** [Å][a]	5.07(1)	5.12(1)	5.05(1)
Φ_1[b] [°]	32(1)	32(1)	32(1)
C1-N2 [Å][c]	1.416(6)	1.418(6)	1.407(3)
N2-C3 [Å][c]	1.281(6)	1.274(6)	1.268(3)
C3-C4 [Å][c]	1.457(6)	1.457(7)	1.439(3)
C4-C5 [Å][c]	1.410(6)	1.410(6)	1.415(3)
C5-O6 [Å][c]	1.352(6)	1.354(6)	1.347(3)
O6-H7 [Å][c]	0.80(6)	0.83(6)	0.83(4)
H7···N2 [Å][c]	1.87(7)	1.84(7)	1.85(3)
H7···H_β [Å][c]	2.22(7)	2.25(7)	2.30(4)
M-N1 [Å]	2.138(4)	2.150(4)	2.085(2)
M-N4 [Å]	2.067(4)	2.107(4)	2.108(2)
M-N101 [Å]	2.241(4)	2.193(4)	2.087(2)
M-N104 [Å]	2.118(4)	2.123(4)	2.061(2)
M-N201 [Å]	2.041(4)	2.074(4)	2.088(2)
M-N204 [Å]	2.225(4)	2.178(5)	2.081(2)
$\sum$ [°][d]	74(2)	80(2)	62(1)

[a]Distance between M and the centroid of **1**.[b]Dihedral angle between phenolic and benzoic rings of **1**. [c]Atoms numbering with respect to Scheme 20.[e]Distortion parameter following the equation $\Sigma = \sum_{i=1}^{12} (|\varphi_i - 90|)$ where φ corresponds to N-M-N angle.

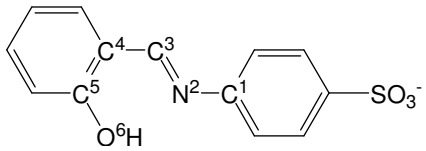

Scheme 20 Molecular scheme of the anion **1** inserted in $\mathbf{H^1}$ and $\mathbf{H^2}$ hybrid materials.

Table 55 Intra- and intermolecular H-bonds in the crystal structure of **H[1]** at 120 K and 250 K.

T [K]	D-H···A	D-H [Å]	H···A [Å]	D···A [Å]	D-H···A [°]
120(2)	O415-H415···N408	0.81(7)	1.87(7)	2.605(5)	150(7)
	0501-H1A···O417[a]	0.90(4)	2.01(5)	2.888(5)	165(5)
	O501-H1B···O418	0.92(4)	1.97(4)	2.824(5)	153(5)
	O502-H2A···O501	0.91(5)	1.94(5)	2.804(5)	159(5)
	O502-H2B···O503	0.89(4)	2.00(5)	2.879(6)	172(6)
	O503-H3A···O504[b]	0.88(5)	1.88(5)	2.753(5)	170(5)
	O503-H3B···O415[c]	0.90(5)	2.36(5)	3.167(5)	150(4)
	O504-H4A···O419	0.91(5)	1.96(5)	2.855(5)	170(5)
	O504-H4B···Cl1	0.91(3)	2.28(3)	3.181(4)	171(4)
	C602-H60D···O505	0.98	1.83	2.46(1)	120
	C702-H70C···O505[a]	0.98	1.90	2.54(1)	121
250(2)	O415-H415···N408	0.84(7)	1.84(7)	2.606(5)	151(7)
	O501-H1A···O417[a]	0.90(4)	2.13(5)	2.935(5)	149(5)
	O501-H1B···O418	0.93(4)	1.96(4)	2.816(6)	153(5)
	O502-H2A···O501	0.89(6)	1.98(6)	2.801(6)	152(6)
	O502-H2B···O503	0.89(4)	2.03(5)	2.900(7)	167(6)
	O503-H3A···O504[b]	0.91(6)	1.95(6)	2.732(7)	144(5)
	O504-H4A···O419	0.91(6)	1.98(6)	2.862(7)	162(6)
	O504-H504···Cl1	0.93(4)	2.28(4)	3.187(5)	168(6)
	C702-H70C···O505[a]	0.97	1.95	2.61(1)	123

[a]O417 and O505 are generated by the symmetry operation: 1-x, 1-y, 1-z. [b] O504, Cl1 and O4: x, 1+y, z. [c]O415: -x, 1-y, 1-z.

Table 56 Intra- and intermolecular C-H···π and π-π stacking interactions in the crystal structure of **H[1]** at 120 and 250 K.

T [K]	Moiety 1	Moiety 2	d [Å]	Φ [°]
120 (2)	C202-C203-C208-C210-C209-C211	C401-C402-C403-C404-C405-C406	3.592(3)	6.9(2)
	N1-C2-C11- C12-C13-C14	C2-C3-C8- C9-C10-C11[a]	3.631(3)	3.0(2)
	C2-C3-C8-C9-C10-C11	C2-C3-C8-C9-C10-C11[a]	3.706(3)	0(1)
	C102-C103-C108-C109-C110-C111	C102-C103-C108-C109-C110-C111[b]	3.65(3)	0(1)
	C107-H107	C401-C402-C403-C404-C405-C406	2.69(4)	14(1)
	C14-H14	N201-C202-C211-C212-C213-C214	2.95(4)	26(1)
	C702-H70E	N1-C2-C11-C12-C13-C14[c]	2.95(4)	20(1)
250 (2)	N1-C2-C11-C12-C13-C14	C2-C3-C8-C9-C10-C11[a]	3.670(3)	2.7(2)
	C2-C3-C8-C9-C10-C11	C2-C3-C8-C9-C10-C11[a]	3.764(3)	0(1)
	C102-C103-C108-C109-C110-C11	C409-C410-C411-C412-C413-C414	3.945(3)	30.0(2)
	C202-C203-C208-C210-C209-C211	C401-C402-C403-C404-C405-C406	3.622(3)	7.2(3)
	C14-H14	N201-C202-C211-C212-C213-C214	2.96	26.05
	C107-H107	C401-C402-C403-C404-C405-C406[c]	2.75	15.33

[a]Rings are generated by the symmetry operation: -x, 1-y, -z. [b] -x, 1-y, 1-z. [c] -x, -y, 1-z.

Table 57 Intra- and intermolecular C-H···π and π-π stacking interactions in the crystal structure of $\mathbf{H^2}$.

Moiety 1	Moiety 2	d [Å]	Φ [°]
C202-C203-C208- C210-C209-C211	C401-C402-C403- C404-C405-C406	3.625(2)	6.1(1)
N1-C2-C11- C12-C13-C14	C2-C3-C8- C9-C10-C11[a]	3.610(2)	1.9(1)
C2-C3-C8- C9-C10-C11	C2-C3-C8- C9-C10-C11[a]	3.745(2)	0(1)
C102-C103-C108- C109-C110-C111	C102-C103-C108- C109-C110-C111[b]	3.693(2)	0(1)
C107-H107	C401-C402-C403- C404-C405-C406[a]	2.71(3)	15(1)
C14-H14	N201-C202-C211- C212-C213-C214	2.82(4)	27(1)
C10-H10	N204-C203-C208- C207-C206-C205[c]	2.97(4)	24(1)

[a]Rings are generated by the symmetry operation: -x, 1-y, -z. [b] -x, 1-y, 1-z. [c] -x, -y, 1-z.

Table 58 Intra- and intermolecular H-bonds in the crystal structure of **H²**.

D-H···A	D-H [Å]	H···A [Å]	D···A [Å]	D-H···A [°]
O415-H415···N408	0.83(4)	1.85(3)	2.608(3)	151(4)
O501-H51A···O417[a]	0.84(4)	2.03(3)	2.855(3)	169(3)
O501-H51B···O418	0.80(4)	2.04(4)	2.800(3)	159(3)
O502-H52A···O503	0.86(4)	2.03(4)	2.895(3)	177(3)
O502-H52B···O501	0.74(4)	2.01(4)	2.753(3)	177(4)
O503-H53A···O504[b]	0.82(4)	1.89(4)	2.713(3)	175(3)
O503-H53B···O415[c]	0.86(3)	2.35(3)	3.192(3)	164(3)
O504-H54A···O419	0.93(4)	1.91(4)	2.835(3)	172(3)
O504-H54B···Cl1	0.84(3)	2.29(3)	3.126(2)	175(4)
O505-H55B···O502	1.03(3)	1.73(2)	2.747(3)	169(3)
O506-H56A···Cl1[b]	0.88(4)	2.34(4)	3.220(2)	173(3)
O506-H56B···Cl1[d]	0.91(3)	2.27(3)	3.177(3)	172(3)
O507-H57A···O506[a]	0.97(3)	1.73(3)	2.702(4)	178(5)
O507-H57B···O70A[e]	0.91(3)	1.78(3)	2.687(4)	177(2)
C6-H6···O418[f]	0.96(3)	2.48(3)	3.365(3)	154(3)
C106-H106···O417[g]	0.94(3)	2.49(3)	3.078(3)	121(3)
C406-H406···O419[h]	0.95(3)	2.47(3)	3.399(3)	165(3)
C413-H413···O417	1.00	2.45(4)	2.888(3)	106(2)

[a] O417 and O506 are generated by the symmetry operation: 1-x, 1-y, 1-z. [b] O504, Cl1 and O4: x, 1+y, z. [c] O415: -x, 1-y, 1-z. [d] Cl1: 1-x, 1-y, 2-z. [e] O70A: 1-x, 1-y, -z.[f] O418 and O2: -x, 1-y, -z. [g] O417: x-1, y, z. [h] O419: 1-x, -y, 1-z.

Table 59 Selected distances and angles in $\mathbf{H^3}$ and $\mathbf{H^4}$.

	$\mathbf{H^3}$	$\mathbf{H^4}$
M···M [Å]	10.81 (1)	10.75 (1)
2···M [Å][a]	5.79 (1)	5.74 (1)
Φ_1[b] [°]	13(1)	12 (1)
C22-N11 [Å]	1.431 (3)	1.427 (2)
N11-C21 [Å]	1.278 (3)	1.282 (2)
C21-C20 [Å]	1.456 (3)	1.453 (3)
C20-C15 [Å]	1.419 (3)	1.417 (3)
C15-O1 [Å]	1.341 (3)	1.344 (2)
O1-H1 [Å]	0.84	0.96
H1···N11 [Å]	1.88	1.73
H21···H27 [Å]	2.12	2.22
M-N1 [Å]	2.024 (2)	2.080 (2)
M-N10 [Å]	2.170 (2)	2.094 (2)
M-N101 [Å]	2.189 (2)	2.099 (2)
$\sum$ [°][c]	72 (2)	65 (1)

[a]Distance between M and the centroid of the anion. [b]Dihedral angle between aromatic rings. [c]Distortion parameter following the equation $\Sigma = \sum_{i=1}^{12} (|\varphi_i - 90|)$ where φ corresponds to N-M-N angle.

Table 60 Intra- and intermolecular H-bonds in **H^3** and **H^4** crystal structures.

	D-H···A	D-H [Å]	H···A [Å]	D···A [Å]	D-H···A
H^3	O1-H1···N11	0.84	1.88	2.621 (3)	147
	C2-H2···O3[a]	0.95	2.37	3.068 (3)	130
	C4-H4···O3[b]	0.95	2.48	3.396 (4)	162
	C7-H7···O4[c]	0.95	2.52	3.376 (4)	150
	C102-H102···O2[d]	0.95	2.44	3.241(3)	143
H^4	O1-H1···N11	0.96	1.73	2.623 (2)	153
	C2-H2···O3[a]	0.95	2.23	3.074 (3)	131
	C4-H4···O3[b]	0.95	2.48	3.401 (3)	162
	C6-H6···O4[c]	0.95	2.59	3.418 (3)	146
	C7-H7···O4[c]	0.95	2.51	3.361 (3)	149
	C25-H25···O3	0.95	2.58	2.926 (3)	102
	C102-H102···O2[d]	0.95	2.44	3.227 (2)	140

[a]O3 is generated following the symmetry operation: x, 1-y, 1/2+z ; [b] 1/2-x, 1/2+y, 1/2-z ; [c]O4: x, 1+y, z ; [d]O2: -x, 1-y, -z .

Table 61 Intra- and intermolecular C-H···π and π-π stacking interactions in **H³** crystal structures.

Moiety 1	Moiety 2	d [Å]	Φ [°]†
Cu1-N101-C106-C106-N101	C22-C23-C24-C25-C26-C27	4.907 (2)	14.3 (1)
N101-C102-C103-C104-C107-C106	C15-C16-C17-C18-C19-C20[a]	4.662 (2)	2.4 (1)
N101-C102-C103-C104-C107-C106	C22-C23-C24-C25-C26-C27	3.646 (2)	12.5 (1)
C105-C107-C106-C106-C107-C105	C15-C16-C17-C18-C19-C20	4.860 (2)	2.7 (1)
C105-C107-C106-C106-C107-C105	C22-C23-C24-C25-C26-C27	4.802 (2)	13.3 (1)
C105-C107-C106-C106-C107-C105	C22-C23-C24-C25-C26-C27[a]	4.802 (2)	13.3 (1)
C15-C16-C17-C18-C19-C20	C105-C107-C106-C106-107-C105[a]	4.801 (2)	2.7 (1)
C15-C16-C17-C18-C19-C20	C15-C16-C17-C18-C19-C20[b]	4.004 (2)	0 (1)
C22-C23-C24-C25-C26-C27	Cu1-N101-C106-C106-N101[a]	4.907 (2)	14.3 (1)
C5-H5	C22-C23-C24-C25-C26-C27[c]	2.87	21.8
C27-H27	N1-C2-C3-C4-C13-C12	2.74	13.6
C105-H105	N10-C9-C8-C7-C14-C11[d]	2.95	17.4

[a]The rings are generated following the symmetry operation: -x, y, 1/2-z ; [b]1/2-x, 1/2-y, 1-z ; [c]1/2-x, 1/2+y, 1/2-z ; [d]x, -1+y, z. †Dihedral angle between aromatic rings.

Table 62 Intra- and intermolecular C-H···π and π-π stacking interactions in **H[4]** crystal structures.

Moiety 1	Moiety 2	d [Å]	Φ [°][†]
Ni1-N101-C106-C106-N101	C22-C23-C24-C25-C26-C27	4.911 (2)	15.1 (1)
Ni1-N101-C106-C106-N101	C22-C23-C24-C25-C26-C27[a]	4.911 (2)	15.1 (1)
N101-C102-C103-C104-C107-C106	C15-C16-C17-C18-C19-C20[a]	4.688 (2)	3.5 (1)
N101-C102-C103-C104-C107-C106	C22-C23-C24-C25-C26-C27	3.639 (2)	12.5 (1)
C105-C107-C106-C106-C107-C105	C15-C16-C17-C18-C19-C20	4.881 (2)	3.1 (1)
C105-C107-C106-C106-C107-C105	C15-C16-C17-C18-C19-C20[a]	4.881 (2)	3.1 (1)
C105-C107-C106-C106-C107-C105	C22-C23-C24-C25-C26-C27	4.778 (2)	13.6 (1)
C105-C107-C106-C106-C107-C105	C22-C23-C24-C25-C26-C27[a]	4.778 (2)	13.6 (1)
C15-C16-C17-C18-C19-C20	C15-C16-C17-C18-C19-C20[b]	3.953 (2)	0 (1)
C5-H5	C22-C23-C24-C25-C26-C27[c]	2.83	19.11
C27-H27	N1-C2-C3-C4-C13-C12	2.70	12.36
C105-H105	N10-C9-C8-C7-C14-C11[d]	2.96	18.34

[a]The rings are generated following the symmetry operation: -x, y, 1/2-z ; [b]1/2-x, 1/2-y, 1-z ; [c]1/2-x, 1/2+y, 1/2-z ; [d]x, -1+y, z. [†]Dihedral angle between aromatic rings.

Table 63 Crystal data and structure refinement for **K1**.

Empirical formula	$C_{13}H_{10}KNO_4S$	ρ_{calc} [Mg.m^{-3}]	1.342
fw	315.38	F(000)	648
T [K]	120 (2)	μ [mm^{-1}]	0.484
Crystal system	Orthorhombic	θ max [°]	24.41
space group	$Pca2_1$ (No 29)	Reflections collected/ unique	11680/ 2489
a [Å]	8.491 (2)	R_{int}	0.059
b [Å]	19.788 (5)	R_1 [I>2σ(I)]	0.1209
c [Å]	9.287 (3)	wR_2	0.3666
V [Å^3]	1560. (7)	Largest peak and hole	2.410 and -0.886
Z	4		

Additional material

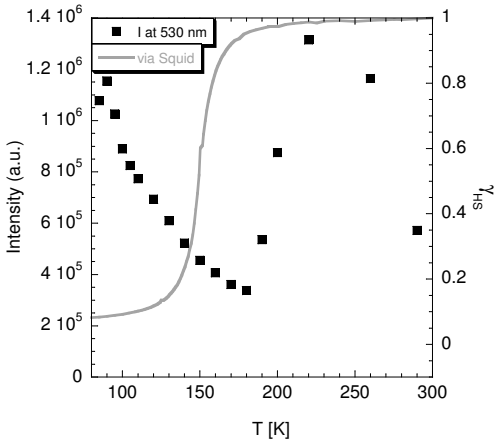

Figure 131 Temperature dependence of the emission intensity of cis* in the emission spectra at 400 nm of **Hsaltrz** versus the molar fraction of HS iron(II) ions obtained by the SQUID measurements for **C**[7]. The evolution is complicated because of the slow decrease of the fluorescence intensity to approximately 190 K, followed by an increase to 220 K and by a decrease to 290 K. No clear explanation is actually proposed but a modification of most stable conformations and/or a change of favoured relaxation scheme is suggested.

Materials

Solvents (acetone, chloroform, diethylether and toluene analytical reagent, absolute ethanol, n-hexane HPLC grade, methanol analytical and technical grade from Prolabo; DMSO-d^6 from Aldrich, toluene for analysis from Fisher Chemicals; benzene ≥ 99 % from Fluka and ethylene glycol 99 % from Acros Organics) and reagents (2-aminopyridine, 3-aminopyridine and 4-aminopyridine from Lancaster; 1,10-phenanthroline, 4-amino-4H-1,2,4-triazole 99 %, 2-cyanopyridine 99 %, ethanolamine 99 %, hydrazine dihydrochloride 99 %, L(+)-ascorbic acid, o-vanillin 99 %, salicylaldehyde, triethylorthoformate 98 %, 5-chlorosalicylaldehyde, $FeCl_2•4H_2O$, $Fe(NH_4)_2(SO_4)_2$, $CoSO_4•7H_2O$, $CuCl_2•2H_2O$, $Cu(NO_3)_2•3H_2O$, $MnCl_2•4H_2O$, KNCSe and NH_4NCS extra pure from Acros Organics; (1,10)-phenanthrolin-5-amine 97 %, 2-hydroxy-1-naphtaldehyde technical grade, 2-(aminomethyl)pyridine 99 %, 3-(aminomethyl)pyridine ≥ 99 %, 4-(aminomethyl)pyridine 98 %, 3-hydroxysalicylaldehyde, 4-hydroxysalicylaldehyde 98 %, 3,4-dihydroxysalicylaldehyde 98 %, 5-aminotetrazole 97 %, 5-bromosalicylaldehyde 98 %, calcium hydroxide 95+%, ethylformate 97 %, molecular sieves 4 Å-beads 4-8 mesh, hydrazine monohydrate 98 %, Sulfanilic acid 99 %, $CoCl_2•6H_2O$ ACS Reagent, $ZnBr_2$ > 98 % from Aldrich; sodium hydroxide, analytical reagent from Fisher Scientific; 3-aminobenzenesulfonic acid, > 98 %, $ZnCl_2$ 98 % and ZnI_2 pure from Fluka; $CuSO_4•5H_2O$, ZnF_2 and potassium hydroxide analytical reagent from Riedel-de Haën and $NiCl_2$ from UCB; CD_3OD-d^4 $HDO+D_2O$ < 0.03 % from Euriso-top) were obtained commercially and used as received.

Sonications were made with a Branson 3510 ultrasonic bath. ^1H and ^{13}C NMR spectra were recorded on a Brüker AC 300 MHz instrument with DMSO protons peak as internal standard. H and C atoms attributions were done, when it was possible, following the atoms numbering found in the crystal structure (see CIF files and figures in the text) and confirmed by COSY and HMQC 2D experiments. ^1H-NMR of $\mathbf{C^{14}}$ and $\mathbf{C^{15}}$ were measured with a Brüker Advance DRX 500 MHz equiped with a Dual $^1H/^{13}C$ probe. Infrared spectra were recorded on a Shimadzu FTIR-8400S spectrometer with KBr discs. Peaks attributions were found following Ref. [404, 405]. Mass

spectral data were obtained on Thermofinnigan LCQ ion trap spectrometer using an ESI ionization mode for **Hsaltz** (+), **Hsalphen** (+), **Ksaltz** (-), **Na2** (-), **K1** (-), **Ca1** (-), **Na1Cl** (-), **Na1Br** (-) and **C**$^{14\text{-}16}$ (+) and APCI ionization mode for **Habs** (+), **Hsaltrz** (+), **Na1** (-), **CH$_2$L^4 (+)**, **CH$_2$L^6** (+) and **Rsaltrz** (+). Elementary analyses were performed at University College London. Atomic absorptions were carried out with a Varian SpectrAA-300. Sampling was done in aqueous nitric acid solutions and standard solutions were prepared with Möhr salt.

The TGA/DTA instrument used was a TA instrument SDT2960 Simultaneous DSC-TGA with alumina crucibles filled with approximately 10 mg of sample. Crystalline sample of **C**^{17} was taken from the solution and directly sampled under dried air. The temperature program for this compound was: (i) isotherm 25°C, 2h; (ii) heating to 130°C, 1°C/min; (iii) isotherm 130°C, 1h; (iv) cooling down to 25°C, 1°C/min; (v) stabilization at 25°C, 5 min; (vi) heating to 450°C, 10°C/min. For **C**^{18}, The sample was filtered and stored under dried atmosphere and rapidly measured to avoid moisture absorption. The temperature program was: (i) stabilization at 30°C; (ii) heating to 150°C, 1°C/min; (iii) isotherm 150°C, 20 min; (iv) cooling down to 25°C, 1°C/min; (v) stabilization at 25°C; (vi) heating to 500°C, 5°C/min. The TGA instrument combined with a mass spectrometer (Pfeiffer Vacuum Thermostat) was a Mettler Toledo TGA/SDTA 851e TGA with alumina crucibles filled with approximately 10 mg of sample. DSC measurements above the room temperature were carried out at a scanning rate of 10 K/min, over the temperature range (298-873 K) on a Mettler Toledo DSC20, calibrated with pure aluminium (s/l) and indium (s/l), used with an alumina sample holders. Measurements below 298 K were carried under a helium atmosphere by using a Perking-Elmer DSC Pyris 1 instrument equipped with a liquid nitrogen cryostat. Aluminium capsule containing **C**^{7} was loaded with 79 mg of crystalline sample. The heating and cooling rate were fixed at 5 K.min^{-1}. Temperatures and enthalpies were calibrated over the temperature range of interest using the solid-solid transitions of pure cyclopentane (≥ 99 %).

X-ray powder diffractograms were performed on a Siemens D5000 X-ray diffractometer, with a Cu anticathode ($\lambda K\alpha$ = 1.5418 Å) in Bragg-Brentano

geometry (θ/θ mode). Samples were deposited on silicon after calibration with a quartz standard. UV/Visible absorption spectra of solutions were obtained on a Varian Cary 50conc spectrometer using a quartz cell (1 x 1 x 4.5 cm). Solution emission spectra were performed with a Cary Eclipse spectrometer using a quartz cell (1 x 1 x 4.5 cm).

Diffuse Reflectance spectra were obtained on a Varian Cary 5E spectrometer using PTFE as a reference. Spectra were measured on pure solids to avoid matrix effects.[14, 103-113] Eventual distortions in the Kubelka-Munk spectra,[396] that could result from the study of pure compounds, have not been considered because no comparison with absorption spectra was necessary. Diffuse reflectance spectra were sometimes normalized to allow meaningful comparisons. Signals assignment was supported by reported band ranges obtained with diluted samples of *N*-salicylidene aniline derivatives.[89] Light irradiations were carried out either with a standard lamp used for visualizing TLC plates (ROC; intensity at 15 cm from filter: 440 μW cm^{-2} at 254 nm) for $\mathbf{L}^{2\text{-}5}$ or with a LOT-ORIEL 200 W high-pressure mercury arc lamp combined with selected band pass filter and a water cooling setup to avoid infrared light exposure. Kubelka-Munk spectra were taken before and after UV irradiation which was undertaken during the time described in the text. The reversibility of the *cis-trans* isomerisation was checked with a LOT-ORIEL 200 W high pressure mercury arc lamp combined with a water cooling setup to avoid infrared light exposure. In situ irradiations were carried out for 10 min with appropriate filters. Data that were accumulated each 30 s by diffuse reflectance spectroscopy were normalized. Solid-state emission and excitation spectra were obtained with a Fluorolog-3 (Jobin-Yvon-Spex Company) spectrometer equipped with an adapted liquid nitrogen Oxford optistat. Temperature dependent experiments were carried out in warming mode because no hysteresis was expected and because of the instability of some compounds at high temperatures. No influence of the light irradiation during fluorescence measurements was noted (e.g. LIESST effect in the case of $\mathbf{C}^{7}$). Reproducibility of temperature dependent emission and excitation spectra was checked on fresh samples that provided the same spectroscopic results.

Variable temperature ^{57}Fe Mössbauer spectra were recorded in transmission geometry with a constant acceleration mode conventional spectrometer equipped with a WISSEL or IKS motor, 45 mCi ^{57}Co(Rh) source, several bethcryostats including an Oxford optistat DN and a Reuter Stokes proportional counter. Powder sample was sealed in aluminium foil and spectra were recorded over the temperature range using a liquid nitrogen cryostat. The spectra were fitted using Recoil 1.05 Mössbauer Analysis Software.[406] The isomer shift values are given with respect to α-Fe at room temperature. **C^{7}** was only measured up to 208 K to avoid problems linked to solvent lost. Magnetic susceptibility of **C^{17}** was measured with a Quantum Design SQUID magnetometer MPMS-XL. M vs. H measurements were performed at 100 K to check for the presence of ferromagnetic impurities; none were observed. The magnetic data were corrected for the sample holder and diamagnetic contributions. Magnetic susceptibilities of **C^{18}** and **C^{19}** were not recorded because of the too low available sample quantity of **C^{18}** and the likely Curie paramagnetism of **C^{19}**. Magnetic susceptibilities were measured with a 5T SQUID magnetometer for **C^{7}**. The magnetic data were corrected for the sample holder and diamagnetic contributions. The crystal sample was quickly loaded into a gelatin capsule and immediately inserted within the SQUID cavity.

Lifetime of excited states were measured for **Habs** and related complexes in collaboration with Dr. B. Muls and Prof. Habib Jiwan. The time resolved fluorescent measurements were performed by time correlated single photon counting (TCSPC). In those measurements, the distribution of the time delays between the absorption of a photon and the emission of the fluorescent photon is determined. This distribution is constructed by repeatedly exciting the sample with a pulsed laser and measuring the time needed to detect the first photon after the pulse. The time is measured using a time-to-amplitude converter (TAC). The events (photon detection) are collected in a memory by adding a count in a location of the multi-channel analyzer (MCA) with an address corresponding to the detected time delay. After many photon detections in the memory, the histogram of the detected times is built.[407, 408] The laser pulses were generated by a Mira femtosecond laser which delivers femtosecond pulses (130 fs) at a repetition frequency of

76 MHz. A Verdi 10 W 532 nm continuous wave Nd-YAG laser is used to pump the Miar laser. The wavelength is tunable in the range of 710 to 1000 nm thanks to the use of a Titanium-sapphire crystal. The repetition frequency is then decreased to 3.8 MHz using a Coherent 9200 pulse picker. At the output of this setup, 1 % of the laser beam is deviated to a photodiode delivering the synchronization pulses. The wavelength of the pulsed laser beam is then divided by two using a Coherent 9300 doubler (doubling the frequency of the photons). The resulting pulses are directed into a Fluotime 200 (Picoquant) where the sample is located. The fluorescence was detected by a micro-channel plate (MCP). The pulses delivered by the MCP as well as the synchronizing pulses are directed to a single photon counting card (SPC-630, Bercker and Hickl). The card is used in TCSPC mode (4096 channels). The obtained histograms are analysed with TRFA software.[408]

Fluorescence quantum measurements were carried out in Lausanne in Prof. J.-C. Bünzli's laboratory by F. Gumy. The experiments were done with a home-made analyser where the solid samples were irradiated with a selected light. The wavelength was chosen at 430 nm to avoid photo-bleaching phenomena. The emission was quantified using a detector combined with an integration sphere allowing absolute measurements.

X-ray Structure Data Collection and Refinement: X-ray intensity data were collected for all compounds with a MAR345 image plate using MoKα (λ= 0.71069Å) radiation except for **Ksaltz** which was analysed with a Xcalibur CCD diffractometer (Gemini Ultra Mo) in Prof. J. Wouters's lab in Namur. The crystal was chosen, mounted in inert oil and transferred quickly to the cold gas stream for flash cooling. Crystal data and data collection parameters are summarized in Table 19 to Table 62. The unit cell parameters were refined using all the collected spots after the integration process. Except for **Ksaltz**, the data were not corrected for absorption, but the data collection mode partially takes the absorption phenomena into account. (See the total number of collected reflections versus the independent number of reflections in Table 19, Table 24, Table 28, Table 32, Table 36, Table 42, Table 46 and Table 53).

All structures were solved by direct methods with SHELXS97.[409] The structures of **C**$^{2-5}$ are isomorphous with that of **C**^{1}. All structures were refined by full-matrix least-squares on F^2 using SHELXL97.[409] All the non-hydrogen atoms were refined with anisotropic temperature factors. When it was possible (e.g. for **L**^{4}, **L**^{5}, **Habs**, **Hsaltrz**, **Hsaltz**, **Hsalphen** and **H**^{3}) all the hydrogen atoms were localized by Fourier-difference synthesis. For some compounds (e.g. **Ksaltz** and **C**$^{1-5}$), only H atom of the hydroxyl group was localized, the other H atoms were calculated with AFIX. When the H could not be localized, they were calculated with AFIX or if it was not possible not included (see cif files in appendix). The H atoms were included in the refinement with a common isotropic temperature factor.

When disorder was observed, some constraints were applied on bond lengths and bond angles. The final R index and all the refinement parameters are listed in Table 19, Table 24, Table 28, Table 32, Table 36, Table 42, Table 46 and Table 53. The R values of structures **C**^{2}, **C**^{5} and **K1** are abnormally high. A second data set with crystal from a new crystallization batch was collected for both compounds but we did not obtain better results probably because of poor crystal quality. Tables of distances and angles were obtained using PLATON software.[410]

Computational Details: For isolated molecules of **L**$^{3-4}$, the geometry optimization of ground and excited states was performed at the UB3LYP/6-31G(d,p) level of theory using Jaguar 6.5 pseudospectral program package.[411] For isolated molecules of **Habs** and **Hsalphen**, the geometry optimization of ground and excited states was performed at the UB3LYP/6-31G(d,p) and CIS/6-31G(d,p) levels of theory, respectively. Enol, *cis*-keto and *trans*-keto forms (and the cyclised intermediate in the case of **Habs**) were fully geometry optimized. Energy profile for *cis/trans*-keto isomerisation was obtained by performing a set of constrained geometry optimization at successively larger values of the C14-C9-C8-N7 torsion angle (for **L**$^{3-4}$) and at similar values of C4-C3-C2-N1 (see Scheme 10 and Scheme 11, p. 57 and 59) angles for **Habs** and **Hsalphen**. All energies are given after single point calculations at the CIS/6-311+G(d,p) level using Gaussian 03 program.[412] For calculations taking crystal packing into account, systems were taken so as to be constituted of one molecule

surrounded by others in every direction (i.e., about 10-12 molecules for $\mathbf{L}^{3\text{-}4}$, 4 molecules for **Habs** and 5 molecules for **Hsalphen**. Crystal environment created by neighbouring molecules was taken from X-Ray crystal structures. Optimization was performed at the CIS/6-31G(d,p) levels of theory (S^1) for **Habs** and **Hsalphen** and AM1 pour $\mathbf{L}^{3\text{-}4}$. The position of every atom of such molecules was frozen during optimization calculations with only the central molecule being fully geometry optimized, excepted for the TS obtained during *cis/trans*-keto isomerization which were obtained by freezing the torsion angle at 90°. Energies were obtained by single point calculations with the central molecule and crystal packing (surrounding molecules) treated at the B3LYP/6-31G(d) and B3LYP/6-31G level of theory, respectively. Stabilization energy induced by the packing was estimated by eq. (a):

$$E_{stab} = E_{system} - E_{isolated\ molecule} - E_{surrounding\ molecules} \qquad (a)$$

where E_{system} is the energy of the full system (i.e. central molecule and surrounding molecules), $E_{isolated\ molecule}$ is the energy (B3LYP/6-31G(d)) of the central molecule of interest without its surrounding, $E_{surrounding\ molecules}$ is the energy (B3LYP/6-31G) of the surrounding molecules (without the molecule of interest). The relative stabilization energy respective to the enol form was estimated according to eq. (b):

$$\text{Rel. } E_{stab} = \mathbf{E}_{\mathbf{stab}}^{\mathbf{intermediate}} - \mathbf{E}_{\mathbf{stab}}^{\mathbf{enol}} \qquad (b)$$

Calculations of interaction energies are susceptible to basis set superposition error (BSSE). In order to eliminate this error, $E_{isolated\ molecule}$ and $E_{surrounding\ molecules}$ were estimated by single point calculations using a mixed basis set containing 'ghost orbitals' corresponding to the surrounding molecules and the central molecule, respectively.

In the case of metallic complexes, only ground state structures were investigated (using Jaguar 6.5 pseudospectral program package). All structures were fully geometry optimized at the UB3LYP/6-31G(d,p) level of theory with the LACV3P basis set on the metallic atom. Energy profile for rotation around the N-metal bond was obtained by performing a set of constrained geometry optimization at successively larger values of the N-M-

N-C torsion angle. All energies are given after single point calculations at the UB3LYP/6-311+G(d,p) levels of theory with the LACV3P basis set on the metallic atom. The metallic atoms (Ni and Cu) have been considered in their +2 oxidative / high spin state.

Experimental section

Organic molecules

Synthetic schemes

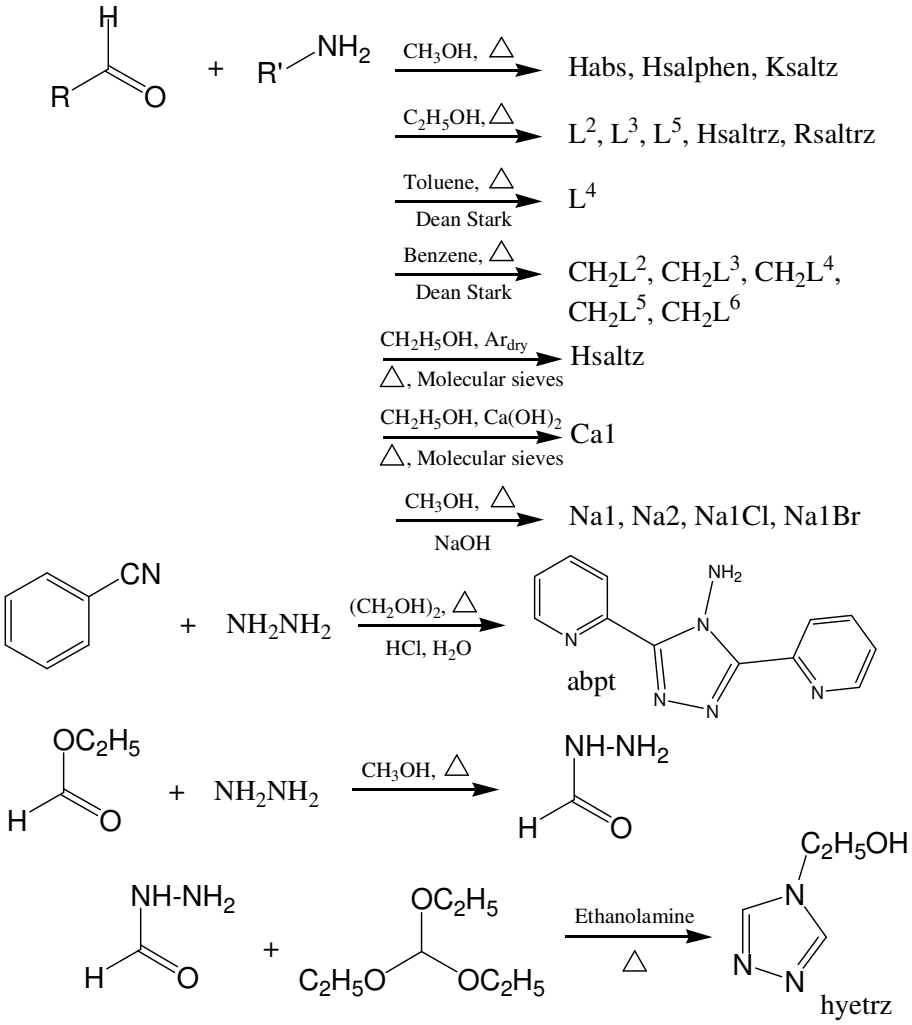

Chapter 1

L² (*N*-salicylidene 2-aminopyridine), **L³** (*N*-salicylidene 3-aminopyridine) and **L⁵** (5-chloro-*N*-salicylidene 3-aminopyridine) were synthesized by condensation reaction in ethanol.[156]

L²: 2-aminopyridine (4.75 g, 1 equiv, 50.4 mmol) in 100 mL of refluxing ethanol was reacted with salicylaldehyde (5.3 mL, 1 equiv, 50.3 mmol) to give a crude yellow solid after solvent evaporation. Pure **L²** was obtained as a yellow powder by washing the product with 10 mL of diethylether (5.51 g, yield 55 %). ^{1}H-NMR (300 MHz, d^{6}-DMSO, in ppm, 298 K): δ = 13.08 (s, 1 H, *H10*, Numbering relative to Figure 12), 9.53 (s, 1 H, *H5*), 8.57 (m, 1 H, C12-*H*), 7.92 (m, 1 H, C10-*H*), 7.81 (dd, 1 H, J_1 = 7.92 *Hz*, J_2 = 1.68 *Hz*, C10-*H*), 7.49 (m, 2 H, C4-*H* and C9-*H*), 7.39 (m, 1 H, C11-*H*), 7.02 (m, 2 H, C3-*H* and C5-*H*). ^{13}C-NMR (300 MHz, d^{6}-DMSO, in ppm, 298 K): δ = 165.39 (*C7*), 161.78 (*C8*), 158.41 (*C2*), 149.93 (*C12*), 139.97 (*C10*), 135.02 (*C4*), 134.19 (*C6*), 123.88 (*C11*), 120.70 (*C9*), 120.28 (*C5*), 119.94 (*C1*), 117.66 (*C3*). FTIR (KBr disk, cm^{-1}): 453 (m), 561 (m), 528 (s), 503 (m), 577 (m), 623 (m), 675 (w), 732 (s), 744 (m), 758 (s), 789 (s), 847 (s), 877 (w), 914 (s), 949 (w) 993 (m), 1030 (w), 1043 (w), 1095 (w), 1111 (m), 1146 (s, *C-O*), 1186 (s), 1230 (w), 1257 (m), 1277 (m), 1323 (w), 1350 (m), 1429 (s), 1454 (s), 1466 (s), 1556 (s), 1574 (s), 1587 (s), 1608 (s, *C=N*). X-ray powder diffraction (°): 7.5 (w), 11.9 (w), 15.2 (w), 16.22 (s), 16.6 (w), 18.9 (w), 20.1 (w), 24.2 (w), 25.4 (w), 25.9 (w), 34.1 (w), 28.6 (w), 32.5 (w).

L³: 3-aminopyridine (4.75 g, 1 equiv, 50.4 mmol) in 75 mL of ethanol was reacted with salicylaldehyde (5.3 mL, 1 equiv, 50.3 mmol) to give **L³** as a yellow powder (8.91 g, yield 89 %). ^{1}H-NMR (300 MHz, d^{6}-DMSO, in ppm, 298 K): δ = 12.65 (s, 1 H, *H10*, Numbering relative to Figure 13), 9.03 (s, 1 H, *H5*), 8.66 (d, 1 H, *J* = 2.5 *Hz*, C11-*H*), 8.54 (dd, 1 H, J_1 = 4.7 *Hz*, J_2 = 1.3 *Hz*, C6-*H*), 7.88 (m, 1 H, C10-*H*), 7.71 (dd, 1 H, J_1 = 7.9 *Hz*, J_2 = 1.6 *Hz*, C3-*H*), 7.49 (m, 2 H, C5-*H* and C9-*H*), 7.02 (m, 2 H, C4-*H* and *H9*). ^{13}C-NMR (300 MHz, d^{6}-DMSO, in ppm, 298 K): δ = 165.91 (*C7*), 160.86 (*C8*), 148.49 (*C6*), 145.32 (*C2*), 144.26 (*C11*), 134.53 (*C9*), 133.25 (*C3*), 128.70 (*C10*), 124.93 (*C5*), 120.16 (*C1*), 120.10 (*C4*), 117.45 (*C12*). Anal. calcd. for $C_{12}H_{10}N_2O$ (Mol. wt.: 198.22 g/mol) : C, 72.71 % ; H, 5.08 % ; N, 14.13 %.

Found: C, 72.61 %; H, 5.09 %; N, 14.14 %. FTIR (KBr disk, cm^{-1}): 496 (w), 523 (m), 546 (m), 577 (w), 619 (m), 665 (w), 702 (s), 754 (s), 781 (m), 810 (s), 825 (m), 849 (w), 910 (m), 947 (m), 947 (w), 987 (w), 1020 (m), 1099 (m), 1111 (m), 1150 (m, *C-O*), 1184 (s), 1196 (m), 1230 (w), 1246 (w), 1284 (s), 1321 (w), 1340 (w), 1373 (s), 1412 (m), 1423 (m), 1454 (m), 1479 (m), 1500 (m), 1570 (s), 1614 (s, *C=N*), 2700 (w, br, *OH*). X-ray powder diffraction (°): 8 (m), 9.2 (m), 11.9 (s), 12.6 (w), 16.0 (s), 18.0 (m), 19.6 (m), 20.6 (m), 24 (m), 31.4 (w), 32.2 (m), 33.0 (w), 34.1 (w), 42.2 (w), 45.9 (w). Single crystals were obtained by sublimation under reduced pressure (~ 75°C, over a period of a week) on the cold finger condenser of a sublimator apparatus. A X-ray investigation revealed same cell parameters as in ref. [157].

L^5: 3-aminopyridine (0.90 g, 1 equiv, 9.6 mmol) in 8 mL of ethanol was reacted with 5-chlorosalicylaldehyde (1.50 g, 1 equiv, 9.6 mmol) in 7 mL of ethanol to give **L^5** as a yellow powder (1.83 g, yield 82 %). ^{1}H-NMR (300 MHz, d^6-DMSO, in ppm, 298 K): 12.4 (s, 1 H, *H15*, Numbering relative to Figure 16), 8.99 (s, 1 H, C8-*H*), 8.64 (d, 1 H, J = 2.5 *Hz*, C2-*H*), 8.53 (dd, 1 H, J_1 = 4.7 *Hz*, J_2 = 1.4 *Hz*, C6-*H*), 7.86 (m, 1 H, C14-*H*), 7.79 (d, 1 H, J = 2.7 *Hz*, C4-*H*), 7.50 (m, 2 H, C5-*H* and C12-*H*), 7.04 (d, 1 H, J = 8.8 *Hz*, C11-*H*). ^{13}C-NMR (300 MHz, d^6-DMSO, in ppm, 298 K): 164.13 (*C8*), 159.50 (*C10*), 148.80 (*C6*), 144.27 (*C3*), 144.12 (*C2*), 134.00 (*C12*), 131.49 (*C4*), 128.82 (*C14*), 125.03 (*C5*), 123.58 (*C9*), 121.62 (*C13*), 119.58 (*C11*). Anal. calcd. for $C_{12}H_9N_2OCl$ (Mol. wt.: 232.67 g/mol): C, 61.95 %; H, 3.90 %; N, 12.04 %. Found: C, 61.75 %; H, 3.85 %; N, 11.96 %. X-ray powder diffraction pattern (°): 9.1 (s), 14.9 (w), 15.5 (w), 17.5 (w), 18.4 (s), 19.9 (m), 20.3 (w), 24.2 (w), 27.1 (w), 27.7 (s), 28.8 (w), 30.9 (w), 31.5 (w), 33.3 (m), 40.3 (w), 52.6 (w). M. p.: onset temperature observed by DSC: 136 (1)°C. FTIR (KBr disk, cm^{-1}): 1616 (s, *C=N*), 1558 (s), 1477 (s), 1425 (w), 1385 (w), 1356 (s), 1275 (s), 1182 (s), 1171 (s, *C-O*), 1097 (w), 1018 (w), 978 (w), 922 (w), 881 (w), 862 (m), 810 (s), 783 (m), 698 (s), 650 (m), 619 (m), 565 (m), 519 (w), 455 (w). Single crystals were obtained by recrystallisation in methanol and slow evaporation at room temperature.

L^4: 4-aminopyridine (2.38 g, 25.54 mmol, 1 equiv) was suspended in 50 mL of toluene in a 100 mL round bottom flask with a Dean-Stark setup.

Salicylaldehyde (2.7 mL, 25.26 mmol, 1 equiv) was added to the solution leading to a slight yellow coloration. A clear solution was obtained after 24h reflux and was concentrated. The resulting yellow oil was cooled in a salt/ice bath and a small amount of precipitated impurities was filtered. Solution was collected and dried under a vacuum line to afford a pure yellow precipitate (yield: 66 %, 3.29 g). ^{1}H-NMR (300 MHz, d^{6}-DMSO, in ppm, 298 K, Numbering relative to Figure 14): 12.30 (s, 1 H, O15-*H*, Numbering relative to Figure 14), 9.00 (s, 1 H, C8-*H*), 8.65 (m, 2 H, C2-*H* and C6-*H*), 7.75 (dd, 1 H, J_1 = 7.9 *Hz*, J_2 = 1.7 *Hz*, C14-*H*), 7.49 (m, 1 H, C12-*H*), 7.37 (m, 2 H, C3-*H* and C5-*H*), 7.03 (m, 2 H, C11-*H* and C13-*H*). ^{13}C-NMR (300 MHz, d^{6}-DMSO, in ppm, 298 K): 166.96 (*C8*), 161.28 (*C10*), 156.46 (*C4*), 151.89 (*C2* and *C6*), 135.27 (*C12*), 133.44 (*C14*), 120.40 (*C13*), 120.28 (*C9*), 117.78 (*C11*), 117.36 (*C3* and *C5*).Anal. calcd for $C_{12}H_{10}N_2O$ (Mol. wt. : 198.22 g/mol): C, 72.71 % ; H, 5.08 % ; N, 14.13 %. Found: C, 70.92 %; H, 5.30 %; N, 14.03 %. FTIR (KBr disk, cm^{-1}): 418 (m), 440 (w), 496 (w), 534 (s), 561 (m), 656 (w), 754 (s), 777 (m), 820 (s), 854 (s), 876 (s), 910 (s), 939 (w), 953 (w), 991 (m), 976 (m), 1031 (w), 1148 (s, *C-O*), 1186 (s), 1213 (w), 1232 (w), 1242 (w), 1275 (s), 1331 (m), 1362 (m), 1394 (w), 1418 (s), 1452 (s), 1485 (s), 1566 (s), 1587 (s), 1612 (s, *C=N*), 2700 (w, br, *O-H*). X-ray powder diffraction pattern (°): 7.5 (s), 12.0 (w), 15.1 (s), 17.0 (m), 19.3 (m), 19.5 (m), 20.1 (w), 22.9 (m), 24.1 (s), 25.2 (m), 28.7 (m), 29.6 (m), 30.7 (m), 48.3 (w). Single crystals were obtained by sublimation under reduced pressure (~ 75°C, over a period of a week) on the cold finger condenser of a sublimator apparatus.

Chapters 2 and 4

Sodium salt of *N*-salicylidene para-aminobenzenesulfonate (**Na1**): Sodium salt of *N*-salicylidene para-aminobenzenesulfonate was firstly prepared as precursor for single crystals growing of Hsaltrz. 5 g of sulfanilic acid (28.8 mmol, 1 equiv.) is suspended in 50 mL of methanol and deprotonated by adding 1.16 g of solid sodium hydroxide (28.8 mmol, 1 equiv.) under reflux for 1 h. Afterwards, 3 mL of salicylaldehyde (28.8 mmol, 1 equiv.) is added to the white suspension to give a yellow solution. The mixture was stirred for 2 h at r.t. and then concentrated. The resulting solution was filtered to

give 11.94 g of crystalline yellow product which was washed with 10 mL of methanol and dried under vacuum. The pure product (7.44 g, yield = 86 %) is obtained after recrystallisation in 100 mL of hot methanol. ^{1}H-NMR (300 MHz, d^{6}-DMSO, in ppm, 298 K): δ = 13.06 (s, 1H, O*H*), 9.00 (s, 1H, C*H*=N), 7.70 (m, 3H, C*H*-C-CH=N and C*H*-CSO_3), 7.42 (m, 3H, C*H*-CH-COH and C*H*-CH-SO_3), 7.00 (m, 2H, C*H*-COH and C*H*-CH-CH-COH). ^{13}C-NMR (300 MHz, d^{6}-DMSO, in ppm, 298 K): δ = 164.47 (*C*-OH), 161.05 (*C*H=N), 148.73 (*C*-N), 147.61 (*C*-SO_3), 134.14 (*C*H-CH-C-OH), 133.37 (*C*H-C-C-OH), 127.54 (*C*-H-C-SO_3), 121.44 (*C*H-C-N), 120.07 (*C*-C-OH), 119.94 (*C*H-CH-CH-C-OH), 117.36 (*C*H-C-OH). Anal calcd. for $C_{13}H_{10}NSO_4Na$ (Mol. Wt.: 299.28 g/mol): C, 52.17 %; H, 3.61 %; N, 4.68 %; S, 10.71 % Found: C, 52.31 %; H, 3.30 %; N, 4.40 %; S, 10.47 %. MS: m/z = 276 (M^-), 212 (M^- - SO_2), 196 (M^- - SO_3), 118 ($C_7H_4NO^-$). X-ray powder diffraction (°): 3.24 (s), 6.42 (m), 9.64 (s), 12.8 (w), 16.04 (w), 18.38 (w), 19.67 (s), 20.81 (w), 21.68 (w), 23.30 (w), 23.58 (w), 25.40 (w), 25.80 (w), 27.08 (w), 25.80 (w), 26.00 (w), 27.08 (w), 30.34 (w), 31.12 (w), 32.40 (w), 32.62 (w). FTIR (KBr disk, cm^{-1}): 418 (w), 442 (w), 459 (w), 494 (w), 528 (w), 552 (m), 565 (m), 577 (s), 634 (m), 650 (s), 716 (s), 731 (s), 779 (w), 812 (m), 835 (s), 850 (s), 912 (m), 935 (w), 982 (m), 1011 (m), 1032 (m, *SO_3*), 1051 (s, *C-O*), 1107 (m), 1032 (s), 1150 (m), 1174 (s, *SO_3*), 1186 (s), 1236 (s), 1261 (w), 1281 (s), 1319 (w), 1362 (m), 1404 (m), 1456 (m), 1489 (s), 1528 (w), 1576 (s), 1591 (m), 1626 (s, *C=N*), 1664 (w), 3250 (m, br, *OH*).

Sodium salt of *N*-salicylidene para-aminobenzenesulfonate (**Na2**): 5 g of 3-aminobenzene sulfonic acid (28.8 mmol, 1 equiv.) was suspended in 55 mL of hot methanol and deprotonated by adding 1.18 g of solid sodium hydroxide (28.8 mmol, 1 equiv.) under reflux for 1 h. Afterwards, 3 mL of salicylaldehyde (28.8 mmol, 1 equiv.) were added to the mixture to give a yellow solution which was stirred for 2 h at r.t. and concentrated. The crystalline yellow powder is filtered and washed with 10 mL of methanol (7.09 g, yield = 82 %) ^{1}H-NMR (300 MHz, d^{6}-DMSO, 298 K, ppm): 7.01 (m, 2 H, COH-C*H* and COH-CH-CH-C*H*), 7.43 (m, 3 H, CSO_3-CH-C*H*, CSO_3-CH-C-C*H* and COH-CH-C*H*), 7.62 (m, 1 H, CSO_3-C*H*-C), 7.57 (m, 1 H, CSO_3-C*H*-CH), 7.73 (m, 1 H, COH-C-C*H*), 9.01 (s, 1 H, N=C*H*), 13.07

(s, 1 H, O*H*). ^{13}C-NMR (300 MHz, d^6-DMSO, 298 K, ppm): 117.3 (COH-*C*), 119.0 (CSO_3-*C*H-C), 119.9 (COH-CH-CH-*C*H), 120.0 (COH-*C*), 122.4 (N-C-*C*H), 124.8 (CSO_3-*C*H-CH), 129.7 (CSO_3-CH-*C*H), 133.4 (COH-C-*C*H), 134.1 (COH-CH-*C*H), 148.2 (*C*-SO_3), 150.2 (N-*C*), 161.0 (*C*H=N), 164.4 (*C*-OH). Elemental analysis calcd (%) for $C_{13}H_{10}NSO_4Na$ (Mr = 299.28 g.mol^{-1}): C 52.17, H 3.37, N 4.68 ; found: C 51.79, H 3.31, N 4.66. MS: m/z = 276 (M^-), 212 (M^- - SO_2), 196 (M^- - SO_3), 118 ($C_7H_4NO^-$), 574 (NaM_2^-). Degradation temperature by TGA/DTA: 340 (1)°C. X-ray powder diffraction (°): 7.26 (m), 10.92 (s), 14.52 (w), 14.46 (w), 18.12 (w), 21.82 (m), 25.06 (w), 25.54 (w), 26.44 (w), 27.26 (w), 29.28 (m), 30.20 (w), 35.62 (w), 36.74 (w), 38.88 (w), 43.34 (w). FTIR (KBr disk, cm^{-1}): 445 (w), 467 (w), 498 (w), 534 (m), 548 (w), 573 (w), 611 (m), 629 (m), 662 (w), 692 (m), 725 (m), 742 (m), 752 (s), 810 (m), 839 (w), 885 (w), 904 (w), 912 (w), 928 (w), 984 (w), 995 (w), 1032 (w), 1047 (m, *C-O*), 1092 (w), 1111 (m), 1148 (m), 1186 (s, *SO_3*), 1219 (s), 1281 (m), 1362 (w), 1385 (m), 1414 (w), 1429 (w), 1460 (w), 1474 (m), 1498 (m), 1572 (s), 1593 (s), 1622 (s, *C=N*), 3466 (w, br, *OH*).

Potassium salt of *N*-salicylidene para-aminobenzenesulfonate (**K1**). Sulfanilic acid (5 g, 28.8 mmol, 1 equiv.) were suspended in methanol (60 mL) at 80°C. Solid potassium hydroxide (1.62 g, 28.8 mmol, 1 equiv.) was added in order to deprotonate the compound. After a reflux of a few minutes, 3.04 mL of salicylaldehyde (28.8 mmol, 1 equiv) was added to the mixture to give a yellow solution which was refluxed for 1 h. The resulting precipitate was re-dissolved in methanol (500 mL) at 80 °C. The insoluble impurities were filtered and the solution was allowed to cool to 0°C by plunging in an ice bath. The yellow precipitate was filtered to give a crude crystalline yellow product which was washed with 5 mL of methanol and dried under vacuum. Impurities were then extracted by two subsequent sonication of the compound in ether. The pure yellow compound was filtered and dried under vacuum (1.87 g, yield: 20 %). ^{1}H-NMR (300 MHz, d^6-DMSO, 298 K, ppm): 7.02 (m, 2 H, C*H*-COH and C*H*-CH-CH-COH), 7.43 (m, 3 H, C*H*-CH-COH and C*H*-CH-SO_3), 7.72 (m, 3 H, C*H*-C-CH=N and C*H*-CSO_3), 9.01 (s, 1 H, C*H*=N), 13.08 (s, 1 H, O*H*). ^{13}C-NMR (300 MHz, d^6-DMSO, 298 K, ppm): 117.5 (*C*H-C-OH), 120.1 (*C*H-CH-CH-COH) ,

120.2 (*C*-COH), 121.6 (*C*H-C-N), 127.7 (*C*H-C-SO3), 133.5 (*C*H-C-COH), 134.3 (*C*H-CH-COH), 147.8 (*C*-SO_3), 148.9 (*C*-N), 161.2 (*C*H=N), 164.5 (*C*-OH). Elemental analysis calcd (%) for $C_{13}H_{10}NSO_4K•0.5H_2O$ (Mr = 324.40 g.mol^{-1}): C 48.13, H 3.42, N 4.32. Found: C 47.98, H 3.13, N 4.38. MS: m/z = 276 (M^-), 212 (M^- - SO_2), 196 (M^- - SO_3), 118 ($C_7H_4NO^-$), 575 (NaM_2^-), 591 (KM_2^-). Degradation temperature by TGA-TDA: 349 (1)°C. X-ray powder diffraction (°): 9.86 (s), 10.46 (s), 14.02 (m), 14.92 (s), 15.40 (s), 16.36 (m), 16.94 (s), 17.10 (m), 20.46 (s), 20.98 (s), 21.92 (m), 23.86 (m), 23.98 (w), 24.84 (m), 25.90 (m), 27.76 (m), 28.3 (m), 29.16 (m), 30.12 (s), 40.72 (m). FTIR (KBr disk, cm^{-1}): 436 (w), 467 (w), 500 (w), 534 (m), 611 (m), 629 (m), 662 (w), 692 (s), 725 (s), 752 (s), 810(s), 839 (m), 912 (m), 928 (w), 984 (m), 1032 (m, *SO_3*), 1048 (s, *C-O*), 1186 (s, *SO_3*), 1219 (s), 1281 (s), 1362 (m), 1414 (m), 1460 (m), 1474 (s), 1499 (s), 1572 (s), 1593 (s), 1622 (s, *C=N*).

Calcium salt of *N*-salicylidene para-aminobenzenesulfonate (**Ca1**). Sulfanilic acid (2 g, 11.5 mmol, 1 equiv.) was suspended in methanol (60 mL) at 80°C in a round bottom flash mounted by a desiccant setup made with molecular sieves. Calcium hydroxide (0.43 g, 5.8 mmol, 0.5 equiv.) was added to the suspension in order to deprotonate the compound. After a reflux of 3 h, salicylaldehyde (1.41 mL, 11.5 mmol, 1 equiv) was added to the mixture to give a yellow solution which was refluxed for 24 h. The resulting milky suspension was filtered and the precipitate was washed with 5 mL of absolute ethanol and dried under vacuum line (2.87 g, yield: 84 %). ^{1}H-NMR (300 MHz, d^6-DMSO, 298 K, ppm): 7.02 (m, 2 H, C*H*-COH and C*H*-CH-CH-COH), 7.45 (m, 3 H, C*H*-CH-COH and C*H*-CH-SO_3), 7.71 (m, 3 H, C*H*-C-CH=N and C*H*-CSO_3), 9.01 (s, 1 H, C*H*=N), 13.06 (s, 1 H, O*H*). ^{13}C-NMR (300 MHz, d^6-DMSO, 298 K, ppm): 117.5 (*C*H-C-OH), 120.1 (*C*H-CH-CH-COH) , 120.2 (*C*-COH), 121.6 (*C*H-C-N), 127.7 (*C*H-C-SO3), 133.5 (*C*H-C-COH), 134.3 (*C*H-CH-COH), 147.6 (*C*-SO_3), 149.0 (*C*-N), 161.2 (*C*H=N), 164.6 (*C*-OH). Elemental analysis calcd (%) for $C_{26}H_{20}N_2S_2O_8Ca•H_2O$ (Mr = 610.68 g.mol^{-1}): C 51.14, H 3.63, N 4.59 ; found: C 51.76, H 3.19, N 4.67. MS: m/z = 276 (M^-), 212 (M^- - SO_2), 196 (M^- - SO_3), 118 ($C_7H_4NO^-$), 575 (NaM_2^-), 591 (KM_2^-). Degradation temperature by DSC: 346 (1) °C. X-ray powder diffraction (°): 6.60 (m),

9.80 (m), 12.96 (w), 16.22 (m), 19.50 (m), 19.92 (m), 20.54 (w), 21.58 (w), 22.42 (s), 23.56 (m), 23.52 (m), 25.00 (m), 25.98 (m), 27.26 (m), 27.30 (m), 28.7 (m), 30.76 (w), 31.80 (w), 32.56 (w), 33.40 (w), 33.48 (w), 36.38 (w), 36.54 (w), 39.10 (w), 40.02 (w), 41.60 (w), 41.52 (w), 45.04 (m), 46.14 (w), 47.12 (w), 49.56 (w), 53.08 (w). FTIR (KBr disk, cm^{-1}): 403 (s), 457 (m), 501 (s), 552 (s), 567 (s), 575 (s), 590 (s), 634 (s), 852 (s), 729 (s), 746 (s), 754 (s), 781 (s), 825 (s), 849 (s), 812 (s), 972 (m), 1009 (s), 1030 (s, *SO_3*), 1049 (s, *C-O*), 1068 (s), 1111 (s), 1142 (s), 1180 (s, *SO_3*), 1202 (s), 1227 (s), 1258 (s), 1280 (s), 1358 (s), 1408 (s), 1456 (s), 1489 (s), 1572 (s), 1591 (s), 1620 (s, *C=N*), 2714 (w, br, *OH*).

Sodium salt of 5-chloro-N-salicylidene para-aminobenzenesulfonate (**Na1Cl**). Sulfanilic acid (3.87 g, 22 mmol, 1 equiv.) was suspended in methanol (50 mL) at 80°C. Solid sodium hydroxide (0.89 g, 22 mmol, 1 equiv.) was added to the white suspension. After stirring for 1 h, 5-chlorosalicylaldehyde (3.87 g, 22 mmol, 1 equiv.), dissolved in 5 mL of methanol, was added to the mixture to give a yellow solution which was refluxed for 1 h. The resulting suspension was filtered to give 6.24 g (84 %) of crystalline yellow product which was washed with 5 mL of methanol and dried under vacuum. ^{1}H-NMR (250 MHz, d^{6}-DMSO, 298 K, ppm): 7.0 (d, J_1 = 8.7 *Hz*, 1 H, C*H*-COH), 7.4 (d, J_1 = 8.7 *Hz*, 2 H, N-C-C*H*), 7.6 (dd, J_1 = 8.7 *Hz*, J_2 = 2.4 *Hz*, 1 H, COH-CH-C*H*), 7.7 (d, J_1 = 8.7 *Hz*, 2 H, CSO_3-C*H*), 7.9 (d, J_1 = 2.8 *Hz*, 1 H, COH-C-C*H*), 9.0 (s, 1 H, C*H*=N). ^{13}C-NMR (500 MHz, d^{6}-DMSO, 298 K, ppm): 119.1 (*C*H-COH), 120.7 (COH-*C*), 121.2 (N-C-C*H*), 126.6 (*C*-Cl), 126.8 (CSO_3-*C*H), 134.0 (COH-C-*C*H), 135.6 (COH-CH-*C*H), 147.2 (N-*C*), 147.8 (*C*-SO_3), 159.3 (*C*H=N), 162.0 (*C*-OH). Elemental analysis calcd (%) for $C_{13}H_9NSO_4BrNa$ (Mr = 378.17 $g.mol^{-1}$): C 41.29, H 2.57, N 3.70, S 8.48 ; found: C 41.26, H 2.52, N 3.45, S 8.78. MS: m/z = 356 (M^-), 354 (M^-), 275 (M^- - SO_3), 274 (M^- - Br). Degradation temperature by TGA/TDA: 400(1)°C. X-ray powder diffraction (°): 2.78 (w), 5.88 (s), 8.80 (w), 11.78 (w), 27.7 (w), 29.98 (w), 36.18 (w). FTIR (KBr disk, cm^{-1}): 498 (s), 530 (s), 553 (s), 565 (m), 579 (m), 629 (s), 665 (w), 719 (s), 741 (m), 779 (s), 827 (m), 847 (m), 862 (m), 887 (s), 918 (s), 978 (s), 1011 (m), 1051 (m, *C-O*), 1074 (s), 1109 (s), 1134 (w), 1174 (w), 1188 (m,

SO_3), 1238 (w), 1275 (m), 1310 (s), 1346 (s), 1389 (s), 1402 (s), 1437 (s), 1474 (w), 1495 (s), 1564 (m), 1591 (m), 1622 (m, *C*=*N*).

Sodium salt of 5-bromo-N-salicylidene para-aminobenzenesulfonate (**Na1Br**). Sulfanilic acid (3.4 g, 19.9 mmol, 1 equiv.) was suspended in methanol (50 mL) at 80°C and deprotonated by adding solid sodium hydroxide (0.79 g, 19.9 mmol, 1 equiv.) under reflux for 1 h. Afterwards, 5-bromo-salicylaldehyde (4 g, 19.9 mmol, 1 equiv.), dissolved in 5 mL of methanol, was added to give a yellow solution. The mixture was refluxed for 1 h. The resulting suspension was filtered to give 8.24 g (yield: 83 %) of crystalline yellow product which was washed with 5 mL of methanol and dried under vacuum. ^{1}H-NMR (250 MHz, d^6-DMSO, 298 K, ppm): 7.0 (d, J_1 = 9.1 *Hz*, 1 H, COH-C*H*), 7.4 (d, J_1 = 8.3 *Hz*, 2 H, N-C-C*H*), 7.5 (dd, J_1 = 8.7 *Hz* and J_2 = 2.8 *Hz*, 1 H, COH-CH-C*H*), 7.7 (d, J_1 = 8.3 *Hz*, 2 H, CSO_3-C*H*), 7.8 (d, J_1 = 2.4 *Hz*, 1 H, COH-C-C*H*), 9.0 (s, 1 H, C*H*=N). ^{13}C-NMR (500 MHz, d^6-DMSO, 298 K, ppm): 118.6 (COH-*C*H), 120.6 (N-C-*C*H), 120.7 (*C*-Br), 122.6 (COH-*C*), 126.8 (CSO_3-*C*H), 131.0 (COH-C-*C*H), 132.8 (COH-CH-*C*H), 147.2 (*C*-SO_3), 147.8 (N-*C*), 158.9 (C*H*=N), 162.1 (*C*-OH). Elemental analysis calcd (%) for $C_{13}H_9NSO_4ClNa$ (Mr = 310.73 g.mol^{-1}): C 46.79, H 2.91, N 4.20, S 9.61 ; found: C 46.51, H 2.71, N 4.03, S 9.25. MS: m/z = 312 (M^-), 310 (M^-), 246 (M^- - SO_2), 230 (M^- - SO_3), 152 (C_7H_3NOCl), 118 (C_7H_4NO). Degradation temperature by TGA/DTA: 401(1)°C. X-ray powder diffraction (°): 3.00 (s), 6.02 (s), 9.04 (s), 15.00 (w), 18.50 (w), 18.16 (w), 21.88 (w), 23.76 (w), 24.22 (w), 30.36 (w), 36.64 (w). FTIR (KBr disk, cm^{-1}): 446 (w), 469 (w), 500 (w), 532 (w), 557 (m), 579 (s), 648 (m), 677 (s), 719 (w), 746 (m), 781 (w), 835 (s), 868 (m), 887 (w), 926 (m), 978 (m), 1011 (m), 1051 (s, *C*-*O*), 1090 (w), 1109 (w), 1134 (s), 1174 (s), 1188 (s, *SO_3*), 1238 (s), 1275 (s), 1312 (w), 1348 (m), 1389 (w), 1402 (w), 1477 (s), 1570 (m), 1591 (w), 1624 (m, *C*=*N*).

Chapter 2

N-salicylidene 4-amino-1,2,4-triazole (**Hsaltrz**): 1.25 mL of salicylaldehyde (11.8 mmol, 1 equiv.) dissolved in 5 mL of ethanol was added to 1 g of 4-amino-1,2,4-triazole (11.8 mmol, 1 equiv.) dissolved in 5 mL of ethanol.

The resulting slightly yellow solution was stirred for 15 min and, afterwards, refluxed for 45 min. The resulting pale yellow solution was allowed to cool to r.t. to give a crystalline white powder. The product was filtered, washed with 1 mL of ethanol and 1 mL of diethylether and dried under vacuum (2 g, yield : 90 %). ^{1}H-NMR (300 MHz, d^{6}-DMSO, in ppm, 298 K, Numbering relative to Figure 27): δ = 10.50 (s, 1H, O-*H14*), 9.20 (m, 3H, C3-*H*, C5-*H*,C7-*H*), 7.63 (m, 1 H, C13-*H*), 7.46 (m, 1H, C11-*H*), 7.01 (m, 2H, C10-*H* and C12-*H*). ^{13}C-NMR (300 MHz, d^{6}-DMSO, in ppm, 298 K): δ = 158.93 (*C9*), 155.71 (*C7*), 139.76 (*C3* and *C5*), 134.70 (*C11*), 128.50 (*C13*), 120.45 (*C10*), 118.99 (*C8*), 117.52 (*C12*). Anal calcd. for $C_9H_8N_4O$ (Mol. Wt.: 188.19 g/mol): C, 57.44 %; H, 4.28 %; N, 29.77 %. Found: C, 57.44 %; H, 4.30 %; N, 29.80 %. M. p.: onset temperature by DSC: 206(1)°C. Degradation temperature (onset) by DSC: 220(1)°C. MS: m/z = 189 ($M + H^+$), 120 ($C_7H_6NO^{\cdot+}$), 70 ($C_2N_3H_5^{\cdot+}$). X-ray powder diffraction (°): 7.86 (s), 9.48 (m), 11.72 (m), 14.26 (m), 14.86 (s), 15.78 (m), 16.2 (w), 17.0 (m), 16.88 (w), 18.06 (w), 18.78 (w), 19.08 (s), 19.84 (m), 20.48 (w), 21.2 (m), 22.06 (m), 22.76 (m), 23.74 (w), 26.1 (w), 28.38 (w), 28.8 (w), 28.7 (w), 30.96 (w), 34.94 (w). FTIR (KBr disk, cm^{-1}): 461 (m), 515 (w), 598 (s), 623 (s, *trz*), 729 (w), 762 (s), 833 (w), 854 (m), 949 (w), 974 (w), 1057 (s, *C-O*), 1105 (w), 1155 (s), 1194 (m, *trz*), 1259 (s), 1300 (s), 1373 (m), 1412 (w), 1456 (s), 1516 (s), 1605 (s, *C=N*), 2710 (s, br), 3117 (s), 3435 (s, br, *O-H*).

Single crystals were obtained following an unconventional procedure. 0.30 g of **Na1** (1 mmol, 2 equiv.) was added to a solution of 0.12 g (0.5 mmol, 1 equiv.) of $CuCl_2$•$2H_2O$ in 10 mL of methanol. 0.13 g of 4-amino-1,2,4-triazole (1.5 mmol, 3 equiv.), dissolved in 10 mL of methanol, was allowed to slowly diffuse into the copper solution through a diffusion H-tube filled with 100 mL of methanol. After 1 year, diffusion was assumed to be complete and the whole solution was allowed to slowly evaporate at r.t. Long uncoloured needles of diffractable quality were obtained within the resulting concentrated green solution after 6 months. These crystals were then analyzed by X-ray diffraction.

4-amino-3,5-bis(pyridin-2-yl)-1,2,4-triazole (**abpt**): Abpt was obtained following a reported procedure[298] (yield = 55 %). ^{1}H-NMR: (300 MHz, d^{6}-DMSO, in ppm, 298 K, Numbering relative to the atoms number in the **Habs**

cif file displayed in Figure 28): δ = 8.78 (m, 2H, C17-*H* and C23-*H*), 8.24 (m, 2H, C20-*H* and C26-*H*), 8.08 (dt, 2H, J_1 = 7.8 *Hz*, J_2 = 1.77 *Hz*, C19-*H* and C25-*H*), 7.83 (s, 2H, NH_2), 7.59 (m, 2H, C18-*H* and C24-*H*). ^{13}C-NMR (300 MHz, d^6-DMSO, in ppm, 298 K): δ = 149.67 (*C17* and *C23*), 149.52 (*C3* and *C5*), 147.78 (*C15* and *C21*), 138.52 (*C19* and *C25*), 125.30 (*C18* and *C24*), 123.55 (*C20* and *C26*).

N-salicylidene 4-amino-3,5-bis(pyridin-2-yl)-1,2,4-triazole (**Habs**): 2.5 g of abpt (10.5 mmol, 1 equiv.) were dissolved in 25 mL of hot methanol to give a clear solution where 1.1 mL of salicylaldehyde (10.5 mmol, 1 equiv.) were added to afford a clear pale yellow solution. The mixture was refluxed for 48 h and then allowed to cool down to r.t.. The resulting crystalline yellow precipitate was filtered and re-crystallised in 60 mL of hot methanol to give 2.58 g of pure product (7.5 mmol, yield = 72 %). ^{1}H-NMR (300 MHz, d^6-DMSO, in ppm, 298 K, Numbering relative to Figure 28): δ = 10.66 (s, 1 H, *H14*), 8.98 (s, 1H, C7-*H*), 8.66 (m, 2 H, C20-*H* and C26-*H*), 8.18 (d, 2 H, J_1 = 7.89 *Hz*, C17-*H* and C23-*H*), 8.06 (dt, 2 H, J_1 = 7.76 *Hz*, J_2 = 1.69 *Hz*, C19-*H* and C25-*H*), 7.59 (m, 3 H, C12-*H*, C18-*H* and C24-*H*), 7.47 (dt, 1 H, J_1 = 7.80 *Hz*, J_2 = 1.68 *Hz*, C11-*H*), 6.97 (m, 2 H, C10-*H* and C13-*H*). ^{13}C-NMR (300 MHz, d^6-DMSO, in ppm, 298 K): δ = 168.30 (*C7*), 159.54 (*C9*), 150.65 (*C15* and *C21*), 150.34 (*C20* and *C26*), 147.29 (*C3* and *C5*), 138.48 (*C19* and *C25*), 135.40 (*C11*), 130.48 (*C18* and *C24*), 125.76 (*C17* and *C23*), 125.33 (*C12*), 120.61 (*C13*), 118.52 (*C10*), 117.74 (*C8*). Anal calcd. for $C_{19}H_{14}N_6O$ (Mol. Wt.: 342.36 g/mol): C, 66.66 %; H, 4.12 %; N, 24.55 %. Found: C, 66.34 %; H, 4.06 %; N, 24.68 %. MS: m/z = 343 (M + H^+), 224 ($C_{12}H_{10}N_5$). FTIR (KBr disk, cm^{-1}): 472 (w), 554 (w), 604 (m), 623 (m, *trz*), 642 (m), 690 (s), 731 (w), 739 (s), 760 (s), 787 (s), 914 (w), 895 (w), 910 (m), 964 (w), 993 (m), 1036 (w), 1091 (w), 1115 (w), 1150 (m), 1196 (m, *trz*), 1254 (w), 1271 (s), 1367 (m), 1406 (m), 1429 (s), 1448 (s), 1460 (s), 1487 (s), 1519 (w), 1568 (s), 1587 (s), 1622 (s, *C=N*), 3040 (m), 3153 (m, br, *OH*). M. p.: onset temperature by DSC: 161(1)°C. Degradation temperature by TGA (onset point): 261(1)°C. X-ray powder diffraction (°): 4.92 (w), 7.86 (s), 9.9 (m), 10.62 (m), 14.48 (w), 14.88 (m), 15.34 (w), 16.1 (s), 18.2 (m), 18.96 (m), 19.8 (w), 21.3 (w), 23.18 (m), 24.16 (w), 24.88 (w), 26.1 (w), 32.54 (w), 34.3 (w), 35.1 (w), 38.34 (w), 39.84 (w), 42.68 (w),

45.14 (m), 45.32 (w), 51.28 (w). Single crystals were obtained by sublimation under reduced pressure (110°C, over a period of 3 months) on the cold finger condenser of a sublimator setup.

N-salicylidene (1,10)-phenanthrolin-5-amine (**Hsalphen**): 0.50 g of (1,10)-phenanthrolin-5-amine (2.6 mmol, 1 equiv.) was dissolved in 15 mL of hot methanol. 3 mL of salicylaldehyde (28.5 mmol, 11 equiv.) was added to give a pale yellow solution. The mixture was refluxed during 16 h and then allowed to cool to r.t.. The unreacted (1,10)-phenanthrolin-5-amine was filtered and the solvent was removed under vacuum. The residual yellow oil was triturated with 20 mL of hexane and sonicated 30 min. The supernate containing excess of salicylaldehyde was pipetted out without disturbing the oil. After repeating 6 times the last manipulation, a pure yellow precipitate (0.6638 g, 2.21 mmol, yield = 86 %) was isolated from the oil, filtered and dried under vacuum. ^{1}H-NMR (300 MHz, d^{6}-DMSO, in ppm, 298 K, Numbering relative to Figure 29): δ = 12.37 (s, 1 H, *H23*), 9.21 (d, 1 H, J_1 = 1.68 *Hz*, C9-*H*), 9.20 (s, 1 H, C16-*H*), 9.09 (dd, 1 H, J_1 = 4.32 *Hz*, J_2 = 1.71 *Hz*, C2-*H*), 8.70 (dd, 1 H, J_1 = 8.28 *Hz*, J_2 = 1.71 *Hz*, C7-*H*), 8.52 (dd, 1 H, J_1 = 8.13 *Hz*, J_2 = 1.68 *Hz*, C4-*H*), 7.89 (m, 3 H, C6-*H*, C8-*H* and C18-*H*), 7.81 (m, 1 H, C3-*H*), 7.53 (m, 1 H, C21-*H*), 7.08 (m, 2 H, C19-*H* and C20-*H*). ^{13}C-NMR (300 MHz, d^{6}-DMSO, in ppm, 298 K): δ = 165.10 (*C16*), 160.87 (*C22*), 151.20 (*C9*), 150.12 (*C2*), 146.48 (*C5*), 145.64 (*C11*), 145.34 (*C12*), 136.96 (*C4*), 134.81 (*C21*), 132.77 (*C18*), 132.44 (*C7*), 129.40 (*C14*), 125.83 (*C13*), 124.46 (*C6*), 124.31 (*C3*), 120.76 (*C17*), 120.33 (*C20*), 117.54 (*C19*), 113.72 (*C8*). MS: m/z = 300 ($M + H^+$), 599 ($M_2^{\cdot+}$), 322 ($M + Na^+$), 621 ($M_2 + Na^+$), 107 (C_7H_7O). FTIR (KBr disk, cm^{-1}): 517 (w), 565 (w), 608 (w), 621 (w), 656 (w), 702 (w), 742 (s), 752 (m), 781 (w), 806 (w), 833 (w), 881 (w), 893 (w), 922 (w), 991 (w), 1024 (w), 1036 (w), 1059 (m, *C-O*), 1084 (w), 1115 (w), 1140 (w), 1151 (w), 1197 (w), 1275 (s), 1300 (w), 1366 (w), 1394 (m), 1420 (m), 1460 (w), 1481 (w), 1560 (m), 1574 (m), 1601 (s, *C=N*), 1616 (s), 3022 (w, br), 3448 (w, br, *OH*). M. p.: onset temperature by DTA: 185(1)°C. Degradation temperature by DTA (onset point): 254(1)°C. Anal calcd. for $C_{19}H_{13}N_3O$ (Mol. Wt.: 299.10 g/mol): C, 76.23 %; H, 4.38 %; N, 14.04 %. Found: C, 75.35 %; H, 4.19 %; N, 13.40 %. X-ray powder diffraction (°): 7.72 (s), 11.38 (m), 11.7 (s), 12.7 (w), 13.42 (w), 14.24 (w),

14.94 (w), 15.4 (m), 15.98 (m), 16.74 (m), 17.08 (m), 17.54 (m), 18.36 (m), 18.96 (m), 19.8 (s), 20.28 (w), 20.32 (w), 21.6 (m), 22.1 (m), 22.44 (m), 23.44 (s), 24.58 (m), 25 (m), 26.4 (s), 27.36 (s), 28.26 (w), 28.68 (w), 29.34 (m), 30.06 (w), 31.92 (w), 33.02 (w), 33.56 (w), 34.36 (w), 37.96 (w), 38.86 (w). White single crystals of X-ray quality were obtained by slow evaporation of a saturated solution in diethylether.

N-salicylidene 5-aminotetrazole (**Hsaltz**): Synthesis was performed under a dried argon atmosphere. 5 g of 5-aminotetrazole (58.8 mmol, 1 equiv.) were degassed under vacuum. 50 mL of ethanol, dried and kept over molecular sieves, was bubbled with argon during 30 min. 5-amino-tetrazole is dissolved in hot ethanol using Schlenk techniques. Salicylaldehyde (5.6 mL, 58.8 mmol, 1equiv.) was slowly added leading to a pale green solution. The mixture was refluxed during 5 h under argon and then filtered, washed with few millilitres of degassed and dried methanol, and then dried under vacuum. The resulting yellow precipitate was suspended in 75 mL of diethylether and sonicated in an ultrasonic bath for 1 h. 6 g of pure product (31.7 mmol, yield = 54 %) was obtained and dried under vacuum. ^{1}H-NMR (300 MHz, d^{6}-DMSO, in ppm, 298 K, Numbering relative to Figure 30): δ =11.52 (s, 1 H, *H14*), 9.53 (s, 1 H, C7-*H*), 7.92 (d, J_1 = 7.32 *Hz*, 1 H, C13-*H*), 7.52 (t, J_1 = 7.23 *Hz*, 1 H, C11-*H*), 7.03 (m, 2 H, C10-*H* and C12-*H*), 6.48 (s, 1 H, *H4*). ^{13}C-NMR (300 MHz, d^{6}-DMSO, in ppm, 298 K): δ =167.79 (*C7*), 162.64 (*C9*), 161.35 (*C5*), 157.60 (*C8*), 136.39 (*C11*), 131.45 (*C13*), 120.70 (*C12*), 117.90 (*C10*). MS: m/z = 190 (M), 162 (M - N_2). X-ray powder diffraction (°):7.40 (w), 8.98 (s), 10.38 (w), 10.48 (w), 12.34 (w), 12.48 (w), 13.92 (w), 14.64 (w), 15.88 (m), 16.86 (w), 17.82 (w), 19.00 (m), 20.16 (m), 20.28 (w), 21.44 (w), 22.98 (w), 23.56 (m), 23.74 (w), 24.34 (w), 25.28 (m), 25.16 (w), 26.60 (m), 27.12 (m), 27.84 (w), 28.32 (m), 28.38 (m), 29.1 (w), 31.56 (w), 35.48 (w). White single crystals of good quality were obtained by slow evaporation of a saturated solution of diethylether.

Potassium salt of *N*-salicylidene 5-aminotetrazolate (**Ksaltz**): In a first step, 2.51 g (29.5 mmol, 1 equiv) of 5-aminotetrazole was dissolved in 50 mL of distillated water. 1.66 g (29.5 mmol, 1 equiv.) of potassium hydroxide pellets were slowly added to the solution. The mixture was refluxed overnight, concentrated under vacuum and then, the resulting white

precipitate was dried (3.93 g, yield = 78 %). The product was dissolved in 50 ml of methanol and 3.36 ml of salicylaldehyde (32 mmol, 1 equiv.) were added. The mixture was refluxed overnight to give a clear yellow solution which was concentrated under vacuum. The crude product contained 10 % of unreacted salicylaldehyde. It was sonicated 3 times with 50 ml of hexane to give 5.51 g of pure product (yield = 76 %). Potassium salt of 5-aminotetrazolate: ^{1}H-NMR (300 MHz, d^{6}-DMSO, in ppm, 298 K): δ = 4.73 (s, 2H, N*H*$_2$). ^{13}C-NMR (300 MHz, d^{6}-DMSO, in ppm, 298 K): δ = 163.68 (*C*-NH$_2$). **Ksaltz**: ^{1}H-NMR (300 MHz, d^{6}-DMSO, in ppm, 298 K, Numbering relative to Figure 31): δ = 13.25 (s, br, 1 H, *H1*), 9.35 (s, 1 H, C8-*H*), 7.72 (dd, 1 H, J_1 = 7.98 *Hz*, J_2 = 1.50 *Hz*, C6-*H*), 7.43 (dt, 1 H, J_1 = 7.30 *Hz*, J_2 = 1.62 *Hz*, C4-*H*), 6.98 (m, 2 H, C3-*H* and C5-*H*). ^{13}C-NMR (300 MHz, d^{6}-DMSO, in ppm, 298 K): δ = 166.06 (*C2*), 163.04 (*C8*), 160.97 (*C9*), 133.64 (*C4*), 132.78 (*C6*), 119.98 (*C7*), 119.71 (*C5*), 117.13 (*C3*). MS: m/z = 188 (M^{+}). Anal calcd. for $C_8H_6N_5OK$ (Mol. Wt.: 171.24 g.mol^{-1}): C, 42.28 %; H, 2.66 %; N, 30.82 %. Found: C, 42.92 %; H, 2.73 %; N, 31.14 %. X-ray powder diffraction (°): 13.34 (w), 13.86 (w), 14.80 (m), 15.44 (s), 16.46 (w), 18.52 (s), 18.84 (w), 19.82 (w), 20.68 (w), 22.58 (w), 23.22 (m), 24.26 (m), 25.40 (m), 26.86 (s), 27.80 (s), 28.82 (s), 29.00 (w), 30.48 (w), 31.84 (w), 33.16 (w), 34.7 (w), 36.66 (m), 42.2 (w), 43.68 (m), 45.12 (w), 46.50 (w), 48.42 (w), 49.64 (w), 50.62 (w). Yellow single crystals of good quality were obtained by slow evaporation of a saturated solution in methanol. X-ray diffraction measurements were done at r.t. because of the instability of crystals at low temperature (120 K).

5-chloro-*N*-salicylidene 4-amino-1,2,4-triazole (**Clsaltrz**): 3.05 g of 5-chloro-salicylaldehyde (19.1 mmol, 1 equiv.) dissolved in 50 mL of ethanol was added to 1.62 g of 4-amino-1,2,4-triazole (19.1 mmol, 1 equiv.) dissolved in 50 mL of ethanol. The resulting slightly yellow solution was stirred for 15 min and, afterwards, refluxed for 12 h under dry argon atmosphere. The resulting pale yellow solution was allowed to cool to r.t. to give a powdered compound. The product was filtered, washed with 10 mL of ethanol and dried under vacuum (1.49 g, yield: 35 %). ^{1}H-NMR (300 MHz, d^{6}-DMSO, in ppm, 298 K, Numbering relative to Figure 27): 10.84 (s, 1H, *H14*), 9.22 (s, 2H, C5-*H* and C3-*H*), 9.13 (s, 1H, C7-*H*), 7.80 (d, 1H, J_1 = 2.7

Hz, C13-*H*), 7.47 (dd, 1H, J_1 = 6.12 *Hz* and J_2 = 2.73 *Hz*, C11-*H*), 7.05 (d, 1H, J_1 = 8.85*Hz*, C10-*H*).^{13}C-NMR (300 MHz, d^6-DMSO, in ppm, 298 K): δ = 157.67 (*C9*), 153.46 (*C7*), 139.84 (*C3* and *C5*), 134.02 (*C11*), 126.86 (*C13*), 124.09 (*C8*), 120.73 (*C10*), 119.42 (*C12*). Anal calcd. for $C_9H_7N_4OCl$ (Mol. Wt.: 222.63 g.mol^{-1}): C, 48.55 %; H, 3.17 %; N, 25.17 %. Found: C, 48.62 %; H, 2.97 %; N, 25.09 %. MS: m/z = 223 ($M^{\cdot+}$), 154 (C_7H_5NOCl), 70 ($C_2N_3H_4$). X-ray powder diffraction (°): 11.90 (w), 16.06 (s), 18.70 (s), 21.08 (m), 23.72 (m), 24.64 (m), 26.96 (s), 27.94 (s). FTIR (KBr disk, cm^{-1}): 727 (w), 773 (m), 825 (s), 881 (w), 943 (m), 975 (m), 1089 (m, *C-Cl, C-O*), 1168 (s), 1186 (s, *trz*), 1230 (m), 1267 (s), 1303 (m), 1371 (m), 1400 (w), 1481 (s), 1500 (s), 1518 (s), 1566 (m), 1604 (s, *C=N*), 1666 (w), 3076 (w, br, *OH*).

5-bromo-*N*-salicylidene 4-amino-1,2,4-triazole (**Brsaltrz**): 3.01 g of 5-bromo-salicylaldehyde (14.9 mmol, 1 equiv.) dissolved in 50 mL of ethanol was added to 1.26 g of 4-amino-1,2,4-triazole (14.9 mmol, 1 equiv.) dissolved in 50 mL of ethanol. The resulting slightly yellow solution was stirred for 15 min and, afterwards, refluxed for 12 h under dry argon atmosphere. The resulting pale yellow solution was allowed to cool to r.t. to give a powdered compound. The product was filtered, washed with 10 mL of ethanol and dried under vacuum (1.63 g, yield: 41 %). ^{1}H-NMR (300 MHz, d^6-DMSO, in ppm, 298 K, Numbering relative to Figure 27): 10.84 (s, 1H, *H14*), 9.22 (s, 2H, C5-*H* and C3-*H*), 9.12 (s, 1H, C7-*H*), 7.92 (d, 1H, J_1 = 2.5 *Hz*, C13-*H*), 7.58 (dd, 1H, J_1 = 8.79 *Hz* and J_2 = 2.58 *Hz*, C11-*H*), 6.99 (d, 1H, J_1 = 8.79 *Hz*, C10-*H*).^{13}C-NMR (300 MHz, d^6-DMSO, in ppm, 298 K): δ = 158.06 (*C9*), 153.32 (*C7*), 139.85 (*C3* and *C5*), 136.79 (*C11*), 129.84 (*C13*), 121.32 (*C8*), 119.85 (*C10*), 111.52 (*C12*). Anal calcd. for $C_9H_7N_4OBr$ (Mol. Wt.: 267.08 g.mol^{-1}): C, 40.47 %; H, 2.64 %; N, 20.98 %. Found: C, 40.39 %; H, 2.45 %; N, 20.73 %. MS: m/z = 268 ($M^{\cdot+}$), 136 (C_7H_5NOBr), 70 ($C_2N_3H_4$). X-ray powder diffraction (°): 13.08 (m), 14.76 (w), 16.62 (m), 18.18 (w), 19.1 (w), 19.7 (s), 20.46 (w), 20.94 (w), 20.90 (w), 22.30 (w), 23.96 (m), 23.88 (m), 25.30 (w), 25.64 (w), 26.88 (s), 27.76 (m), 27.72 (m), 29.46 (w), 29.62 (w), 31.00 (w), 33.10 (w), 34.32 (w), 34.80 (w), 37.02 (w), 38.64 (w), 39.98 (w), 40.38 (w), 43.90 (w), 45.28 (m), 48.56 (w). FTIR (KBr disk, cm^{-1}): 729 (w), 765 (w), 829 (m), 854 (w), 918 (w), 943 (m), 985 (w),

1053 (s, *C-O*), 1080 (m, *C-O*, *C-Br*), 1166 (m), 1188 (m, *trz*), 1211 (w), 1269 (s), 1307 (m), 1330 (w), 1367 (m), 1404 (w), 1463.87 (m), 1485 (s), 1494 (s), 1514 (s), 1562 (m), 1608(s, *C=N*).

3-hydroxy-*N*-salicylidene 4-amino-1,2,4-triazole (**3OHsaltrz**): 2 g of 3-hydroxy-salicylaldehyde (14.5 mmol, 1 equiv.) dissolved in 50 mL of ethanol was added to 1.22 g of 4-amino-1,2,4-triazole (14.5 mmol, 1 equiv.) dissolved in 50 mL of ethanol. The resulting slightly yellow suspension was stirred for 15 min and, afterwards, refluxed for 12 h under dry argon atmosphere. The resulting pale yellow solution was allowed to cool to r.t. to give a powdered compound. The product was filtered, washed with 10 mL of ethanol and dried under vacuum (2.26 g, yield: 76 %). ^{1}H-NMR (300 MHz, d^{6}-DMSO, in ppm, 298 K, Numbering relative to Figure 27): 9.20 (m, 5 H, *H14*, OH_{ortho}, C7-*H*, C3-*H* and C5-*H*), 7.28 (dd, 1H, J_1 = 7.92 *Hz* and J_2 = 1.29 *Hz*, C13-*H*), 7.00 (m, 1H, C11-*H*), 6.82 (m, 1H, C10-*H*).^{13}C-NMR (300 MHz, d^{6}-DMSO, in ppm, 298 K): δ = 158.06 (*C9*), 153.32 (*C7*), 139.85 (*C3* and *C5*), 136.79 (*C11*), 129.84 (*C13*), 121.32 (*C8*), 119.85 (*C10*), 111.52 (*C12*). Anal calcd. for $C_9H_8N_4O_2$ (Mol. Wt.: 204.19 g.mol^{-1}): C, 52.94 %; H, 3.95 %; N, 27.44 %. Found: C, 52.95 %; H, 3.82 %; N, 27.34 %. MS: m/z = 205 ($M^{\cdot}$ + H^{+}), 136 ($C_7H_6NO_2$), 70 ($C_2N_3H_4$). X-ray powder diffraction (°): 8.14 (m), 16.14 (s), 19.50 (w), 24.18 (w), 27.20 (w).FTIR (KBr disk, cm^{-1}): 700 (w), 727 (w), 779 (m), 831(m), 885 (w), 960 (w), 995 (m), 1056 (s, *C-O*), 1163 (s, *trz*), 1218 (m), 1249 (s), 1286 (s), 1313 (m), 1363 (m), 1382 (m), 1479 (s), 1517(s), 1579 (m), 1614 (m, *C=N*), 1670 (w), 1758 (w), 1830 (w), 3028 (s, br, *OH*).

4-hydroxy-*N*-salicylidene 4-amino-1,2,4-triazole (**4OHsaltrz**): 5 g of 4-hydroxy-salicylaldehyde (36.2 mmol, 1 equiv.) dissolved in 50 mL of ethanol was added to 3.04 g of 4-amino-1,2,4-triazole (36.2 mmol, 1 equiv.) dissolved in 50 mL of ethanol. The resulting slightly yellow suspension was stirred for 15 min and, afterwards, refluxed for 12 h under dry argon atmosphere. The resulting pale yellow solution was allowed to cool to r.t. to give a powdered compound. The product was filtered, washed with 10 mL of ethanol and dried under vacuum (4.14 g, yield: 56 %). ^{1}H-NMR (300 MHz, d^{6}-DMSO, in ppm, 298 K, Numbering relative to Figure 27): 10.35 (m, 2 H, *H14* and OH_{meta}), 9.11 (s, 2H, C3-*H* and C5-*H*), 9.00 (s, 1H, C7-*H*), 7.64 (m,

1H, C13-*H*), 6.39 (m, 2 H, C10-*H* and C12-*H*).[13]C-NMR (300 MHz, d^6-DMSO, in ppm, 298 K): δ = 163.82 (*C7*), 161.02 (*C11*), 156.41 (*C9*), 139.77 (*C3* and *C5*), 130.60 (*C13*), 110.72 (*C8*), 109.47 (*C12*), 103.38 (*C10*). Anal calcd. for $C_9H_8N_4O_2$ (Mol. Wt.: 204.19 $g.mol^{-1}$): C, 52.94 %; H, 3.95 %; N, 27.44 %. Found: C, 52.39 %; H, 3.83 %; N, 27.80 %. MS: m/z = 205 ($M^{\cdot} + H^+$), 136 ($C_7H_6NO_2$), 70 ($C_2N_3H_4$). X-ray powder diffraction (°): 8.42 (m), 16.88 (s), 17.08 (w), 18.02 (m), 20.32 (w), 20.92 (m), 23.24 (w), 24.00 (w), 24.10 (w), 24.66 (w), 25.54 (m), 26.60 (s), 26.82 (w), 28.26 (w), 31.28 (w), 32.30 (w), 34.30 (w), 36.34 (w), 36.60 (w). FTIR (KBr disk, cm^{-1}): 711 (w), 738 (w), 786 (w), 833 (m), 877 (w), 964 (w), 975 (w), 1004 (w), 1062 (s, *C-O*), 1110 (m), 1172 (m, *trz*), 1191 (s), 1205 (m), 1245 (s), 1265 (s), 1303 (w), 1334 (w), 1392 (w), 1454 (m), 1473 (w), 1521 (m), 1577 (s), 1614 (s, *C=N*), 3112 (s, br, *OH*).

3,4-dihydroxy-*N*-salicylidene 4-amino-1,2,4-triazole (**34OHsaltrz**): 2 g of 3,4-dihydroxy-salicylaldehyde (12.9 mmol, 1 equiv.) dissolved in 50 mL of ethanol was added to 1.09 g of 4-amino-1,2,4-triazole (12.9 mmol, 1 equiv.) dissolved in 50 mL of ethanol. The resulting slightly yellow suspension was stirred for 15 min and, afterwards, refluxed for 12 h under dry argon atmosphere. The resulting pale yellow solution was allowed to cool to r.t. to give a powdered compound. The product was filtered, washed with 10 mL of ethanol and dried under vacuum (2.34 g, yield: 81 %). [1]H-NMR (300 MHz, d^6-DMSO, in ppm, 298 K, Numbering relative to Figure 27): 9.90 (m, 2 H, *H14* and OH_{ortho}), 9.12 (s, 2H, C3-*H* and C5-*H*), 9.01 (s, 1H, C7-*H*), 7.76 (s, 1 H, OH_{meta}), 7.12 (d, 1H, J_1 = 8.64 *Hz*, C13-*H*), 6.51 (m, 1 H, C12-*H*).[13]C-NMR (300 MHz, d^6-DMSO, in ppm, 298 K): δ = 157.96 (*C9*), 151.50 (*C11*), 149.30 (*C7)*, 140.38 (*C3* and *C5*), 133.74 (*C10*), 120.88 (*C13*), 111.31 (*C8*), 109.21 (*C12*). Anal calcd. for $C_9H_8N_4O_3$ (Mol. Wt.: 220.19 $g.mol^{-1}$): C, 49.09 %; H, 3.66 %; N, 25.45 %. Found: C, 49.23 %; H, 3.66 %; N, 24.33 %. MS: m/z = 221 ($M^{\cdot} + H^+$), 152 ($C_7H_6NO_3$), 70 ($C_2N_3H_4$). X-ray powder diffraction (°): 15.12 (s), 16.64 (w), 19.10 (w), 25.14 (w), 26.52 (s), 27.46 (m). FTIR (KBr disk, cm^{-1}): 694 (w), 763 (w), 798 (s), 842 (w), 923 (w), 975 (m), 1018 (w), 1058 (s, *C-O*), 1089 (s), 1166 (w), 1190 (m, *trz*), 1213 (m), 1247 (s), 1284 (m), 1313 (s), 1343 (m), 1367 (s), 1440 (w), 1469 (m), 1506 (s), 1604 (m), 1633 (s, *C=N*), 3143(s, br, *OH*)

3-methoxy-*N*-salicylidene 4-amino-1,2,4-triazole (**omesaltrz**): 5 g of o-vanillin (32.8 mmol, 1 equiv.) dissolved in 50 mL of ethanol was added to 2.76 g of 4-amino-1,2,4-triazole (32.8 mmol, 1 equiv.) dissolved in 50 mL of ethanol. The resulting slightly yellow solution was stirred for 15 min and, afterwards, refluxed for 12 h under dry argon atmosphere. The resulting pale yellow solution was allowed to cool to r.t. to give a powdered compound. The product was filtered, washed with 10 mL of ethanol and dried under vacuum (4.58 g, yield: 64 %). ^{1}H-NMR (300 MHz, d^{6}-DMSO, in ppm, 298 K, Numbering relative to Figure 27): 9.16 (m, 3 H, C3-*H*, C5-*H* and C7-*H*), 7.37 (dd, 1 H, J_1 = 8.00 *Hz*, J_2 = 1.28 *Hz*, C13-*H*), 7.14 (dd, 1 H, C12-*H*), 6.90 (m, 1 H, C11-*H*), 3.84 (s, 3 H, O-CH_3).^{13}C-NMR (300 MHz, d^{6}-DMSO, in ppm, 298 K): δ = 155.37 (*C9*), 148.91 (*C11*), 148.60 (*C7*), 139.65 (*C3* and *C5*), 120.10 (*C13*), 119.37 (*C8*), 119.19 (*C12*), 115.84 (*C10*). Anal calcd. for $C_{10}H_8N_4O_3$ (Mol. Wt.: 218.22 g.mol^{-1}): C, 55.04 %; H, 4.62 %; N, 25.68 %. Found: C, 55.01 %; H, 3.88 %; N, 25.80 %. MS: m/z = 220 ($M^{\cdot}$ + H^{+}), 150 ($C_8H_8NO_2$), 70 ($C_2N_3H_4$). X-ray powder diffraction (°): 6.18 (m), 8.80 (m), 12.50 (s), 13.98 (m), 17.72 (w), 18.82 (w), 19.88 (s), 22.30 (w), 22.34 (w), 22.58 (w), 15.18 (w), 26.02 (m), 28.28 (w), 29.72 (w), 31.68 (w). FTIR (KBr disk, cm^{-1}): 696 (w), 732 (s), 779 (m), 838 (w), 887 (w), 933 (m), 979 (m), 1058 (m, *C-O*), 1076 (s), 1083 (s), 1157 (s), 1188 (w, *trz*), 1220 (s), 1228 (s), 1255 (s), 1288 (s), 1352 (m), 1438 (s), 1481 (s), 1506 (m), 1521 (s), 1581 (m), 1606 (m), 1670 (w, *C=N*), 1764 (w), 1953 (w), 3089 (w, br, *OH*).

1-naphtalene-*N*-salicylidene 4-amino-1,2,4-triazole (**naphsaltrz**): 3 g of 2-hydroxy-1-naphtaldehyde (17.4 mmol, 1 equiv.) dissolved in 50 mL of ethanol was added to 1.47 g of 4-amino-1,2,4-triazole (17.4 mmol, 1 equiv.) dissolved in 50 mL of ethanol. The resulting slightly yellow solution was stirred for 15 min and, afterwards, refluxed for 12 h under dry argon atmosphere. The resulting pale yellow solution was allowed to cool to r.t. to give a powdered compound. The product was filtered, washed with 10 mL of ethanol and dried under vacuum (0.58 g, yield: 14 %). ^{1}H-NMR (300 MHz, d^{6}-DMSO, in ppm, 298 K): 11.39 (s, 1 H, O*H*), 9.70 (s, 1 H, C*H*=N$_{imine}$), 9.33 (s, 2 H, CH_{trz}), 8.89 (d, 1 H, J_1 = 8.49 *Hz*, COH-C-C-C*H*), 8.09 (d, 1 H, J_1 = 9 *Hz*, COH-CH-C*H*), 7.95 (d, 1 H, J_1 = 7.53 *Hz*, COH-CH-CH-C-C*H*),

7.66 (m, 1 H, COH-C-C-CH-C*H*), 7.48 (m, 1 H, COH-C-C-CH-CH-C*H*), 7.32 (d, 1 H, J_1 = 9 *Hz*, COH-C*H*).^{13}C-NMR (300 MHz, d^6-DMSO, in ppm, 298 K): δ = 160.27 (*C*OH), 157.34 (*C*H=N_{imine}), 139.74 (*C*H_{trz}), 136.20 (COH-*C*H-CH), 132.47 (COH-C-*C*), 129.70 (COH-CH-CH-*C*), 129.16 (COH-CH-CH-C-*C*H), 128.81 (COH-C-C-CH-*C*H), 124.76 (COH-CH-CH-C-CH-*C*H), 124.31 (COH-C-C-*C*H), 119.26 (COH-*C*H), 109.24 (COH-*C*). Anal calcd. for $C_{10}H_8N_4O_3$ (Mol. Wt.: 238.25 g.mol^{-1}): C, 65.54 %; H, 4.23 %; N, 23.52 %. Found: C, 64.98 %; H, 4.35 %; N, 23.22 %. MS: m/z = 239 ($M^{\cdot}$ + H^+), 170 ($C_{11}H_8NO$), 70 ($C_2N_3H_4$). X-ray powder diffraction (°): 7.98 (m), 10.06 (s), 12.68 (m), 13.10 (s), 16.08 (m), 18.06 (w), 19.36 (w), 20.04 (w), 20.26 (m), 21.58 (m), 22.16 (s), 24.28 (s), 26.06 (w), 28.76 (m), 30.24 (w), 30.58 (w), 35.26 (w). FTIR (KBr disk, cm^{-1}): 700 (m), 727 (s), 734 (s), 780 (m), 819 (m), 873 (m), 943 (w), 964 (m), 1031 (w), 1058 (s, *C-O*), 1066 (m), 1164 (s), 1178 (s, *trz*), 1240 (s), 1301 (s), 1334 (m), 1411.80 (w), 1463 (s), 1504 (s), 1573 (s), 1620 (s, *C=N*).

Chapter 3

N-salicylidene 2-aminomethylpyridine (**CH_2L^2**): 2-aminomethylpyridine (0.61 mL, 1 equiv., 5.88 mmol) was dissolved in benzene (25 mL) in a 100 mL round-bottom flask with a Dean-Stark setup. Salicylaldehyde (0.62 mL, 1 equiv., 5.88 mmol) was added to the solution. The coloration immediately turned to light yellow. After refluxing for 24 h, the dark yellow solution was concentrated to obtain orange oil. This crude product was triturated in hexane in order to obtain a pure light yellow solid which was filtered (0.40 g, yield: 32 %). ^{1}H-NMR (300 MHz, d^6-DMSO, 298 K, in ppm): 13.41 (s, 1H, O*H*), 8.74 (s, 1H, C7-*H*), 8.55 (d, J_1 = 4.83 *Hz*, 1 H, C12-*H*), 7.80 (m, 1 H, C14-*H*), 7.50 (dd, J_1 = 7.60 *Hz*, J_2 = 1.59 *Hz*, 1 H, C3-*H*), 7.35 (m, 2 H, C15-*H*, C13-*H*, C6-*H*), 6.91 (m, 2 H, C4-*H*, C5-*H*), 4.91 (s, 2 H, C9-*H*). ^{13}C-NMR (300 Mhz, d^6-DMSO, 298 K, in ppm): 167.42 (*C7*), 160.52 (*C2*), 157.78 (*C10*), 149.26 (*C12*), 136.99 (*C14*), 132.50 (*C13*), 131.79 (*C3*), 122.49 (*C6*), 122.09 (*C15*), 118.72 (*C1*), 118.64 (*C4*), 116.47 (*C5*), 63.86 (*C9*). Anal calcd. for $C_{13}H_{12}N_2O$ (Mol. Wt.: 212.25 g.mol^{-1}): C, 73.57; N, 13.20; H, 5.70. Found: C, 72.97; N, 11.44; H, 5.45. FTIR (KBr, cm^{-1}): 3057 (m, br, *OH*), 2867 (m) 1630 (s, *C=N*), 1589 (m), 1491 (m), 1474 (m), 1458

(m), 1435 (m), 1389 (w), 1335 (w), 1279 (m), 1259 (w), 1220 (w), 1151 (w), 1116 (w), 1099 (w), 1047 (m), 1007 (w), 893 (w), 839 (w), 802 (m), 754 (s). Single crystals were obtained in hexane by solvent evaporation.

N-salicylidene 3-aminomethylpyridine (**CH_2L^3**): 3-aminomethylpyridine (2.40 mL, 1 equiv., 23.56 mmol) was dissolved in benzene (100 mL) in a 250 mL round-bottom flask with a Dean-Stark setup. Salicylaldehyde (2.48 mL, 1 equiv., 23.56 mmol) was added to the solution giving rise to an immediate coloration change to yellow. After refluxing the mixture for 24 h, the dark yellow solution was evaporated to give a crude solid which was triturated in hexane in order to obtain pure **CH_2L^3** (4.99 g, yield: 99 %). ^{1}H-NMR (300 MHz, d^6-DMSO, 298 K, in ppm, Numbering following cif files avalaible in Ref. [204]): 13.22 (s, 1 H, O*H*), 8.76 (s, 1 H, C7-*H*), 8.60 (d, J_1 = 1.90 *Hz*, 1 H, C11-*H*), 8.51 (dd, J_1 = 4.8 *Hz*, J_2 = 1.6 *Hz*, 1 H, C10-*H*), 7.76 (d, J_1 = 7.9 *Hz*, 1 H, C12-*H*), 7.49 (dd, J_1 = 7.65 *Hz*, J_2 = 1.68 *Hz*, 1 H, C12-*H*), 7.42 (dd, 1 H, J_1 = 6.36 *Hz*, J_2 = 0.48 *Hz*, C5-*H*), 7.35 (m, 2H, C3-*H* and C13-*H*), 6.92 (m, 2H, C2-*H* and C4-*H*), 4.85 (s, 2 H, C8-*H*). ^{13}C-NMR (300 Mhz, d^6-DMSO, 298 K, in ppm): 168.36 (*C7*), 161.56 (*C4*), 150.34 (*C11*), 149.78 (*C10*), 136.84 (*C12*), 135.52 (*C1*), 133.79 (*C3*), 133.06 (*C5*), 124.97 (*C13*), 120.01 (*C9*), 119.93 (*C6*), 117.68 (*C2*), 60.67 (*C8*). Anal calcd. for $C_{13}H_{12}N_2O$ (Mol. Wt.: 212.25 g.mol^{-1}): C, 73.57; N, 13.20; H, 5.70. Found: C, 73.12; N, 12.87; H, 5.59. X-ray powder diffraction (°): 9.66 (m), 15.18 (w), 17.92 (m), 19.34 (m), 19.70 (m), 20.50 (m), 21.18 (w), 21.62 (m), 23.86 (s), 27.42 (m), 32.98 (m). FTIR (KBr, cm^{-1}): 3030 (w, br, *OH*), 2891 (w), 1630 (s, *C=N*), 1575 (m), 1491 (m), 1458 (m), 1421 (m), 1400 (m), 1350 (w), 1317 (w), 1275 (m), 1213 (w), 1198 (w), 1147 (w), 1113 (w), 1057 (m, *C-O*), 1028 (m), 993 (m), 970 (w), 924 (w), 876 (m), 856 (m), 795 (m), 770 (s), 712 (m). Single crystals were obtained in hexane by solvent evaporation. An X-ray investigation has revealed the same cell parameters as those in ref.[204].

N-salicylidene 4-aminomethylpyridine (**CH_2L^4**): 4-aminomethylpyridine (2.38 mL, 1 equiv., 23.56 mmol) was dissolved in benzene (100 mL) in a 250 mL round bottom flask with a Dean-Stark setup. Salicylaldehyde (2.48 mL, 1 equiv., 23.56 mmol) was added in the mixture which has immediately turned to yellow. After refluxing for 24 h, the solution was concentrated

leading to a yellow solid which was triturated in hexane in order to obtain pure **CH_2L^4** (4.90 g, yield: 98 %). ^{1}H-NMR (300 MHz, d^6-DMSO, 298 K, in ppm): 13.20 (s, 1H, O*H*), 8.73 (s, 1 H, N=C*H*), 8.56 (dd, J_1 = 4.41 *Hz*, J_2 = 1.62 *Hz*, 2 H, N-CH_2-C-CH-C*H*), 7.49 (m, 1 H, N=CH-C-C*H*), 7.35 (m, 3 H, HO-C-CH-C*H* and N-CH_2-C-CH-C*H*), 6.93 (m, 2 H, HO-C-C*H* and HO-C-CH-CH-C*H*), 4.91 (s, 2 H, N-CH_2). ^{13}C-NMR (300 Mhz, d^6-DMSO, 298 K, in ppm): 167.75 (N=*C*H), 160.31 (HO-*C*), 149.83 (N-CH_2-C-CH-*C*H), 147.59 (HO-C-*C*), 132.66 (N-CH_2-C-*C*H), 131.86 (N=CH-C-*C*H), 122.67 (HO-C-CH-*C*H), 118.84 (HO-C-CH-CH-*C*H), 118.69 (N-CH_2-*C*), 116.47 (HO-C-*C*H), 60.68 (N-*C*H_2). MS: m/z = 213 (M + H^+), 196 ($C_{13}H_{10}N_2$). Anal calcd. for $C_{13}H_{12}N_2O$ (Mol. Wt.: 212.25 g.mol^{-1}): C, 73.57; N, 13.20; H, 5.70. Found: C, 72.57; N, 11.02; H, 5.70. FTIR (KBr, cm^{-1}): 3049 (m, br, *OH*), 2868 (m), 2725 (m, l), 1630 (s), 1602 (s, C=N), 1580 (m), 1489 (m), 1458 (s), 1413 (m), 1389 (w), 1279 (m), 1250 (m), 1219 (w), 1151 (w, *C-O*), 1116 (w), 1065 (w), 1034 (m), 1009 (w), 800 (m), 754 (s).

5-chloro-*N*-salicylidene 3-aminomethylpyridine (**CH_2L^5**): 3-aminomethylpyridine (2.40 mL, 1 equiv., 23.56 mmol) was dissolved in benzene (70 mL) in a 250 mL round bottom flask with a Dean-Stark setup. 5-chloro-salicylaldehyde (3.69 g, 1 equiv., 23.56 mmol) was added in the mixture which has immediately turned to dark yellow. After refluxing for 24 h, the solution was concentrated leading to a dark crude oil which was triturated in hexane in order to obtain pure **CH_2L^5** (5.44 g, yield: 93 %). ^{1}H-NMR (300 MHz, d^6-DMSO, 298 K, in ppm, Numbering following Figure 46): 8.76 (s, 1 H, C8-*H*), 8.59 (d, J_1 = 1.80 *Hz*, 1 H, C13-*H*), 8.51 (dd, J_1 = 4.80 *Hz*, J_2 = 1.60 *Hz*, 1 H, C11-*H*), 7.76 (dt, J_1 = 7.83 *Hz*, J_2 = 1.83 *Hz*, 1 H, C14-*H*), 7.61 (d, J_1 = 2.67 *Hz*, 1 H, C6-*H*), 7.40 (m, 2 H, C15-*H*, C4-*H*), 6.92 (d, J_1 = 8.85 *Hz*, 1 H, C3-*H*), 4.85 (s, 2 H, C9-*H*). ^{13}C-NMR (300 Mhz, d^6-DMSO, 298 K, in ppm): 165.67 (*C7*), 159.12 (*C5*), 149.13 (*C13*), 148.59 (*C11*), 135.66 (*C14*), 134.04 (*C2*), 132.15 (*C4*), 130.56 (*C6*), 123.72 (*C15*), 121.01 (*C1*), 119.84 (*C10*), 118.48 (*C3*), 61.58 (*C9*). Anal calcd. for $C_{13}H_{12}N_2O$ (Mol. Wt.: 212.25 g.mol^{-1}): C, 63.29; N, 11.36; H, 4.43. Found: C, 63.29; N, 11.49; H, 4.43. X-ray powder diffraction (°): 6.6 (s), 13.12 (w), 16.14 (m), 16.84 (w), 19.62 (m), 20.5 (m), 20.84 (w), 21.62 (s), 24.00 (s), 24.10 (m), 25.02 (m), 25.46 (m), 25.74 (m), 26.12 (s), 28.16 (m), 29.16 (m),

30.08 (m), 30.16 (m), 30.54 (w), 32.26 (m), 35.64 (w), 36.46 (w), 39.56 (w), 41.84 (w), 44.34 (w), 45.04 (w), 48.20 (w), 49.48 (w). FTIR (KBr, cm^{-1}): 3057 (w, br, *OH*), 2995 (w), 2914 (w), 2850 (w), 1633 (s, *C=N*), 1576 (m), 1558 (w), 1448 (w), 1450 (m), 1416 (m), 1394 (w), 1369 (m), 1338 (m), 1308 (w), 1277 (s), 1232 (w), 1203 (w), 1184 (m), 1107 (m), 1092 (w), 1036 (m), 1022 (s), 955 (w), 910 (w), 891 (w), 833 (w), 820 (s), 802 (m), 777 (w), 716 (m), 710 (s). Single crystals were obtained in hexane by slow solvent evaporation.

5-chloro-*N*-salicylidene 4-aminomethylpyridine (**CH_2L^6**): 4-Aminomethylpyridine (2.38 mL, 1 equiv., 23.56 mmol) was dissolved in benzene (70 mL) in a 250 mL round bottom flask with a Dean-Stark setup. 5-chloro-salicylaldehyde (3.69 g, 1 equiv., 23.56 mmol) was added in the mixture which has immediately turned to yellow. After refluxing for 24 h, the solution was concentrated giving crude orange oil which was triturated in hexane in order to obtain a pure **CH_2L^6** (5.48 g, yield: 94 %). ^{1}H-NMR (300 MHz, d^6-DMSO, 298 K, in ppm): 13.11 (s, 1 H, O*H*), 8.73 (s, 1 H, N=C*H*), 8.56 (m, 2 H, N-CH_2-C-CH-C*H*), 7.63 (d, J_1 = 3 *Hz*, 1 H, N=CH-C-C*H*), 7.36 (m, 3 H, N-CH_2-C-C*H* and HO-C-CH-C*H*), 6.95 (d, J_1 = 8.85 *Hz*, 1 H, HO-C-C*H*), 4.85 (s, 2 H, N-CH_2). ^{13}C-NMR (300 Mhz, d^6-DMSO, 298 K, in ppm): 167.22 (N=*C*H), 160.05 (HO-*C*), 150.79 (N-CH_2-C-CH-*C*H), 147.30 (HO-C-*C*), 133.21 (N-CH_2-C-*C*H), 131.50 (N=CH-C-*C*H), 123.64 (HO-C-CH-*C*H), 121.79 (Cl-*C*), 120.86 (N-CH_2-*C*), 119.49 (HO-C-*C*H), 61.58 (N-*C*H_2). MS: m/z = 247 (M - H^+), 230 ($C_{13}H_9N_2Cl$), 210 ($C_{13}H_{10}N_2O$). Anal calcd. for $C_{13}H_{12}N_2O$ (Mol. Wt.: 212.25 $g.mol^{-1}$): C, 63.29; N, 11.36; H, 4.43. Found: C, 63.81; N, 12.15; H, 4.70. X-ray powder diffraction (°) 6.74 (w), 16.06 (m), 16.78 (w), 19.60 (m), 20.60 (w), 21.60 (w), 21.64 (s), 23.98 (m), 25.10 (m), 25.22 (m), 26.16 (m), 26.22 (m), 28.18 (w), 29.14 (m), 30.08 (m), 30.16 (m), 30.24 (w), 32.36 (m), 35.64 (w), 39.62 (w), 41.96 (w), 44.34 (w), 44.44 (m), 46.74 (w), 49.48 (w). FTIR (KBr, cm^{-1}): 3069 (w, br, *OH*), 2922 (w), 2899 (w), 2856 (w), 1633 (s, *C=N*), 1597 (m), 1575 (w), 1560 (m), 1481 (s), 1450 (m), 1416 (m), 1389 (m), 1367 (m), 1337 (m), 1327 (w), 1308 (w), 1277 (s), 1219 (m), 1182 (m), 1117 (w), 1092 (m), 1068 (w), 1032 (m), 991 (m), 960 (m), 889 (w), 827 (m), 808 (m), 777 (w), 706 (m).

Chapter 9

4-(2'-hydroxy-ethyl)-1,2,4-triazole (**hyetrz**) was synthesized following Ref. [413]. Ethylformate (76.5 mL, 1 mol, 1 equiv.) was mixed with 200 mL of methanol. Hydrazine monohydrate (49 mL, 1.2 mol, 1.2 equiv.) was then added to the mixture before refluxing 1 h. The solution was concentrated to 1/3 of its initial volume and allowed to cool to r.t. Large pink crystals were formed after few hours, filtered, washed with few mL of methanol and dried under vacuum to give 18.26 g of monoformylhydrazine (yield: 30 %). This product (18.26 g, 0.30 mol, 1 equiv.) and triethylformate (61 mL, 0.36 mol, 1.2 equiv.) was dissolved in 400 mL of methanol. The mixture was refluxing for 2 h before adding 18.5 mL of ethanolamine (0.30 mol, 1 quiv.). After refluxing 4 h, the solution was evaporated under vacuum at 70°C to give a crude yellow oil which was kept at -10°C for 12 h. The resulting yellow solid is then washed 6 times with 100 mL of acetone at -10°C to give pure white powder of hyetrz (26.67 g, yield: 78 %). ^{1}H-NMR (300 MHz, d^{6}-DMSO, in ppm, 298 K): 3.68 (t, J_1 = 5.4 *Hz*, 2 H, N-CH_2), 4.09 (t, J_1 = 5.3 *Hz*, 2 H, CH_2-OH), 5.12 (s, br, 1 H, O*H*), 8.49 (s, 2 H, N*H*).^{13}C-NMR (300 MHz, d^{6}-DMSO, in ppm, 298 K): δ = 47.94 (*C*H_2-OH), 61.02 (*C*H-N), 144.33 (*C*H_{trz}).

Inorganic molecules

Synthetic shemes

$M^{II}Cl_2 \cdot xH_2O + 2NH_4NCS + 2L^3 \xrightarrow{\text{crystallisation}} C^{1\text{-}5}$

$Fe^{II}Cl_2 \cdot 4H_2O + 2NH_4NCS + 2L^3 \xrightarrow[\text{Ascorbic acid}]{\text{precipitation}} C^6$

$Fe^{II}Cl_2 \cdot 4H_2O + 2NH_4NCS + 2.5Hsaltrz \xrightarrow[\text{Ascorbic acid}]{\text{Schlenk, } CH_3OH_{dry}} C^7$

$Fe^{II}(NH_4)(SO_4)_2 + 2NH_4NCS + 2Hsaltrz \xrightarrow[\text{Ascorbic acid}]{CH_3OH} C^8$

$Fe^{II}Cl_2 \cdot 4H_2O + 2NH_4NCS + 2Hsaltrz \xrightarrow[\text{Ascorbic acid}]{CH_3OH} C^9$

$Co^{II}SO_4 + 2NH_4NCS + 2Hsaltrz \xrightarrow{CH_3OH,\ H_2O} C^{10}$

$Fe^{II}Cl_2 \cdot 4H_2O + 2NH_4NCS + 2Habs \xrightarrow{C_2H_5OH} C^{11}$

$M^{II}X_2 \cdot xH_2O + 3Habs \xrightarrow{C_2H_5OH,\ \triangle} C^{12\text{-}16}$

$Ni^{II}Cl_2 + 2NH_4NCS + 4CH_2L^3 \xrightarrow{CH_3OH} C^{19}$

$4Cu^{II}(NO_3)_2 \cdot 3H_2O + 4L^2 +$ 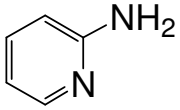 $\xrightarrow[(C_2H_5)_2O_{diffusion}]{CH_3OH} C^{17}$

$5Cu^{II}(NO_3)_2 \cdot 3H_2O + 5L^2 +$ 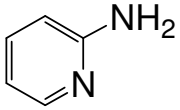 $\xrightarrow[(C_2H_5)_2O_{diffusion}]{CH_3OH} C^{18}$

Chapter 5

$[Co(\mathbf{L^3})_2(NCS)_2(CH_3OH)_2]$ ($\mathbf{C^1}$): $CoCl_2 \bullet 6H_2O$ (0.09 g, 0.4 mmol, 1 equiv) and NH_4NCS (0.06 g, 0.8 mmol, 2 equiv) were each dissolved in 5 mL of methanol. The clear solution of NH_4NCS was added to the red cobalt(II) solution to give a pink solution. The resulting solution was slowly added to a

yellow solution of $\mathbf{L^3}$ (0.15 g, 0.8 mmol, 2 equiv., dissolved in 10 mL of methanol) to give a clear red solution which was kept in dark. After seven days, red needles of X-ray diffraction quality were obtained. All analyses carried out with $\mathbf{C^{7\text{-}6}}$ were done on crystals in order to avoid purity problem.

$[Co(\mathbf{L^3})_2(NCSe)_2(CH_3OH)_2]$ ($\mathbf{C^2}$): 0.09 g of $CoCl_2 \bullet 6H_2O$ (0.4 mmol, 1 equiv) and 0.11 g of KNCSe (0.8 mmol, 2 equiv) were each dissolved in 5 mL of methanol and 0.15 g of $\mathbf{L^3}$ (0.8 mmol, 2 equiv) was dissolved in 10 mL of methanol. The clear solution of KNCSe was added to the red solution of cobalt to give a pink solution. The resulting mixture was slowly added to the yellow solution of $\mathbf{L^3}$ to give a clear red solution. It was placed in a controlled atmosphere container, equilibrated with diethyl ether vapours and covered to avoid exposure to light. After 7 days, ether diffusion provided red needles.

$[Mn(\mathbf{L^3})_2(NCS)_2(CH_3OH)_2]$ ($\mathbf{C^3}$): 0.05 g of $MnCl_2 \bullet 4H_2O$ (0.4 mmol, 1 equiv) and 0.06 g of NH_4NCS (0.8 mmol, 2 equiv) were each dissolved in 5 mL of methanol and 0.15 g of $\mathbf{L^3}$ (0.8 mmol, 2 equiv) was dissolved in 10 mL of methanol. The solution of NH_4NCS was added to the manganese solution to give a colourless mixture which was slowly added to $\mathbf{L^3}$ to afford a clear yellow solution. This methanol solution containing the targeted compound was placed in dark. After slow solvent evaporation during six months, few black single crystals.

$[Ni(\mathbf{L^3})_2(NCS)_2(CH_3OH)_2]$ ($\mathbf{C^4}$): 0.09 g of $NiCl_2$ (0.4 mmol, 1 equiv) and 0.06 g of NH_4NCS (0.8 mmol, 2 equiv) were each dissolved in 5 mL of methanol, mixed and added to 0.15 g of $\mathbf{L^3}$ (0.8 mmol, 2 equiv) dissolved in 10 mL of methanol. Pale green needles were obtained from this green solution after keeping for seven days in darkness.

$[Cu(\mathbf{L^3})_2(NCS)_2(CH_3OH)_2]$ ($\mathbf{C^5}$): 0.06 g of $CuCl_2 \bullet 2H_2O$ (0.4 mmol, 1 equiv) and 0.06 g of NH_4NCS (0.8 mmol, 2 equiv) were each dissolved in 5 mL of methanol and 0.15 g of $\mathbf{L^3}$ (0.8 mmol, 2 equiv) was dissolved in 10 mL of methanol. The colourless solution of NH_4NCS was added to the green copper solution. The resulting mixture was heated to ~ 70°C and slowly added to $\mathbf{L^3}$ to give a green solution with a green precipitate, which was filtered. After cooling to r.t., small single crystals were obtained as a result

of immediate nucleation. These crystals were allowed to grow during 6 months in darkness, within the methanol mother solution.

$[Fe(\mathbf{L^3})_2(NCS)_2(CH_3OH)_2]$ ($\mathbf{C^6}$): 0.01 g of $FeCl_2 \cdot 4H_2O$ (0.5 mmol, 1 equiv) with a pinch of ascorbic acid (to avoid iron oxidation) was dissolved in 5 mL of methanol. 0.08 g of NH_4NCS (1 mmol, 2 equiv) was also dissolved in 1 mL of the same solvent. The iron solution was added under stirring to NH_4NCS to form a clear solution. Then, 0.20 g of $\mathbf{L^3}$ (1 mmol, 2 equiv) in 2 mL of methanol was added leading to a red solution which was kept under stirring for 10 minutes. A dark precipitate, was obtained, filtered, washed with 2 mL of methanol and dried under vacuum (0.30 g, yield: 93.5 %). Anal. calcd for $FeC_{28}H_{28}N_6S_2O_4$ (Mol. wt. : 632.55 $g.mol^{-1}$): Fe: 8.83 %, C: 53.17 %, H: 4.46 %, N: 13.29 %. Found: Fe: 8.96 %, C: 53.42 %, H: 5.52 %, N: 12.93 %. With TGA, we have observed a mass loss of 11 % between 83°C (onset point) and 130°C which corresponds to the loss of the two coordinated methanol molecules (calcd. loss: 10 %), FTIR (KBr disk, cm^{-1}): 3294 (br, m, *OH*), 2079 (s), 1618 (s, *C=N*), 1568 (m), 1475 (w), 1427 (w), 1388 (w), 1286 (m), 1202 (m), 1180 (m),1153 (m, *C-O*), 1030 (w), 1005 (m), 910 (m), 860 (w), 827 (w), 804 (w), 768 (m), 700 (m), 642 (w), 579 (w), 553 (w), 449 (w), 480 (w). X-ray powder diffraction (°): 6.1 (w), 12.0 (s), 13.0 (s), 17.4 (w), 19.0 (s), 21.9 (m), 23.3 (m), 24.1 (m), 25.9 (s), 26.6 (s), 26.9 (s), 27.9 (w), 29.7 (w).

Chapter 6

$[Fe^{II}_2(\mathbf{Hsaltrz})_5(NCS)_4] \cdot 4\ CH_3OH$ ($\mathbf{C^7}$): The synthesis was made under Schlenck conditions allowing a strict control of the moisture presence. **Hsaltrz** (0.25 g, 1.3 mmol, 2.5 equiv.), NH_4NCS (0.081 g, 1.1 mmol, 2 equiv.) and $Fe^{II}Cl_2 \cdot 4H_2O$ (0.106 g, 0.5 mmol, 1 equiv.) with a pinch of ascorbic acid were kept under vacuum in 3 different flasks during 4 h. Methanol was mixed with molecular sieves and degassed by bubbling dried argon during 3 h. The reactants were dissolved in 5, 5 and 10 mL of hot methanol, respectively. The NH_4NCS solution was slowly added to the iron solution. The mixture was then added, drop wise, to the **Hsaltrz** solution to give a yellow suspension which was filtered after 30 min. The resulting clear

solution was then kept during 5 days under dried argon to give large yellow crystals (0.159 g, yield: 22 %). All analyses were done on fresh samples because of the strongly marked degradation of the compound in air atmosphere (see optical properties described in the text). Elementary analysis calcd (%) for $[Fe^{II}_2(\mathbf{Hsaltrz})_5(NCS)_4]\bullet 3CH_3OH\bullet 2H_2O$: $C_{52}H_{56}N_{24}O_{10}S_4Fe_2$ (Mr = 1417.13 g.mol^{-1}): C 44.07, H 3.98, N 23.72 ; found: C 43.62, H 3.48, N 24.24. Elementary analysis clearly demonstrated the lost of methanol guest molecules with time as suggested in the optical properties section in the text. Moreover, **C^7** appears to be hygroscopic as shown by the presence of water molecules. FTIR (KBr, cm^{-1}): 434 (w), 428 (w), 511 (w), 548 (m), 555 (m), 606 (s), 623 (s, *trz*), 764 (s), 804 (m), 860 (m), 883 (w), 810 (m), 972 (m), 986 (m), 1014 (m), 1059 (s, *C-O*), 1117 (w), 1151 (m), 1173 (m), 1200 (s), 1217 (m, *trz coordinated*), 1240 (m), 1269 (s), 1313 (m), 1327 (m), 1392 (m), 1456 (m), 1472 (m), 1485 (s), 1522 (s), 1573 (s), 1618 (s, *C=N*), 2077 (s, *NCS*), 3097 (s, br, *OH*), 3240 (s, br, *OH*), 3429 (s, br, *OH*).

$[Fe^{II}_2(\mathbf{Hsaltrz})_5(NCS)_4]\bullet 3H_2O\bullet CH_3OH$ (**C^8**): 0.39 g of $Fe^{II}(NH_4)_2(SO_4)_2$ (1 mmol, 1 equiv.) with a pinch of ascorbic acid was dissolved in 5 mL of methanol. The resulting solution was added to 0.152 g of NH_4NCS (2 mmol, 2 equiv.) dissolved in 3 mL of methanol. The mixture was stirred for few minutes and then added to a clear solution of 0.376 g of **Hsaltrz** (2 mmol, 2 equiv.) in 15 mL of hot methanol. After 10 minutes, the yellow solution was filtered and kept at room temperature for 1 day to give yellow crystals of diffractable quality (0.288 g, yield = 21 %). Elementary analysis calcd (%) $C_{50}H_{50}N_{24}O_9S_4Fe_2$ (Mr = 1371.06 g.mol^{-1}): C 43.80, H 3.68, N 24.52. Found: C 43.48, H 3.67, N 24.43. FTIR (KBr, cm^{-1}): 556 (w), 607 (m), 622 (m, *trz*), 768 (w), 806 (w), 1064 (s, *C-O*), 1150 (w), 1199 (m), 1271 (m), 1331 (w), 1478 (w), 1525 (m), 1574 (w), 1619 (s, *C=N*), 2066 (s, *NCS*), 3101 (w), 3444 (w, br, *OH*).

$[Fe^{II}_2(\mathbf{Hsaltrz})_5(NCS)_4]\bullet 4H_2O$ (**C^9**): To a solution of 0.07 g of NH_4NCS (1 mmol, 2 equiv.) in 4 mL of methanol, a pinch of ascorbic acid and 0.1 g of $Fe^{II}Cl_2\cdot 4H_2O$ (0.5 mmol, 1 equiv.) was successively added to give a clear solution after few minutes of stirring at 70°C. The mixture was then added to 0.19g of **Hsaltrz** (1 mmol, 2 equiv.) in 5 mL of methanol. The flash was

purged with nitrogen and kept closed during 3 days to give yellow crystals (0.07 g, yield: 26%). Elementary analysis calcd (%) for **C^{9}**•H_2O: $C_{49}H_{50}N_{24}O_{10}S_4Fe_2$ (Mr = 1375.05 g.mol^{-1}): C 42.80, H 3.66, N 24.45. Found: C 42.42, H 3.06, N 24.37. Compound **C^{9}** appears to be hygroscopic as shown by the presence of 5 water molecules in the elementary analysis. FTIR (KBr, cm^{-1}): 552 (w), 604(m), 620 (s, *trz*), 766 (m), 802 (m), 855 (w), 907(w), 968 (w), 1063 (s, *C-O*), 1151 (m), 1175 (m), 1199 (m), 1217 (m, *trz coordinated*), 1241 (m), 1270 (s), 1304 (m), 1372 (w), 1478 (m), 1525 (s), 1573 (m), 1607 (s), 1619 (s, *C=N*), 2066 (s, *NCS*), 3099 (m, br, *OH*), 3231 (m, br, *OH*), 3446 (m, br, *OH*).

[Co^{II}_2(**Hsaltrz**)$_5$($NCS)_4$]•$4H_2O$ (**C^{10}**): 0.281 g of $Co^{II}SO_4$ (1 mmol, 1 equiv.) was dissolved in a mixture of 10 mL of methanol and 5 mL of distillate water. 0.152 g of NH_4NCS (2 mmol, 2 equiv.), dissolved in 5 mL of methanol, was added to the previous solution. The mixture was then added to a solution of 0.376 g of **Hsaltrz** (2 mmol, 2 equiv.) in 10 mL of methanol to give an orange suspension which was filtered. The resulting clear red solution was kept at room temperature during 6 months to give a few orange crystals of diffractable quality.

Chapter 7

[Fe^{II}(**Habs**)$_2$($NCS)_2$]·$4H_2O$ (**C^{11}**): **Habs** (0.3 g, 0.88 mmol, 2 equiv.) was dissolved in 30 mL of ethanol at 60°C. $FeCl_2$·$4H_2O$ (0.09 g, 0.44 mmol, 1 equiv.) with a pinch of ascorbic acid, in 5 mL of ethanol was slowly added to a solution of NH_4NCS (0.07 g, 0.88 mmol, 2 equiv., in 5 mL of ethanol) to give a colourless solution. The mixture was transferred, drop by drop, to the **Habs** solution. A colour change to red was immediately observed demonstrating the coordination of **Habs** to the metal ions. The solution was stirred for 36 h in order to give a pink precipitate which was filtered, washed with 5 mL of ethanol and dried in air (0.24 g, yield: 59 %). Elementary analysis calcd (%) for **C^{11}**: $C_{40}H_{36}N_{14}S_2O_6Fe$ (Mr = 928.79 g.mol^{-1}): C, 51.73; H, 3.91; N, 21.11; S, 6.90. Found: C, 51.89; H, 3.25; N, 22.01; S, 6.16. FTIR (KBr, cm^{-1}): 417 (m), 482 (w), 598 (w), 638 (w), 700 (s), 744 (s), 789 (s), 837 (w), 891 (w), 986 (w), 1012 (m), 1049 (m), 1092 (m), 1151 (m,

C-O), 1256 (s), 1298 (w), 1348 (m), 1427 (m), 1448 (s), 1475 (s), 1570 (m), 1585 (m), 1603 (s, *C=N*), 2058 (s, *NCS*), 3099 (m, br, *OH*). X-ray powder diffraction (°): 6.88 (s), 7.38 (s), 9.56 (w), 10.98 (m), 12.26 (m), 14.02 (m), 15.00 (m), 16.84 (m), 17.40 (m), 17.54 (w), 19.52 (m), 20.94 (m), 22.04 (m), 22.54 (m), 24.50 (m), 25.98 (s). ^{57}Fe Mössbauer parameters at (a) 113K. δ^{HS1}: 1.09 (1) mm.s^{-1}, $\Delta E_Q{}^{HS1}$: 3.69 (1) mm.s^{-1}, $\Gamma^{HS1}/2$: 0.10 (3) mm.s^{-1}, RAF^{HS1} (Relative Area Fraction): 15 (1) %; δ^{HS2}: 1.09 (1) mm.s^{-1}, $\Delta E_Q{}^{HS2}$: 3.96 (1) mm.s^{-1}, $\Gamma^{HS2}/2$: 0.12 (2) mm.s^{-1}, RAF^{HS2}: 24 (1) %; δ^{HS3}: 1.11 (1) mm.s^{-1}, $\Delta E_Q{}^{HS3}$: 3.30 (2) mm.s^{-1}, $\Gamma^{HS3}/2$: 0.16 (1) mm.s^{-1}, RAF^{HS3}: 40 %; δ^{BS}: 0.495 (2) mm.s^{-1}, $\Delta E_Q{}^{BS}$: 0.40 (4) mm.s^{-1}, $\Gamma^{BS}/2$: 0.14 (2) mm.s^{-1}, RAF^{BS}: 13 (2) %; $\delta^{Fe(III)}$: 0.02 (1) mm.s^{-1}, $\Delta E_Q{}^{FeIII}$: 0.82 (8) mm.s^{-1}, $\Gamma^{FeIII}/2$: 0.18 (8) mm.s^{-1}, RAF^{FeIII}: 8 (3) %. (b) 193 K. δ^{HS1}: 1.00 (1) mm.s^{-1}, $\Delta E_Q{}^{HS1}$: 3.48 (1) mm.s^{-1}, $\Gamma^{HS1}/2$: 0.14 (1) mm.s^{-1}, RAF^{HS1} (Relative Area Fraction): 30 (4) %; δ^{HS2}: 1.00 (1) mm.s^{-1}, $\Delta E_Q{}^{HS2}$: 3.87 (8) mm.s^{-1}, $\Gamma^{HS2}/2$: 0.14 (4) mm.s^{-1}, RAF^{HS2}: 29 (2) %; δ^{HS3}: 1.00 (1) mm.s^{-1}, $\Delta E_Q{}^{HS3}$: 3.09 (9) mm.s^{-1}, $\Gamma^{HS3}/2$: 0.13 (6) mm.s^{-1}, RAF^{HS3}: 19 (2) %; RAF^{BS}: 0 %; $\delta^{Fe(III)}$: 0.03 (4) mm.s^{-1}, $\Delta E_Q{}^{FeIII}$: 0.71 (6) mm.s^{-1}, $\Gamma^{FeIII}/2$: 0.23 (5) mm.s^{-1}, RAF^{FeIII}: 22 (3) %. ^{57}Fe Mössbauer spectra are complicated and the origin of the signals is unknown and thus difficult to fit with accuracy. Nevertheless, the SCO phenomenon is clearly observed by the quenching of the LS site.

$[Fe^{II}(\mathbf{Habs})_2Cl_2]\cdot 1.5H_2O$ (**C^{12}**): $Fe^{II}Cl_2\cdot 4H_2O$ (0.5 g, 0.24 mmol, 1 equiv.) with a pinch of ascorbic acid, in 5 mL of ethanol was slowly added to a solution of **Habs** (0.25 g, 0.73 mmol, 3 equiv.) in 30 mL of ethanol at 60°C. The resulting red solution was refluxing for 4 days affording the slow formation of a yellow precipitate which was filtered, washed with few mL of ethanol and dried in air (0.16 g, yield: 77 %). Elementary analysis calcd (%) for **C^{12}**: $C_{38}H_{31}N_{12}O_{3.5}Cl_2Fe$ (Mr = 838.49 g.mol^{-1}): C, 54.43; H, 3.73; N, 20.05; Fe, 6.66. Found: C, 55.10; H, 4.5; N, 18.68; Fe, 6.85. Small deviations in elementary analyses should come from the small amount of $[Fe^{II}(\mathbf{Habs})_3]$ impurities detected in ^{57}Fe Mössbauer spectra, as described in the text. FTIR (KBr, cm^{-1}):424 (w), 480 (m), 500 (m), 615 (m), 615 (m), 638 (m), 692 (m), 708 (s), 731 (m), 752 (s), 781 (m), 795 (s), 841 (w), 878 (m), 893 (m), 989 (m), 1012 (s), 1038 (s), 1066 (w), 1094 (m), 1138 (w), 1155 (s, *C-O*), 1190 (w), 1230 (m), 1259 (s), 1269 (s), 1294 (m), 1312 (s), 1356 (s),

1375 (w), 1427 (m), 1452 (s), 1497 (s), 1514 (w), 1537 (w), 1580 (s), 1603 (s, *C=N*), 2978 (s, br, *OH*). X-ray powder diffraction (°): 8.44 (m), 9.52 (w), 10.26 (s), 12.08 (w), 12.98 (m), 13.54 (w), 14.48 (m), 15.04 (m), 15.98 (w), 16.88 (m), 17.24 (s), 19.78 (w), 20.60 (w), 21.24 (s), 21.8 (m), 22.36 (m), 24.04 (m), 2.12 (m), 25.06 (w), 26.16 (w), 30.26 (w).

$[Zn^{II}(\mathbf{Habs})_2F_2]$ (**C[13]**): $Zn^{II}F_2$ (0.025 g, 0.24 mmol, 1 equiv.) was suspended in 5 mL of hot ethanol. The mixture was slowly added to a solution of **Habs** (0.25 g, 0.73 mmol, 3 equiv.) in 30 mL of ethanol at 60°C. The resulting yellow solution was refluxing for 3 days affording the slow formation of a strong yellow precipitate which was filtered, washed with few mL of ethanol and dried in air (0.12 g, yield: 63 %). Elementary analysis calcd (%) for **C[13]**: $C_{38}H_{28}N_{12}O_2F_2Zn$ (Mr = 788.10 g.mol^{-1}): C, 57.91; H, 3.58; N, 21.33. Found: C, 58.37; H, 3.34; N, 21.57. FTIR (KBr, cm^{-1}): 447 (w), 521 (m), 677 (x), 706 (w), 756 (m), 781 (w), 814 (w), 808 (w), 1045 (s), 1059 (s, br), 1120 (m), 1142 (m), 1151 (m, *C-O*), 1182 (m), 1282 (m), 1317 (w), 1352 (w), 1375 (w), 1383 (w), 1420 (w), 1446 (m), 1466 (m), 1531 (m), 1570 (s), 1616 (s, *C=N*), 3061 (m, br, *OH*). MS and NMR experiments did not give relevant result because of the strong insolubility of the complex. X-ray powder diffraction (°): 9.22 (s), 9.40 (w), 11.58 (m), 12.42 (m), 13.88 (w), 15.28 (w), 15.92 (w), 16.30 (m), 18.30 (w), 18.42 (w), 18.86 (w), 20.88 (m), 22.44 (m), 23.10 (w), 23.96 (m), 24.78 (w), 25.26 (m), 26.86 (w), 27.50 (w), 28.60 (w), 28.98 (w), 30.76 (w), 34.48 (w), 34.5 (w).

$[Zn^{II}(\mathbf{Habs})_2Cl_2]\cdot 12\ H_2O$ (**C[14]**): $Zn^{II}Cl_2$ (0.034 g, 0.24 mmol, 1 equiv.) was dissolved in 10 mL of hot ethanol. The mixture was slowly added to a solution of **Habs** (0.25 g, 0.73 mmol, 3 equiv.) in 30 mL of ethanol at 60°C. The resulting yellow solution was refluxing for 24 h affording the formation of a white precipitate which was filtered, washed with few mL of ethanol and dried in air (0.09 g, yield: 38 %). Elementary analysis calcd (%) for **C[14]**: $C_{38}H_{52}N_{12}O_{14}Cl_2Zn$ (Mr = 1037.19 g.mol^{-1}): C, 44.00; H, 5.05; N, 16.21. Found: C, 43.52; H, 5.77; N, 16.63. FTIR (KBr, cm^{-1}): 698 (s), 746 (s), 770 (m), 791 (s), 837 (w), 899 (w), 987 (m), 1012 (s), 1041 (m), 1053 (m), 1090 (m), 1151 (m, *C-O*), 1169 (m), 1227 (m), 1261 (s), 1299 (m), 1315 (m), 1342 (m), 1386 (w), 1396 (w), 1429 (s), 1452 (s), 1487 (m), 1608 (s, *C=N*), 3211 (m, br, *OH*). MS: 785 ($M^{\cdot+}$ – Cl^- + H^+), 747 (M – 2 Cl^- – 1H^+), 575

([$Zn^{II}(abpt)_2Cl$] – H^+), 374 (M -2 Cl^-), 343 (Habs) and 239 (abpt). ^{1}H-NMR (500 MHz, CD_3OD, in ppm, 298 K): 10.05 (s, 1 H), 9.08 (s, 1 H, C*H*=N), 8.95 (d, J_1 = 4.6 *Hz*, 2 H), 8.81 (m, 2 H), 8.68 (d, J_1 = 7.65 *Hz*, 2 H), 8.36 (d, J_1 = 7.5 *Hz*, 2 H), 8.21 (m, 2 H), 8.16 (m, 2 H), 7.94 (d, J_1 = 7.70 *Hz*, 1 H), 7.75 (m, 2 H), 7.68 (m, 1 H), 7.51 (m, 1 H), 7.04 (m, 1 H), 6.97 (d, J_1 = 8.3 *Hz*, 1 H). X-ray powder diffraction (°): 6.28 (s), 9.86 (m), 10.86 (m), 11.12 (m), 12.38 (m), 13.82 (m), 14.08 (m), 15.66 (m), 17.78 (m), 19.42 (m), 22.28 (m), 27.78 (s).

[Zn^{II}(**Habs**)$_2Br_2$]·12 H_2O (**C^{15}**): $Zn^{II}Br_2$ (0.06 g, 0.24 mmol, 1 equiv.) was dissolved in 5 mL of hot ethanol. The mixture was slowly added to a solution of **Habs** (0.25 g, 0.73 mmol, 3 equiv.) in 30 mL of ethanol at 60°C. The resulting yellow solution was refluxing for 1 days affording the formation of a white precipitate which was filtered, washed with few mL of ethanol and dried in air (0.08 g, yield: 63 %). Elementary analysis calcd (%) for **C^{15}**: $C_{38}H_{52}N_{12}O_{14}Br_2Zn$ (Mr = 1126.10 g.mol^{-1}): C, 40.53; H, 4.65; N, 14.93; Br, 14.19. Found: C, 38.31; H, 2.58; N, 20.47; Br, 15.42. MS: 751 (M – 2 Br^- + H^+). ^{1}H-NMR (500 MHz, CD_3OD, in ppm, 298 K): 9.16 (s, 1 H, C*H*=N), 8.97 (d, J_1 = 4.4 *Hz*,4 H), 8.84 (m, 2 H), 8.74 (d, J_1 = 7.1 *Hz*, 4 H), 8.40 (d, J_1 = 7.7 *Hz*, 2 H), 8.22 (m, 4 H), 8.19 (m, 2 H), 8.01 (d, J_1 = 7.6 *Hz*, 1 H), 7.78 (m, 4 H), 7.72 (m, 2 H), 7.52 (m, 1 H), 7.05 (m, 1 H), 6.97 (d, J_1 = 8.4 *Hz*, 1 H). X-ray powder diffraction (°): 9.22 (s), 9.40 (w), 11.58 (m), 12.42 (m), 13.88 (w), 15.28 (w), 15.92 (w), 16.30 (m), 18.30 (w), 18.42 (w), 18.86 (w), 20.88 (m), 22.44 (m), 23.10 (w), 23.96 (m), 24.78 (w), 25.26 (m), 26.86 (w), 27.50 (w), 28.60 (w), 28.98 (w), 30.76 (w), 34.48 (w), 34.5 (w).

[Zn^{II}(**Habs**)$_2I_2$]·2 H_2O (**C^{16}**): $Zn^{II}I_2$ (0.08 g, 0.24 mmol, 1 equiv.) was dissolved in 5 mL of hot ethanol. The mixture was slowly added to a solution of **Habs** (0.25 g, 0.73 mmol, 3 equiv.) in 30 mL of ethanol at 60°C. The resulting yellow solution was refluxing for 1 days affording the formation of a white precipitate which was filtered, washed with few mL of ethanol and dried in air (0.13 g, yield: 50 %). Elementary analysis calcd (%) for **C^{16}**: $C_{38}H_{32}N_{12}O_4I_2Zn$ (Mr = 1039.95 g.mol^{-1}): C, 43.89; H, 3.10; N, 16.16. Found: C, 37.93; H, 2.55; N, 20.26. MS: 1081 (M + 2 K^+ - H^+), 875 (M - I - 2 H), 747 (M - 2 I), 343 (Habs), 239 (abpt). FTIR (KBr, cm^{-1}): 652 (m), 696 (s), 748 (s), 795 (s), 986 (m), 1012 (s), 1040 (s), 1053 (s, *C-O*),

1076 (w), 1095 (m), 1151 (m), 1258 (m), 1288 (w), 1298 (m), 1338 (w), 1400 (w), 1429 (s), 1450 (s), 1458 (s), 1495 (s), 1517 (w), 1572 (m), 1589 (s), 1605 (s, *C=N*), 1624 (w), 3051 (m, br, *OH*). X-ray powder diffraction (°): 11.46 (w), 12.36 (w), 21.64 (w), 26.20 (m), 33.72 (w).

Chapter 8

$[Cu^{II}_4(\mathbf{L}\text{-}^{\mathbf{2}})_4(NO_3)_3(CH_3OH)][Cu^{II}(\mathbf{L}\text{-}^{\mathbf{2}})(NO_3)_2]$(2-aminopyridinium)$(NO_3)$•5 CH_3OH ($\mathbf{C^{17}}$): A solution of $Cu(NO_3)_2$•$3H_2O$ (0.37 g, 1.51 mmol, 4 equiv.) dissolved in methanol (5 mL) was slowly added to a solution of $\mathbf{L^2}$ (0.3 g, 1.51 mmol, 4 equiv.) dissolved in hot methanol (10 mL). 2-aminopyridine (0.04 g, 0.4 mmol, 1 equiv.) dissolved in methanol (5 mL) was then added to the mixture to give a dark green solution which was kept in darkness and under a diethyl ether saturated atmosphere over few weeks. A crystalline sample, constituted by a large number of green crystalline blocks, was obtained (0.16 g, 0.08 mmol, 21 %). It was essential to control the ether diffusion rate to obtain large single crystals. Elemental analysis calcd (%) for $[Cu^{II}_4(\mathbf{L}\text{-}^{\mathbf{2}})_4(NO_3)_3(CH_3OH)][Cu^{II}(\mathbf{L}\text{-}^{\mathbf{2}})(NO_3)_2]$ (2-aminopyridinium) (NO_3)• CH_3OH• $6H_2O$: $C_{67}H_{77}N_{18}O_{31}Cu_5$ (Mr = 1948.18 g mol^{-1}): C, 41.31; H, 3.98; N, 12.94. Found: C, 40.93; H, 3.05; N, 12.55. This analysis reveals that four non coordinated methanol molecules have been replaced by six water molecules, provided the samples are stored in air. Indeed, a perfect match was obtained between TGA and X-ray analyses when fresh crystals were quickly transferred from the mother solution to the thermogravimetric analyser. TGA weight lost at onset temperatures: 25°C, -1.1%, -1 CH_3OH; 122°C, -3.8%, -2 CH_3OH; 130°C, -2.7%, -3 CH_3OH; Degradation temperature: 218(1)°C. FTIR (KBr, cm^{-1}): 3366 (l, s, *NH_2*), 1763 (w), 1666 (m), 1601 (s, *C=N*), 1568 (m), 1545 (s), 1481 (m), 1470 (s), 1435 (s), 1385 (s, *NO_3*), 1306 (m), 1290 (s), 1267 (m), 1200 (s), 1155 (m, *C-O*), 1128 (w), 1065 (w), 1036 (w), 1022 (w), 989 (w), 933 (w), 864 (m), 825 (w, *NO_3*), 806 (m), 783 (w), 762 (m), 741 (w), 675 (w), 646 (w), 627 (w), 598 (w), 555 (m), 538 (w), 521 (w), 465 (w).

$[Cu^{II}_4(\mathbf{L}\text{-}^{\mathbf{2}})_4(NO_3)_2(OH)_2]$(2-aminopyridinium)(OH)•$CH_3OH$ ($\mathbf{C^{18}}$): A solution of $Cu(NO_3)_2$•$3H_2O$ (0.37 g, 1.51 mmol, 5 equiv.) dissolved in

methanol (5 mL) was slowly added to a solution of **L²** (0.3 g, 1.51 mmol, 5 equiv.) dissolved in hot methanol (10 mL). 2-aminopyridine (0.03 g, 0.3 mmol, 1 equiv.) dissolved in methanol (5 mL) was then added to the mixture to give a dark green solution which was kept in darkness and under a diethylether saturated atmosphere over few weeks. A single crystal of **C[18]** was isolated on the glassware and rapidly taken out from the mother solution to be measured by X-ray diffraction. The presence of free hydroxide and 2-aminopyridinium groups in the structure is proposed because such molecules are consistent with the composition of **C[17]** but the possibility to have free water and 2-aminopyridine cannot be excluded.

$[Ni^{II}_2(\mathbf{CH_2L^3})_4(NCS)_2(CH_3OH)_2]\bullet 2CH_3OH$ (**C[19]**): $NiCl_2$ (0.056 g, 0.24 mmol, 1 equiv.) was dissolved in methanol (5 mL) and added to a solution of NH_4NCS (0.036 g, 0.47 mmol, 2 equiv.) dissolved in methanol (5 mL). The resulting blue-green solution was then added to $\mathbf{CH_2L^3}$ (0.2 g, 0.94 mmol, 4 equiv.) dissolved in methanol (7 mL). A yellow precipitate (17 mg of crude product) was filtered and the resulting clear green solution was kept over one month in darkness. **C[19]** (0.08 g, 0.07 mmol, 58 %) was obtained as green single crystals. Elemental analysis calcd (%) for $[Ni_2(\mathbf{CH_2L^3})_4(NCS)_2(CH_3OH)_2]\bullet 2CH_3OH\bullet H_2O$: $C_{56}H_{56}N_{10}O_7S_2Ni_2$ (Mr = 1162.64 g mol^{-1}): C, 57.85; H, 4.85; N, 12.05; S, 5.52. Found: C, 57.50; H, 4.55; N, 12.22; S, 5.61. TGA weight lost at onset temperatures: 46°C, -4.2%, -1.5 CH_3OH; 69°C, -6.3%, - 2.3 CH_3OH; Degradation temperature: 169(1)°C. FTIR (KBr, cm^{-1}): 3055 (w, br, *OH*), 2080 (s, *NCS*), 1624 (s, *C=N*), 1533 (w), 1479 (w), 1468 (m), 1452 (m), 1429 (m), 1400 (w), 1348 (w), 1329 (w), 1279 (w), 1215 (w), 1190 (m), 1126 (w), 1117 (w), 1036 (w), 984 (w), 903 (w), 841 (w), 806 (w), 756 (m), 706 (m).

Hybrid materials

Synthetic schemes

$$2Na1 + M^{II}Cl_2 \cdot xH_2O + 3\ phen \xrightarrow[\text{crystallisation}]{CH_3OH} H^1, H^2$$

$$2Na2 + Cu^{II}SO_4 \cdot 5H_2O + 3\ phen \xrightarrow[\text{crystallisation}]{CH_3OH} H^3$$

$$2Na2 + Ni^{II}Cl_2 + 3\ phen \xrightarrow[\text{crystallisation}]{CH_3OH} H^4$$

$$FeCl_2 \cdot 4H_2O + 2Na1 \text{ or } 2Na1Br + 3\ hyetrz \xrightarrow{\text{Schlenk, } CH_3OH} H^5 \text{ or } H^6$$

where phen = 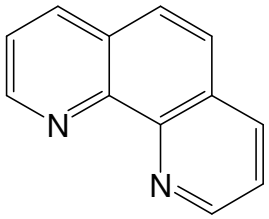

Chapter 9

$[Cu^{II}(phen)_3](\mathbf{1})Cl{\bullet}5H_2O{\bullet}2CH_3CH_2OH$ (**H^1**). **Na1** (0.2 g, 0.7 mmol, 2 equiv.) was dissolved in technical grade methanol (20 mL) at 80°C to give a yellow solution. $CuCl_2 \cdot 2H_2O$ (0.06 g, 0.4 mmol, 1 equiv.), dissolved in 5 mL of methanol, was added drop by drop to **Na1** (0.3 mmol, 1 equiv.) to give a clear brown solution. 1,10-phenantholine (0.18 g, 1 mmol, 3 equiv.) was dissolved in methanol (5 mL) and then added to the mixture to give a clear green solution. The mixture was allowed to slowly evaporate in the darkness during 15 days. A few green single crystals of good quality were formed and freshly taken out from the mother solution for X-ray diffraction analysis.

$[Ni^{II}(phen)_3](\mathbf{1})Cl{\bullet}7H_2O{\bullet}CH_3OH$ (**H^2**). **Na1** (0.2 g, 0.7 mmol, 2 equiv.) was dissolved in technical grade methanol (20 mL) at 80°C to give a yellow solution. $NiCl_2$ (0.08 g, 0.3 mmol, 1 equiv.), dissolved in methanol (5 mL), was added drop by drop to **Na1** to give a clear green solution. 1,10-phenantholine (0.18 g, 1 mmol, 3 equiv.) was dissolved in methanol (5 mL)

and then added to the mixture to give a clear orange solution. The mixture was allowed to slowly evaporate in the darkness during 10 days. A few orange/red single crystals of good quality were formed and freshly taken out from the mother solution for X-ray diffraction analysis.

$[Cu^{II}(phen)_3](\mathbf{2})_2$ ($\mathbf{H^3}$): **Na2** (0.2 g, 0.7 mmol, 2 equiv.) was dissolved in hot methanol (60 mL) to give a yellow solution. $CuSO_4 \bullet 5H_2O$ (0.06 g, 0.5 mmol, 1 equiv.) dissolved in methanol (5 mL) was added drop wise to **Na2** to give a clear brown solution. 1,10-phenantholine (0.18 g, 1 mmol, 3 equiv.) was dissolved in methanol (5 mL) and then added to the mixture to give a clear green solution. The mixture was allowed to slowly evaporate in darkness during 15 days. Green crystals of good quality were formed and freshly taken out from the mother solution for analyses. Elemental analysis calcd (%) for $C_{62}H_{44}CuN_8O_8S_2 \cdot H_2O$ (Mr = 1174.77 g.mol^{-1}): C, 63.39; H, 3.95; N, 9.54. Found: C, 63.12; H, 3.68; N, 9.43. Degradation temperature by TGA/DTA: 309(1) °C. FTIR (KBr disk, cm^{-1}): 418 (w), 500 (w), 523 (m), 542 (w), 559 (w), 617 (s), 658 (m), 685 (m), 719 (s), 750 (m), 781 (m), 795 (m), 854 (s), 864 (m), 914 (m), 957 (w), 995 (m), 1032 (s), 1082 (m), 1103 (s), 1146 (s), 1209 (s, br, *SO$_3$*), 1278 (s), 1342 (w), 1358 (w), 1421 (m), 1454 (m), 1470 (s), 1470 (s), 1516 (s), 1568 (s), 1587 (s), 1616 (s, *C=N*), 3053 (w, br, *OH*).

$[Ni^{II}(phen)_3](\mathbf{2})_2$ ($\mathbf{H^4}$): **Na2** (0.15 g, 0.5 mmol, 2 equiv.) was dissolved in hot methanol (50 mL) at 80°C to give a yellow solution. $NiCl_2$ (0.06 g, 0.25 mmol, 1 equiv.), dissolved in 5 mL of methanol was added drop by drop to 1 to give a clear orange solution. 1,10-phenantholine (0.14 g, 0.8 mmol, 3 equiv.) was dissolved in 5 mL of methanol and then added to the mixture to give a red solution. The mixture was allowed to slowly evaporate in the darkness during 15 days. Orange crystals of good quality were formed and freshly taken out from the mother solution for analyses (0.21 g, yield = 22 %). Elemental analysis calcd (%) for $C_{62}H_{44}NiN_8O_8S_2$ (Mr = 1151.89 g.mol^{-1}): C, 64.65; H, 3.85; N, 9.73. Found: C, 64.52; H, 3.81; N, 9.73. FTIR (KBr disk, cm^{-1}): 422 (w), 442 (w), 507 (w), 523 (m), 542 (m), 559 (w), 573 (w), 617 (s), 644 (w), 658 (w), 687 (m), 723 (s), 752 (m), 781 (w), 795 (w), 841 (w), 854 (s), 866 (m), 914 (m), 966 (w), 995 (m), 1032 (s), 1092 (w), 1105 (s), 1134 (m), 1145 (s), 1211 (s, *SO$_3$*), 1281 (m), 1344 (w), 1360 (w), 1396

(m), 1420 (s), 1431 (s), 1454 (m), 1470 (m), 1493 (m), 1518 (s), 1568 (s), 1587 (m), 1616 (m, *C=N*), 3053 (w), 3433 (w, br, *OH*). Degradation temperature by TGA-TDA: 370 (1) °C.

$[Fe^{II}_3(hyetrz)_6(H_2O)_6](\mathbf{1})_4Cl_2$ (**H^5**) was synthesised using Schlenk techniques. Under nitrogen atmosphere, $Fe^{II}Cl_2 \cdot 4\ H_2O$ (0.12 g, 1 equiv., 0.6 mmol) was dissolved in 2 mL of degassed methanol and then added to 11 mL of a solution of **Na1** (0.35 g, 2 equiv., 1.2 mmol) dissolved in degassed methanol. The resulting solution was added to 2 mL of a solution of 4-(2'-hydroxyethyl)-1,2,4-triazole (0.20 g, 3 equiv., 1.8 mmol) in degassed methanol. A beige powder (0.18 g, yield: 33 %) was filtered, washed with 2 mL of degassed methanol and dried under a vacuum line. Elemental analysis calcd (%) for $Fe_3C_{76}H_{94}N_{22}S_4O_{28}Cl_2$ (Mr = 2130.42 g.mol^{-1}): C, 42.85; H, 4.45; N, 14.46; S, 6.02; Cl, 3.33. Found: C, 45.57; H, 4.34; N, 16.43; S, 6.24; Cl, 3.35. The error present in elemental analysis is however significant and could come from the presence of a small amount of iron (III) impurity as shown in the Mössbauer analyses or to the presence of a more statistical ratio of **1**/Cl anions. X-ray powder diffraction (°): 3.66 (s), 6.62 (w), 7.34 (m), 8.10 (w), 9.62 (w), 11.02 (w), 13.74 (w), 13.54 (w), 19.6 (m), 22.3 (w), 27.68 (w). FTIR (KBr disk, cm^{-1}): 552 (w), 575 (m), 586 (w), 644 (s, *trz*), 667 (w), 719 (m), 754 (m), 850 (m), 1005 (m), 1030 (s), 1071 (m), 1092 (w), 1122 (s), 1190 (s, *SO_3*), 1207 (s, *trz*), 1281 (w), 1398 (w), 1456 (w), 1489 (w), 1556 (m), 1574 (m), 1593 (w), 1624 (m, *C=N*), 3011 (w), 3076 (m), 3385 (s, br, *OH*).

$[Fe^{II}_3(hyetrz)_6(H_2O)_6](\mathbf{1Br})_4Cl_2$ (**H^6**) was synthesised using the Schlenk techniques. Under nitrogen atmosphere, $Fe^{II}Cl_2 \cdot 4\ H_2O$ (0.08 g, 1 equiv., 0.4 mmol) was dissolved in 2 mL of degassed methanol and then added to 11 mL of a solution of **Na1Br** (0.30 g, 2 equiv., 0.8 mmol) in degassed methanol. The resulting solution was added to 2 mL of a solution of 4-(2'-hydroxyethyl)-1,2,4-triazole (0.14 g, 3 equiv., 1.2 mmol) in degassed methanol. A beige powder (0.05 g, 5 %) was filtered, washed with 2 mL of degassed methanol and dried under a vacuum line. Elemental analysis calcd (%) for $Fe_3C_{76}H_{90}N_{22}S_4O_{28}Br_4Cl_2$ (Mr = 2446.00 g.mol^{-1}): C, 37.32; H, 3.71; N, 12.60; S, 5.24. Found: C, 39.90; H, 3.54; N, 13.23; S, 5.03. The error present in elemental analysis is however significant and could come from the

presence of a small amount of iron (III) impurity as shown in the Mössbauer analyses or to the presence of a more statistical ratio of **1Br/**Cl anions. X-ray powder diffraction (°): 3.68 (w), 6.00 (w), 7.30 (w), 8.1(w), 9.48 (w), 13.72 (w), 19.30 (w), 19.54 (w), 22.16 (w), 27.38 (w). FTIR (KBr disk, cm^{-1}): 554 (w), 575 (w), 627 (m, *trz*), 660 (s), 735 (w), 825 (w), 862 (w), 916 (w), 1007 (s), 1032 (s), 1072 (m), 1092 (w), 1122 (s), 1180(s, SO_3), 1215 (s, *trz*), 1277 (m), 1350(w), 1400 (w), 1475 (m), 1558 (m), 1589 (w), 1618 (m, *C*=*N*), 3107 (m), 3389 (m, br, *OH*). Although $\mathbf{H^6}$ is less crystalline than $\mathbf{H^5}$, the compounds are isostructural as shown by similar X-ray powder diffraction patterns.